Measurements and Modeling of Deposition Rates from Near-Supercritical, Aqueous, Sodium Sulfate and Potassium Sulfate Solutions to a Heated Cylinder

by

Marc S. Hodes

B.S.M.E., University of Pittsburgh (1990)
M.S.M.E., University of Minnesota (1994)

Submitted to the Department of Mechanical Engineering in Partial Fulfillment of the Requirements for the Degree of
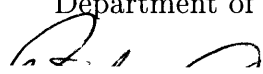
DOCTOR OF PHILOSOPHY IN MECHANICAL ENGINEERING AT THE MASSACHUSETTS INSTITUTE OF TECHNOLOGY

September 1998

Signature of Author...
Department of Mechanical Engineering
July 14th, 1998
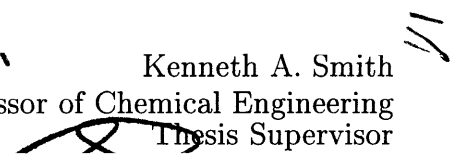
Certified by.. .
Peter Griffith
Professor of Mechanical Engineering
Thesis Supervisor

Certified by..
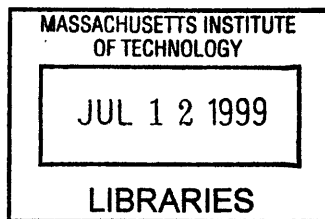Kenneth A. Smith
Edwin R. Gilliland Professor of Chemical Engineering
Thesis Supervisor

Accepted by...
Ain A. Sonin
Professor of Mechanical Engineering
Chairman, Committee for Graduate Students

Measurements and Modeling of Deposition Rates from Near-Supercritical, Aqueous, Sodium Sulfate and Potassium Sulfate Solutions to a Heated Cylinder

by

Marc S. Hodes

Submitted to the Department of Mechanical Engineering
on July 14th, 1998 in Partial Fulfillment of the
Requirements for the Degree of Doctor of Philosophy
in Mechanical Engineering

ABSTRACT

In the Supercritical Water Oxidation (SCWO) process, a technology emerging for the disposal of hazardous organic wastes, organic compounds containing heteroatoms such as S, Cl and P are oxidized to the corresponding acid. In order to reduce corrosion, bases are therefore often injected into the reactor. The salts that are formed upon neutralization (sulfates, chlorides, phosphates, etc.) have low solubility in supercritical water (SCW) and consequently precipitate as solid phases. These salts can form agglomerates and coat internal surfaces, leading to plugging of transport lines and inhibition of heat transfer. The purpose of this dissertation is to develop an understanding of salt deposition kinetics and nucleation phenomena at conditions relevant to SCWO.

Solubility and deposition experiments were performed with aqueous sodium sulfate and aqueous potassium sulfate solutions at elevated temperatures and pressures typical of the SCWO process. For both the solubility and deposition experiments, the test cell is a six-port chamber which was fabricated by modifying a 1.91 cm (3/4 inch) diameter Swagelok cross. One port was used to mount a 0.200 inch (5.08 mm) diameter internally heated cylinder into the center of the chamber and the remaining ports provided fluid cross flow, visual observation capability and instrumentation access. Aqueous salt solutions containing up to 10 wt% salt were pumped at about 250 bar through preheaters that brought the solution to a temperature close to that at which precipitation occurs. Inside the test cell, the heated cylinder raised the temperature of the nearby solution above this precipitation temperature, thus limiting deposition almost exclusively to the heated cylinder. Experimental deposition rate data from sodium sulfate- and potassium sulfate-containing SCW streams to the heated cylinder were obtained by removing the heated cylinder from the cell following each run and measuring the mass of salt deposited on it. The deposition rate data were obtained as a function of time and concentration of salt in the solution entering the test cell. Salt concentration and time in the deposition experiments were varied between 2 and 8 wt% and 6 and 12 minutes respectively. In the solubility experiments, the solubility temperature of sodium sulfate and potassium sulfate in water at a pressure of 250 bar was measured for salt concentrations up to 10 wt%. Natural convection dominates transport at all of the conditions investigated in the solubility and deposition rate experiments.

The equations governing the transport of salt to the interface that develops between the salt layer which forms on the heated cylinder/hot finger and the solution in the adjoining boundary layer are developed in a fairly rigorous context. Then, the equations governing transport are scaled to determine a set of criteria which, when satisfied or partially satisfied, allows various terms, e.g., those accounting for the Sorét effect and Dufour effect in the species and energy conservation equations respectively, to be neglected or simplified. All of the criteria are evaluated for the conditions in the deposition experiments, justifying a relatively simple set of ordinary differential equations which govern the deposition rate of salt at the salt layer-solution interface. The simplified model is numerically solved to predict the rate of transport of salt to the salt layer-solution interface for all the conditions investigated in the deposition experiments as a function of time. The theoretical deposition rate predictions are then compared to the deposition rate data in the context of a sensitivity analysis. For the deposition experiments in which the sodium sulfate and potassium sulfate concentrations in the solution entering the test cell were 4 wt% or less, the theory and data compare well. In

fact most, but not all, of the experimental data for these experiments fall within the bounds predicted by a sensitivity analysis accounting for uncertainties in thermophysical properties and experimentally measured variables input into the theoretical deposition rate formulation. For higher salt concentrations, however, the model underpredicts the experimental data by up to a factor of about two. It is shown that, as the concentration of salt in the solution entering the test cell increases, deposition of salt within the porous salt layer formed on the hot finger is likely to become more significant. Thus it is hypothesized that the theory and deposition data do not compare as well at higher salt concentrations because the predictive model accounts for deposition at the salt layer-solution interface, but not deposition within the porous salt layer.

In the model developed for the deposition rate of salt at the salt layer-solution interface it is assumed that salt nucleation occurs exclusively at the salt layer-solution interface, i.e., there is no homogeneous nucleation of salt in the boundary layer. This assumption is validated, to some extent, by visual observations during the experiments. Additionally, a major chapter of this dissertation is devoted to nucleation modeling. A model to predict whether or not homogeneous nucleation and/or supersaturation will occur in the boundary layer formed around the salt layer-solution interface is developed. It predicts that homogeneous nucleation and/or supersaturation are unlikely, if not impossible, at the conditions investigated in the deposition experiments. This justifies the formulation used to solve for the rate of mass transfer at the salt layer-solution interface a posteriori.

Thesis Supervisors: Peter Griffith
                        Professor of Mechanical Engineering

                        Kenneth A. Smith
                        Edwin R. Gilliland Professor of Chemical Engineering

ACKNOWLEDGMENTS

SCWO. He continually kept very much abreast of the research we were performing and provided fruitful input during many discussions. Finally, I would like to thank Ms. Maria Aquino-Class for performing x-ray diffraction analyses of various salt samples given to her by me.

I'd also like to acknowledge all of the other members of the SCWO research team here at MIT. Matt DiPippo continuously attempted to explain various thermodynamic principles to me, despite the fact that many of them remain beyond my comprehension. I look forward to reading his upcoming book entitled "Ken Smith: The Unauthorized Biography." I am also grateful to Phil Marrone for many informative discussions about SCWO, a bemusing discussion about the United Stated judiciary system and some fun trips. I thank Joanna Dinaro as well. Joanna was the first person to successfully explain the concept of SCWO to me despite the efforts of numerous others. Joanna also coordinated numerous group activities including trips to Maine for lobster and Vermont for skiing. However, I still don't understand why Joanna insists on personally selecting the restaurant at which "Group Tester" will celebrate my graduation. I would also like to acknowledge Brian Phenix. I enjoyed discussing chemical kinetics, heat transfer and various Richard Rhodes works with him. I also appreciate the fact that his moderate skiing skills enabled me to ski with somebody in the group who would also not have a good chance at making the US Olympic team. Jason Cline provided a resource where all of my UNIX questions could be competently answered and a partner with whom to occasionally attend arcane physics seminars. I'd further like to acknowledge Randy Weinstein. Although Randy was not truly a part of the SCWO group at MIT since he worked exclusively on supercritical carbon dioxide, I enjoyed having him around the laboratory. I further wish to acknowledge all the remaining members of the MIT SCWO group including Mike Kutney, Josh Taylor, Matt Reagan Dr. William Peters, Howard Herzog, Frederic Vogel and Stephan Pilz. Finally, I acknowledge Professor Jefferson W. Tester himself. Jeff was not my advisor, but made me feel very welcome in the SCWO group at MIT led by him.

There are also many individuals I wish to thank in the Department of Mechanical Engineering. Back when I arrived at MIT in 1993, Kevin Wasson and I were cohorts on a number of homework problems in a course we completed on generalized engineering aka Advanced Heat Transfer. Kevin and I also enjoyed many good times outside of MIT at the cost of a pumpkin. "Mean" Shereen Eletribi was nice company in the Warren M. Rohsenow Heat Transfer Laboratory. SăngjunE Hân provided nice company in our office some of the time. Leslie Regan, Joan Kravitz and Mellisa Gillis in the Mechanical Engineering Department Graduate Office were continual sources of camaraderie and personal support. Professor Ain Sonin showed genuine concern at a critical stage of my studies. Finally, Dr. Wayne Bidstrup was a wonderful office mate and friend. I further acknowledge the agencies which sponsored the work contained in my dissertation. These included the United States Army Research Office (ARO) through Bob Shaw and the ARO-University Research Initiative program, NIST and NSF.

Some other individuals also must be acknowledged. Eric Chivian provided truly invaluable and desperately needed advice with genuine concern over a three year period. Professor Steven Rogak of the University of British Columbia and I exchanged a number of fruitful emails and publications relevant to salt deposition kinetics in SCWO. Bonnie Caputo, Loretta May and John O'Brien of the MIT Energy Laboratory and Elaine Aufiero of the Chemical Engineering Department were very helpful to me at various stages. The following individuals provided me with respites from work: Pete Wyckoff, Ted Ogata, Steve Borsellino, Joachim Hadeler, Craig Aamlie, Mark Caputo, Craig Darden, Ari Kaplan (Not only did I write this, but I also spelled your name correctly!), R.J. Nelson, Matt Sutin and Kelly Dodge. Other individuals who should not go unmentioned include Jerry Rice (obviously), Victor Hugo, Mr. Steven Tyler, Michael Jordan, John Grisham, Ken Follet, Terrell Owens and Phil Rizzuto to name but a few. My compliments are passed to two, but only two, chefs, namely Bob Kinkead of Kinkeads in Washington D.C. and Gray Kunz of Lespinasse in New York city. Incidentally, it is noted that neither one of these restaurants are within 200 miles of the city of Boston. I would like to acknowledge the developers of UNIX, LATEXand gnuplot for providing far better alternatives to such appalling trash as Windows 95, Microsoft Word and Cricket Graph respectively. At the bottom of the list I would like to thank Todd Kaplan, my twin brother of sorts. To all those who are conspicuously absent it was on purpose and I vow to continue to harbor my spite. I'm only happy when it rains.

<u>DEDICATION</u>

This dissertation is dedicated to the late James A. Michener, 1907-1997. Although I never had the privilege of meeting this distinguished writer, he shall remain my foremost role model and my cherished friend.

Contents

List of Figures

13

15

19

20

List of Tables

24

Nomenclature

Symbol	Description
a	activity [dimensionless]
A	area [m^2]
$A1 - A11$	arbitrary dimensionless parameters [dimensionless]
$A\left(Le, Pr, \tilde{N}\right)$	$Nu_x Le^{\frac{1}{3}}/Sh_x$ [dimensionless]
A_P	annular fin parameter [m^2]
Bi	Biot number [dimensionless]
Br	Brinkman number [dimensionless]
c	concentration in molality units [moles of solute/kg of solvent]
c	total molar concentration $\left[\frac{gmoles}{m^3}\right]$
C	concentration [$wt\%$]
$\overline{C}_{eff}$	average salt concentration in the effluent [wt%]
C_{in}	salt concentration in the inlet stream [$wt\%$]
C_{out}	salt concentration in the stream exiting the test cell [$wt\%$]
C_P	constant pressure specific heat $\left[\frac{J}{kgK}\right]$
$\overline{C}_P$	mole based constant pressure specific heat $\left[\frac{J}{gmoleK}\right]$
C_s	solubility concentration [$wt\%$]
D	diameter [m]
D	Ratio of "Dufour" to "Fourier" diffusive energy flux terms [dimensionless]
$\mathfrak{D}_{AA}$	self diffusion coefficient $\left[\frac{m^2}{s}\right]$

$\mathfrak{D}_{AB}$ binary molecular diffusion coefficient $\left[\frac{m^2}{s}\right]$

$D_A^{(T)}$ binary thermal diffusion coefficient for species A in system A-B $\left[\frac{kg}{m \cdot sec}\right]$

D_{io} diameter of the hot finger [m]

D_T ID of the Inconel 625 tube leading to test cell [m]

E separation efficiency [dimensionless]

$\dot{E}'''$ rate of energy generation per unit volume $\left[\frac{W}{m^3}\right]$

f   similarity variable [dimensionless]

g   gravitational acceleration $\left[\frac{m}{sec^2}\right]$

Gr   Grashof number [dimensionless]

h   specific enthalpy $\left[\frac{J}{kgK}\right]$

h heat transfer coefficient $\left[\frac{W}{m^2K}\right]$

H enthalpy [J]

H_{diss} (mass based) heat of dissolution $\left[\frac{J}{kg}\right]$

h_m mass transfer coefficient $\left[\frac{m}{s}\right]$

$h_{m,c}$ critical mass transfer coefficient $\left[\frac{m}{s}\right]$

$\dot{I}''$ internal energy flux into a control volume $\left[\frac{W}{m^2}\right]$

J   Jacobian matrix

J_{i,x_j} mass diffusive flux of species "i" in the x_j direction $\left[\frac{kg\ i}{m^2 sec}\right]$

k Boltzman's constant $(1.38*10^{-23})$ $\left[\frac{J}{K \cdot molecule}\right]$

k thermal conductivity $\left[\frac{W}{mK}\right]$

K_A transport constant defined by Eq. 3.175

K_B	transport constant defined by Eq. 3.178
k_T	thermal diffusion ratio [dimensionless]
K_W	ion product $\left[\frac{gmoles}{kg}\right]^2$
L	length [m]
L	length of protruding portion of hot finger [m]
$L(x,t)$	value of y at salt layer-solution interface [m]
L_c	annular fin parameter [m]
Le	Lewis number [dimensionless]
Le_c	critical Lewis number [dimensionless]
m	fin calculation parameter $\left(\frac{hP}{kA_{CS}}\right)$ $\left[\frac{1}{m}\right]$
m	mass [kg]
$\dot{m}$	mass flow rate $\left[\frac{kg}{sec}\right]$
$\frac{dm''}{dt}$	mass flux $\left[\frac{kg}{m^2 sec}\right]$
M	Ratio of energy transfer by a mass diffusion term to the Fourier term in energy equation [dimensionless]
M_{dep}	mass of salt deposited during a run [kg]
M_i	molecular weight of species "i" $\left[\frac{gm}{gmole}\right]$
MW_i	molecular weight of species of "i" $\left[\frac{gm}{gmole}\right]$
n	exponent in analogy between heat and mass transfer
n	number density $\left[\frac{molecules}{m^3}\right]$

$\tilde{N}$	ratio of concentration induced buoyancy to temperature induced buoyancy terms [dimensionless]
Nu	Nusselt number [dimensionless]
$\dot{O}$	rate of energy leaving a control volume [W]
P	Perimeter [m]
P	Power [Watts]
P	Pressure [bar (generally)]
$P(a, x)$	incomplete gamma function
Pr	Prandtl number [dimensionless]
q''	heat flux $\left[\frac{W}{m^2}\right]$
Q	heat transfer rate [Watts]
r	radius [m]
R	universal gas constant $\left[\frac{J}{gmoleK}\right]$
R'	thermal resistance per unit length $\left[\frac{mK}{W}\right]$
Ra	Rayleigh number [dimensionless]
Re	Reynolds number [dimensionless]
S	ratio of Sorét diffusion to "Fick" diffusion terms [dimensionless]
Sc	Schmidt number $\left(\frac{\mu}{\rho \mathcal{D}_{AB}}\right)$ [dimensionless]
Sh	Sherwood number $\left(\frac{h_m D}{\mathcal{D}_{AB}}\right)$ [dimensionless]
t	thickness [m]
t	time [sec]

31

T	temperature [$°C$ or K]
T_o	solubility temperature at (pragmatically) zero salt solubility [$°C$]
$\overline{T_W}$	average hot finger surface temperature [$°C$]
T_s	solubility temperature [$°C$]
u	specific internal energy $\left[\frac{J}{kgK}\right]$
u	velocity in x direction $\left[\frac{m}{s}\right]$
U	characteristic u-velocity in the boundary layer $\left[\frac{m}{s}\right]$
v	velocity in y direction $\left[\frac{m}{s}\right]$
V	characteristic v-velocity in the boundary layer $\left[\frac{m}{s}\right]$
V	volume [m^3]
v_{A,x_j}	species velocity of component "i" in the x_j direction $\left[\frac{m}{sec}\right]$
x	axial direction [m]
x	azimuthal direction [m]
x	distance from pipe inlet [m]
x	mole fraction [dimensionless]
y	normal direction [m]
y	radial direction [m]
z	distance from pipe inlet [m]

Greek Symbols

α	thermal diffusion factor [dimensionless]
α	thermal diffusivity $\left[\frac{m}{s^2}\right]$

β	volumetric thermal expansion coefficient $\left[\frac{1}{K}\right]$
β^*	species expansion coefficient $\left[\frac{m^3}{kg}\right]$
Γ	incomplete gamma function
δ	boundary layer thickness [m]
Δ	difference in value of a quantity at interface and bulk conditions
ϵ	potential well depth [J]
ϵ	static dielectric constant [dimensionless]
η	efficiency [dimensionless]
η	similarity variable [dimensionless]
η	wall platelet effectiveness ratio [dimensionless]
θ	temperature minus base temperature in fin calculations [K]
μ	viscosity $\left[\frac{kg}{ms}\right]$
ν	kinematic viscosity $\left[\frac{m^2}{sec}\right]$
ρ	solution density $\left[\frac{kg}{m^3}\right]$
ρ_i	density of species "i" $\left[\frac{kg\ i}{m^3}\right]$.
ρ_s	density of solid salt $\left[\frac{kg}{m^3}\right]$.
σ	Sorét coefficient $\left[\frac{1}{K}\right]$
σ_{AB}	collision diameter [Ångstroms]
τ	time constant associated with material capacitance of the test cell [minutes]
ϕ	void fraction/porosity [dimensionless]
Φ	viscous dissipation function $\left[\frac{1}{sec^2}\right]$

χ	"dense" gas correction factor to Chapman-Enskog equation [dimensionless]
ω_i	mass fraction of species i [dimensionless]
Ω_D	collision integral for diffusivity [dimensionless]

Subscripts	Description
∞	bulk condition as y $\rightarrow$ ∞
∞	steady state
A	salt component in binary solution
B	bulk
B	H_2O component of binary solution
c	characteristic
c	concentration
c	cylinder
cs	cross sectional
E	experiment
f	film
F	forced convection
i	salt layer-solution interface
L	total fin length
m	momentum
N	natural convection
o	value of a parameter at t or z = 0

PSL	porous salt layer
s	salt
t	thermal
T	theoretical
T	total
x_j	direction

Superscripts Description

D	Dufour
F	Fourier

Chapter 1

Introduction

Supercritical Water Oxidation (SCWO) is an emerging technology for the disposal of organic wastes. However, corrosion and fouling during the SCWO process can be problematic. The research performed for this dissertation was motivated by the fouling problems often present during the SCWO process. This introductory chapter begins with a discussion of the behavior of water beyond its critical temperature and pressure, i.e., supercritical water (SCW), and an overview of SCWO technology. Next, the technologies which have been developed to control corrosion and fouling in the SCWO process are discussed. A summary of existing research studies on salt deposition kinetics in the context of SCWO follows. Then, the measurements and modeling of deposition rates from near-supercritical, aqueous, sodium sulfate and potassium sulfate solutions to a heated cylinder accomplished in the dissertation are motivated in the context of developing a better understanding of fouling problems in the SCWO process. Finally, the contents of the remaining chapters of this dissertation are presented.

1.1 Supercritical Water (SCW) and Supercritical Water Oxidation (SCWO)

Toxic organic wastes and "mixed wastes," composed of toxic organic compounds and radioactive elements, are a major environmental management problem. Supercritical water oxidation (SCWO) shows promise for

effective remediation of these wastes by destroying their organic constituents and, when necessary, concentrating their radioactive ingredients in forms suited to safe disposal. Shaw et al. [78] and Tester et al. [87] elucidate the principles behind SCWO and review relevant fundamental research. More recent research pertinent to SCWO has been summarized by Gloyna and Li [33].

SCWO is defined as oxidation in water at temperatures and pressures exceeding the critical temperature (371 $°C$) and critical pressure (221 bar) of pure water. The SCWO process unites water, organic waste and oxidant at high pressures (25 MPa or more) and moderate temperatures (400°C and above). When processing some types of wastes, auxiliary fuel and/or caustic are added to the reactor as well. At supercritical conditions a single fluid phase generally exists, thereby eliminating transport limitations inherent in multiphase systems and leading to high destruction efficiencies in short reactor residence times. When salts are present a solid phase and, occasionally, two fluid phases may be present.

At supercritical conditions, water is a highly disordered fluid which behaves like an ordinary non-polar solvent; therefore, oxidants and organics are highly soluble in SCW. (See, for example, Smith et al. [80].) A qualitative explanation for the solvation properties of SCW may be developed by examining the effect of density on the hydrogen bond structure in H_2O. The highly ordered, three-dimensional (tetrahedral) structure of ice as depicted by Némethy and Scheraga [65] is shown in Fig. 1-1. Intermolecular covalent bonds between O and H atoms are represented by short solid lines and intramolecular hydrogen bonds between O and H atoms are represented by long dashed lines. Each O atom is covalently bonded to two H atoms and hydrogen bonded to two H atoms. The intramolecular covalent bonds are stronger than the intermolecular hydrogen bonds. The highly ordered three-dimensional structure of ice causes H_2O molecules to be spaced further apart than in (liquid) water; hence, water expands upon freezing. Interestingly, at its melting point and up to 4 $°C$ (at atmospheric pressure) water expands upon cooling because molecules possessing sufficient kinetic energy to break their hydrogen bonds are subsequently "trapped" within cavities of the three-dimensional bond structure of water causing a reduction in density [17]. Above 4 $°C$, kinetic energy effects dominate the "trapping" effect and water expands upon heating. In liquid water at normal conditions much of the structure in Fig. 1-1 is preserved; however, the number of hydrogen bonds per oxygen atom is reduced to approximately 3.5 [80] because more water molecules possess sufficient kinetic energy to
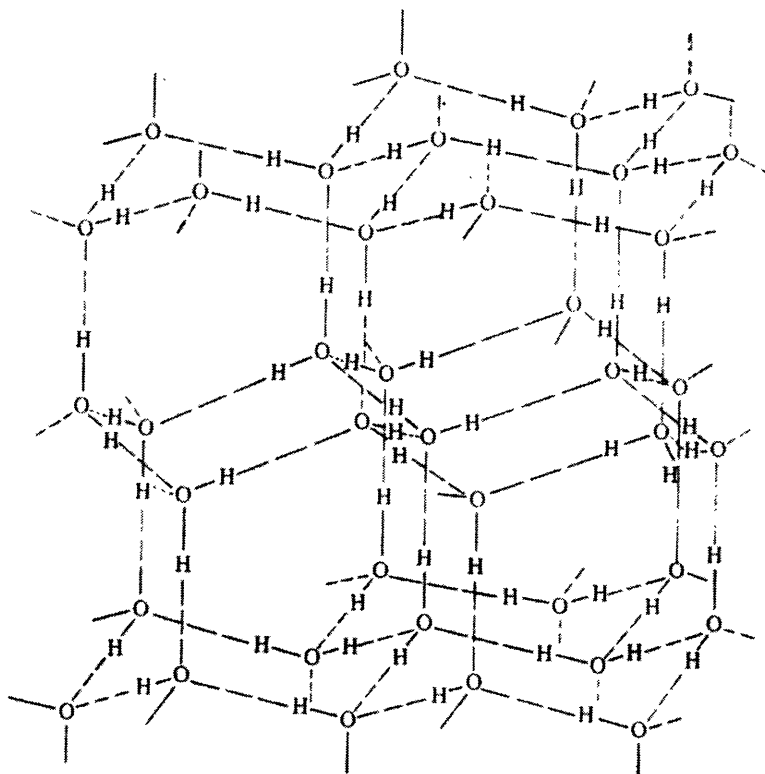
Figure 1-1: The three-dimensional structure of ice extracted from Némethy and H.A. Scheraga [65].

break free of hydrogen bonds.

At temperatures and pressures typical of the reaction zone in an SCWO reactor, i.e., in the neighborhood of 550 $^\circ C$ and 250 bar, the density of water is of order 100 kg/m^3. This is substantially below the density of ice (about 920 kg/m^3) and liquid water at STP (about 1000 kg/m^3); consequently, geometric constraints prevent the retention of any kind of organized three-dimensional structure. Moreover, the extent of hydrogen bonding is considerably reduced and hydrogen bonds which do form are comparatively weak. The result is that supercritical water is a largely disordered fluid which behaves like a non-polar solvent at the conditions in the reaction zone of an SCWO reactor. Not surprisingly, the static dielectric constant and ion product of H$_2$O at conditions typical of the SCWO process are about 40 and 10^9 times smaller than their respective values at STP. It is noted that, despite the overwhelming amount of information available on H$_2$O at liquid and gas-like conditions, comparatively little is known about H$_2$O at near-supercritical conditions. The knowledge-base for aqueous electrolyte solutions at near-supercritical conditions is even less mature. The

term "near-supercritical" is used liberally, but not precisely, throughout this dissertation to describe pure H_2O and aqueous salt solutions near the critical temperature and pressure of the fluid. It is noted, however, that thermodynamically a fluid is classified as either supercritical or not supercritical.

The solubility of salts in supercritical water is low and very often approaches zero at conditions relevant to SCWO. This is largely attributable to the drastic reduction in the static dielectric constant of water near its critical temperature. The static dielectric constant and density of pure H_2O at 250 bar for temperatures between 0 and 700 $°C$ are plotted in Fig. 1-2. The static dielectric constant of H_2O as a function of temperature at 250 bar was computed from an equation developed by Uematsu and Franck [90] based on their critical evaluation of the data available for the static dielectric constant of (pure) H_2O up to the year 1980. Uematsu and Franck's expression provides the static dielectric constant of pure H_2O as a function of temperature and density. It is rigorously valid for temperatures and densities in the ranges 0 to 555 $°C$ and 0 to 1150 kg/m^3 respectively; therefore, the portion of the static dielectric constant curve plotted for temperatures between 555 and 700 $°C$ in Fig. 1-2 is an extrapolation. To generate the static dielectric constant curve shown in Fig. 1-2, the NBS Steam Tables were used to compute density as a function of temperature at 250 bar. Then temperatures and densities of interest at 250 bar were inserted into the Uematsu and Franck expression to compute the static dielectric constant as a function of temperature at 250 bar. It is noted that to be completely rigorous, the sources for the density of pure water as a function of temperature and pressure cited by Uematsu and Franck should be used to compute the static dielectric constant from their expression. However, use of the NBS Steam Tables does not introduce any significant error. The density curve in Fig. 1-2 was generated directly from the NBS Steam Tables [30].

At a pressure of 250 bar, the static dielectric constant is a relatively smooth function of density, but not temperature as per Fig. 1-2. This is especially true near the pseudocritical temperature of pure H_2O at 250 bar (385 $°C$). (The critical temperature of pure H_2O (371 $°C$) is close to its pseudocritical temperature at a pressure 250 bar. Moreover, 250 bar exceeds the critical pressure of pure water (221 bar) by only about 12%.) Franck [27] plotted curves of constant static dielectric constant and pressure on the temperature-density diagram for pure H_2O and the results are shown in Fig. 1-3 [27]. This figure conclusively shows that the static dielectric constant of water is a much smoother function of density than temperature in

general. Earlier in this section, it was shown that the hydrogen bond structure of H_2O is especially sensitive to density; therefore, it is not surprising that its static dielectric constant is a smoother function of density than temperature. At typical SCWO conditions, SCW has a static dielectric constant below 2. Conversely, the static dielectric constant of pure H_2O is 78.46 at 1 bar and 25 $°C$. (The static dielectric constant is a weak function of pressure. Increasing pressure from 1 bar to 250 bar at 25 $°C$, for example, causes the static dielectric constant to rise from 78.46 to 79.44, a very modest amount [90].) In short, increasing the temperature and decreasing the density of H_2O significantly increases the kinetic energy of the molecules; consequently, the strength and cohesiveness of the hydrogen bonds are greatly reduced. This "attenuation" in hydrogen bonding decreases the net orientation of permanent dipoles resulting in a lower static dielectric constant.

The drop in the static dielectric of constant H_2O with decreasing density is accompanied by an even more pronounced drop in its ion product. The ion product and density of H_2O for temperatures between 0 and 700 $°C$ at 250 bar are plotted in Fig. 1-4. The ion product curve was computed by using an equation developed by Marshall and Franck [56] and the density curve was generated using the NBS Steam Tables [30]. At conditions typical of the SCWO process, the ion product of water is of order 10^{-23} $(mole/kg)^2$, or nine orders of magnitude smaller than its value at STP. Obviously, at such conditions ions are not well shielded from one another by SCW and, hence, salts precipitate. Of course, the low ion product and static dielectric constant of H_2O at supercritical conditions are the primary reasons it behaves as a non-ionic/non-polar solvent. This explains why salts have low solubility in SCW and oxygen and organics have high solubility (and miscibility) in SCW, i.e., "like dissolves like."

The corrosion rate during the SCWO process is closely tied to the ion product of the aqueous solution at conditions of interest. At 250 bar, the ion product of water is an increasing function of temperature up to 255 $°C$, and, moreover, it is especially high within the temperature interval of roughly 150 $°C$ to 335 $°C$ as per Fig. 1-4. Corrosion rates are often higher in the preheaters of an SCWO system than in the main reactor vessel because of the high concentration of positive hydrogen ions in the aforementioned temperature range. Corrosion resulting from hydrolysis of halogen-containing wastes due to the formation of the corresponding acid, e.g., methylene chloride leading to hydrochloric acid, during preheating in the SCWO process can be
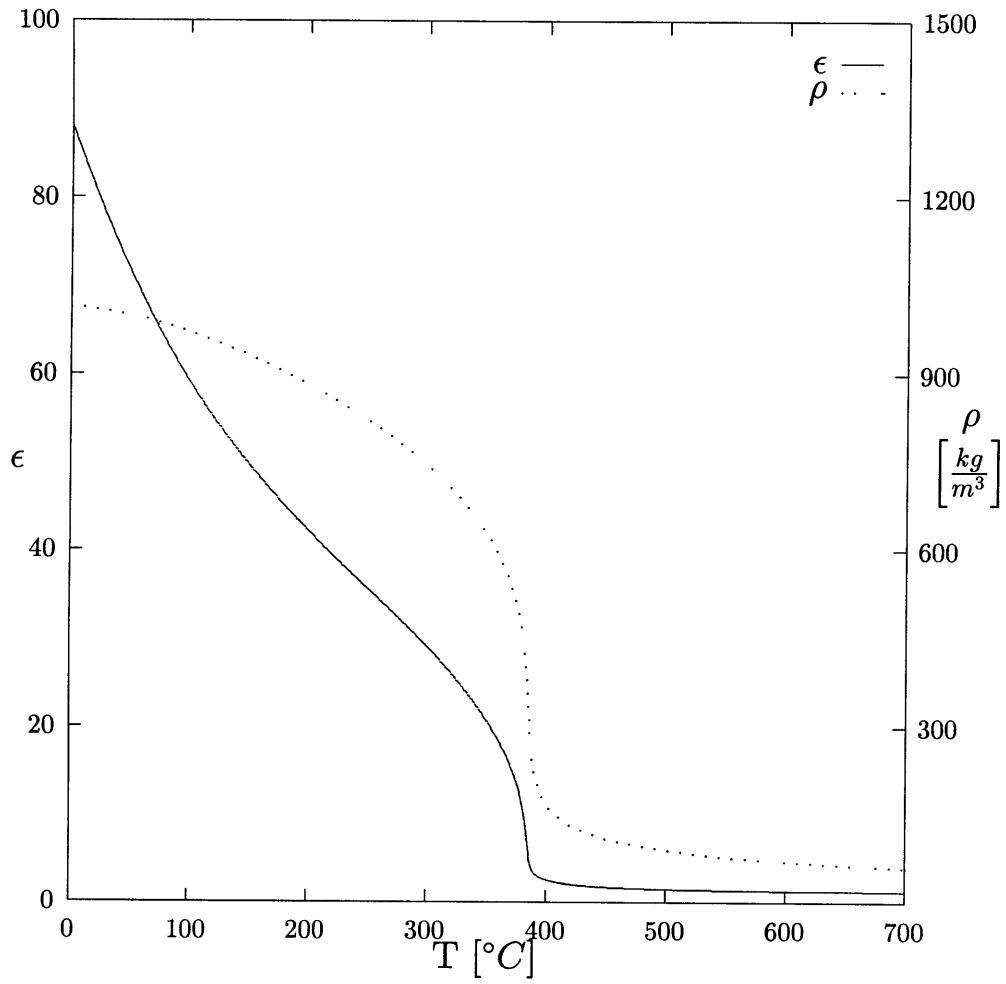
Figure 1-2: Static dielectric constant and density of pure H_2O as a function of temperature at 250 bar [90, 30].
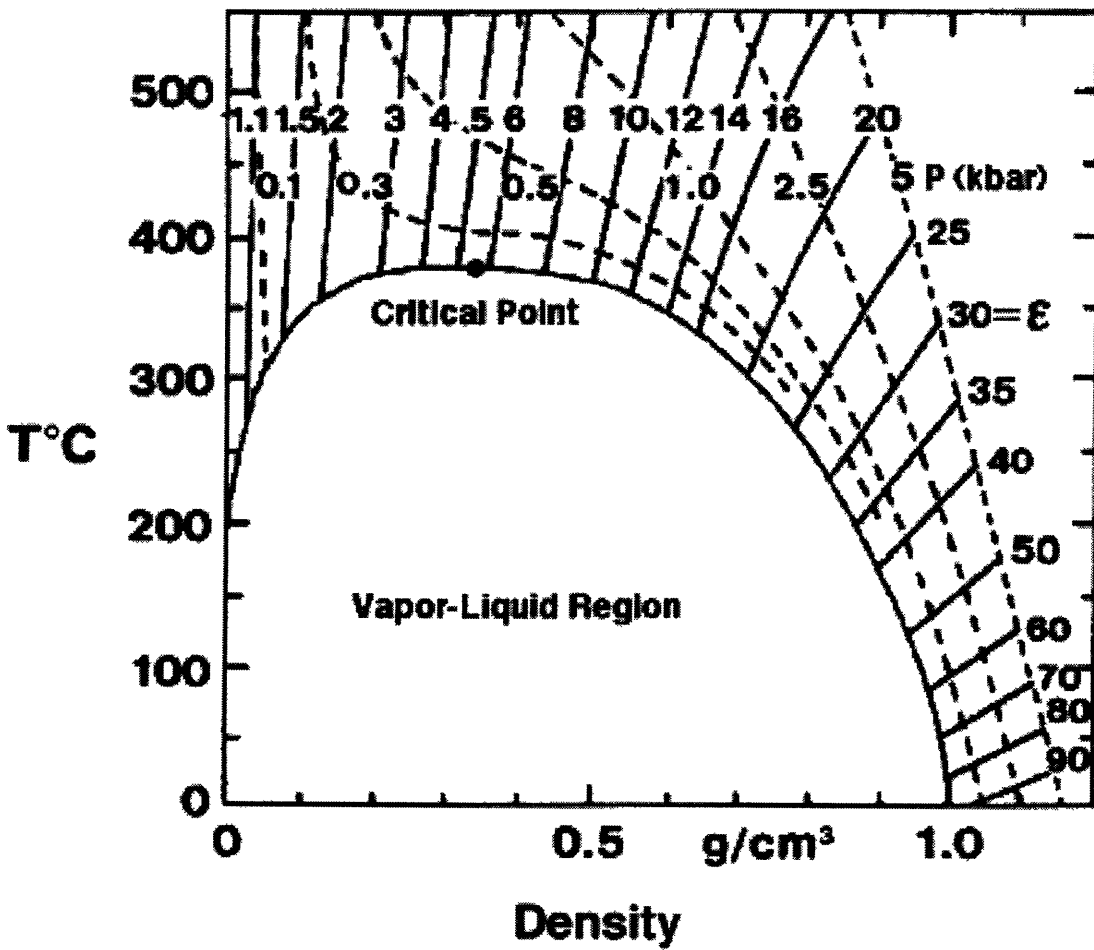
Figure 1-3: Temperature-density diagram for pure H_2O with curves of constant pressure and static dielectric constant. This figure was constructed by E.U. Franck based on what he published in reference [27].
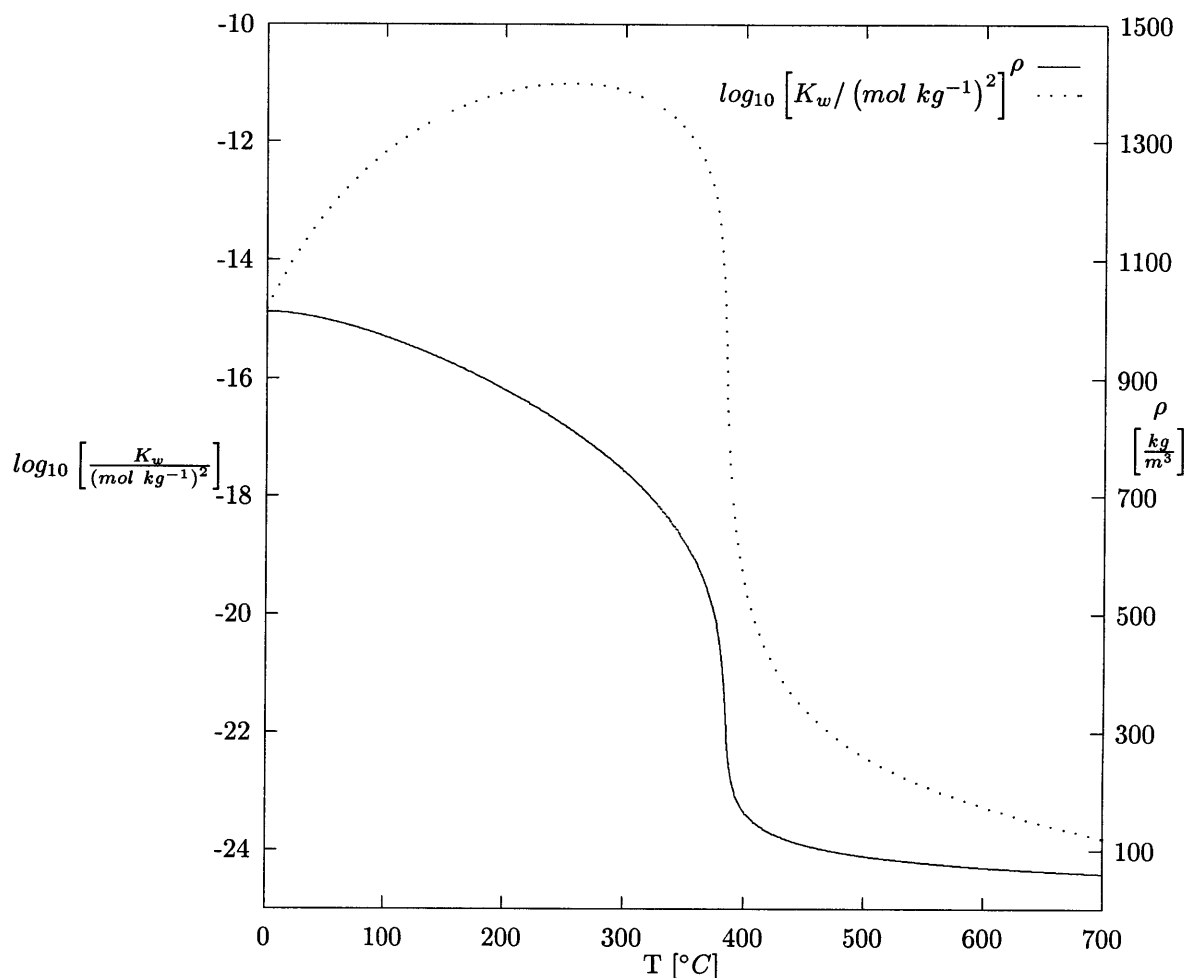
Figure 1-4: Ion product and density of pure H_2O as a function of temperature at 250 bar [56, 30].

especially severe.

Many different types of SCWO reactors have been designed and/or implemented. In general, rapid and near-complete destruction of a very wide array of organic wastes has been achieved by SCWO. These wastes include aromatics, chlorinated hydrocarbons, fermentation wastes, pulp mill sludge, propellants and military smokes and dyes [72]. The "MODAR" SCWO reactor, shown in Fig. 1-5, has probably been the most extensively investigated type of SCWO reactor to date. It is a continuous flow reactor and was developed by MODAR Inc. (Natick, MA) which has been subsequently acquired by General Atomics (San Diego, CA). MODAR constructed both laboratory scale (71 mm diameter) and pilot scale (254 mm diameter)

reactors and successfully oxidized a wide array of waste feed materials. Destruction efficiencies of the various organic materials were generally 99.9% or better. Barner et al. [7] describe the MODAR reactor/process in considerable detail and an overview of it is given here.

In the MODAR process, an aqueous waste stream, typically containing 2-20 wt% organic, is preheated to temperatures of 300 °C or more, depending on the concentration of the waste, exothermicity of the subsequent oxidation process and desired conversion. (If necessary auxiliary fuel and/or caustic are added to the aqueous waste stream.) Next, the aqueous organic waste stream and oxidant are simultaneously injected into the top of the MODAR reactor through a coaxial nozzle. The oxidant can be can be pure oxygen, but it is generally air or hydrogen peroxide. The two steams mix in the reaction zone and the exothermicity of the oxidation process causes the "reaction zone" of the reactor to reach a temperature of 550 °C or more. Most effluent leaves the top of the reactor as a single phase mixture at 250 bar. This effluent is cooled as it passes through a heat exchanger which preheats incoming aqueous waste. Next, it passes through a back pressure regulator and becomes a two-phase mixture. The vapor phase of the effluent is generally almost exclusively CO_2, H_2O and molecular nitrogen; therefore, it can be vented to the atmosphere. Alternatively, the CO_2 offgas may be captured for future use, e.g., the production of dry ice. The liquid phase portion of the effluent is nearly pure water. When present, heavy metals may be removed from the liquid phase portion of the effluent if potable water is desired or it may simply be discharged. Handling of corrosion and fouling in the MODAR process are discussed in Section 1.3.

Incineration is by far the most commonly used method for the remediation of hazardous organic wastes; hence, a comparison between incineration and SCWO is apropos. Under appropriate conditions, a wide array of hazardous organic wastes treated by SCWO are oxidized to lower molecular weight compounds. Subsequently, these lower molecular weight compounds are oxidized to, predominantly, water, carbon dioxide and molecular nitrogen. Generally the moderate temperatures associated with the SCWO process (400 to 600 °C) prevent significant NO_x and SO_x production. (NO_x levels in the gaseous effluent released from SCWO reactors are routinely measured to be less than 1 mg/m^3 [11]. SO_2 emissions are generally of order 1 mg/m^3 [7].) Conversely, incineration of hazardous wastes often results in significant NO_x and SO_x production because of the relatively high temperatures (above 1000 °C) required to achieve specified

44
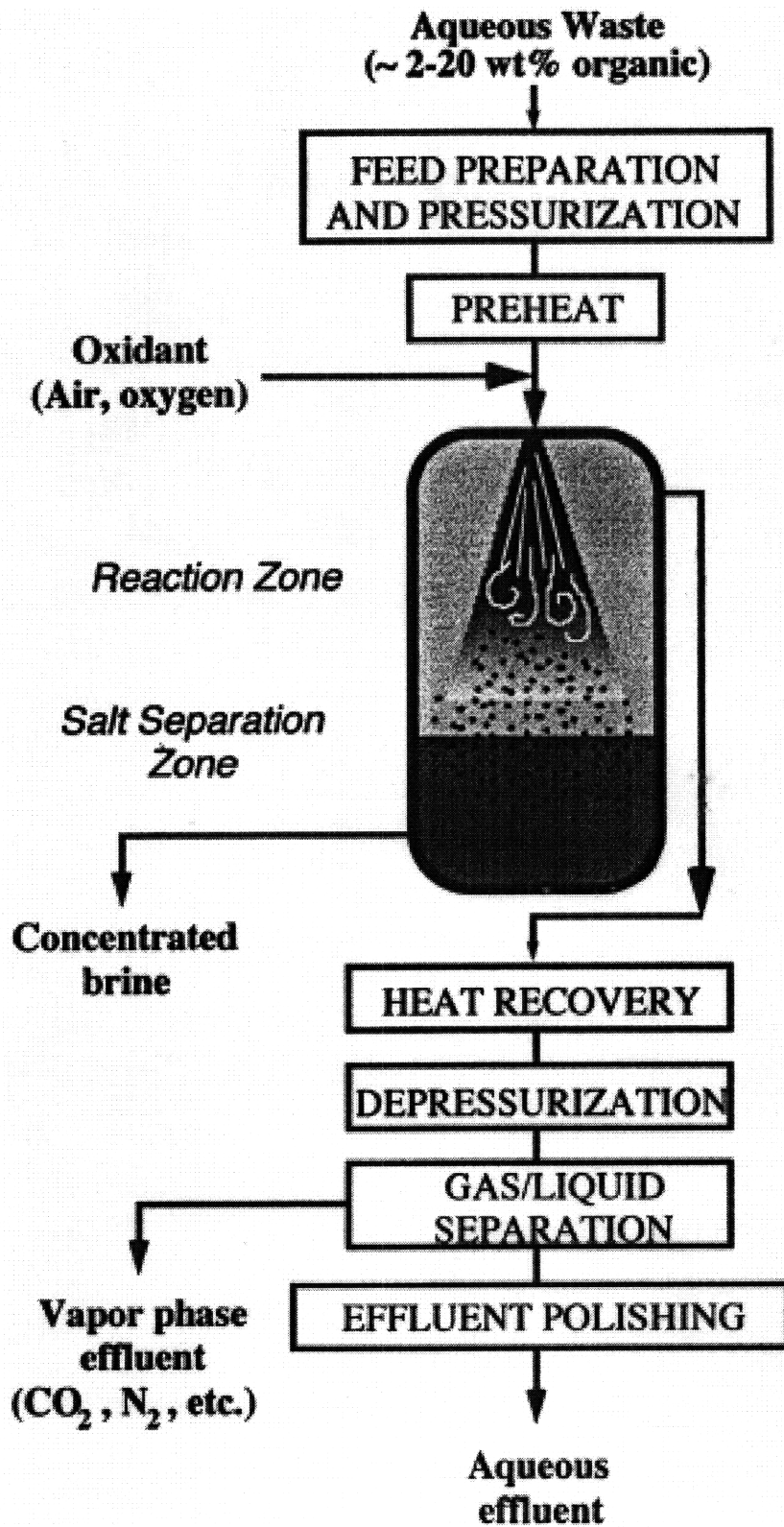
Figure 1-5: Schematic of the Modar SCWO Process. (This schematic was produced by the SCWO group at MIT.)

conversions. Typical fluid densities and temperatures in the reaction zone of an SCWO reactor are of order $100 \, \text{kg/m}^3$ and 400-600 °C respectively. The temperature of the gas mixture in an incinerator is considerably higher (above 1000 °C), and the gas density is considerably lower (of order $1 \, \text{kg/m}^3$). This makes SCWO better suited to dilute aqueous wastes (1-20 wt% organics) than incineration for the following reasons. First, for dilute aqueous wastes incineration is very expensive because auxiliary fuel is required to reach the high temperatures necessary for desired levels of conversion. Conversely, due to the comparatively low temperatures and high fluid density in the SCWO process, auxiliary fuel is generally unnecessary to maintain a self-sustaining reaction in an SCWO reactor when processing dilute aqueous wastes. Typically, a waste containing 5 wt% or more organic is autogenic, i.e., after startup, the SCWO process is self sustaining [25]. Moreover, the low gas density ($\sim 1 \, \text{kg/m}^3$) associated with incineration makes containment during an upset virtually impossible; whereas SCWO systems are easily contained, if necessary, in an emergency. For very dilute aqueous wastes (< 1 wt% organics), activated carbon absorption and biological oxidation may or may not be more suitable/economical than SCWO [87].

Another advantage SCWO possesses relative to incineration is its portability. A small SCWO facility can be assembled and removed from a contaminated site, but this is virtually impossible with an incinerator. Moreover, transportation of hazardous and/or toxic wastes for offsite incineration causes safety concerns and is expensive. Even when installation of an incinerator is economical, deservedly or not, incineration has developed an unsavory reputation in the eyes of the general public; therefore, obtaining the permits required for new sites is especially difficult. It is noted that many persons in the SCWO community currently refer to SCWO as Hydrothermal Oxidation because of the negative connotations the general public associates with the term "supercritical."

Of course incineration is an extremely mature technology and has many virtues. It is more cost-effective than SCWO when the waste stream is concentrated, i.e., it contains 20 wt% or more organic. Moreover, incinerator reactor materials are cheaper than the high nickel alloys required to withstand the hostile SCWO environment. Also, incinerators operate near atmospheric pressure; whereas SCWO reactors operate at about 250 bar. Furthermore, it is unnecessary to add water to the organic waste fed into an incinerator and some solid wastes are suitable to incineration. (It is possible to remediate solid wastes with SCWO.

For example, a CSTR recently constructed in our SCWO laboratory at MIT is equipped with a basket to accommodate solid wastes; however, SCWO has not been used to a significant extent to dispose of solid organic wastes to date.) The corrosion and fouling problems associated with the implementation of SCWO are discussed in the next section.

1.2 Corrosion and Fouling in the SCWO Process

For widespread commercialization of SCWO technology to be realized corrosion and scale buildup/fouling, caused by the production of "sticky" salts, must be controlled. Oxide solids often precipitate from solution as well, but have generally been found to be "non-sticky and flowable" [7]. However, oxide solids tend to be less soluble than salts in SCW and can cause erosion and, occasionally, scale buildup problems. Moreover, some oxide solids produced from corrosion are virtually insoluble even at ordinary temperatures and pressures and, therefore, are very difficult to dislodge once adhered to surfaces inside an SCWO system. Although precipitated salt particles and suspended solids erode various surfaces in an SCWO system, corrosion and scale buildup tend to be more problematic. Corrosion and scale buildup are generally most severe in the preheater and the main reactor of an SCWO system. Erosion is generally most severe when the pressure of the effluent stream from an SCWO reactor is let down [77]. This happens because the expansion of the gas contained in the effluent can cause inert solid particles and/or oxides to impact surfaces at high velocities. The reasons that corrosion, fouling and erosion are often problematic during the SCWO process are elucidated in this in the remainder of this section.

Corrosion of SCWO reactor materials caused by acidic solutions that result from the oxidation of organic compounds containing heteroatoms such as S, Cl or P is often minimized by injecting neutralizing bases into the reactor. The salts formed upon neutralization (sulfates, chlorides, phosphates, etc.) have low solubility in SCW and, consequently, precipitate as solid phases. It is noted that salts may also be present in the waste stream itself. Because the salts formed tend to be "sticky", they can form agglomerates and coat internal surfaces thereby leading to plugging of transport lines and inhibition of heat transfer. After a reactor or transport line becomes plugged, it must be flushed with solution or water at a temperature sufficiently low

47

to dissolve the scale causing the plug. Often, this results in substantial and costly downtime in the SCWO process. In extreme cases, mechanical means can be necessary to remove scale. For example, products resulting from the pyrolysis of pyrotechnic dyes and charring in the study by Chan et al. [16] had to be removed by mechanical honing. Moreover, some sodium sulfate deposits in an SCWO reactor during the investigations by Haroldsen et al. [36] had to be removed using "a screwdriver and hammer" when the reactor was not flushed with cold water.

It is important to recognize that, despite leading to fouling and erosion problems, the insolubility of salts and other solids in SCW provides a convenient means to separate them from solution. This can be important when, for example, regulatory laws prohibit the discharging of certain salts/brines to the environment. It is also advantageous not to have solids present upstream of an SCWO reactor to limit erosion during pressure letdown. Precipitation of salts from SCW is not an economical means to produce potable water from salt water.

Examining the global reactions during the oxidation of a typical halogen-containing aqueous waste by SCWO further elucidates the corrosion and fouling problems. For example, during the oxidation of methyl chloride and subsequent neutralization of the hydrochloric acid produced with sodium hydroxide, the global reactions are:

$$CH_3Cl + \frac{3}{2}O_2 \quad \rightarrow \quad HCl + H_2O + CO_2 \tag{1.1}$$

$$HCl + NaOH \quad \rightarrow \quad H_2O + NaCl \text{ (s)} \tag{1.2}$$
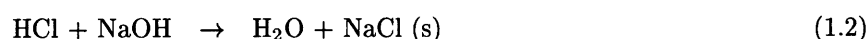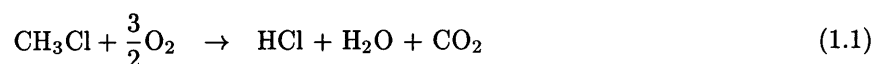
When the methyl chloride reacts with oxygen the hydrochloric acid produced is highly corrosive; therefore, sodium hydroxide or some other base is normally injected into the reactor to neutralize the solution. This reduces, but does not eliminate, corrosion. However, sodium chloride is virtually insoluble in water above 450 $°C$; therefore, it precipitates and fouling generally occurs. The next section describes the many technologies which have been developed to control the scale buildup problem in the SCWO process.

In closing this section, it is noted that designing commercial sized SCWO units by scale-up from laboratory or pilot sized reactors is especially difficult [48, 7]. Many different parameters, e.g., Grashof number, Reynolds

48

number, surface area to volume ratio, are important to transport and kinetics during the SCWO process. Therefore, for practical purposes, similitude is impossible. The fact that the role of catalysis during SCWO remains largely ambiguous [48] further complicates matters. Corrosion and fouling aside, scale-up is probably the most critical issue which needs to be addressed before SCWO can be widely commercialized.

1.3 Methods to Control Scale Buildup During SCWO

1.3.1 Introduction

A fair number of strategies to limit corrosion and fouling during the SCWO process have been implemented and many of them have met with considerable success. Nonetheless, continuous processing of heteroatom-containing wastes without encountering corrosion and fouling problems to some degree is not possible in the foreseeable future. Technologies currently available to limit corrosion and scale buildup during SCWO are described in this section. From a corrosion control perspective, only technologies which lead to the precipitation of "sticky" salts are presented. The use of exotic materials, e.g., titanium and even platinum, to withstand the extremely corrosive environment produced during SCWO of halogen-containing wastes without the addition of caustic has, however, been investigated as well. (See, for example, Leistikow [50].)

1.3.2 The MODAR Process

In the MODAR process shown in Fig. 1-5 most, but not all, salt precipitation occurs in the reaction zone away from the walls of the main vessel and the majority of precipitated salts are eventually redissolved in the "cold" brine located at the bottom of the reactor. The majority of salts precipitated in the reaction zone of the MODAR reactor are directed or "thrust" towards the bottom of the reactor for two primary reasons. First, the aqueous waste and oxidant enter the reactor as a vertical jet moving downward; therefore, most precipitated salts are moving towards the bottom of the reactor a priori. Secondly, the salts which precipitate from solution are, roughly, an order of magnitude more dense than the solution itself; therefore, gravity causes them to settle at the bottom of the reactor. Extraneous solids which may be suspended in the aqueous waste and precipitated oxide solids tend to be directed towards the bottom of the reactor as well.

49

Cold water is continuously injected into the bottom of the MODAR reactor to maintain it at approximately 200 $°C$ [7], a temperature at which virtually all relevant salts are sufficiently soluble in SCW. The resulting brine or slurry is continuously drained from a discharge nozzle located at the bottom of the reactor. A fraction of the salts which precipitate in the reaction zone of the MODAR reactor inevitably stick to the walls in the higher temperature (supercritical) region of the reactor where they are insoluble [11]. To be sure, the flow in the supercritical region of the reactor does have a nonzero radial velocity component, albeit small. Moreover, certain salts do precipitate from solution in the preheater lines and at other locations in the SCWO system. Thus, scale buildup problems do occur in the MODAR process when remediating heteroatom-containing wastes. Moreover, maintaining the bottom portion of the MODAR reactor at a temperature a few hundred degrees centigrade cooler than the reaction zone in order to control scale buildup causes thermal stresses in the walls of the reactor vessel.

Control of scale buildup during the MODAR process is discussed in more detail in the article by Barner et al. [7]. It is also noted that Oh et al. [67] modeled particle trajectories in the MODAR (pilot scale) reactor as a function of particle size and nucleation location. The diameter of the particles for which trajectories were computed ranged from 5 to 1000 microns and each particle was 50% (by volume) void and 50% NaCl. To compute particle trajectories, the steady state velocity field in the reactor was determined by numerically solving the equations governing transport in the reactor under typical SCWO operating conditions. (Apparently the computational transport software program FLUENT (Lebanon, NH) was used for this purpose.) Then trajectories of individual particles were determined by (Lagrangian) force balances marching forward in time. Since the flow is turbulent, the particle trajectories were statistical in nature. In general, particles less than 20 microns in diameter deposited in the top half of the reactor and particles with diameters larger than 500 microns settled in the bottom of the reactor. Particles of diameter twenty microns or smaller occasionally reached the outlet port located at the top of the reactor. Oxides and inert solid particles egressing from the top of the MODAR reactor are known to cause downstream erosion problems; therefore, it is encouraging that this investigation could predict that solids (of sufficiently small diameter) can egress from the top of the reactor.

1.3.3 SCWO Reactors with Transpiring Walls

Recently, the use of transpiring walls to bathe the surfaces of SCWO reactors with pure, "cold" water to reduce corrosion and deposition has received attention [36, 37, 59, 2]. Under sponsorship primarily by ARDEC, the U.S. Army Armament Research, Development and Engineering Center (Picatinny, NJ), and the U.S. Department of Energy; Sandia National Laboratories (Livermore, CA), Foster Wheeler Development Corporation (Livingston, NJ) and Gencorp, Aeorjet (Rancho Cordova, CA) have collaboratively developed a transpiring wall SCWO reactor using a platelet device to reduce fouling and corrosion rates [36, 37, 2]. The recent tests run by Haroldsen et al. [36] at Sandia National Laboratories with and without transpiration in this reactor show that transpiration can appreciably reduce the rate of scale buildup during SCWO. The reactor is described next and an account of some of the deposition experiments performed using it follows.

Platelets are liners that distribute fluid uniformly through small transpiration pores along surfaces using an intricate network of manifolding and metering channels. The resulting boundary layer formed along the surface of a platelet protects it from an adjacent hostile environment. (The flow through a platelet may be delivered nearly parallel to its surface when necessary.) It is noteworthy that platelets may be fabricated from numerous materials including Inconels as well as ceramics and differ from conventional porous liners by providing precise flow control to prevent the formation of "hot spots". Additionally, the pressure difference across a platelet in an SCWO reactor can be relatively small. For example, it was less than 200 psi during the tests run at Sandia National Laboratories. Thus for SCWO applications platelets may be manufactured from materials that are highly resistant to corrosion and can withstand high temperatures, but have a relatively low yield strength.

The transpiring wall platelet SCWO reactor constructed at Sandia National Laboratories (Livermore, CA) is shown in Fig. 1-6. It is a 1/4 scale model of a transpiring wall platelet SCWO reactor about to come on-line at the Army's Pine Bluff Arsenal facility (Arkansas, US). A description of it follows below and a more detailed description of it may be found in the technical reports by Haroldsen et al. [37, 36] and, to a lesser extent, the proceeding by Ahluwalia et al. [2]. The reactor is approximately 3 feet long, oriented vertically and housed within a 2.5 inch OD X 1.75 inch ID Inconel 625 pressure-containment tube. The annulus between the pressure containment tube and (tubular) platelet is divided into three separate

51

distribution plenums. The porous platelet liner is centered inside the Inconel 625 pressure-containment tube by welded rings. It was manufactured by Gencorp, Aerojet from stainless steel 304L. It is comprised of two identical platelets which are each 1.5 feet long and have a 1.419 inch OD and 1.115 inch ID. The two sections of the reactor are assembled as mirror images of one another; therefore, the top (inlet) section is identical to the (bottom) outlet section. The two platelets are mechanically joined by a flange. The oxidation process occurs inside the circular cross section within the platelet. The geometry of the platelets, i.e., pore size, etc., was not provided in any of the aforementioned references. During the experiments performed by Ahluwalia et al. [2] the pressure in the distribution plenums between the Inconel 625 pressure-containment tube and porous platelet liner was about 4200 psi and the pressure inside the porous platelet liner was about 4000 psi. (Similar pressures were measured in all the experiments performed using the transpiring wall platelet reactor at Sandia National Laboratory.)

When this reactor operates, the aqueous waste and oxidizer are preheated to, typically, 320 $°C$ at a pressure of about 4000 psi. (During the deposition studies of interest here, aqueous sodium sulfate solutions containing up to 3 wt% salt were preheated to temperatures where the salt remained soluble, i.e, up to about 300 $°C$.) The feed enters the top of the reactor through a perforated plate which acts as a flow diffuser and enhances mixing. As already mentioned, the distribution plenum between the Inconel 625 pressure vessel and porous platelet liner is divided into three separate sections. In the top 5 inches of this plenum, "hot" (pure) supercritical water (typically at a temperature of about 600 $°C$) is injected through several large diamond-shaped holes which are interspersed among the transpiration pores of the platelet. This injected SCW mixes with and heats the waste and oxidant stream in this section of the reactor causing the oxidation process to proceed. (In the deposition experiments of interest here, the injected "hot" water causes sodium sulfate to precipitate from solution.) The temperature in the reaction zone is controlled by adjusting the relative flow rates of "hot water" injected and feed. In the middle 26 inches of the distribution plenum, two separate pumps supply SCW (generally at a temperature of about 450 $°C$) for transpiration through the porous platelet liner to protect its inner surface. The streams of SCW supplied by these two pumps are subsequently referred to as the "upper" and "lower" transpiration streams. Finally, in the bottom five inches of the distribution plenum, room temperature water is injected through diamond-shaped holes interspersed
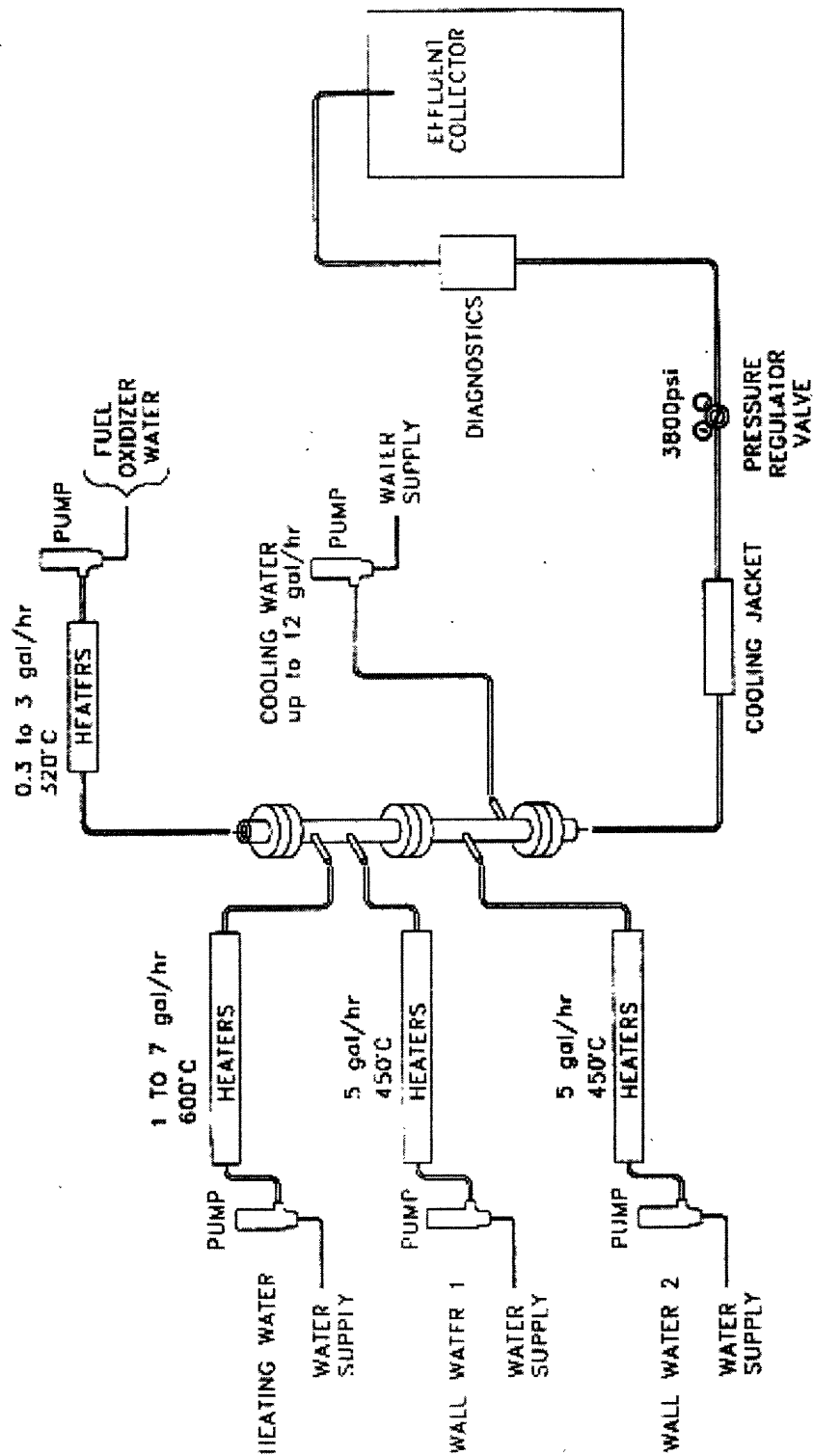
Figure 1-6: The Transpiring Wall Platelet SCWO system at Sandia National Laboratories (Livermore, CA). This figure was extracted from reference [2].

amongst the transpiration pores of the platelet. This causes salt particles which precipitated in the upper portions of the reactor to redissolve and form a brine before exiting the reactor.

The solution exiting the reactor is cooled in a heat exchanger and then passes through a back pressure regulator. The electrical conductivity and pH of the effluent leaving the back pressure regulator are measured to monitor sodium sulfate concentration in the effluent as a function of time. (The pH of the effluent was measured to determine what fraction of its electrical conductivity was accountable to H^+ and OH^- ions. The electrical conductivity not attributable to these ions was attributed to dissolved sodium sulfate molecules.) The system is purged with nitrogen and subsequently disassembled after each run to inspect the location, morphology, etc. of the sodium sulfate deposits.

As per Fig. 1-6, five separate pumps supply the aqueous waste stream/oxidant/fuel (or aqueous sodium sulfate solution), injected "hot" water, two streams of transpiration water and injected room temperature water. Only oxygen-free, deionized water is supplied through the platelet because its small internal passages are susceptible to corrosion. Haroldsen et al. [36] note that conductive heat transfer along the platelet liner and cooling of the transpiring water as it flows azimuthally through the (annular) distribution plenum between the Inconel 625 pressure-containment tube and platelet both cause significant undesirable thermal gradients. Moreover, since the thermodynamic and transport properties of water are a function of temperature, despite pressures being essentially constant within the distribution plenum and porous platelet liner, the flow rate of solution and water are a function of both axial and azimuthal position. The mass flow rate of subcritical water is larger than that of supercritical water for the same pressure drop (and geometry); therefore, flow rates are highest at the bottom of the reactor.

Ahluwalia et al. note the "hot" water jets injected through the diamond-shaped holes at the top of the porous platelet liner do reach the center of the reactor to insure complete mixing, but do not disrupt the fluid on the opposite side of the inner wall of the porous platelet liner. However, in a later publication, Haroldsen et al. [36] caution that turbulence generated by the liquid jets and the presence of the diamond-shaped injection holes may be responsible for the alarmingly high deposition rates observed at the top of the reactor. It is critical that the protective boundary layer formed by the transpiring SCW is not disturbed because its purpose is to form a "nonreacting barrier" between the inner wall of the platelet and

the adjacent hostile reaction zone. By way of this "nonreacting barrier", corrosion of the platelet by acid attack and salt deposition on the platelet are both very substantially reduced. Obviously, from a corrosion perspective, pure water is more benign to the surface of the platelet than the products of SCWO, particularly during the oxidation of halogen-containing wastes. Ahluwalia et al. note that another reason transpiration reduces corrosion rates is that when corrosion does occur on the inner surface of the platelet, the corrosion products are immediately diluted. If the transpiring wall works as intended, presumably, little, if any, nucleation occurs on the inner surface of the platelet, i.e., the majority of nucleation is homogeneous and/or secondary in the bulk fluid. Armellini [4] observed the diameter of sodium sulfate particles which nucleated homogeneously in solution at conditions typical of SCWO operating conditions was generally in the range of 1 to 3 microns. The Reynolds numbers of the flows through the platelet in the experiments performed at Sandia National Laboratories are on the order of 10000. Particles of diameter of order 2 microns are likely deposited by Brownian diffusion when the mass transfer mechanism is forced convection to the wall of a tube at a Reynolds number of order 10000. (For lager diameter particles inertial deposition mechanisms become important.) Brownian diffusion coefficients of particles in this diameter range are orders of magnitude smaller than molecular diffusion coefficients of sodium sulfate molecules in SCWO. (See Section 5.1.) Furthermore, for turbulent forced convective mass transfer, the mass transfer coefficient scales as the diffusion coefficient to (roughly) the 2/3 power. Thus, one expects that, if transpiration inhibits heterogeneous nucleation on the inner surface of the platelet, then a substantial reduction in deposition rate may be realized.

Not surprisingly, corrosion of the stainless steel 304L porous platelet liner did occur when sodium sulfate solution was run through the transpiring wall reactor at Sandia National Laboratories. Ahluwalia et al. [2] suggest that corrosion of a stainless steel platelet could be quantified by monitoring the concentration of chromium, nickel and iron in the effluent. Ahluwalia et al., further note it would be interesting to simultaneously place a stainless steel witness wire in the center of the reactor and compare the rates of corrosion on the witness wire and inner wall of the platelet. Another potential advantage of the Sandia reactor is that by heating the aqueous waste stream with H_2O (or fuel) injected through the diamond-shaped holes in the porous platelet liner it is possible for the solution entering and leaving the main reactor to be at (subcritical) temperatures which are low enough to reduce corrosion. Moreover, temperatures in preheat

lines can be maintained below the solubility temperature of salts which may be contained within the aqueous waste stream. However, as already noted, fouling rates were especially high near the diamond-shaped holes where the high temperature water was injected into the top of the reactor. Nonetheless, one wonders, if, under appropriate conditions, it may be possible to reduce corrosion and deposition rates in preheaters in SCWO systems, using cleverly designed injection heating methods in the presence of transpiration.

McGuinness [59] deems it will be possible to operate the central reaction zone of transpiring wall SCWO reactors at temperatures higher than those currently possible in existing SCWO reactors. (The SCWO process is exothermic; therefore, the hottest location in the reactor occurs in the reaction zone and not along the inner surface of the transpiring wall.) Higher oxidation temperatures may permit waste remediation within shorter residence times. McGuinness does note, however, that surfaces of SCWO reactors may be significant catalysts; therefore, the gains in conversion caused by higher temperatures may be offset by reduced surface areas. For example, Webley et al. [91] showed that oxidation of ammonia in the SCWO process was partially catalyzed by an Inconel 625 reactor wall. McGuinness further suggests that the transpiring walls may be fabricated from materials which could not withstand the elevated temperature of the reaction zone, but are more corrosion resistant. However, failure to design an entire SCWO reactor vessel to withstand the highest temperatures possible at any location within it would cause safety concerns.

The tests run by Haroldsen et al. [36] at Sandia National Laboratories which demonstrate transpiration can appreciably reduce salt deposition rates at conditions relevant to SCWO are described next. In the baseline test, pure water was run through the reactor to bring it up to temperature. Once steady state conditions were reached, a 1.5 wt% salt, aqueous sodium sulfate solution was run through the reactor for two hours without transpiration water to quantify the rate of salt deposited in the reactor when it was not "protected" by transpiration. During this test, the aqueous sodium sulfate solution entered the top of the reactor at a temperature of 235 °C and a mass flow rate of 1.7 grams/sec. Hot water at a temperature of 625 °C and a mass flow rate of 3.5 grams/sec was injected through the diamond-shaped holes located at the top of the platelet. Room temperature water at a mass flow rate of 8 grams/sec was injected through the diamond-shaped holes located at the bottom of the platelet. The electrical conductivity of the effluent leaving the system as a function of time during this baseline test is shown in Fig. 1-7. (The units of electrical
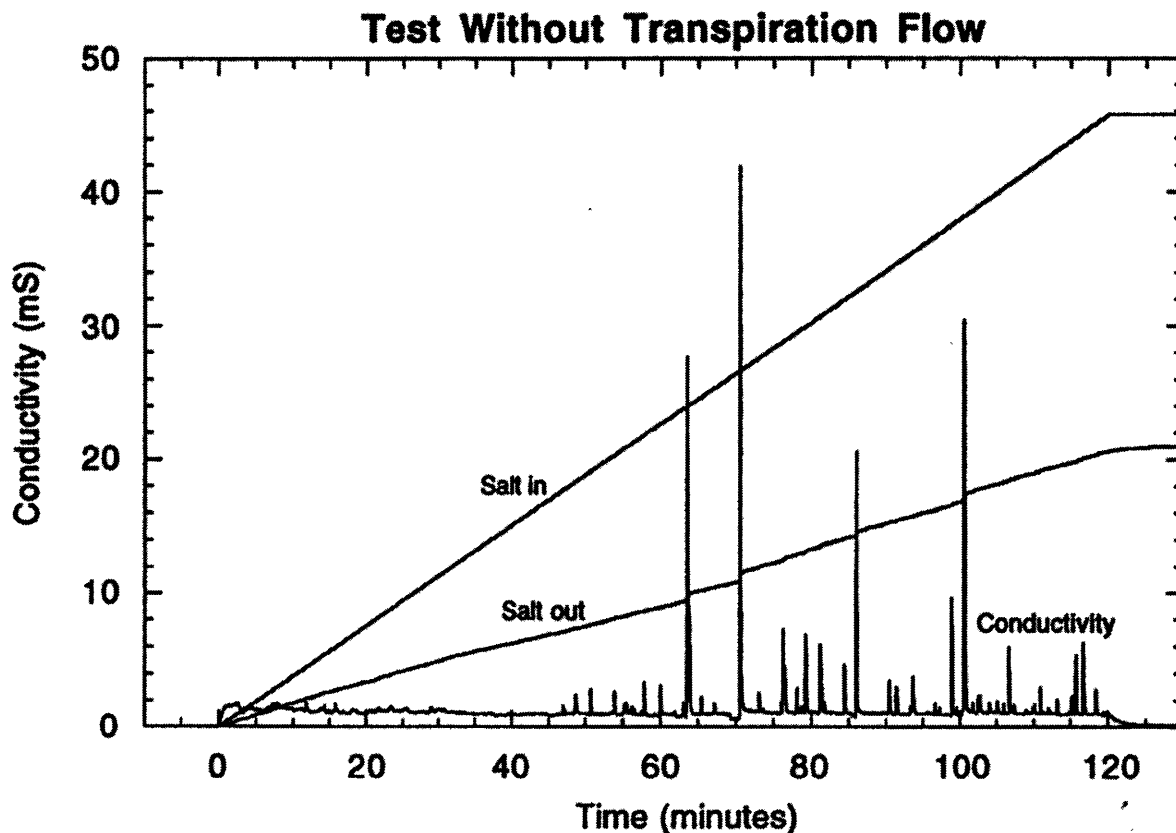
Figure 1-7: Electrical conductivity of the effluent without transpiration. Integrated electrical conductivity of the salt supplied to the reactor and in the effluent are shown by the curves labelled "salt in" and "salt out" respectively. This figure was extracted from Haroldsen et al. [36].

conductivity in Fig. 1-7, "mS", are, presumably, milli-Siemens.)

The spikes in the electrical conductivity signal were attributed to pieces of salt intermittently dislodging

from the inner wall of the platelet. The curves labelled "salt in" and "salt out" are the accumulated quantities

of salt which have been supplied to the reactor and have egressed from the reactor respectively as a function

of time. The "salt out" curve was computed by integrating the electrical conductivity of the effluent with

respect to time. However, the short duration of the spikes in the electrical conductivity signal introduced

uncertainty when "salt out" curves were determined by integration. Small variations in mass flow rates

during the experiment and not compensating for temperature in the electrical conductivity measurement

added more uncertainty to the computed "salt out" curves [36]. Unfortunately, the uncertainty in the "salt

out" curves was not quantified. Approximately 55% of the salt supplied to the reactor did not egress over the

entire two hours of the baseline test as per Fig. 1-7. It is, perhaps, somewhat surprising that the percentage of total salt supplied to the reactor during the run which had egressed was essentially independent of time.

Since such a large fraction of the salt supplied to the reactor deposited on the platelet in the absence of transpiration, one suspects a substantial amount of salt was diffusing to the inner surface of the platelet in molecular form and subsequently nucleating heterogeneously there. We investigated this assessment by performing two simple mass transfer calculations. In the first calculation, all of the salt in the bulk solution was assumed to be present in the form of 2 micron diameter (spherical) particles. In the second calculation, it was assumed that (associated) salt molecules diffused to the inner wall of the platelet and subsequently nucleated heterogeneously there. The sticking efficiency of the particles which reached the inner wall of the platelet was assumed to equal unity. In the molecular diffusion calculation, it was assumed the solubility on the inner wall of the platelet was equal to zero since sodium sulfate is essentially insoluble in water at 400 $^\circ C$ and 250 bar as per Section 4.3. For both situations, a simple mass exchanger calculation shows that the the bulk salt concentration as a function of the axial distance from the inlet to the reactor (denoted by x) equals:

$$\frac{\omega_{A_x}}{\omega_{A_o}} = exp\left(-\frac{h_m P \rho}{\dot{m}}x\right),$$ (1.3)

where ω_{A_x}, ω_{A_o}, h_m, P, ρ and $\dot{m}$ denote the mass fraction of salt in the bulk solution at a distance x from the inlet of the reactor, mass fraction of salt in the bulk solution at the inlet to the reactor, mass transfer coefficient between the bulk solution and wall of the reactor, interior perimeter of the platelet, solution density and mass flow rate of solution respectively.

The Sherwood numbers for deposition of Brownian particles and sodium sulfate molecules on the inner wall of the platelet are functions of the Reynolds number of the flow and the Schmidt number of the solution. The Brownian diffusion coefficient of 2 micron diameter (spherical) particles in SCW at the bulk temperature and pressure characterizing the experiments, i.e., 260 bar and 400 $^\circ C$ is about $1.9*10^{-11}$ m^2/s based on the Stokes-Einstein equation. The molecular diffusion coefficient of (associated) sodium sulfate in SCW at this temperature and pressure is estimated to be about $0.25*10^{-7}$ m^2/s. (See Section 3.7.5.) It follows

that the Schmidt numbers characterizing Brownian and molecular transport are approximately 8500 and 6.5 respectively. The Reynolds number characterizing the flow through the reactor in the experiment run without transpiration was about 7700. The mass transfer coefficients required in Eq. 1.3 were determined by applying the analogy between heat and mass transfer to the "Colburn" equation [20] for turbulent forced convective heat transfer in a tube. (Inertial deposition of the particles was assumed to be unimportant.) The length of the reactor not including the bottom section where cold water was injected is 78.7 cm. The Brownian and molecular diffusion models predict that about 10 and 100% respectively of the salt supplied to the reactor will have deposited at 78.7 cm from its inlet. In the experiment without transpiration, approximately 55% of the salt supplied to the reactor deposited. Thus, perhaps, both Brownian and molecular diffusion mechanisms were important.

Haroldsen et al. [36] conducted experiments to quantify the rate of deposition of sodium sulfate in the reactor as a function of the wall platelet effectiveness ratio, η, defined by,

$$\eta = \frac{C_{core} - C_{wall}}{C_{core} - C_{transpiration}}, \tag{1.4}$$

where C is the *calculated* concentration of waste at the center of the reactor (core), on the surface of the reactor (wall) and in the transpiration flow. Since the transpiration flow is always pure water $C_{transpiration}$ equals 0. System parameters for "low" (0.83), "medium" (0.91), and "high" (0.94) effectiveness ratios (averaged over the length of the reactor) were determined by Gencorp, Aerojet using an (apparently proprietary) computer design code; however, the details of this procedure were not provided. Intentions are to use this code to design larger transpiring wall SCWO reactors, e.g., the reactor at Pine Bluff Arsenal facility, by assuming that the rates of deposition measured at Sandia can be correlated with the effectiveness ratio as the sole scaling parameter. However, Haroldsen et al. [36] did not find any identifiable correlation between the average effectiveness ratio and deposition rate in their experiments. Moreover, it seems virtually impossible that one dimensionless parameter would suffice for the scale-up of such a complicated system.

Operating conditions for the "low" effectiveness ratio (0.83) test were closest to the conditions in the baseline test without transpiration; therefore, this experiment is discussed here. During the "low" effective-

ness ratio experiment, a 3 wt% salt, aqueous sodium sulfate solution entered the top of the reactor at a temperature of 235 $^\circ C$ and a mass flow rate of 1.4 grams/sec. Hot water at a temperature of 560 $^\circ C$ and mass flow rate of 3.8 grams/sec was injected through the diamond-shaped holes located at the top of the reactor and room temperature water was injected through the diamond-shaped holes located at the bottom of the reactor at a mass flow rate of 10.7 grams/sec. Pure H_2O at a temperature of 455 $^\circ C$ was supplied to the middle distribution plenum by the "upper" and "lower" transpiration streams at mass flow rates of 4.7 and 4.9 grams/sec respectively.

The electrical conductivity of the effluent as a function of time during the "low" effectiveness ratio test is shown in Fig. 1-8. During the first 50 minutes of this experiment the amount of "salt out" of the reactor was close to the amount of "salt in", i.e., roughly 80% of the salt supplied to the reactor egressed. Spikes in the electrical conductivity of the effluent appeared virtually as soon as the run began; whereas, spikes did not appear until after about 45 minutes elapsed in the absence of transpiration as per Fig. 1-7. Haroldsen et al. [36] hypothesize this happens because salt which adheres to the platelet is more easily dislodged in the presence of transpiration . At approximately 135 minutes into this run, a plug dislodged from near the top of the reactor and the final twenty minutes of the run resembled the first 20 minutes of the run. However, during the five minutes prior to the dislodging of this plug the effluent was, somewhat alarmingly, essentially pure water. (As per Figure 1-6, the electrical conductivity of the effluent was essentially zero for the 5 minutes prior to the dislodging of this plug.) By the end of the run, virtually all of the salt which had been supplied to the reactor egressed. This proves transpiration can dramatically affect the rate of scale buildup during SCWO. Haroldsen et al. [36] note that the virtually complete closure attained on the sodium sulfate mass balance was unexpected, even in the absence of deposition, because of the aforementioned uncertainties when computing the "salt out" curves. Not surprisingly, a modest amount of salt was, in fact, left in the reactor after this experiment; therefore, the "salt out" curve should have been below the "salt in" curve at the end of the experiments. It is, perhaps, somewhat surprising that even 20% of the salt supplied to the reactor deposited. One would suspect the transpiration to cause nucleation to be predominantly homogeneous and/or secondary and thus, perhaps, a lower deposition rate. It is noteworthy that most of the deposition which did occur in the reactor during the "low" effectiveness ratio test was in the top region near the injected hot
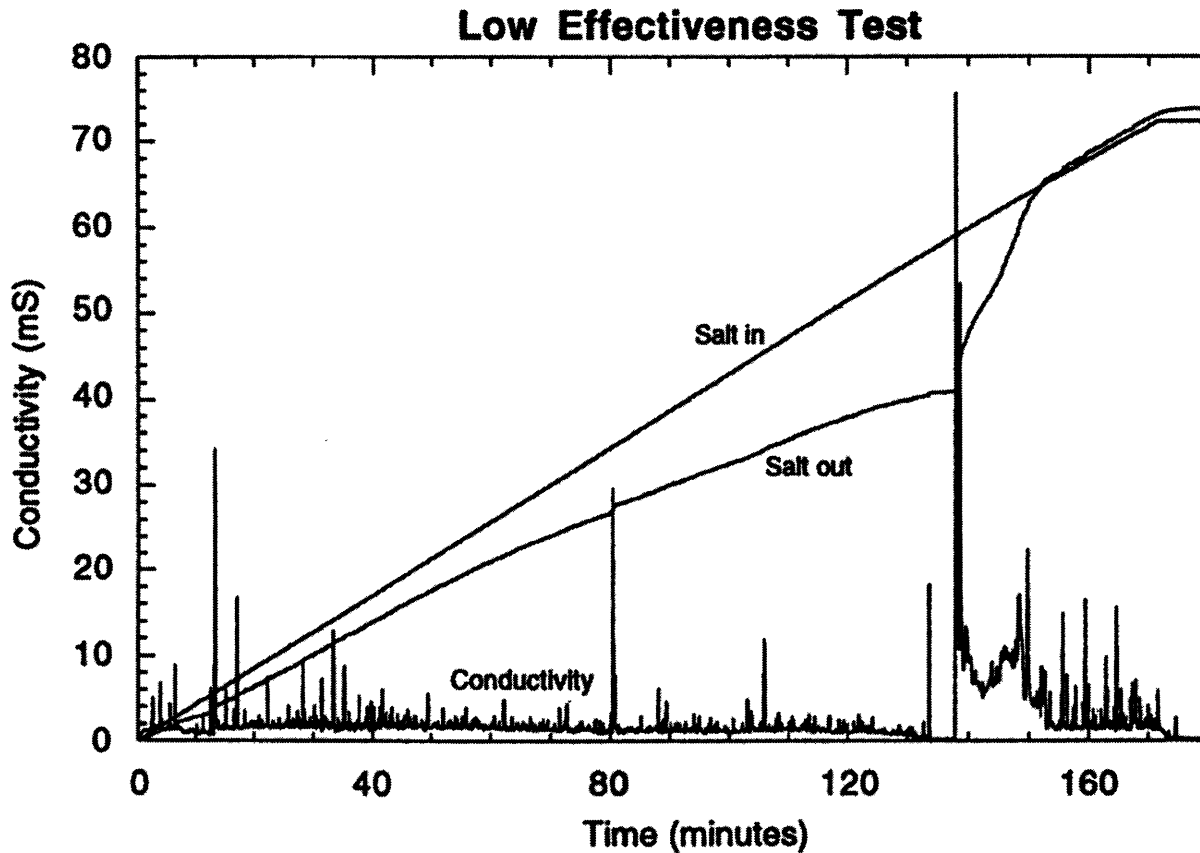
Figure 1-8: Electrical conductivity of effluent as a function of time in the "low" effectiveness ratio experiment. Integrated electrical conductivity of the salt supplied to the reactor and in the effluent are shown by the curves labelled "salt in" and "salt out" respectively. This figure was extracted from Haroldsen et al. [36].

water. In fact, inspection of the reactor after the tests run without transpiration and at "low" effectiveness ratio showed that the amount of salt deposited in the middle portion of the reactor was *very dramatically* reduced by the presence of transpiration. This is a very significant observation. The "medium" and "high" ratio effectiveness tests run by Haroldsen et al. were less conclusive for reasons explained in reference [36]. A different (coaxial) method of injection heating did not alleviate the high fouling rate near the top of the reactor.

In the "low" effectiveness test, the mass flow rate of sodium sulfate was only 0.28% of the sum of the mass flow rates of aqueous sodium sulfate solution, injected hot water and transpiration water. All of these streams must be preheated at some cost. In the "medium" and "high" effectiveness ratio tests this ratio was even lower, i.e., 0.05% and 0.02% respectively. Even in the test run without transpiration the mass flow rate

of salt was only 0.49% of the mass flow rate of aqueous sodium sulfate solution plus injected hot water. In commercial applications restricting the mass flow rate of salt supplied to the reactor to such low fractions of the sum of the mass flow rates of preheated solution and preheated water would make SCWO of many important wastes uneconomical. Haroldsen et al. [36] note that injecting fuel instead of hot water into the top of the reactor could alleviate this problem to a large extent. It would be interesting to determine if this could also help alleviate the severe deposition problems near and in the diamond-shaped holes located at the top of the reactor.

The tests run by Haroldsen et al. demonstrate that transpiration can appreciably reduce, but unlikely eliminate, scale buildup during SCWO; therefore, a subsequent test was run to determine how quickly and to what extent salt could be removed from the reactor by periodically flushing it with cold water. At the beginning of this test the "upper" and "lower" transpiration streams supplied pure water at a temperature of 450 $^\circ C$ to the middle section of the distribution plenum at mass flow rates of 5.1 and 4.7 grams/sec respectively. Simultaneously, pure water entered the top of the reactor at a mass flow rate of 0.71 grams/sec and temperature of 100 $^\circ C$ and (room temperature) cooling water was injected through the diamond-shaped holes located at the bottom reactor at a mass flow rate of 9.5 grams/sec. (Heating water was not injected through the diamond-shaped holes in the platelet at the top of the reactor at any point during this test.) Once steady state conditions were established, a 2.7 wt% salt, aqueous sodium sulfate solution at a temperature of 100 $^\circ C$ and a mass flow rate of 0.71 grams/sec was fed into the top of the reactor instead of pure water for 30 minutes and salt deposited throughout the reactor. (The time when the feed supplied to the reactor was switched from pure water to aqueous sodium sulfate solution was designated as time equal to "zero".) After 30 minutes elapsed, the stream fed into the top of the reactor was switched from aqueous sodium sulfate solution back to pure water at the same temperature and mass flow rate. The temperature of the water supplied to the "upper" and "lower" transpiration streams was lowered to approximately 445 and 425 $^\circ C$ respectively at about this time as well. The results of this test are shown in Fig. 1-9. After about 11 minutes (41 minutes of total run time), the conductivity of the effluent approached zero, i.e., salt was no longer leaving the reactor as per Fig. 1-9. At this point "cold rinse water" (at a temperature of 35 $^\circ C$) was injected through the diamond-holes at the top of the reactor at a mass flow rate of 3.3 grams/sec. As

shown in Fig. 1-9, at about 41 minutes into the experiment, i.e., virtually as soon as the "cold rinse water" was injected through the diamond-shaped holes at the top of the reactor, a large spike in the electrical conductivity of the effluent appeared. (Another large spike appeared about 2 minutes later.) This suggests large pieces of salt were quickly dislodged upon injecting the cold water. After about 10 minutes of cold water injection (50 minutes of total elapsed time) virtually all of the salt which had been supplied to the reactor during the entire test had egressed. Repeating this procedure several times in succession demonstrated the reactor could be fouled and flushed/cleaned in a cyclic manner. However, during the 30 minute deposition period of this test the ratio of the mass flow rate of salt fed into the reactor to the sum of the mass flow rates of aqueous sodium sulfate solution, injected hot water and transpiration water was only 0.18%. Thus, the mass flow rate of sodium sulfate supplied to the reactor compared to the mass flow rate of heated solution plus heated water sent through reactor are still very low for important potential commercial applications of SCWO. Also, after 30 minutes had elapsed only about half of the salt fed into the reactor had egressed. It is noted that the rinsing concept can, obviously, be applied in the absence of transpiration.

The presence of transpiration in the tests run at Sandia National Laboratories dramatically reduced the deposition rate in the middle 26 inches of the reactor, i.e., where transpiration was present. Thus, the use of transpiring walls to reduce fouling (and corrosion) of the walls of SCWO reactors may hold much potential. However, deposition was always problematic in the heating zone near the top of the reactor and the fraction of salt supplied to the reactor which deposited was often alarmingly high. For example, the medium effectiveness ratio test (the results of which are not shown here) was terminated after virtually no salt had egressed from the reactor over a 40 minute period. The effectiveness ratio and the deposition rate in the reactor showed no identifiable relationship. Although part of this problem may be attributable to the excessive fouling rates near the top of the reactor, it is hard to fathom that one scaling parameter could suffice for scale-up purposes under such complicated conditions. Conclusive evidence was provided that an SCWO reactor could be fouled by scale and cleaned by "cold rinse water" in a cyclic manner. The amount of salt supplied to the reactor in the tests run at Sandia was a very small fraction, always less than 0.49%, of the amount of heated water/heated solution supplied to the reactor on a mass per unit time basis. This is insufficient for many commercial wastes for which SCWO offers advantages over incineration. Further tests
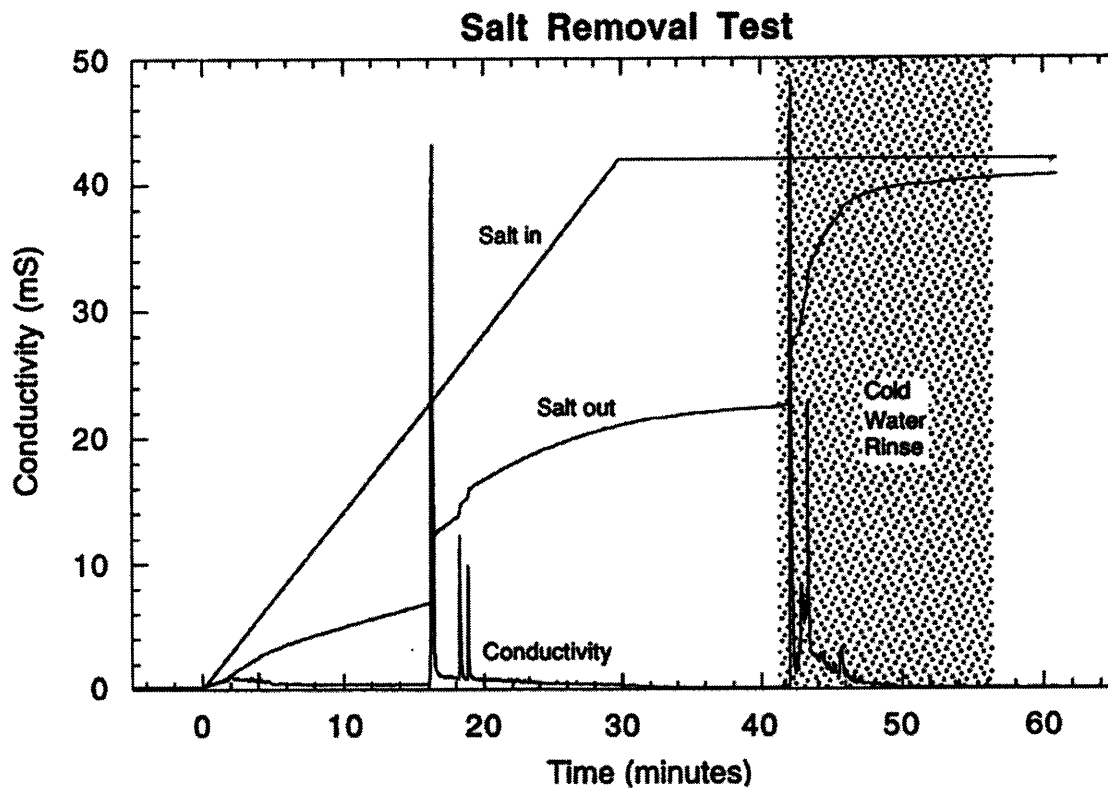
Figure 1-9: Electrical conductivity of the effluent as a function of time during the salt removal test. Integrated conductivity of the salt supplied to the reactor and in the effluent are shown by the curves labelled "salt in" and "salt out" respectively. This figure was extracted from Haroldsen et al. [36].

with higher mass fractions of salt using the transpiring wall platelet reactor at Sandia National Laboratories may prove fruitful. Running deposition experiments using salts with different phase behavior in SCW, e.g., NaCl, would also be interesting.

In the spring of 1998, the United States Army will begin disposing colored smoke and dye using a transpiring wall SCWO reactor at its Pine Bluff Arsenal facility in Arkansas. The platelet for this reactor was manufactured from Inconel 625 and has a platinum liner; therefore, it is more resistant to corrosion than the one used at Sandia National Laboratories. There are other substantial differences between the (1/4 scale) Sandia test reactor and the reactor at the Pine Bluff Arsenal Facility. For example, hot water is not injected to heat the waste in the Army's reactor. Instead feed will be heated using a small amount of hot water and the injection of supplementary fuel. (See Haroldsen et al. [36] for more detail.) However, platelets are used to control corrosion and deposition in both reactors and the design of the reactor about to come on-line at the Pine Bluff Arsenal facility was based largely on the studies performed at Sandia National Laboratories. The effectiveness of the transpiring wall platelet used in this new reactor in limiting corrosion and deposition rates will be very interesting.

1.3.4 Assisted Hydrothermal Oxidation Reactor

SRI (Palo Alto, CA) recently proposed a process called Assisted Hydrothermal Oxidation (AHO), a modification of conventional SCWO, to alleviate the corrosion and fouling problems during SCWO of chlorinated wastes. Conceptually the AHO reactor houses a stirred or fluidized source of sodium carbonate (Na_2CO_3). The operating temperature and pressure of the AHO reactor are about 380 $°C$ and 223 bar respectively. Sodium carbonate is insoluble at AHO operating conditions and acts as an in-situ base. Thus, hydrochloric acid produced by oxidation of the chlorinated waste reacts with the sodium carbonate and the sodium carbonate gradually changes to sodium chloride. According to SRI, an added benefit of AHO is accelerated oxidation because the sodium carbonate surfaces catalyze oxidation.

1.3.5 Cross Flow Microfiltration

Goemans et al. [34] recently evaluated the efficacy of a cross flow microfilter, capable of operating within an SCWO environment, for the removal of sodium nitrate from an aqueous sodium nitrate solution at supercritical conditions. Sodium nitrate was selected because its solubility under supercritical conditions has been previously investigated [22] and it is molten at supercritical conditions. (The melting point of sodium nitrate is 306.8 °C.) Goemans et al. note that other salts commonly present in the SCWO process effluent including sodium hydroxide, sodium bicarbonate, magnesium hydroxide, aluminum nitrate and aluminum hydroxide also have melting points below the critical temperature of pure water. Small quantities of the aforementioned molten salts mixed with salts which are solids at SCWO conditions, e.g., solid sodium sulfate and sodium chloride, may explain why even solid salts are considered "sticky" at SCWO conditions.

The cross flow microfiltration system used by Goemans et al. is shown in Fig. 1-10. The filter element was fabricated from stainless steel 316L. It is 2.1 meters long with an OD of 25.40 mm and an ID of 19.05 mm. The pore size is 0.5 mm. Aqueous sodium nitrate solutions containing 0.477 to 2.25 wt% salt, were pumped through the system at 276 bar and temperatures ranging from 400 to 470 °C. Feed flow rates ranged from 63 to 111 kg/hour and filtrate flowrates were between 80 and 100% of the feed flow rates. During each experiment representative samples of filtrate and retentate effluent corresponding to known volumes of effluent were collected. At the end of each experiment, "rinse water" below the critical temperature of pure H_2O was circulated through the system. Sodium nitrate is soluble in water below the critical temperature; therefore, the "rinse water" redissolved most of the sodium nitrate deposits which accumulated within the filter pores and on the equipment walls. The mass of sodium nitrate remaining in the system after each filtration experiment could then be determined by analyzing the rinse water. The sum of the mass of sodium nitrate detected in the filtrate, retentate and "rinse water" ranged from 82 to 126% of the amount of sodium nitrate supplied to the system. Goemans et al. attributed the imprecision in the sodium nitrate mass balances to sodium precipitated with corrosion products that was retained in the apparatus prior to flushing it with "rinse water" and molten sodium nitrate which had precipitated in dead end connecting tubes.
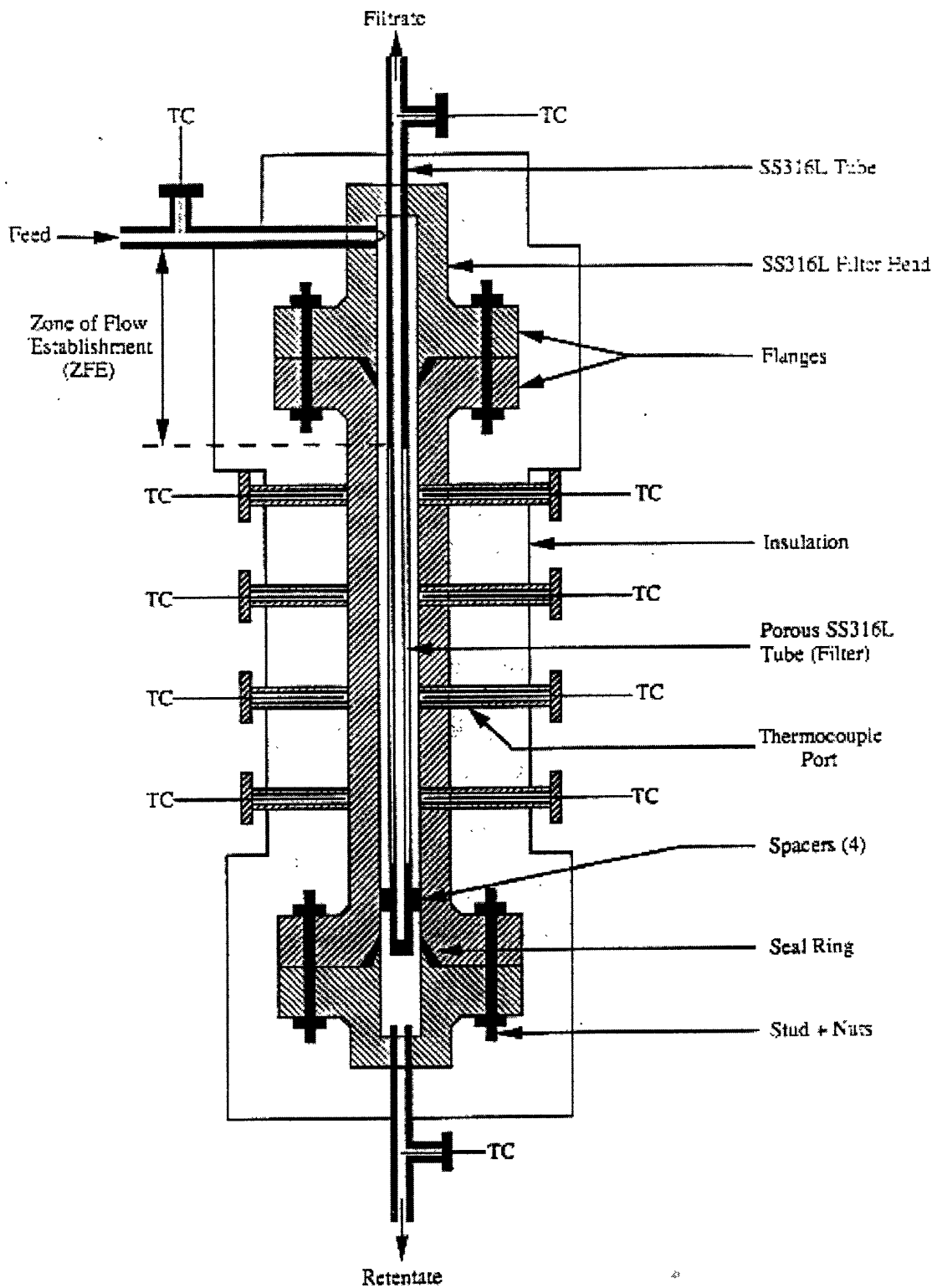
Figure 1-10: Schematic of the cross flow microfilter used by Goemans et al. [34]. This figure was extracted directly from reference [34].

The separation efficiency of the cross flow microfilter was defined as:

$$E = 100 \left(1 - \frac{C_{filtrate}}{C_{feed}} \right),$$ (1.5)

where C is the concentration of sodium nitrate in wt%. The separation efficiency ranged from 60 to 80% for the experiments conducted at temperatures between 420 and 470 °C, but was reduced to 40% for the experiment run at 400 °C. The success of the cross flow microfilter was attributed to the different relative permeability of it for molten salt and supercritical solution. No fouling of the filter membrane was observed, however, it did corrode. Perhaps it is surprising that a molten salt like sodium nitrate was able to flow through the pores in the filter without plugging it.

In a related study, Goemans et al. [35] evaluated the effectiveness of cross flow microfiltration for the purpose of separating α-alumina particles from SCWO. The motivation behind this study was to test the viability of cross-flow microfiltration for separating "non-sticky" metal oxides during SCWO. The filter element was again constructed from stainless steel 316L with a nominal pore size of 0.5 microns. The diameter of the α-alumina particles ranged from 0.8 to 5 microns and the mean particle diameter was 3 microns. All the experiments were run at close to isothermal conditions at a temperature of approximately 400 °C and a pressure of 276 bar. Separation efficiencies were high, ranging from 97.3 to 99.9% by weight. Thus the tests were successful.

1.3.6 Cycling of SCWO Reactors

Recently, Abitibi-Price, Inc. (Mississouga, Canada) and General Atomics (San Diego, CA) jointly patented a method to control scale buildup during SCWO by alternatively supplying a "feeding" stream and a "flushing" stream to a pair of SCWO reactors operating simultaneously when oxidizing heteroatom-containing wastes [13]. The "feeding" stream contains the waste being oxidized and the "flushing" stream is a solution in which scale built up on reactor surfaces is soluble. (The "flushing" stream can be the "feed" stream itself after it has been cooled to a temperature for which the deposited scale is soluble.) In short, scale is permitted to buildup on the surface of one reactor as the "feed" stream passes through it while the "flushing"

stream is dissolving any scale present in the other reactor. At appropriate time intervals, the feed stream is redirected towards the reactor freed from scale deposits and the "flushing" stream is redirected towards the reactor which has a new scale layer. This cycle is repeated continuously. It is noted that this process can accommodate more than two reactors simultaneously. Flushing of SCWO reactors with cold water to remove salt deposits is not a new technology (see for example the 1994 study by Chan et. al. [16]); however, it had not been patented before.

1.3.7 Additional Studies

RPC Waste Management Incorporated (Austin, TX) recently patented a method to add solid particles to inhibit the fouling of SCWO reactors [77]. In brief, when solid salts are present during the SCWO process, e.g., NaCl, additional salts are added, e.g., $NaNO_3$, to form a "blend" of salt with a melting point below the operating temperature of the reactor. Apparently, the molten salt "blends" are less likely to plug the reactor.

MODEC (Waltham, MA), sent stainless steel brushes through their tubular reactors approximately every ten minutes to minimize scale buildup. Other separation techniques have also been looked at in the context of SCWO. For example, Killilea et al. [43] investigated microgravity and impingement/filtration as potential methods for removing metal oxide particles from SCW and Dell'Orco et al. [23] reported cyclone removal efficiencies of up to 99% for micron-sized silica, zirconium oxide and titanium oxide particles. However, salts were not amenable to separation using cyclones because they adhered to the walls of the cyclone.

1.4 Salt Deposition Kinetics Research Studies at SCWO Conditions

1.4.1 Sandia National Laboratories Study

Chan et al. [16] at Sandia National Laboratories (Livermore, CA) studied solubility and salt deposition kinetics in the Na_2SO_4-H_2O system at conditions relevant to SCWO. A 750 cm long, Inconel 625 tube

wrapped with six 375 Watt cable heaters served as the (tubular) reactor. The OD and the ID of the reactor were 1.43 cm and 0.477 cm respectively. When collecting solubility data, a (preheated) 0.5 wt% salt, aqueous sodium sulfate solution was pumped through the reactor at 250 bar. The last 600 cm of the reactor were isothermal to within "several" degrees and, apparently, at the highest temperature in the system. Solution exiting the reactor was rapidly cooled and the concentration of sodium sulfate in the effluent was measured using an ion specific electrode. The concentration of sodium sulfate measured in the effluent was assumed to equal the solubility concentration at the temperature in the isothermal portion of the reactor and 250 bar; therefore, it was assumed that all salt beyond the solubility concentration corresponding to the temperature of the isothermal section of the reactor deposited. Solubility data points were collected at temperatures of approximately 360, 375, 380 and 400 °C and fit by,

$$T_s = 326.6 - 15.55 log_{10}(C) \tag{1.6}$$

where C is the wt% of sodium sulfate in solution. However, the solubility data measured by Chan et al. have been shown to be inconsistent with solubility data from other sources [85]. Solubility data in the Na_2SO_4-H_2O system from a number of different studies are presented in Section 4.3. If, Chan et al. were to measure solubility concentrations at the same temperatures while varying the mass flow rate of solution through their reactor, a la the Teshima [85] study discussed in Section 1.4.2, their data may be better interpreted. Teshima was able to validate his solubility data to a considerable extent by measuring the same concentration of sodium sulfate in the effluent for a given isothermal reactor temperature while varying the mass flow rates of aqueous sodium sulfate solution supplied to the reactor as described in Section 1.4.2.

Deposition experiments were also performed by Chan et al. using the same reactor and following a procedure similar to that used for the solubility experiments. In the deposition experiments, however, over much of the length of the reactor, fluid temperature was an increasing function of (axial) distance from the inlet. The fluid temperature near the exit of the reactor was, apparently, near 400 °C in all the deposition experiments. In each deposition experiment a 0.5 wt% salt, aqueous sodium sulfate solution was pumped through the reactor at various mass flow rates all on the order of 1 gram/sec. Experiments were conducted

for "gradual" and "steep" temperature profiles within the test section. The aqueous sodium sulfate solution was heated at (average) rates of approximately 0.8 °C per cm of reactor length and 1 °C per cm of reactor length in the experiments with "gradual" and "steep" temperature profiles respectively. Each deposition experiment was run until fouling by sodium sulfate deposits plugged the reactor. At time equal to zero in each experiment the pressure drop between the reactor inlet and back pressure regulator was essentially zero. When this pressure drop increased to 70 bar it was assumed that the reactor had been plugged. The time this happened was designated as the plugging time, $t_{p,exp}$, at the conditions of interest.

Chan et al. [16] also developed a simple deposition rate model and compared plugging time predictions by this model to the measured plugging times in their five deposition experiments. The model assumed that the temperature of the aqueous sodium sulfate solution flowing through the reactor was solely a function of the distance from its inlet, i.e., the dependence of the fluid temperature on time, radius, and azimuthal location was assumed to be unimportant. Perhaps, this is a valid assumption, but it was not justified. It is questionable whether or not the radial temperature distribution can be neglected as salt deposits and the flow becomes constricted. It was further assumed that supersaturation did not occur and all salt which precipitated immediately deposited on the reactor walls at the same location. Eqn. 1.6 was used to determine the solubility concentration as a function of temperature at 250 bar. It follows from a simple mass balance, that the cross sectional area of salt deposited on the reactor wall as a function of time and distance from the reactor inlet may be determined from the measured bulk temperature profile. The plugging time predicted by the model simply equals the time required for sodium sulfate to fill the cross section of the reactor tube at the axial location where the deposition rate is maximum. The mass flow rate of aqueous sodium sulfate solution through the reactor, nature of the temperature profile within the reactor, measured plugging time, calculated plugging time and discrepancy between the calculated and measured plugging time are given in Table 1.1.

The plugging times calculated from the deposition model, $t_{p,calc}$, compare well with the five measured plugging times. (For four out of the five data points the model predicted the measured plugging time to within 20%.) However, the results of the model are highly suspect for several reasons. First, the model can not predict the correct axial distance from the inlet at which deposition begins. This is because the wall

Test #	Flow Rate $\frac{gram}{sec}$	Temperature Profile	$t_{p,exp}$ minutes	$t_{p,calc}$ minutes	% Error percent
1	0.6	"gradual"	48	49.1	2%
2	0.6	"gradual"	41	49.1	20%
3	1.2	"gradual"	23	24.5	7%
4	1.5	"gradual"	37	19.6	-47%
5	0.6	"steep"	28	23.0	-18%

Table 1.1: Mass flow rates, temperatures profiles, measured plugging times, calculated plugging times and percent discrepancy between calculated and measured plugging times in the Chan et al. study [16].

temperature of the reactor is, obviously, above the bulk temperature and, therefore, salt will be insoluble at the wall of the reactor before the bulk temperature of the solution has been increased to the solubility temperature of a 0.5 wt% salt, aqueous sodium sulfate solution at 250 bar. For sufficiently high wall-to-bulk temperature differences, this could cause severe error; however, Chan et al. do not quantify the wall-to-bulk temperature differences present in their experiments. Secondly, to calculate plugging time, Chan et al. implicitly assume the porosity of the salt layer is zero by using the density of anhydrous sodium sulfate to compute the thickness of the scale layer from the mass of salt deposited at each axial location as a function of time. This assumption is highly questionable. (At the conditions investigated in this dissertation, for example, porosity in sodium sulfate scale layers formed at conditions relevant to SCWO were consistently measured to be around 2/3.) Moreover, Chan et al. do not provide any information concerning their measurements of "fluid temperature", but their plugging time calculations and solubility data are highly dependent on "fluid temperature." Furthermore, the Chan et al. solubility data were inconsistent with those from other studies, but used to determine the concentration of sodium sulfate in the solution flowing through the reactor as a function of "fluid temperature" and, hence, calculate plugging times. A substantial attempt to determine the nucleation mechanism in their experiments was not made by Chan et al., but as previously discussed in this chapter the nucleation mechanism and deposition rate are very closely related. In fact, Chan et al. claim that analysis of the salt formed inside their reactor after their experiments indicated that it was "anhydrous sodium sulfate that was precipitated *homogeneously* from the fluid as it was heated." If this is true, it is inconsistent with all salt depositing on the surface of the reactor at the location where it precipitates because the mass transport of salt particles (as opposed to salt molecules) to the wall of the

reactor must be very slow. Finally, the possibility of mass transfer inside the porous salt layer formed in the reactor is not considered by Chan et al. Although the Chan et al. deposition model is crude, it may be very useful under certain conditions; however, it must be better justified when applied. Significant virtues of the Chan et al. model are its simplicity and the ease with which it may be implemented.

1.4.2 University of British Columbia (UBC) Study

Recently, solubilities and salt deposition kinetics in the Na_2SO_4-H_2O system at conditions relevant to SCWO were also measured in an interesting study performed at the University of British Columbia (UBC). Limited results from this study are given by Teshima et al. [86] and a very detailed and lucid account of it is provided in the recent Master's Thesis by Teshima [85]. The experiments and analyses conducted by the UBC group are summarized in this section.

Aqueous sodium sulfate solutions are pumped through the SCWO system at UBC at a pressure of 250 bar and high mass flow rates of up to 2.2 liter/min at STP. Once pressurized, the feed passes through a regenerative heat exchanger and then two separately controlled preheaters. (Power is supplied to the preheaters by running AC current through their Inconel 625 walls.) The test section/reactor of the SCWO system at UBC is comprised of four sections of 0.952 cm ID X 0.622 cm OD Inconel 625 tube. Unions separate the four sections and Inconel-sheathed thermocouples inserted into the unions measure the bulk solution temperature at 5 different (axial) locations along the reactor. At the beginning and the end of the reactor are 0.30 m long unheated lengths. Between the unheated lengths of the reactor are two heated sections. Each one is 1.52 m long and heated independently by direct electrical heating. The total (tubular) reactor length is 3.8 m and the length to (inner) diameter ratio is about 400. All heated sections of the UBC SCWO system are insulated in 15.2 X 15.2 cm boxes of ceramic board.

The Reynolds number, based on the diameter of the test section is maintained between 33000 and 180000 and natural convection is unimportant. (Obviously, the flow through the reactor is turbulent.) Thermocouples spot welded to the external wall of the reactor measure its temperature at twenty and nine locations along its top and bottom respectively. (The top to bottom temperature differences measured were sufficiently small to confirm the analysis performed by Teshima [85] which showed natural convection to

be irrelevant at the conditions investigated.) Differential pressure cells measure the pressure drop across each of the two (1.52 m long) heated sections of the reactor. Solution leaving the reactor passes through a regenerative heat exchanger, a process cooler and, finally, a back pressure regulator. During selected experiments the electrical conductivity of the effluent is measured to determine the concentration of sodium sulfate in it.

During the solubility experiments performed at UBC the entire test section was maintained as isothermal as possible. (The difference in bulk solution temperature between the inlet and the outlet of the test section was approximately 1 $°C$ in the solubility experiments.) The pressure in the test section was approximately 250 bar during all of the solubility experiments. To determine the solubility concentration at the temperature of interest, it was assumed that, as the aqueous sodium sulfate solution passed through the (isothermal) reactor, *all* salt above the solubility limit deposited on its walls. Provided this is true, the concentration of sodium sulfate in the effluent leaving the system equals the solubility concentration at the temperature of the isothermal reactor and 250 bar. The assumption that all sodium sulfate in solution beyond the solubility concentration corresponding to the temperature in the (isothermal) reactor and 250 bar deposited was tested by running aqueous sodium sulfate solution through the system at different mass flow rates, but at the same inlet concentration and reactor temperature. The solubility data collected at different mass flow rates and the same inlet concentration and reactor temperature were consistent; therefore, the assumption seems credible. Moreover, the solubility data from the UBC study agrees reasonably well with those from other studies as per Section 4.3. Twenty-two solubility data points were collected at temperatures between about 340 and 510 $°C$ and a pressure of 250 bar. This is a considerable number of solubility data. Selected results are provided in Section 4.3, along with those from other studies.

The UBC group also conducted fourteen sodium sulfate deposition experiments. The concentration of sodium sulfate in the solution supplied to the system in the deposition experiments ranged from 0.652 to 1.066 wt% and the mass flow rate of solution through the system was between 0.62 and 2.22 kg/min. The solutions entered the reactor at temperatures between 363 and 375 $°C$. Direct electrical heating of the reactor caused the bulk solution temperature at its outlet to range from 384 to 386 $°C$. (At 363 and 386 $°C$, sodium sulfate is soluble in water to 2.32 and 0.055 wt% respectively at 250 bar based on the Teshima [85]

solubility data.) Each deposition experiment was run until a pressure difference approaching 55 kPa across one of the two heated sections of the reactor was detected. (Pressure excursions of this magnitude were assumed to signify the reactor was about to plug.) The duration of the experiments ranged from about 1 minute to about half an hour and was, obviously, a function of the concentration of sodium sulfate in the feed, mass flow rate of solution through the reactor, bulk solution temperature at the inlet to the reactor and power supplied to the reactor. At the end of each run, the system was flushed with cool distilled water to remove all of the scale deposited.

In six of the deposition experiments the concentration of sodium sulfate in the effluent during the deposition and flushing periods was measured. For these six runs mass balances were performed to check if the mass of sodium sulfate supplied to the system during the deposition period was consistent with that which egressed during the deposition period and subsequent flushing. The percentages of the mass of salt supplied to the system measured in the effluent were -19.2%, -17.7%, 74.2%, 23.0%, 16.7% and 7.7%. (Negative numbers signify less salt was collected than delivered to the system over the course of an experiment.) The run in which 74% more sodium sulfate exited the system than was supplied to it according to the measurements was alarming and there were some uncertainties in the mass balances. However, the mass balances for the other five runs seemed quite reasonable. (See the Master's thesis by Teshima [85] for more detail.)

The mass of salt deposited in the reactor as a function of distance from its inlet was inferred from the measured external wall temperature profiles *at the time at which 0.024 kg of sodium sulfate had been supplied to the reactor.* (It was desirable to compare the mass/volume of salt deposited in different deposition experiments at a time for which the same mass of salt had been supplied to the reactor. At least 0.024 kg of salt was supplied to the reactor in every run before a plug was detected; therefore, it was the logical datum.) The mass of salt as a function of distance from the inlet of the reactor at the time 0.024 kg of salt had been supplied to the reactor was also independently predicted using four different mass transfer models. Then, the results were compared for each run. The remainder of this section describes the procedure followed to accomplish this task and provides some representative results.

The UBC group developed a program to compute the external wall temperature profile of their reactor at steady state conditions when pure (near-supercritical) water flowed through it. This program was validated

by the measured external wall temperature profiles in two simple heat transfer experiments. The inputs to this program were the ID of the reactor, OD of the reactor, rate of heat generation in the reactor walls caused by direct electrical heating, bulk fluid temperature at the reactor inlet and pressure of the system (250 bar). The reactor was divided into a series of control volumes, each of which was assumed isothermal in the axial direction. The bulk temperature of each control volume was calculated from a simple energy balance which assumed the exterior wall of the (heated) reactor was perfectly insulated. For each control volume, a Nusselt number was calculated from the correlation proposed by Swenson et al. [84] using thermodynamic and transport properties evaluated at the bulk temperature of each control volume and 250 bar. (The Swenson et al. correlation is one of many which attempt to account for the complex variable property effects often present when heat is being transferred by forced convection to/from supercritical water.) Next, the heat transfer coefficient resulting from the Swenson correlation based on fluid properties evaluated at the bulk temperature (and 250 bar) of the solution in each control volume was used to determine the wall temperature of each control volume. Then, the same procedure was repeated, but the thermodynamic and transport properties used in the Swenson et al. correlation were based on the bulk *and* wall temperatures. Iterations were performed until refining the evaluation of the thermodynamic and transport properties used in the Swenson et al. correlation changed the wall-to-bulk temperature difference by 0.01 °C or less in every control volume. The results of this procedure provide the bulk and inner wall temperature profiles as a function of distance from the inlet of the reactor at steady state conditions. All of the heat generated in the walls of the Inconel 625 reactor is assumed to be transferred to the water flowing through it and the bulk temperature has been calculated as a function of position as above. Thus, the solution of a simple one-dimensional heat conduction problem (with a heat generation term) provides the external wall temperature profile of the reactor. The pure water heat transfer computations were validated by comparing the measured and predicted bulk and external wall temperature profiles in the two simple heat transfer experiments with pure water. In both cases the agreement was extremely good. (See the Teshima Master's Thesis [85] for more details.)

The thermal conductivity of sodium sulfate at temperatures pertinent to the Teshima et al. deposition experiments, i.e., above 365 °C, is currently unavailable. (Even at room temperature the thermal conduc-

tivity of (crystalline) sodium sulfate does not seem to be available.) Inferring the mass/volume of scale deposited as a function of the distance from the inlet to the UBC reactor from the measured external wall temperature profiles necessitated estimation of the thermal conductivity of the scale layer. The UBC group developed an interesting procedure to accomplish this task. It was applied to the six experiments for which a mass balance on the sodium sulfate was performed. It was assumed that the thermal conductivity of the scale layer was equivalent to a network of salt and (stagnant) water columns in parallel, i.e.,

$$k_{layer} = (1 - \phi) k_{salt} + \phi k_{water} \tag{1.7}$$

The porosity in the expression for the thermal conductivity of the salt layer was assumed to equal 0.71 based on the results of the study by Hodes et al. [40]. The thermal conductivity of the aqueous sodium sulfate solutions at near-supercritical conditions is not available; therefore, it was approximated as that of pure water. At a temperature of 375 $°C$ and a pressure of 250 bar, for example, the thermal conductivity of pure water is 0.41 W/m/K [30]. (The aqueous sodium sulfate solutions were approximated as pure water to determine the thermodynamic and transport properties, other than molecular diffusivity, necessary for all heat and mass transfer calculations. The molecular diffusivity of sodium sulfate in water was estimated to equal $0.25*10^{-7}$ m^2/sec at conditions of interest.)

The thermal conductivity *of the sodium sulfate* within the scale layer was estimated for the six runs a mass balance on sodium sulfate was performed. Subsequently, Eq. 1.7 was applied to compute the thermal conductivity of the scale layer. For each run, an initial guess of the thermal conductivity of the sodium sulfate in the scale layer was made and iterations were performed until a thermal conductivity value yielded results consistent with the measured external wall temperature profile *and* mass of salt deposited in the reactor *at the conclusion of the deposition period in a given experiment*. The following procedure was applied to determine if each guess of the thermal conductivity of the sodium sulfate in the scale layer was "correct." First, the procedure described above was used to compute the external wall temperature profile of the reactor assuming deposition did not occur at the operating conditions of interest. Next, a thin layer of salt was added to each control volume for which the calculated and measured external wall temperature were inconsistent.

Then, the external wall temperature of each control volume was recalculated. In the control volumes in which thin layers of salt were added, the additional thermal resistance and decreased cross sectional area caused by them was accounted for. The updated external wall temperature profile was then compared to that measured and thin salt layers were gradually added to the control volumes as necessary until the measured and computed external wall temperatures were consistent. Then, based on the total volume of salt "added" to the reactor by the creation of the scale layer, the mass deposited over the course of the run was calculated. This calculated mass of salt deposited was compared to the mass of salt deposited measured experimentally. New thermal conductivity values for the sodium sulfate were "guessed" until the mass of salt which was added to the reactor to force the measured and calculated external wall temperature profiles to match equaled the experimentally measured mass of salt deposited.

For the six runs to which the foregoing procedure was applied, the estimates of the thermal conductivity of the sodium sulfate in the scale layer ranged from 2.5 to 9.8 W/m/K. Based on the these 6 experiments, the mean value for the thermal conductivity of the sodium sulfate in the scale layer was 5.8 W/m/K. This value was subsequently used to infer the salt layer thickness profile in the reactor as a function of the external wall temperature profile measured in each experiment at the time 0.024 kg of salt had been supplied to the reactor by the procedure described by Teshima [85]. As already mentioned, the thermal conductivity of sodium sulfate at pertinent conditions is presently unavailable. However, the thermal conductivity of sodium chloride up to a temperature of approximately 175 $°C$ is available [88]. The thermal conductivity of sodium chloride is about 6 and 4 W/m/K at room temperature and 175 $°C$ respectively. Extrapolation of the sodium chloride thermal conductivity data to 375 $°C$, a temperature which typifies the deposition experiments performed at UBC, yields a value of slightly less than 3 W/m/K. (Obviously, the thermal conductivity of sodium chloride is a substantial function of temperature.) It is unknown how different the thermal conductivity of sodium sulfate and sodium chloride are at relevant conditions. However, if the difference is not substantial, the Teshima et al. estimates for the thermal conductivity appear high for some runs.

A complete mass balance on sodium sulfate could be performed only when the system was flushed with cold water after a run. Thus, the thermal conductivity of the sodium sulfate in the scale layer could not

be accurately estimated as a function of time during a given run. Estimates of the thermal conductivity of the sodium sulfate in the scale layer as a function of time during a run could, however, be ascertained by performing a series of experiments at the same operating conditions, but for different lengths of time. This would be interesting because it may place the importance (or lack thereof) of densification of the salt layer in better context. To be sure, a driving force for mass transfer is present inside the porous salt layer formed on the surface of the reactor. Moreover, the thermal conductivity of sodium sulfate and water at relevant conditions are considerably different. The thermal conductivity of the sodium sulfate in the scale layer was estimated to range from 2.5 to 9.8 W/m/K and the thermal conductivity of (pure) SCW at 375 °C and 250 bar, for example, is about 0.4 W/m/K. Therefore, the effective thermal conductivity of the scale layer is a substantial function of porosity. For example, if the thermal conductivity of the aqueous sodium sulfate solution and sodium sulfate are set equal to 0.4 W/m/K and 3 W/m/K respectively, the thermal conductivity of the scale layer would be 1.44 and 0.92 for porosity values of 0.60 and 0.80 respectively according to Eq. 1.7.

If the thermal conductivity of the scale layer varies with time it is probably attributable to changes in porosity. This is because the thermal conductivity of solid sodium sulfate at conditions of interest probably is essentially constant and it is unlikely significant convection occurs within the scale layer. If porosity of the scale layer is, in fact, a constant then one expects the effective thermal conductivity of the scale layer to be largely independent of time during each run and, moreover, to be approximately the same in different runs. Conversely, if the porosity is a substantial function of time and erroneously approximated as a constant one would expect the thermal conductivity of the sodium sulfate in the scale layer to vary with time. (Porosity may also be a considerable function of radius because one expects the porosity of the salt layer to decrease as the wall of the reactor is approached.) The assumption of constant porosity within the scale layer produced different estimates for the value of the thermal conductivity of the sodium sulfate in the scale layer at virtually the same temperature. This, in fact, suggests porosity may have been different in each run. If accurate data for the thermal conductivity of sodium sulfate becomes independently available, it would be interesting to check if porosity was a substantial function of run time by the procedure suggested above.

Four different models were used to predict the mass/volume of salt deposited in the UBC reactor as a

function of the distance from its inlet at the time 0.024 kg of sodium sulfate had been supplied to it in each fouling experiment. The time step used for all the computations was 1/10 of the experimentally measured time at which a plug was detected. At time equal to zero, the wall temperature profile in the reactor is calculated following the procedure described above for the pure water heat transfer experiments. Next, the UBC solubility data are used to compute the wall concentration profile from the wall temperature profile at time equal to zero and solubility relationship. Then, each of the four different mass transfer models are used to predict the mass of sodium sulfate deposited on the reactor wall in each control volume during each time step. "Model 2" is described in detail below, followed by a brief account of the other three models.

"Model 2" assumes nucleation occurs exclusively at the interface between the salt layer deposited on the reactor wall and adjacent solution. This interface is subsequently referred to as the salt layer-solution interface and is equivalent to the inner wall of the reactor at time equal to zero. In "Model 2", if the bulk solution became supersaturated, it was considered metastable. Mass transfer coefficients between the bulk solution and salt layer-solution interface were determined by applying the analogy between heat and mass transfer to the Swenson et al. Nusselt number correlation. Then, from the definition of the mass transfer coefficient the mass of salt deposited in the first control volume during the first time step was computed. The bulk concentration of sodium sulfate in control volume "i" was computed from a simple mass balance on the mass of salt entering, depositing within, and leaving control volume "i-1" starting with control volume 2 in the first time step. The mass of salt deposited in control volume "i" during each time step was calculated the same way as in control volume 1 during the first time step. In time steps 2-10, the diameter through which solution flows and surface area available for deposition are, obviously, decreasing in the control volumes where salt is depositing. At the end of each simulation, the mass of salt deposited in the reactor as a function of distance from the inlet is converted to a volume to determine the salt layer thickness profile at the time when 0.024 kg of salt has been supplied to the reactor. (The porosity was assumed to equal 0.71 when converting mass to volume as when estimating the thermal conductivity of the sodium sulfate in the scale layer.)

In mass transfer "Model 1", it was assumed that the bulk concentration of dissolved sodium sulfate in each control volume was identically equal to the solubility concentration at the corresponding bulk temperature and 250 bar. All salt in excess of this solubility concentration was assumed to homogeneously nucleate and

form particles in the bulk solution. The particles were not permitted to deposit at the salt layer-solution interface, and egressed from the reactor at its exit. For "Model 3", the UBC group applied the Chan et al. model described above, i.e., the mass of salt depositing on the walls was determined by assuming all salt in excess of the solubility limit at the bulk solution temperature immediately deposited on the reactor wall. "Model 4", the "complete" model, accounted for the deposition of both particles formed due to homogeneous nucleation in the bulk fluid and molecules diffusing to the salt layer-solution interface and, subsequently, nucleating heterogeneously there. The rate of deposition by molecular diffusion of dissolved salt molecules to the salt layer-solution interface and subsequent nucleation was calculated as in "Model 1." All sodium sulfate in the bulk solution beyond the solubility limit was assumed to be present in the form of 2 micron diameter particles. (Supersaturation was not permitted.) Mass transport coefficients necessary to compute the rate at which the 2 micron particles deposited at the salt layer-solution interface were determined using a correlation proposed by Papavergos and Hedley [70] applicable to the mass transfer of particles in turbulent flows through horizontal tubes.

The salt layer thickness profiles inferred from the external wall temperature measurements and predicted by the four mass transfer models at the time when 0.024 kg of salt had been supplied to the reactor in "Run 1" and "Run 12" are shown in Figs. 1-11 and 1-12 respectively. (The unheated lengths at the beginning and end of the reactor are not included in Figs. 1-11 and 1-12.) In "Run 1", a 0.652 wt% salt, aqueous sodium sulfate solution was pumped through the reactor at a mass flow rate of 1.21 kg/min. The bulk temperature of the solution measured at the inlet of the reactor was 373 °C. The bulk temperature measured at the outlet was up to 384 °C. In "Run 12", a 1.066 wt% salt, aqueous sodium sulfate solution was pumped through the reactor at a mass flow rate of 2.16 kg/min. The bulk temperatures of the solution measured at the inlet of the reactor in "Run 12" was 363 °C. The bulk temperature at the outlet was up to 386 °C. The curves labelled "Experimental" in Figs. 1-11 and 1-12 correspond to the salt layer thickness profiles inferred from the measured external wall temperature profile at the time for which 0.024 kg of salt had been delivered to the test section. It is critical to bear in mind that the "Experimental" salt deposition profiles are not measured directly, but inferred from the external wall temperature profiles. The major advantage of this is that the reactor does not have to be disassembled after each run to measure the mass of sodium

sulfate deposited inside it. The major disadvantage is that the inferences are only as good as the estimate of the thermal conductivity of the scale layer and the heat transfer model. The curves labelled "Suspended Particles", "No Nucleation", "Chan et al.", and "Complete" correspond to the predictions of "Model 1" through "Model 4" respectively at the time when 0.024 kg of salt had been delivered to the reactor.

Some general features of the results of "Run 1" and "Run 12" may be observed. First, the predictions of Models 1, 2 and 4 were essentially the same. Even in "Model 4", the "complete" model, accounting for particle deposition did not alter the deposition rate significantly. Since particles were predicted to form in two of the fourteen deposition experiments, but did not affect the predictions, molecular diffusion is a far stronger mechanism of mass transport than inertial deposition of particles at the conditions investigated. "Model 3", the Chan et al. model, produced results that were inconsistent with the other three models. In the Chan et al. model salt is permitted to remain in solution until the bulk solution temperature exceeds the solubility temperature at the concentration of interest. Thus, as discussed in the previous section, it can not predict the correct axial location at which deposition begins because the wall temperature exceeds the solubility temperature before the bulk temperature. This does not cause any significant discrepancy in "Run 1." However, in "Run 14", the Chan et al. model predicts deposition does not begin until after about 20% of the distance between the inlet and outlet of the heated portion of the reactor, but deposition appears to begin at the inlet.

In "Run 1", Models 1, 2 and 4 overpredict the inferred salt layer thickness profile by at least 50% throughout the reactor. The Chan et al. model is closer to the inferred salt layer thickness profile near the inlet of the reactor because it predicts that deposition does not begin until the bulk temperature exceeds the solubility temperature. The Chan et al. model is high by about a factor of 5 at 1.0 meter from the inlet of the reactor and gradually becomes fairly consistent with the other models by the end of the reactor. The thickness of the scale layer peaks after about 1.7 m from the inlet to the heated portion of the reactor according to the salt deposition profile inferred from the external wall temperature measurements. Based on Models 1, 2 and 4, it peaks at about 0.9 m from the inlet to the heated portion of the reactor and based on the Chan et al. model it peaks after about 1.0 m.

The inferred salt layer thickness profile compares much better with Models 1, 2 and 4 in "Run 12" as

per Fig. 1-12. After about 1/5 of the distance between the beginning and end of the heated section of the reactor, the discrepancy does not exceed about 30% and often does much better. Moreover, the overall trends between the inferred and predicted salt deposition profiles are similar. The Chan et al. model is poor for about the first 30% of the distance between the beginning and end of the heated section of the reactor and then does about as well as Models 1, 2 and 4. The peak salt layer thickness inferred from the measured external wall temperature profiles occurs at about 1 m after the beginning of the heated section of the reactor. It occurs at about 0.6 and 0.8 m after the beginning of the heated section of the reactor according to Models 1, 2 and 4 and the Chan et al. model respectively. Runs "1" and "12" were selected for the preceding discussion because for some experiments the results of mass transfer Models 1, 2 and 4 were quite consistent with the inferred salt layer profile, but in others the consistency was not as good.

It would be interesting to estimate what fraction of the power supplied to the test section was consumed by the precipitation of sodium sulfate at the conditions investigated in the UBC deposition experiments. In Section 3.8, it is estimated that, during the sodium sulfate deposition experiments performed for this dissertation, about 20% of the heat supplied to the test section was consumed by (endothermic) precipitation. If the heat of precipitation is important to transport it would affect the predicted and inferred salt layer thickness profiles.

The results of the UBC investigation are very interesting and contribute very substantially to our knowledge on salt deposition kinetics at SCWO conditions. It would also be interesting to see how the inferred and predicted salt deposition profiles compare throughout the various runs in addition to at the time for which 0.024 kg of salt has been supplied to the reactor. Finally, in all studies to date of salt deposition kinetics in the context of SCWO, including this dissertation, the importance (or lack thereof) of heat and mass transfer inside the porous salt layer needs to be more thoroughly investigated.

1.5 Motivation for Dissertation Research

At the present time, limited means are available to predict the rate of scale buildup for a given set of SCWO operating conditions, to evaluate the relative merits of existing scale buildup control strategies, or
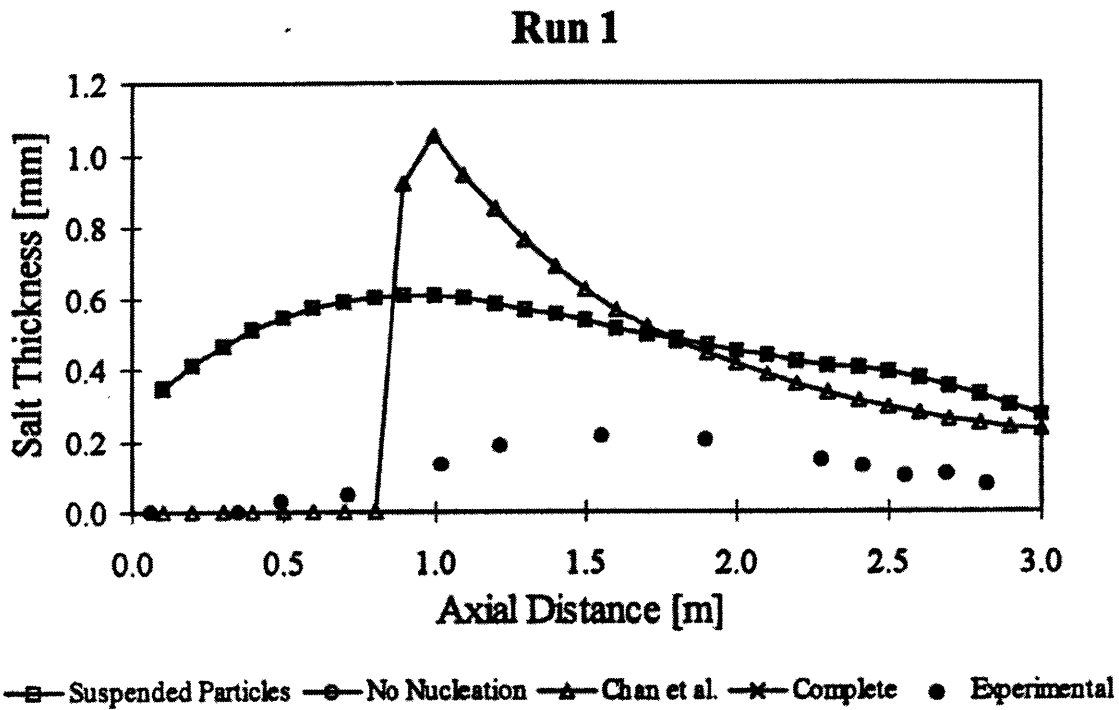
Figure 1-11: Results of "Run 1" in the UBC sodium sulfate deposition experiments. Extracted from Teshima [85].
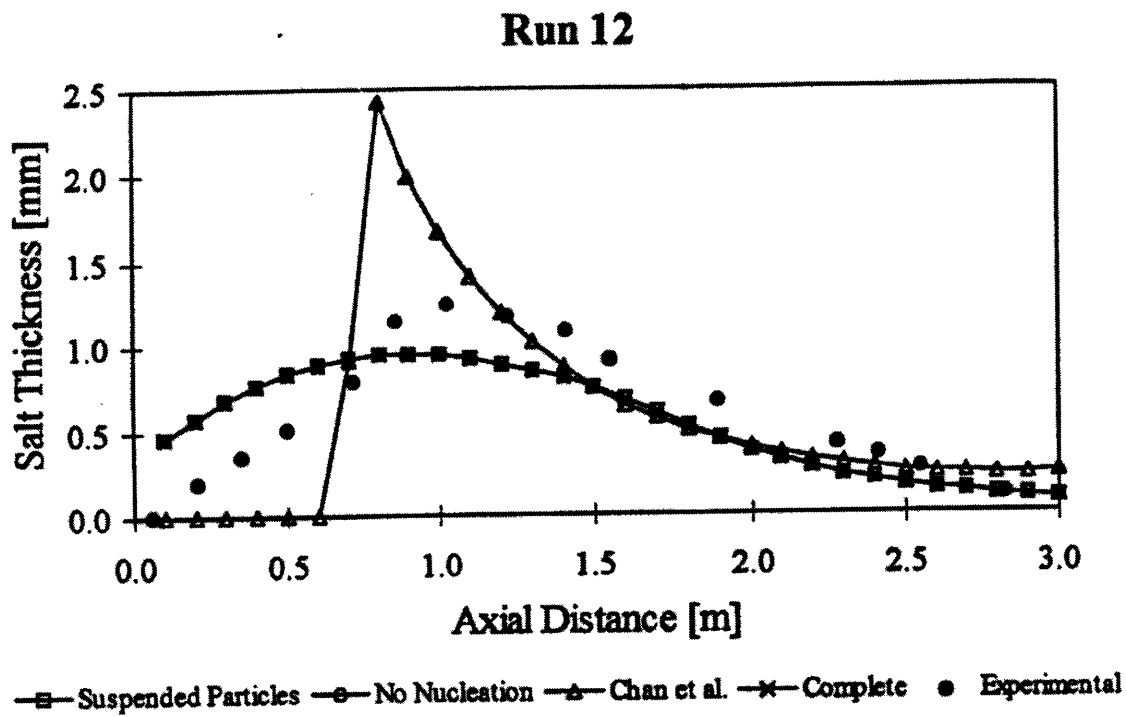
Run 12

Figure 1-12: Results of "Run 12" in the UBC sodium sulfate deposition experiments. Extracted from Teshima [85].

to effectively guide the development of new ones. Thus, control of scale buildup still remains a key enabling technology for SCWO. This dissertation contributes to the knowledge base necessary to understand and control scale buildup in SCWO reactors by presenting experimental deposition rate data and concomitant analyses. Only from a fundamental understanding of salt deposition kinetics in the context of SCWO will it be possible to use the results of laboratory or pilot scale experiments to design commercial SCWO reactors which effectively limit scale buildup. This dissertation is, admittedly, "academic" in nature to a substantial extent.

1.6 Contents of Dissertation

The primary contents of the remaining chapters of this dissertation are outlined in this section. The next chapter of this dissertation begins with a description of the apparatus constructed at the National Institute of Standards and Technology (NIST) to measure solubility data in the Na_2SO_4-H_2O and K_2SO_4-H_2O systems at elevated temperatures and pressures and deposition rates from near-supercritical, aqueous, sodium sulfate and potassium sulfate solutions to a heated cylinder. (This was a collaborative effort between the MIT and NIST SCWO groups as described in Chapter 2.) Next, the procedures to measure solubility and deposition rate data are given. After providing the results of some simple heat transfer experiments to validate the apparatus, the solubility data collected for sodium sulfate and potassium sulfate in SCW at 250 bar are presented. Finally, the results of the deposition experiments are provided.

Chapter 3-5 are devoted to the modeling of deposition rates at the conditions investigated in the deposition experiments. Chapter 3 begins with a development of the, sometimes counter intuitive, relationship between transport coefficients and deposition rate at the salt layer-solution interface from a simple transport model. Then, the conservation laws and boundary conditions are stated in a fairly rigorous context assuming that the deposition mechanism is exclusively molecular diffusion of salt to the salt layer-solution interface and subsequent heterogeneous nucleation there. Next, a set of criteria to justify a simpler transport formulation is derived. The thermodynamic and transport properties of aqueous sodium sulfate and potassium sulfate solutions required in the transport formulation are then estimated. Next, the criteria are evaluated and

a simpler transport formulation is justified. Finally, the transport formulation is recast into a form which improves its numerical tractability.

Chapter 4 begins with a comparison of the results of the simple heat transfer experiments run to validate the apparatus to the predictions of standard heat transfer correlations. Then the solubility data that was presented in Chapter 2 is compared to solubility data collected by other investigators. The remainder of Chapter 4 is devoted to the solution of the transport formulation given at the end of Chapter 3. The rate of mass transfer from the bulk solution to the salt layer-solution interface predicted by the model is compared to the results of the sodium sulfate and potassium sulfate deposition experiments. Finally, an explanation for the discrepancy between model and experiment, when present, is proposed.

In Chapters 3 and 4 it was assumed that deposition at the salt layer-solution interface was exclusively by molecular diffusion across the boundary layer and subsequent heterogeneous nucleation there. Chapter 5 develops a criterion which must be satisfied for this to be true. The criterion is then applied to the conditions investigated in the deposition experiments. It is satisfied in all cases and justifies, a posteriori, the transport formulation solved in Chapter 4 for the deposition rate at the salt layer-solution interface. Some other nucleation issues relevant to the conditions investigated in the deposition experiments are also discussed/analyzed. Chapter 6 presents the conclusions of this dissertation and recommendations for future work related to it.

Chapter 2

Experimental Apparatus, Procedure and Data

2.1 Introduction

The experimental program described in this chapter focuses on solubility and mass transfer measurements in supercritical water at conditions relevant to the implementation of SCWO. Solubilities of sodium sulfate and potassium sulfate in supercritical water at 250 bar were measured. Also measured was the rate of salt deposition from near-supercritical, aqueous, sodium sulfate and potassium sulfate solutions to a heated cylinder. In this chapter the aqueous sodium sulfate and aqueous potassium sulfate systems at conditions of interest are discussed briefly in the context of the experiments. Then the experimental apparatus and procedure used for the measurements are presented, followed by a discussion of uncertainties in the measurements. Next, the solubility and deposition rate data are presented. Results from some related heat transfer experiments are also presented. It is noted that no organic compounds or oxidizer were supplied to the system in any of the experiments performed for this dissertation.

The temperature-composition diagrams for the aqueous sodium sulfate and aqueous potassium sulfate systems at 250 bar are shown in Figs. 2-1 and 2-2 respectively. (A more detailed discussion of these two

temperature-composition diagrams may be found in Section 4.3 where solubility data from additional studies are also provided.) In both systems, the solubility curve separates a single phase fluid region from a fluid plus solid salt region. Experimental determinations of solubilities were acquired by maintaining the surface temperature of a hot finger approximately 15 $^{\circ}C$ above the bulk temperature of the solution surrounding it while gradually increasing the bulk solution temperature by additional preheating. The hot finger surface temperature at which precipitation first occurs is the solubility temperature. In the deposition experiments, the aqueous salt solution flowing past the hot finger was preheated to a temperature close to that at which precipitation begins and the salt layer-solution interface was maintained slightly above this precipitation temperature, thus limiting deposition almost exclusively to the salt layer-solution interface. (At the beginning of each deposition experiment the surface of the hot finger corresponds to the salt layer-solution interface.)

Fig. 2-3 shows before and after photographs of a 5.08 mm OD hot finger inserted into the cross flow of a 4 wt% salt, aqueous sodium sulfate solution flowing (laminarly) at 10.47 gm/min at a pressure of 250 bar after about 15 minutes of exposure. Note that the cross flow is directed vertically upward, i.e., in the direction opposite to that of the gravity vector. It is further noted that it will be shown in Chapter 3 that natural convection dominates transport at all conditions of interest to this dissertation. Upstream and downstream views of the hot finger after same the experiment are shown in Fig. 2-4. The initial bulk solution condition and (estimated) initial hot finger surface condition are shown on the Na_2SO_4-H_2O temperature-composition diagram in Fig. 2-1. Figs. 2-5 and 2-6 show before and after photographs of the same hot finger inserted into the cross flow of a 4 wt% salt, aqueous potassium sulfate solution flowing (laminarly) at 10.39 grams per minute at a pressure of about 250 bar after about 10 minutes of exposure. Unfortunately, the quality of the photographs in Figs. 2-5 and 2-6 is not great. The structure of the potassium sulfate formed on the hot finger is clearly dendritic. (The needle-like/dendritic structure is more obvious from visual observations of the salt, than from the photograph in Fig. 2-6.) Dendrites were not observed in the sodium sulfate layer deposited on the hot finger. For both of the experiments the thickness of the salt layer formed on the hot finger is on the order of the radius of the hot finger after only 10 minutes. One begins to appreciate the seriousness of the scale buildup problem in SCWO from the foregoing discussion and illustrations. It is noted that the potassium sulfate was very easy to remove from the hot finger with one's fingers. The sodium

sulfate generally had to be removed by mechanical means unless is was loosened with tap water.

2.2   Experimental Apparatus

The experimental apparatus used for this study was designed, constructed and operated at the National Institute of Standards and Technology (NIST). The design and construction of the apparatus was in collaboration with Dr. Wilbur Hurst and Mr. Walter J. Bowers, Jr. from the Process Measurements Division of the Chemical Science and Technology Laboratory (CSTL) at NIST. The design of the optically-accessible test cell used for this study was largely based on a similar one designed for studying SCWO kinetics by Dr. Vern Bean of the Process Measurements Division of the CSTL at NIST. Finally, Dr. Hurst and Mr. Kentaro Saco, a visiting scientist from Asahi Chemical Company (Japan), assisted in collecting the solubility and deposition rate data.

The apparatus is shown schematically in Fig. 2-7. Two ISCO 260D syringe pumps, controlled by an ISCO Series D controller, deliver up to 25 ml/min (at STP) of pure distilled water or aqueous salt solution to the system. It is noted that the ISCO pump system eliminates flow pulsations. The pump which is temporarily inoperative gradually takes over when the amount of fluid remaining in the operating pump falls below a certain level. After the pump which was inoperative has completely taken over the near empty pump refills and the cycle is repeated. A pair of Sensotec Model GM pressure transducers accompanied by Sensotec Model LM signal conditioners measure the pressure of the fluid leaving the pump system and entering the back pressure regulator yielding the pressure drop across the system.

The fluid leaving the pump system enters the preheater which consists of an approximately 2 m length of 2 mm wall thickness, 2 mm ID Hastelloy C276 tube shaped into 6 straight runs of about 25 cm each which are connected by U-bends with radii of about 2 cm. Heat is transferred to this tube by 3 strips of Omega STH101-020 ultra-high temperature heating tape, each capable of supplying about 300 watts at 120 volts. Three Omega CN9000A Series controllers supply power to the heating tapes based on temperatures relayed to them by type K thermocouples attached to the walls of the preheater tube at appropriate locations. The entire preheater tube is embedded in a 15 cm thick section of Marinite I insulation manufactured by BNZ
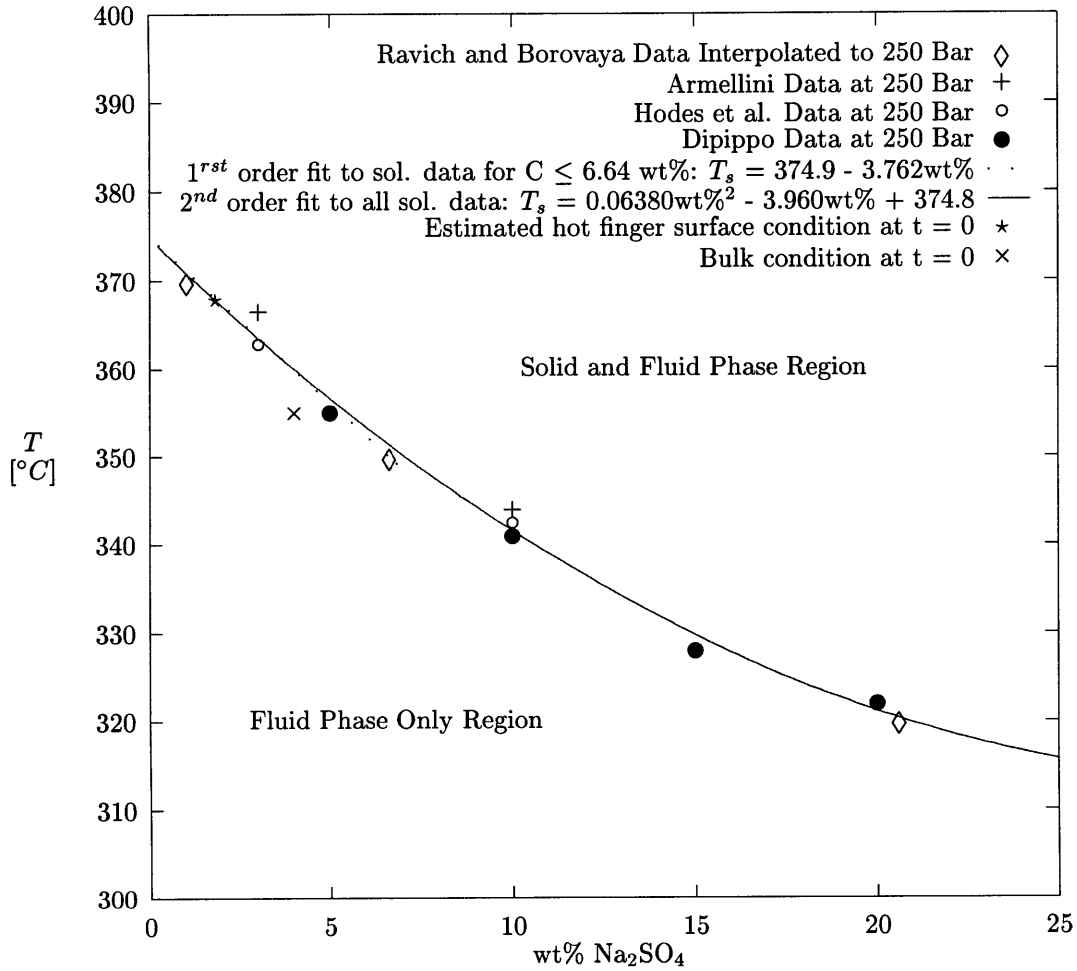
Figure 2-1: Temperature-composition Na_2SO_4-H_2O diagram at 250 bar and linear and 2nd order curve fits to selected existing solubility data. The initial bulk solution condition and the estimated initial hot finger surface condition for the experiments conducted in which the sodium sulfate concentration in the inlet stream was 4 wt% are also shown.
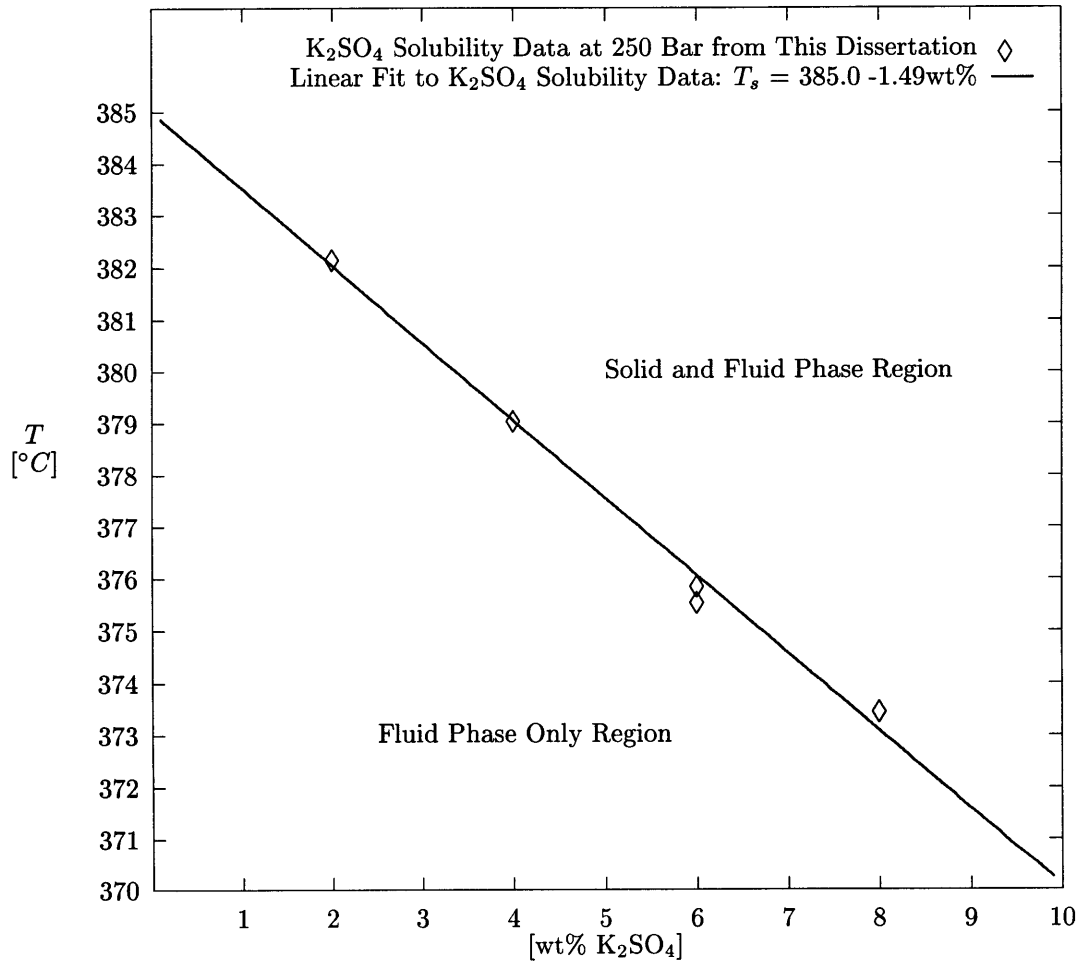
Figure 2-2: Temperature-composition K_2SO_4-H_2O diagram at 250 bar and linear fit to the solubility data.

gravity ↓

flow dir'n ↑

After ≅ 15 minutes

Before Run
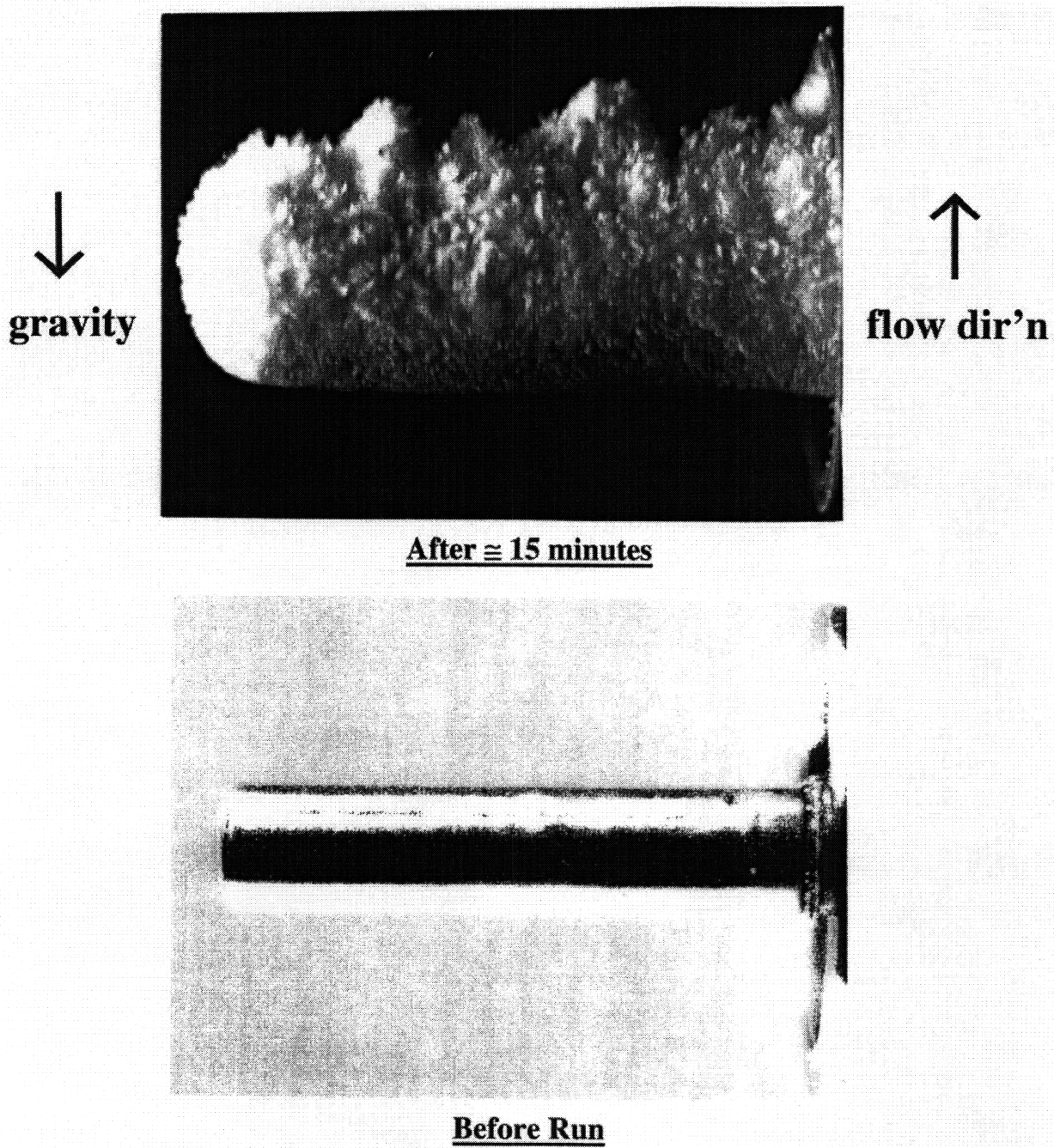
Figure 2-3: Photographs of the 5.08 mm OD hot finger before it was inserted into the cross flow of a 4 wt% salt, aqueous sodium sulfate solution flowing (laminarly) at 10.47 gm/min and after about 15 minutes of exposure. The bulk temperature of the solution surrounding the hot finger was about $356°C$ and the pressure in the system was about 250 bar. Note the flow is directed vertically upward, i.e., opposite to the direction of the gravity vector.
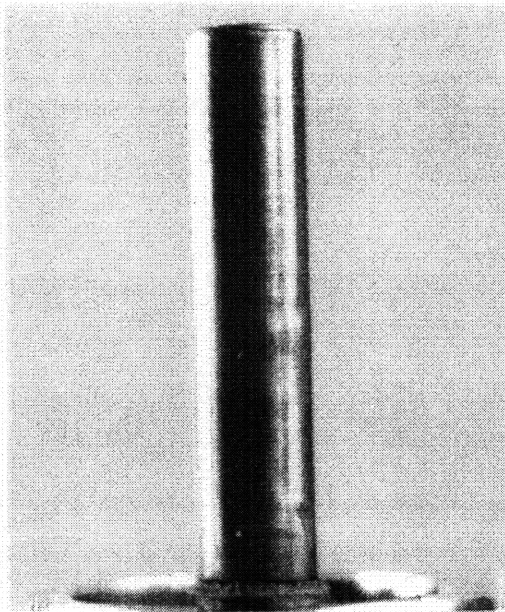
Before Run
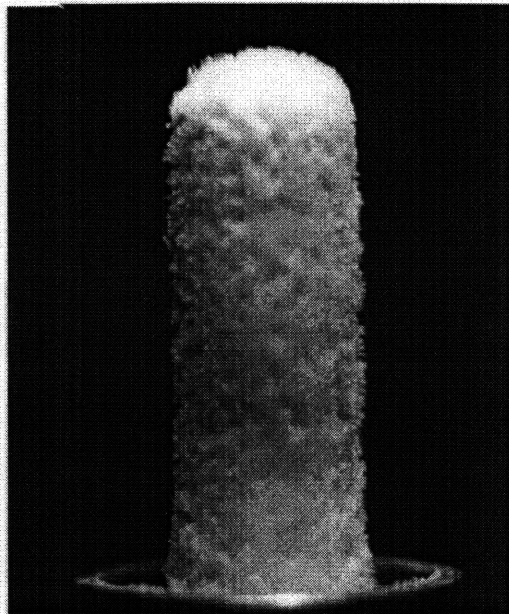
Upstream View
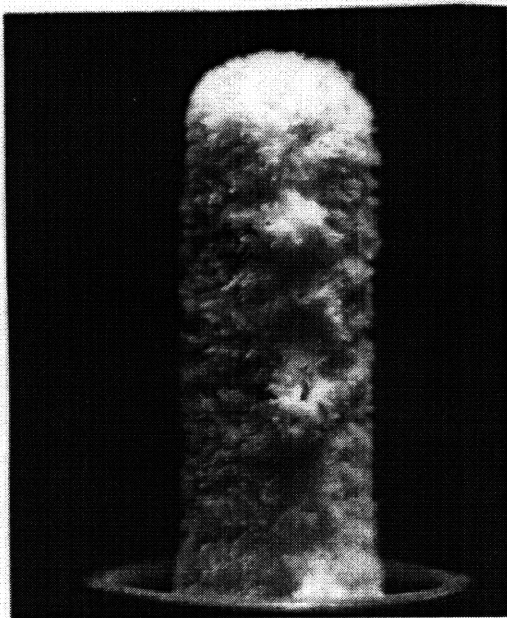
Downstream View
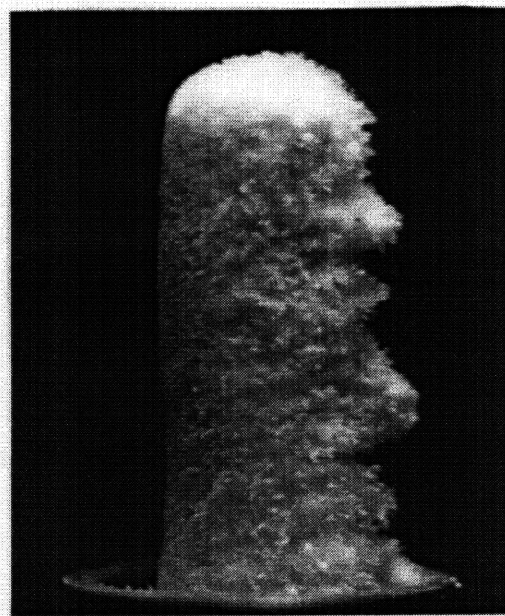
Side View

Figure 2-4: Photograph of the 5.08 mm OD hot finger before it was inserted into the cross flow of a 4 wt% salt, aqueous sodium sulfate solution flowing (laminarly) at 10.47 gm/min and upstream, downstream and side views of the hot finger after about 15 minutes of exposure. The bulk temperature of the solution surrounding the hot finger was about $356°C$ and the pressure in the system was about 250 bar.

Figure 2-5: Photograph of the 5.08 mm OD hot finger before it was inserted into the cross flow of a 4 wt% salt, aqueous potassium sulfate solution flowing (laminarly) at 10.39 gm/min.
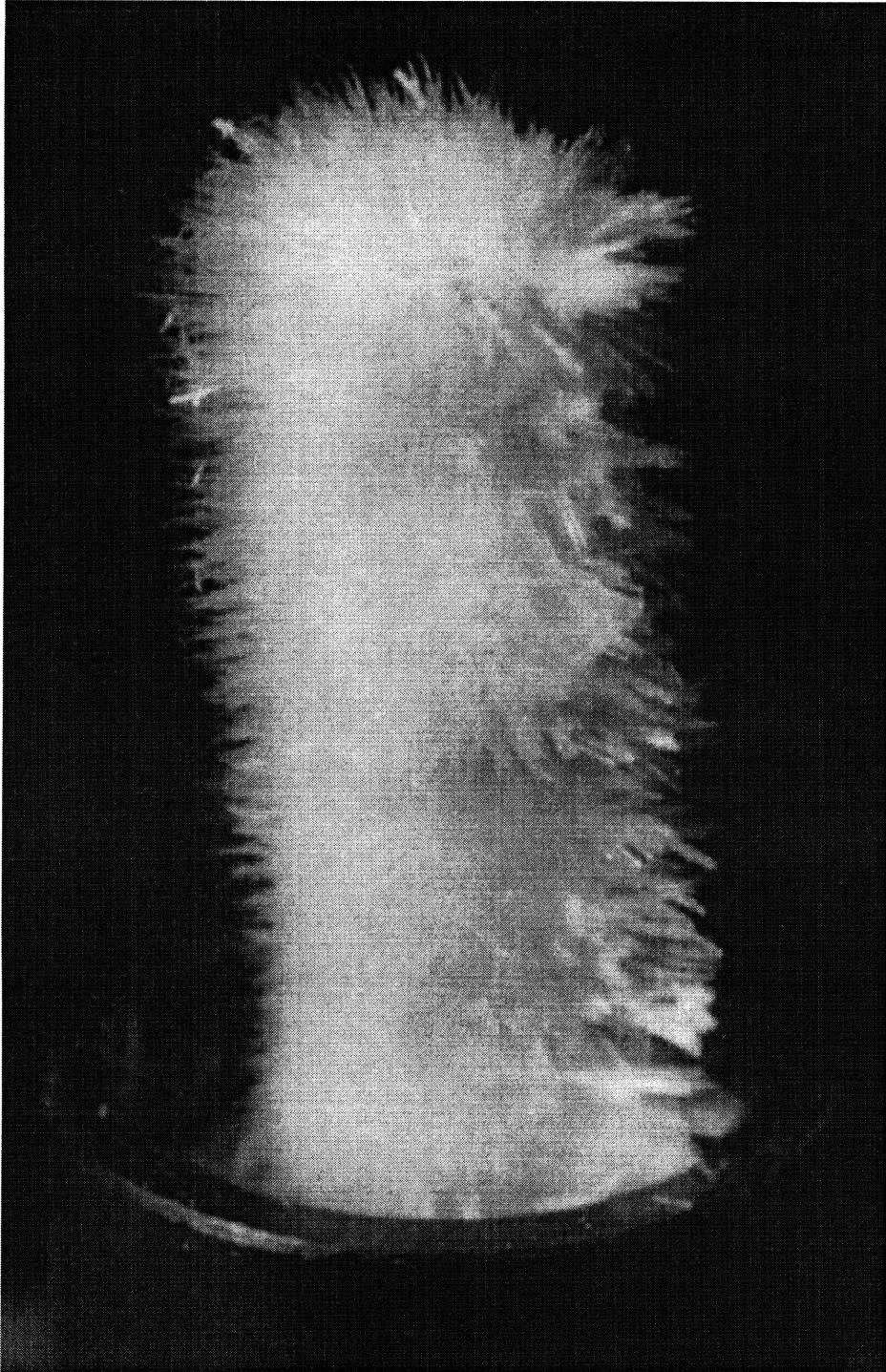
Figure 2-6: Photograph of the 5.08 mm OD hot finger after it was inserted into the cross flow of a 4 wt% salt, aqueous potassium sulfate solution flowing (laminarly) at 10.39 gm/min for about 10 minutes. The bulk temperature of the solution surrounding the hot finger was about $373°C$ and the pressure in the system was about 250 bar.

Materials Corporation primarily from a calcium silicate hydrate mixture.

After leaving the preheater, the solution flows horizontally through an approximately 1/3 m long section of 2 mm wall thickness, 2 mm ID Hastelloy C276 tube which has a Hastelloy C276 "hot valve", labelled valve A in Fig. 2-7, installed in it that is operable in elevated temperature and pressure environments. (The plastic handle of the "hot valve" is accessible and cool enough to be operated manually.) The solution then flows vertically upward through a 28 cm length of 1.59 cm OD, 1.34 cm ID Inconel 625 tube which is welded to the test section inlet. Two Cole Parmer L-03117-20 heavy-insulated heating tapes, each capable of supplying about 315 Watts at 120 V, are wrapped around the Hastelloy C276 tube leaving the preheater, the "hot valve" and the Inconel 625 tube leading to the cell. The amount of power supplied to these heating tapes is controlled by two Omega CN9000A Series controllers based on temperatures relayed to them by appropriately located thermocouples. This insures solution enters the test cell at the desired temperature. A 1/16 inch OD type K Incoloy-sheathed thermocouple is fed up through the Inconel 625 tube leading to the test cell and its junction sits about 15 cm below the hot finger. All the lines between the preheater and the test section are very heavily insulated with Fiberfrax.

The test section was fabricated from a 3/4 inch stainless steel 316 Swagelok Cross and it is shown schematically in Fig. 2-8. The inner surfaces of the cross were gold plated by Brushtronics Corporation in Laurel, MD to protect against corrosion. The cross is oriented such that all four ports are parallel to the floor and the Inconel 625 tube connecting the preheater to the cross is welded into a hole machined into its bottom. A 3/4 inch Swagelok weld connector is welded into a hole machined into the top of the cross and provides an extra 3/4 inch port there. A laser beam or white light source is directed at the sapphire window located in this port to illuminate the cell. A 25 cm run of 2 mm ID, 2 mm wall Hastelloy C276 tube is welded to this connector 1.32 cm above the top of the cross and serves as the flow exit. This tube is downwardly inclined by about 10 degrees to prevent cool fluid from reentering the cell. A 1/16 inch OD stainless steel 316 capillary tube which carries the nitrogen for blow-down enters the exit tube from the cell about 12 inches downstream and runs inside the exit line to the cross itself. The four ports on the cross itself are used to mount sapphire windows, plugs, hot fingers and thermocouples at desired locations in the cell. In the majority of the experiments presented in this dissertation the ports were occupied as shown in

97
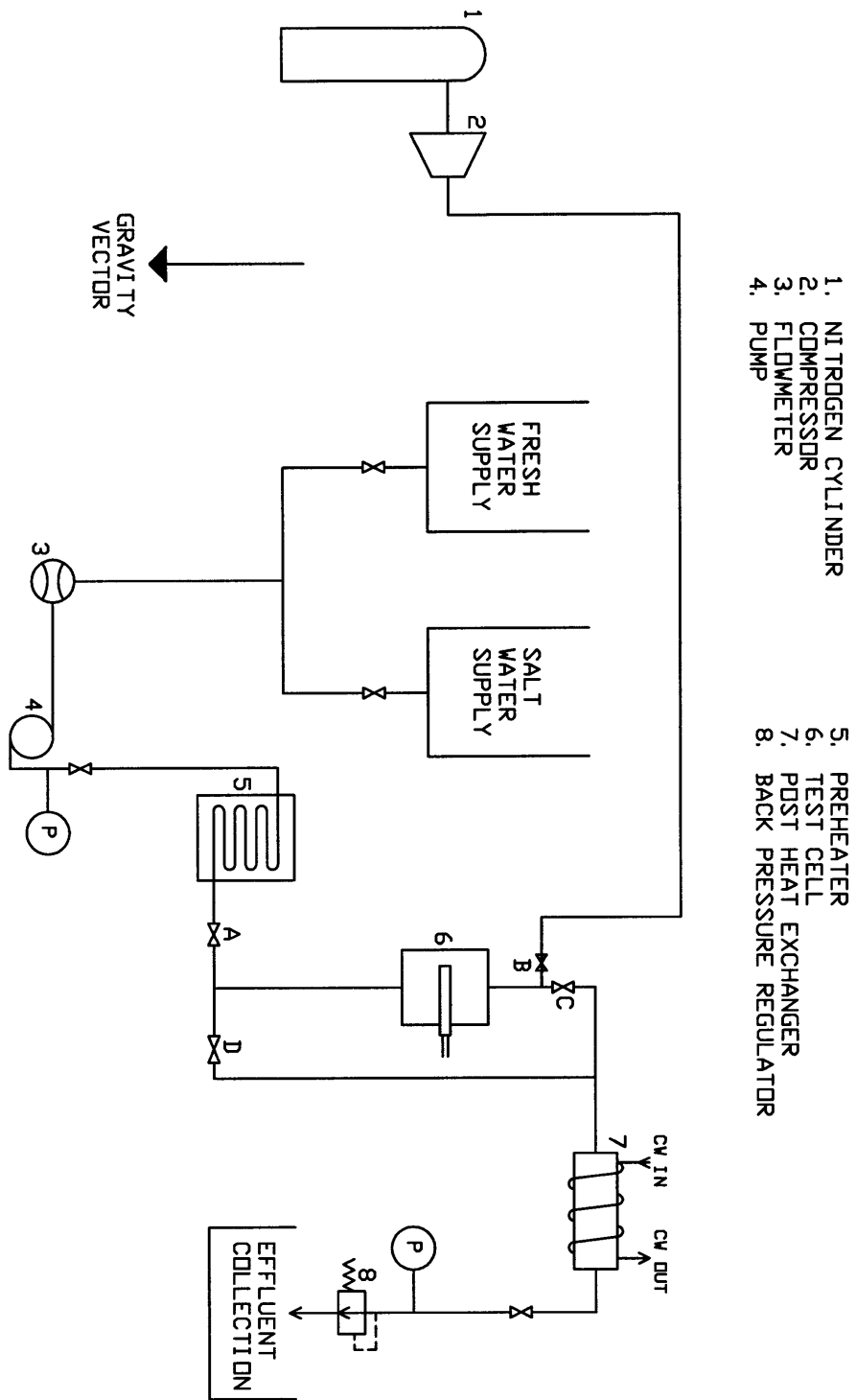
Figure 2-7: Schematic representation of the apparatus.

Fig. 2-8. (In some of the early experiments an Inconel 625 plug instead of a sapphire window occupied the port directly across from the hot finger.) The cell is particularly versatile because a plug, sapphire window, thermocouple or hot finger may occupy any of the five 3/4 inch ports on the modified Swagelock cross. Generally, a telescope is directed at the hot finger through the port directly opposite the thermocouple's port to visually observe it during the experiments.

The part which serves as the heated cylinder in cross flow or "hot finger", is shown in Fig. 2-9. The Hastelloy C276-sleeved copper portion of the hot finger protrudes into the test section and serves as the actual heated cylinder in cross flow along with a small part of the Inconel 625 base. The length of the cylindrical portion of the hot finger on which salt deposits is 1.086 inches (27.58 mm) and its diameter is 0.200 inches (5.08 mm), except for the 0.135 inches (3.43 mm) closest to the base where the diameter increases to 0.220 inches (5.59 mm). A 1.25 inch long, 1/8 inch diameter Watlow C1E14 Firerod cartridge heater coated by Watlub lubricant slides into the 0.125 inch diameter hole in the hot finger. There is a 1/4 inch unheated length at both ends of the cartridge heater and the 32.5 mil thick copper sleeve surrounding it serves as a heat spreader. The 5 mil thick Hastelloy C276 sleeve around the copper is added to protect the hot finger from corrosion and allow salt to deposit/nucleate on a surface typical of actual SCWO reactors. The backside of the base of the hot finger is threaded to facilitate the removal of the hot finger from the test cell between runs. When the hot finger is inserted into its port on the cross, it rests against a lip where the ID of the cross is reduced from 0.75 to 0.62 inches and the cylindrical portion of it extends approximately 0.25 inches beyond where the ID of the cross again becomes 0.62 inches, following the center of the cross as per Fig. 2-8. Tightening the nut on the cross in the port where the hot finger resides forces a set of ferrules into the 90 mil deep groove machined into the hot finger which prevents it from being capable of bursting out of the cell under pressure and creates the two metal-to-metal seals required. The threads on the port where the hot finger is inserted are lubricated by Silver Goop, a high temperature silver-based thread lubricant manufactured by Swagelok Company, which *greatly* facilitates installation and removal of the hot finger between runs. Generally about 85 ft-lbs of torque are sufficient to maintain a seal at the conditions investigated. The leads of the cartridge heater inside the hot finger are electrically insulated with a pair of ceramic sleeves and sent to a Variac. The supply side voltage to the Variac is maintained relatively constant
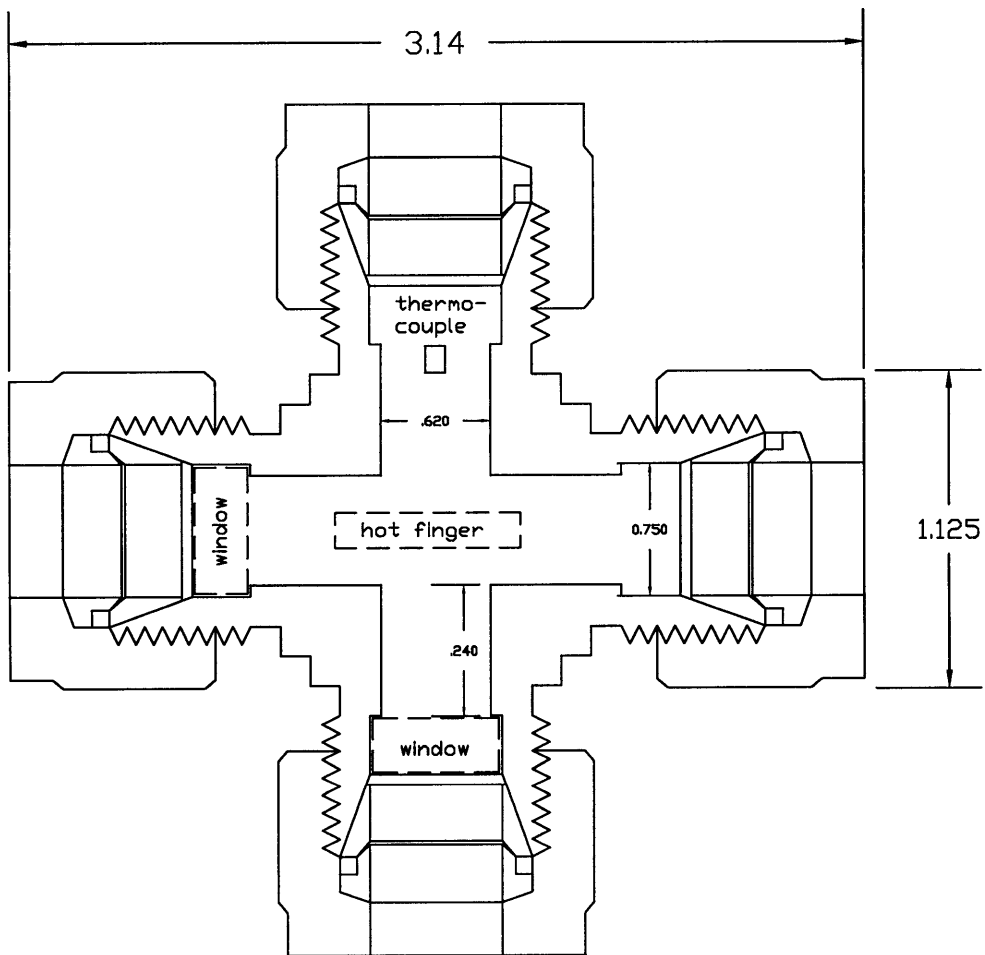
Figure 2-8: Schematic drawing of the 3/4 inch Swagelok cross from which the test cell for the experiments was fabricated showing hot finger, sapphire window, plug and thermocouple locations. The flow is in and out of the page, all dimensions are in inches and the figure is not drawn to scale.

100

by an AC regulator. For all of the experimental data reported in this study the power dissipated by the cartridge heater was 10.61 watts.

Two hot fingers were fabricated. One of them was instrumented with five 10 mil diameter, Incoloy-sheathed, type K thermocouples to measure axial and azimuthal temperature profiles along its surface at the locations shown in Fig. 2-9. (The locations of the thermocouples are to scale in Fig. 2-9) Thermocouple "F4" is located at the forward stagnation point on the upstream side of the hot finger exactly in the middle of the protruding portion of it, i.e., 0.543 inches from its tip. Thermocouples "F3" and "F2" are located 90 and 180 degrees azimuthally downstream of thermocouple "F4" respectively. Thermocouples "F1" and "F5" are located 0.84 and 0.25 inches away from the tip of the hot finger respectively at the same azimuthal location as thermocouple "F3." The thermocouples were fed through a hole drilled into the base of the hot finger to the stated locations and silver solder was used to plug the hole and secure them in place. A second identical hot finger was fabricated but not instrumented with thermocouples. When collecting deposition rate data the hot finger must be installed and removed for each run. Since the 10 mil diameter thermocouples are extremely fragile, the hot finger without the thermocouples was used to collect all of the deposition rate data. (The thermocouples and silver solder used to secure them in place also disturb the cylindrical geometry of the hot finger surface to some extent.) After the deposition rate data were collected, the hot finger instrumented with the thermocouples was installed and surface temperature profiles were measured under various conditions.

The stainless steel mounts that house the sapphire windows are shown in Fig. 2-10. A 2 mil gold gasket rests on the base mount and a 0.177 inch thick, 5/8 inch diameter sapphire window is placed on top of the gold gasket. The sapphire windows were supplied by Meller Optics (Providence, RI). Between the window and the cap are one or two spring loaded washers which were supplied by Schnorr Corporation (Woodside, NJ). The fluid pressure in the cell presses the window firmly against the gold gasket during the experiments and creates a seal, except when the pressure in the system is too low to sufficiently deform the gold gasket in which case the resilence of the spring loaded washer(s) is sufficient to seal the windows. A 1/8 inch OD, type K, Incoloy-sheathed, grounded thermocouple probe is installed in the remaining port as per Fig. 2-8.

The entire test cell rests in a 7.87 by 7.87 by 7.87 cm aluminum block equipped with four Omega CIR-

Figure 2-9: Assembly drawing of the hot finger. The copper heat spreader is silver soldered to the Inconel 625 base and the Inconel 625 cap is silver soldered to the copper heat spreader. The Hastelloy C276 sleeve is press fit on to the copper heat spreader. All dimensions are in inches and the drawing is to scale.

FLUID

0.512

0.218

0.368

.020

CAP

0.632

0.750

SPRING WASHER

0.177

SAPPHIRE WINDOW

0.625

GOLD GASKET

0.760

0.750

0.673

0.120

0.025

0.709

BASE

9/16-18
threads

0.300

0.515

Figure 2-10: Exploded assembly drawing of the sapphire window system. The base and cap are machined from stainless steel 316. The drawing is to scale except for the gold gasket and spring washer.

3031/120 cartridge heaters, each with its own controller, and the block temperature is maintained as close as possible to the temperature of the fluid exiting the preheater. The cartridge heaters are 7.62 cm long and have a diameter of 1.27 cm. They are rated for 250 W at 120 volts. The aluminum block rests in a massive 25 cm by 25 cm by 25 cm section of Marinite I insulation that has a number of ports machined into it to provide visual access to the sapphire windows and accommodate electrical leads and plumbing as needed.

Effluent from the cell is cooled in a heat exchanger and passes through a back pressure regulator, which is generally set at 250 bar. System effluent is only a few degrees Celsius above room temperature. The system is connected to a high pressure compressed nitrogen line and a bypass line is available in order to flush out the aqueous salt solution after a deposition run as described in the Experimental Procedure section. It is noted that valves C and D needed to be water cooled during the experiments to prevent their packings from melting. The volume of the test cell and reservoir leading up to it are approximately 17 ml and 39 ml respectively and the total volume of the system is about 125 ml.

2.3 Experimental Procedure

2.3.1 Heat Transfer Experiments

A series of heat transfer experiments were performed using the hot finger instrumented with thermocouples and pure, distilled water to validate the system. In each of these experiments the power supplied to the cartridge heater inside the hot finger was 10.61 watts. The surface temperature of the hot finger and bulk temperature of the water as a function of time were recorded for different flow rates of water, pressures in the system and amounts of preheating. The measured wall-to-bulk temperature differences are compared to those predicted by standard heat transfer correlations in Section 4.2.

2.3.2 Solubility Experiments

Prior to each solubility (and deposition) experiment pure distilled water at a temperature ranging from 20 °C to 100 °C is circulated through the entire system for approximately one hour at a pressure of 250 bar. Sodium sulfate and potassium sulfate are highly soluble in pure water at these conditions. Therefore,

circulating pure water through the system is expected to remove any salt that may remain there from the previous experiment. Next, with pure water still circulating through the system, the amount of preheating is gradually increased until the thermocouple measuring the bulk temperature of the solution in the cell reads 250 °C. Then both pumps are completely drained and refilled with aqueous salt solution. Next, the aqueous salt solution is systematically pumped through the system until all the distilled water has been flushed out of it.

At this point a voltage corresponding to 10.61 watts of power is supplied to the cartridge heater inside the hot finger which creates about a 15 °C temperature difference between the hot finger surface and bulk fluid. Then all the controller setpoints are gradually stepped upward until the surface temperature of the hot finger surface is about 15 °C below the temperature at which salt is expected to precipitate from the solution at the concentration of interest and 250 bar. Next, all the controller setpoints are stepped upward at the rate of approximately 1 °C every 15 minutes until precipitation occurs on the hot finger. Each 1 °C increase in the setpoint temperatures causes the bulk fluid temperature and the hot finger surface temperature to increase by about 1 °C until a scale layer forms. (In the runs designated "F" and "H", the controller setpoints were increased (stepwise) at the rate of approximately 2 °C every 15 minutes.) Fig. 2-11 illustrates the dynamics of the solubility experiments as the bulk solution temperature is gradually stepped upward until salt begins to deposit on the hot finger. In this figure, a single symbol is used to represent the bulk solution temperature and average hot finger surface temperature as a function of time.

After an appreciable scale layer forms on the hot finger, its surface temperature increases sharply, by about 5 °C or more for a 1 °C increase in the controller setpoints, because of the thermal resistance of the scale layer. This effect is shown in Fig. 2-12 where the average temperature of the five thermocouples attached to the hot finger is plotted versus the bulk fluid temperature for the 6 wt% salt, aqueous potassium sulfate solution flowing through the system at 10.56 gm/min in run I. For the first three data points shown in this figure, a 1 °C increase in controller setpoint temperatures caused both the bulk fluid and average hot finger surface temperatures to increase by about 1 °C after 15 minutes. For the last 1 °C increase in the controller setpoint temperatures, the bulk fluid temperature increased by 1 °C, but, due to scale buildup, the average surface temperature of the hot finger increased by 6.3 °C. The scale layer was continuing to
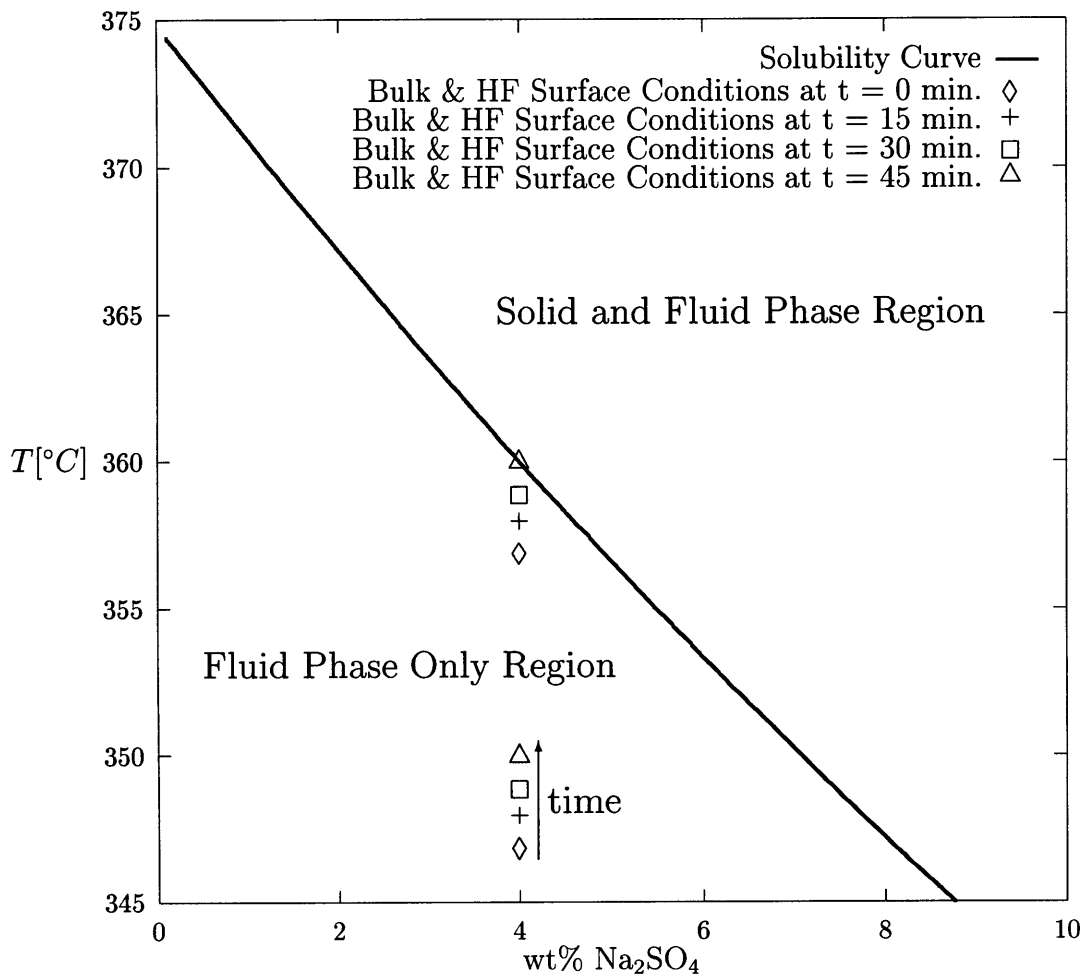
Figure 2-11: Dynamics of the sodium sulfate solubility experiments.

grow and, therefore, the average hot finger surface temperature was still increasing when the experiment was terminated after about a half an hour.

The variation in the temperatures measured at the five different locations along the surface of the hot finger remained less than 3 °C until the scale layer began to form and increased by about 1 °C, if at all, after the scale layer formed. (The uncertainty associated with each thermocouple reading is ± 3.2 °C as per Section 2.4.2; therefore, the measured axial and azimuthal variations are of limited significance.) The average surface temperature of the hot finger at which precipitation begins is assumed to equal the solubility temperature for the aqueous salt solution at the concentration of interest and 250 bar. (The "average temperature" is the mean temperature measured by the five thermocouples.) This temperature is determined by visual observation of nucleation on the surface of the hot finger and/or a large increase in surface temperature of the hot finger for a small increase in bulk fluid temperature caused by a scale layer of salt forming on the hot finger. In most, but not all, runs nucleation was visually observed before the temperature difference between the hot finger surface and bulk fluid sharply increased. As shown in Fig. 2-12, the solubility temperature of the salt at the concentration of interest lies somewhere between the highest steady state temperature of the hot finger surface prior to deposition and the approximately 1 °C surface temperature increase that would have occurred once the setpoints on the controllers were raised by 1 °C had deposition not begun. Thus the solubility temperature is assumed to be the steady state average temperature along the surface of the hot finger, as measured by the five thermocouples attached to it, corresponding to the last set of temperature controller setpoints input before deposition occurred plus 0.5 °C. (In runs F and H, the controller setpoints were increased at the rate of approximately 2 °C per 15 minutes. Hence, the solubility temperature at the concentration of interest is assumed to be the highest average hot finger surface temperature measured before deposition plus 1.0 °C instead of 0.5 °C.)

The method used to collect solubility data in this dissertation is valid only if the nucleation mechanism when salt begins to deposit is exclusively heterogeneous nucleation on the surface of the hot finger. To be sure, the solubility temperature at the concentration of interest is measured at the hot finger surface. Hence, if homogeneous nucleation occurs anywhere in the boundary layer, the concentration of salt at the hot finger surface, i.e., where solubility temperature is measured, is unknown. The nucleation model developed in
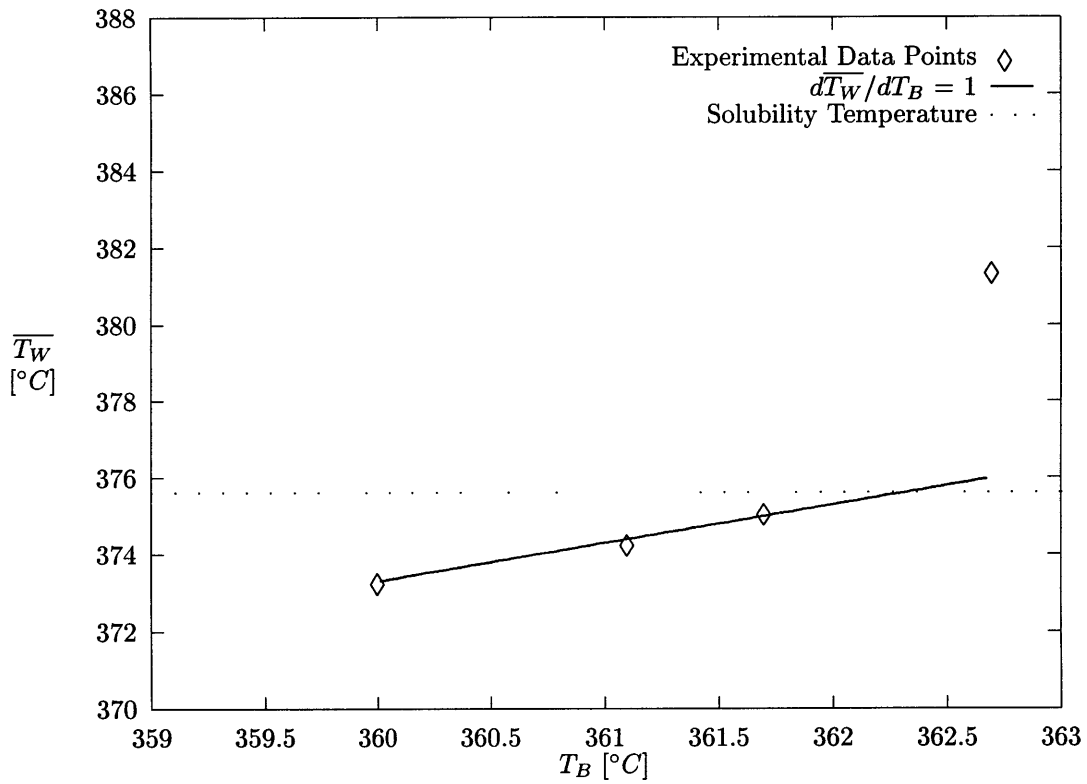
Figure 2-12: Average hot finger surface temperature versus bulk fluid temperature as the controller setpoints are stepped upward at the rate of approximately 1 °C every 15 minutes and a 6 wt% salt, aqueous potassium sulfate solution flows through the system at 10.56 gm/min and 250 bar. The solubility temperature is shown by the dotted line. The variation in the temperatures measured by the five thermocouples attached to the hot finger surface was less than 4 °C before and after deposition on the hot finger.

Chapter 5 predicts sodium sulfate and potassium sulfate will not nucleate homogeneously in the boundary layer at conditions of interest. Moreover, visual observations during the solubility experiments yielded no evidence of homogeneous nucleation in the boundary layer.

2.3.3 Deposition Experiments

The procedure for the deposition experiments follows that for the solubility experiments until the point at which aqueous salt solution flows through the system at 250 $°C$ and 250 bar. Then with the bypass line closed, i.e., valve D in Fig. 2-7 is closed, the controller setpoints are gradually stepped upward until the aqueous salt solution in the cell reaches the desired bulk temperature. After the desired bulk temperature of the fluid in the cell is stable, the resistance of the cartridge heater inside the hot finger is measured and a voltage corresponding to 10.61 watts of power to the heater is supplied. The moment the voltage is supplied to the cartridge heater is designated as t = 0.

Fig. 2-13 illustrates the dynamics of a deposition experiment. A 4 wt% salt, aqueous sodium sulfate solution is preheated to about 355 $°C$, i.e., 7 $°C$ below the temperature at which sodium sulfate precipitates at 250 bar. When the cartridge heater inside the hot finger is turned on, its surface temperature increases to about 368 $°C$. Sodium sulfate is soluble to approximately two weight percent in water at 368 $°C$ and 250 bar. The 2 wt% difference in bulk salt concentration and solubility concentration of salt at the hot finger surface drives mass transfer. The transient dynamics of the deposition experiments are explained in Chapter 3.

Throughout a run, deposition is visually observed through a telescope or CCD camera directed at the hot finger through the sapphire window located directly opposite the port in the cross containing the thermocouple. Temperatures are recorded at 1 to 2 minute intervals for the preheater walls, the wall of the Inconel 625 tube leading to the cell, the fluid inside the Inconel 625 tube leading to the cell, the fluid inside the cell, the Al block and the surface of the cross. The pressure drop across the system is also recorded.

The procedure by which the system is purged of solution using high pressure nitrogen at the end of each run takes approximately 1.5 minutes; therefore, 1.5 minutes before the desired run time has elapsed, it is started. First, power to the preheaters and heating tapes between the preheater and the test cell is cut off.
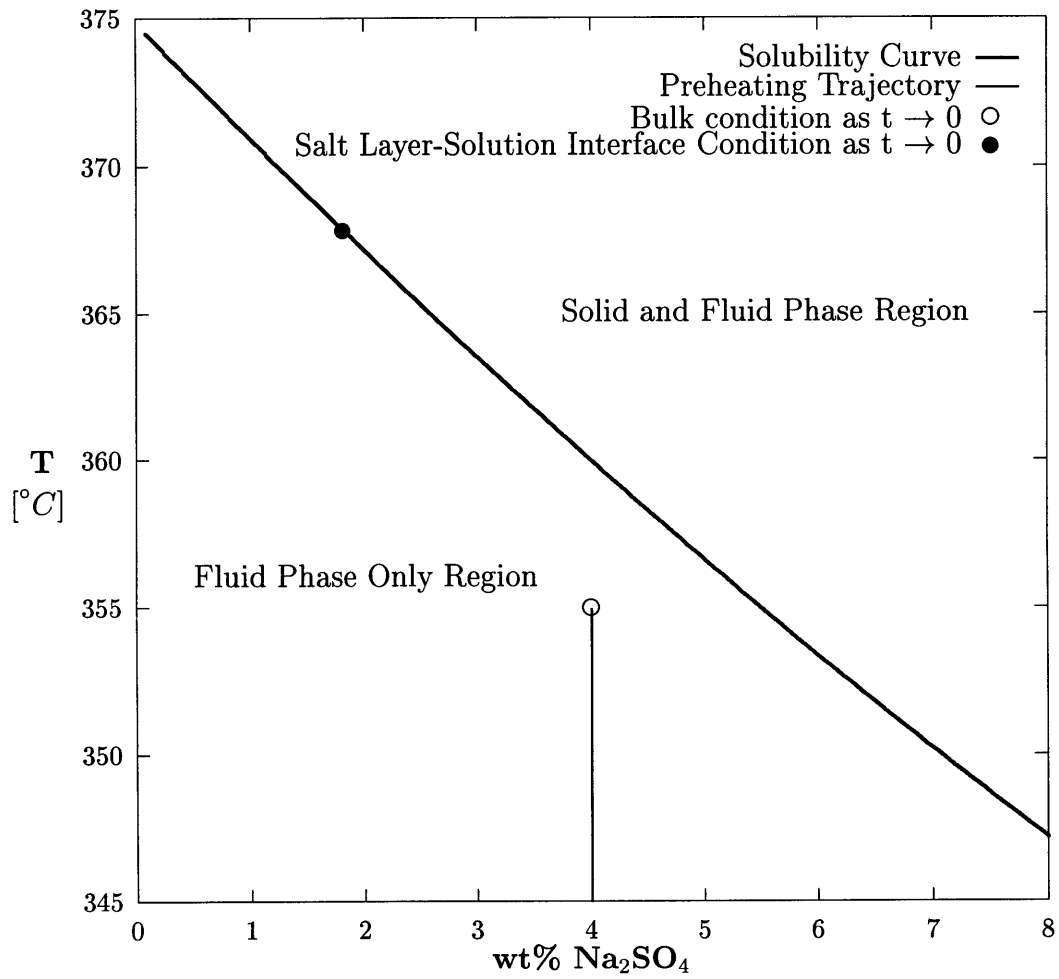
Figure 2-13: Dynamics of the sodium sulfate deposition experiments.

Then the pump is turned off and all solution upstream of the "hot valve" (valve A) is isolated by closing it. Next, valve B is opened and nitrogen flows into the capillary tube inside the Hastelloy C276 cell exit line and pushes the solution in the Hastelloy C276 cell exit line through the heat exchanger used to cool the cell effluent down and out the back pressure regulator. By monitoring the effluent from the back pressure regulator, the time at which these lines are free of solution is determined. At this time, bypass valve D is opened and then valve C is closed. After a few seconds, a nitrogen-solution interface clears the hot finger and the time this happens is recorded as the end of the run. Once the effluent is all nitrogen again, valve C is reopened, and the nitrogen is pumped through the entire system for at least a half hour to make sure it is completely free of solution, insuring that no water vapor condenses on the salt deposited on the hot finger before it is removed.

After the cell cools down, which takes about 10 hours, the hot finger is carefully removed from the cell with the salt intact and weighed on a precision balance. Then the salt that has deposited on the hot finger is loosened with tap water and easily removed using a Q tip. Once dry, the hot finger is weighed again. Subtraction of the weight of the hot finger without the salt from the weight of the hot finger with the salt intact yields the mass of salt deposited on the hot finger during a run. The salt on the hot finger when it is removed from the cell is entirely free of water, i.e., "dry", because scraping the salt off the hot finger with a dry instrument and exposing it to a dessicant under vacuum for a three week period produced no measurable change in its mass. (This procedure was done after both sodium sulfate and potassium sulfate deposition experiments.)

Between experiments, the hot finger is handled only with gloves and the surface of the protruding part is cleaned sequentially with soapy water, isopropanol and acetone. Then the hot finger is immersed in boiling tap water for a few minutes to dissolve any salt that is left on or near the ferrules which could prevent the Swagelok seal from working. (In retrospect it would be better to use the solvents after immersing the hot finger in boiling tap water.)

2.4 Experimental Data

2.4.1 Introduction

All experimental data and accompanying uncertainties are presented in this section. First, uncertainties in the experiments are discussed. Then the wall temperature profiles measured along the surface of the hot finger during the heat transfer experiments and a selected deposition experiment are provided. The results of the solubility experiments follow. The deposition rate data is presented next. Finally, the results of x-ray diffraction analyses performed on the salt deposited on the hot finger are discussed.

2.4.2 Uncertainties

Instrumentation Uncertainties

Type K commercial-grade thermocouples were used for all temperature measurements. The calibration tolerance for them is $\pm$ 3.00 $^\circ C$ at temperatures up to 400 $^\circ C$ as per ASTM Standard E320-87 in the 1992 Annual Book of ASTM Standards [5]. The total uncertainty due to thermocouple calibration and instrumentation error in all temperatures reported was $\pm$ 3.2$^\circ C$. The mass flow rate of fluid delivered by the ISCO pump system is within $\pm$ 0.05 ml/min at STP of that selected and constant to within $\pm$ 0.01 ml/min at STP during operation according to ISCO literature provided with the pump system. Deposition did not reduce the mass flow rate of solution through the system by more than about 2%. (Volumetric flow rates at STP for all the deposition experiments are provided in Table 2.12 and the volumetric flow rate of solution was 10 ml/min at STP in all the solubility experiments.) The Sensotec Model GM pressure transducers and Sensotec Model LM signal conditioners which accompany them are factory calibrated to $\pm$ 1.5 bar. Finally, the uncertainty of the power dissipated by the cartridge heater inside of the hot finger was $\pm$ 4% (0.42 Watts) based on measured fluctuations in the voltage supplied to it. (The resistance of the cartridge heater is measured before the beginning of each run and is essentially constant during each run.)

Mass of Salt Deposited Measurement

A fraction of the salt deposited on the hot finger over the course of a run is eroded off of it during the procedure by which the system is purged of aqueous salt solution. A rigorous quantitative assessment of the magnitude of this fraction was not undertaken and would be difficult. However, based on visual observations of the blow-down process, it is estimated that from 5 to 20% of the salt on the hot finger is eroded off of it during the procedure by which the system is purged of aqueous salt solution. (A method to reduce the amount of erosion during blow down in proposed in Section 6.2.) Formation of the bumps shown in Fig. 2-4 and of the pronounced dendrites shown in Fig. 2-6 on the downstream side of the hot finger during the sodium sulfate and potassium sulfate deposition experiments respectively is visually observed during the deposition process and is not a consequence of erosion during blow-down. After the hot finger is removed from the test cell, the mass of salt on it is measured using an Ohaus Model AP210S balance accurate to within ± 0.02 grams.

Thermal Capacitance of the Hot Finger

The thermal capacitance ($\rho V C_P$) of the protruding portion of the hot finger including both the copper heat spreader and C276 sleeve is about 1 J/K. (Specific heat values required to calculate the thermal capacitance values used in this section were those at a temperature characteristic of the deposition experiments.) The surface temperature profiles measured along the outer Hastelloy C276 surface of the protruding portion of the hot finger, which are presented later in this section, show that the temperature of the protruding portion of the hot finger increases by up to about 35 °C by the end of a deposition experiment. Moreover, radial temperature gradients within the hot finger wall are negligible as shown later in this chapter. The power supplied to the cartridge heater inside the hot finger is 10.61 watts and the minimum run duration is about 6 minutes. Therefore, at least 3500 Joules of energy are delivered to the hot finger over the duration of a deposition experiment and the 35 Joules of energy required to raise the temperature of the protruding portion of the hot finger by 35 °C are negligible.

The thermal capacitance of the Inconel 625 base of the hot finger is about 13 J/K. However, the temperature of the base of the hot finger most likely remains close to the temperature of the surface of the

cross, which is measured to be within about ± 5 °C of the bulk fluid temperature during each run using thermocouples attached to the cross with tie wire. At a power of 10.61 watts, it would take approximately 6 seconds to change the temperature of the base of the hot finger by 5 °C. Hence, the thermal capacitance of the base of the hot finger is unimportant.

Bulk Fluid Temperature

A 0.125 inch OD, type K thermocouple with a 0.018 inch thick Incoloy sheath is used to measure the bulk fluid temperature in the test cell. The error in this measurement which is caused by (axial) heat conduction along this thermocouple is quantified in this section. The thermocouple is fed through a hole machined into an Inconel 625 plug and welded to this plug. The plug-thermocouple assembly occupies the port of the test cell directly opposite the port through which the hot finger is viewed as per Fig. 2-8. Only 0.1 inches of the thermocouple protrude into the solution, thus the length to diameter ratio of the portion of the thermocouple exposed to fluid in the cell is 0.8. Obviously, this length to diameter ratio is far less than optimal.

The average velocity of the solution flowing through the cell based on its entire cross sectional area at the location of the thermocouple used to measure bulk temperature is about 0.43 mm/sec (0.017 in/sec) at conditions which typify the experiments. (Pure water flowing through the cell at 10 gm/min, 355 °C and 250 bar was assumed to typify the experiments.) The Reynolds number based on this velocity and the 0.125 inch diameter of the thermocouple is about 12. However, the actual Reynolds number is probably significantly less than 12 because the fluid near the thermocouple is likely relatively stagnant, but in the Reynolds number calculation the velocity was assumed to be uniform over the entire cross sectional area of the cell. When the Grashof number based on the diameter of the hot finger becomes larger than Re^2, natural convection begins to dominate transport. The Grashof number is defined by Eq. 2.1, where β is the volumetric thermal expansion coefficient, ΔT the temperature difference driving natural convection, ν the kinematic viscosity and α the thermal diffusivity.

$$Gr = \frac{g\beta\Delta T D^3}{\nu^2} \tag{2.1}$$

114

Only about a 0.0015 °C temperature difference between the thermocouple surface and bulk fluid is required for the Grashof number based on the thermocouple diameter to equal the Reynolds number squared based on the thermocouple diameter. Hence natural convection is the dominant mode of heat transfer between the surface of the thermocouple and bulk fluid if there is a significant temperature difference present between them.

The difference between the surface temperature of the cross, as measured by thermocouples attached to it using tie wire, and the bulk fluid temperature is generally within ± 5 °C. (In general, temperature measured at different locations on the surface of the cross are both above and below the measured bulk solution temperature during each run.) Approximating the thermocouple used to measure bulk fluid temperature as a fin, it is possible to determine the temperature of the tip of the thermocouple when the temperature of the "base" of the thermocouple is assumed to be 5 °C higher than the bulk fluid temperature. (The "base" of the thermocouple is designated as the part of it that is flush with the Inconel 625 plug to which it is silver soldered.) There is a significant thermal resistance between the surface temperature of the cross and the "base" of the thermocouple, thus the temperature of the "base" of the thermocouple is probably closer than 5 °C to the fluid temperature. However, 5 °C serves as a conservative estimate. Radial temperature gradients within the Incoloy sheath of the thermocouple are negligible and it may be approximated as a fin provided that the Biot number characterizing it is about 0.1 or less. The Biot number for the Incoloy sheath is defined by Eq. 2.2, where h is the heat transfer coefficient between the Incoloy sheath and the bulk fluid; t is the thickness of the Incoloy sheath; and k is the thermal conductivity of the Incoloy sheath. The Biot number characterizing the Incoloy sheath of the thermocouple is about 0.05; therefore, radial temperature gradients within it are small enough to approximate it as a fin. (The heat transfer coefficient between surface of the thermocouple and bulk solution is a function of the temperature difference between them; therefore, the Biot number calculation had to be done a posteriori to the fin calculation.) The tip of the thermocouple in the fin analysis is assumed to be hollow and, thus, to have a cross sectional area equal to $\frac{\pi}{4}(OD_{INC} - 2t)^2$, where, OD_{INC}, is the outside diameter of the thermocouple (0.125 inches), and t is the wall thickness of the Incoloy sheath (0.018 inches). However, the actual area of the thermocouple tip is closer to $\frac{\pi OD_{INC}^2}{4}$. The assumption that the thermocouple tip is hollow for the purposes of the fin analysis is acceptable because it

reduces the total surface area of the Incoloy sheath exposed to solution by only about 14%.

$$Bi = \frac{ht}{k} \qquad (2.2)$$

The temperature distribution for a fin with convective heat transfer at its tip is given by:

$$\frac{\theta}{\theta_L} = \frac{cosh(m(L-x)) + \frac{h}{mk}sinh(m(L-x))}{cosh(mL) + \frac{h}{mk}sinh(mL)} \qquad (2.3)$$

where, $\theta = T - T_{BASE}$, L is the length of the fin, x is the axial distance from the base of the fin and m $=$ $\frac{hP}{kA_{cs}}$. P and A_{cs} are the external perimeter and cross sectional area respectively of the fin. For pure natural convection, the mean Nusselt number for heat transfer from an isothermal heated cylinder in a quiescent medium can be determined from Eq. 2.4 [64]. (The fin is assumed isothermal for the purpose of calculating the heat transfer coefficient between it and the fluid in the test cell.) The constants C and n in Eq. 2.4 are 0.48 and 0.25 respectively in the 10^4-10^7 Rayleigh number range and 0.125 and 1/3 respectively in the 10^7-10^{12} Rayleigh number range and D_c is the diameter of the cylinder.

$$\overline{Nu}_{D_c} = CRa_{D_c}^n \qquad (2.4)$$

The Rayleigh number is equal to the Grashof number times the Prandtl number and $\overline{Nu} = \frac{\overline{h}D_c}{k}$.

The heat transfer coefficient between the fin and the surrounding fluid is coupled to the temperature distribution along the fin; consequently, an iterative procedure must be invoked to solve for the temperature distribution along the fin. The fin calculation is begun by guessing a characteristic temperature difference between the fin and bulk fluid. Next the heat transfer coefficient between the fin surface and surrounding fluid is calculated and the temperature distribution along the fin determined. Iterations are performed until the average fin temperature minus the bulk fluid temperature equals the temperature difference used to calculate the natural convective heat transfer coefficient between the fin and the surrounding fluid. The average temperature of the fin is approximated as its base temperature plus its tip temperature divided by

116

two. The iterations converge when the average temperature difference between the fin and bulk fluid is 3.9 °C. Thus when the temperature of the thermocouple's base is 360 °C and the bulk fluid temperature is 355 °C, for example, the fin analysis predicts the temperature of the thermocouple tip is 357.7 °C which is 2.7 °C larger than the actual bulk temperature being measured. Similarly, if the base of the thermocouple were 5 °C cooler than the bulk solution temperature, one expects the thermocouple to read about 2.7 °C too low. Since the junction of the thermocouple is grounded to the tip of the Incoloy sheath the thermocouple measures the tip temperature calculated in the fin analysis. Hence, $\frac{\theta_L}{\theta_B} = 0.54$ typifies the measurement and the fin analysis predicts that the thermocouple essentially provides the mean value of the temperatures of the base of the thermocouple and the bulk fluid.

In the pure water heat transfer experiments and in the single deposition experiment which was run with the hot finger instrumented with five 10 mil thermocouples, before the cartridge heater inside the hot finger is turned on the temperature of the surface of the hot finger should be essentially equal to the temperature of the bulk solution. As per Tables 2.5, 2.7 and 2.8 at conditions relevant to the deposition experiments the average temperature of the surface of the hot finger before the cartridge heater inside it is turned on is measured to be 1.7 to 2.8 °C higher than the measured bulk fluid temperature. This is consistent with the fin analysis which predicted that the bulk temperature measurement is inaccurate by up to about 2.5 °C since in all three experiments the temperature measured at at least one location on the cross was below the measured temperature of the bulk solution. There is also an inherent 3.2 °C instrumentation error associated with each thermocouple as per Section 2.4.2. In conclusion it is, unfortunately, possible that the bulk temperature measurement is too low or, less likely, too high by a couple of degrees centigrade during the solubility and deposition experiments. In Section 4.2, further evidence is provided that the bulk temperature measurements are more likely to be low than high at the conditions investigated in the solubility and deposition experiments.

Conduction of Heat Through the Inconel 625 Base and into the Surrounding Fluid

A small fraction of the power supplied to the cartridge heater within the hot finger is conducted through the Inconel 625 base and into the bulk fluid over an area where salt is not depositing. The analyses in this

section quantify the magnitude of this fraction. To simplify the subsequent fin analysis it is first shown that the copper heat spreader may be assumed isothermal for the purpose of the fin calculation.

The thermal resistances to heat transfer per unit length in the radial direction by conduction through the copper heat spreader and the Hastelloy C276 sleeve of the protruding portion of the hot finger, and natural convection from the Hastelloy C276 sleeve to the adjoining fluid are given by R_1', R_2' and R_3' respectively:

$$R_1' = \frac{ln(r_2/r_1)}{2\pi k_{Cu}} \tag{2.5}$$

$$R_2' = \frac{ln(r_3/r_2)}{2\pi k_{C276}} \tag{2.6}$$

$$R_3' = \frac{1}{2\pi r_3 h_{NC}} \tag{2.7}$$

The radii r_1, r_2 and r_3 are the inner radius of the copper heat spreader (62.5 mils), outer radius of the copper heat spreader/inner radius of the Hastelloy C276 sleeve (95 mils) and outer radius of the Hastelloy C276 sleeve (100 mils) respectively. The thermal conductivity of copper and Hastelloy C276 at conditions of interest are approximately 375 and 15 $\frac{W}{mK}$ respectively. Based on the measured temperature differences between the hot finger surface and bulk solution, the natural convection heat transfer coefficient along the surface of the hot finger is about 2450 W/m^2/K. It follows from the foregoing equations that the (radial) thermal resistances per unit length R_1', R_2' and R_3' are equal to 1.78*10^{-4}, 5.44*10^{-4} and 2.56*10^{-2} mK/W respectively. Obviously, natural convection between the Hastelloy C276 sleeve and the fluid is the dominant thermal resistance. (No attempt is made to account for contact resistances between the cartridge heater and the copper heat spreader and between the copper heat spreader and the Hastelloy C276 sleeve.)

Radial temperature gradients within the copper heat spreader are negligible provided that the (radial) Biot number characterizing it is about 0.1 or less. The Biot number for the copper part of the hot finger is defined by Eq. 2.8, where U is the overall heat transfer coefficient between the copper-Hastelloy C276 interface and the bulk fluid, t, the thickness of the copper, and, k, the thermal conductivity of the copper. Neglecting the contact resistance between the copper heat spreader and the Hastelloy C276 sleeve, the overall heat transfer coefficient between the copper part of the hot finger and the bulk fluid is calculated using Eq. 2.9, where h is the natural convection heat transfer coefficient between the outer surface of the

Hastelloy C276 sleeve and the bulk fluid and t and k are the thickness and thermal conductivity of the Hastelloy C276 sleeve respectively. As already mentioned, at the beginning of the deposition experiments, the heat transfer coefficient between the Hastelloy C276 sleeve and bulk fluid is about 2450 $\frac{W}{m^2 K}$. (Once salt begins to deposit on the hot finger the thermal resistance between the Hastelloy C276 sleeve and bulk solution increases because of the added thermal resistance of the salt layer. This is accounted for below.) The thickness and thermal conductivity of the Hastelloy C276 sleeve are about 0.13 mm and 15 $\frac{W}{mK}$ respectively. Its thermal resistance is negligible compared to the thermal resistance due to natural convection from the C276 sleeve to the bulk fluid, thus the overall heat transfer coefficient between the copper heat spreader and bulk fluid is approximated as 2450 $\frac{W}{m^2 K}$ at the beginning of the experiments. Noting that the thermal conductivity and thickness of the copper are about 375 $\frac{W}{mK}$ and 0.8 mm respectively, the resulting Biot number characterizing it is about 0.005; therefore, significant radial temperature gradients do not exist within the hot finger. Moreover, the temperature profiles measured along the hot finger which are provided later in this chapter show that there are no appreciable temperature gradients axially or azimuthally along it. Additionally, the fin parameter m for the copper heat spreader is approximately 100 meters^{-1}. The temperature of a fin changes from its base temperature to that of its surroundings over a length scale of order 1/m, i.e., 0.01 meters. Thus, since the length of the copper heat spreader is equal to about 0.00025 m, it makes sense that no significant axial variations in the surface temperature of the hot finger are measured. In conclusion, radial, axial and azimuthal temperature variations within the copper heat spreader are negligible; therefore, it may be assumed isothermal for the purpose of calculating the rate of heat conducted from the copper heat spreader to the Inconel 625 base.

$$Bi = \frac{Ut}{k} \tag{2.8}$$

$$U = \frac{1}{\frac{1}{h} + \frac{t}{k}} \tag{2.9}$$

From the location where the copper heat spreader is silver soldered to the Inconel 625 base, the Inconel 625 base can be modeled as an annular fin with a rectangular profile. A portion of the heat supplied by the

cartridge heater inside the hot finger is conducted through the Inconel 625 base/annular fin and into the surrounding fluid. The base of this fin is set equal to the temperature of the copper heat spreader. Between the location where the Inconel 625 base is silver soldered to the copper heat spreader and the location where it becomes flush with the Swagelock cross, it is primarily composed of sections which are 43, 62 and 75 mils thick as per Fig. 2-9. Thus, to approximate the Inconel 625 base as an annular fin, it is assumed to have a uniform thickness of 60 mils. Heat transfer on the backside of the annular fin is very weak relative to that on the front side because the backside is exposed to air and metal. Thus the backside of the annular fin is assumed to be adiabatic. The rate of heat transfer from the annular fin to the fluid in the test cell equals half the rate of heat transfer from a hypothetical annular fin which is twice as thick as the real annular fin. Both the front and back surfaces of the hypothetical annular fin are exposed to the same conditions as the front side of the real annular fin which is exposed to the fluid. The midplane of the hypothetical annular fin is adiabatic due to symmetry; consequently, the front or back half of the hypothetical annular fin exactly corresponds to the actual fin which has one side exposed to the fluid and the other side adiabatic. The thickness of the hypothetical fin is set equal to 120 mils and the actual rate of heat transfer between the Inconel 625 base and fluid equals half the rate of heat transfer from the hypothetical annular fin to the fluid. The radius of the base of the annular fin where the copper heat spreader is silver soldered to the Inconel 625 is about 0.11 inches and the total surface area of the fin which is exposed to the fluid is about 0.67 square inches. To determine an appropriate outer radius of the annular fin, the inner radius and total surface area of the fin are set equal to 0.11 inches and 0.67 square inches respectively, resulting in an outer radius of 0.475 inches.

For a laminar natural convection boundary layer on an object of any shape, Lienhard [52] suggests that the average Nusselt number is correlated by:

$$\overline{Nu}_L = 0.52 Ra_L^{\frac{1}{4}} \tag{2.10}$$

where the characteristic length L is the length of the boundary layer. For the purpose of calculating the heat transfer coefficient characterizing the annular fin, L is set equal to 0.2 inches. Incropera and Dewitt [41]

provide the fin efficiency, η_f, of an annular fin as a function of the parameter $L_c^{\frac{3}{2}}\left(\frac{h}{kA_P}\right)^{\frac{1}{2}}$, where, L_c is the outer radius minus the base radius of the annular fin plus the thickness of the fin divided by two and A_P equals L_c multiplied by the thickness of the fin. The fin efficiency, defined by Eq. 2.11, is the rate of heat transfer from the fin to the fluid divided by the rate of heat transfer from the fin to the fluid for the hypothetical case when the temperature of the entire fin equals its base temperature. Moreover, the temperature difference averaged over the entire surface area of the annular fin exposed to solution equals $\eta_f\theta_B$.

$$\eta_f = \frac{Q_{fin}}{hA_{fin}\theta_B} \tag{2.11}$$

An iterative procedure is required to solve for the rate of heat transfer from the copper heat spreader through the Inconel 625 base and into the fluid. First, the average temperature of the fin is guessed. Next, the Rayleigh number characterizing natural convection between the fin and the fluid is calculated. The temperature difference required to calculate the Rayleigh number is set equal to the average temperature of the annular fin minus the bulk fluid temperature. Eq. 2.10 is used to determine the heat transfer coefficient between the annular fin and the fluid. (The natural convective flow induced by the transfer of heat from the annular fin to the bulk fluid is laminar; therefore, Eq. 2.10 applies.) Next, the parameter $L_c^{\frac{3}{2}}\left(\frac{h}{kA_P}\right)^{\frac{1}{2}}$ is calculated and used to determine the fin efficiency. From the fin efficiency the average temperature of the fin is calculated and iterations are performed until the average fin temperature used in the fin calculation equals the average fin temperature based on the resulting η_f. The rate of heat transfer through the Inconel 625 base and into the fluid may then be determined using Eq. 2.11 and dividing the result by 2.

The procedure developed above was used to determine the rate of heat transfer through the Inconel 625 base and into the fluid for a selected pure water experiment. In run D (see Table 2.7) the mass flow rate of the pure water was 9.98 gm/min and the pressure in the system was maintained at approximately 3610 psig. The cartridge heater inside the hot finger was dissipating 10.61 watts and the bulk fluid (water) temperature was maintained between 355.8 and 358.4 °C. As per Table 2.7, the temperature of the copper heat spreader

for these conditions was about 12.3 $°C$ above the bulk fluid temperature. At these conditions the fin analysis predicts that 1.65 watts will be conducted through the Inconel 625 base and into the fluid. 1.65 watts equals 15.6% of the power supplied to the cartridge heater. However, a fraction of this 1.65 watts will be dissipated through the portion of the Inconel 625 base directly adjacent to where it is silver soldered to the copper heat spreader and salt will deposit. To be sure, the iterative fin calculation converged at a fin efficiency equal to 18.5%. Hence the fin is relatively "long", i.e., the tip temperature is close to the temperature of the surrounding medium. Hence, the "heat leak" to the fraction of the annular fin's surface on which salt does not deposit is estimated to be less than 1 Watt. It is noted that the Biot number based on the representative thickness of the actual Inconel 625 base, i.e., 60 mils is about 0.17 for these conditions, thus treating it as an annular fin is acceptable.

As salt deposits on the hot finger, the thermal resistances between the portion of the surface of the annular fin where salt deposits and the surrounding fluid and between the Hastelloy C276 sleeve and surrounding fluid increase substantially. Estimation of the fraction of the heat supplied to the cartridge heater inside the hot finger which is conducted through its Inconel 625 base and into the fluid over a surface area of the Inconel 625 base where salt does not deposit may be accomplished with an annular fin calculation similar to that above. However, it would be far more complex; consequently, an alternative procedure is used. During a typical deposition experiment, the diameter of the salt layer-solution interface is of order 0.6 inches. The thermal boundary layer formed around the salt layer-solution interface is very thin compared to the diameter of the hot finger (see Section 3.8). Therefore, the surface temperature of the Inconel 625 base at the diameter of the nominal salt layer-solution can not exceed the saturation temperature corresponding to the bulk concentration. Otherwise; salt would deposit on the Inconel 625 base of the hot finger at a diameter beyond the salt layer-solution interface and visual observations of the hot finger after the deposition experiments show it does not. The fraction of the Inconel 625 base extending from the salt layer-solution interface to where it rests against the Swagelock cross corresponds to a fraction of the same annular fin used to estimate the "heat leak" above. In the sodium sulfate experiments in which the concentration of salt in the inlet stream was 4 wt%, for example, the saturation temperature corresponding to the bulk concentration is about 362.5 $°C$ and the bulk solution temperature is about 356 $°C$. Thus the base temperature of a second

122

annular fin is set equal to 362.5 $°C$ and the surrounding fluid temperature is 356 $°C$. Following the same procedure as before, it is estimated that the efficiency of this fin is about 32% and the heat transfered from it into the fluid is about 1.15 watts. Based upon the foregoing fin analyses it is subsequently assumed that 90% of the power supplied to the cartridge heater inside the hot finger drives the deposition process and 10% of it is simply convected into the fluid. Thus for the purposes of theoretically predicting the deposition rate in subsequent chapters, the power supplied to the hot finger is set equal to ηP, where η equals 0.9 and P equals 10.61 Watts.

2.4.3 Hot Finger Surface Temperature Profiles for Pure Water Heat Transfer Experiments

A series of simple heat transfer experiments were run using the hot finger instrumented with the 10 mil diameter thermocouples. The purpose of these experiments was to validate the heat transfer characteristics of the test cell. This is accomplished in Section 4.2 by comparing the measured temperature differences between the hot finger surface and bulk solution against those predicted by standard heat transfer correlations. The conditions for which the temperature distribution along the hot finger surface was measured in the pure water heat transfer experiments are summarized in Table 2.1. In Run A the temperature profile along the surface of the hot finger was measured under purely natural convective conditions, i.e., with the pump turned off. In this experiment the cartridge heater inside of the hot finger was dissipating 10.61 watts and all other heaters were turned off. The pressure in the cell was approximately atmospheric and the initial bulk fluid temperature was 21.0 $°C$. The results are presented in Table 2.2 where $\overline{T_W}$ represents the average temperature of the five thermocouples attached to the surface of the hot finger at the locations shown in Fig. 2-9 and ΔT_{W-B} is the wall-to-bulk temperature difference based on $\overline{T_W}$ and T_{bulk}. A plot of the results is shown in Fig. 2-14. This experiment was repeated with pure water flowing through the system at 40 gm/min at approximately atmospheric pressure and the results are tabulated in Table 2.3 and plotted in Fig. 2-15. In Table 2.4 results are provided for the case when the there was not cross flow, pure water filled the cell at approximately 2750 psig and the initial bulk fluid temperature was 21.5 $°C$.

Pure water heat transfer experiments were also conducted at conditions typical of deposition experiments

Run	T_{bulki}	P	Flow Rate
-	°C	bar	$\frac{gm}{min}$
A	21.0	atm.	0
B	21.9	atm.	40.0
32	21.5	2750	0
C	314.5	3560	0
34	314.0	3650	10.1
D	355.8	3610	10.1

Table 2.1: Initial bulk fluid temperature, system pressure and pure water mass flow rate for the the experiments in which the temperature distribution along the surface of the hot finger was measured to validate the heat transfer characteristics of the system.
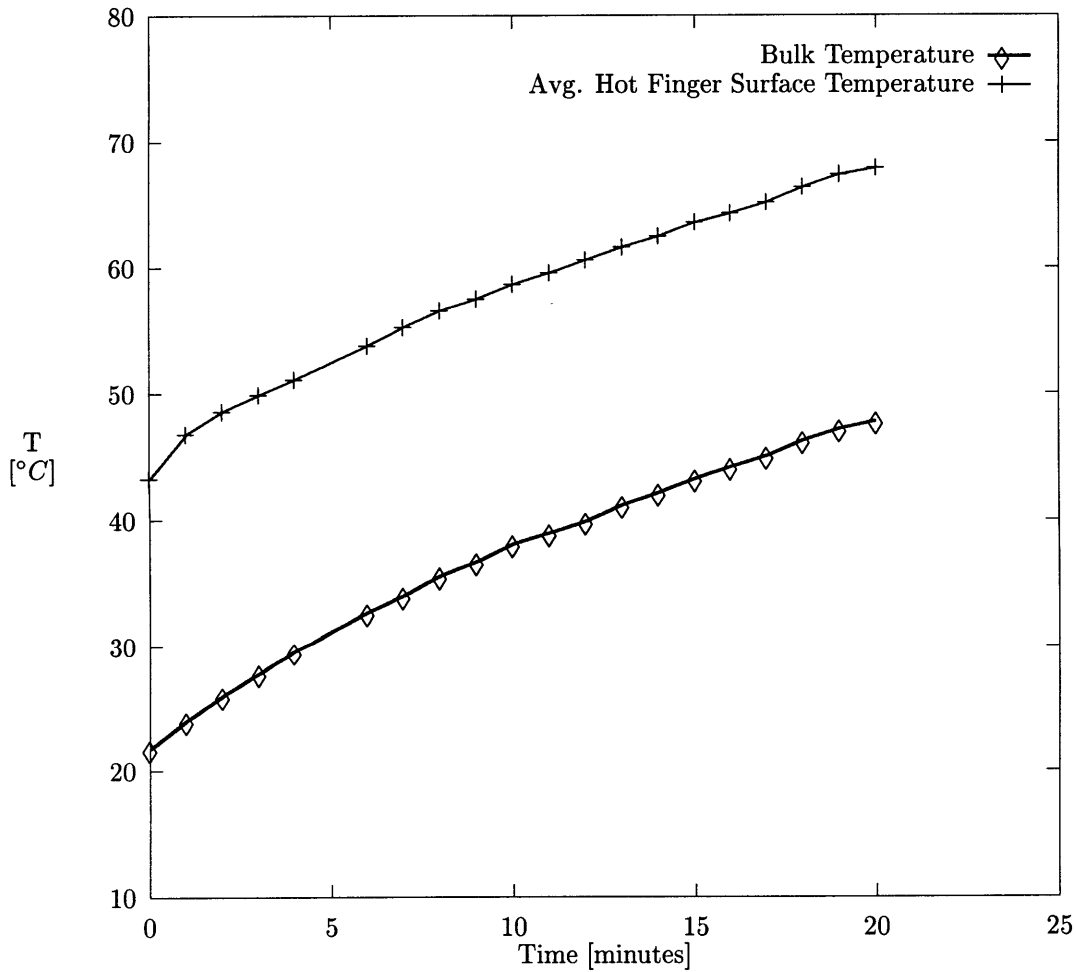
Figure 2-14: Bulk solution temperature and average hot finger surface temperature versus time for the pure water heat transfer experiment at atmospheric pressure with the pump turned off. The solution was not preheated before entering the test cell. (Data is contained in Table 2.2 and corresponds to Run A.)
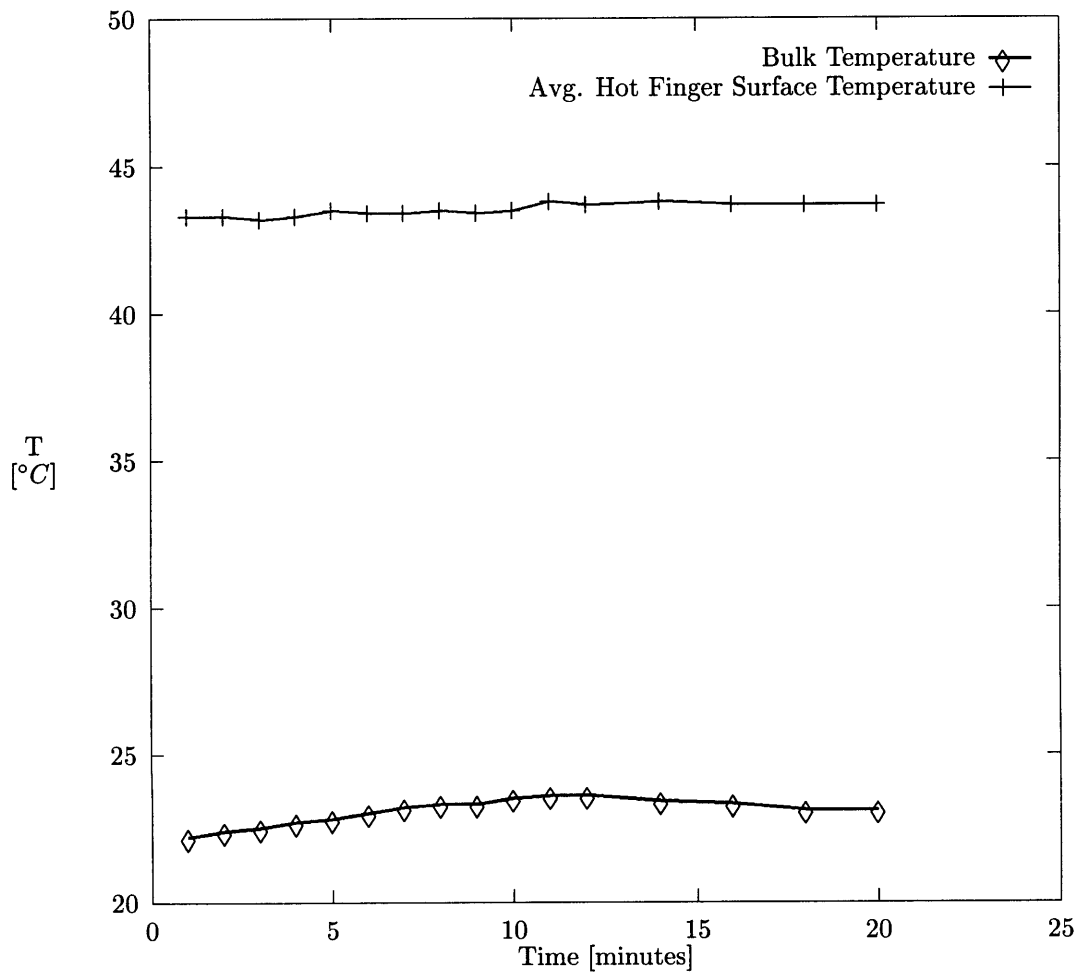
Figure 2-15: Bulk solution temperature and average hot finger surface temperature versus time for the pure water heat transfer experiment at atmospheric pressure with water circulating through the system at 40.0 gm/min. The solution was not preheated before entering the test cell. (Data is contained in Table 2.3 and corresponds to Run B.)

Time [min]	T_{bulk} [°C]	T_{F1} [°C]	T_{F2} [°C]	T_{F3} [°C]	T_{F4} [°C]	T_{F5} [°C]	T_W [°C]	ΔT_{W-B} [°C]
<0	21.0	21.2	21.2	21.1	21.1	21.1	21.1	0.1
0	21.8	40.3	43.4	44.6	44.4	44.0	43.3	21.5
1	24.0	45.1	46.2	48.6	46.0	48.1	46.8	22.8
2	26.0	47.4	49.2	50.2	47.9	48.2	48.6	22.6
3	27.8	49.0	50.7	50.2	49.7	49.8	49.9	22.1
4	29.6	50.3	50.7	51.4	50.9	52.3	51.1	21.5
5	31.0	52.5	53.3	-	-	-	-	-
6	32.7	53.0	54.1	54.6	52.8	54.5	53.8	21.1
7	34.0	54.4	54.8	56.0	55.0	56.1	55.3	21.3
8	35.6	55.6	56.6	57.1	56.0	57.5	56.6	21.0
9	36.7	57.0	57.0	58.5	56.6	58.6	57.5	20.8
10	38.1	58.0	58.4	59.6	57.6	59.8	58.7	20.6
11	39.0	59.1	59.1	60.6	58.6	60.6	59.6	20.6
12	39.9	60.0	60.0	61.1	60.4	61.5	60.6	20.7
13	41.2	61.2	61.1	62.5	60.6	62.5	61.6	20.4
14	42.2	62.1	61.7	63.5	61.5	63.5	62.5	20.3
15	43.3	63.0	63.0	65.3	62.5	64.4	63.6	20.3
16	44.2	64.1	63.7	65.6	63.3	64.8	64.3	20.1
17	45.1	65.0	64.9	66.1	64.1	66.0	65.2	20.1
18	46.3	65.8	65.8	68.1	65.2	67.1	66.4	20.1
19	47.2	67.1	66.8	67.7	67.3	68.1	67.4	20.2
20	47.8	67.9	67.5	68.7	68.1	67.1	67.9	20.1

Table 2.2: Temperatures measured along the surface of the hot finger when the cell was filled with pure water at atmospheric pressure and at an initial temperature of 21.0 °C. The cartridge heater inside the hot finger was dissipating 10.61 watts and all the other heaters were turned off. The pump was turned off. (Run A)

and the results are shown to be consistent with standard natural convection heat transfer correlations in Section 4.2. In runs C and 34, the pure water flow rate was 0 and 10.1 gm/min respectively and the pressure in the system was maintained at about 3600 psig. The bulk temperature of the solution around the hot finger was about 315 °C at the beginning of these runs, the cartridge heater inside the hot finger was dissipating 10.61 watts and the data are presented in Tables 2.5 and 2.6. Finally, in Run D pure water was flowing through the system at 10.1 gm/min, the system pressure was about 3610 psig, the initial bulk fluid temperature in the cell was 355.8 °C and the results are presented in Table 2.7.

2.4.4   Hot Finger Surface Temperature Profile during a Deposition Experiment

The temperature profile along the surface of the hot finger was also measured during a sodium sulfate deposition experiment. The hot finger surface temperature profile data for a deposition run in which the

Time [min]	T_{bulk} [°C]	T_{F1} [°C]	T_{F2} [°C]	T_{F3} [°C]	T_{F4} [°C]	T_{F5} [°C]	T_W [°C]	ΔT_{W-B} [°C]
<0	21.9	21.2	21.2	21.2	21.2	21.5	21.3	-0.6
1	22.2	43.2	43.5	43.7	43.7	42.6	43.3	20.9
2	22.4	43.4	43.8	43.9	42.6	42.8	43.3	20.9
3	22.5	43.5	43.7	43.8	42.5	42.7	43.2	20.7
4	22.7	43.5	43.6	43.9	42.6	42.9	43.3	20.6
5	22.8	43.7	43.7	43.9	43.1	43.0	43.5	20.7
6	23.0	43.6	43.6	43.9	42.7	43.2	43.4	20.4
7	23.2	43.7	43.6	43.9	42.6	43.2	43.4	20.2
8	23.3	43.7	43.5	44.1	42.7	43.3	43.5	20.2
9	23.3	43.7	43.6	43.9	42.8	43.1	43.4	20.1
10	23.5	43.8	43.6	44.3	42.8	43.2	43.5	20.0
11	23.6	44.9	43.7	44.2	42.8	43.2	43.8	20.2
12	23.6	44.0	43.8	44.4	43.0	43.3	43.7	20.1
14	23.4	44.1	44.1	44.5	42.9	43.2	43.8	20.4
16	23.3	44.1	44.1	44.2	42.8	43.3	43.7	20.4
18	23.1	44.1	44.1	44.1	42.7	43.3	43.7	20.6
20	23.1	44.1	44.2	44.4	42.8	43.1	43.7	20.6

Table 2.3: Temperatures measured along the surface of the hot finger with pure water pure water flowing through the cell at a flow rate of 40 $\frac{gm}{min}$ at atmospheric pressure. The cartridge heater inside the hot finger was dissipating 10.61 watts and all other heaters were turned off. (Run B)

Time [min]	T_{bulk} [°C]	T_{F1} [°C]	T_{F2} [°C]	T_{F3} [°C]	T_{F4} [°C]	T_{F5} [°C]	T_W [°C]	ΔT_{W-B} [°C]
0	21.5	20.9	20.6	19.9	19.8	21.4	20.3	1.2
.5	22.2	46	49	48	48	48	47.8	25.6
2	23.0	51	51	51	51	51	51.0	28.0
7	31.6	53	53	53	54	52	53.0	21.4
14	37.2	58	58	58	59	57	58.0	20.8
20	43.1	63	62	63	64	63	63.0	19.9
25	46.6	66	67	66	67	66	66.4	19.8

Table 2.4: Temperatures measured along the surface of the hot finger when the cell was filled with pure water at a pressure of about 2750 psig and the cartridge heater inside the hot finger was dissipating 10.61 watts. The pump was turned off. (Run 32)

Time [min]	T_{bulk} [°C]	T_{F1} [°C]	T_{F2} [°C]	T_{F3} [°C]	T_{F4} [°C]	T_{F5} [°C]	$\overline{T_W}$ [°C]	ΔT_{W-B} [°C]
<0	314.5	316.7	318.7	318.6	317.9	314.5	317.3	2.8
2	317.1	329.9	331.7	331.5	329.7	330.3	330.6	13.5
4	318.2	330.9	332.9	332.5	330.9	-	331.8	13.6
6	318.7	331.3	333.3	333.2	331.2	331.6	332.1	13.4
8	318.9	331.8	333.8	333.7	331.8	332.2	332.7	13.8
10	319.2	332.2	334.0	334.0	331.8	332.5	332.9	13.7
12	319.5	332.2	332.6	333.9	331.7	332.7	332.6	13.1
14	319.6	332.2	334.3	334.1	332.2	332.8	333.1	13.5
16	319.6	332.4	334.5	334.2	332.5	332.9	333.3	13.7
18	319.7	332.4	334.5	334.2	332.3	332.9	333.3	13.6
20	319.7	332.4	334.3	334.3	332.3	333.0	333.3	13.6

Table 2.5: Temperatures measured along the surface of the hot finger when the cell was filled with pure water at a pressure of about 3560 psig and the cartridge heater inside the hot finger was dissipating 10.61 watts. The pump was turned off and the initial bulk temperature in the cell was 314.5 °C. (Run C)

Time [min]	T_{bulk} [°C]	T_{F1} [°C]	T_{F2} [°C]	T_{F3} [°C]	T_{F4} [°C]	T_{F5} [°C]	$\overline{T_W}$ [°C]	ΔT_{W-B} [°C]
34	314.0	326	328	327	328	327	327.2	13.2
39	314.7	327	328	328	328	327	327.6	12.9
44	315.3	327	329	328	329	328	328.2	12.9
49	315.8	328	329	329	329	328	328.6	12.8
54	316.2	328	330	329	330	328	329.0	12.8

Table 2.6: Temperatures measured along the surface of the hot finger. The mass flow rate of the pure water was 10.1 gm/min and the pressure in the system was maintained at approximately 3650 psig. The heater inside the hot finger was dissipating 10.61 watts. (Run 34)

Time [min]	T_{bulk} [°C]	T_{F1} [°C]	T_{F2} [°C]	T_{F3} [°C]	T_{F4} [°C]	T_{F5} [°C]	$\overline{T_W}$ [°C]	ΔT_{W-B} [°C]
<0	355.8	357.2	359.9	359.7	358.7	355.8	358.3	2.5
2	357.4	368.5	371.0	370.9	368.9	369.6	369.8	12.4
4	357.8	368.8	371.3	371.2	369.1	370.0	370.1	12.3
6	358.0	369.2	371.6	371.7	369.4	370.2	370.4	12.4
8	358.1	369.1	371.4	371.6	369.3	370.1	370.3	12.2
10	358.2	369.3	371.8	371.8	369.4	370.4	370.5	12.3
12	358.4	369.4	371.9	371.8	369.7	370.5	370.7	12.3
14	358.3	369.3	371.7	371.8	369.5	370.4	370.5	12.2
16	358.4	369.3	371.7	371.7	369.5	370.4	370.5	12.1
18	358.3	369.4	371.9	371.9	369.7	370.5	370.7	12.4
20	358.4	369.4	371.9	371.7	369.6	370.5	370.6	12.2

Table 2.7: Temperatures measured along the surface of the hot finger. The mass flow rate of the pure water was 10.1 gm/min and the pressure in the system was maintained at approximately 3610 psig. The heater inside the hot finger was dissipating 10.61 watts. (Run D)

Time [min]	T_{bulk} [°C]	T_{F1} [°C]	T_{F2} [°C]	T_{F3} [°C]	T_{F4} [°C]	T_{F5} [°C]	T_W [°C]	ΔT_{W-B} [°C]
0	21.5	20.9	20.6	19.9	19.8	21.4	20.3	1.2
< 0	354.9	355	357	358	357	356	356.6	1.7
0	354.9	361	365	366	368	366	365.2	10.3
0.5	-	367	369	369	371	369	369.0	-
1.0	355.4	373	376	375	379	377	376.0	20.6
1.5	-	375	380	379	380	379	378.6	-
2.0	356.0	378	381	381	382	381	380.6	24.6
2.5	-	378	382	382	383	381	381.2	-
3.0	356.6	379	383	383	384	382	382.2	25.6
3.5	-	380	383	383	384	383	382.6	-
4.0	356.8	380	384	384	385	383	383.2	26.4
4.5	-	381	384	384	385	384	383.6	-
5.0	356.8	381	381	385	384	384	383.0	26.2
5.5	-	381	385	385	384	384	383.8	-
6.0	357	382	385	385	386	385	384.6	27.6
6.5	-	382	386	386	386	385	385.0	-
7.0	357.1	382	386	386	387	386	385.4	28.3
7.5	-	383	387	387	387	386	386.0	-
8.0	357.1	383	387	387	387	386	386.0	28.9
8.5	-	383	387	387	387	386	386.0	-
9.0	357.0	384	387	388	387	386	386.4	29.4
9.5	-	384	388	388	388	387	387.0	-
10.0	356.9	384	388	389	388	388	387.4	30.5
10.5	-	385	388	389	388	388	387.6	-
11.0	356.8	385	389	389	388	388	387.8	31.0
11.5	-	385	389	390	388	389	388.2	-
12.0	356.8	385	389	390	389	389	388.4	31.6

Table 2.8: Temperatures measured along the surface of the hot finger. The mass flow rate of the 4 wt% salt, aqueous sodium sulfate solution was 10.47 gm/min and the pressure in the system was maintained at approximately 3625 psig. The cartridge heater inside the hot finger was dissipating 10.61 watts. (Run 35)

concentration of sodium sulfate in the inlet steam was 4 wt%, the solution flowrate was 10.49 gm/min, the cell pressure was about 3550 psig and the cartridge heater inside the hot finger was dissipating 10.61 watts are provided in Table 2.8 and plotted in Fig. 2-16.

2.4.5 Solubility Data

The solubility data for Na_2SO_4 and K_2SO_4 in water at 250 bar are presented in Table 2.9. In runs F and H, the controller setpoints were increased (stepwise) at the rate of approximately 2 °C every 15 minutes and in all other runs the controller setpoints were increased (stepwise) at the rate of approximately 1 °C every 15 minutes. It is also noted that thermocouple "F5" was not working in runs L and O and, thus, the solubility
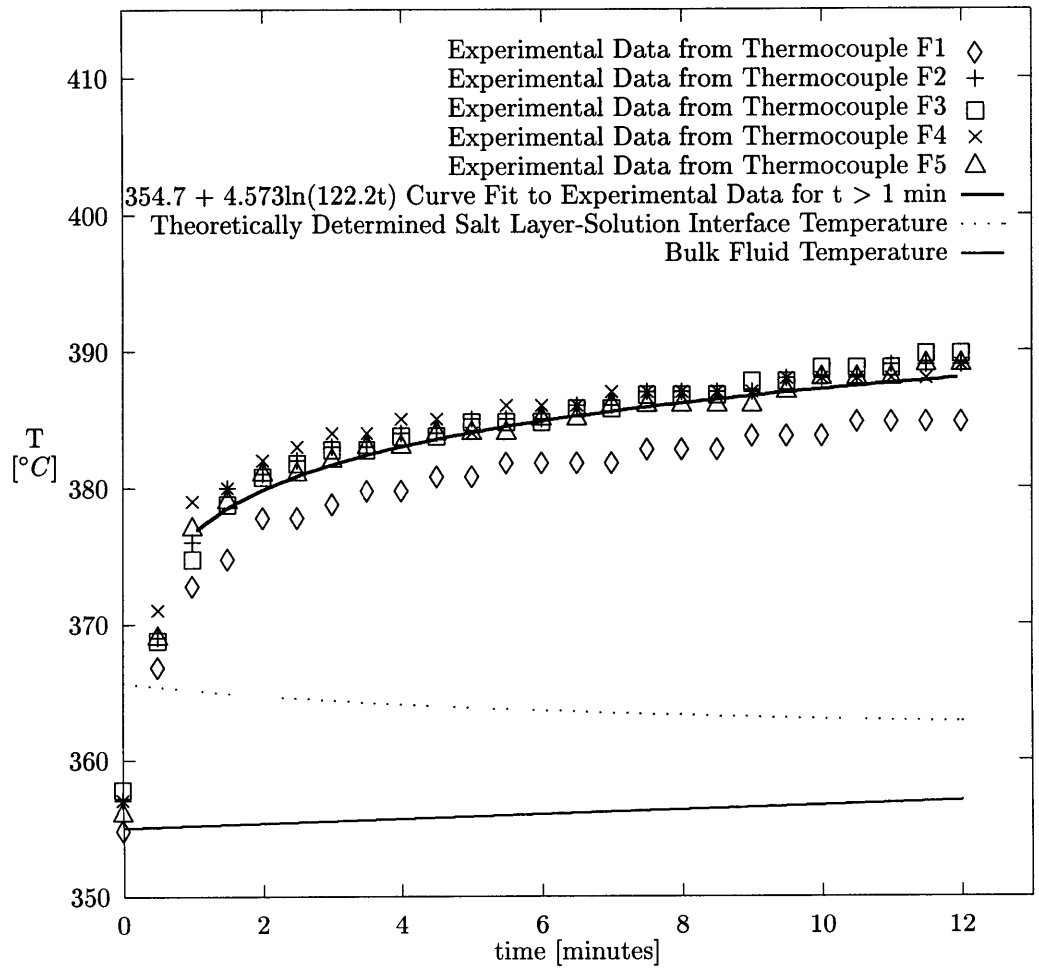
Figure 2-16: Measured temperature profile along the surface of the hot finger and in the bulk solution. The theoretically estimated salt layer-solution interface temperature profile as a function of time is also shown. Conditions correspond to the experiments in which a 4 wt% salt, aqueous sodium sulfate solution was pumped through the system at 3625 psig and the cartridge heater inside the hot finger dissipated 10.61 watts. (Data is contained in Table 2.8.)

Run	Salt	wt%	T_s
F	K_2SO_4	6	375.9 $^\circ C$
H	K_2SO_4	4	379.1 $^\circ C$
I	K_2SO_4	6	375.6 $^\circ C$
J	K_2SO_4	2	382.2 $^\circ C$
K	K_2SO_4	8	373.5 $^\circ C$
L	Na_2SO_4	10	342.5 $^\circ C$
O	Na_2SO_4	3	362.8 $^\circ C$

Table 2.9: Solubility of Na_2SO_4 and K_2SO_4 in water at 250 bar.

temperature for these two runs was based on the output of thermocouples "F1" through "F4". All of the solubility experiments were run at a pressure of 250 bar.

2.4.6 Deposition Rate Data

All of the experimental deposition rate data are reported in Table 2.12. The volumetric flow rate of solution delivered by the pump was either 10 or 25 ml/min at about 20$^\circ C$ and 250 bar for all runs. Although the results of the deposition experiments for which the volumetric flow rate of the solution through the system was 25 ml/min are provided, they are not subsequently analyzed. This is because some particles, presumably salt particles, were visually observed to be present in the test cell during these experiments. The particles formed because the inner wall of the cross exceeded the solubility temperature of the bulk solution at certain locations. (The temperature difference between the surface of the cross and bulk solution was much higher in the experiments run at 25 ml/min than at 10 ml/min because of heating problems.)

To convert the volumetric flow rate of the solutions to their corresponding mass flow rates, the density of the aqueous sodium sulfate and aqueous potassium sulfate solutions as a function of composition at 20 $^\circ C$ and 250 bar are required, but not directly available. However, these densities can be extrapolated from existing data. The density of an aqueous sodium sulfate solution as a function of composition is available at 20 $^\circ C$ and atmospheric pressure and is plotted Fig. 2-17 using data taken from Isono [42]. Furthermore, increasing the pressure of pure water from 1 atmosphere to 250 bar causes its density to increase by only 1.1% [30]. Thus to estimate the density of the aqueous sodium sulfate solution in the pump, the curve fit to the Isono data in Fig. 2-17 is used to determine the density at the composition of interest and 20 $^\circ C$. Then
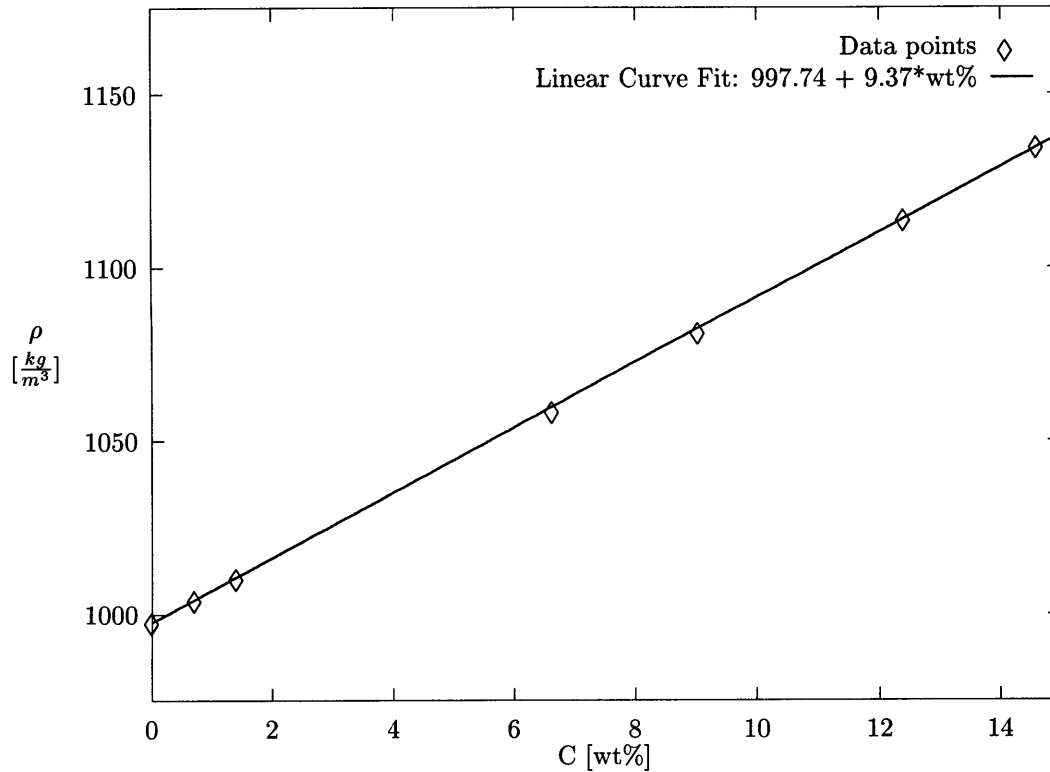
Figure 2-17: Density of an aqueous sodium sulfate solution as a function of salt concentration at a temperature of 20 °C and atmospheric pressure and linear curve fit to the data. All data is taken from Isono [42] except for the pure water data point which is taken from the NIST steam tables [30].

it is assumed that the solution density increases by a factor of 1.011 when pressurized to 250 bar by the pump. The results are shown in Table 2.10. The addition of sodium sulfate to pure water changes its density by only a modest amount at salt concentrations pertinent to this study. Even when the sodium sulfate concentration is 8 wt%, the density of the solution is just 7.5% higher than that of pure water at the same temperature and pressure. The density of an aqueous potassium sulfate solution at 25 °C and atmospheric pressure is provided in [55]. Extrapolation of this data to a temperature of 20 °C and a pressure of 250 bar is provided in Table 2.11

Two values for the bulk temperature of the solution in the cell as measured by the thermocouple residing in the cell are reported. The values in column T_{bulki} are the bulk temperatures of the solution in the cell measured at the beginning of each run and the values in column T_{bulkf} are the measured bulk temperatures

C wt%	ρ at 1 atm. $\frac{kg}{m^3}$	ρ at 250 bar $\frac{kg}{m^3}$
0	998.2	1009.3
2	1016.5	1027.7
4	1035.2	1046.6
6	1054.0	1065.6
8	1072.7	1084.5

Table 2.10: Density of an aqueous sodium sulfate at atmospheric pressure and 20 °C ([30, 42]) and estimation of density of an aqueous sodium sulfate solution at 20 °C and 250 bar as a function of salt concentration.

C wt%	ρ $\frac{kg}{m^3}$
2	1022.9
4	1039.4
6	1055.9
8	1072.3

Table 2.11: Density of an aqueous potassium sulfate solution at 20 °C and 250 bar based on extrapolation of the density of an aqueous potassium sulfate solution at 25 °C and atmospheric pressure as per the data provided in [55].

of the solution in the cell two to three minutes before the end of each run. (Bulk solution temperature was not monitored during the blow-down process, i.e., during the last 1-2 minutes of the runs.) The bulk temperature of the solution in the cell increased by up to about 3°C during each run.

The porosity, ϕ, is defined as the void volume within the porous salt layer formed on the hot finger divided by the total volume of the layer including voids. Thus, denoting the salt volume, total volume of salt including voids, and porosity by V_s, V_T, and ϕ respectively it follows:

$$\phi = \frac{V_T - V_s}{V_T} \tag{2.12}$$

The volume of salt including voids on the hot finger was determined using photographs similar to those in Figs. 2-4 and 2-6 and the volume occupied by only the salt on the hot finger was calculated from the mass of salt deposited during a run using values of 2680 and 2662 kg/m³ for the densities of Na_2SO_4 and K_2SO_4 respectively [51]. Porosity could be calculated only for the limited number of runs for which the hot finger was photographed following the experiment. The bumps/dendrites formed on the downstream side of

the hot finger were neglected when determining the total volume of the salt including voids in the porosity calculation and the porosity values are given in Table 2.12.

The mean sodium sulfate concentration in the system effluent, denoted by $\overline{C}_{eff}$, for the duration of each run was calculated from the mass of salt deposited on the hot finger and the mass flow rate of sodium sulfate in solution flowing into the cell according to Eq. 2.13 and is also given in Table 2.12. The concentration of salt in the effluent stream was at most about 2 wt% less than that in the inlet stream according to these calculations. Therefore, deposition did not decrease the mass flow rate of solution through the system by more than about 2 wt%.

The measured pressure drop across the system was less than 1 atmosphere in all runs. In fact, during some experiments, the upstream pressure transducer read less than the downstream pressure transducer. This is a consequence of the 1.5 bar uncertainty associated with each pressure transducer. Finally, it is noted that x-ray diffraction (XRD) analyses were performed by Ms. Maria Aquino-Class of the Process Measurements Division at NIST on the salt deposited on the hot finger during the deposition experiments after several runs. XRD analyses after sodium sulfate deposition experiments showed that the salt deposited on the hot finger was exclusively sodium sulfate. After potassium sulfate deposition experiments they showed that the salt deposited was exclusively potassium sulfate.

$$M_{deposited}[kg] = \dot{m}_{soln} \left[C_{in} - \overline{C}_{eff} \right] t/100 \qquad (2.13)$$

Run #	Salt	Q_{STP} $[\frac{ml}{min}]$	$\dot{m}$ $[\frac{g}{min}]$	C_{inlet} [wt%]	Time [min]	T_{bulki} [°C]	T_{bulkf} [°C]	M_{dep} [grams]	$\overline{C}_{eff}$ [wt%]	ϕ
18	Na_2SO_4	10	10.47	4	5.92	355.0	357.2	0.45	3.27	82%
6	Na_2SO_4	10	10.47	4	6.22	355.0	355.5	0.51	3.22	-
8	Na_2SO_4	10	10.47	4	9.1	355.0	357.6	0.58	3.39	-
17	Na_2SO_4	10	10.47	4	9.33	355.0	357.3	0.62	3.37	81%
19	Na_2SO_4	10	10.47	4	11.92	355.0	357.6	0.88	3.29	71%
9	Na_2SO_4	10	10.47	4	11.95	355.0	357.5	0.92	3.26	-
15	Na_2SO_4	10	10.28	2	9.27	363.3	365.8	0.37	1.61	-
14	Na_2SO_4	10	10.66	6	9.08	347.7	349.9	1.39	4.56	71%
13	Na_2SO_4	10	10.85	8	8.85	340.8	343.9	1.77	6.16	76%
27	Na_2SO_4	25	26.17	4	8.5	355.0	355.6	0.97	3.56	-
28	Na_2SO_4	25	26.17	4	5.92	355.0	356.3	0.54	3.65	-
29	Na_2SO_4	25	26.17	4	12	355.0	355.7	1.23	3.61	-
Q	K_2SO_4	10	10.39	4	8.83	371.9	373.6	0.97	2.94	68.4
R	K_2SO_4	10	10.72	8	8.82	366.1	368.1	1.92	5.97	66.5
S	K_2SO_4	10	10.56	6	9.02	369.0	371.1	1.37	4.56	67.2
T	K_2SO_4	10	10.23	2	8.95	374.7	376.7	0.27	1.71	-
U	Na_2SO_4	10	10.85	8	9.00	340.8	343.1	1.55	6.41	63.2
V	Na_2SO_4	10	10.66	6	9.03	347.7	350.2	1.06	4.90	62.6
W	Na_2SO_4	10	10.66	6	9.28	347.7	350.0	1.13	4.86	60.2
Y	K_2SO_4	10	10.72	8	8.98	366.2	369.0	1.73	6.20	66.0
Z	K_2SO_4	10	10.39	4	9.60	372.0	373.5	0.91	3.09	67.9

Table 2.12: Experimental deposition rate data and associated parameters.

Chapter 3

Equations Governing Transport and Solution Properties

3.1 Introduction

At the beginning of this chapter the mechanisms of convective transport that can cause deposition at the salt layer-solution interface are described. Then those which are important at the operating conditions of the deposition experiments are placed in context. Next, a simple model to compute the deposition rate at the salt layer-solution interface is presented. Despite the model's simplicity, it provides a useful qualitative framework for understanding the deposition process at the salt layer-solution interface. Next, the conservation laws and accompanying boundary conditions which govern the deposition rate at the salt layer-solution interface for the conditions investigated in the experiments are developed in a far more rigorous context. Then, by scale analysis, a set of criteria is derived which, when satisfied to a sufficient extent, justify a considerably simpler, but still formidable, set of conservation laws and accompanying boundary conditions which govern the deposition rate at the salt layer-solution interface. Next, it is confirmed that natural convection is the dominant transport mode at the conditions investigated in the experiments. The conservation laws are subsequently non-dimensionalized and the applicability of the analogy between heat

and mass transfer to the conditions investigated in the deposition rate experiments is evaluated. Next, the thermodynamic and transport properties required to evaluate the criteria which justify simplification of the equations governing transport are assembled. This chapter ends with an evaluation of all of the criteria developed and justification of the simplified formulation used to calculate the deposition rate at the salt layer-solution interface in Chapter 4. (The calculations are compared against the experimental deposition rate data later in Chapter 4.)

The primary diffusion and convection mechanisms that can be responsible for deposition at the salt layer-solution interface are summarized in the matrix contained in Table 3.1. The two possible convection mechanisms are forced and natural convection denoted by FC and NC respectively. When both natural and forced convection are relevant the term mixed convection is used to describe transport. Diffusion of particles and molecules to the salt layer-solution interface are possible. To further complicate matters, particles can be deposited by a Brownian mechanism, an inertial mechanism or both. Under some conditions diffusion of both molecules and particles will be important. Depending on the relevant mechanisms for a particular set of operating conditions, the deposition calculation can be relatively simple or extremely complex. For example, if heat and mass transfer to the salt layer-solution interface approach a forced convection limit and if nucleation does not occur in the bulk, then the mean and/or local Nusselt and Sherwood numbers may be computed relatively simply from standard correlations available in introductory transport texts. (Of course this is provided that the thermal-fluid properties of the solution are known and do not vary dramatically in the region of interest.) Conversely, if forced and natural convective transport are on the same order and both particle and molecular diffusion are important, etc., accurate models capable of predicting relevant Nusselt and Sherwood numbers may be particularly difficult to develop. At the conditions investigated in the deposition experiments natural convection of dissolved salt molecules dominates transport at the salt layer-solution interface. Fortunately, under these conditions calculation of the deposition rate at the salt layer-solution interface is a tractable problem. Another key issue which must be assessed to perform the deposition calculations accurately (and efficiently) is whether or not deposition within the porous salt layer formed on the hot finger is relevant. Treatment of this topic is deferred until Section 4.5. Finally, to be completely rigorous, the nature of the deposits needs to be considered, i.e., their shape, structure, porosity,

	FC	NC	MIXED
MD PD BOTH			

Table 3.1: Matrix depicting the different combinations of convective and diffusive mechanisms that may be relevant to deposition at the salt layer-solution interface.

etc.

3.2 A Simple Deposition Rate Model

A model to predict the rate of salt deposition at the salt layer-solution interface under a simplifying set of assumptions is developed in this section. The qualitative results produced by the simple model are very general and apply to the conditions investigated in the deposition experiments. Moreover, the analysis in this section elucidates the somewhat surprising relationship between transport coefficients and deposition rate at the salt layer-solution interface. It is assumed that the relationship between salt solubility and temperature is linear and the simplest form of the analogy between heat and mass transfer applies. The depletion of salt in the bulk solution because of deposition is not addressed. Furthermore, the coupling between heat and mass transfer which results because both the temperature and concentration differences across the boundary layer induce significant buoyancy forces is neglected. Finally, the transient nature of the deposition process is not considered. All of these assumptions are relaxed in the more rigorous model which follows this section. The relationships developed in this section assume that the heat flux at the salt layer-solution interface is constant.

Contrary to what one might expect, a reduction in transport coefficients may increase, decrease or not affect the deposition rate at the salt layer-solution interface. Temperatures, concentrations and graphic illustrations of some of the principles required to derive the relationship between the transport coefficients and the deposition rate are shown in Fig. 3-1. The solubility relationship is assumed to be linear and is given by $T_s = T_o - K_1 C$. The temperatures T_B, T_s, T_i and T_o are the bulk solution temperature, solubility

temperature corresponding to the bulk salt concentration, salt layer-solution interface temperature and solubility temperature corresponding to zero salt concentration respectively. The heat transfer coefficient relates the heat flux at the salt layer-solution interface to the temperature difference driving heat transfer as shown. Thus,

$$T_i = T_B + \frac{q''}{h} \tag{3.1}$$

Similarly, the mass transfer coefficient relates the mass flux of salt to the salt layer-solution interface to the mass transfer driving force as shown. Thus,

$$\frac{dm''}{dt} = h_m \left(C_B - C_i \right) 0.01 \rho_{soln} \tag{3.2}$$

Concentrations in this dissertation are often expressed in wt% units because that is the unit most often used when providing solubility data. The factor of $0.01 \rho_{soln}$ is used to convert them from wt% to kg/m^3 when necessary. Alternatively, concentrations could have been expressed in mass fraction units and the 0.01 conversion factor eliminated.

Provided the salt layer-solution interface temperature does not exceed the temperature corresponding to zero salt solubility or fall below the solubility temperature corresponding to the concentration of salt in the bulk solution, the slope of the solubility line may be used to express the driving force for mass transfer to the salt layer-solution interface $(C_B - C_i)$ in terms of the temperature difference $(T_i - T_s)$ as:

$$C_B - C_i = \left(-\frac{dC_s}{dT_s} \right) (T_i - T_s) \quad \text{for} \quad T_s \leq T_i \leq T_o \tag{3.3}$$

Substituting the foregoing expression for the mass transfer driving force as well as the expression for T_i given by Eq. 3.1 into Eq. 3.2, it follows that the mass flux of salt to the salt layer solution interface when $T_s \leq T_i \leq T_o$ is:

$$\frac{dm''}{dt} = \left(-\frac{dC_s}{dT_s} \right) \left[\frac{h_m}{h} q'' - h_m (T_s - T_B) \right] 0.01 \rho_{soln} \quad \text{for} \quad T_s \leq T_i \leq T_o \tag{3.4}$$
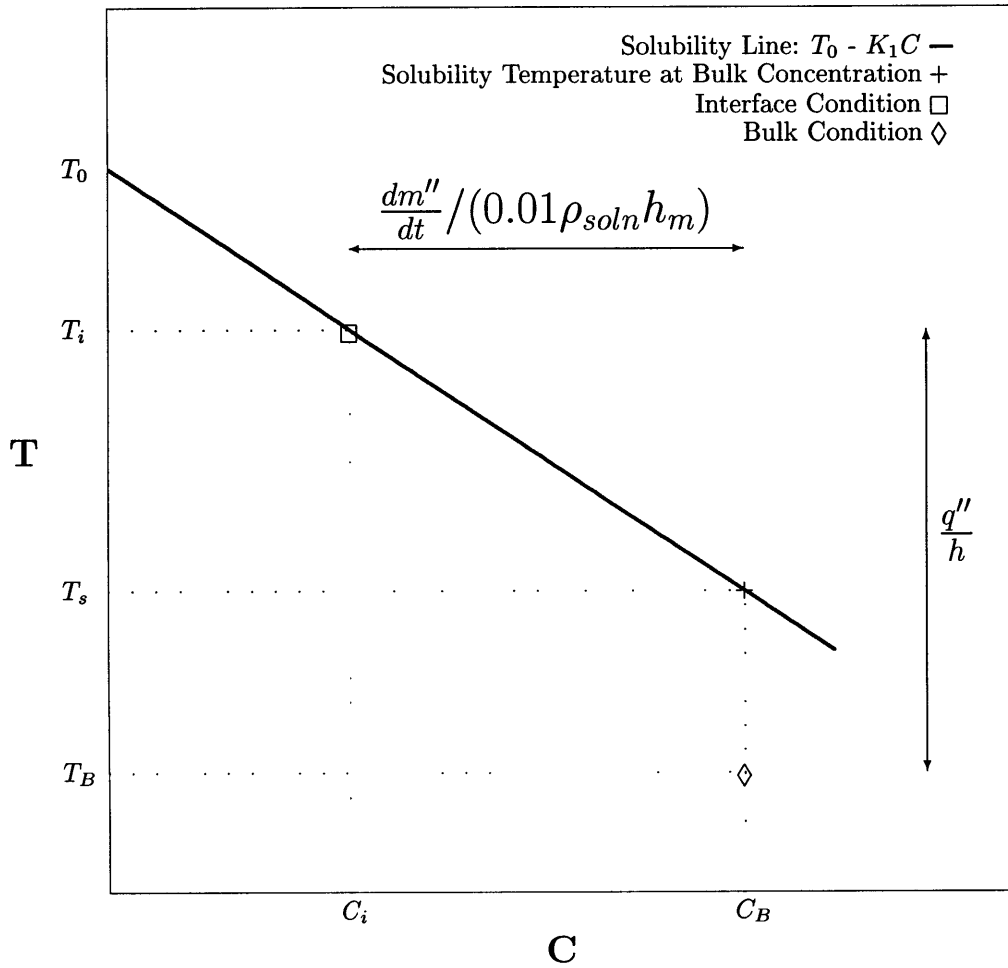
Figure 3-1: Temperatures, concentrations and graphic illustrations of some of the principles relevant to the relationship between transport coefficients and deposition rate at the salt layer-solution interface.

For sufficiently weak transport the salt layer-solution interface temperature is greater than or equal to the temperature corresponding to zero salt solubility. Then the concentration of salt at the salt layer-solution interface equals zero and the mass flux of salt to it is simply:

$$\frac{dm''}{dt} = 0.01\rho_{soln}h_m C_B \quad \text{for} \quad T_i \geq T_o \tag{3.5}$$

Conversely, for sufficiently strong transport the salt layer-solution interface temperature is less than or equal to the solubility temperature corresponding to the concentration of salt in the bulk solution. Then the mass transfer rate equals zero. This condition is stated by Eq. 3.6. Interestingly, increasing the mass flow rate of solution through the cell until the efficacy of transport causes the salt layer-solution interface temperature to be less than or equal to the solubility temperature corresponding to the bulk salt concentration prevents deposition.

$$\frac{dm''}{dt} = 0 \quad \text{for} \quad T_i \leq T_s \tag{3.6}$$

For both natural and forced convective transport, the Nusselt and Sherwood numbers are generally similar, if not identical, functions of the same set of dimensionless groups, with the exception that the Nusselt number is functionally dependent on the Prandtl number whereas the Sherwood number is functionally dependent on the Schmidt number. Moreover, for the majority of convection problems the Nusselt number scales as the Prandtl number to some power n and the Sherwood number scales as the Schmidt number to the same power n. Thus, generally:

$$\frac{Nu}{Sh} \cong \frac{1}{Le^n} \tag{3.7}$$

For example, in the next chapter the following expression is derived for the Sherwood number characterizing natural convection on a vertical flat plate when the Prandtl number equals one and the Schmidt is larger

than 165:

$$Sh_x = 0.5422Le^{\frac{1}{3}}Ra_x^{\frac{1}{4}} \tag{3.8}$$

Equation 3.9 is provided by Gebhart et al. [31] for natural convection heat transfer on the surface of a vertical flat plate when the Prandtl number equals unity.

$$Nu_x = 0.4010Ra_x^{\frac{1}{4}} \tag{3.9}$$

Dividing the Nusselt number expression given by Eq. 3.9 by the Sherwood number expression given by Eq. 3.8 approximately results in the form of the heat and mass transfer analogy given by Eq. 3.7. (It will be shown in Section 3.6.3 that the analogy between heat and mass transfer rigorously applies to natural convection boundary layer flows only when the Lewis number equals unity.) Applying the definitions of the Nusselt and Sherwood numbers to Eq. 3.7 the analogy between heat and mass transfer may also be expressed by:

$$\frac{h}{h_m} = \rho C_P Le^{1-n} \tag{3.10}$$

Equations 3.7 and 3.10 are the simplest forms of the analogy between heat and mass transfer and, typically, n is about 1/3. Combining Eq. 3.4 with the analogy between heat and mass transfer, it follows that:

$$\frac{dm''}{dt} = \left(-\frac{dC_s}{dT_s}\right)\left[\frac{q''}{\rho_{soln}C_P Le^{1-n}} - h_m(T_s - T_B)\right]0.01\rho_{soln} \quad \text{for} \quad T_s \leq T_i \leq T_o \tag{3.11}$$

When the heat flux at the salt layer-solution interface, relevant solution properties and bulk solution temperature are constant and $T_s \leq T_i \leq T_o$, the mass flux of salt to the salt layer-solution interface increases linearly with a decreasing mass transfer coefficient. This phenomenon occurs because a reduction in the mass transfer coefficient is accompanied by an increase in the mass transfer driving force and the net effect is an increase in the mass flux of salt to the salt layer-solution interface.

An absolute maximum in the mass flux of salt to the salt layer-solution interface as a function of the

142

mass transfer coefficient occurs at the value of the mass transfer coefficient for which the salt layer-solution interface temperature equals the temperature corresponding to zero salt solubility. After this maximum a further reduction in the mass transfer coefficient does not change the mass transfer driving force and, thus, decreases the mass flux to the salt layer-solution interface. The mass transfer coefficient at this condition is subsequently referred to as the critical mass transfer coefficient and may be determined from Eq. 3.1 and the analogy between heat and mass transfer. It is given by:

$$h_{m,c} = \frac{q''}{\rho C_P Le^{1-n}(T_o - T_B)} \tag{3.12}$$

The rate of mass transfer at the absolute maximum is given by:

$$\left. \frac{dm''}{dt} \right|_{max} = 0.01 \rho_{soln} h_{m,c} C_B \tag{3.13}$$

When the temperature of the salt layer-solution interface is greater than or equal to the temperature corresponding to zero salt solubility or, equivalently, the mass transfer coefficient is less than or equal to the critical mass transfer coefficient, the mass flux of salt to the salt layer-solution interface decreases linearly with a decreasing mass transfer coefficient as per Eq. 3.5. The condition for $T_i \leq T_s$ may also be expressed in terms of the mass transfer coefficient. From Eq. 3.1 and the analogy between heat and mass transfer it follows that if $T_i \leq T_s$ then $h_m \geq \frac{q''}{\rho_{soln} C_P Le^{1-n}(T_s - T_B)}$.

Eqs. 3.15 through 3.18 summarize the relationships between the deposition rate and the mass transfer coefficient under the assumptions stated at the beginning of this section. These relationships are illustrated in Fig. 3-2 for an arbitrary set of conditions. The mass flux of salt to the salt layer-solution interface is nondimensionalized by the maximum mass flux and the mass transfer coefficient by the critical mass transfer coefficient. The maximum mass flux occurs when $h_m = h_{m,c}$ and may be determined from Eq. 3.13. The dimensionless mass flux increases linearly with the dimensionless heat transfer coefficient until the critical mass transfer coefficient is reached. Moreover, the derivative of the dimensionless mass flux with respect to the dimensionless mass transfer coefficient equals one when $h_m \leq h_{m,c}$. For $h_m > h_{m,c}$ dimensionless mass flux decreases linearly with dimensionless mass transfer coefficient until mass transfer ceases which happens

when $h_m \geq \frac{q''}{\rho C_P Le^{1-n}(T_s - T_B)}$. For $h_{m,c} \leq h_m \leq \frac{q''}{\rho C_P Le^{1-n}(T_o - T_B)}$ the derivative of the dimensionless mass flux with respect to the dimensionless mass transfer coefficient is a function of the solution properties and heat flux at the salt layer-solution interface. (It may be determined from Eqs. 3.15, 3.16 and 3.18).

The numerical solution of a more rigorous formulation for the deposition rate at the salt layer-solution interface is presented in Section 3.11 and predicts that the temperature at the salt layer-solution interface is larger than the temperature corresponding to zero salt solubility at only one set of conditions which were experimentally investigated in this dissertation. These are the conditions corresponding to the run in which the concentration of potassium sulfate in the inlet stream was 2 wt%. Even when the concentration of potassium sulfate in the inlet stream is 2 wt%, the solution of the formulation predicts that the salt layer-solution interface temperature exceeds the temperature corresponding to zero salt solubility for only the first 2-3 minutes of the run. Since the mass transfer coefficients associated with all the other conditions investigated in the deposition experiments are between $h_{m,c}$ and $\frac{q''}{\rho C_P Le^{1-n}(T_s - T_B)}$, a reduction in the mass transfer coefficient leads to an increase in the deposition rate at the salt layer-solution interface. An example of this phenomenon is shown in Section 4.4.2.

$$h_{m,c} = \frac{q''}{\rho C_P Le^{1-n}(T_o - T_B)} \tag{3.14}$$

$$\frac{dm''}{dt} = \left(-\frac{dC_s}{dT_s}\right)\left[\frac{h_m}{h}q'' - h_m(T_s - T_B)\right]0.01\rho_{soln} \quad \text{for} \quad h_{m,c} \leq \frac{q''}{\rho C_P Le^{1-n}(T_s - T_B)} \tag{3.15}$$

$$\frac{dm''}{dt} = 0.01\rho h_m C_B \quad \text{for} \quad h_m \leq h_{m,c} \tag{3.16}$$

$$\frac{dm''}{dt} = 0 \quad \text{for} \quad h_{m,c} \leq h_m \leq \frac{q''}{\rho C_P Le^{1-n}(T_s - T_B)} \tag{3.17}$$

$$\left.\frac{dm''}{dt}\right|_{max} = 0.01\rho h_{m,c} C_B \tag{3.18}$$

Fig. 3-3 also illustrates the relationship between transport coefficients and the deposition rate at the salt layer-solution interface when the heat flux at the salt layer-solution interface is constant. When transport coefficients are "very high", the hot finger surface temperature is below the solubility temperature corresponding to the bulk concentration and deposition does not occur. When transport coefficients are "high", salt deposits on the hot finger. When transport coefficients are "medium", the maximum deposition rate occurs, i.e., the mass transfer coefficient is equal to the critical mass transfer coefficient. As transport coef-
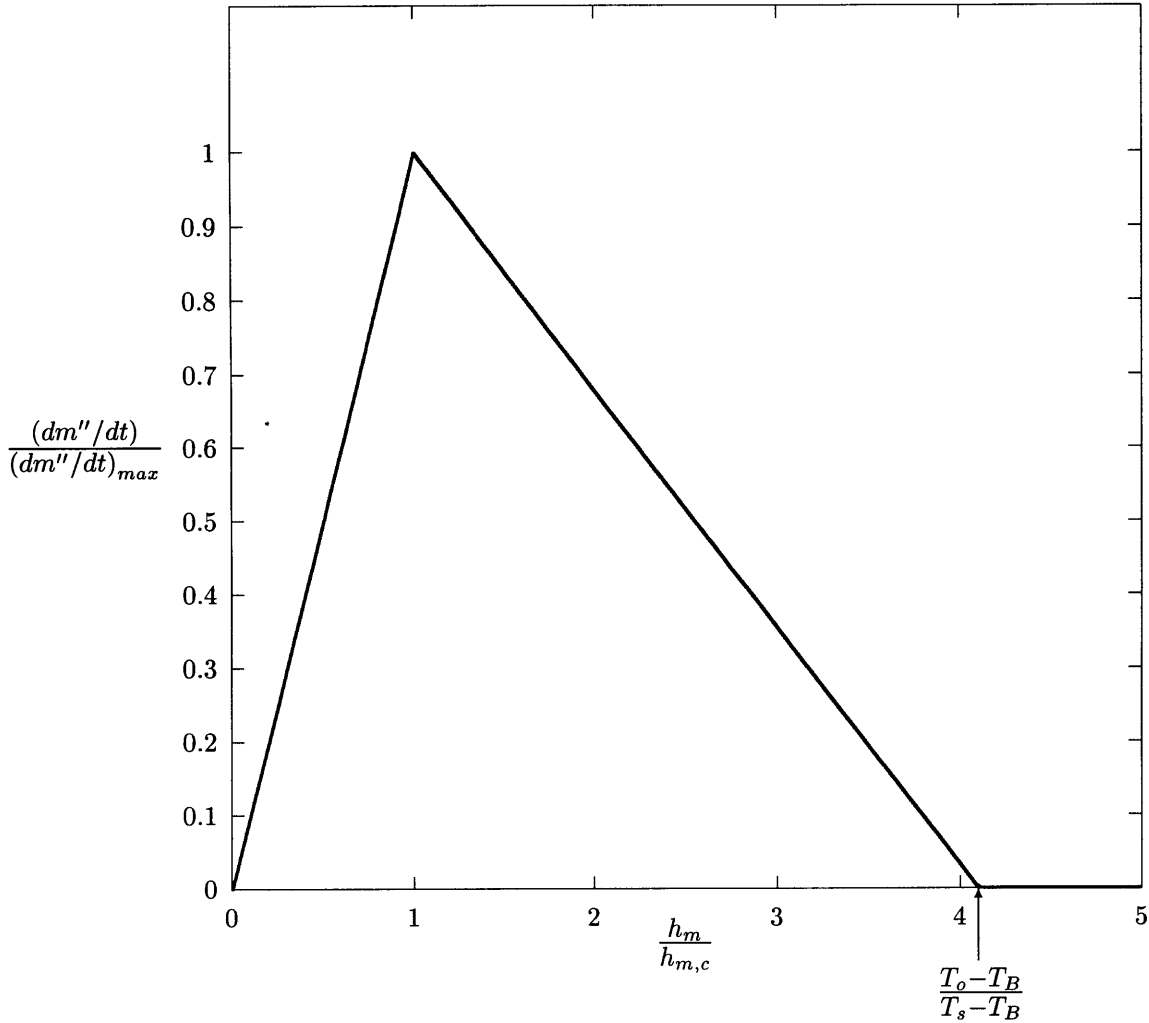
Figure 3-2: Relationship between the dimensionless mass flux and dimensionless mass transfer coefficient at the salt-layer solution interface.

ficients become "low", the mass transfer driving force does not increase further, and the deposition rate is reduced.

It is important to bear in mind that this section focused exclusively on the deposition rate at the salt layer-solution interface. To be sure, changes in the transport coefficients at the salt layer-solution interface can also affect the rate of deposition inside the porous salt layer. Treatment of this subject is, however, beyond the scope of this dissertation.
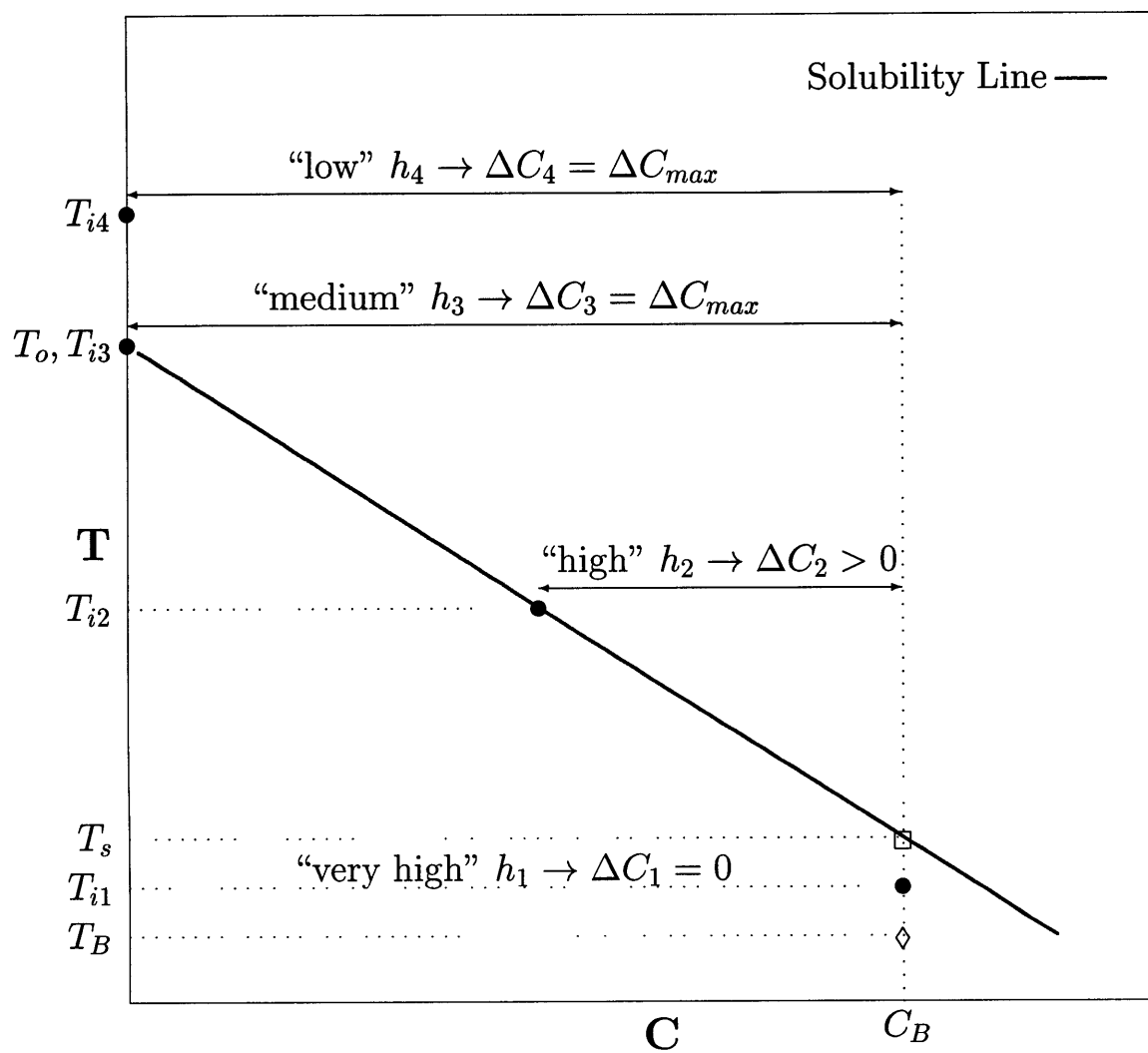
Figure 3-3: Relationship between transport coefficients and deposition rate at the salt layer-solution interface.

3.3 Introduction to Rigorous Model

The assumptions stated at the beginning of Section 3.2 were necessary to develop the simple deposition rate model provided therein. For the deposition rate formulation developed beginning in this section all of these assumptions are relaxed at the cost of substantially increasing the model's complexity. Thus the relationship between salt solubility and temperature is not assumed to be linear and the analogy between heat and mass transfer is not applied. Moreover, the depletion of salt in the bulk solution because of deposition and the coupling between heat and mass transfer are an integral part of the formulation. Finally, the increasing surface area of the salt layer-solution interface is accounted for.

Two major assumptions are still invoked a priori in the development of the equations governing transport in the more rigorous model. First, it is assumed that deposition inside the porous salt layer formed on the hot finger is unimportant. However, the results of the deposition experiments suggest that this is a valid assumption only when the salt concentration in the inlet stream is sufficiently low as per Section 4.5. Secondly, it is assumed that homogeneous nucleation does not occur in the boundary layer formed around the salt layer-solution interface. Evidence that this is a valid assumption is given in Chapter 5. It follows from these two assumptions that in the model developed in this chapter salt is deposited on the hot finger exclusively by salt molecules diffusing to the salt layer-solution interface and subsequently nucleating heterogeneously there. It is reiterated that natural convection is the dominant mode of transport at the conditions investigated in the deposition experiments. Forced convective transport is shown to be negligible in Sections 3.5.12 and 4.2. Thus, the transport problem formulated in this chapter is one of molecular transport by natural convection. The reader is cautioned that this is not necessarily true for an arbitrary set of operating conditions.

3.4 General Form of the Equations Governing Transport

3.4.1 Introduction

The mathematical statements of the conservations laws and accompanying boundary and initial conditions for the free convection, laminar boundary layer flow around the salt layer-solution interface are developed in this section. Sodium sulfate and potassium sulfate dissolved in solution are assumed to be completely

associated and the solution is assumed to contain only two components, namely H_2O molecules and associated salt molecules. Evidence exists that, at near-supercritical conditions, salts are present predominantly in the form of associated ion pairs. For example, Spohn and Brill [82] calculated from Raman spectroscopy data that about 80% of the ions present were in the form of associated ion pairs in a 6.82 m aqueous sodium nitrate solution at 450 $°C$ and 300 bar. Spohn and Brill noted that "no precipitation or decomposition of the sample occurred up to the 450 $°C$ limit of this study." Quist and Marshall [75] measured the electrical conductances of 0.001-0.1 m or, equivalently, $5.8*10^{-3}$ to 0.58 wt% salt, aqueous sodium chloride solutions up to temperatures and pressures of 800 $°C$ and 4000 bars respectively. Conventional equilibrium constants for the dissociation of NaCl into Na^+ and Cl^- were derived from the electrical conductance measurements. At conditions of interest to the deposition rate experiments in this dissertation sodium chloride was predominantly associated. In a 0.5 wt% salt, aqueous sodium chloride solution at a density of 500 kg/m^3 and temperature of 400 $°C$, for example, sodium chloride is 73.6% associated based on the Quist and Marshall equilibrium constant tabulation. (A density of 500 kg/m^3 typifies the deposition experiments.)

Salts dissolved in supercritical water are often hydrated (see, for example, Butenhoff et al. [15]). Moreover, hydration can dramatically affect the magnitude of the driving force for the mass transport of salt from the bulk solution to the salt layer-solution interface. For example, if the concentrations of (anhydrous) sodium sulfate in the bulk solution and at the salt layer-solution interface are 6 and 8 wt% respectively, the driving force for mass transport of salt to the salt layer-solution interface is, obviously, 2 wt%. However, if each sodium sulfate molecule is hydrated with 10 water molecules, say, i.e., sodium sulfate is present exclusively in the form of $Na_2SO_4 \cdot 10H_2O$ ("Glauber's salt"), the mass transfer driving force is dramatically increased. Specifically, 6 and 8 wt% anhydrous Na_2SO_4 in solution correspond to 13.61 and 18.14 wt% $Na_2SO_4 \cdot 10H_2O$ in solution respectively; therefore, ten water of molecules of hydration per salt molecule would increase the mass transfer driving force from 2 wt% to 4.53 wt%.

The results from ex-situ XRD analyses of the salt on the hot finger after the cell was purged with nitrogen and the hot finger removed the day(s) after each deposition experiment were discussed briefly in Chapter 2. The spectra show conclusively that the salt remaining on the hot finger after both the sodium sulfate and potassium sulfate deposition experiments was uniformly anhydrous. However, this does not

eliminate the possibility of salt diffusing to the salt-layer solution interface in hydrated form and subsequently releasing its water molecules during and/or after the deposition process. $Na_2SO_4 \cdot xH_2O$ hydrated ion pairs are, depending on the hydration number, substantially larger and heavier than anhydrous, associated salt molecules; therefore, hydration may also substantially decrease the binary molecular diffusion coefficient of the solution. (The molecular weight of $Na_2SO_4 \cdot 10H_2O$, for example, is approximately 2.3 times larger than that of Na_2SO_4.) Unfortunately, insufficient information is presently available to account for the importance (or lack thereof) of hydration on mass transport. It is noted, however, that the optically accessible test cell used in the experiments performed for this dissertation is amenable to in-situ Raman spectroscopy which may be a viable means to determine whether or not the salts in solution are hydrated and, if so, to what extent.

A number of other assumptions are invoked a priori in the development of the conservation laws and boundary conditions governing transport and subsequently justified. First, the boundary layer approximation is assumed to apply. This is justified in Sections 3.8 by showing that, in the boundary layer formed around the salt layer-solution interface, the characteristic azimuthal velocity is much greater than the characteristic radial velocity and the momentum, thermal and concentration boundary layers are all very thin compared to the diameter of the hot finger. The flow in the boundary layer formed around the salt layer-solution interface is assumed to be laminar. This assumption is justified in Section 4.4.2 a posteori to the solution of the transport formulation. The Boussinesq approximation is assumed to apply, i.e., except for density in the buoyancy force terms in the momentum equation, all thermodynamic and transport properties are treated as constants. The Boussinesq approximation applies provided the temperature and concentration differences across the boundary layer are sufficiently small such that all thermodynamic and transport properties except density can be treated as constants and the variation in the density itself is small, i.e., $\frac{\Delta \rho}{\rho} \lesssim 0.1$. This is shown to be the case for the conditions investigated in the deposition experiments in Section 4.4.2 a posteriori to the solution of the transport formulation. As already noted, natural convection is the dominate transport mode and forced convection is completely neglected in formulating the conservations laws and accompanying boundary conditions. The forced convective cross flow of solution past the hot finger does, however, affect the salt concentration in the bulk solution and this accounted for in the deposition rate formulation. (See

Section 3.11.2).

The flow around the salt layer-solution interface is approximated as two-dimensional. At the beginning of each deposition rate experiment, the length to diameter ratio of the protruding portion of the hot finger is 6.43 and by the end of each deposition experiment this ratio is reduced to about 3; therefore, "edge effects" must play a minor role in transport. Moreover, the walls of the test cell will affect transport to a small extent as well. A substantial computational investment would be required to incorporate "edge effects" into the deposition rate formulation, but it is not deemed worthwhile. This is because many other sources of error in the deposition rate computation, e.g., the uncertainties in the thermodynamic and transport properties of the aqueous salt solutions, are likely to be far more serious than "edge effects".

The salt layer-solution interface is modeled as a vertically oriented flat plate. A vertical flat plate is aligned with the gravitational vector. Thus when a vertical plate is heated or cooled, the buoyancy force generated acts exclusively to induce fluid motion in the surrounding fluid parallel to the plate. For the case of the nominally cylindrical salt layer-solution interface natural convection is more complex. Letting x = 0° correspond to the bottom of the horizontal cylinder, the buoyancy force has a component normal as well as parallel to the salt layer-solution interface, except at x values of 0, 90, 180 and 270°. For -90° < x < 90°, the normal component of the buoyancy force acts to maintain contact between the ascending boundary layer flow and the salt layer-solution interface and the x component of the buoyancy forced is reduced relative to the vertical flat plate case. Thus, in this region one might expect fluid velocities and transport coefficients be be reduced relative to a vertical flat plate. On the upper surface of an inclined, heated plate and the lower surface of an inclined, cooled plate the discharging of parcels of fluid as a consequence of the buoyancy force normal to the plate results in a three dimensional flow field and enhanced transport [41]. For 90° < x < 270°, the normal component of the buoyancy force acts to move fluid away from the salt layer-solution interface. Hence in this region one might expect boundary layer development to be interrupted by discharges of parcels of fluid from it. This would increase transport coefficients.

Based on the preceding arguments one might expect that for a cylinder transport would be reduced for -90° < x < 90° and enhanced for 90° < x < 270° relative to a vertically oriented flat plate and, thus, a small net effect on the transport coefficients. Not surprisingly, little effect on the transport coefficients is

observed when a standard correlation for a vertically oriented flat plate is used to approximate a circular

cylinder for the case when the species expansion coefficient of the surrounding fluid is equal to zero, i.e., when

natural convection is driven solely by the temperature difference across the boundary layer. For example,

McAdams [58] gives $\overline{Nu_L} = 0.59Ra_L^{\frac{1}{4}}$ for a vertically oriented flat plate of height L in the 10^4 to 10^9 Rayleigh

number range. Replacing L with $\frac{\pi D}{2}$ in both $\overline{Nu_L}$ and Ra_L, the McAdams expression can be expressed as

$\overline{Nu_D} = 0.42Ra_D^{\frac{1}{4}}$. For natural convection on a horizontal cylinder Morgan [64] gives $\overline{Nu_D} = 0.48Ra_D^{\frac{1}{4}}$ in

the 10^4 to 10^7 Rayleigh number range. The average Nusselt number scales as $Ra_D^{\frac{1}{4}}$ when either the Morgan

correlation is used directly or the McAdams correlation is used to approximate the cylinder as a vertically

oriented flat plate of height $\frac{\pi D}{2}$. Moreover, there is only a 12.5% difference in the constants multiplying

$Ra_D^{\frac{1}{4}}$ in the McAdams-based expression for $\overline{Nu_D}$ and Morgan correlation for $\overline{Nu_D}$. The preceding discussion

justifies the subsequent use of the results from a study by Gebhart and Pera [32] to determine transport

coefficients between the salt layer-solution interface and bulk solution by approximating it as a vertical flat

plate of height $\frac{\pi D}{2}$. It is noted that, typically, to determine natural convective heat transfer coefficients on

the upper surface of a moderately-inclined, heated plate or the lower surface of a moderately-inclined, cooled

plate a vertical plate correlation is used; however, g is replaced by $g\cos\theta$, where θ is the angle between the

plate and ground, in the Rayleigh number. This procedure is not directly applicable to the case of a circular

cylinder, however, because there is no logical choice for θ.

Temperature, (salt) concentration and velocity profiles for natural convection adjacent to a heated, ver-

tical flat plate are shown in Fig. 3-4. During subsequent deposition rate calculations, the surface of the

flat plate corresponds to the salt layer-solution interface. The u-velocity is zero at the surface of the plate

and at the edge of the boundary layer. Salt concentration, denoted by ρ_A, is lowest at the surface of the

plate and increases to its bulk solution value at the edge of the boundary layer. Conversely, temperature

is highest at the surface of the plate and decreases to its bulk solution value at the edge of the boundary

layer. The subsequent statements of the conservation laws and accompanying boundary conditions follow

the nomenclature displayed in Fig. 3-4.
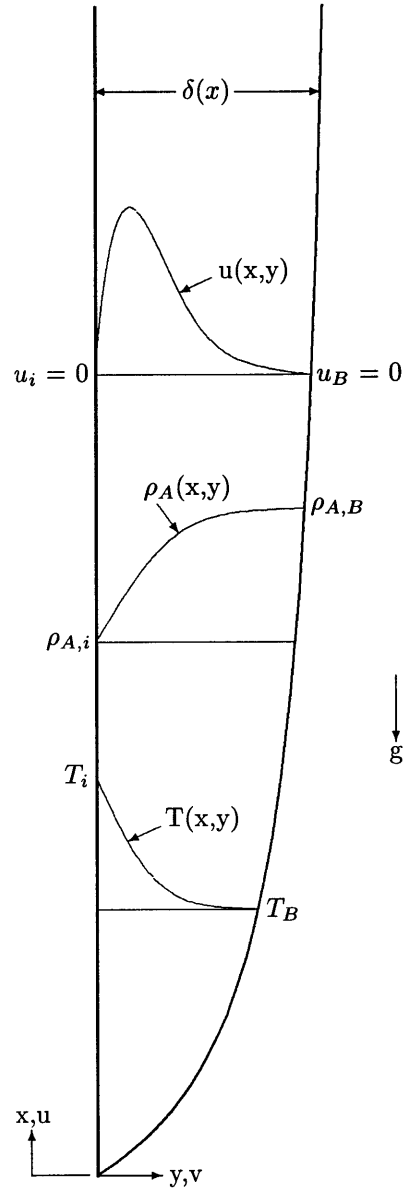
Figure 3-4: Velocity, concentration and temperature profiles for buoyancy-induced, laminar boundary layer flow adjacent to a heated, vertical plate. (It is assumed that the thicknesses of the temperature, concentration and velocity boundary layers are the same for all x.)

3.4.2 Conservation Laws

The continuity equation for two-dimensional incompressible flow is:

$$\frac{\partial u}{\partial x} + \frac{\partial v}{\partial y} = 0 \tag{3.19}$$

The associated ion pairs of salt and H_2O molecules in solution are designated as species A and B respectively and the boundary layer form of the species equation for species A is:

$$\frac{\partial \rho_A}{\partial t} + u \frac{\partial \rho_A}{\partial x} + v \frac{\partial \rho_A}{\partial y} = \frac{\partial J_{A,x_j}}{\partial y} \tag{3.20}$$

In this dissertation, ρ_i represents the density of species "i" in solution in units of $\frac{kg\ i}{m^3}$ and J_{i,x_j} represents the *mass* diffusive flux of species i in the x_j direction in units of $\frac{kg\ i}{m^2 s}$. An equation for the conservation of species B is unnecessary because it is not independent of continuity and conservation of species A.

It is assumed that the Sorét effect, i.e., diffusion of mass along temperature gradients, is present at this stage of the transport formulation. Bird, Stewart and Lightfoot [12] provide the following expression for the mass diffusive flux of species A in the the x_j direction in a two-component system,

$$J_{A,x_j} = -\frac{c^2}{\rho} M_A M_B \mathfrak{D}_{AB} \left[\frac{dx_A}{dx_j} + \frac{k_T}{T} \frac{dT}{dx_j} \left(\frac{\partial\ ln\ x_A}{\partial\ ln\ a_A} \right)_{T,P} \right], \tag{3.21}$$

where c is total molar concentration in $\frac{gmoles\ soln}{m^3}$, ρ is solution density in $\frac{kg\ soln}{m^3}$, M_A and M_B are the molecular weights of species A and B respectively in $\frac{kg\ i}{gmole\ i}$, $\mathfrak{D}_{AB}$ is the binary diffusivity for system A-B in $\frac{m^2}{sec}$, x denotes mole fraction, a denotes activity, and P denotes pressure. The transport coefficient k_T is the thermal diffusion ratio which is defined as:

$$k_T = \left(\frac{\rho}{c^2 M_A M_B} \right) \left(\frac{D_A^{(T)}}{\mathfrak{D}_{AB}} \right) \left(\frac{\partial\ ln\ a_A}{\partial\ ln\ x_A} \right)_{T,P}, \tag{3.22}$$

where $D_A^{(T)}$ is the binary thermal diffusion coefficient for species A in system A-B in units of $\frac{kg}{m \cdot sec}$ [12]. Extreme care should be exercised to be sure the thermal diffusion ratio has the correct sign. It is noted

that $D_A^{(T)} = -D_B^{(T)}$ [12]. Eq. 3.21 is valid for both liquids and gases [12] and it is assumed to be valid in near-supercritical aqueous salt solutions at conditions relevant to this dissertation as well.

From the definition of the thermal diffusion ratio and Eq. 3.21 it follows that for a positive thermal diffusion ratio the Sorét effect will cause species A to diffuse from a "hot" region to a "cold" region. Generally if species A has a larger molecular weight than species B the thermal diffusion ratio will be a positive quantity [21]. Since the molecular weights of sodium sulfate and potassium sulfate are 142.04 $\frac{gm}{gmole}$ and 174.27 $\frac{gm}{gmole}$ respectively and the molecular weight of water is considerably smaller (18.02 $\frac{gm}{gmole}$), it is expected that the Sorét effect will decrease the deposition rate for the conditions investigated in the experiments. Measurements by Butenhoff et al. [15] corroborate that the thermal diffusion ratio is a positive quantity, as one would expect, in a 1.0 m aqueous $NaNO_3$ solution at 450 $^\circ C$ between pressures of 407.3 and 900 bars. The relevance of the Sorét effect at the conditions investigated in the deposition experiments is evaluated in Sections 3.5.2 and 3.8.

The appropriate boundary layer form of the x-momentum equation is:

$$\frac{\partial u}{\partial t} + u\frac{\partial u}{\partial x} + v\frac{\partial u}{\partial y} = \nu\frac{\partial^2 u}{\partial y^2} + g\beta(T - T_\infty) + g\beta^*(\rho_A - \rho_{A,\infty}), \qquad (3.23)$$

where the quantities β and β^* are the volumetric thermal expansion coefficient and species expansion coefficient respectively, i.e.,

$$\beta = -\frac{1}{\rho}\frac{\partial \rho}{\partial T}\bigg|_{P,C} \qquad (3.24)$$

$$\beta^* = -\frac{1}{\rho}\frac{\partial \rho}{\partial \rho_A}\bigg|_{P,T} \qquad (3.25)$$

The units assigned to β and β^* in this dissertation are $\frac{1}{K}$ and $\frac{m^3}{kg\,A}$ respectively. The subscripts ∞ and B are used interchangeably to designate bulk conditions. Two buoyancy terms are included in the momentum equation because the magnitudes of the buoyancy forces induced by the temperature and concentration differences across the boundary layer are of the same order. (See Sections 3.5.3 and 3.8.) Moreover, the buoyancy terms couple the momentum equation to the energy and species equations in addition to continuity.

$$\left[\dot{I}''_y + \frac{\partial}{\partial y}\left(\dot{I}''_y\right)dy\right]dx(1)$$

$$\dot{I}''_x dy(1) \longrightarrow \boxed{\dot{E}'''dxdy(1)} \longrightarrow \left[\dot{I}''_x + \frac{\partial}{\partial x}\left(\dot{I}''_x\right)dx\right]dy(1)$$

$$\dot{W}$$

$$\dot{I}''_y dx(1)$$
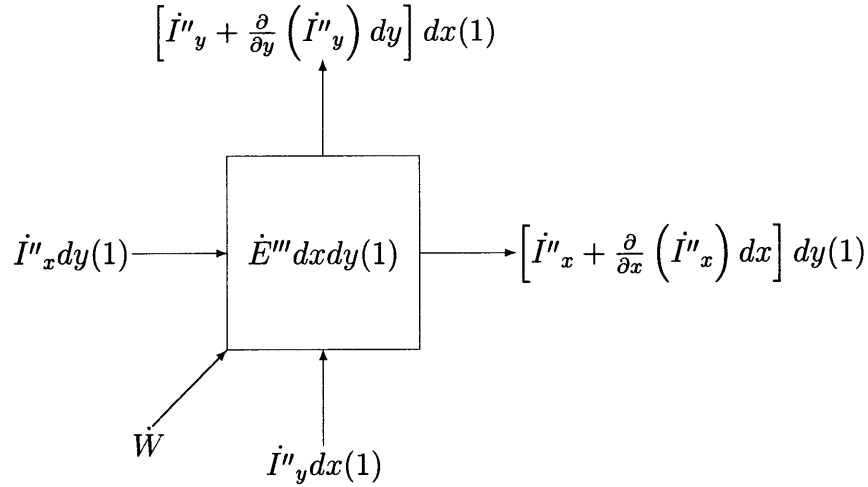
Figure 3-5: Control volume (of unit depth) used to develop the energy equation.

Obviously, solution of the transport problem at hand is not amenable to purely analytical methods.

The appropriate boundary layer form of the energy equation is considerably more complex than the conservation laws presented thus far. The energy equation is developed using the control volume (of unit depth) shown in Fig. 3-5. Terms which account for kinetic and potential energy and "vdP" work in the energy equation are assumed negligible a priori. The variables $\dot{I}''$, $\dot{E}'''$ and $\dot{W}$ represent the rates at which internal energy flows into the control volume (per unit area), internal energy is generated within the control volume (per unit volume) and work is performed on the control volume respectively. Internal energy is transported into and out of the control volume by advection, flow work, diffusion of mass along temperature and concentration gradients, and diffusion of energy along temperature and concentration gradients. Accordingly, the fluxes of internal energy into the control volume in the x and y directions respectively are:

$$\dot{I}''_x = [(\rho_A C_{P_A} + \rho_B C_{P_B})uT + J_{A,x}C_{P_A}T + J_{B,x}C_{P_B}T + q''_x] \tag{3.26}$$

$$\dot{I}''_y = [(\rho_A C_{P_A} + \rho_B C_{P_B})vT + J_{A,y}C_{P_A}T + J_{B,y}C_{P_B}T + q''_y] \tag{3.27}$$

The q'' terms in the foregoing expressions represent diffusive energy fluxes along both temperature and concentration gradients. The diffusive flux of energy along a temperature gradient in the x_j direction is

155

given by Fourier's Law, i.e.,

$$q_{x_j}^{''F} = -k\frac{dT}{dx_j} \tag{3.28}$$

The Dufour effect accounts for the diffusion of energy along concentration gradients. It is substantially more complex than the Sorét effect and, apparently, a general expression for it which is suitable for all fluids does not exist [21]. Deen [21] provides the following expression for the Dufour energy flux in a binary gas mixture:

$$q_{x_j}^{''D} = \frac{RTD_A^{(T)}}{\mathcal{D}_{AB}} \left(\frac{x_A}{M_B} + \frac{x_B}{M_A} \right) \left(v_{A,x_j} - v_{B,x_j} \right), \tag{3.29}$$

where R is the universal gas constant in units of $\frac{J}{gmoleK}$, and v_{i,x_j} denotes the species velocity of component i in the x_j direction, e.g.,

$$\dot{m}_{A,y}^{''} = \rho_A v + J_{A,y} = \rho_A v_{A,y} \tag{3.30}$$

The Dufour energy flux expression provided by Deen derives from a general expression for the Dufour energy flux in a ν-component mixture of monatomic gases obtained by Hirschfelder, Curtiss and Bird [39] using rigorous methods. It is assumed to be valid at near-supercritical conditions for the purposes of this transport formulation and for evaluating the importance of the Dufour effect in the context of the deposition rate experiments.

In the current transport formulation it is convenient to express the Dufour energy flux in a form different from that given by Deen. From the definition of species velocity,

$$v_{A,x_j} - v_{B,x_j} = J_{A,x_j} \left(\frac{1}{\rho_A} + \frac{1}{\rho_B} \right) \tag{3.31}$$

and, therefore, the Dufour energy flux may be expressed as

$$q_{x_j}^{''D} = \frac{RTD_A^{(T)}}{\mathcal{D}_{AB}} J_{A,x_j} \left[\frac{M}{M_A M_B} \right] \left[\frac{\rho}{\rho_A \rho_B} \right], \tag{3.32}$$

156

Denoting the mass fraction of species "i" by ω_i and noting $\frac{M}{\rho_B} = \frac{1}{\omega_B c}$, Eq. 3.32 becomes:

$$q_{x_j}''^D = \frac{RT D_A^{(T)}}{\mathfrak{D}_{AB}} \frac{J_{A,x_j}}{M_A M_B \omega_A \omega_B c} \tag{3.33}$$

Expressing the binary thermal diffusion coefficient for species A in system A-B in terms of the thermal diffusion ratio using Eq. 3.22, Eq. 3.33 becomes:

$$q_{x_j}''^D = \frac{k_T RT J_{A,x_j}}{M \omega_A \omega_B} \left(\frac{\partial \ln x_A}{\partial \ln a_A} \right)_{T,P} \tag{3.34}$$

The foregoing expression for the Dufour energy flux is consistent with that used by Sparrow et al. [81]. (Conversion of Eq. 3.34 to the form given by Sparrow et al. [81] requires setting $k_T = \alpha x_A x_B$, performing some algebraic operations, and assuming the solution is ideal, i.e., activity is proportional to mole fraction. The variable α is called the thermal diffusion factor.)

The total diffusive flux of energy in the x_j direction including both the Fourier and Dufour terms is:

$$q_{x_j}'' = -k \frac{\partial T}{\partial x_j} + \frac{k_T RT J_{A,x_j}}{M \omega_A \omega_B} \left(\frac{\partial \ln x_A}{\partial \ln a_A} \right)_{T,P} \tag{3.35}$$

At conditions of interest to the deposition experiments, k_T is assumed positive and J_{A,x_j} is negative at the salt layer-solution interface; therefore, the Dufour effect results in diffusive energy transport toward the interface. Thus the temperature of the salt layer-solution interface must increase in the presence of the Dufour effect to maintain a surface energy balance there. This temperature increase will generally cause a decrease in salt concentration at the salt layer-solution interface and a concomitant increase in the mass transfer driving force and deposition rate at the salt layer-solution interface. (See Section 3.2 for a more detailed discussion about transport dynamics at the salt layer-solution interface.) Returning to the energy balance, the net outflows of internal energy from the control volume in the x and y directions are:

$$\dot{O}_x = \frac{\partial}{\partial x} \left(\dot{i}_x'' \right) dx dy (1) \tag{3.36}$$

$$\dot{O}_y = \frac{\partial}{\partial y} \left(\dot{i}_y'' \right) dy dx (1) \tag{3.37}$$

Substituting Eqs. 3.26 and 3.27 into Eqs. 3.36 and 3.37 respectively, it follows

$$\dot{O}_x = \frac{\partial}{\partial x}\left[(\rho_A C_{P_A} + \rho_B C_{P_B})uT + J_{A,x}C_{P_A}T + J_{B,x}C_{P_B}T + q_x''\right]dy(1)dx \tag{3.38}$$

$$\dot{O}_y = \frac{\partial}{\partial y}\left[(\rho_A C_{P_A} + \rho_B C_{P_B})vT + J_{A,y}C_{P_A}T + J_{B,y}C_{P_B}T + q_y''\right]dx(1)dy \tag{3.39}$$

Noting that $J_{A,x,} = -J_{B,x,}$ because the net (mass) diffusive flux in each direction equals zero and expanding Eqs. 3.38 and 3.39 yields,

$$\dot{O}_x = \left[C_{P_A}T\frac{\partial(\rho_A u)}{\partial x} + \rho_A u C_{P_A}\frac{\partial T}{\partial x} + J_{A,x}(C_{P_A} - C_{P_B})\frac{\partial T}{\partial x} + \right. \tag{3.40}$$
$$\left.(C_{P_A} - C_{P_B})T\frac{\partial J_{A,x}}{\partial x} + C_{P_B}T\frac{\partial(\rho_B u)}{\partial x} + \rho_B u C_{P_B}\frac{\partial T}{\partial x} + \frac{\partial q_x''}{\partial x}\right]dy(1)dx$$

$$\dot{O}_y = \left[C_{P_A}T\frac{\partial(\rho_A v)}{\partial y} + \rho_A v C_{P_A}\frac{\partial T}{\partial y} + J_{A,y}(C_{P_A} - C_{P_B})\frac{\partial T}{\partial y} + \right. \tag{3.41}$$
$$\left.(C_{P_A} - C_{P_B})T\frac{\partial J_{A,y}}{\partial y} + C_{P_B}T\frac{\partial(\rho_B v)}{\partial y} + \rho_B v C_{P_B}\frac{\partial T}{\partial y} + \frac{\partial q_y''}{\partial y}\right]dx(1)dy$$

Addition of the expressions for $\dot{O}_x$ and $\dot{O}_y$ provides the net outflow of internal energy from the control volume:

$$\dot{O}_{net} = \left\{C_{P_A}T\overbrace{\left[\frac{\partial(\rho_A u)}{\partial x} + \frac{\partial(\rho_A v)}{\partial y} + \frac{\partial J_{A,x}}{\partial x} + \frac{\partial J_{A,y}}{\partial y}\right]}^{0} + C_{P_B}T\overbrace{\left[\frac{\partial(\rho_B u)}{\partial x} + \frac{\partial(\rho_B v)}{\partial y} + \frac{\partial J_{B,x}}{\partial x} + \frac{\partial J_{B,y}}{\partial y}\right]}^{0}\right.$$
$$+ (\rho_A C_{P_A} + \rho_B C_{P_B})u\frac{\partial T}{\partial x} + (\rho_A C_{P_A} + \rho_B C_{P_B})v\frac{\partial T}{\partial y} + J_{A,x}(C_{P_A} - C_{P_B})\frac{\partial T}{\partial x} + J_{A,y}(C_{P_A} - C_{P_B})\frac{\partial T}{\partial y}$$
$$\left.+ \frac{\partial q_x''}{\partial x} + \frac{\partial q_y''}{\partial y}\right\}dxdy(1) \quad (3.42)$$

The terms set equal to zero in Eq. 3.42 are identically equal to the species equations for the salt and water components of the aqueous salt solution. Moreover, the boundary layer approximation dictates that $J_{A,x}\frac{\partial T}{\partial x} \ll J_{A,y}\frac{\partial T}{\partial y}$ and $\frac{\partial q_x''}{\partial x} \ll \frac{\partial q_y''}{\partial y}$; therefore, the net outflow of internal energy from the control volume

becomes:

$$\dot{O}_{net} = (\rho_A C_{P_A} + \rho_B C_{P_B}) \left(u\frac{\partial T}{\partial x} + v\frac{\partial T}{\partial y} \right) + J_{A,y}(C_{P_A} - C_{P_B})\frac{\partial T}{\partial y} + \frac{\partial q_y''}{\partial y} \tag{3.43}$$

The rate of internal energy change within the control volume, $\left((\rho_A C_{V_A} + \rho_B C_{V_B})\frac{\partial T}{\partial t}\right)$, plus the net outflow of internal energy from the control volume equals the rate at which work is performed on the control volume plus the rate at which energy is generated within it. In addition to flow work, which has already been accounted for, work is done on the control volume by body forces and (viscous) surface forces. Viscous effects cause mechanical energy to be irreversibly converted to thermal energy in the fluid and are accounted for by the viscous dissipation function term in the energy equation ($\mu\Phi$); therefore, the energy equation becomes:

$$(\rho_A C_{V_A} + \rho_B C_{V_B})\frac{\partial T}{\partial t} + (\rho_A C_{P_A} + \rho_B C_{P_B})\left(u\frac{\partial T}{\partial x} + v\frac{\partial T}{\partial y} \right) + J_{A,y}(C_{P_A} - C_{P_B})\frac{\partial T}{\partial y} + \frac{\partial q''}{\partial y} = \mu\Phi + \dot{E}''',$$

$$\tag{3.44}$$

where Φ is the viscous dissipation function and $\dot{E}'''$ is the rate of energy generation per unit volume. The appropriate form of the viscous dissipation function for boundary layer flow adjacent to a vertical flat plate is $\Phi = \left(\frac{\partial u}{\partial y}\right)^2$. If there is homogeneous nucleation in the boundary layer, the heat released or absorbed during precipitation must be accounted for in the generation term of the energy equation. However, for the conditions investigated in the deposition experiments visual inspection of the deposition process yielded no evidence of homogeneous nucleation. (See Chapter 2.) Moreover, the visual observations are supported by the nucleation model developed in Chapter 5. Thus the generation term in the energy balance, $\dot{E}'''$, is set equal to zero. The heat of dissolution during heterogeneous nucleation at the salt layer-solution interface is subsequently accounted for in a boundary condition.

An expression relating the rate of propagation of the salt layer-solution interface in the y direction to the net inflow of mass at the interface completes the transport formulation. It is developed using the (moving) differential control volume (of unit depth) shown in Fig. 3-6. The rectangular control volume shown in this figure is an approximation because the value of y at the salt layer solution interface, i.e., L, is a function of

159

both x and t. However, it can be shown that using a rectangular control volume (as opposed to a trapezoid control volume) does not affect the results of the balances at the interface and it is possible to capture the behavior of L as a function of x and t with the current formulation. For the purposes of this transport formulation, the porosity in the salt layer is assumed to be constant. However, this likely represents a shortcoming of the transport formulation as discussed in Section 4.5. As the thickness of the salt layer increases, a porous salt layer replaces aqueous salt solution and the rate of accumulation of mass in the differential control volume equals the net rate of mass flow into it. Thus, at a given x,

$$\frac{\partial m(x,t)}{\partial t}\bigg|_x = \dot{m}_{in,net}(x) \tag{3.45}$$

At time equal to t, the mass of solution in the control volume is:

$$m(x,t) = \rho dx dL \tag{3.46}$$

(This holds for all x.) After time δt elapses, a porous salt layer occupies the control volume and the total mass inside it is:

$$m(x, t + \delta t) = [\rho\phi + \rho_s(1 - \phi)]\, dx dL \tag{3.47}$$

(The density of solid salt is denoted by ρ_s.) It follows from Eqs. 3.46 and 3.47 that the rate of accumulation of mass in the control volume is:

$$\frac{\partial m(x,t)}{\partial t}\bigg|_x = (\rho_s - \rho)\,(1 - \phi)\, dx \frac{\partial L}{\partial t}\bigg|_x \tag{3.48}$$

where $\frac{\partial L}{\partial t}\big|_x$ is the rate of propagation of the salt layer-solution interface at a given x.

Mass enters and leaves the control volume exclusively at the salt layer-solution interface and the net
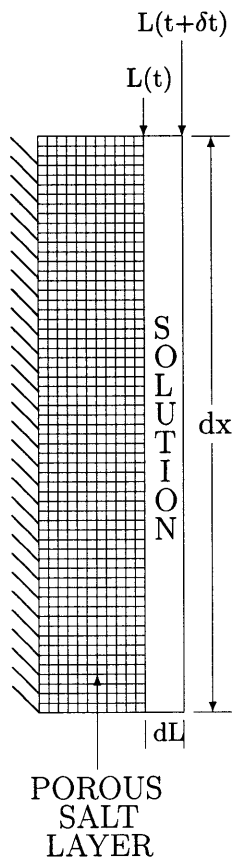
Figure 3-6: Moving differential control volume (of unit depth) used to derive boundary conditions at the salt layer-solution interface. (At time equal to zero the porous salt layer has yet to form.)

inflow of mass there at time equal to "t" is:

$$\dot{m}_{in,net} = -\left[\rho_A v(x, L, t) + \rho_B v(x, L, t) + J_{A,y}(x, L, t) + J_{B,y}(x, L, t)\right] dx \qquad (3.49)$$

(The v-velocity and (mass) diffusive fluxes in the preceding equation are assumed to be functions of (x,y,t).) All velocities in the transport formulation are mass based; therefore, the net mass diffusive flux in the y direction equals zero. Moreover, $\rho_A v(x, L, t) + \rho_B v(x, L, t) = \rho v(x, L, t)$; therefore, at a given x, the mass balance at time "t" becomes,

$$(\rho_s - \rho)(1 - \phi)\left.\frac{\partial L}{\partial t}\right|_x = -\rho v(x, L, t) \qquad (3.50)$$

Since the porous salt layer is propagating outward, i.e., $\partial L/\partial t > 0$, the induced convective velocity at the salt layer-solution interface must always be negative, i.e., *towards* the interface.

Combining the conservation laws and mass balance at the salt layer-solution interface results in the following system of partial differential equations which govern transport in the boundary layer formed adjacent to the salt layer-solution interface:

$$\frac{\partial u}{\partial x} + \frac{\partial v}{\partial y} = 0 \qquad (3.51)$$

$$\frac{\partial \rho_A}{\partial t} + u\frac{\partial \rho_A}{\partial x} + v\frac{\partial \rho_A}{\partial y} = \frac{\partial J_{A,y}}{\partial y} \qquad (3.52)$$

$$\frac{\partial u}{\partial t} + u\frac{\partial u}{\partial x} + v\frac{\partial u}{\partial y} = \nu\frac{\partial^2 u}{\partial y^2} + g\beta(T - T_\infty) + g\beta^*(\rho - \rho_\infty) \qquad (3.53)$$

$$(\rho_A C_{V_A} + \rho_B C_{V_B})\frac{\partial T}{\partial t} + (\rho_A C_{P_A} + \rho_B C_{P_B})\left(u\frac{\partial T}{\partial x} + v\frac{\partial T}{\partial y}\right) + J_{A,y}(C_{P_A} - C_{P_B})\frac{\partial T}{\partial y} + \frac{\partial q_y''}{\partial y} = \mu\left(\frac{\partial u}{\partial y}\right)^2$$

$$\qquad (3.54)$$

$$(\rho_s - \rho)(1 - \phi)\frac{\partial L}{\partial t} = -\rho v(y = L) \qquad (3.55)$$

162

where,

$$J_{A,x_j} = -\frac{c^2}{\rho} M_A M_B \mathfrak{D}_{AB} \left[\frac{dx_A}{dx_j} + \frac{k_T}{T} \frac{dT}{dx_j} \left(\frac{\partial \ln x_A}{\partial \ln a_A} \right)_{T,P} \right] \tag{3.56}$$

$$q''_{x_j} = -k\frac{\partial T}{\partial x_j} + \frac{k_T R T J_{A,x_j}}{M \omega_A \omega_B} \left(\frac{\partial \ln x_A}{\partial \ln a_A} \right)_{T,P} \tag{3.57}$$

Setting x_A equal to $\frac{\rho_A}{cM_A}$ in Eqs. 3.56 and 3.57 and assuming c to be a constant eliminates mole fraction from the transport formulation; therefore, increasing its numerical tractability. However, when the deposition rate is computed in the next Chapter the Sorét and Dufour effects are neglected and a mass based form of Fick's law is used. Therefore, this simplification is unnecessary because terms containing mole fraction are set equal to zero when the transport formulation is solved for the deposition rate at the salt layer-solution interface.

3.4.3 Boundary and Initial Conditions

In the system of partial differential equations governing transport: u-velocity is first order in x, second order in y and first order in t; v-velocity is first order in y; ρ_A is first order in x, second order in y and first order in t; T is first order in x, second order in y and first order in t; and L is first order in t. Thus the order of the system is 14. Three and seven boundary conditions are required on x and y respectively and four initial condition are required on t. These conditions are presented in Table 3.2 and discussed below.

The first three boundary conditions in Table 3.2 state that at x = 0, salt concentration, temperature and u-velocity equal their respective bulk values. Boundary condition number four invokes the no slip condition at the salt layer-solution interface, i.e., y = L(x,t). The interface between the salt layer and adjacent solution is assumed to be at saturation conditions. Thus, temperature-concentration equilibrium at the salt layer-solution interface represents another boundary condition on y at L(x,t). (The temperature-concentration equilibrium relationships for the aqueous sodium sulfate and potassium sulfate systems at conditions of interest were presented in Chapter 2.) The next three boundary conditions on y state that as y approaches infinity u-velocity, temperature and salt concentration equal their respective bulk values.

The relationship between the rate of increase of the mass of salt in the porous salt layer as it propagates

Number	Variable	(x,y,t)	Condition
1	x	$(0, y \geq L(0,t), t)$	$u = 0$
2	x	$(0, y \geq L(0,t), t)$	$T = T_B$
3	x	$(0, y \geq L(0,t), t)$	$\rho_A = \rho_{A,B}$
4	y	$(x, L(x,t), t)$	$u = 0$
5	y	$(x, L(x,t), t)$	T,C equilibrium
6	y	(x, ∞, t)	$u = 0$
7	y	(x, ∞, t)	$T = T_B$
8	y	(x, ∞, t)	$\rho_A = \rho_{A,B}$
9	y	$(x, L(t), t)$	$(\rho_s - \rho_A)(1 - \phi)\frac{\partial L}{\partial t} = -[\rho_A v + J_{A,y}]$
10	y	$(x, L(t), t)$	$\eta P'' + \rho_s H_{diss}(1 - \phi)\frac{\partial L}{\partial t} = q_y''$
11	t	$(x,y,0)$	$u = 0$
12	t	$(x,y,0)$	$T = T_B$
13	t	$(x,y,0)$	$\rho_A = \rho_{A,B}$
14	t	$(x,0)$	$L=0$

Table 3.2: Boundary and initial conditions for the transport formulation.

in the y direction to the total mass flux of salt at the salt layer-solution interface provides another boundary condition on y at L(x,t). Following the same procedure used to develop the overall mass balance at the salt layer-solution interface, the mass of salt within the control volume (denoted by m_s) shown in Fig. 3-6 at time t is:

$$m_s(x,t) = \rho_A dx dL \tag{3.58}$$

After the time δt elapses, the mass of salt in the control volume is:

$$m_s(x, t + \delta t) = \rho_A dx dL \phi + \rho_s dx dL(1 - \phi) \tag{3.59}$$

Thus the rate of accumulation of salt in the control volume, is:

$$\frac{\partial m_s(x,t)}{\partial t} = (\rho_s - \rho_A)(1 - \phi) dx \frac{\partial L}{\partial t} \tag{3.60}$$

The net inflow of salt at the salt layer-solution interface is:

$$\dot{m}_{s-in,net} = -[\rho_A v + J_{A,y}] dx \tag{3.61}$$

164

and the mass balance for the salt becomes:

$$(\rho_s - \rho_A)(1 - \phi)\frac{\partial L}{\partial t} = -[\rho_A v + J_{A,y}] \tag{3.62}$$

Derivation of a mass balance on species B at the salt layer-solution interface is unnecessary because it is not independent of the preceding total mass balance and mass balance on species A.

An energy balance at the salt layer-solution interface, i.e., y = L(x,t), provides the final boundary condition on y and is also developed using the control volume in Fig. 3-6. In the subsequent energy balance, (specific) internal energy is denoted by the variable u and has units of J/kg and u_s, u_A and u_B represent the internal energy of solid salt, associated ion pairs of salt in solution and H_2O in solution respectively. The internal energy in the control volume at time t is:

$$u(x,t) = \rho_A u_A dx dL + \rho_B u_B dx dL \tag{3.63}$$

After the time δt elapses, the internal energy in the control volume is:

$$u(x, t + \delta t) = [(\rho_A u_A + \rho_B u_B)\phi + \rho_s u_s (1 - \phi)]dx dL \tag{3.64}$$

Thus the rate of accumulation of internal energy in the control volume is:

$$\frac{\partial u}{\partial t} = [\rho_s u_s - \rho_A u_A - \rho_B u_B](1 - \phi)dx\frac{\partial L}{\partial t} \tag{3.65}$$

The rate of accumulation of internal energy in the control volume equals the net inflow of internal energy at the salt layer-solution interface as per Eq. 3.66. The variable h_i represents the specific enthalpy of species "i" *in solution* and has units of $\frac{J}{kg\ i}$. The first term on the R.H.S. of Eq. 3.66 accounts for the power supplied to the hot finger. The next two terms account for the energy fluxes associated with the mass fluxes of species A and B and flow work performed on the control volume. Diffusion of energy along temperature

and concentration gradients is accounted for by the last term.

$$\frac{\partial u}{\partial t} = \left[\frac{P}{dx} - [\rho_A v + J_{A,y}] h_A - [\rho_B v + J_{B,y}] h_B - q_y''\right] dx \qquad (3.66)$$

The net mass diffusive flux in the y direction equals zero, i.e., $J_{A,y} = -J_{B,y}$; therefore, the energy balance may be expressed as:

$$[\rho_s u_s - \rho_A u_A - \rho_B u_B](1-\phi)\frac{\partial L}{\partial t} = \frac{P}{dx} - [\rho_A h_A + \rho_B h_B]v + J_{A,y}[h_B - h_A] - q_y'' \qquad (3.67)$$

It is assumed that the specific internal energies of solid salt, associated ion pairs of salt in solution and H_2O in solution are equal to their respective specific enthalpies in solution, i.e.,

$$u_s \cong h_s \qquad (3.68)$$

$$u_A \cong h_A \qquad (3.69)$$

$$u_B \cong h_B \qquad (3.70)$$

Enthalpy and internal energy are essentially equal for solid phases because of their small specific volume. Similarly, the enthalpy of a condensed solid phase in solution, i.e., dissolved salt in the form of associated ion pairs, may be set equal to its internal energy in solution for the same reason. Fig. 3-7 is a plot of the internal energy and enthalpy of pure water between 300 and 400 $^\circ C$ at 250 bar, i.e., the region of interest to the deposition rate experiments [30]. The enthalpy does not exceed the internal energy by more than 6.2% in this region. Moreover, the internal energy and enthalpy of H_2O in aqueous salt solutions at salt concentrations of interest to this dissertation are unlikely to substantially differ from the internal energy and enthalpy of pure H_2O at the same temperature and pressure; therefore, setting the internal energy of H_2O in solution equal to its corresponding enthalpy in solution is deemed appropriate.

Upon setting all internal energies in Eq. 3.67 equal to their respective enthalpies it becomes:

$$[\rho_s h_s - \rho_A h_A - \rho_B h_B](1-\phi)\frac{\partial L}{\partial t} = \frac{P}{dx} - [\rho_A h_A + \rho_B h_B]v + J_{A,y}[h_B - h_A] - q_y'' \qquad (3.71)$$

166
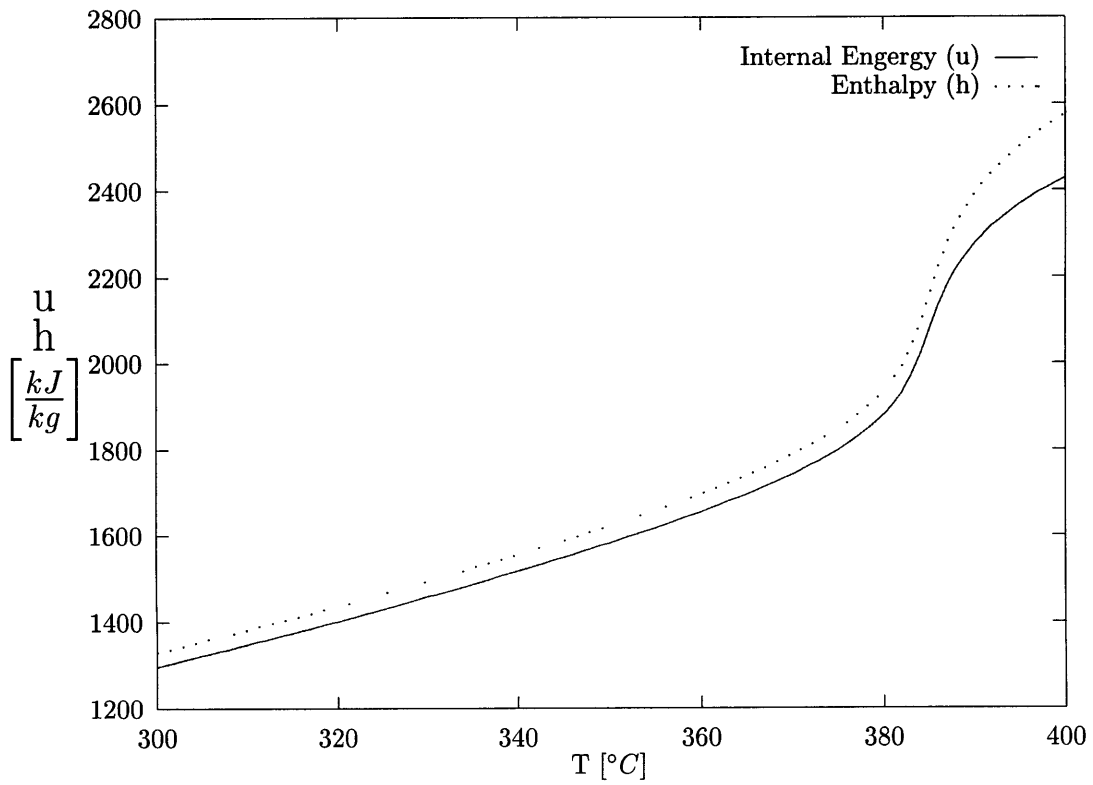
Figure 3-7: Specific internal energy and specific enthalpy of pure H_2O as a function of temperature between 300 and 400 $^\circ C$ at 250 bar [30].

Subtracting Eq. 3.62 from Eq. 3.50, it follows,

$$\rho_B \left(1 - \phi\right) \frac{\partial L}{\partial t} = \rho_B v - J_{A,y} \tag{3.72}$$

Eq. 3.72 is equivalent to a mass balance on the H_2O at the salt layer-solution interface. However, as already noted, it is not independent of the total mass balance and salt mass balance at the salt layer-solution interface; therefore, it was unnecessary to derive it from first principles. Multiplying Eq. 3.72 by h_B and subsequently adding it to Eq. 3.71 gives,

$$[\rho_s h_s - \rho_A h_A] \left(1 - \phi\right) \frac{\partial L}{\partial t} = \frac{P}{dx} - \rho_A h_A v - J_{A,y} h_A - q_y'' \tag{3.73}$$

Multiplying Eq. 3.62 by h_A and subtracting it from the foregoing equation gives:

$$\rho_s \left[h_s - h_A\right] \left(1 - \phi\right) \frac{\partial L}{\partial t} = P'' - q_y'' \tag{3.74}$$

The quantity $(h_A - h_s)$ equals the (mass based) heat of dissolution and is denoted by H_{diss}; therefore, the energy balance at the salt layer-solution interface may be expressed as:

$$P'' + \rho_s H_{diss} \left(1 - \phi\right) \frac{\partial L}{\partial t} = q_y'' \tag{3.75}$$

Initial conditions 11 through 13, state that at time equal to zero u-velocity, temperature and salt concentration equal their respective bulk values for all (x,y). The initial condition on L simply states that salt has yet to deposit on the hot finger at time equal to zero.

3.5 Scaling of the Conservation Laws and Criteria for Neglecting Various Terms

3.5.1 Introduction

In this section, scale analysis is used to develop a set of criteria to systematically simplify the equations governing transport to the salt layer-solution interface. When satisfied to the extent shown in Section 3.8, these criteria justify computation of the deposition rate at the salt layer-solution interface using the relatively simple numerical procedure developed in the next Chapter.

3.5.2 Sorét and Dufour Effects

Criteria to neglect the Sorét and Dufour effects are developed in this section. The criteria are derived assuming the Sorét and/or Dufour effects do not affect the thicknesses of the concentration and thermal boundary layers; consequently, the Lewis number to the 1/3 power scales (roughly) as the ratio of the thermal boundary thickness to the concentration boundary layer thickness. (This relationship applies to the laminar natural convection boundary layer flow around the salt layer-solution interface and it is derived in Section 3.6.) However, it is noted that if either or both criteria developed in this section are not satisfied the relationship is invalidated because the thermal diffusion ratio must be accounted for to properly determine the relative boundary layer thicknesses when the Sorét and/or Dufour effects are important. Conversely, provided both criteria are satisfied it may be assumed that the magnitude of the relative boundary layer thicknesses has been computed correctly and the Sorét and Dufour effects are negligible. It is emphasized that *both* the Sorét effect and the Dufour effect must be negligible for either of the criteria derived in this section to rigorously apply.

169

Sorét Effect

The ratio of the mass diffusive flux along temperature gradients to that along concentration gradients may be estimated by scaling the two terms bracketed in Eq. 3.21. This ratio is denoted by S and equals:

$$S = \left| \frac{k_T \Delta T}{T \Delta x_A} \left(\frac{\Delta \, ln \, x_A}{\Delta \, ln \, a_A} \right)_{T,P} \left(\frac{\delta_C}{\delta_T} \right) \right| \tag{3.76}$$

The symbol Δ designates the magnitude of the difference of a quantity at the bulk condition and salt layer-solution interface condition. Setting $\left(\frac{\delta_t}{\delta_c} \right) = Le^{\frac{1}{3}}$ and further assuming the solution is ideal, i.e., activity proportional to mole fraction, S becomes:

$$S = \left| \frac{k_T \Delta T}{T \Delta x_A Le^{\frac{1}{3}}} \right| \tag{3.77}$$

If S $\lesssim$ 0.1, it is assumed that the Sorét effect can be safely neglected. It is noted that if, the Sorét effect is important, then at steady state conditions the bulk concentration and salt layer-solution interface concentration are not equal at steady state conditions. This is because even at steady state conditions a temperature difference between the salt layer-solution interface and bulk solution must be present.

Dufour Effect

Scaling the Fourier diffusion term with the term accounting for the Dufour effect in the diffusive energy flux expression given by Eq. 3.35 shows that a criterion to neglect the Dufour effect is D $\lesssim$ 0.1, where D is defined by:

$$D = \left| \frac{k_T RT J_{A,y} \delta_T}{M \omega_A \omega_B k \Delta T} \left(\frac{\Delta \, ln \, x_A}{\Delta \, ln \, a_A} \right)_{T,P} \right| \tag{3.78}$$

The magnitude of the total mass diffusive flux in the boundary layer equals that by mass diffusion along concentration gradients multiplied by (1 - S) to account for the Sorét effect, i.e.,

$$J_{A,y} \backsim \frac{c^2 M_A M_B \mathfrak{D}_{AB} \Delta x_A}{\rho \delta_c} (1 - S) \tag{3.79}$$

Assuming that the thermal diffusion ratio of aqueous sodium sulfate and potassium sulfate solutions is a positive quantity at the conditions in the deposition experiments as discussed in Section 3.4.2, the Sorét effect causes salt to diffuse away from the salt layer-solution interface. Since, diffusion along concentration gradients causes diffusion of salt towards the interface, the presence of the Sorét effect will *decrease* the characteristic diffusive flux in the boundary layer.

Combining Eqs. 3.78 and 3.79, D becomes,

$$D = \left| \frac{k_T R T c^2 M_A M_B \mathfrak{D}_{AB} \Delta x_A \delta_T}{\rho \delta_c M \omega_A \omega_B k \Delta T} \left(\frac{\Delta \ln x_A}{\Delta \ln a_A} \right)_{T,P} (1 - S) \right| \tag{3.80}$$

Noting that $\frac{M_i}{M\omega_i} = \frac{1}{x_i}$ and again assuming that the ratio of the thermal boundary layer thickness to the concentration boundary layer thickness scales as the Lewis number to the 1/3 power and that the solution is ideal, D becomes:

$$D = \frac{k_T R T c \mathfrak{D}_{AB} \Delta x_A Le^{\frac{1}{3}}}{x_A x_B k \Delta T} (1 - S) \tag{3.81}$$

Bird, Stewart and Lightfoot [12] note that the quantity $k_T/(x_A x_B)$, commonly referred to as the thermal diffusion factor or α, is almost independent of concentration for gases. Since the thermal diffusion factor appears explicitly in the expression for D and not S; perhaps, the importance of the Sorét effect is more concentration dependent than that of the Dufour effect in the context of the deposition experiments.

3.5.3 Buoyancy Induced by Concentration Gradients

Scaling the buoyancy terms induced by the concentration and temperature differences across the boundary layer in the x-momentum equation (given by Eq. 3.23) against one another, it follows that a criterion to neglect the buoyancy forces generated by concentration difference across the boundary layer is $\tilde{N} \lesssim 0.1$, where:

$$\tilde{N} = \frac{\beta^* \Delta \rho_A}{\beta \Delta T} \tag{3.82}$$

3.5.4 Viscous Dissipation

Assuming that the Dufour effect is unimportant, if the viscous dissipation term in the energy equation is small compared to the Fourier diffusion term, viscous dissipation may be neglected. This is true provided that the Brinkman number (Br) is small relative to one, i.e., Br $\lesssim$ 0.1. The Brinkman number is defined by:

$$Br = \frac{\mu U^2}{k \Delta T},$$ (3.83)

where U is the characteristic u-velocity in the boundary layer.

3.5.5 Energy Transfer by Mass Diffusion

The net mass diffusive flux relative to the (mass averaged) convective velocities, i.e., u and v, equals zero. However, because species A (associated ion pairs of salt in solution) and species B (H_2O in solution) possess different constant pressure specific heat capacities, a net energy flux accompanies mass diffusion in the x and y directions. Energy transfer accompanying mass diffusion is negligible in the x direction compared to the y direction because of the boundary layer approximation and in the y direction it is accounted for by the term $J_{A,y} (C_{P_A} - C_{P_B}) \frac{\partial T}{\partial y}$ in the energy equation. Assuming the Sorét and Dufour effects are negligible, this term may be scaled against the Fourier diffusion term in the energy equation to determine whether or not energy transfer accompanying mass diffusion is important. The result is that it is unimportant provided the dimensionless group M is $\lesssim$ 0.1, where,

$$M = \frac{c^2 M_A M_B \mathcal{D}_{AB} \Delta x_A (C_{P_A} - C_{P_B})}{\rho k} Le^{\frac{1}{3}}$$ (3.84)

3.5.6 Specific Heat of Aqueous Salt Solutions

To simplify the energy equation (Eq. 3.54), it is subsequently assumed:

$$(\rho_A C_{P_A} + \rho_B C_{P_B}) = \rho C_{P_B} = \text{constant}$$ (3.85)

If the quantity A1 defined by Eq. 3.86 is between 0.9 and 1.1, say, this assumption is valid:

$$A1 = \frac{\omega_A C_{P_A} + \omega_B C_{P_B}}{C_{P_B}} \tag{3.86}$$

The quantity A1 simply equals the ratio of the (mass based) constant pressure specific heat of the aqueous salt solution to the constant pressure specific heat of pure H_2O at the temperature and pressure of the aqueous salt solution. (Dimensionless quantities for which standard nomenclature do not exist are designated by A1 through A11 in this section.)

3.5.7 Heat of Dissolution

Based on extrapolation of the heat of dissolution data presented in Section 3.7.9, the precipitation of sodium sulfate and of potassium sulfate at relevant conditions are endothermic events. If the amount of heat absorbed due to precipitation at the salt layer-solution interface is small compared to the power supplied to the hot finger, then the heat of dissolution may be neglected in the transport formulation. This criteria is expressed as A2 $\lesssim$ 0.1, where,

$$A2 = \left| \frac{\dot{m}_c H_{diss}}{P} \right| \tag{3.87}$$

The variable $\dot{m}_c$ is the characteristic deposition rate.

3.5.8 Induced Convective Velocity at the Salt Layer-Solution Interface

In the computation of the deposition rate at the salt layer-solution interface in Chapter 4, the normal velocity at the interface is set equal to zero. However, the (mass based) convection velocity at this interface is not identically equal to zero. It may be estimated by scaling the overall mass balance at the salt layer-solution interface given by Eq. 3.50, i.e.,

$$V_i = \frac{\rho_s - \rho}{\rho} \left. \frac{\partial L}{\partial t} \right|_c (1 - \phi) \tag{3.88}$$

If the induced convective velocity at the salt layer-solution interface is small compared to the characteristic v-velocity in the boundary layer (V), it may be neglected. This criterion is expressed as A3 $\lesssim$ 0.1, where, A3 is:

$$A3 = \left| \frac{V_i}{V} \right| \tag{3.89}$$

The characteristic v-velocity in the boundary layer may be estimated from Eq. 3.114 in the next section.

3.5.9 Transport Mechanisms at the Salt Layer-Solution Interface

It is also of interest to place the relative importance of advection and diffusion at the salt layer-solution interface in context. To be sure, the concentration gradient of salt in the boundary layer is positive, i.e., $\partial \rho_A / \partial y > 0$ because salt diffuses towards the interface. Therefore, an opposing concentration gradient of H_2O and associated mass diffusion flux of H_2O away from the interface is present as well. As the diameter of the salt layer-solution interface increases, H_2O is replaced by salt and Eq. 3.72 relates the rate of increase of this diameter to the advective and diffusive mass fluxes of H_2O at the interface. The relative importance of advective and diffusive transport of H_2O at the salt layer-solution interface may be evaluated by scaling this equation. As described below, under certain conditions the H_2O mass balance at the salt layer-solution interface may be used to corroborate the estimate of the induced convective velocity at the salt layer-solution interface based on the total mass balance at the interface.

The ratio of the diffusive term to the accumulation term in Eq. 3.72 is denoted by A4 and equal to:

$$A4 = \frac{c^2 M_A M_B \mathfrak{D}_{AB} \Delta x_A (1 - S)}{\rho \delta_c \rho_B (1 - \phi) \left. \frac{dD_i}{dt} \right|_c}, \tag{3.90}$$

where $\left. \frac{dD_i}{dt} \right|_c$ is the characteristic rate at which the diameter of the salt layer-solution interface increases. It is shown in the next section (assuming the Sorét and Dufour effects are negligible) that the concentration

174

boundary layer thickness scales roughly as $D_i / \left(Ra_{D_i}^{\frac{1}{4}} Le^{\frac{1}{3}} \right)$. Therefore assuming S equals zero, A4 becomes:

$$A4 = \frac{c^2 M_A M_B \mathfrak{D}_{AB} \Delta x_A Ra_{D_i}^{\frac{1}{4}} Le^{\frac{1}{3}}}{\rho^2 \omega_{B,film} D_i (1 - \phi) \left. \frac{dD_i}{dt} \right|_c} \tag{3.91}$$

The ratio of the advection term to the accumulation term in the water mass balance at the salt layer-solution interface is denoted by A5 and equals:

$$A5 = \frac{(1 - \phi) \, dL/dt}{V_i} \tag{3.92}$$

It was shown in Section 3.4.2 that water and salt are advected *towards* the salt layer-solution interface, i.e., the mass averaged v-velocity is a negative quantity at the salt layer-solution interface. Moreover, as salt deposits the net mass transfer of water must be directed away from the salt layer-solution interface, i.e., towards the bulk. Since diffusion is the only mechanism transporting water away from the salt layer-solution interface the diffusive term in Eq. 3.72 can not be small small compared to the accumulation term, i.e., A4 must be at least of order unity. If A4 is of order unity, the water mass balance can not be scaled to determine the characteristic v-velocity at the salt layer-solution interface and Eq. 3.88 should be used to determine the characteristic v-velocity there. For $A4 \gtrsim 10$, the amount of H_2O diffusing away from the salt layer-solution substantially exceeds the amount of H_2O being displaced as the porous salt layer propagates outward. Under this condition, the diffusive and advective terms in the mass balance on the H_2O at the salt layer-solution interface must be of the same order and it follows that the characteristic value of the induced convective velocity at the interface is:

$$V_i = \frac{c^2 M_A M_B \mathfrak{D}_{AB} \Delta x_A Ra_D^{\frac{1}{4}} Le^{\frac{1}{3}}}{\omega_B \rho^2 D} \quad \text{for} \quad A4 \gtrsim 10 \tag{3.93}$$

For $A4 \gtrsim 10$, Eq. 3.93 may be used to corroborate the estimate of V_i based on the overall mass balance at the salt layer-solution interface.

Equation 3.62 relates the rate of increase of the diameter of the salt layer-solution interface to the advective and diffusive fluxes of salt at the interface. It may be scaled to determine the relative importance

175

of advection and diffusion to the transport of salt at the salt layer-solution interface. The Sorét and Dufour effects are neglected in the subsequent scaling. The ratio of the diffusion term to the accumulation term is:

$$A6 = \frac{c^2 M_A M_B \mathfrak{D}_{AB} \Delta x_A Ra_D^{\frac{1}{4}} Le^{\frac{1}{3}}}{\rho (\rho_s - \rho_A) D (1 - \phi) \frac{dD_i}{dt}\Big|_c}$$

(3.94)

Similarly, the ratio of the advective term to the accumulation term in this equation is:

$$A7 = \frac{\rho_A V_i}{(\rho_s - \rho_A) \frac{dD_i}{dt}\Big|_c}$$

(3.95)

3.5.10 Transient Terms in the Conservation Laws

In the expressions for conservation of species "A" and x-momentum (Eqs. 3.52 and 3.53 respectively) scaling a transient term with a convective term shows that, provided the characteristic v-velocity in the boundary layer is large compared to the characteristic rate at which the diameter of the salt layer-solution interface increases, the transient term is negligible. Thus the criterion for quasisteady conditions to hold in the expressions for conservation of species "A" and x-momentum is that A8 $\lesssim$ 0.1, where, A8 is:

$$A8 = \frac{\frac{dD_i}{dt}\Big|_c}{V}$$

(3.96)

The rate of increase of the diameter of the salt layer-solution interface, $\frac{dD_i}{dt}\Big|_c$, may be estimated directly from the experimental results or from the computation of the deposition rate at the salt layer-solution interface in Chapter 4.

The criterion for quasisteady conditions to hold in the energy equation is A9 $\lesssim$ 0.1, where, A9 is:

$$A9 = \frac{\rho_A C_{V_A} + \rho_B C_{V_B}}{\rho_A C_{P_A} + \rho_B C_{P_B}} \frac{\frac{dD_i}{dt}\Big|_c}{V}$$

(3.97)

In the ratio $(\rho_A C_{V_A} + \rho_B C_{V_B}) / (\rho_A C_{P_A} + \rho_B C_{P_B})$, the terms corresponding to species B will dominate the numerator and denominator. Moreover, the constant pressure specific heat of water exceeds its constant volume specific heat; therefore, A8 must always be smaller than A7. Thus, if the transient terms in the

species "A" and x-momentum conservation equations are negligible, then the transient term in the energy equation is negligible as well, i.e.,

$$A9 < A8 \tag{3.98}$$

3.5.11 Justification of the Boundary Layer Approximation

As already mentioned in Section 3.4.1, if the characteristic v-velocity is small compared to the characteristic u-velocity in the boundary layer and the thicknesses of the momentum, thermal and concentration boundary layers are small compared to the diameter of the hot finger, the boundary layer approximation is justified. Expressions for the characteristic values of the aforementioned velocities and boundary layer thicknesses are developed in the next section. It follows from them that the criterion for the characteristic u-velocity to be much greater than the characteristic v-velocity is A10 $\lesssim$ 0.1, where,

$$A10 = \frac{1}{Ra_{D_{io}}^{\frac{1}{4}}} \tag{3.99}$$

The criterion for the momentum and thermal boundary layer thicknesses to be small compared to the diameter of the hot finger is also that A10 is $\lesssim$ 0.1. Finally, if A11 is small compared to 0.1, the concentration boundary layer is small compared to the diameter of the hot finger as well.

$$A11 = \frac{1}{Ra_{D_{io}}^{\frac{1}{4}} Le^{\frac{1}{3}}} \tag{3.100}$$

Thus for the boundary layer approximation to be valid A10 and A11 must both be small compared to unity.

3.5.12 The Relative Importance of Natural and Forced Convection

For pure forced convection, the Reynolds number characterizing flow past a cylinder in cross flow is given by Eq. 3.101 where D_c is the OD of the cylinder.

$$Re_{D_c} = \frac{\rho V D_c}{\mu} \tag{3.101}$$

To determine a characteristic value for the quantity ρV in the experiments, continuity is applied to the flow in the Inconel 625 tube leading up to the cell, i.e., $\rho V = \frac{4\dot{m}}{\pi D_T^2}$, where D_T is the ID of the Inconel 625 tube. Approximating the salt layer-solution interface as a cylinder, Eq. 3.101 becomes:

$$Re_{D_i} = \frac{4\dot{m} D_i}{\pi \mu D_T^2} \tag{3.102}$$

During the deposition experiments when the concentration of sodium sulfate was 4 wt%, for example, the Reynolds number at time equal to zero (based on the diameter of the hot finger) is about 95. As salt deposits on the hot finger, the diameter of the salt layer-solution interface increases by a factor of up to about 2; consequently, the maximum Reynolds number in these experiments is of order 200. The Reynolds numbers characterizing the experiments in which the sodium sulfate concentration in the inlet stream is 4 wt% are typical of all of the deposition experiments.

At a Reynolds numbers between 40 and 150, in the absence of natural convection, the flow in the boundary layer formed around a cylinder in cross flow is laminar and the vortex street formed on the downstream side of the cylinder is laminar as well [61]. For $150 < Re_{D_i} < 3*10^5$, the flow in the boundary layer remains laminar up to the separation point, but the vortex street is turbulent and its structure increasingly three-dimensional [61]. Thus by the end of each deposition experiment some turbulence due to the forced convective cross flow is expected on the downstream side of the hot finger. This turbulence likely plays a role in the formation of the bumps shown in Fig. 2-4 and pronounced dendrites shown in Fig. 2-6 during the sodium sulfate and potassium sulfate deposition experiments respectively. Towards the end of some experiments the downstream side of the natural convection boundary may be turbulent as well as discussed in Section 4.4.2.

This turbulence may also affect the morphology of the salt on the downstream side of the hot finger. Finally, stability may also play a role in the formation of the downstream morphology. Examining Fig. 2-3 it is apparent that the fluid between the bumps and pronounced dendrites formed on the downstream side of the hot finger is buoyantly unstable because it is at a lower concentration and higher temperature than the bulk fluid. Thus substantial natural convective transport may occur between these irregularities on the downstream side of the hot finger. Conversely, if there were bumps and/or pronounced dendrites formed on the upstream side of the hot finger the fluid in between them would be far less buoyant and natural convective transport weaker.

For the conditions investigated in this dissertation, forced convection is weak relative to natural convection. The relative importance of natural and forced convective transport in the experiments may be evaluated by comparing the square of the characteristic velocities associated with the two convection regimes. Using scale analysis it is simple to show that the square of the ratio of the characteristic velocity for natural convection to that for forced convection scales as $\frac{Gr_{D_i}}{Re_{D_i}^2}$ where Gr_{D_i} represents the Grashof number defined by:

$$Gr_{D_i} = \frac{\Delta \rho g D_i^3}{\rho \nu^2} \tag{3.103}$$

In Eq. 3.103 $\Delta \rho$ is the difference between the bulk solution density and the solution density at the salt layer-solution interface and ν is the kinematic viscosity. The dimensionless group $\frac{Gr_L}{Re_L^2}$ is commonly referred to as the Richardson number. At the beginning of the deposition experiments in which the concentration of sodium sulfate in the inlet stream was 4 wt%, the Grashof number is about $1.3*10^7$ according to the analyses in Chapter 4 resulting in a Richardson number of about 1300. Thus transport is dominated by natural convection near the beginning of these experiments. After 12 minutes of deposition the Richardson number is estimated to be about 1100; therefore, natural convection dominates transport during the entire run. Similar Richardson numbers characterize all of the deposition experiments; hence, in subsequent transport analyses forced convection is neglected. The pure water heat transfer experiments presented in Chapter 2 corroborate that natural convection dominates transport at conditions of interest as per the analyses in

3.6 Dimensionless Conservation Laws

3.6.1 Introduction

In this section a scale analysis is performed to non-dimensionalize the conservation laws and estimate characteristic values of u, v and y. (The characteristic value of x is, obviously, of order $\pi D_i/2$ or simply D_i.) Then the criteria for the analogy between heat and mass transfer to be valid are presented. Next, the functional form of the Nusselt number for double-diffusive laminar natural convection along a vertical plate is derived. Then an expression for the ratio of the thermal boundary layer thickness to the concentration boundary layer thickness is developed. Finally, the functional form of the Sherwood number for double-diffusive laminar natural convection along a vertical flat plate is developed. All of the criteria developed in the previous section, except $\tilde{N} \lesssim 0.1$, are assumed to be satisfied. Justification of this may be found in Section 3.8. The salt layer-solution interface is approximated as a vertical flat plate of height L. (L is of order $\pi D_i/2$ or simply D_i.) The appropriate form of the conservation laws in this context is:

$$\frac{\partial u}{\partial x} + \frac{\partial v}{\partial y} = 0 \tag{3.104}$$

$$u\frac{\partial u}{\partial x} + v\frac{\partial u}{\partial y} = \nu\frac{\partial^2 u}{\partial y^2} + g\beta(T - T_\infty) + g\beta^*(\rho - \rho_\infty) \tag{3.105}$$

$$u\frac{\partial T}{\partial x} + v\frac{\partial T}{\partial y} = \alpha\frac{\partial^2 T}{\partial y^2} \tag{3.106}$$

$$u\frac{\partial \rho_A}{\partial x} + v\frac{\partial \rho_A}{\partial y} = \mathfrak{D}_{AB}\frac{\partial^2 \rho_A}{\partial y^2} \tag{3.107}$$

The Prandtl number of (pure) water at conditions relevant to the deposition experiments is of order unity, as per Fig. 3-14; therefore, the momentum boundary layer thickness (δ_m) and the thermal boundary layer thickness (δ_t) are of the same order and, thus, both are subsequently denoted by δ. For scaling purposes both of the buoyancy terms contained in the momentum equation are treated as a single term by setting the order of the (combined) buoyancy terms equal to $\beta g\left(1 + \tilde{N}\right)$. In this way, the buoyancy forces induced by both the temperature and concentration differences across the boundary layer are accounted for in the scale

180

analysis.

3.6.2 Dimensionless Conservation Laws

Scaling the buoyancy term(s) with the viscous term in the x-momentum equation and the first convective term with the diffusive term in the energy equation as well as setting the characteristic lengths in the x and y directions equal to D and δ respectively yields,

$$\delta^2 \quad \sim \quad \frac{\nu U}{g\beta\Delta T \left(1 + \tilde{N}\right)} \tag{3.108}$$

$$U \quad \sim \quad \frac{\alpha D}{\delta^2} \tag{3.109}$$

The Rayleigh number is defined conventionally as:

$$Ra_D = \frac{g\beta\Delta T D^3}{\nu\alpha} \tag{3.110}$$

However, because buoyancy in this study is induced by both temperature and concentration differences, the Rayleigh number herein is defined as:

$$Ra_D = \frac{g\left(\beta\Delta T + \beta^*\Delta\rho_A\right)D^3}{\nu\alpha} \tag{3.111}$$

It then follows from Eqs. 3.108 and 3.109 that characteristic values for the boundary layer thickness and u-velocity scale as:

$$\delta \quad \sim \quad \frac{D}{Ra_D^{\frac{1}{4}}} \tag{3.112}$$

$$U \quad \sim \quad \frac{\alpha Ra_D^{\frac{1}{2}}}{D} \tag{3.113}$$

181

Then, by scaling the continuity equation it follows that the characteristic v-velocity is:

$$V \sim \frac{\alpha Ra_D^{\frac{1}{4}}}{D} \qquad (3.114)$$

Finally, scaling temperature and concentration conventionally, it follows that an appropriate set of dimensionless variables is:

$$\tilde{x} = \frac{x}{D} \qquad (3.115)$$

$$\tilde{y} = \frac{y Ra_D^{\frac{1}{4}}}{D} \qquad (3.116)$$

$$\tilde{u} = \frac{uD}{\alpha Ra_D^{\frac{1}{2}}} \qquad (3.117)$$

$$\tilde{v} = \frac{vD}{\alpha Ra_D^{\frac{1}{4}}} \qquad (3.118)$$

$$\tilde{T} = \frac{T - T_B}{T_i - T_B} \qquad (3.119)$$

$$\tilde{\rho} = \frac{\rho - \rho_B}{\rho_i - \rho_B} \qquad (3.120)$$

The resulting dimensionless form of the conservation laws is:

$$\frac{\partial \tilde{u}}{\partial \tilde{x}} + \frac{\partial \tilde{v}}{\partial \tilde{y}} = 0 \qquad (3.121)$$

$$\tilde{u}\frac{\partial \tilde{u}}{\partial \tilde{x}} + v\frac{\partial \tilde{u}}{\partial \tilde{y}} = Pr\left[\frac{\partial^2 \tilde{u}}{\partial \tilde{y}^2} + \frac{\tilde{T} + \tilde{\rho}_A \tilde{N}}{1 + \tilde{N}}\right] \qquad (3.122)$$

$$\tilde{u}\frac{\partial \tilde{T}}{\partial \tilde{x}} + \tilde{v}\frac{\partial \tilde{T}}{\partial \tilde{y}} = \frac{\partial^2 \tilde{T}}{\partial \tilde{y}^2} \qquad (3.123)$$

$$\tilde{u}\frac{\partial \tilde{\rho}_A}{\partial \tilde{x}} + \tilde{v}\frac{\partial \tilde{\rho}_A}{\partial \tilde{y}} = \frac{1}{Le}\frac{\partial^2 \tilde{\rho}_A}{\partial \tilde{y}^2} \qquad (3.124)$$

3.6.3   Applicability of the Analogy Between Heat and Mass Transfer

It is evident from examination of Eqns. 3.123 and 3.124 that, when the Lewis number equals unity, the energy and species conservation equations are of the same form and the analogy between heat and mass transfer may apply. However, for the analogy between heat and mass transfer to rigorously apply the energy and species conservation equations must have the same set of boundary conditions in x and y, e.g., all three boundary

182

conditions Dirichlet on both equations. The Lewis number of the aqueous salt solutions is estimated to be of order 6 at conditions of interest in Section 3.7.6. However, a computational study by Gebhart and Pera [32] shows that the Nusselt and Sherwood numbers at conditions of interest to the deposition experiments are relatively weak functions of the Lewis number. Moreover, all the boundary conditions on both the energy and species equations are, at least to a first approximation, of the first kind. Hence, the analogy between heat and mass transfer should suffice for "crude", but meaningful, estimates of the deposition rate. It was applied in Section 3.2.

3.6.4 Form of Nusselt and Sherwood Numbers and Scale of Relative Boundary Layer Thicknesses

From Eqs. 3.121 through 3.124, it is evident that $\left(\frac{\partial \tilde{T}}{\partial \tilde{y}}\right)\Big|_{y=0}$ for the prescribed geometry is a function of Prandtl number, Lewis number and $\tilde{N}$, i.e.,:

$$\left(\overline{\frac{\partial \tilde{T}}{\partial \tilde{y}}}\right)\Big|_{y=0} = f\left(Pr, Le, \tilde{N}\right) \tag{3.125}$$

Furthermore, if $\overline{\frac{\partial \tilde{T}}{\partial \tilde{y}}}\Big|_{y=0}$ is expressed in dimensional form, it follows from the definition of the heat transfer coefficient that the mean Nusselt number (based on diameter) is of the form:

$$\overline{Nu_D} = Ra_D^{\frac{1}{4}} g\left(Pr, Le, \tilde{N}\right) \tag{3.126}$$

If Sc $\gg$ 1, in addition to Pr $\sim$ 1, scaling either of the inertial terms with the diffusive term in the species conservation equation yields:

$$\frac{\delta_c}{\delta} \cong Le^{\frac{1}{3}} \tag{3.127}$$

Combining the foregoing expression with the characteristic thermal/momentum boundary layer thickness given by Eq. 3.112, it follows that the concentration boundary layer thickness scales as:

$$\delta_c = \frac{D}{Ra_D^{\frac{1}{4}} Le^{\frac{1}{3}}} \tag{3.128}$$

Even at the estimated Lewis number of 6 for the aqueous salt solutions, or, equivalently, Schmidt number of 6 (since the Prandtl number of SCW is about 1), Eq. 3.127 suffices in the context of a scale analysis. Since the mean Sherwood number scales as the mean Nusselt number multiplied by δ_t/δ_C, it follows that it scales as $Le^{\frac{1}{3}} Ra_D^{\frac{1}{4}} g\left(Pr, Le, \tilde{N}\right)$. Bejan [9] performed a scale analysis similar to that above and determined the functional form of the Sherwood number for various permutations of the Prandtl and Lewis/Schmidt numbers in the context of convection driven solely by "thermal" buoyancy.

3.7 Estimation of Thermodynamic and Transport Properties

3.7.1 Introduction

The thermodynamic and transport properties necessary to evaluate the criteria developed Section 3.5 and compute the deposition rate at the salt layer-solution interface in Chapter 4 are provided in this section. Currently, most thermodynamic and transport properties of aqueous sodium sulfate and potassium sulfate solutions at the conditions investigated in the deposition rate experiments are unavailable. Hence the aqueous salt solutions are generally approximated as pure H_2O at the temperature and pressure of interest to determine relevant thermodynamic and transport properties. This is accomplished using the NBS Steam Tables [30] as per the next section. Estimates of the density, volumetric thermal expansion coefficient, species expansion coefficient, thermal diffusivity, binary molecular diffusion coefficient, constant pressure specific heat, heat of dissolution and thermal diffusion ratio of the aqueous salt solutions at relevant conditions are possible and provided in Sections 3.7.3 through 3.7.9. Using the data for the constant pressure specific heat of aqueous sodium sulfate solutions presented in Section 3.7.8, the constant pressure specific heat of the salt and the water components of solution are estimated as well. In Section 3.7.5 a brief evaluation of the

applicability of kinetic theory of gases to predicting molecular diffusion coefficients in supercritical fluids is given.

3.7.2 NBS Steam Tables

The density, viscosity, constant pressure specific heat, and thermal conductivity of pure H_2O at 250 bar as a function of temperature between 0 and 700 $^\circ C$ were extracted directly from the NBS Steam Tables [30] and are plotted in Figs. 3-8 through 3-11. The kinematic viscosity ($\nu = \frac{\mu}{\rho}$), thermal diffusivity ($\alpha = \frac{k}{\rho C_P}$) and Prandtl number ($Pr = \frac{\nu}{\alpha}$) of pure H_2O at 250 bar, computed using NBS Steam Table values for ρ, C_P, μ and k, are plotted in Figs. 3-12 through 3-14. Figs. 3-8 through 3-14 are used to determine thermodynamic and transport properties as necessary in subsequent sections of this dissertation. Each of the aforementioned properties varies most dramatically around the pseudocritical temperature of pure H_2O at 250 bar (385 $^\circ C$). Density (at 250 bar), for example, decreases from 625.7 kg/m^3 at 350 $^\circ C$ to 166.6 kg/m^3 at 400 $^\circ C$. It is noted that the thermophysical properties of H_2O along a given isobar are far smoother functions of density than temperature as discussed in Chapter 1. Finally, it is noted that 250 bar exceeds the critical pressure of H_2O by 13.2%; consequently, variations in properties near the critical temperature (371 $^\circ C$), despite being large, are less dramatic than along the critical isobar.
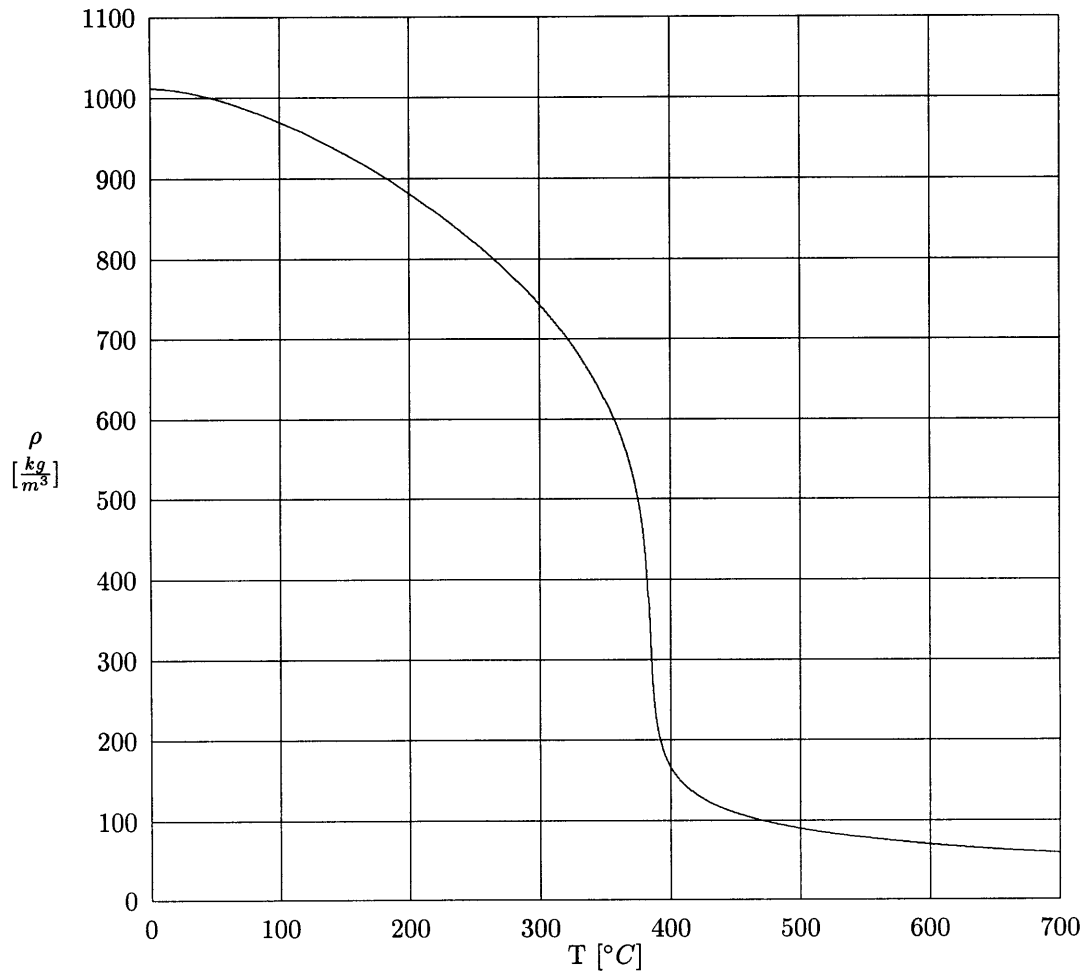
Figure 3-8: Density of H_2O as a function of temperature at 250 bar [30].
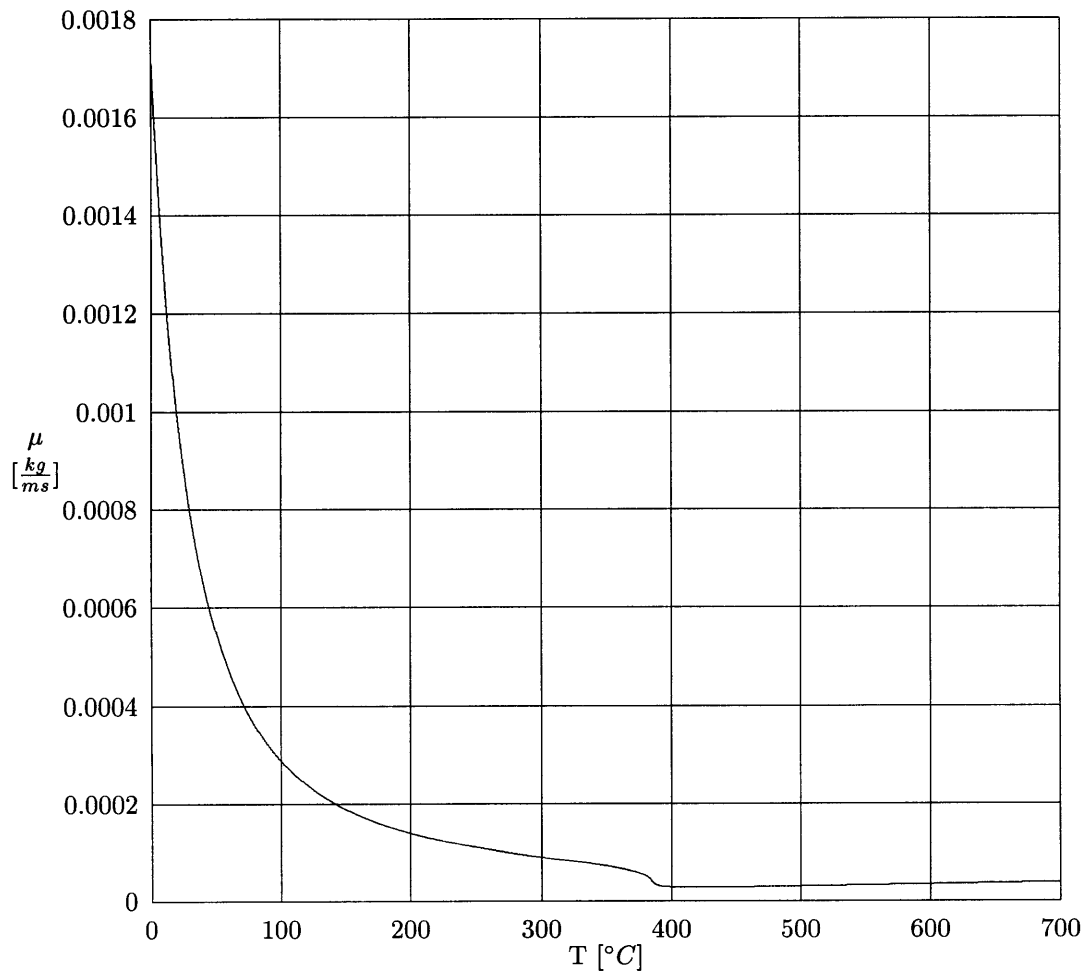
Figure 3-9: Viscosity of H_2O as a function of temperature at 250 bar [30].
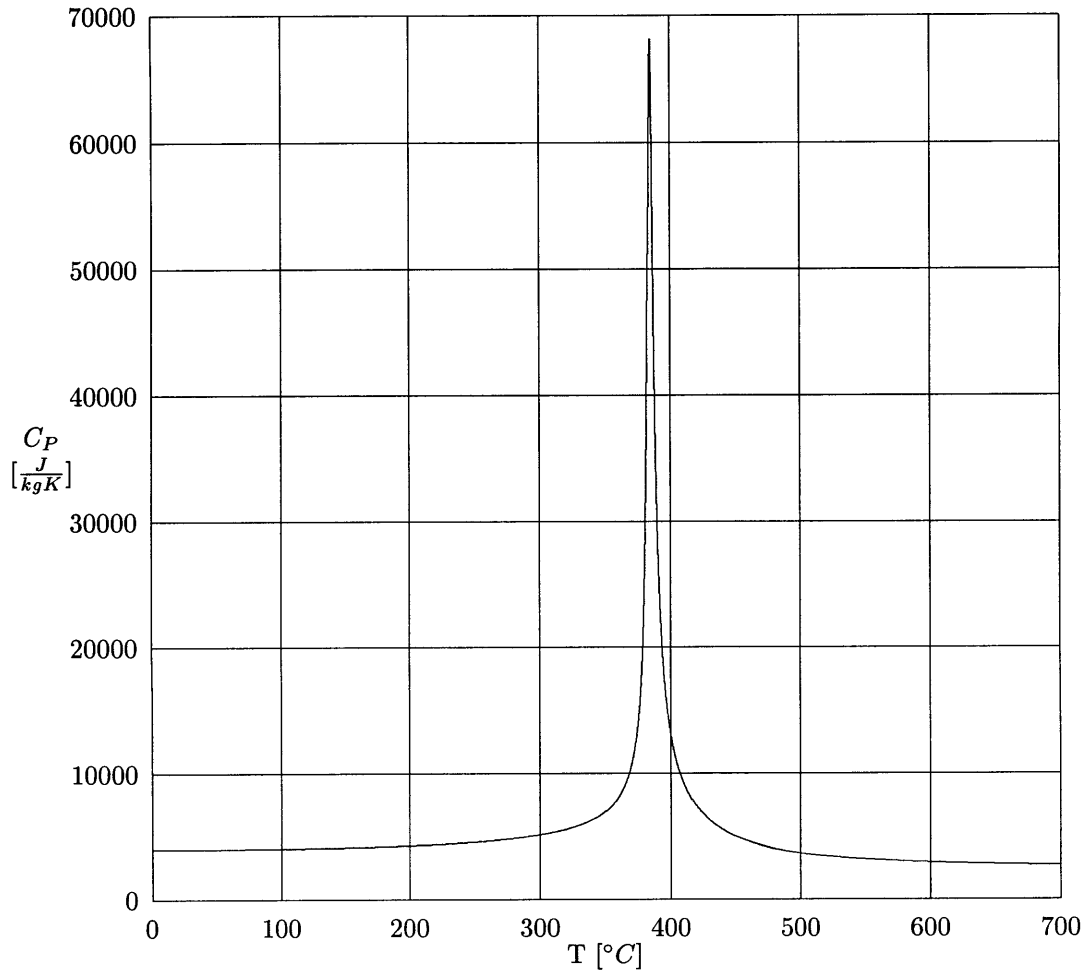
Figure 3-10: Constant pressure specific heat of H_2O as a function of temperature at 250 bar [30].
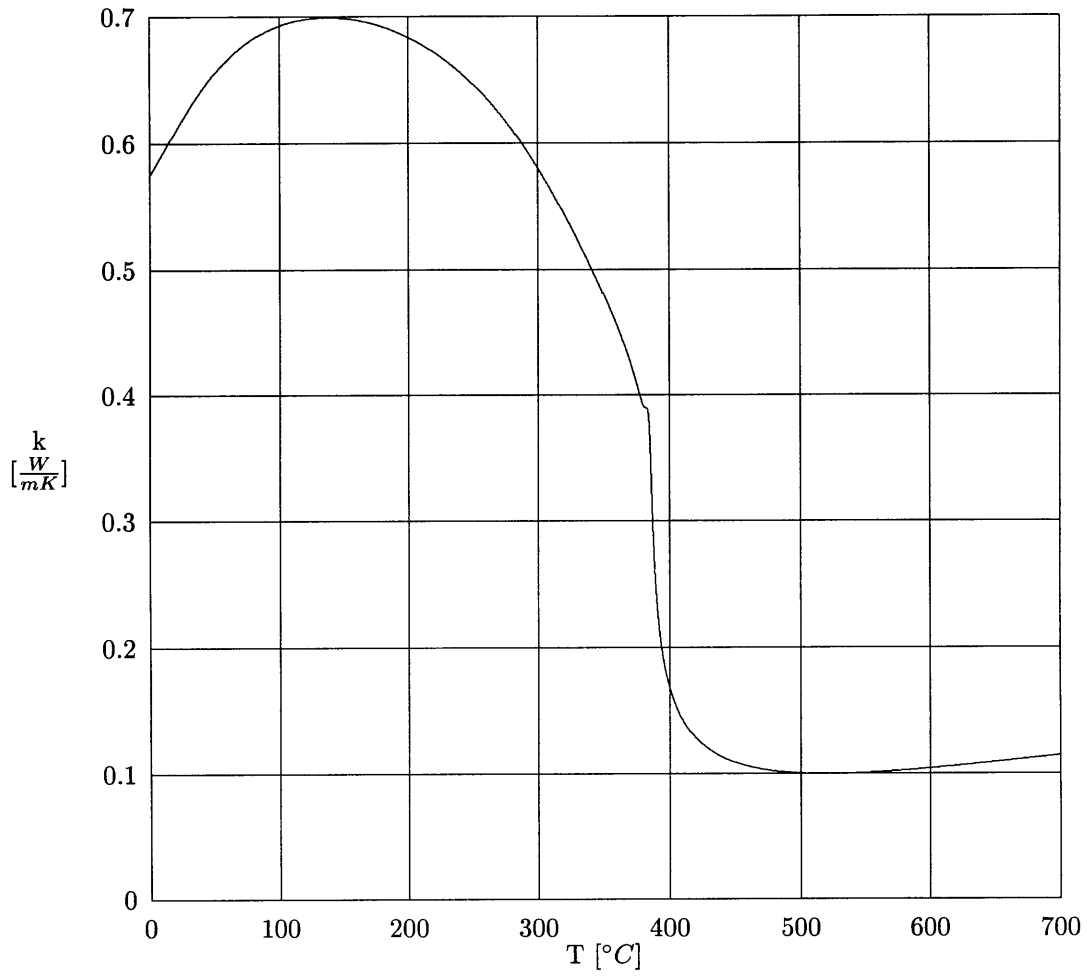
Figure 3-11: Thermal conductivity of H_2O as a function of temperature at 250 bar [30].
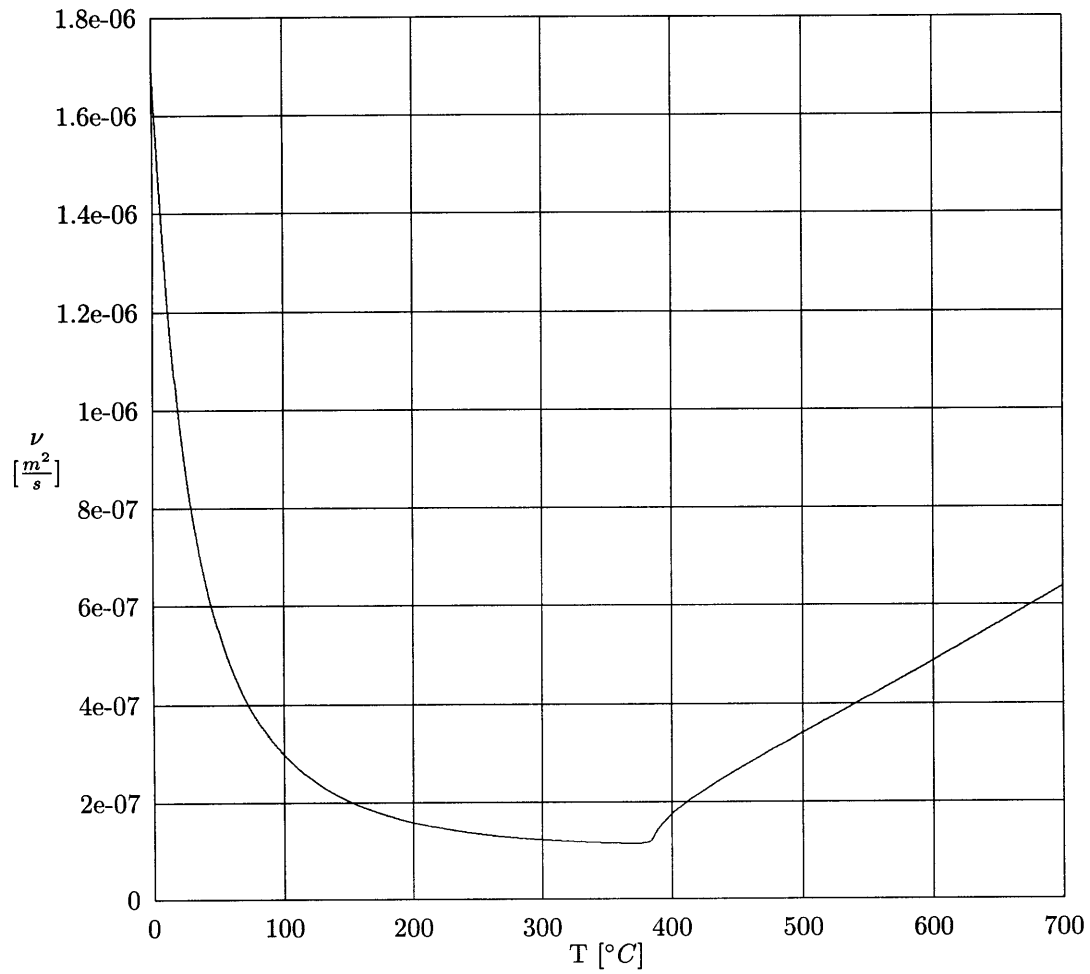
Figure 3-12: Kinematic viscosity of H_2O as a function of temperature at 250 bar [30].
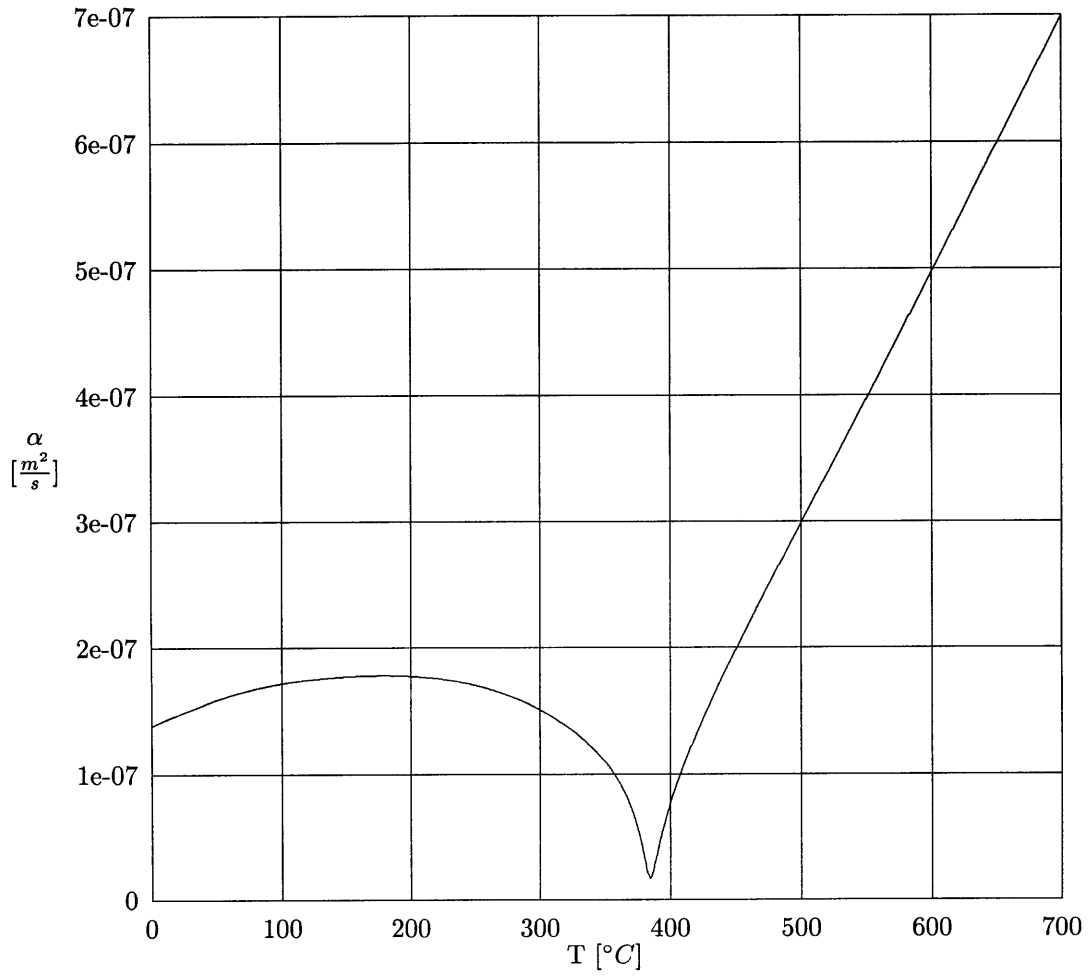
Figure 3-13: Thermal diffusivity of H_2O as a function of temperature at 250 bar [30].
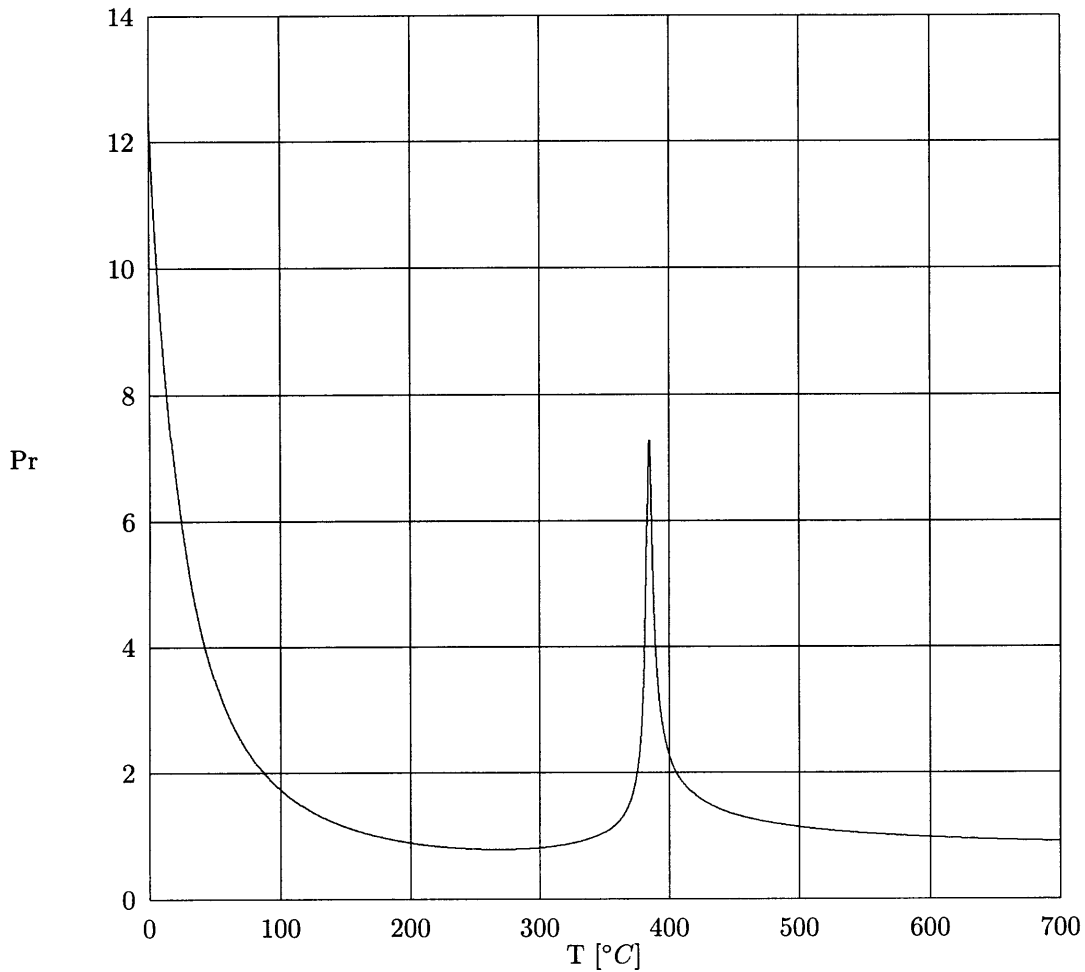
Figure 3-14: Prandtl number of H_2O as a function of temperature at 250 bar [30].

The volumetric thermal expansion coefficient is defined according to Eq. 3.24. For pure H_2O it may be computed along a given isobar using density as a function of temperature data extracted from the NBS Steam Tables. The quantity $\frac{\partial \rho}{\partial T}\Big|_P$ is computed using a central difference formula, i.e.,

$$\rho'(T_i) = \left(\frac{\rho(T_{i+1}) - \rho(T_{i-1})}{2h}\right)_P + \text{error} \tag{3.129}$$

where h represents the number of degrees Kelvin between equispaced temperature values. One h value is inappropriate over large temperature ranges because of the form of the variation of ρ with T. Thus in the FORTRAN 77 program written to compute $\frac{\partial \rho}{\partial T}\Big|_P$ over the temperature range from 0 to 700 °C (at

192
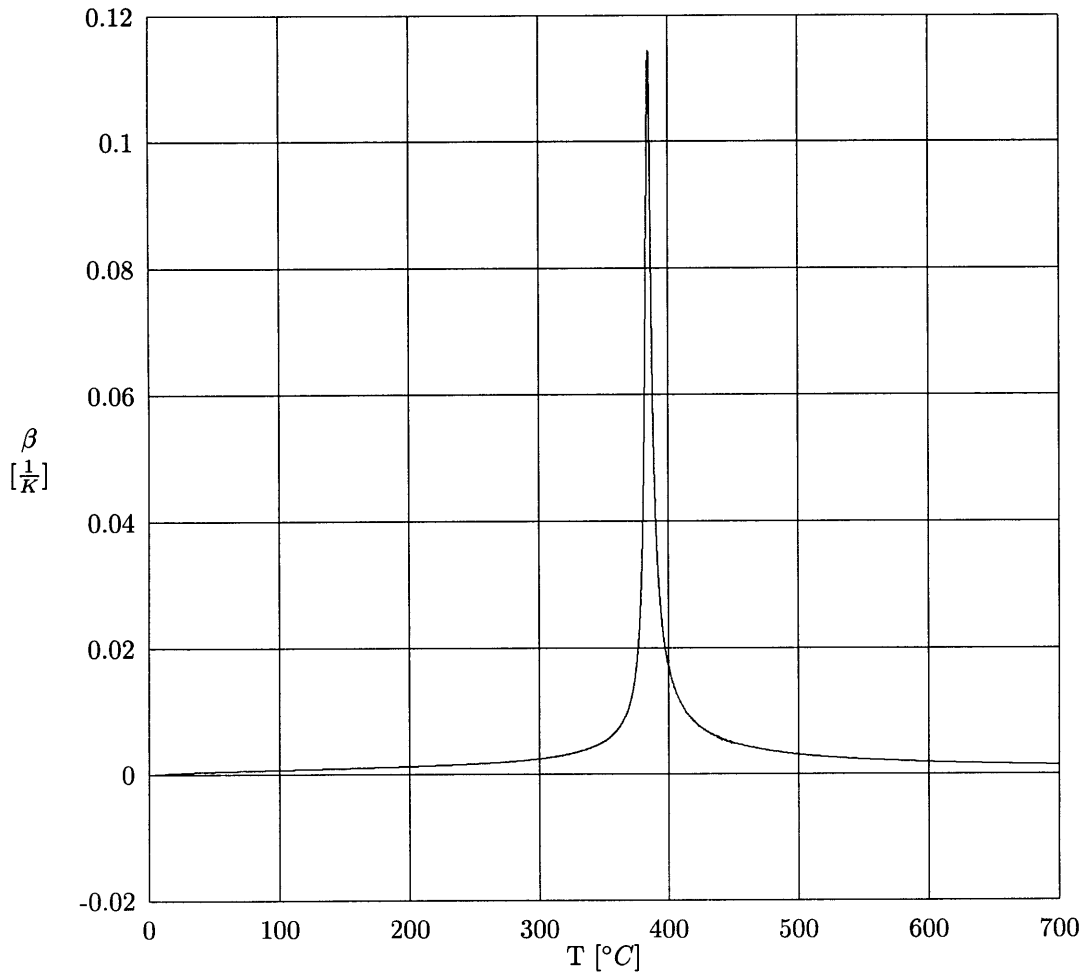
Figure 3-15: Volumetric thermal expansion coefficient of pure H_2O as a function of temperature at 250 bar computed from density data provided by Gallagher and Haar [30].

250 bar), different h values were used in different temperature intervals. The variation of the volumetric thermal expansion coefficient with temperature for pure H_2O at 250 bar is plotted in Fig. 3-15. Pure water is especially compressible in the temperature range pertinent to the deposition experiments, i.e., from about 350 to 400 °C.

3.7.3 Density and Expansion Coefficients of Aqueous Sodium Sulfate Solutions

Dr. John Gallagher of the Chemical Science and Technology Laboratory (CSTL) at NIST has provided us with a FORTRAN 77 program to compute the density of aqueous sodium sulfate solutions as a function

193

of temperature, concentration and pressure at conditions relevant to the deposition rate experiments [29]. (Gallagher developed the program by applying the equation of state developed by Anderko and Pitzer [3] for the NaCl-H_2O system above 573 K to the Na_2SO_4-H_2O system.) The program is valid for the single-phase fluid and liquid-vapor regions of the Na_2SO_4-H_2O system for temperatures between 200 and 500 $°C$ and pressures up to 1000 bar. Temperature, pressure and salt concentration and whether the (T,P,C) state of interest lies in the single-phase fluid or liquid-vapor region are the inputs to the program and density is output. (If the state of interest lies in the liquid-vapor region the program outputs the densities of both phases.) The density of pure H_2O as a function of temperature between 330 and 375 $°C$ at 250 bar was determined using both the Gallagher program and the NBS Steam Tables and the results are plotted in Fig. 3-16. This parametric range of temperatures and pressures characterizes the conditions investigated in the deposition experiments and the discrepancy between the two sources of density data does not exceed 2.41% within it.

The density of 0, 2, 4, 6, and 8 wt% salt, aqueous sodium sulfate solutions between temperatures of 330 and 375 $°C$ at 250 bar computed using the Gallagher program in the single phase region are shown in Fig. 3-17. Each of the curves in Fig. 3-17 terminates at the phase boundary separating the single phase and solid-fluid phase regions of the Na_2SO_4-H_2O system at 250 bar. (This phase boundary and a 2nd order curve fit to it are contained in Fig. 2-1.) Increasing salt concentration from 0 wt% to 8 wt% results in about a 20% increase in solution density at temperatures and pressures pertinent to the sodium sulfate deposition experiments. The K_2SO_4-H_2O and Na_2SO_4-H_2O systems have similar temperature-composition diagrams at relevant conditions and sodium and potassium are both group 1A elements; therefore, it is possible, or perhaps probable, that the addition of sodium sulfate and potassium sulfate increase the density of pure H_2O by similar amounts. Conversely, the Na_2SO_4-H_2O and NaCl-H_2O systems have dramatically different temperature-composition diagrams at 250 bar and density data shows that in the single phase region similar changes in the concentration of sodium sulfate and sodium chloride can change solution density by substantially different amounts. For example, at 300 $°C$ and 250 bar an 8 wt% salt, aqueous sodium chloride solution is about 20% more dense than pure H_2O at the same temperature and pressure [4, 73], whereas an 8 wt% sodium sulfate solution is only about 4% more dense than pure H_2O at 300 $°C$ and 250 bar [30].
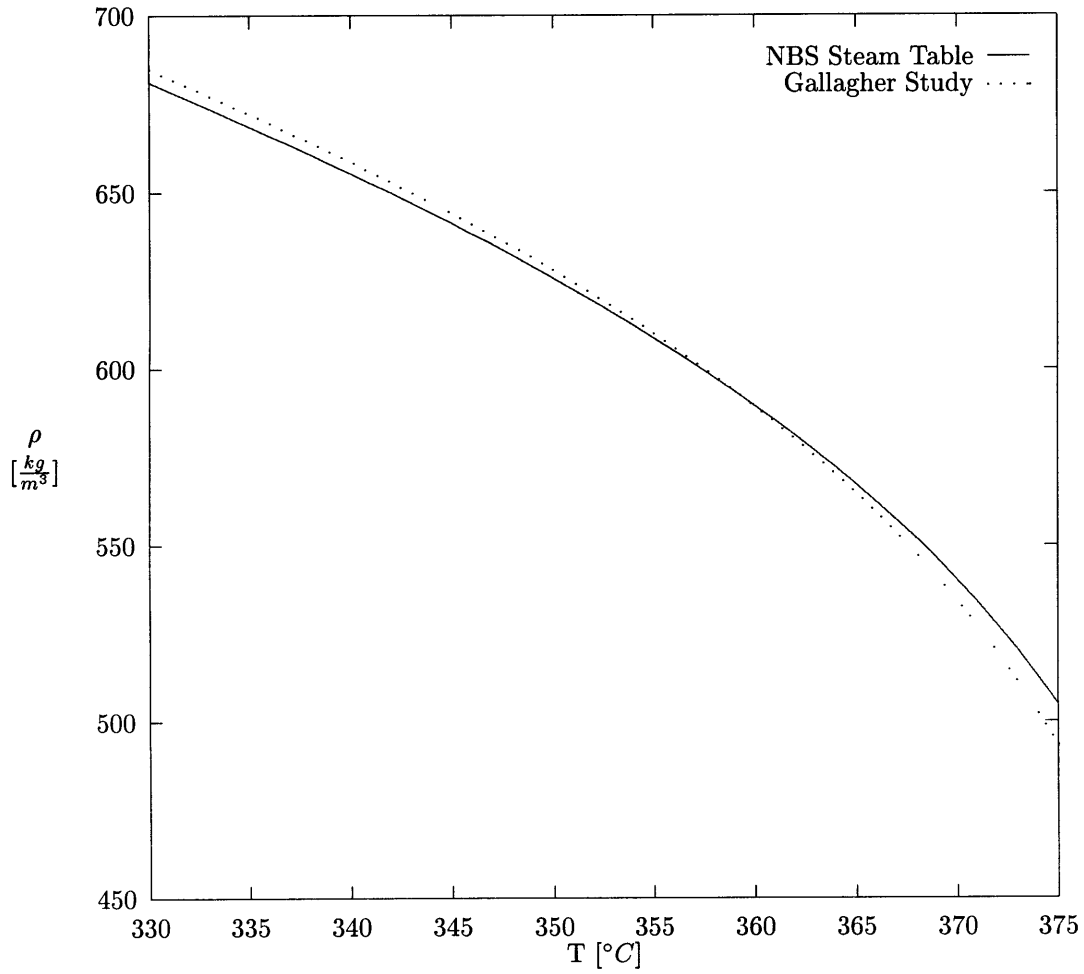
Figure 3-16: Density of pure H_2O at 250 bar as a function of temperature based on the NBS Steam Tables [30] and Gallagher study [29].
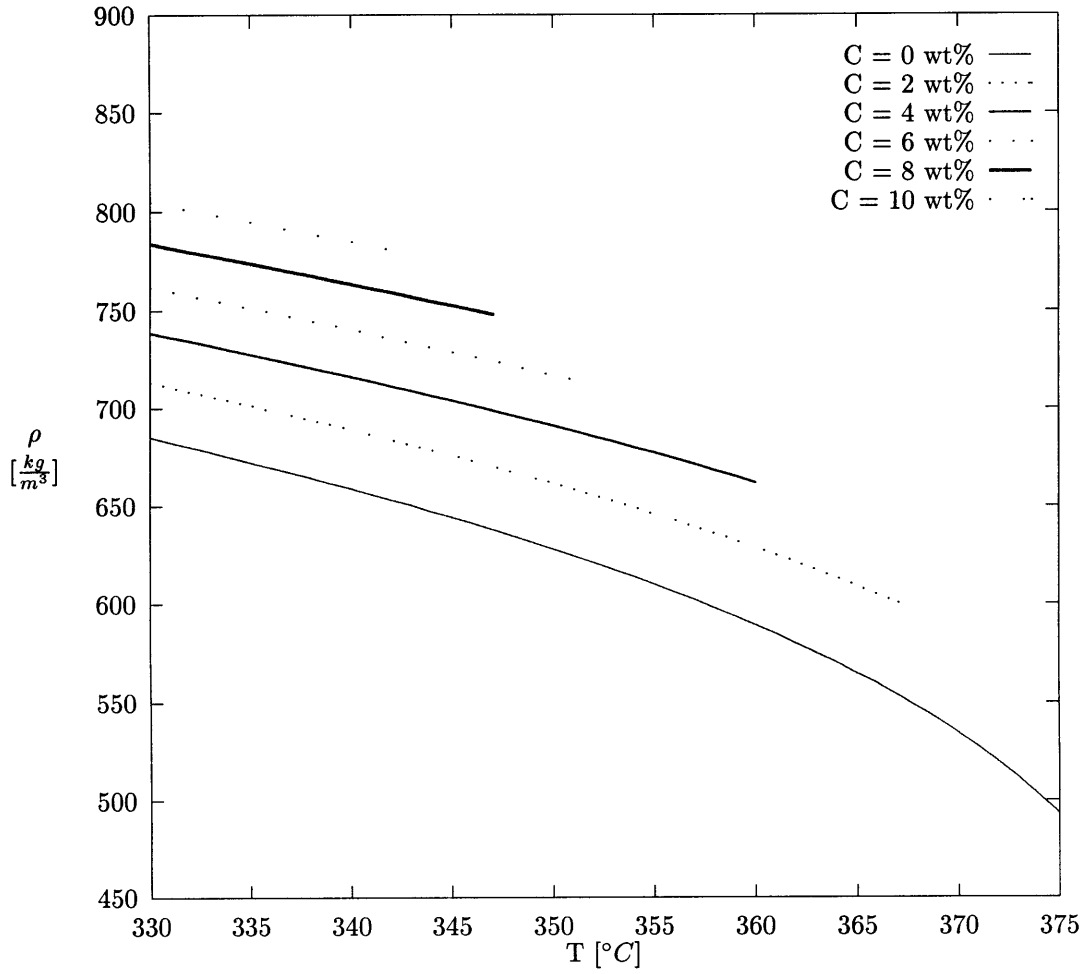
Figure 3-17: Density of pure water and 2, 4, 6, 8 and 10 wt% salt, aqueous sodium sulfate solutions as a function of temperature at 250 bar based on the Gallagher study [29]

A central difference formula was used to evaluate $\frac{\partial \rho}{\partial T}\big|_{P,C}$ and $\frac{\partial \rho}{\partial \rho_A}\big|_{P,T}$ from densities computed using the Gallagher program over temperature and concentration ranges relevant to the sodium sulfate deposition experiments and 250 bar. The volumetric thermal and species expansion coefficients were computed from Eqs. 3.24 and 3.25 respectively. Resulting tabulations of the volumetric thermal expansion coefficient as a function of temperature at sodium sulfate concentrations of 0, 2, 4, 6 and 8 wt% and species expansion coefficient as a function of sodium sulfate concentration at temperatures of 345, 350, 355, 360 and 365 °C were fitted to polynomials and the results are plotted in Figs. 3-18 and 3-19 respectively. In Fig. 3-18, the volumetric thermal expansion coefficient for pure H_2O based on the Gallagher study (at 0 wt% salt) and the NBS Steam Tables, as per Section 3.7.2, are both plotted over the temperature range of 330 to 375 °C at 250 bar and agree to within about 10% throughout this parametric range. (Some of this discrepancy is attributable to errors in the central difference approximations of $\left(\frac{\partial \rho}{\partial T}\right)\big|_{P,C}$ and the polynomial curve fits to the tabulations of discrete values of volumetric thermal expansion coefficients.) Each curve in Figs. 3-18 and 3-19 terminates at the solubility temperature corresponding to the concentration of interest. As per Fig. 3-18, increasing the sodium sulfate concentration from 0 to 8 wt% at constant temperature causes the volumetric thermal expansion coefficient to decrease by a factor of up to about 1/3 at conditions relevant to the deposition experiments. Similarly, increasing the sodium sulfate concentration from 0 to 8 wt% (at constant temperature) can decrease the species expansion coefficient by a factor of up to about 1/2 at conditions relevant to the deposition experiments as per Fig. 3-19. Not surprisingly, as the critical temperature of pure H_2O (371 °C) is approached there are substantial increases and decreases in the volumetric thermal expansion coefficient and species expansion coefficient respectively.

3.7.4 Thermal Diffusivity

Butenhoff et al. recently measured the thermal diffusivity of aqueous sodium nitrate solutions at near-supercritical conditions as a function of pressure (270 to 1000 bar), temperature (400 to 500 °C) and salt concentration (0.25 to 3.0 m) using the laser-induced grating technique [15]. Their results are provided in Table 3.3. (Other transport variables measured in the Butenhoff et al. study are reported in Table 3.3 as well and discussed below.) The thermal (and molecular) diffusivities reported by Butenhoff et al. were
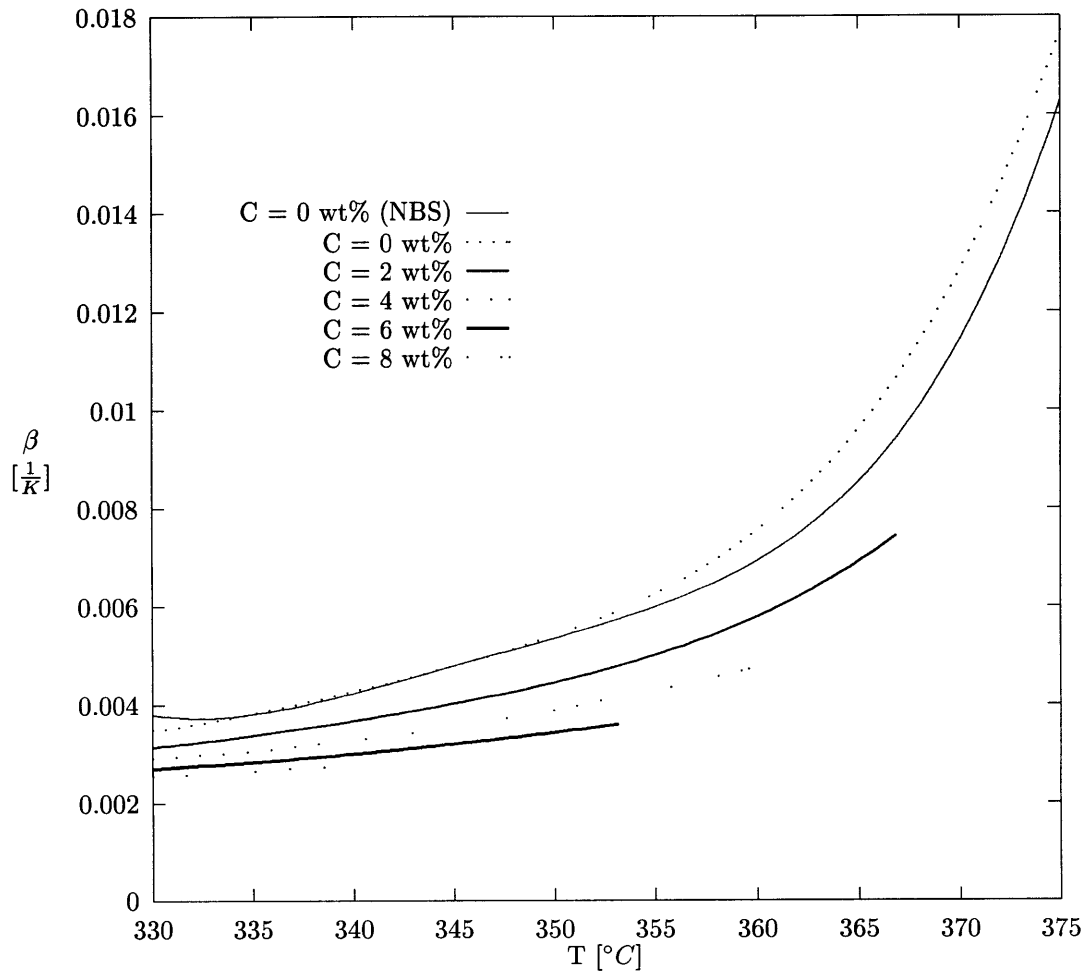
Figure 3-18: Volumetric thermal expansion coefficient as a function of temperature and salt concentration for an aqueous sodium sulfate solution at 250 bar.
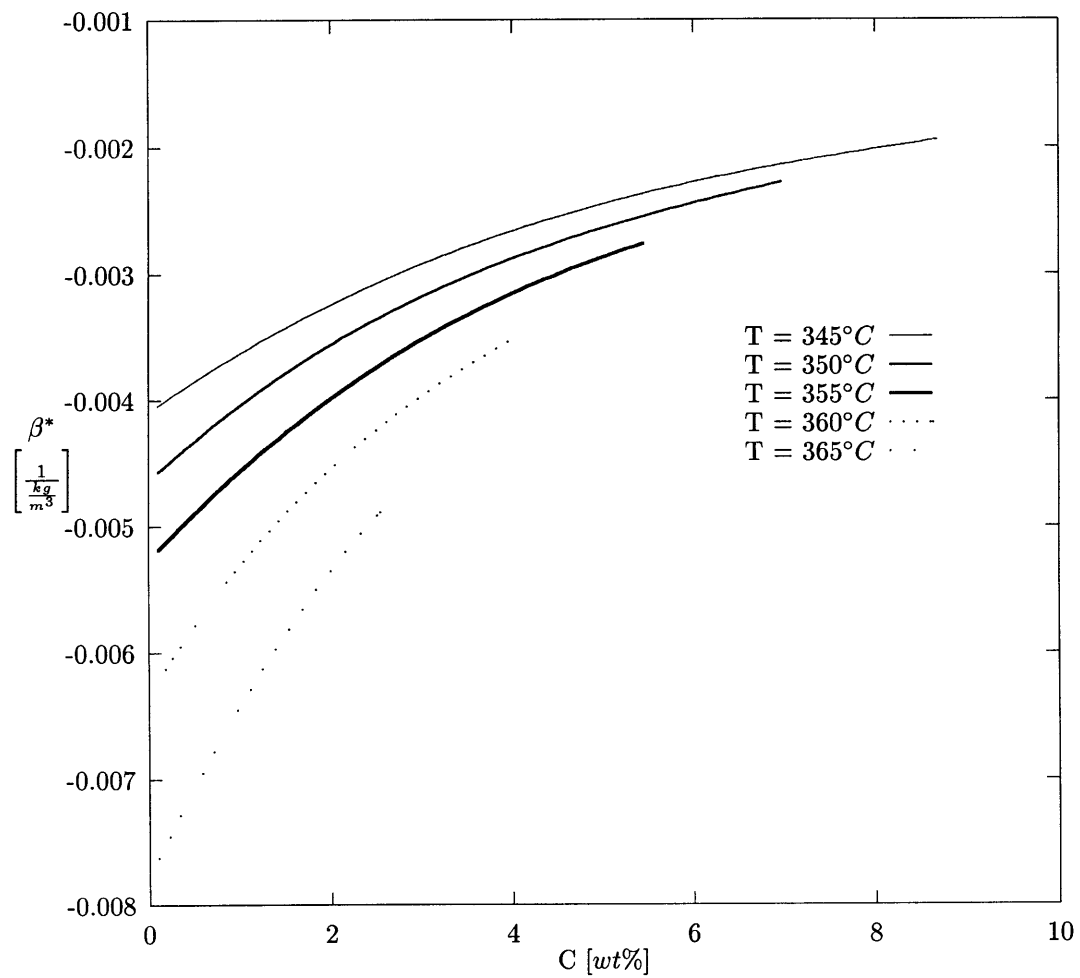
Figure 3-19: Species expansion coefficient as a function of temperature and salt concentration for an aqueous sodium sulfate solution at 250 bar.

averaged over 6-12 measurements and the numbers given in parenthesis represent one standard deviation in the last digit(s). For example, when c = 0.25 m, T = 450 °C and P = 409.5 bar, α is reported as $70.9(12)*10^{-9}$ m²/sec, i.e., it was measured as $(70.9 \pm 1.2)*10^{-9}$ m²/sec within one standard deviation over 6-12 measurements. Modest systematic errors, of up to about 3%, were also present in the diffusivity measurements performed by Butenhoff et al. [15]. The molecular weight of sodium nitrate is 84.99 $\frac{gm}{mole}$ and the 0.25, 1.0 and 3.0 molality solutions in the Butenhoff et al. study correspond to 2.08, 7.83, and 20.32 wt% $NaNO_3$ in solution respectively. All of the Butenhoff et al. measurements were in the single-phase fluid region of the $NaNO_3$-H_2O system.

The thermal diffusivity of pure water (α_{H_2O}) based on the NBS Steam Tables at the temperatures and pressures investigated by Butenhoff et al. is also provided in Table 3.3. The ratio of the thermal diffusivity of the aqueous sodium nitrate solutions to that of pure water at the same temperature and pressure is given in the next column and ranges from 0.76 to 2.39 over the parametric range investigated by Butenhoff et al. However, it is generally close to unity and subsequently assumed equal to unity for the purpose of calculating the deposition rate at the salt layer-solution interface. Fig. 3-20, for example, is a plot of the thermal diffusivity of a 1 m, aqueous, sodium nitrate solution and pure H_2O as a function of pressure at 450 °C and the agreement is close, with a maximum discrepancy of about 33%.

3.7.5 Molecular Diffusion Coefficient

Introduction

Experimental measurements of (self and binary) molecular diffusion coefficients at conditions relevant to the deposition experiments are provided at the beginning of this section. Then a limited evaluation of the applicability of the kinetic theory of gases, without and with a correction factor for "dense" gases, to predict molecular diffusion coefficients in supercritical fluids is undertaken.

Experimental Data

Data for the binary molecular diffusion coefficient of salts in water at near-supercritical conditions is sparse. Recently, Butenhoff et al. [15] measured binary molecular diffusion coefficients of sodium nitrate ($NaNO_3$)
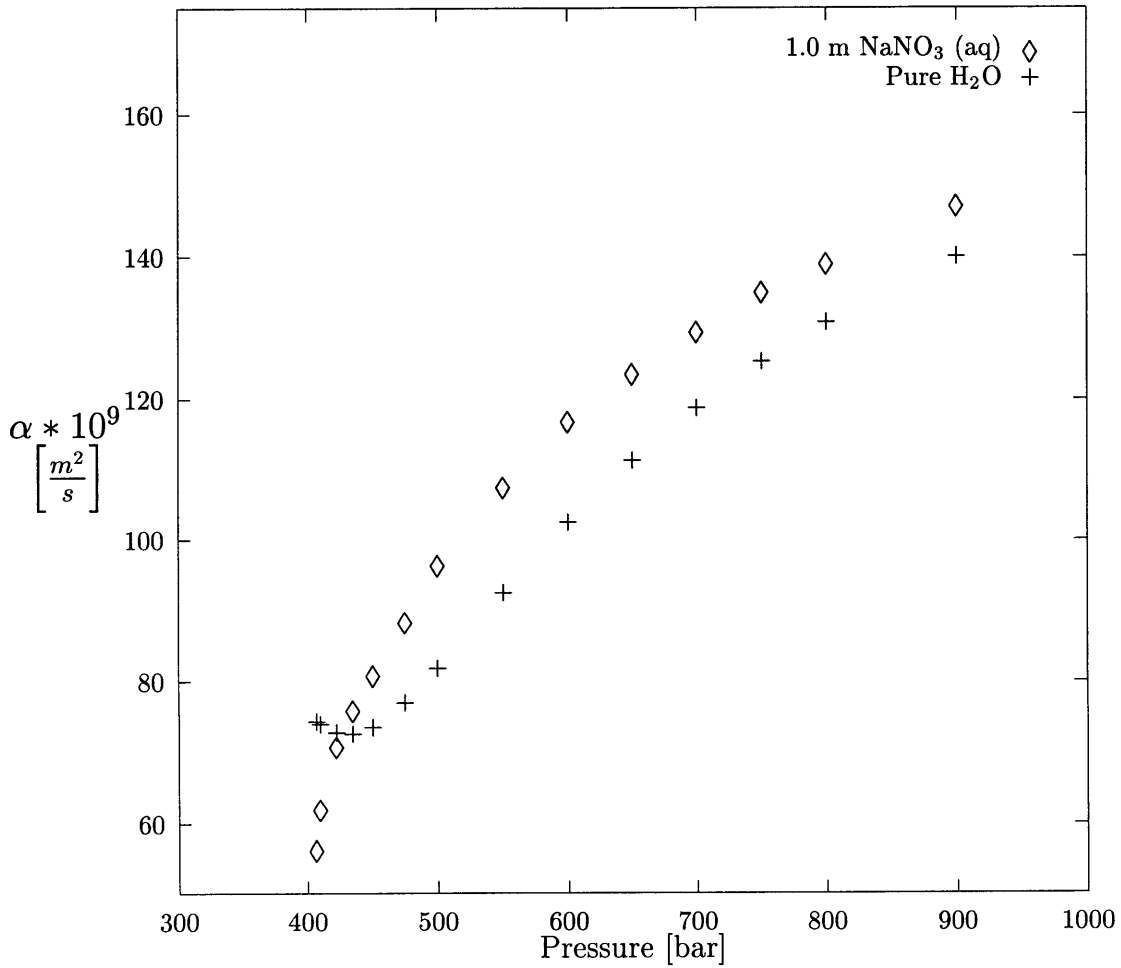
Figure 3-20: Thermal diffusivity of pure water (computed using the NBS Steam Tables [30]) and a 1.0 m, aqueous sodium nitrate solution (from the Butenhoff et al. data [15]) as a function of pressure at 450 °C.

c m	T $^\circ C$	P Bar	$10^9 \mathfrak{D}_{AB}$ $\frac{m^2}{sec}$	$10^9 \alpha$ $\frac{m^2}{sec}$	$10^9 \alpha_{H_2O}$ $\frac{m^2}{sec}$	ρ_{H_2O} $\frac{kg}{m^3}$	Le
0.25	450	409.5	13.0(8)	70.9(12)	74.1	285.1	5.5
0.25	450	425.1	14.7(7)	72.5(10)	72.7	308.3	4.9
0.25	450	450.1	17.0(11)	75.8(16)	73.6	343.5	4.5
0.25	450	500.0	19.8(13)	86.9(18)	81.8	402.3	4.4
0.25	450	550.3	18.3(14)	97.7(17)	92.5	446.5	5.3
0.25	450	600.1	20.2(19)	107.0(16)	102.5	479.9	5.3
1.0	400	271.6	10.6(3)	68.8(14)	45.7	225.9	6.5
1.0	400	276.9	12.1(5)	73.7(7)	39.9	247.3	6.1
1.0	400	300.0	15.8(5)	87.8(11)	36.7	358.1	5.6
1.0	400	350.0	20.1(8)	105.6(6)	69.4	474.9	5.3
1.0	400	399.9	21.2(13)	116.5(12)	90.7	523.6	5.5
1.0	400	500.0	23.2(19)	132.3(17)	115.1	578.0	5.7
1.0	400	600.0	21.7(15)	141.8(13)	129.7	612.5	6.5
1.0	450	407.3	1.42(9)	56.6(8)	74.4	281.8	39.9
1.0	450	410.3	2.72(8)	62.3(9)	74.0	286.3	22.9
1.0	450	422.8	6.35(26)	71.2(9)	72.8	304.9	11.2
1.0	450	435.0	9.04(35)	76.3(11)	72.7	322.6	8.4
1.0	450	450.1	11.4(6)	81.2(12)	73.6	343.5	7.1
1.0	450	475.0	14.6(6)	88.7(11)	77.0	374.9	6.1
1.0	450	500.0	17.1(9)	96.8(14)	81.8	402.3	5.7
1.0	450	550.1	20.3(10)	107.8(10)	92.5	446.4	5.3
1.0	450	600.0	21.7(12)	117.2(13)	102.5	479.9	5.4
1.0	450	650.0	23.1(12)	123.9(10)	111.3	506.6	5.4
1.0	450	700.0	23.1(20)	129.8(15)	118.7	528.6	5.4
1.0	450	750.0	24.8(15)	135.4(10)	125.2	547.4	5.5
1.0	450	800.0	24.7(13)	139.4(20)	130.8	563.7	5.6
1.0	450	900.0	24.0(21)	147.4(24)	140.0	591.1	6.1
1.0	500	544.0	4.0(3)	78.0(11)	102.4	293.8	19.5
1.0	500	550.2	5.4(4)	81.8(6)	101.9	298.9	15.1
1.0	500	600.1	12.2(3)	93.8(10)	100.3	338.5	7.7
1.0	500	700.0	19.6(5)	110.2(9)	106.3	405.8	5.6
1.0	500	800.1	22.7(9)	122.3(7)	116.3	457.0	5.4
1.0	500	900.0	25.0(13)	133.7(13)	127.0	496.5	5.3
1.0	500	1001	27.1(21)	141.9(18)	134.5	528.5	5.2
3.0	450	401.0	8.9(2)	94.3(17)	75.7	272.4	10.6
3.0	450	412.1	11.0(6)	100.5(13)	73.8	289.0	9.1
3.0	450	425.2	12.8(9)	105.0(8)	72.7	308.4	8.2
3.0	450	450.0	14.7(8)	111.9(31)	73.6	343.4	7.6
3.0	450	475.1	16.3(5)	118.2(11)	77.1	375.0	7.3
3.0	450	500.0	17.5(9)	123.1(23)	81.8	402.3	7.0
3.0	450	550.1	19.0(9)	129.8(18)	92.5	446.4	6.8
3.0	450	601.2	19.6(16)	137.1(13)	102.7	480.6	7.0
3.0	450	650.4	20.5(11)	142.1(20)	111.3	506.8	7.1
3.0	450	699.2	19.6(11)	145.8(13)	118.6	528.3	7.4
3.0	450	751.5	20.5(13)	149.3(20)	125.4	547.9	7.3

Table 3.3: Butenhoff et al. [15] measurements of binary molecular diffusivity and thermal diffusivity in aqueous, sodium nitrate solutions as a function of salt concentration, temperature and pressure. The thermal diffusivity and density of pure water based on the NBS Steam Tables at the corresponding temperature and pressure are also given. Lewis numbers calculated from the diffusivity data are provided in the last column.

in water at near-supercritical conditions in the aforementioned investigation and their results are reported in Table 3.3. The Butenhoff et al. measurements of the binary molecular diffusivity of a 1 m, aqueous sodium nitrate solution at temperatures of 400, 450 and 500 $°C$ as a function of pressure are plotted in Fig. 3-21. Fig. 3-22 is the same binary molecular diffusion coefficient data plotted as a function of the density of pure H_2O. Unfortunately the density of aqueous sodium nitrate solutions at the conditions investigated by Butenhoff et al. is presently unavailable; therefore, the NBS Steam Tables were used to determine pure H_2O densities at the temperatures and pressures reported in Table 3.3. (Gallagher [29] and Potter and Brown [73] studied the effect of salt concentration on the density of aqueous sodium sulfate and sodium chloride solutions respectively. Based upon their results, it is estimated, albeit crudely, that at the temperatures and pressures investigated by Butenhoff et al., a 1 m (7.83 wt%) aqueous sodium nitrate solution would be about 20% more dense than pure water.) It was noted in Chapter 1 that the thermophysical properties of SCW are generally smoother functions of density than other variables such as temperature and pressure. Hence, not surprisingly, the scatter is substantially less when the binary molecular diffusion coefficient of a 1 m aqueous sodium nitrate solution is plotted as a function of (pure water) density rather than pressure.

The "critical slowing down process" causes a dramatic drop in the binary molecular diffusivity in the vicinity of the critical point. It occurs at higher pressures as temperature is increased from 400 to 500 $°C$ (see Fig. 3-21); however, as per Fig. 3-22, it appears to become important at about the same (pure water) density, i.e., about 500 kg/m^3. (The critical density of pure H_2O is 317.0 kg/m^3.) Butenhoff et al. note that for all five (T,C) pairs in which they measured the binary molecular diffusion coefficient as a function of pressure, it is "at a minimum near the phase separation pressure and appears to plateau at higher pressures" where "ordinary mass diffusion" dominates. (For all five pairs of salt concentrations and temperatures investigated by Butenhoff et al., the lowest pressure in Table 3.3 corresponds to the phase separation pressure [15].)

The Butenhoff et al. measurements of the binary molecular diffusivity in 0.25, 1.0 and 3.0 m aqueous sodium nitrate solutions as a function of pressure at a temperature of 450 $°C$ are plotted Fig. 3-23. Variations in salt concentration within this parametric range change the binary molecular diffusivity by up to, but generally substantially less than, about 20%. Moreover, salt concentration differences in the deposition rate experiments are substantially less than the 0.125 to 3.0 m (2.08 to 20.32 wt%) range of salt concentrations
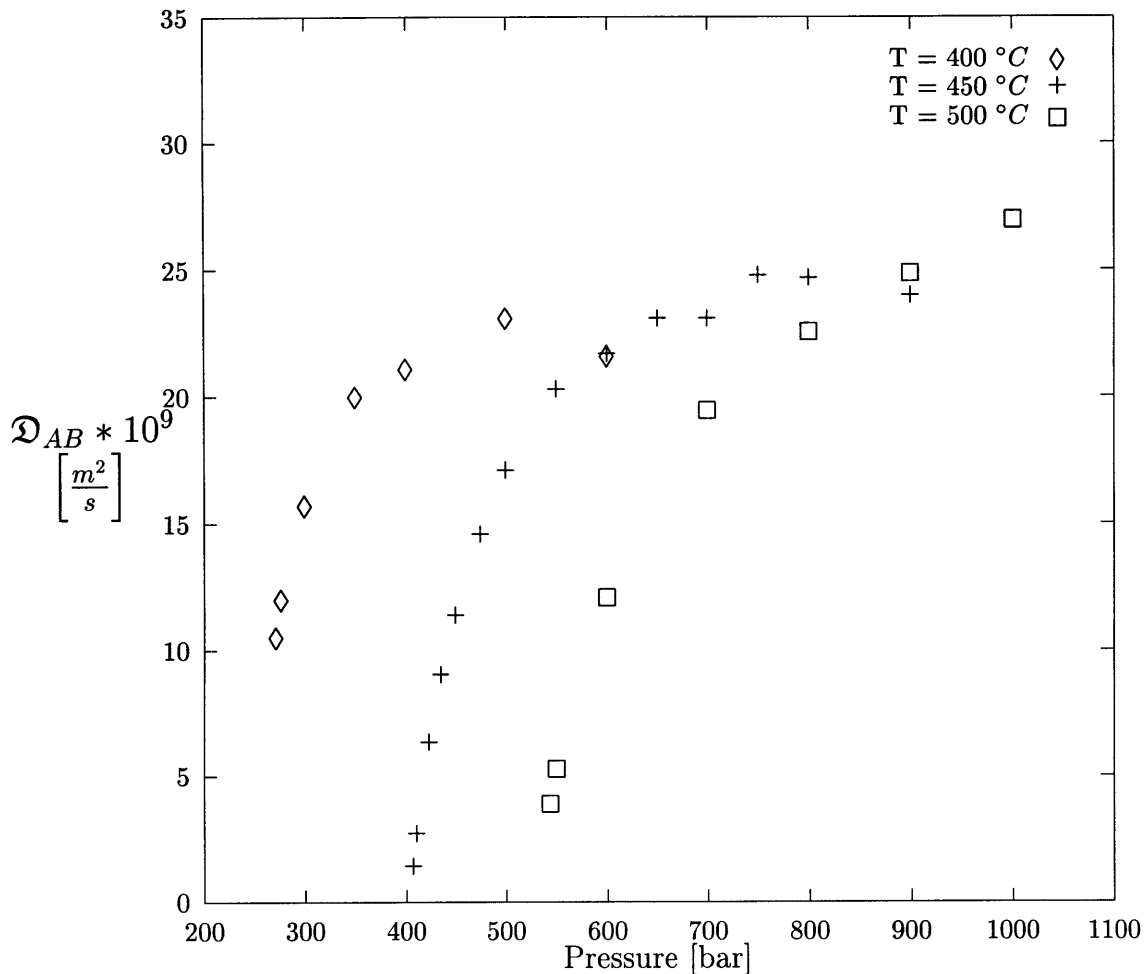
Figure 3-21: Butenhoff et al. [15] measurements of the binary molecular diffusion coefficient of sodium nitrate in a 1.0 m, aqueous solution as a function of pressure at temperatures of 400, 450 and 500 °C.

shown in Fig. 3-23. (The maximum salt concentration in the deposition experiments was 8 wt%.) The temperature difference across the boundary layer in all of the deposition experiments is of order 10 °C and examination of the Butenhoff et al. data shows that a 10 °C temperature difference does not significantly change the binary molecular diffusion coefficient in the $NaNO_3$-H_2O system at relevant conditions. Thus, the Butenhoff et al. data suggest that for the purpose of calculating the deposition rate at the salt layer-solution interface assuming a constant binary molecular diffusivity is legitimate for the Na_2SO_4-H_2O and K_2SO_4-H_2O systems.

Lamb et al. [47] measured the self diffusion coefficient of H_2O over a range of pressures (199 to 1056

204
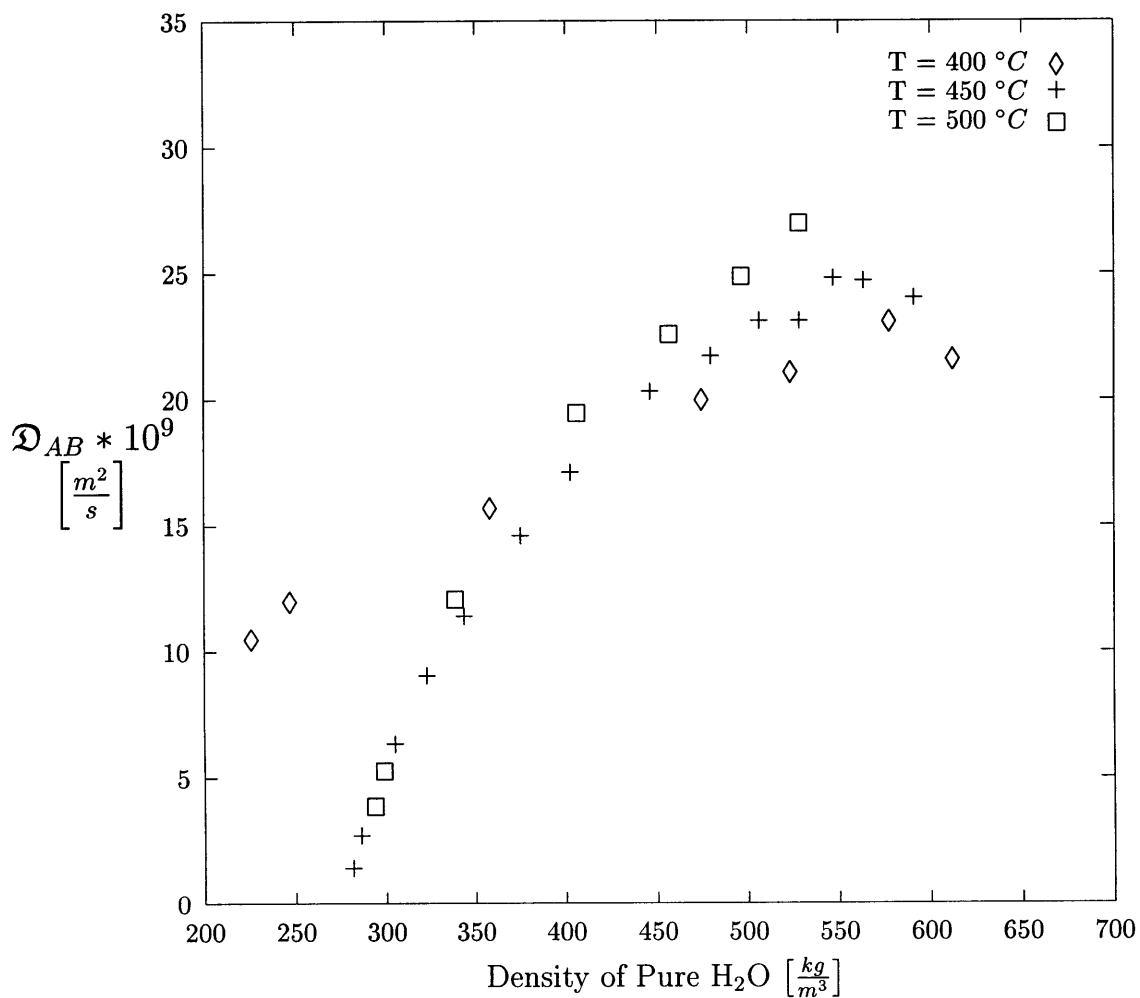
Figure 3-22: Butenhoff et al. [15] measurements of the binary molecular diffusion coefficient of sodium nitrate in a 1.0 m, aqueous solution as a function of the density of pure water. (The NBS Steam Tables [30] were used to determine the density of pure water at the temperatures and pressures reported by Butenhoff et al.)
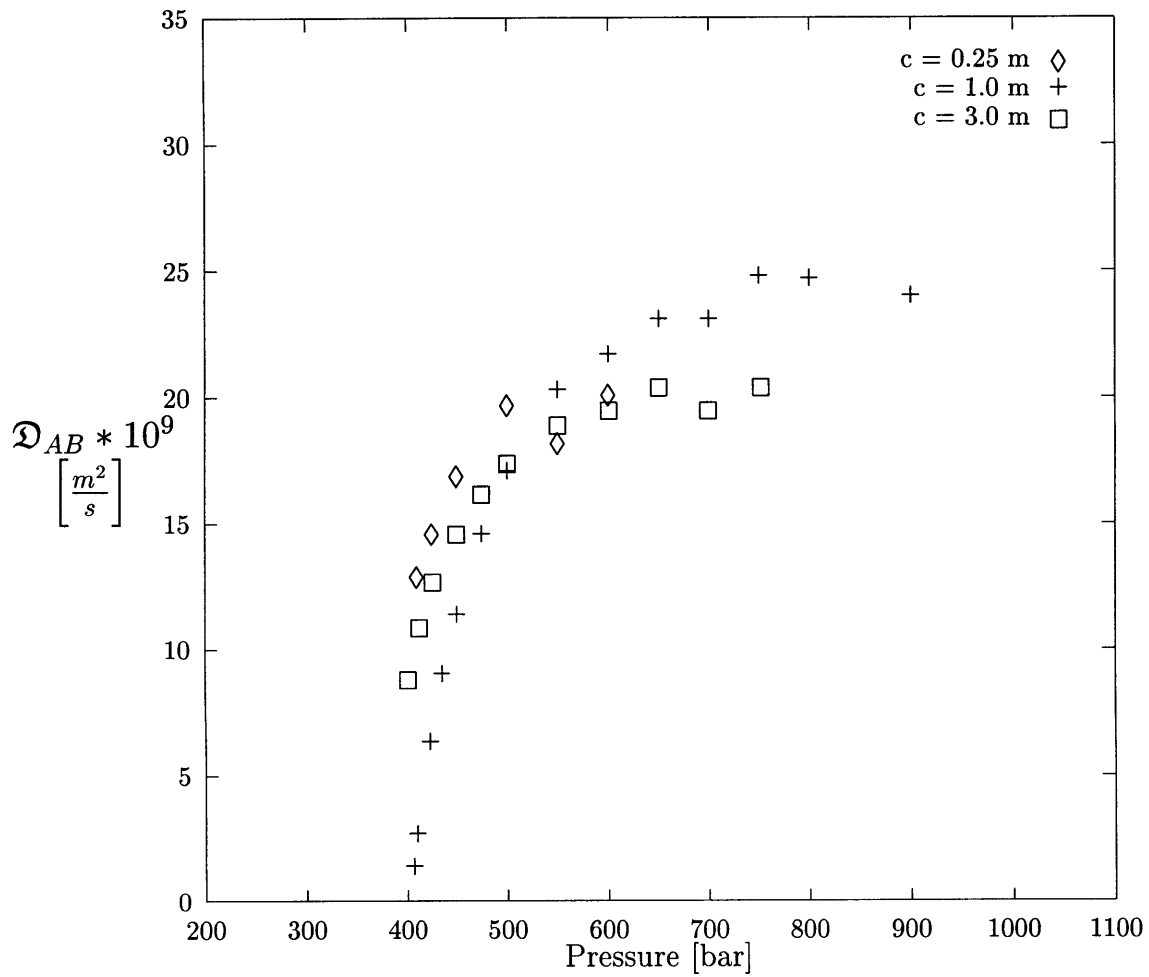
Figure 3-23: Binary molecular diffusion coefficient of sodium nitrate in 0.25, 1.0 and 3.0 m aqueous sodium nitrate solutions as a function of pressure at a temperatures of 450 °C. Adapted from the data of Butenhoff et al. [15].

bar) and temperatures (400 to 700 °C) relevant to the deposition experiments using the NMR spin-echo technique. This range corresponds to $0.315 \leq \frac{\rho}{\rho_c} \leq 2.21$, where ρ_c is the critical density of pure water. Lamb et al. estimated their diffusivity measurements to be accurate to within $\pm 10\%$ and their results are reported in Table 3.4. The Lamb et al. measurements of self diffusion coefficient as a function of density at temperatures of 400, 500, 600 and 700 °C are plotted in Fig. 3-24. In the parametric range investigated by Lamb et al. the self diffusion coefficient of pure water correlates well with density and, moreover, is a weak function of temperature at a given density. The semi-empirical equation,

$$\rho \mathfrak{D}_{AA} = 2.24 * 10^{-6} T^{.763}, \tag{3.130}$$

where $\mathfrak{D}_{AA}$, ρ and T are in cm^2/s, g/cm^3 and K respectively proposed by Lamb et al. fits all of their data to within 10%.

The Butenhoff et al. data for the binary molecular diffusion coefficient in a 1 m, aqueous sodium nitrate solution and the Lamb et al. self diffusion coefficient data for H$_2$O at temperatures of 400 and 500 °C as a function of pressure are plotted in Fig. 3-25. The binary molecular diffusion coefficient data and self diffusion coefficient data appear to plateau at approximately 0.25 and 0.5 m^2/s respectively. Thus the self diffusion coefficient of pure water exceeds the binary molecular diffusion coefficient in a 1 m, aqueous sodium nitrate solution in the "plateau" region by a factor of about 2 which is not surprising because sodium nitrate molecules are considerably larger (and heavier) than water molecules. As critical phenomena become important the self diffusion coefficient of H$_2$O and the binary molecular diffusion coefficient of aqueous sodium nitrate solutions are decreasing and increasing functions of pressure/density respectively and dramatically different in magnitude. It is noted that the self diffusion coefficient at the critical point of a pure fluid is identically equal to zero.

The film density in the boundary layer formed around the salt layer-solution interface is defined conventionally, i.e.,:

$$\rho_f = \frac{\rho_B + \rho_i}{2} \tag{3.131}$$

T $^\circ C$	ρ $\frac{kg}{m^3}$	P bar	$10^9\mathfrak{D}_{ABEXP}$ $\frac{m^2}{s}$	$10^9\mathfrak{D}_{ABKT}$ $\frac{m^2}{s}$	R1	ρ_{ideal} $\frac{kg}{m^3}$	χ_E	χ_T	R2
400	100	199	286	707	2.47	64.1	1.43	1.09	1.31
400	125	221	243	637	2.62	71.2	1.49	1.11	1.34
400	150	241	213	584	2.74	77.6	1.42	1.13	1.26
400	200	265	161	531	3.30	85.3	1.41	1.18	1.19
400	250	280	120	503	4.19	90.2	1.51	1.22	1.24
400	300	291	112	484	4.32	93.7	1.35	1.26	1.07
400	400	314	89.7	448	4.99	101.1	1.26	1.35	0.93
400	500	378	70.0	372	5.31	121.7	1.29	1.44	0.90
400	600	565	57.1	249	4.36	181.9	1.32	1.53	0.86
400	700	1056	47.4	133	2.81	340.0	1.36	1.62	0.84
500	100	256	326	692	2.12	71.7	1.52	1.09	1.39
500	125	314	251	564	2.25	87.9	1.58	1.11	1.42
500	150	359	213	493	2.31	100.5	1.55	1.13	1.37
500	200	403	189	440	2.33	112.8	1.31	1.18	1.11
500	250	491	141	361	2.56	137.5	1.41	1.22	1.16
500	300	551	125	321	2.57	154.3	1.32	1.26	1.05
500	400	691	95.6	256	2.68	193.5	1.30	1.35	0.96
500	500	910	74.5	195	2.62	254.8	1.33	1.44	0.92
500	600	1313	61.7	135	2.19	367.6	1.34	1.53	0.88
600	100	336	361	644	1.78	83.3	1.49	1.09	1.37
600	125	403	282	537	1.90	99.9	1.52	1.11	1.37
600	150	467	242	463	1.91	115.8	1.48	1.13	1.31
600	200	584	194	370	1.91	144.8	1.38	1.18	1.17
600	250	696	156	311	1.99	172.6	1.38	1.22	1.13
600	300	809	125	267	2.14	200.6	1.43	1.26	1.13
600	400	1074	97.0	201	2.07	266.4	1.38	1.35	1.02
600	500	1459	76.4	148	1.94	361.8	1.40	1.44	0.97
700	100	397	471	630	1.34	88.5	1.18	1.09	1.08
700	125	480	346	521	1.51	107.0	1.29	1.11	1.16
700	150	568	285	440	1.54	126.7	1.30	1.13	1.15
700	200	731	226	342	1.51	163.0	1.23	1.18	1.04
700	250	893	172	280	1.63	199.1	1.30	1.22	1.07
700	300	1060	155	236	1.52	236.4	1.20	1.26	0.95
700	400	1455	108	172	1.59	324.5	1.29	1.35	0.96

Table 3.4: Lamb et al. [47] data for the self diffusion coefficient of H_2O at temperatures of 400, 500, 600 and $700^\circ C$ over a range of pressures/densities. Theoretical estimates of the self diffusion coefficient data using the kinetic theory of dilute, nonpolar gases without and with a "dense" gas correction factor are also provided and compared to the data. (R1, χ_E, χ_T and R2 are defined in the text.)
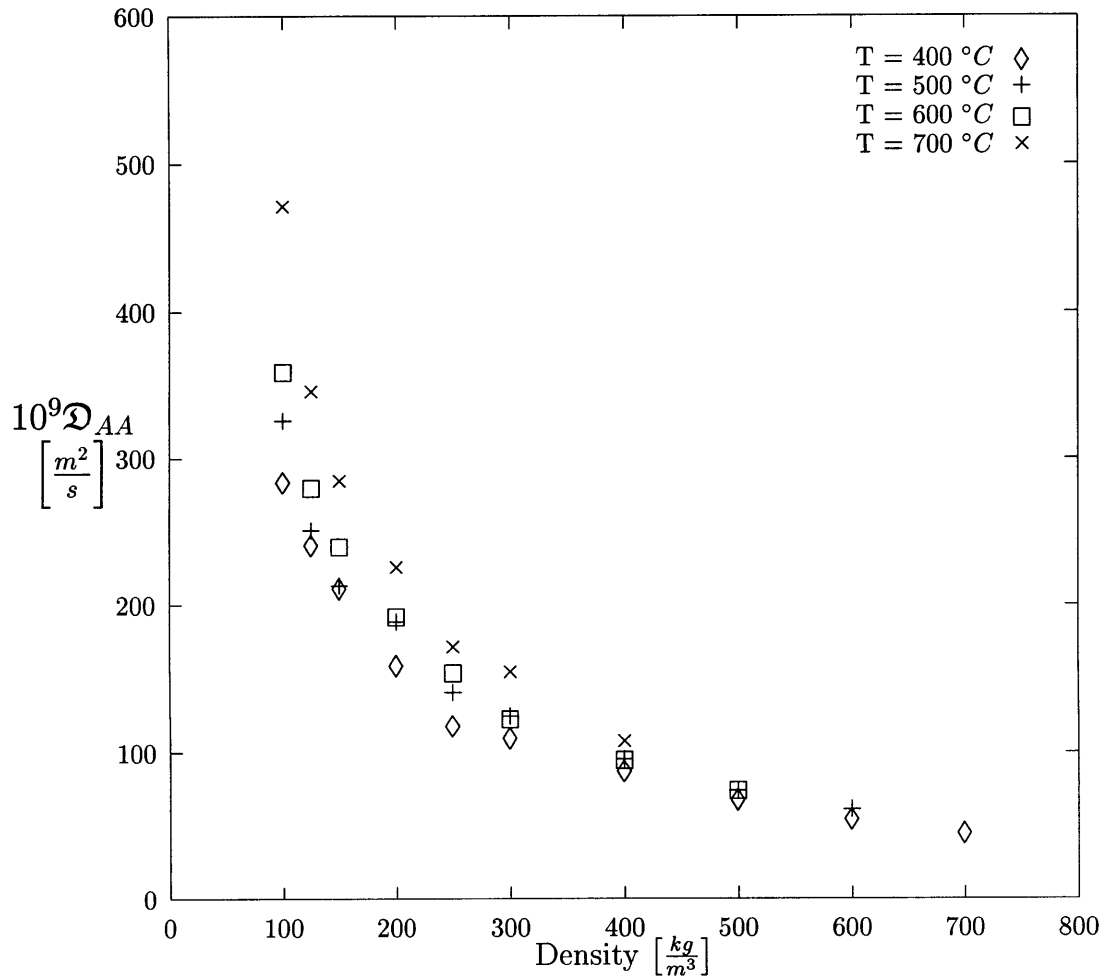
Figure 3-24: Lamb et al. [47] self diffusion coefficient data for H_2O at temperatures of 400, 500, 600 and 700 $^\circ C$ as a function of density.
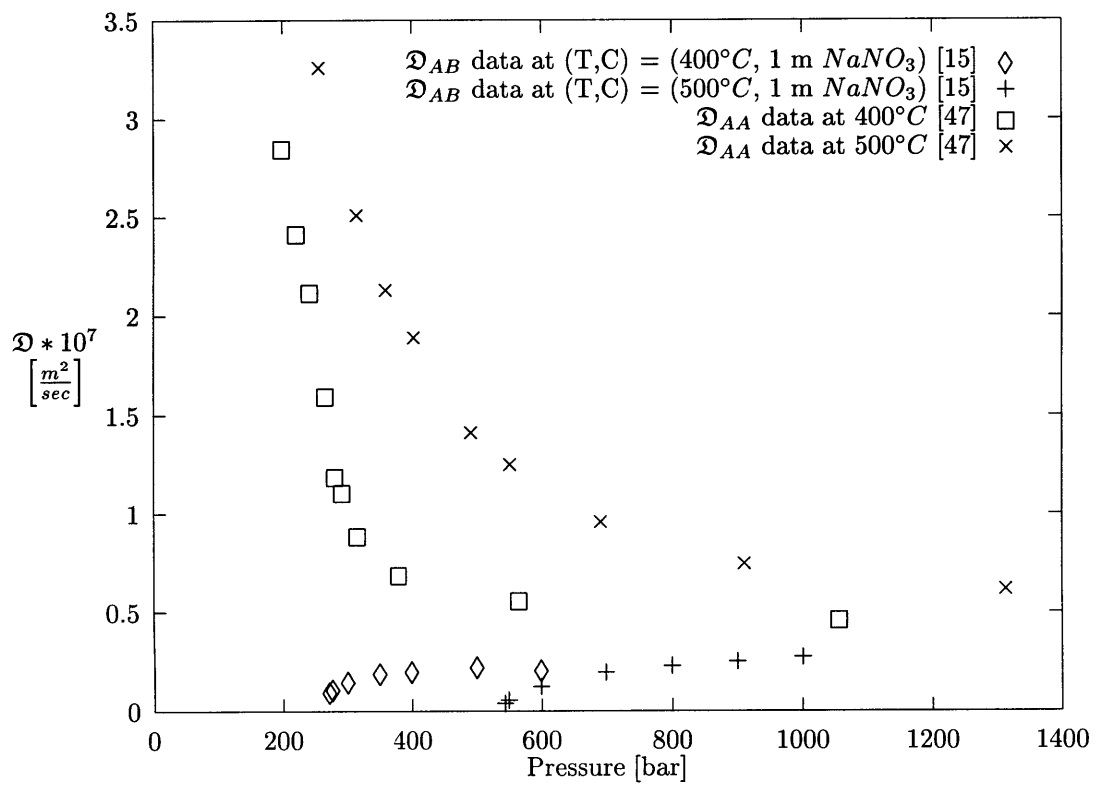
Figure 3-25: Plot of the self diffusion coefficient of water measured by Lamb et al. [47] and binary molecular diffusion coefficient in a 1 m, aqueous $NaNO_3$ solution measured by Butenhoff et al. [15] as a function of pressure at temperatures of 400 and 500 °C.

In Chapter 4 the film densities of the aqueous sodium sulfate and potassium sulfate solutions are estimated to range from about 550 to 750 kg/m^3 as per Table 4.4 and 425 to 525 kg/m^3 as per Table 4.7 respectively at conditions relevant to the deposition rate experiments. (Aqueous sodium sulfate solution densities were estimated using the Gallagher program and the aqueous potassium sulfate solutions were approximated as pure water to determine density.) Film densities also characterize the solution density at the bulk condition and salt layer-solution interface condition because the density difference across the boundary layer is small relative to the film density, i.e., $\frac{\Delta\rho}{\rho} \lesssim 0.1$. (See Section 4.4.2 for justification.) The "plateau" region in Fig. 3-22 where "ordinary mass diffusion" dominates begins at a (pure water) density of about 500 kg/m^3 which is typical of the lowest (estimated) film densities in the deposition experiments. This suggests that binary molecular diffusion coefficient values in the "plateau region" may well characterize aqueous sodium sulfate and potassium sulfate solutions at conditions of interest; therefore, $\mathcal{D}_{AB}$ is subsequently set equal 0.25 m^2/s when computing the deposition rate at the salt layer-solution interface, except when the sensitivity analysis in Section 4.4.2 is performed. Butenhoff et al. mention that the phase behavior of the NaNO$_3$-H$_2$O system appears to be qualitatively similar to that of the NaCl-H$_2$O system according to unpublished results. The temperature-composition diagram/phase behavior of the NaCl-H$_2$O system is dramatically different from that of the Na$_2$SO$_4$-H$_2$O and K$_2$SO$_4$-H$_2$O systems at relevant conditions. In the NaCl-H$_2$O system, salt precipitates in a shock-like manner from a liquid-vapor region at conditions of interest to SCWO. (See, for example, [4].)

Kinetic Theory of Gases

Theoretical estimation of self and binary molecular diffusion coefficients in supercritical fluids may be approached from two extremes, i.e., using the kinetic theory of gases or, at the other extreme, the Stokes-Einstein Equation for molecular diffusion in liquids. Only the kinetic theory of gases is discussed in this dissertation. However, it is noted that both Lamb et al. [47] and Butenhoff et al. [15] applied the Stokes-Einstein equation to their results with some success. Hirschfelder, Curtiss and Bird [39] derive the following

expression for the binary molecular diffusion coefficient from the kinetic theory of dilute, nonpolar gases:

$$\mathfrak{D}_{AB} = \frac{1.8583 * 10^{-7} T^{\frac{3}{2}}}{P \sigma_{AB}^2 \Omega_D} \sqrt{\frac{1}{M_A} + \frac{1}{M_B}} \qquad (3.132)$$

where P, T and $\mathfrak{D}_{AB}$ are in atm, K and m^2/s respectively. Equation 3.132 is generally referred to as the Chapman-Enskog equation.

The quantities σ_{AB} and Ω_D are the collision diameter (in Ångstrom units) and dimensionless collision integral for diffusivity. The collision cross section is a function of the collision diameters of species A and B in a binary gas mixture. The collision cross section is defined as "An area characteristic of a collision reaction between atomic or nuclear particles or systems, such that the number of reactions which occurs equals the product of the number of target particles or systems and the number of incident particles or systems which would pass through this area if their velocities were perpendicular to it." [71]. Collision integrals result from kinetic theory calculations and are a function of the potential well depth, ϵ, and temperature. The potential well depth is a measure of the energy required to separate two molecules of the same type.

The collision diameter for selected species is tabulated by Lienhard [53] and the value reported for H$_2$O is 2.655 Ångstroms. It is noted, however, that the collision diameter is a weak function of temperature because as temperature increases molecules can penetrate to smaller distances of separation. Based on a review article by Wilhelm [92], the collision diameter of water is, for example, 2.67 Ångstroms at 400 $^\circ C$ and 2.60 Ångstroms at 700 $^\circ C$. Hence in the temperature range investigated by Lamb et al. the collision diameter is essentially constant. Therefore, it is set equal to the value given by Lienhard, i.e., 2.655 Ångstroms, when the kinetic theory of gases is used to predict self diffusion coefficients in the parametric range of temperatures and pressures investigated by Lamb et al. The value of the collision diameter is assumed to be independent of pressure/density following Lamb et al. To determine the dimensionless collision integral for diffusivity, the potential well depth (divided by Boltzman's constant) is set equal to 263 K as given in the table in Lienhard [53]. The dimensionless collision integral for mass diffusivity is tabulated as a function of the quantity kT/ϵ by Hirschfelder, Curtiss and Bird [39]. All the collision integrals required for the diffusion coefficient predictions in this section are determined by interpolating within this table. Interestingly, H$_2$O

is the only species in Lienhard's table where the potential well depth computed from mass diffusion data is not equal to the potential well depth computed from viscosity and/or thermal conductivity data.

Theoretical estimations of the self diffusion coefficient of H_2O using the kinetic theory of dilute, nonpolar gases, without and with a "dense" gas correction factor were compared to the Lamb et al. data. A summary of the basic assumptions inherent in the Chapman-Enskog equation is apropos and provided following Mills [61]. First, the density of the gas must be low enough for only two body collisions to be important. The (empirical) Lennard-Jones 6-12 intermolecular potential function is used to approximate the attraction and repulsion forces between molecules. To be sure, this potential function describes a spherically symmetric force field; consequently, it is rigorously valid only for nonpolar, symmetric molecules. Nonetheless, it often works adequately for polar molecules, e.g., H_2O, especially when the compressibility factor of the mixture is close to unity. Generally, experimental viscosity data (near STP) are used to determine the exact form of the Lennard-Jones 6-12 intermolecular potential function. However, it tends to work well at higher temperatures and for estimation of thermal conductivity and mass diffusivity in addition to viscosity under appropriate conditions. (As already noted, water is atypical because its potential well depth, and, hence, Lennard-Jones intermolecular potential function, differs substantially when it is determined from mass diffusion data as opposed to viscosity and/or thermal conductivity data.) It is noted that the value of the binary molecular diffusion coefficient predicted by the Chapman-Enskog equation is independent of solute concentration.

The conditions in the deposition experiments are not typical of those under which the Chapman-Enskog equation is generally applied. First, the density of water at near-supercritical conditions is of order 100 kg/m^3, whereas the density of an ideal gas is typically about two orders of magnitude less. Secondly, salt concentrations reach 8 wt%; therefore, the solute is not especially "dilute" in the solvent. Moreover, water is a polar molecule and hydrogen bonds play a substantial role in molecular dynamics even at near supercritical conditions. Thus, applying the kinetic theory of dilute, nonpolar gases to the conditions investigated by Lamb et al. to theoretically predict the self diffusion coefficient is suspect a priori. Nonetheless, the density of water at near-supercritical conditions is about an order of magnitude less than in liquid water at STP and water exhibits the solvation properties of an ordinary nonpolar solvent at supercritical conditions. Hence, the Chapman-Enskog equation without and with a correction factor for "dense" gases was applied to the

conditions investigated by Lamb et al. and the results are summarized in Table 3.4. (It was not applied to the Butenhoff et al. data since the necessary molecular parameters, i.e., collision diameter and potential well depth, for sodium nitrate are unavailable because the Lennard-Jones intermolecular potential function is inappropriate for such polar molecules.)

The quantities $\mathcal{D}_{ABEXP}$ and $\mathcal{D}_{ABCE}$ reported in Table 3.4 are the Lamb et al. measurements and Chapman-Enskog predictions respectively. The quantity R1 is the ratio of the self diffusion coefficient predicted by the kinetic theory of dilute, nonpolar gases, i.e., the Chapman-Enskog equation, to that measured by Lamb et al. This theory overpredicts the measured self diffusion coefficients by a factor ranging from about 2 to 5. Nonetheless, this is somewhat encouraging considering the narrow range of conditions for which the Chapman-Enskog equation rigorously applies.

Chapman and Cowling [18] derived a correction factor which improves the accuracy of the Chapman-Enskog equation when it is used to predict self diffusion coefficients in a "dense" gas. H.H. Thorne [19] generalized the correction factor given by Chapman and Cowling to apply to binary mixtures. When Thorne's result is applied to self diffusion it becomes identical to Chapman and Cowling's correction factor. The correction factor accounts for two effects which become more important with increasing density. First, it accounts for the volume occupied by individual (spherical) gas molecules so that one molecule can not occupy any of the space occupied by another. Secondly it accounts for the shielding of one molecule by another, i.e., "If an area S of the sphere associated with a given molecule lies within the sphere associated with a second, no other molecule can collide with the first in such a way that at collision its center lies on S." [18]. The correction factor, χ, is defined as [18]:

$$\chi = \frac{(\rho \mathcal{D}_{AB})_{IDEAL}}{(\rho \mathcal{D}_{AB})_{REAL}} \qquad (3.133)$$

Correction factors can be determined from experiment and theory and are subsequently denoted by χ_E and χ_T respectively. The numerator of both χ_E and χ_T equals the density of an ideal gas at the temperature and pressure of interest multiplied by the (self or binary) molecular diffusion coefficient determined from the kinetic theory of dilute, nonpolar gases, i.e., the Chapman-Enskog equation. The denominator of χ_E equals

the real density of the gas multiplied by the measured (binary or self) diffusion coefficient. (Hence χ_E can be computed only if the diffusion coefficient has been measured.) The theoretical expression for the correction factor that Chapman and Cowling derived for self diffusion is:

$$\chi_T = 1 + \frac{5\pi}{12} n\sigma_3 \tag{3.134}$$

where, n is number density in molecules per m^3 and σ is collision cross diameter in Ångstroms. For self diffusion in H_2O, χ_T reduces to,

$$\chi_T = 1 + 1.8184 * 10^{-4} \rho \tag{3.135}$$

where ρ is H_2O density in units of kg/m^3. In theory, the effect of increasing pressure at constant temperature is to decrease the self diffusion coefficient by the ratio of $\rho_{ID}/(\rho\chi_T)$ because of the increase in the number of collisions between unlike molecules [18].

The ratio χ_T/χ_E equals the theoretically predicted value of the diffusion coefficient divided by its measured value and is tabulated as R2 in Table 3.4. The dense gas correction factor dramatically improves the estimates of the self diffusion coefficient of water in the parametric range investigated by Lamb et al. Specifically, the Chapman-Enskog equation overpredicts the measured self diffusion coefficient from 34 to 531%, but this discrepancy is reduced to between 2 and 42% by the "dense" gas correction factor. For the 34 self diffusion coefficients measured by Lamb et al., the Chapman-Enskog equation with the correction factor is off by an average of less than 17%. (One should bear in mind, that Lamb et al. report their measurements to be accurate to within ±10%.) Moreover, the correction factor improves the theoretical predictions over the entire parametric range investigated by Lamb et al. as per Table 3.3. Finally, it is noted that the Chapman-Enskog equation without the correction factor always overpredicts the measured value of the diffusion coefficient, but when the correction factor is added it overpredicts some data points and underpredicts others.

Lamb et al. also compared their measured self diffusion coefficients with predictions based on a dilute polar gas model proposed by Monchick and Mason [62]. Collision integrals for mass diffusivity were evaluated

with a Stockmayer (12-6-3) potential and the temperature dependence of the collision cross section of water reported by Wilhelm [92] was accounted for. Predictions of the self diffusion coefficient using the Monchick and Mason model compared very well with the Lamb et al. self diffusion coefficient data. In fact, this model was accurate to within 10% over the entire parametric range Lamb et al. investigated. However, it is noted that one of the parameters in the Stockmayer (12-6-3) potential used by Lamb et al. is empirical and, therefore, was fit to their data. The Chapman-Enskog equation with the Chapman and Cowling correction factor for "dense" gases does not predict the Lamb et al. data as accurately as the dilute polar gas model proposed by Monchick and Mason. (It is inaccurate by up to 42%.) However, it is considerably easier to implement and all the molecular parameters used to do so above were determined from mass diffusivity data at STP.

A brief evaluation of the applicability of the Chapman-Enskog equation without and with the "dense" gas correction factor for predicting molecular diffusion coefficients in supercritical fluids in general is given here. Aside from the Butenhoff et al. study, limited experimental data for binary molecular diffusion coefficients in SCW exists. Recently, two data points for the binary molecular diffusion coefficient of benzene in SCW were collected by Bartle et al. [8] using the Taylor dispersion technique. Moreover, a considerable amount of data for binary molecular diffusion coefficients in other supercritical fluids, particularly CO_2, exists [26].

The Bartle et al. [8] measurements of the molecular diffusion coefficient of benzene in water from sub to supercritical conditions are given in Table 3.5. The measurements are reported to be accurate to within 20% and the two diffusivities measured at conditions above the critical temperature of water (647 K) are accompanied by predictions from the Chapman-Enskog equation without the "dense" gas correction factor. At a temperature of 653 K the kinetic theory value is too large by a factor of 2.73, about the same factor as in all the CO_2-benzene data points discussed below, and when temperature is increased to 673 K, the discrepancy is reduced to 19%. Not surprisingly, when the kinetic theory of gases is applied to a subcritical data point the results are poor, e.g., it overpredicts the molecular diffusion coefficient by a factor of almost 20 for the 573 K data point. When the "dense" gas correction factor was applied to the two supercritical data points the agreement between experiment and theory deteriorated by a factor of about two.

The molecular diffusion coefficient of benzene in supercritical CO_2 was measured by Feist and Schnei-

| T | ρ | D_{ABEXP} | D_{ABKT} |
K	$\frac{kg}{m^3}$	$\frac{m^2}{s}$	$\frac{m^2}{s}$
373	970	$1.3 * 10^{-9}$	-
423	930	$1.7 * 10^{-9}$	-
473	881	$5.1 * 10^{-9}$	-
523	821	$5.4 * 10^{-9}$	-
573	743	$7.4 * 10^{-9}$	-
623	626	$25 * 10^{-9}$	-
653	459	$66 * 10^{-9}$	$180 * 10^{-9}$
673	166	$160 * 10^{-9}$	$190 * 10^{-9}$

Table 3.5: Comparison of experimental [8] and kinetic theory of gas values for the binary molecular diffusion coefficient of benzene in SCW over a range of temperatures at a pressure of 250 bar.

der [26] using the chromatographic peak-broadening method. All of their data was collected at a temperature of 40 $°C$ and estimated to be accurate to within 6% [26]. It is provided in Table 3.6. Predictions of the binary molecular diffusion coefficient using the Chapman-Enskog equation without and with the "dense" gas correction factor are given and compared to the Feist and Schneider data in Table 3.6 as well. (When calculating the correction factor, it was assumed that the CO_2 was infinitely dilute in benzene because benzene concentrations were not reported by Feist and Schneider [26].) The Chapman-Enskog equation without the correction factor overpredicts all the diffusion coefficients in this data set by a factor of about 2.5 to 3, lending some confidence that the method may be appropriate for order of magnitude predictions of molecular diffusion coefficients in supercritical fluids. The experimental and theoretical values for the correction factor χ are also given in Table 3.6. The experimental value of the correction factor for all six data points was close to unity, ranging from 0.86 to 1.19 and the theoretical value ranged from 1.43 to 1.96. R2, the ratio of the predicted to measured diffusion coefficient, when the "dense" gas correction factor is included, ranged from 0.48 to 0.89. For all six data points the correction factor brought the predicted diffusion coefficient closer to that measured. It also noted that all the predictions without the correction factor were higher than the experimental data and all the predictions with the correction factor were lower than the experimental data. Balenovic et al. [6] measured binary molecular diffusion coefficients in 11 different "dense" gas mixtures at pressures up to 1360 atmospheres and compared their measurements to predictions of the diffusion coefficients computed from the Chapman-Enskog equation including the "dense" gas correction factor. Agreement between theory and measurements was similar to that found above when "dense" gas

ρ $\frac{kg}{m^3}$	P bar	$log\frac{\mathfrak{D}_{ABEXP}}{m^2/s}$ [26]	$\mathfrak{D}_{ABEXP}$ [26] $\frac{m^2}{s}$	D_{ABKT} $\frac{m^2}{s}$	R1	ρ_{ideal} $\frac{kg}{m^3}$	χ_E	χ_T	R2
284.4	80	-7.48	$3.31*10^{-8}$	$8.28*10^{-8}$	2.50	135.3	1.19	1.33	0.89
362.5	85	-7.53	$2.95*10^{-8}$	$7.79*10^{-8}$	2.64	143.7	1.04	1.43	0.73
447.5	90	-7.55	$2.82*10^{-8}$	$7.36*10^{-8}$	2.61	152.2	0.88	1.54	0.57
585.0	115	-7.65	$2.23*10^{-8}$	$5.76*10^{-8}$	2.58	194.5	0.86	1.64	0.51
662.5	125	-7.76	$1.74*10^{-8}$	$5.30*10^{-8}$	3.05	211.4	0.97	1.79	0.54
797.0	160	-7.83	$1.48*10^{-8}$	$4.14*10^{-8}$	2.80	270.6	0.95	1.96	0.48
Note: σ_{CO_2} and $\sigma_{benzene}$ are 3.941 Ångstroms and 5.349 Ångstroms respectively [53].									

Table 3.6: Comparison of experimental [26] and kinetic theory of gas values for the binary molecular diffusion coefficient of benzene in supercritical CO_2 over a range of pressures at a temperature of $40°C$ (313 K). (R1, χ_E, χ_T and R2 are defined in the text.)

kinetic theory was applied to the data sets of Lamb et al. and Feist and Schneider.

The Chapman-Enskog equation overpredicted the self diffusion coefficient in H_2O, binary diffusion coefficient of benzene in SCW and binary diffusion coefficient of benzene in CO_2 measured in the the Lamb et al., Bartle et al., and Feist and Schneider studies respectively by a factor ranging from about 1 to 5. Excluding the Bartle et al. data, when the "dense" gas correction factor developed by Chapman and Cowling/Thorne was included, the predictions were always accurate to within a factor of about two and often did much better. Moreover, the correction factor *always* improved the agreement between the theoretical predictions and the experimental data excluding the two data points from the Bartle et al. study. A virtue of the correction factor is that it is entirely derived from the kinetic theory of gases and adds no additional empirical parameters to the Chapman-Enskog equation.

3.7.6 Lewis Number

The Lewis number is defined as the thermal diffusivity divided by the molecular diffusivity of a binary mixture, i.e.,

$$Le = \frac{\alpha}{\mathfrak{D}_{AB}} \quad (3.136)$$

It is ubiquitous throughout the remainder of this dissertation and has been implicitly measured by Butenhoff et al. for aqueous sodium nitrate solutions at near-supercritical conditions. It is tabulated in Table 3.3 and

ranges from 4.4 to 39.9, but is generally between 5 and 10. In the "plateau" region, the Lewis number is subsequently assumed to equal 6.

3.7.7 Thermal Diffusion Ratio

Butenhoff et al. [15] also measured the thermal diffusion coefficient of a 1 m, aqueous sodium nitrate solution as a function of pressure at 450 °C. Their results are summarized in Table 3.7. Butenhoff et al. define the thermal diffusion coefficient as the product of the Sorét coefficient, σ, times the binary molecular diffusivity $\mathcal{D}_{AB}$. However, in this dissertation the conventions of Bird, Stewart and Lightfoot [12] are adopted when treating the Sorét and Dufour effects; consequently, the thermal diffusion coefficient is defined differently than in the Butenhoff et al. study. Bird, Stewart and Lightfoot define the "binary thermal diffusion coefficient of species A in system A-B" (D_A^T) according to Eq. 3.22 and it has units of $\frac{kg}{m \cdot s}$, whereas Butenhoff et al. define it as $\sigma \mathcal{D}_{AB}$ in units of $\frac{m^2}{sK}$. The Sorét coefficient (σ) and the quantity $\sigma \mathcal{D}_{AB}$ are defined consistently by Butenhoff et al. and Bird, Stewart and Lightfoot; hence, the Butenhoff results are reported as $\sigma \mathcal{D}_{AB}$ in Table 3.7

Converting the quantity $\sigma \mathcal{D}_{AB}$ reported by Butenhoff et al. to the corresponding thermal diffusion ratio allows the Sorét and Dufour effects to be accounted for with one additional transport property. The Sorét coefficient and thermal diffusion ratio are related by [12]

$$k_T = \sigma x_A x_B T \tag{3.137}$$

The thermal diffusion ratio computed from the Butenhoff et al. data for $\sigma \mathcal{D}_{AB}$ as a function of pressure in a 1.0 m, aqueous sodium nitrate solution at 450 °C is reported in Table 3.7. The density of pure water at the corresponding temperature and pressure is reported in the last column of Table 3.7. Fig. 3-26 is a plot of the thermal diffusion ratio versus the density of pure water at the aforementioned conditions. In a 1 m, aqueous sodium nitrate solution, the thermal diffusion ratio increases as the phase separation pressure is approached, whereas the thermal diffusivity and binary molecular diffusivity decrease. In the "plateau" region, the thermal diffusion coefficient is of order 0.2 and increases to about 6 with decreasing pressure/density as the

P Bar	$10^{10}\sigma\mathfrak{D}_{AB}$ $\frac{m^2}{sK}$	$10^9\mathfrak{D}_{AB}$ $\frac{m^2}{s}$	σ $\frac{1}{K}$	k_T	ρ_{H_2O} $\frac{kg}{m^3}$
900	3.6	24.0	0.0150	0.1886	591.1
800	3.7	24.7	0.0150	0.1886	563.7
750	3.9	24.8	0.0157	0.1974	547.4
700	4.0	23.1	0.0173	0.2175	528.6
650	4.4	23.1	0.0190	0.2389	506.6
600	4.6	21.7	0.0212	0.2665	479.9
550	5.1	20.3	0.0251	0.3156	446.4
500	6.0	17.1	0.0351	0.4413	402.3
475	6.3	14.6	0.0432	0.5432	374.9
450.1	6.6	11.4	0.0579	0.7280	343.5
435	8.5	9.04	0.0940	1.1819	322.6
422.8	8.5	6.35	0.1339	1.6835	304.9
410.3	7.8	2.72	0.2867	3.6047	286.3
407.3	6.8	1.42	0.4789	6.0212	281.8

Table 3.7: Butenhoff et al. [15] measurements of the product $\sigma\mathfrak{D}_{AB}$ and $\mathfrak{D}_{AB}$ as a function of pressure in a 1.0 m, aqueous sodium nitrate solution at 450 °C. Corresponding Sorét coefficients, thermal diffusion ratios and pure water densities are also provided.

phase separation pressure is approached. The Butenhoff et al. measurements show that the binary molecular diffusion coefficient and thermal diffusion ratio are dramatically decreasing and increasing respectively as the pressure is lowered from pressures characterizing the "plateau" region to the phase separation pressure. (See Figs. 3-21 and 3-26.) Butenhoff et al. attribute this to "critical enhancements" dominating transport properties near the (vapor-liquid) critical point. Thus it appears likely that the Sorét and Dufour effects become more important as critical phenomena become more important.

3.7.8 Constant Pressure Specific Heat of Aqueous Sodium Sulfate Solutions and Their Components

Validation of the assumptions that the term accounting for energy transfer accompanying mass diffusion in the energy equation is unimportant (see Eq. 3.84) and $\rho_A C_{P_A} + \rho_B C_{P_B} = \rho C_{P_B}$ (see Eq. 3.86) require values for the constant pressure specific heats of the salt and water components in the aqueous salt solutions. Pabalan and Pitzer measured the constant pressure specific heat of aqueous sodium sulfate solutions as a function of salt molality up to a temperature of 299.59 °C at a pressure of 200 bar [69]. Their measurements are provided in Table 3.8. The constant pressure specific heat of pure H_2O at 299.59 °C and 200 bar is 5.3310
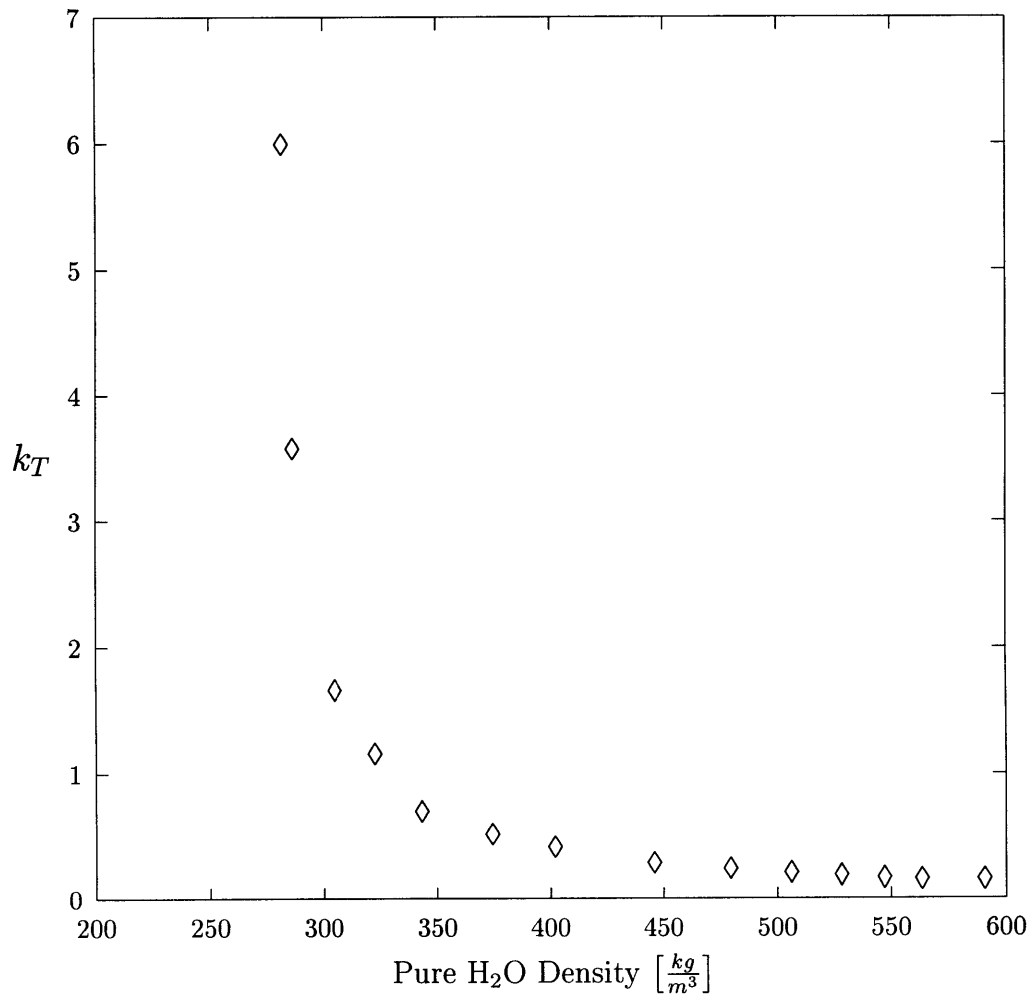
Figure 3-26: Plot of the thermal diffusion ratio of a 1 m, aqueous sodium nitrate solution at 450 $°C$ [15] as a function of the density of pure H_2O corresponding to the temperature and pressure for each data point reported by Butenhoff et al.

J/gram/K [30] and this datum is also included in Table 3.8. Moreover, Brodale and Giauque [14] report that the stable form of pure (solid) sodium sulfate has a constant pressure specific heat of 1.23 J/gram/K at 299.59 °C and this datum is included in Table 3.8 as well. The constant pressure specific heat of an aqueous sodium sulfate solution at 299.57 °C and 200 bar as a function of the mole fraction of sodium sulfate is plotted in Fig. 3-27 from the data reported in Table 3.8.

Solution density in the deposition rate experiments does not appear to be dramatically different from that of a 3.5 wt% aqueous sodium sulfate solution at 200 bar and 300 °C and thermodynamic properties in H_2O at near-supercritical conditions correlate well with density. Thus, estimating the constant pressure specific heat of the aqueous sodium sulfate solution and the partial molal constant pressure specific heat of each component in solution corresponding to the conditions investigated in the deposition rate experiments using the Pabalan and Pitzer data at a pressure, temperature and salt concentration of 200 bar, 299.59 °C and 3.5 wt% is worthwhile. Moreover, no other viable alternative for estimating these thermodynamic properties is available. To be sure, the density of pure H_2O at 200 bar and 299.59 °C is about 735 kg/m^3 and the density of pure H_2O at 250 bar and 362.5 °C, a pressure and temperature which typifies the deposition experiments in which the concentration of salt in the inlet stream was 4 wt% sodium sulfate, is about 20% lower, i.e., about 579 kg/m^3. (The density of a 3.5 wt% salt, aqueous sodium sulfate solution at 250 bar and 362.5 °C is about 646 kg/m^3 based on the Gallagher program, however the program does not converge when the temperature, pressure and concentration input to it are 300 °C, 200 bar and 3.5 wt% sodium sulfate respectively. Hence a comparison of the density of a 3.5 wt% salt, aqueous sodium sulfate solution at 299.59 °C and 200 bar with a 3.5 wt% salt, aqueous sodium sulfate solution at 362.5 °C and 250 bar is not possible.) It is noted, however, that the extent of electrostatic ion-pairing in a 3.5 wt% salt, aqueous sodium sulfate solution at 200 bar and 299.59 °C is unknown and potentially significantly different from the extent of electrostatic ion-pairing that typifies the solutions in the deposition experiments.

The (mole based) constant pressure specific heat of a binary solution, $\overline{C}_P$, is:

$$\overline{C}_P = \left(\frac{\partial \left(\frac{H}{n} \right)}{\partial T} \right)_{P, n_A, n_B}, \qquad (3.138)$$

where H is the enthalpy of solution in Joules and n is the number of moles of solution. It may also be expressed as:

$$\overline{C}_P(T, P, x_A) = \overline{C}_{P_A} x_A + \overline{C}_{P_B} x_B, \tag{3.139}$$

where $\overline{C}_{P_A}$ and $\overline{C}_{P_B}$ are the partial molal constant pressure heat capacities of components A and B in solution respectively, i.e.,

$$\overline{C}_{P_A} = \frac{\partial}{\partial T}\left(\left.\frac{\partial H}{\partial n_A}\right|_{T,P,n_B}\right)_{P,n_A,n_B} \tag{3.140}$$

$$\overline{C}_{P_B} = \frac{\partial}{\partial T}\left(\left.\frac{\partial H}{\partial n_B}\right|_{T,P,n_A}\right)_{P,n_A,n_B} \tag{3.141}$$

Evaluation of $\overline{C}_{P_A}$ and $\overline{C}_{P_B}$ as function of the mole fraction of sodium sulfate in solution may be accomplished using the method of intercepts. (See, for example, Moran and Shapiro [63], for a discussion of the method of intercepts.) At T = 299.59 °C, P = 200 bar and $x_A = 4.58*10^{-3}$ (3.5 wt% sodium sulfate), $\overline{C}_{P_A}$ and $\overline{C}_{P_B}$ are equal to -431.65 J/mole Na_2SO_4/K and 94.89 J/mole H_2O/K respectively as per Fig. 3-27. On a mass basis, the constant pressure specific heats are denoted by C_{P_A} and C_{P_B} and equal to -3038.9 J/kg Na_2SO_4/K and 5265.8 J/kg H_2O/K respectively.

3.7.9 Heat of Dissolution

The heat of dissolution for sodium sulfate and potassium sulfate in water are tabulated as a function of the number of water molecules per salt molecule (denoted by n) and temperature in "Properties of Aqueous Solutions of Electrolytes" [94]. The data are given in Table 3.9. (Pressures were not reported.) This book was translated from Russian and the data for sodium sulfate were referenced to a Russian study by Nikolskii [66]. The potassium sulfate data were referenced to Russian studies by Tsvetkov and Rabinovich [89] and Zarembo and Puchkov [93].

For the infinitely dilute case, the heat of dissolutions for sodium sulfate and potassium sulfate are provided up to 300 °C. The (negative) heat of dissolutions for the infinitely dilute case are plotted versus temperature
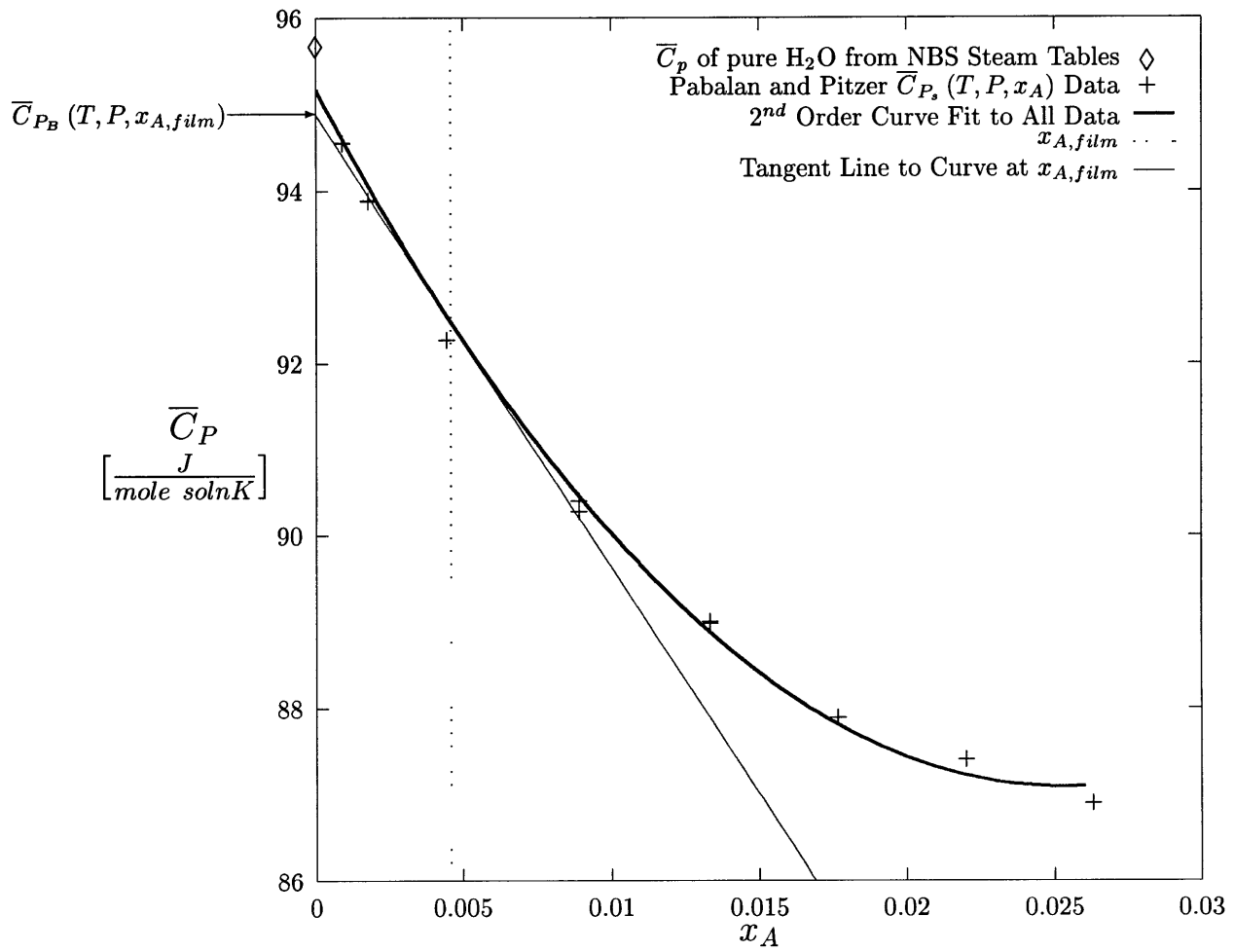
Figure 3-27: Partial molal constant pressure specific heat as a function mole fraction of sodium sulfate in an aqueous sodium sulfate solution at 299.59 $°C$ and 200 bar plotted from the data in Table 3.8. The tangent line required for evaluating the partial molal constant pressure specific heats of the Na_2SO_4 and H_2O in solution when the mole fraction of Na_2SO_4 equals $4.58*10^{-3}$ (3.5 wt%) is also shown.

m $\dfrac{moles\ A}{kg\ B}$	x_A $\dfrac{moles\ A}{mole\ soln}$	x_B $\dfrac{moles\ B}{mole\ soln}$	wt% A	MW_{soln} $\dfrac{gram\ soln}{mole\ soln}$	C_p $\dfrac{J}{gram\ soln\ K}$	$\overline{C}_p$ $\dfrac{J}{mole\ soln\ K}$
0	0	1	0	18.02	5.3110	95.70
0.0500	0.00090	0.99910	0.71	18.13	5.2146	94.55
0.0500	0.00090	0.99910	0.71	18.13	5.2150	94.56
0.1000	0.00180	0.99820	1.40	18.24	5.1462	93.88
0.1000	0.00180	0.99820	1.40	18.24	5.1466	93.89
0.2500	0.00448	0.99551	3.43	18.58	4.9672	92.27
0.4998	0.00893	0.99107	6.63	19.13	4.7262	90.40
0.4998	0.00893	0.99107	6.63	19.13	4.7200	90.28
0.7501	0.01334	0.98666	9.63	19.67	4.5230	88.99
0.7502	0.01334	0.98666	9.63	19.67	4.5242	89.01
1	0.01770	0.98223	12.44	20.22	4.3476	87.89
1.25	0.02203	0.97797	15.08	20.75	4.2122	87.41
1.5008	0.02633	0.97367	17.57	21.29	4.0824	86.90
∞	1	0	100	142.04	1.23	174.71

Table 3.8: Pabalan and Pitzer [69] experimental measurements of the constant pressure specific heat of aqueous sodium sulfate solutions as a function of molality at T = 299.59 $^\circ C$ and P = 200 bar. The constant pressure specific heat of pure water at 299.59 $^\circ C$ and 250 bar [30] and pure Na_2SO_4 (solid-phase I) at 300 $^\circ C$ [14] are also provided.

in Fig. 3-28. Since temperatures characterizing the deposition experiments approach 400 $^\circ C$, the data in Fig. 3-28 were fit to 4th order polynomials which are subsequently used to extrapolate the Russian data to temperatures of interest. Unfortunately, the heat of dissolution as a function of (T,P,C) is unknown at conditions of interest, however, it is likely a stronger function of temperature than pressure and concentration. Moreover, assuming the extrapolations are of the correct sign, the precipitation process is endothermic at conditions relevant to the sodium sulfate and potassium sulfate deposition rate experiments. It is noted that for n = 400 and T = 18 $^\circ C$ the heat of dissolution of $Na_2SO_4 \cdot 10H_2O$ is about 75 times larger than that for Na_2SO_4 and has the opposite sign. Moreover, evidence suggests that salts in SCW are probably hydrated at conditions relevant to the deposition experiments. (See, for example, Butenhoff et al. [15].) The effect (or lack thereof) of hydration on the heat of dissolution of aqueous sodium sulfate and potassium sulfate at near-supercritical conditions has not been studied.

Salt	n	T °C	H_{diss} $\frac{kJ}{kmole}$
Na_2SO_4	∞	25	-2.00
	∞	50	-6.00
	∞	75	-10.00
	∞	100	-17.00
	∞	125	-25.00
	∞	150	-37.00
	∞	175	-51.00
	∞	200	-68.00
	∞	225	-88.00
	∞	250	-115.00
	∞	275	-147.00
	∞	300	-185.00
	∞	18	-1.17
	6400	18	-.066
	3200	18	-0.57
	1600	18	-0.64
	800	18	-0.64
	400	18	-1.07
	200	18	-2.11
	100	18	-4.06
	50	18	-6.82
$Na_2SO_4 \cdot 10H_2O$	400	18	78.51
K_2SO_4	∞	25	24.00
	∞	50	16.00
	∞	75	9.00
	∞	100	2.00
	∞	125	-7.00
	∞	150	-18.00
	∞	175	-31.00
	∞	200	-46.00
	∞	225	-63.00
	∞	250	-84.00
	∞	275	-113.00
	∞	300	-147.00
	500	25	24.81
	∞	18	26.45
	6400	18	27.00
	3200	18	27.11
	1600	18	27.17
	800	18	27.14
	400	18	26.88
	200	18	25.99
	100	18	23.81

Table 3.9: Heat of dissolution of $Na2SO_4$,$Na_2SO_4 \cdot 10H_2O$ and K_2SO_4 as a function of the number of salt molecules per water molecule (n) and temperature [94].
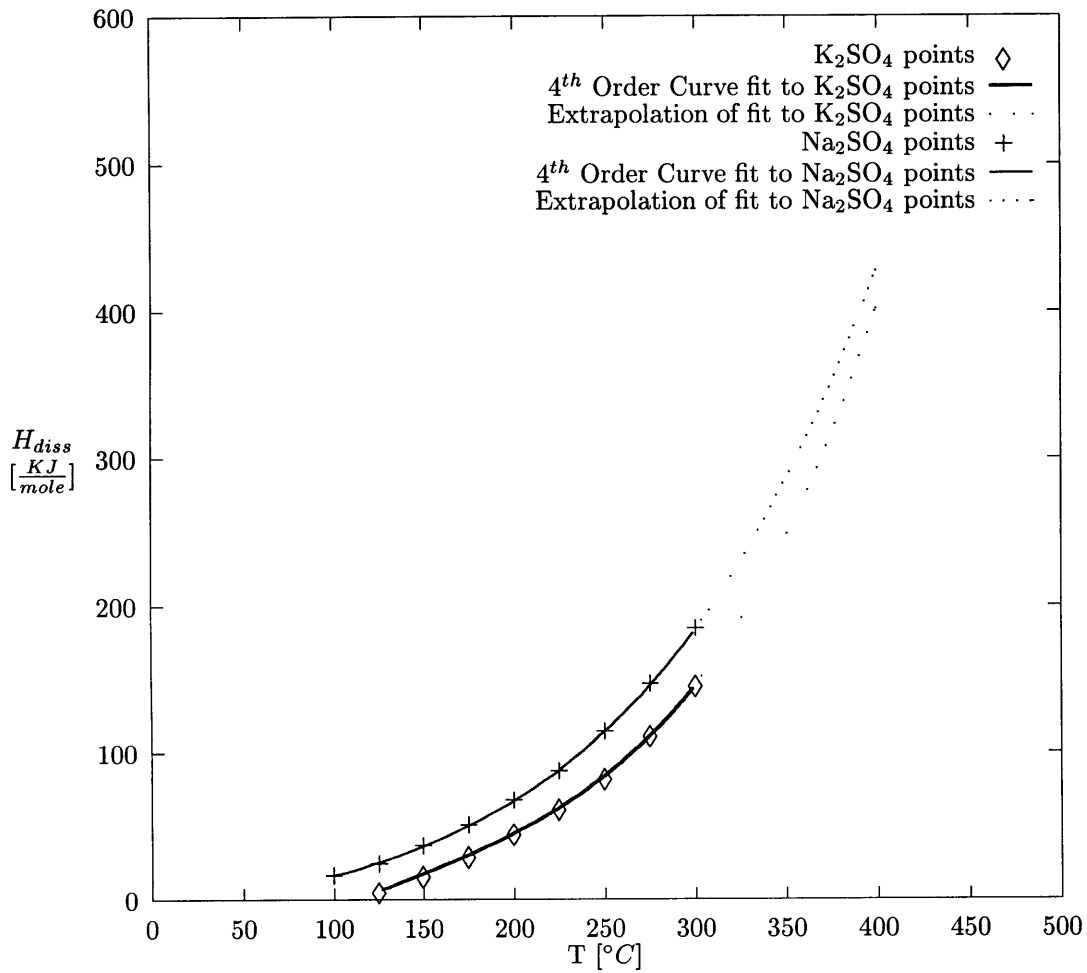
Figure 3-28: (Negative) Heat of dissolution of sodium sulfate and potassium sulfate in H_2O at infinitely dilute conditions [94] as a function of temperature. (Pressures were not reported.) Curve fits used to extrapolate the data to conditions of interest to the deposition experiments are also shown.

3.8 Evaluation and Discussion of Relevant Dimensionless Parameters

The criteria developed in Section 3.5 to justify neglecting the Sorét and Dufour effects, buoyancy forces induced by concentration gradients, viscous dissipation, energy transfer by mass diffusion, changes in the constant pressure specific heat of H_2O caused by the presence of dissolved salt and heat of dissolution are evaluated and discussed first in this section. Next, attention is turned towards the induced convective velocity at the salt layer-solution interface and the relative importance of advective and diffusive transport at the interface. Then the importance of the transient terms in the conservation laws in the equations governing transport is evaluated. Finally, the criteria to validate the use of the boundary layer approximation in the expression of the conservation laws are shown to be satisfied.

The tasks of this section are accomplished in the context of the deposition experiments in which the concentration of salt in the inlet stream was 4 wt% sodium sulfate and it is assumed that the dimensionless parameters of interest are similar in magnitude for all of the deposition experiments. Moreover, within this context, each dimensionless group is evaluated at conditions corresponding to the beginning of the deposition rate experiments. However, the dimensionless groups are largely constant during the deposition experiments, because salt is allowed to deposit for a time which is very small compared to that required to reach steady state conditions. (See Chapter 4.)

Characteristic values of quantities necessary for the tasks of this section are provided in Table 3.10. A deposition rate formulation was solved assuming all the criteria developed in Section 3.5 were valid, except for $\tilde{N} \lesssim 0.1$ and $H_{diss} = 0$, to determine characteristic temperatures and concentrations in the boundary layer. (Iterations were performed until the film temperature and concentration used to estimate the thermodynamic and transport properties required in the deposition rate formulation were consistent with its results.) The bulk, salt layer-solution interface and film temperatures and concentrations required to evaluate the criteria were determined from the results of this deposition rate formulation. All thermodynamic and transport properties are evaluated at the appropriate film temperature, film concentration and 250 bar using the means presented in Section 3.7. The source used to determine each quantity is provided in the last column

228

of Table 3.10 and "DRF" indicates the results of the deposition rate formulation were used directly to determine the characteristic value for the quantity of interest.

Characteristic values for all of the dimensionless groups developed in Section 3.5 are provided in Table 3.11. The quantity S is of order 1 when the thermal diffusion ratio equals 0.2, the value measured by Butenhoff et al. in the "plateau" region of the $NaNO_3$-H_2O system. Nonetheless, the Sorét effect is subsequently neglected when computing the deposition rate at the salt layer-solution interface. There are two primary reasons for neglecting the Sorét effect in the transport formulation. First, only very limited data are currently available for the thermal diffusion ratio of aqueous salt solutions at relevant conditions. Secondly, including the Sorét effect in the transport formulation would greatly reduce its numerical tractability. One should bear in mind, however, that if a thermal diffusion ratio of 0.2 characterizes aqueous sodium sulfate solutions at the conditions investigated in the deposition rate experiments the Sorét effect can not be legitimately neglected. The transport properties of aqueous salt solutions at near-supercritical conditions generally correlate well with density. Moreover, the densities characterizing the deposition rate experiments are estimated to range from approximately 400 to 750 kg/m^3 and the density range over which the thermal diffusion ratio was measured by Butenhoff et al., extends from about 280 to 600 kg/m^3 when the 1.0 m (7.83 wt%), aqueous sodium nitrate solution at 450 $°C$ is approximated as pure water. Thus the higher end of the density range investigated by Butenhoff et al. typifies the density of the aqueous salt solutions in the deposition rate experiments and a thermal diffusion coefficient value of order 0.2 (or higher) appears possible.

When S is of order 1, then D is of order zero according to Eq. 3.81. (The Sorét effect and ordinary (Fick) diffusion cause transport of salt from and to the salt layer-solution interface respectively; therefore; if their magnitudes are equal the net mass diffusive flux to the interface is of order zero.) However, since salt is depositing at the salt layer-solution interface, S can not be unity. To place the Dufour effect in, admittedly crude, context, S is assumed to equal 0 when evaluating D. When the thermal diffusion ratio equals 0.2, the dimensionless parameter D equals about 0.4; therefore, the Dufour effect may not be negligible at the conditions investigated in the deposition rate experiments. If the thermal diffusion ratio is set equal to 6, the maximum measured by Butenhoff et al., S and D are equal to about 30 and 12 respectively. At the very

Property	Characteristic Value	Source
D_{io}	0.00508 m	See Fig. 2-9
T_B	630.7 K	Experimental Measurements
P	10.61 W	Experimental Measurements
ϕ	2/3	Experimental Measurements
$\left.\frac{dD_i}{dt}\right\|_C$	$4.3*10^{-6}$ m/s	Experimental Measurements
$\left.\frac{dD_i}{dt}\right\|_C$	$3.2*10^{-6}$ m/s	DRF
$\dot{m}_{s,c}$	$1.1*10-6$ kg salt/s	DRF/Experimental Measurements
ΔT	10 K	DRF
T_{film}	635.7 K	DRF
$\omega_{A,i}$	0.020	DRF
$\omega_{A,B}$	0.034	DRF
$\omega_{B,i}$	0.980	DRF
$\omega_{B,B}$	0.966	DRF
$\omega_{B,film}$	0.973	DRF
$\Delta\omega_A$	0.014	DRF
$x_{A,i}$	0.0026	DRF
$x_{A,B}$	0.0044	DRF
$x_{A,film}$	0.0033	DRF
$x_{B,film}$	0.9967	DRF
Δx_A	0.0018	DRF
Ra_D	10^7	DRF
M_A	142.04 kg/kmole	Calculated using periodic table
M_B	18.02 kg/kmole	Calculated using periodic table
ρ_s	2680 kg/m^3	CRC Handbook [51] (at STP)
ρ	646 kg/m^3	Gallagher program
β	0.005 1/K	Gallagher program
β^*	-0.004 m^3/kg	Gallagher program
$\overline{C}_{P_A}$	-431.7 J/mole A/K	Computed from Pabalan and Pitzer [69] data
C_{P_A}	-3038.9 J/kg B/K	Computed from Pabalan and Pitzer [69] data
$\overline{C}_{P_B}$	94.89 J/mole A/K	Computed from Pabalan and Pitzer [69] data
C_{P_B}	5266 J/kg B/K	Computed from Pabalan and Pitzer [69] data
H_{diss}	$-2.24*10^6$ J/kg	Nikolskii study [66]
MW_{soln}	18.45 kg/kmole	$MW_{soln} = x_A M_A + x_B M_B$
c	$3.50*10^4$ moles soln/m^3	$c = \rho/MW_{soln}$
μ	$6.68*10^{-5}$ kg/m/s	NBS Steam Tables
k	0.45 W/m/K	NBS Steam Tables
$\mathfrak{D}_{AB}$	$0.25*10^{-7}$ m^2/s	Butenhoff et al. study
Le	6	Butenhoff et al. study
k_T	0.2	Butenhoff et al. study ("plateau" region)
k_T	6	Butenhoff et al. study (maximum measured)
U	0.064 m/s	Scale Analysis in Section 3.6 with DRF results
V	$1.1*10^{-3}$ m/s	Scale Analysis in Section 3.6 with DRF results

Table 3.10: Characteristic temperatures, concentrations, thermodynamic properties, transport properties and flow quantities typifying the deposition rate experiments in which the concentration of sodium sulfate in the inlet stream was 4 wt%.

Dimensionless Group	Characteristic Value	Notes
S	1	for $k_T = 0.2$
S	30	for $k_T = 6$
D	0.4	for S = 0 and $k_T = 0.2$
D	12	for S = 0 and $k_T = 6$
$\tilde{N}$	1	
BR	10^{-7}	
M	$7.3*10^{-3}$	
A1	0.94	
A2	0.25	
A3	$4.1*10^{-3}$	
A4	6.6	
A5	3	
A6	1.5	
A7	0.03	
A8	0.003	
A9	< 0.003	must be smaller than A7
A10	0.02	
A11	0.01	

Table 3.11: Characteritic values of dimensionless quantities relevant to the transport formulation.

least, the magnitudes of the dimensionless quantities S and D determined above indicate that neglecting the Sorét and Dufour effects when computing the deposition rate at the salt layer-solution interface requires far better justification. Unfortunately, at the present time, the thermal diffusion ratio data required to better evaluate the importance of the Sorét and Dufour effects do not exist.

The quantity $\tilde{N}$ is of order 1; therefore, buoyancy forces induced by both the concentration and temperature differences across the boundary layer are accounted for in the model subsequently developed to determine the deposition rate at the salt layer-solution interface. The Brinkman number is of order 10^{-7}; consequently, viscous dissipation is negligible. The dimensionless parameter M is of order $7.3*10^{-3}$; therefore, energy transfer accompanying mass diffusion may be neglected. For a 3.5 wt% salt, aqueous sodium sulfate solution at a temperature of 299.59 $°C$ and a pressure of 200 bar the dimensionless quantity A1 is 0.94; thus, the constant pressure specific heat of an aqueous sodium sulfate solution approximately equals the constant pressure specific heat of pure H_2O at this condition. In all subsequent computations it is assumed that the constant pressure specific heat of the aqueous salt solutions equals the constant pressure specific heat of H_2O at the temperature and pressure of interest. The dimensionless group A2 is of order 0.25; therefore, the heat absorbed when the salts precipitate from solution is accounted for in subsequent

transport computations.

Based upon the scaling of the overall mass balance at the salt layer-solution interface the magnitude of the induced convective velocity at the interface is given by Eq. 3.50 and it is of order $4.5*10^{-6}$ m/s. The characteristic v-velocity in the boundary layer is calculated from Eq. 3.114 and it is of order $1.1*10^{-3}$ m/s. Thus, the dimensionless group A3 is of order $4.1*10^{-3}$ and the induced convective velocity at the salt layer-solution interface may be neglected for the purpose of computing transport coefficients. (It can also be shown that the mass transfer coefficient at the salt layer-solution interface is much larger than the induced convective velocity there to justify neglecting the induced convective velocity when calculating transport coefficients.) Advection does play a major role in transport at the salt layer-solution interface, however. To be sure, the dimensionless quantity A4 is of order 6.6; therefore, diffusive mass transport of H_2O away from the salt layer-solution interface substantially exceeds the mass of H_2O being displaced as the salt layer propagates outward. Obviously, advection of H_2O towards the salt layer-solution interface must be present for the water mass balance at the interface to be satisfied. The ratio of the advection term to the accumulation term in the water mass balance, A5, is, in fact, 3. (It was shown in Section 3.4.2 that the induced convective velocity must be towards the salt layer-solution interface in order for mass to be conserved at the interface and the foregoing analysis is consistent with that assertion.) When A3 equals 6.6 advection and diffusive mass transport of H_2O at the salt layer-solution interface are of the same order. Then it follows from Eq. 3.93 that the induced convective velocity towards the salt layer-solution interface based upon the scaling of the water mass balance at the interface is of order $7.0*10^{-6}$ m/sec. This value is reasonably consistent with the induced convective velocity calculated from the overall mass balance ($4.5*10^{-6}$ m/s) considering Eq. 3.93 is rigorously valid only when A4 $\gtrsim$ 10 and the calculated A4 equals 6.6. A6, the ratio of the diffusion term to the accumulation term in the salt mass balance, equals 1.5. A7, the ratio of the advection term to the accumulation term in the salt mass balance, equals 0.03. It is not surprising that the dominant mode of *salt* transport at the salt-layer solution interface is diffusion because the solution is fairly dilute in salt. The converse is true for the transport of water at the salt layer-solution interface. Specifically, the mass fraction of water at the salt layer-solution interface is high (approaching unity); therefore, it is not surprising that advection is an important transport mode for water at the interface.

The dimensionless group A8 is of order 0.003; therefore, transient terms in all of the conservation laws may be neglected. The dimensionless group A10 equals about 0.02; therefore in the boundary layer the characteristic u-velocity is much greater than the characteristic v-velocity and the thicknesses of the momentum and thermal boundary layers are small compared to the diameter of the hot finger. Moreover, the dimensionless quantity A11 is of order 0.01; consequently, the concentration boundary layer thickness is small compared to the diameter of the hot finger and the boundary layer approximation is valid.

All, except two, of the criteria necessary to simplify the transport formulation were satisfied. Accordingly, buoyancy forces induced by concentration gradients and the heat of dissolution are not neglected in subsequent analyses. The simplified set of equations governing transport becomes:

$$\frac{\partial u}{\partial x} + \frac{\partial v}{\partial y} = 0 \tag{3.142}$$

$$u\frac{\partial \rho_A}{\partial x} + v\frac{\partial \rho_A}{\partial y} = \frac{\partial \rho_A}{\partial y} \tag{3.143}$$

$$u\frac{\partial u}{\partial x} + v\frac{\partial u}{\partial y} = \nu\frac{\partial^2 u}{\partial y^2} + g\beta(T - T_\infty) + g\beta^*(\rho_A - \rho_{A,\infty}) \tag{3.144}$$

$$\rho C_{P_B}\left(u\frac{\partial T}{\partial x} + v\frac{\partial T}{\partial y}\right) = k\frac{\partial^2 T}{\partial y^2} \tag{3.145}$$

$$(\rho_s - \rho)(1 - \phi)\frac{\partial L}{\partial t} = -\rho v(y = L) \tag{3.146}$$

The corresponding boundary conditions and initial condition are provided in Table 3.12. The transient terms in the conservation laws have been shown to be negligible; therefore, only the initial condition on L remains. Moreover, advection was shown to be an unimportant transport mechanism *for salt* at the salt layer-solution interface; consequently, the quantity (-ρv) in boundary condition Number 9 has been dropped. (Boundary condition Number 9 was derived from the salt balance at the salt layer-solution interface.)

3.9 Further Simplification of the Transport Formulation

If the transport coefficients at the salt layer-solution interface are sufficiently weak functions of azimuthal location, then the mass of salt deposited and hence, L, will be independent of x and, thus, solely a function of time. Kuehn and Goldstein [45] numerically solved the *complete* Navier-Stokes equations and energy

Number	Variable	(x,y,t)	Condition
1	x	$(0, y \geq L(x,t), t)$	$u = 0$
2	x	$(0, y \geq L(x,t), t)$	$T = T_B$
3	x	$(0, y \geq L(x,t), t)$	$\rho_A = \rho_{A,B}$
4	y	$(x, L(x,t), t)$	$u = 0$
5	y	$(x, L(x,t), t)$	T, C equilibrium
6	y	(x, ∞, t)	$u = 0$
7	y	(x, ∞, t)	$T = T_B$
8	y	(x, ∞, t)	$\rho_A = \rho_{A,B}$
9	y	$(x, L(x,t), t)$	$(\rho_s - \rho_A)\left(1 - \phi\right)\frac{\partial L}{\partial t} = J_{A,y}$
10	y	$(x, L(x,t), t)$	$P'' + \rho_s H_{diss}\left(1 - \phi\right)\frac{\partial L}{\partial t} = q_y''$
11	t	$t=0$	$L=0$

Table 3.12: Boundary conditions and initial condition for the transport formulation.

equation governing laminar, steady state, natural convection about a horizontal, isothermal, circular cylinder. Buoyancy forces were induced exclusively by temperature gradients and the Boussinesq approximation was assumed to apply in the (single component) fluid surrounding the cylinder. The numerical results of the Kuehn and Goldstein study compare very well with concomitant experimental measurements. In the natural convective boundary layer formed around the salt layer-solution interface, buoyancy forces are induced by both temperature and concentration gradients; nonetheless, the dependence of the transport coefficients on azimuthal location may be placed in perspective by examining the results of the Kuehn and Goldstein study. The Kuehn and Goldstein results for the local Nusselt number as a function of azimuthal angle (θ) and Rayleigh number at a Prandtl number of 0.7 are shown in Fig. 3-29. The bottom of the cylinder corresponds to θ equal to zero and the local Nusselt number and Rayleigh numbers are based on the diameter of the cylinder. (The Prandtl number of SCW at conditions of interest to this dissertation is of order unity; therefore, examining the Kuehn and Goldstein results for Pr = 0.7 is appropriate.) The curve labelled "[12]" in Fig. 3-29 is the local Nusselt number as a function of θ when the boundary layer approximation is applied throughout the entire flow field around the cylinder. It applies as the Rayleigh number approaches ∞ in the boundary layer region, but, obviously, not in the plume region. It was determined by numerically solving the boundary layer form of the conservation laws by Merkin [60].

The Rayleigh number characterizing the natural convection boundary layer formed around the salt layer-solution interface is estimated to be of order 10^7 and larger. (See Section 4.4.2.) At a Rayleigh number of 10^7

234
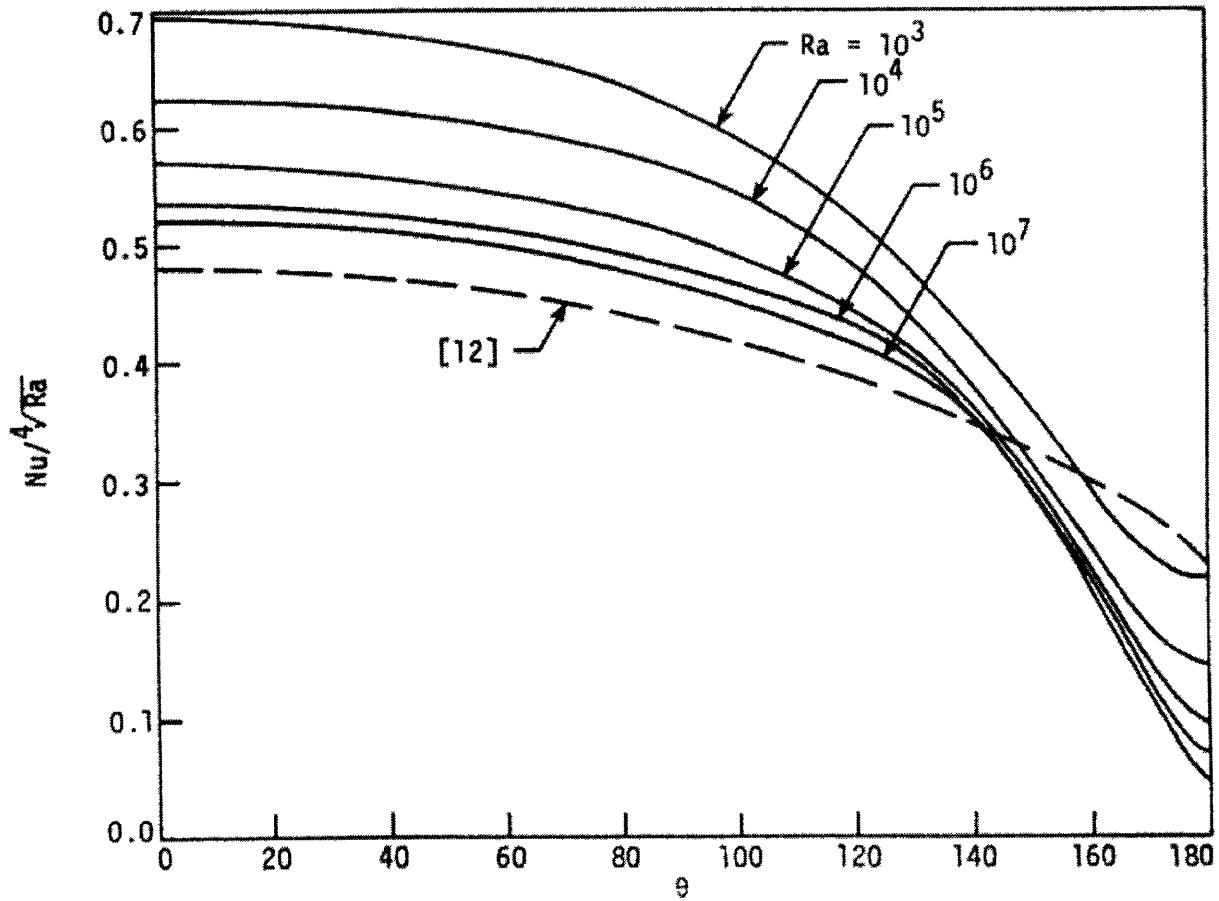
Figure 3-29: Local Nusselt number as a function of Rayleigh number (based on D) and azimuthal angle (θ) for laminar natural convection about a horizontal, isothermal, circular cylinder at a Prandtl number of 0.7. The local Nusselt and Rayleigh numbers are based on the diameter of the cylinder. The bottom of the cylinder corresponds to $\theta = 0$. All curves, except "[12]", are from the numerical solution performed by Kuehn and Goldstein [45]. The curve labelled "[12]" corresponds to Ra → ∞ and was computed by Merkin [60]. This figure was extracted from Kuehn and Goldstein [45].

and Prandtl number of 0.7, the local Nusselt for natural convection about a horizontal, isothermal, circular cylinder number decreases by only approximately 25% between $0 \leq \theta \leq 130°$ as per Fig. 3-29. However, between $130 \leq \theta \leq 180°$, the local Nusselt number drops precipitously. To be sure, the local Nusselt number at $\theta = 180°$ is about a factor of 10 below that at $\theta = 0°$. Qualitatively, the dependence of the local Sherwood number on azimuthal location must be similar to that of the local Nusselt number. (See Section 3.6.4.) Moreover, the local heat and mass transfer coefficients are directly proportional to the local Nusselt and Sherwood numbers (based on the diameter of the cylinder) respectively.

The relationship between the transport coefficients and deposition rate at the salt layer-solution interface is complex and was explained in Section 3.2. In short, at the conditions investigated in the deposition rate experiments, decreases in the transport coefficients lead to increases in the deposition rate at the salt layer solution-interface due to an increased driving force for mass transfer. Thus at time equal to zero, the deposition rate at the salt layer-solution interface is an increasing function of θ. However, asymmetry of the salt layer-solution interface, except on a portion of its downstream side, is inherently limited. (Transport on the downstream side of the salt layer-solution interface is discussed in Section 3.5.12.) The heat flux at the surface of the hot finger is essentially constant. Thus, if the deposition rate is an increasing function of θ, the surface area over an interval $d\theta$ will be an increasing function of θ as well. Hence, the heat flux over an interval $d\theta$ will be a decreasing function of θ. Lower heat fluxes decrease the deposition rate; therefore, the asymmetry of the salt layer-solution interface is inherently limited. In the current transport formulation it is subsequently assumed that the heat and mass transfer coefficients at the salt layer-solution interface are independent of x. The heat and mass transfer coefficients used in the transport formulation correspond to their mean values over a vertical, flat plate of height $\pi D_i/2$.

Admittedly, assuming the heat and mass transfer coefficients and, thus, m and L are independent of x is a shortcoming of the transport model. However, for the aforementioned reasons, it is not expected to be especially serious. Moreover, the salt layer-solution interface during the experiments is virtually circular, except for about a 60° interval on the downstream side. (See the photographs in Figs. 2-4 and 2-6.) Furthermore, accounting for the x-dependence of the various quantities would require a substantial computational investment because solutions to transport problems existing in the literature could not be

applied to compute the deposition rate at the salt layer-solution interface.

Once the heat and mass transfer coefficients are assumed independent of x, the transport formulation becomes considerably simpler. First, the thickness of the salt layer becomes independent of x; therefore, $\partial L/\partial t$ reduces to dL/dt. Secondly, since the heat flux supplied to the hot finger is constant and the transport coefficients around the salt layer-solution interface are assumed constant, the temperature and concentration at the interface are no longer functions of x and t, but exclusively t. With constant transport coefficients, the salt layer-solution interface will be isothermal and constant concentration. Thus, the T-C equilibrium boundary condition can be replaced with two boundary conditions of the first kind. The temperature and concentration boundary conditions of the first kind are still related by the T-C equilibrium expression. Additionally, it was shown above that the v-velocity at the salt-layer solution interface could be assumed equal to zero for the purposes of calculating transport coefficients which gives an additional boundary condition on L(t). Since two "extra" boundary conditions on y have been provided, the salt balance and energy balance at the salt layer-solution interface are no longer necessary and the transport formulation reduces to Eqs. 3.147 through 3.151 with the accompanying boundary conditions given in Table 3.13.

$$\frac{\partial u}{\partial x} + \frac{\partial v}{\partial y} = 0 \tag{3.147}$$

$$u\frac{\partial \rho_A}{\partial x} + v\frac{\partial \rho_A}{\partial y} = \frac{\partial \rho_A}{\partial y} \tag{3.148}$$

$$u\frac{\partial u}{\partial x} + v\frac{\partial u}{\partial y} = \nu\frac{\partial^2 u}{\partial y^2} + g\beta(T - T_\infty) + g\beta^*(\rho - \rho_\infty) \tag{3.149}$$

$$\rho C_{P_B}\left(u\frac{\partial T}{\partial x} + v\frac{\partial T}{\partial y}\right) = k\frac{\partial^2 T}{\partial y^2} \tag{3.150}$$

$$(\rho_s - \rho)(1 - \phi)\frac{dL}{dt} = -\rho v \tag{3.151}$$

When modeling the salt layer-solution interface as a vertically-oriented flat plate, the area of the plate must increase with time as salt deposits because the area of the salt layer-solution interface increases with time. The surface area available for deposition at the salt layer-solution interface is given by:

$$A_i = \pi D_i L\left(1 + \frac{D_i}{4L}\right) \tag{3.152}$$

237

Number	Variable	(x,y,t)	Condition
1	x	$(0, y \geq L(t), t)$	$u = 0$
2	x	$(0, y \geq L(t), t)$	$T = T_B$
3	x	$(0, y \geq L(t), t)$	$\rho_A = \rho_{A,B}$
4	y	$(x, L(t), t)$	$u = 0$
5	y	$(x, L(t), t)$	T,C equilibrium
6	y	(x, ∞, t)	$u = 0$
7	y	(x, ∞, t)	$T = T_B$
8	y	(x, ∞, t)	$\rho_A = \rho_{A,B}$
9	y	$(x, L(t), t)$	$v = 0$
10	t=0	0	L=0

Table 3.13: Boundary conditions and initial condition for the transport formulation.

The factor of $(1 + \frac{D_i}{4L})$ accounts for the area available for deposition at the tip of the hot finger. Setting dL/dt equal to dD_i/dt and expressing the salt mass balance at the salt layer-solution interface (given by Boundary Condition Number 9 in Table 3.12) in terms of overall rate instead of fluxes, Boundary Conditions Number 9 and 10 become:

$$\frac{dm_s}{dt} = \pi D_i L \left(1 + \frac{D_i}{4L}\right)(-J_{A,y=L}) \tag{3.153}$$

$$\eta P'' + \left(\frac{\rho_s}{\rho_s - \rho_A}\right)\frac{dm_s''}{dt}H_{diss} = q_y'' \tag{3.154}$$

The heat and mass transfer coefficients required to calculate the diffusive fluxes fluxes of energy and salt at the salt layer-solution interface may be computed from the solution to the equations governing transport as described below. Written in terms of the heat and mass transport coefficients, Eqs. 3.153 and 3.154 become:

$$\frac{dm_s}{dt} = 0.01 \rho h_m \pi D_i L \left(1 + \frac{D_i}{4L}\right)(C_B - C_i) \tag{3.155}$$

$$\eta P'' + \left(\frac{\rho_s}{\rho_s - \rho_A}\right)\frac{dm_s''}{dt}H_{diss} = h(T_i - T_B) \tag{3.156}$$

The term $\rho_s/(\rho_s - \rho_A)$ is of order unity because salt concentrations at the salt layer-solution interface

238

do not exceed about 0.05 wt%; therefore, Eq. 3.156 may be expressed as:

$$\eta P'' + \frac{dm_s''}{dt} H_{diss} = h\,(T_i - T_B) \tag{3.157}$$

3.10 Double Diffusive Natural Convection

Double diffusive natural convection may result when solution density is coupled to both temperature and solute concentration. It is the dominant mode of transport in the deposition experiments. When buoyancy forces are induced by both temperature and concentration gradients, the continuity, momentum, energy and species equations are coupled; therefore, determination of transport coefficients is complex. The mean Nusselt and Sherwood numbers for pure, double-diffusive natural convective transport from/to an isothermal heated cylinder in a quiescent medium are functions of the Schmidt number (Sc), Prandtl number (Pr), Grashof number (Gr) and dimensionless group $\tilde{N}$. These four dimensionless groups are defined by Eqs. 3.158 through 3.161.

$$Sc = \frac{\nu}{\mathcal{D}_{AB}} \tag{3.158}$$

$$Pr = \frac{\nu}{\alpha} \tag{3.159}$$

$$Gr_D = \frac{g(\beta(T_i - T_B) + 0.01\rho\beta^*(C_i - C_B))D^3}{\nu^2} \tag{3.160}$$

$$\tilde{N} = \frac{\beta^*(\rho_{A,i} - \rho_{A,B})}{\beta(T_i - T_B)} \tag{3.161}$$

The quantities β and β^* are the volumetric thermal expansion coefficient and species expansion coefficient respectively as defined by Eqs. 3.24 and 3.25 respectively. The factor of 0.01ρ in the Grashof number expression converts the concentration units from wt% A to $\frac{kg\,A}{m^3}$ and makes it dimensionally consistent.

Buoyancy forces resulting from both temperature and concentration differences across the boundary layer are included in the Grashof number expression. The dimensionless group $\tilde{N}$ represents the relative importance of buoyancy forces arising from the concentration and temperature differences across the boundary layer. Based on β and β^* values calculated using densities determined from the program produced by the

Gallagher study discussed in Section 3.7.3, it is shown in Section 4.4.2, that $\tilde{N}$ is about 0.5-0.75 at the beginning of the sodium sulfate deposition experiments. As the area of the salt layer-solution interface increases, a smaller driving force for natural convection is required to remove the heat supplied by the hot finger. Moreover, as time increases a smaller fraction of the overall natural convection driving force is provided by the concentration difference across the boundary layer which causes a reduction in $\tilde{N}$. At steady state conditions (neglecting the Sorét and Dufour effects), the temperature of the salt layer-solution interface equals the solubility temperature corresponding to the salt concentration in the bulk solution and the mass transfer driving force and thus $\tilde{N}$ equal 0. This condition is expressed by Eqn. 3.162. Under steady state conditions buoyancy results exclusively from the temperature difference across the boundary layer. The density of an aqueous potassium sulfate solution as a function of temperature, pressure and salt concentration is unavailable at conditions of interest; consequently, the range of $\tilde{N}$ characterizing the potassium sulfate depositions experiments may not be determined directly. However, it is likely to be similar to that of the sodium sulfate sulfate deposition experiments.

$$lim_{t \to \infty} \tilde{N} = 0 \qquad (3.162)$$

The mean Nusselt and Sherwood numbers for double-diffusive natural convection on a horizontal cylinder as a function of the relevant dimensionless groups are not directly available. However, Gebhart and Pera [32] provide the local Nusselt and Sherwood numbers as a function of Sc, Pr, $\tilde{N}$ and the local Grashof number for double-diffusive natural convection on a vertically oriented isothermal and constant concentration flat plate. Gebhart and Pera accomplished this by numerically solving a similarity formulation derived exactly from Eqs. 3.147 through 3.150 and the boundary conditions in Table 3.13 except Number 11.

The expressions for the local Nusselt and Sherwood numbers provided by the Gebhart and Pera study are of the form:

$$Nu_x = \left[\frac{-\phi'(0)}{\sqrt{2}}\right] Gr_x^{\frac{1}{4}} \qquad (3.163)$$

$$Sh_x = \left[\frac{-\tilde{C}'(0)}{\sqrt{2}}\right] Gr_x^{\frac{1}{4}} \qquad (3.164)$$

The quantities $-\phi'(0)$ and $-\tilde{C}'(0)$ are derivatives of dimensionless temperature and concentration respectively with respect to the similarity variable used in the Gebhart and Pera study evaluated at the wall of the flat plate. Dimensionless temperature and concentration are defined according to Eqs. 3.165 and 3.166 respectively by Gebhart and Pera. Both $-\phi'(0)$ and $-\tilde{C}'(0)$ are functions of Sc, Pr and $\tilde{N}$ and are tabulated in Table 3.14 which was extracted directly from the Gebhart and Pera study [32]. The remaining quantity in Table 3.14, $f''(0)$, is used to calculate the shear stress on the flat plate.

$$\tilde{T} = \frac{T - C_B}{T_i - T_B} \tag{3.165}$$

$$\tilde{C} = \frac{C - C_B}{C_i - C_B} \tag{3.166}$$

It is noted that for Rayleigh numbers larger than about 10^9, the natural convective boundary layer formed around a cylinder becomes turbulent [41]. The Rayleigh number is equal to GrPr and defined by Eq. 3.167. The theoretically determined Rayleigh numbers provided in the next Chapter do not exceed 10^9 for time scales on the order of the duration of the deposition experiments. However, before steady state conditions are reached, i.e., mass transfer to the salt layer-solution interface ceases, the deposition rate formulation predicts that for some conditions investigated, the Rayleigh number slightly exceeds 10^9. For example, as shown in Section 4.4.2, for the set of runs in which the sodium sulfate concentration in the solution entering the cell was 4 wt%, the predicted steady state Rayleigh number is about $1.3*10^9$. However, a modest excursion in Rayleigh number beyond 10^9 does not significantly alter the relevant Nusselt and Sherwood number expressions. Moreover, for such modest excursions in Rayleigh number beyond 10^9, most of the flow around the salt layer-solution interface remains laminar. Hence, no adjustments to the deposition rate formulation to account for transition to turbulence are necessary.

$$Ra = \frac{g(\beta(T_i - T_B) + 0.01\rho\beta^*(C_i - C_B))D^3}{\nu\alpha} \tag{3.167}$$

241

Pr	Sc	$\tilde{N}$	$f''(0)$	$-\phi'(0)$	$-C'(0)$
0.7	0.1	0.5	0.74221	0.54913	0.19561
		1	0.77213	0.56620	0.20656
		2	0.80148	0.58125	0.21554
	0.5	-0.5	0.64154	0.45891	0.37536
		0.5	0.69018	0.50768	0.42747
		1	0.69584	0.51125	0.43110
		2	0.70185	0.51559	0.43440
	0.7	All	0.67890	0.49950	0.49950
	0.94	-0.5	0.70824	0.51709	0.59582
		0.5	0.66880	0.49292	0.57019
		1	0.66378	0.48947	0.56659
		2	0.65873	0.48588	0.56286
	5.0	-0.5	0.85198	0.56603	1.29997
		0.5	0.61725	0.46880	1.11689
		1	0.58574	0.45026	1.08559
		2	0.55277	0.42829	1.04962
	10.0	-0.5	0.90099	0.57552	1.71754
		0.5	0.59885	0.46330	1.43962
		1	0.55728	0.44098	1.38965
		2	0.51428	0.41383	1.33242
7.0	7.0	All	0.45069	1.05411	1.05411
	1.0	0.5	0.51983	1.16002	0.48743
		1	0.55161	1.19963	0.51188
		2	0.58246	1.12348	0.53263
	100	-0.5	0.61831	1.21566	3.33176
		0.5	0.38933	0.97593	2.75894
		1	0.35748	0.92855	2.65410
		2	?	0.87121	2.53325
	500	-0.3	0.54994	1.14494	5.58873
		0.5	0.36783	0.96154	4.79946
		1	0.32402	0.90298	4.56087
		2	0.27788	0.82889	4.27465

Table 3.14: Flow and transport quantities for laminar, double-diffusive natural convection flows adjacent to an isothermal and constant concentration vertical surface. Source: Gebhart and Pera [32]. A question mark is indicated for $f''(0)$ at $Pr = 7.0$, $Sc = 100$ and $\tilde{N} = 2$ because the value of 0.03244 given by Gebhart and Pera appears erroneous.

3.11 Deposition Rate Formulation

3.11.1 Introduction

The formulation to theoretically determine the deposition rate at the salt layer-solution interface for the conditions which were experimentally investigated in this dissertation is finalized in this section. Some temperatures, concentrations and principles relevant to the model's development are shown in Fig. 3-30 which is occasionally referred to during the development of the model. The details of this figure are described later in this section. A number of important assumptions are invoked during the development of the formulation for the deposition rate at the salt layer-solution interface contained in this section. Generally, assumptions are introduced when the principle to which they apply is presented. However, assumptions of a more general nature are reiterated here. First, heat and mass transfer within the porous salt layer are neglected in the deposition rate formulation. However, heat and mass transfer within the porous salt layer likely play an important role in the deposition process; therefore, some discussion of them is provided in Section 4.5. The effects of diffusion of mass along temperature gradients and diffusion of energy along concentration gradients, i.e., the Sorét and Dufour effects respectively are not considered. Finally, the detailed morphology of the salt layer-solution interface is not considered and its perimeter is assumed to be circular.

3.11.2 General Formulation

Heat and Mass Transfer

The coupling between heat and mass transfer which occurs because the natural convection transport is doubly diffusive is accounted for by applying the results of the Gebhart and Pera study to determine the relevant transport coefficients in this section. Approximating the salt layer-solution interface as a vertical flat plate of height L and applying the average value theorem to Eqs. 3.163 and 3.164 to determine the mean
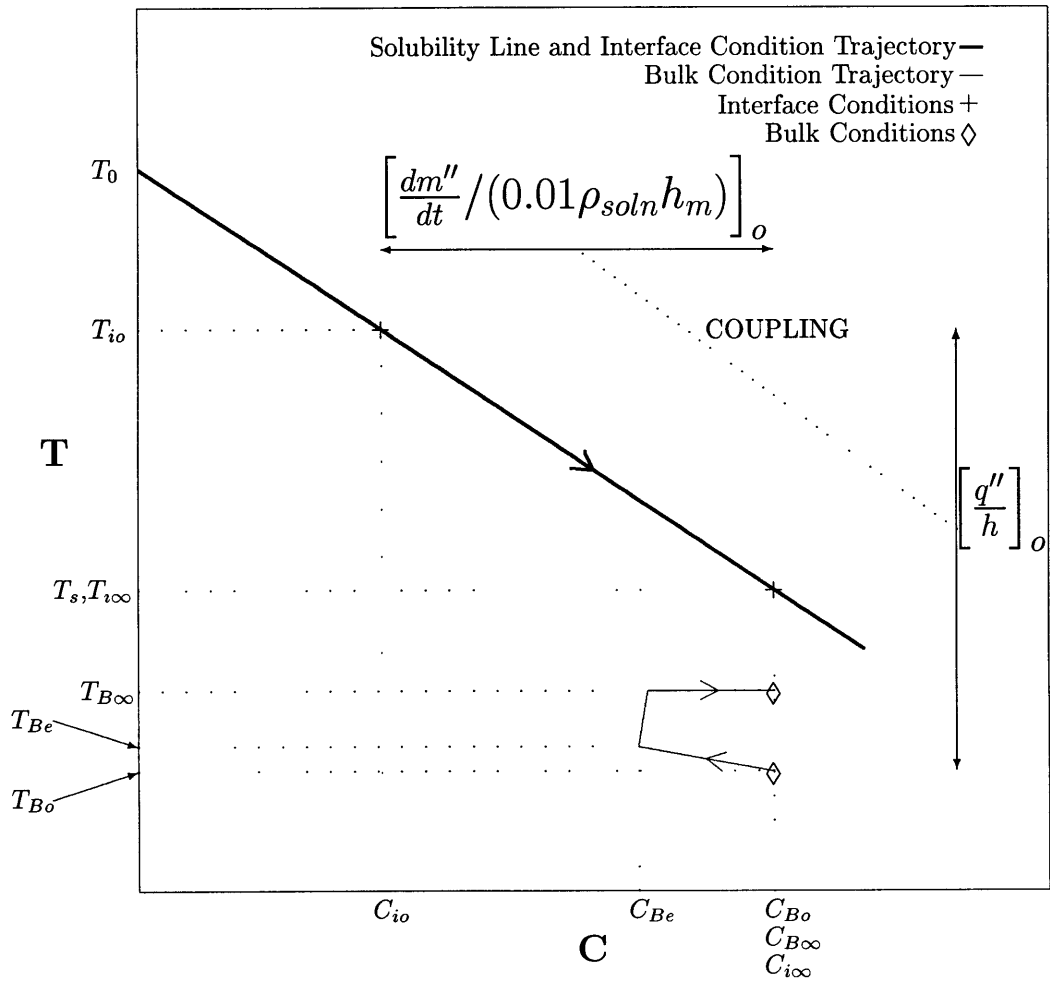
Figure 3-30: Temperatures, concentrations and graphic illustrations of principles relevant to the deposition rate formulation.

Nusselt and Sherwood numbers respectively, over the length of the plate it follows that:

$$\overline{Nu_L} = \frac{4}{3}\left[\frac{-\phi'(0)}{\sqrt{2}}\right]Gr_L^{\frac{1}{4}} \tag{3.168}$$

$$\overline{Sh_L} = \frac{4}{3}\left[\frac{-\tilde{C}'(0)}{\sqrt{2}}\right]Gr_L^{\frac{1}{4}} \tag{3.169}$$

After setting L equal to $\frac{\pi D}{2}$ and performing some algebra, the mean Nusselt and Sherwood numbers are conveniently expressed as:

$$\overline{Nu_D} = 0.84216\left(-\phi'(0)Gr_D^{\frac{1}{4}}\right) \tag{3.170}$$

$$\overline{Sh_D} = 0.84216\left(-\tilde{C}'(0)Gr_D^{\frac{1}{4}}\right) \tag{3.171}$$

The definition of the heat transfer coefficient relates the heat transfer rate at the salt layer-solution interface to the mean heat transfer coefficient, $\overline{h}$, interfacial area between the salt layer and adjoining solution and temperature difference driving heat transfer as:

$$Q = \overline{h}\pi D_i L\left(1 + \frac{D_i}{4L}\right)(T_i - T_B) \tag{3.172}$$

Both the temperature and concentration differences across the boundary layer drive transport. The effect of buoyancy induced by the concentration difference on heat transfer is accounted for by using the Gebhart and Pera results to determine the heat transfer coefficient. It is implicitly assumed in Eq. 3.172 that the salt layer-solution interface and bulk solution are isothermal. The rate of heat transfer from the salt layer-solution interface to the solution is the sum of the power dissipated by the cartridge heater within the hot finger which is conducted through the salt layer (ηP) and the rate at which heat is absorbed or generated as a result of salt precipitation ($\frac{dm}{dt}H_{diss}$). A negative value for H_{diss} implies precipitation is endothermic. Thus Eq. 3.172 becomes:

$$\eta P + \frac{dm}{dt}H_{diss} = \overline{h}\pi D_i L\left(1 + \frac{D_i}{4L}\right)(T_i - T_B) \tag{3.173}$$

245

The preceding equation is consistent with Eq. 3.157. As per Chapter 2, η is about 90%. It is implicit in Eq. 3.173 that homogeneous nucleation does not occur in the bulk fluid, i.e., dissolved salt travels to the salt layer-solution interface exclusively by molecular diffusion where it subsequently nucleates. The nucleation model presented in the Chapter 5 provides strong evidence that homogeneous nucleation does not occur in the bulk solution during the sodium sulfate and potassium sulfate deposition experiments. Moreover, visual observation of deposition during the experiments supports the predictions of the nucleation model.

Determining $\bar{h}$ from Eq. 3.170 and substituting it into Eq. 3.172 results in:

$$\eta P + \frac{dm}{dt} H_{diss} = K_A D_i^{\frac{3}{4}} \left(1 + \frac{D_i}{4L}\right) (\beta(T_i - T_B) + 0.01\rho\beta^*(C_i - C_B))^{\frac{1}{4}} (T_i - T_B) \tag{3.174}$$

where

$$K_A = 0.84216 \left(-\phi'(0)\right) k\pi L \left[\frac{g}{\nu^2}\right]^{\frac{1}{4}} \tag{3.175}$$

Mass transfer calculations for pure natural convective transport may also be conveniently performed provided homogeneous nucleation does not occur in the bulk solution. The subsequent mass transfer model assumes that sodium sulfate and potassium sulfate travel to the salt layer-solution interface exclusively by molecular diffusion under the conditions investigated. For all mass transfer calculations the sticking efficiency of salt transported to the salt layer-solution interface is assumed to be perfect. It is further assumed that once salt adheres to the salt layer-solution interface it can not be subsequently removed by shear stresses present at the interface or any other mechanisms.

The definition of the mass transfer coefficient relates the mass transfer rate at the salt layer-solution interface, $\frac{dm}{dt}$, to the mean mass transfer coefficient, $\overline{h_m}$, interfacial area between the salt layer and adjoining solution and concentration difference driving mass transfer as:

$$\frac{dm}{dt} = 0.01\rho\overline{h}_m\pi D_i L \left(1 + \frac{D_i}{4L}\right) (C_B - C_i) \tag{3.176}$$

The preceding equation is consistent with Eq. 3.155. The rate of mass transfer of salt to the salt layer-solution

246

interface is expressed in kg/sec and the mean mass transfer coefficient in m/sec. Since concentrations in this dissertation are expressed in wt% units, the factor of 0.01ρ is needed to convert them to kg/m^3 units to make Eq. 3.176 dimensionally consistent. The quantity $(C_B - C_i)$ is the mass transfer driving force. Both the temperature and concentration differences across the boundary layer drive natural convective mass transfer. The temperature difference across the boundary layer is accounted for by the solubility relationship between temperature and concentration at the salt layer-solution interface and the application of the Gebhart and Pera results to determine the mass transfer coefficient. It is implicitly assumed in Eq. 3.176 that the salt concentration at the salt layer-solution interface and in the bulk solution are uniform. Determining $\bar{h}_m$ from Eq. 3.171 and substituting it into Eq. 3.176 results in:

$$\frac{dm}{dt} = K_B D_i^{\frac{3}{4}} \left(1 + \frac{D_i}{4L}\right) (\beta(T_i - T_B) + 0.01\rho\beta^*(C_i - C_B))^{\frac{1}{4}}(C_B - C_i) \tag{3.177}$$

where

$$K_B = (0.84216(-\tilde{C}'(0)))0.01\rho\mathfrak{D}_{AB}\pi L \left[\frac{g}{\nu^2}\right]^{\frac{1}{4}} \tag{3.178}$$

Some care must be exercised in the determination of values for the parameters K_A and K_B defined by Eqs. 3.175 and 3.178 respectively. Values of the thermodynamic and transport properties ρ, $\mathfrak{D}_{AB}$, k and ν needed to calculate K_A and K_B are provided in Section 4.4.1 for aqueous sodium sulfate and aqueous potassium sulfate solutions. Values of the thermodynamic and transport properties of the aqueous salt solutions do not change significantly as salt deposits on the hot finger; therefore, for the purposes of calculating K_A and K_B it is a good approximation to treat them as constants. The gravitational constant, g, is set equal to 9.81 m/sec^2 and the length of the hot finger L equals 2.76 cm. The parameters $-\phi'(0)$ and $-C''(0)$ are also required to calculate K_A and K_B and both are functions of Pr, Sc and $\tilde{N}$. Although Pr and Sc remain essentially constant during deposition, $\tilde{N}$ does not as discussed in Section 3.10. Table 3.14 shows the Gebhart and Pera results for $-\phi'(0)$ and $-C''(0)$ as a function of Sc, Pr and $\tilde{N}$. Representative values for Pr and Sc are provided in Section 4.4.1 and are about 1 and 4 respectively for aqueous sodium sulfate solutions at conditions of interest and 2 and 5 respectively for aqueous potassium sulfate solutions at

247

conditions of interest. The solution of the deposition rate formulation shows that $\tilde{N}$ is about 0.5-0.75 at the beginning of the sodium sulfate deposition experiments and decreases by about 15% during the course of a run. However, solution of the deposition rate formulation continues until $\tilde{N}$ equals zero, i.e., steady state conditions are established as per Eq. 3.162. Fortunately, inspection of Table 3.14 shows that both $-\phi'(0)$ and $-C'(0)$ are relatively weak functions $\tilde{N}$. For example, at Pr equal to 0.7 and Sc equal to 5.0 changing $\tilde{N}$ from -0.5 to 2 causes $-\phi'(0)$ and $-C'(0)$ to decrease by only 24.3% and 19.3% respectively. Thus for the purposes of calculating K_A and K_B, $-\phi'(0)$ and $-C'(0)$ are assumed to be constants. Characteristic values for Pr, Sc and $\tilde{N}$ are assumed to be 0.7, 5 and 0.5 respectively; therefore, $-\phi'(0)$ and $-C'(0)$ are set equal to 0.46880 and 1.11689 respectively as per Table 3.14. As discussed in Section 3.10, the species expansion coefficient for aqueous potassium sulfate solutions at conditions of interest is not directly available; consequently, the value of $\tilde{N}$ required to determine $-\phi'(0)$ and $-C'(0)$ using Table 3.14 may not be computed directly. Since $-\phi'(0)$ and $-C'(0)$ are both weak functions of $\tilde{N}$ this is not problematic. The results of the solution of the deposition rate formulation are presented in the context of a sensitivity analysis in which the importance of β^* is quantitatively examined.

The Effect of Deposition on the Mass Transfer Driving Force

Deposition depletes the salt concentration in the bulk solution; therefore, the (average) salt concentration in the bulk solution equals the salt concentration in the inlet stream only before power is supplied to the hot finger and after steady state conditions are established. Hence, it is inappropriate to set the mass transfer driving force equal to the difference between the concentration of salt in the solution entering the cell and the concentration of salt at the salt layer-solution interface. A method to account for the depletion of the mass transfer driving force as a consequence of deposition is developed in this section.

The trajectories of (T,C) states traversed through by the bulk solution and salt layer-solution interface as salt deposits on the hot finger are shown in Fig. 3-30. At the onset of deposition, the salt concentration in the bulk solution and temperature of the bulk solution are designated by C_{Bo} and T_{Bo} respectively. The definitions of the heat and mass transfer coefficients relate the heat flux and mass flux at the salt layer-solution interface to their respective driving forces as shown. The salt concentration in the bulk solution is rapidly

depleted because of deposition. Until the state designated by the subscript "e" is reached, the material capacitance of the test cell is relevant. The deposition rate is a decreasing function of time; consequently, the amount by which the bulk solution is depleted of salt because of deposition decreases with time. However, until state "e" is reached, the material capacitance of the cell is responsible for maintaining the concentration of salt in the bulk solution above the value it would reach if all of the salt deposited on the hot finger were to come from solution which flowed into the test cell after the hot finger was turned on. Thus a minimum in the concentration of salt in the bulk solution is reached at state "e" after which the material capacitance of the cell is unimportant. As shown later in this section, after one minute has elapsed the material capacitance of the test cell is no longer relevant. After the heater inside the hot finger is turned on, the temperature of the bulk solution within the cell drifts upward by about 3 $°C$ in 5 to 10 minutes and is stable thereafter. (Efforts to adjust the settings of the controllers used to send power to the cartridge heaters within the aluminum block surrounding the test cell and thus prevent the upward drift of the bulk solution temperature proved unsuccessful.) Thus the decrease in the concentration of salt in the bulk solution is accompanied by an increase in the bulk solution temperature and before one minute has elapsed the bulk condition reaches the state designated by the subscript "e" in Fig. 3-30. The deposition rate is a decreasing function of time; consequently, after the material capacitance of the cell is no longer important the salt concentration in the bulk solution starts increasing. The deposition rate is equal to zero at steady state conditions and, thus, the steady state salt concentration in the bulk solution equals the salt concentration in the bulk solution at the beginning of the run. Steady state conditions are designated by the subscript ∞ in Fig. 3-30. The steady state bulk solution temperature is reached substantially before deposition ceases as shown in Fig. 3-30.

All of the (T,C) states traversed through by the salt layer-solution interface are assumed to lie on the solubility line (or curve) as shown in Fig. 3-30. The heat flux at the salt layer-solution interface decreases with time because its area increases. Thus, the driving force required to remove the heat supplied to the hot finger decreases with time and the salt layer-solution interface condition moves towards the bulk solution condition. At steady state conditions the concentration is uniform across the boundary layer and, thus, the concentration of salt at the salt layer-solution interface equals the concentration of salt in the bulk solution as shown in Fig. 3-30. At steady state conditions there is heat transfer, but not mass transfer, from the salt

layer-solution interface to the bulk solution.

The depletion of the mass transfer driving force may be conveniently accounted for by assuming the bulk solution in the cell is perfectly well mixed, i.e., there are no spatial variations in salt concentration in the bulk solution. Then the salt concentration in the bulk solution equals the salt concentration in the solution exiting the test cell and may be determined from a material balance on the salt contained in the test cell. The material balance is given by Eq. 3.179 where the rate of change of the mass of salt contained in the bulk solution within the test cell is set equal to the difference between the net mass flow rate of salt into the cell and the deposition rate. In the material balance concentrations are expressed in wt% units and $\frac{dm}{dt}$ and $\dot{m}_{soln}$ are expressed in units of kg/s. (The mass flow rate of solution through the cell, $\dot{m}_{soln}$, decreases by less than 2% because of deposition as per Section 2.4.2 and it is treated as a constant in the material balance.)

$$\frac{\rho_{soln} V_c}{100} \frac{dC}{dt} = \dot{m}_{soln} \frac{(C_{in} - C_{out})}{100} - \frac{dm}{dt} \qquad (3.179)$$

The material capacitance of the test cell, $V\frac{dC}{dt}$, becomes unimportant after the solution initially contained in the test cell has been flushed out by incoming solution. The time for the solution initially contained in the test cell to be flushed out is denoted by τ_c and given by Eq. 3.180, where Q is the volumetric flow rate of solution through the test cell and V_c the volume of the test cell.

$$\tau_c = \frac{V_c \rho_{soln}}{\dot{m}_{soln}} \qquad (3.180)$$

After the material capacitance of the test cell becomes negligible, the concentration of salt in the solution exiting the cell may be determined by solving the material balance for C_{out} and is given by:

$$C_{out} = C_{in} - \frac{100}{\dot{m}_{soln}} \frac{dm}{dt} \qquad (3.181)$$

For $t > \tau_c$ it is assumed that the concentration of salt in the bulk solution (C_B) equals C_{out}, i.e., there are no spatial variations in concentration within the bulk solution.

The deposition experiments were run at solution mass flow rates of approximately 10 and 25 gm/min as per Table 2.12. For the purpose of calculating τ_c, the solution density in both the sodium sulfate and potassium sulfate deposition experiments may be assumed to equal 500 kg/m^3. The volume of the test cell is equal to approximately 17 ml (1 cubic inch) as per Chapter 2. Thus τ_c is about 0.8 and 0.3 minutes for the deposition experiments run at solution mass flow rates of 10 and 25 gm/min respectively. The duration of the deposition experiments ranged from about 6 to 12 minutes. Even when the flow rate of solution through the cell is about 10 gm/min and the duration of the run about 6 minutes, the time required to flush out the solution initially contained in the test cell is only about 13% of the run time.

The concentration of salt in the bulk solution equals the concentration of salt in the inlet stream (C_{in}) at the beginning of each run when the cartridge heater within the hot finger is turned on. After the solution initially contained in the test cell has been flushed out by incoming solution, it is assumed that the concentration of salt in the bulk solution equals the value of C_{out} given by Eq. 3.181. For the purpose of estimating the amount by which including the effect of the material capacitance of the test cell would change the mass of salt deposited on the hot finger before time τ_c, it is assumed that C_B varies linearly between C_{in} and C_{out} between $0 \leq t \leq \tau_c$. Thus

$$C_B = \frac{C_{in} + C_{out}}{2} \quad for \quad 0 \leq t \leq \tau_c \tag{3.182}$$

The deposition rate formulation assumes that $C_B = C_{out}$ for all t and neglects the material capacitance of the test cell. It also predicts that C_i and C_{out} are essentially constant for $0 \leq t \leq \tau_c$. Thus an estimate of the increase in the mass of salt on the hot finger at time equal to τ_c may be determined by setting the bulk solution concentration equal to $\frac{C_{in} + C_{out}}{2}$ instead of C_{out} for $0 \leq t \leq \tau_c$. Thus,

$$m(\tau_c)|_A \cong \frac{\frac{C_{in} + C_{out}}{2} - C_i}{C_{out} - C_i} m(\tau_c) \tag{3.183}$$

where $m(\tau_c)$ is the mass of salt on the hot finger at time τ_c predicted by the deposition rate formulation assuming the material capacitance of the cell is negligible and $m(\tau_c)|_A$ an estimation of the actual mass on the hot finger at time τ_c.

For example, the deposition rate formulation predicts that, for the set of runs in which a 4 wt% salt, aqueous sodium sulfate solution flows into the test cell at 10.47 gm/min, C_{out} and C_i are approximately 3.3 wt% and 1.8 wt% respectively for t $< \tau_c$ and m(τ_c) is about 0.05 g. The increase in $m(\tau_c)$ because of the material capacitance of the cell given by Eq. 3.183 for this set of conditions is 0.012 grams. Since the deposition rate formulation predicts that about 0.50 grams of salt will be deposited on the hot finger during the entire course of a run at these conditions, inclusion of the material capacitance of the test cell increases the mass of salt deposited on the hot finger over the course of a run by only about 2%. Moreover, the importance of the material capacitance of the test cell is about the same for all the conditions investigated and, thus, is neglected in the deposition rate formulation. Hence the bulk salt concentration in Eqs. 3.174 and 3.177 is set equal to the concentration of salt in the stream exiting the test cell given by the material balance and they become:

$$\eta P + \frac{dm}{dt} H_{diss} = K_A D_i^{\frac{3}{4}} \left(1 + \frac{D_i}{4L}\right) \left[\beta(T_i - T_B) + 0.01\rho\beta^* \left(C_i - C_{in} + \frac{100\frac{dm}{dt}}{\dot{m}_{soln}}\right)\right]^{\frac{1}{4}} (T_i - T_B) \quad (3.184)$$

$$\frac{dm}{dt} = K_B D_i^{\frac{3}{4}} \left(1 + \frac{D_i}{4L}\right) \left[\beta(T_i - T_B) + 0.01\rho\beta^* \left(C_i - C_{in} + \frac{100\frac{dm}{dt}}{\dot{m}_{soln}}\right)\right]^{\frac{1}{4}} \left(C_{in} - \frac{100\frac{dm}{dt}}{\dot{m}_{soln}} - C_i\right) \quad (3.185)$$

Relationship Between m(t) and D$_i$(t)

Calculation of the transient deposition rate, requires an expression for the diameter of the salt layer-solution interface as a function of the mass of salt deposited on the hot finger. This can be determined from the experimentally measured porosity in the salt layer on the hot finger and the density of the solid salts which precipitate from solution. As per Chapter 2, the porosity, ϕ, is defined as the void volume within the porous salt layer divided by the total volume of the salt including voids. Thus, denoting the true salt volume, the total volume of salt including voids, and the porosity by V_s, V_T and ϕ respectively it follows that:

$$\phi = \frac{V_T - V_s}{V_T} \quad (3.186)$$

Denoting the length of the protruding portion of the hot finger by L and the diameter of the hot finger at time equal to zero by D_{io}, the total volume occupied by the salt including voids on the hot finger is given by Eq. 3.187.

$$V_T = \frac{\pi(D_i^2 - D_{io}^2)L}{4} \tag{3.187}$$

(The length of the hot finger increases slightly as salt deposits on its tip, but is treated as constant in the total volume of salt including voids expression.) Noting that the mass of salt deposited, m, is equal to $V_S \rho_s$, where ρ_s is the density of solid salt, Eq. 3.186 can be expressed as:

$$D_i = \sqrt{D_{io}^2 + \frac{4m}{\rho_s \pi L(1 - \phi)}} \tag{3.188}$$

Solubility Relationships

The salt layer-solution interface is assumed to be at saturation conditions; therefore, at the salt layer-solution interface concentration and temperature are related by the appropriate solubility curve. Since the pressure is essentially constant in the experiments, the solubility relationship is expressed as:

$$C_i = C_i(T_i) \tag{3.189}$$

For the sodium sulfate-water system, the solubility relationship is defined by Eqn. 3.190 as shown in Fig. 2-1.

$$T_i = 0.06380wt\%^2 - 3.960wt\% + 374.8 \tag{3.190}$$

C_i as a function of T_i is determined by applying the quadratic formula to Eq. 3.190 and discarding the physically unrealistic root. Thus, for the sodium sulfate-water system:

$$C_i = A_1 - \sqrt{B_1 + C_1 T_i} \tag{3.191}$$

where A_1, B_1 and C_1 are 31.034, -4911.469 and 15.674 respectively. For the potassium sulfate-water system at all salt concentrations of interest to this study and the sodium sulfate-water system at salt concentrations less than about 7 wt%, C_i and T_i are linearly related as shown in Figs. 2-1 and 2-2. The resulting solubility relationship is described by Eq. 3.192 where A_2 and B_2 are 99.65 and 0.2658 respectively for the sodium sulfate-water system and 258.39 and 0.6711 respectively for the potassium sulfate-water system.

$$C_i = A_2 - B_2 T_i \qquad (3.192)$$

If the temperature of the salt layer-solution interface exceeds the temperature corresponding to zero salt solubility, the solubility relationships yield a concentration of less than 0 wt%. Obviously, this is physically unrealistic and, thus, if it occurs during the solution of the deposition rate formulation the salt layer-solution interface concentration is set equal to zero.

Overall Formulation

Equations 3.193 through 3.195 govern heat transfer, mass transfer and the relationship between the salt layer-solution interface diameter and the mass of salt deposited on the hot finger respectively. This equation set is first order in m(t) and zero order in all other variables. The single initial condition required to solve the equation set is that the mass of salt deposited on the hot finger equals zero at time equals zero. Equivalently, at time equals zero, the diameter of the salt layer solution interface is equal to the diameter of the hot finger (D_{io}) as stated by Eq. 3.196. K_A and K_B are defined by Eqs. 3.175 and 3.178 respectively. All of the variables in this system of equations are treated as constants, except the deposition rate $(\frac{dm}{dt})$, salt layer-solution interface temperature, diameter of the salt layer-solution interface and the mass of salt deposited on the hot finger. Equations 3.193 through 3.196 are subsequently referred to as the deposition rate formulation. It is noted that the deposition rate formulation does not contain any adjustable parameters.

$$\eta P + \frac{dm}{dt}H_{diss} = K_A D_i^{\frac{3}{4}}\left(1 + \frac{D_i}{4L}\right)\left[\beta(T_i - T_B) + 0.01\rho\beta^*\left(C_i(T_i) - C_{in} + \frac{100\frac{dm}{dt}}{\dot{m}_{soln}}\right)\right]^{\frac{1}{4}} \quad (3.193)$$

$$(T_i - T_B)$$

$$\frac{dm}{dt} = K_B D_i^{\frac{3}{4}}\left(1 + \frac{D_i}{4L}\right)\left[\beta(T_i - T_B) + 0.01\rho\beta^*\left(C_i(T_i) - C_{in} + \frac{100\frac{dm}{dt}}{\dot{m}_{soln}}\right)\right]^{\frac{1}{4}} \quad (3.194)$$

$$\left(C_{in} - \frac{100\frac{dm}{dt}}{\dot{m}_{soln}} - C_i(T_i)\right)$$

$$D_i = \sqrt{D_{io}^2 + \frac{4m}{\rho_s \pi L(1 - \phi)}} \quad (3.195)$$

$$D_i = D_{io} \quad \text{at} \quad t = 0 \quad (3.196)$$

3.11.3 Asymptotic Behavior

At steady state conditions, the salt layer-solution interface temperature approaches the solubility temperature corresponding to the concentration of salt in the solution entering the test cell. Thus at steady state conditions the salt concentration at the salt layer-solution interface approaches the salt concentration in the bulk solution and the deposition rate approaches zero. At steady state conditions, the power supplied to the hot finger is dissipated by natural convection driven solely by the temperature difference between the salt layer-solution interface and bulk solution and Eqn. 3.193 becomes:

$$\eta P = K_A D_{i\infty}^{\frac{3}{4}}\left(1 + \frac{D_{i\infty}}{4L}\right)\beta^{\frac{1}{4}}(T_s - T_B)^{\frac{5}{4}} \quad (3.197)$$

The salt layer-solution interface diameter for which the rate of mass transfer equals zero can be determined from Eqn. 3.197 and is denoted by $D_{i\infty}$. The mass of salt on the hot finger at steady state conditions, m_∞, can be determined from $D_{i\infty}$ using Eq. 3.188, i.e.,

$$m_\infty = \frac{\left(D_{i\infty}^2 - D_{io}^2\right)\rho_s \pi L(1 - \phi)}{4} \quad (3.198)$$

All the thermodynamic and transport properties influence K_A because it is a function of $-\phi'(0)$ which, in

turn, depends on all the solution properties, albeit weakly on some. The mass of salt deposited on the hot finger and salt layer-solution interface diameter at steady state conditions are functions of K_A and, hence, all the solution properties. Inspection of the relevant equations shows that m_∞ is influenced most strongly by P, k, β, T_s, T_B, ρ_s and ϕ. The effects of T_B and ϕ on the steady state value of the mass of salt deposited on the hot finger are very important and, thus, are quantitatively examined in the sensitivity analysis in Section 4.4.2. The time required to establish steady state conditions does not depend on the relevant variables in the same manner as the mass/volume of salt on the hot finger at steady state conditions. For example, the mass of salt on the hot finger at steady state conditions is a very weak function of the binary molecular diffusion coefficient, but doubling the binary diffusion coefficient has a significant effect on the time required to achieve steady state conditions as shown in Section 4.4.2.

Chapter 4

Analyses of Experimental Data

4.1   Introduction

The results of the experiments are analyzed in this section. First, the temperature differences measured between the surface of the hot finger and bulk fluid in the pure water heat transfer experiments are compared to those predicted by standard heat transfer correlations. Then the solubility data collected for this dissertation are compared to solubility data available in the literature. Next, the deposition rate formulation developed in the previous chapter is solved at the conditions of the deposition rate experiments and the results are compared against the experimental data. Finally, transport inside the porous salt layer is examined to explain the discrepancy between the predicted and measured deposition rates at certain operating conditions.

4.2   Analysis of Pure Water Heat Transfer experiments

The results of the pure water heat transfer experiments which were presented in Chapter 2 are compared to the predictions of simple heat transfer correlations in this section. The correlations provided by Morgan [64] and Hilpert [38] for natural and forced convective heat transfer respectively from/to a cylinder are used to determine the required Nusselt numbers. Morgan provides the following expression for the mean Nusselt

Ra_D	C_1	n
10^{-10}-10^{-2}	0.675	0.058
10^{-2}-10^2	1.02	0.148
10^2-10^4	0.850	0.188
10^4-10^7	0.480	0.250
10^7-10^{12}	0.125	0.333

Table 4.1: Constants of Eq. 4.1 for natural convective heat transfer from/to a long, horizontal, isothermal cylinder [64].

Re_D	C_2	m
0.4-4	0.989	0.330
4-40	0.911	0.385
40-4000	0.683	0.466
4000-40000	0.193	0.618
40000-400000	0.027	0.805

Table 4.2: Constants of Eq. 4.2 for the cylinder in cross flow [38, 44].

number for natural convective heat transfer from/to a long, horizontal, isothermal cylinder:

$$\overline{Nu_D} = C_1 Ra_D^n \tag{4.1}$$

The constants C and n in the Morgan expression are a function of the Rayleigh number based on the diameter of the cylinder and given in Table 4.1. Hilpert [38] provides the following empirical expression for the mean Nusselt number for forced convective heat transfer from/to a cylinder in cross flow:

$$\overline{Nu_D} = C_2 Re_D^m Pr^{\frac{1}{3}} \tag{4.2}$$

The constants C and m are functions of the Reynolds number characterizing the flow as per Table 4.2. Following Incropera and Dewitt [41], the effective Nusselt numbers accounting for the combined free and forced convective transport around a cylinder are determined from Eq. 4.3. In Eq. 4.3, Nu is the Nusselt number resulting, from the combined effects of free and forced convection, Nu_F is the Nusselt number for pure forced convection and Nu_N is the Nusselt number for pure natural convection. The buoyancy induced free convection flow and imposed cross flow are both vertically upward; therefore, free convection is enhanced

by forced convection, albeit only slightly.

$$Nu^3 = Nu_F^3 + Nu_N^3 \qquad (4.3)$$

The results of the first pure water heat transfer experiment (Run A) are given in Table 2.2 and plotted in Fig. 2-14. Forced convective cross flow was not present in this experiment, i.e., the pump was turned off, and the experiment was run at atmospheric pressure. The Rayleigh number which characterizes the natural convection around the hot finger is about $1.5*10^5$ and the corresponding Nusselt number according to the Morgan expression is 9.4. It follows that the predicted temperature difference between the surface of the hot finger and bulk solution equals 20.0 $°C$ assuming all of the heat supplied to the hot finger is conducted through the protruding portion of the hot finger and into the water. (Conduction losses should not be significant for the experiments run near room temperature; therefore, "η" is approximately unity.) The measured temperature difference between the hot finger surface and bulk solution ranges from about 20 to 21 $°C$; therefore, theory and experiment are consistent.

The results of the second pure water heat transfer experiment (Run B) are given in Table 2.3 and plotted in Fig. 2-15. The operating conditions for this experiment were the same as in Run A, except that water was pumped through the system at 40 ml/min. The Nusselt number characterizing natural convection for this experiment is approximately the same as that for Run A, i.e., about 9.4. The Reynolds number, based on the diameter of the hot finger, is estimated to equal about 24 from Eq. 3.102. The Nusselt number, based on the Hilpert correlation, characterizing forced convection at this Reynolds number is 4.6. Eq. 4.3 predicts the Nusselt number characterizing combined free and forced convection around the hot finger is only 4% larger than that for free convection alone. The temperature differences measured between the hot finger surface and bulk solution were essentially the same in Run A and Run B as per Tables 2.2 and 2.3. This is consistent with the theoretical prediction that forced convection is too weak to have any significant influence on heat transfer.

Pure water heat transfer experiments were also performed at conditions typical of the deposition experiments. In Run C, the bulk temperature of the solution in the test cell was maintained at approximately 320

259

$^{\circ}C$ and the pump was turned off. The pressure in the system was maintained near 250 bar. The results of this experiment are provided in Table 2.5. It was assumed that 10.0 of the 10.61 Watts of power supplied to the cartridge heater inside of the hot finger were dissipated by natural convection along the surface of the protruding portion of it based on the analysis in Section 2.4.2. The Morgan correlation predicts a temperature difference of 11 $^{\circ}C$ between the hot finger surface and bulk solution at the operating conditions of Run C. The measured temperature difference is 13.5 $^{\circ}C$, i.e., almost 25% higher.

The operating conditions for Run 34 were the same as for Run C, except that pure water was pumped through the system at 10.1 g/min. The Reynolds number, based on the diameter of the hot finger, was estimated to be about 72. Forced convection was predicted to increase the heat transfer coefficient by only 0.5% at these conditions according to Eq. 4.3. The temperature difference between the hot finger surface and bulk solution dropped to about 13.0, i.e., by about 4%. This is more than was expected, but not large enough to cause concern.

In runs C and 34, the temperature difference between the hot finger surface and bulk solution was about 2 $^{\circ}C$ higher than that predicted by the correlations. The hot finger surface temperature and bulk solution temperature before the cartridge heater inside of the hot finger was turned on were measured in two of the pure water heat transfer experiments run at conditions typical of the solubility and deposition rate experiments, namely Run C and Run D. The average hot finger surface temperature exceeded the bulk solution temperature by 2.8 and 2.5 $^{\circ}C$ respectively in Run C and Run D before the hot finger was turned on. This is consistent with the fin analysis performed in Section 2.4.2 to estimate the potential error in the bulk temperature measurement. Thus, perhaps, the reason that the correlations predicted a slightly lower wall-to-bulk temperature difference than measured in Runs C and 34 was because the bulk temperature temperature measurement was slightly high. In conclusion, the temperature differences measured between the surface of the hot finger and the bulk solution in the pure water heat transfer experiments are reasonably consistent with those predicted from standard heat transfer correlations. This validates the heat transfer characteristics of the test cell and shows that natural convection dominates transport in the experiments.

4.3 Solubility Measurements

Solubility data for sodium sulfate and potassium sulfate in water at elevated temperatures and 250 bar was presented in Chapter 2. In this section, solubility data at similar conditions from other investigations is provided. A critical evaluation of the accuracy of the existing solubility data and the many different methods used to acquire them for these two systems is not undertaken. However, the results of the various studies are compared.

A number of investigators have measured the solubility of sodium sulfate in water at pressures in the vicinity of 250 bar. Results from studies at conditions relevant to this dissertation are provided in Fig. 4-1. It is noted, however, that a considerable amount of solubility data at 250 bar exists for sodium sulfate concentrations below 1 wt%, but is not shown in Fig. 4-1. Moreover, Teshima et al. showed that the solubility concentration of sodium sulfate drops from about 0.1 to 0.001 wt% over about a 5 $°C$ temperature interval near the pseudocritical temperature of pure water at 250 bar (385 $°C$). The reader interested in this region is referred to the recent Master's Thesis by Teshima [85]. Ravich and Borovaya [76] obtained solubility data for the Na_2SO_4-H_2O system at pressures ranging from 110 to 1200 bar and temperatures ranging from 320 to 370 $°C$. Data were not obtained exactly at 250 bar in the Ravich and Borovaya study, however, interpolations of their data to 250 bar were performed by DiPippo [24]. The results of DiPippo's interpolations to 250 bar are shown in Fig. 4-1. Using the same apparatus in our SCWO laboratory at MIT, Armellini [4] and, subsequently, DiPippo [24] obtained solubility data for the Na_2SO_4-H_2O system at 250 bar. Their results are also shown in Fig. 4-1. Furthermore, as discussed in some detail in Chapter 1, the SCWO group at the University of British Columbia recently acquired twenty-two solubility data points in the Na_2SO_4-H_2O system at 250 bar [85]. Their solubility data were accurately fit to three curves. Each curve applies to a different concentration/temperature range and that which applies to sodium sulfate concentrations ranging from 0.0732 to 10 wt% at 250 bar is:

$$T = 337.70602 + 49.11281 exp\left(\frac{-C}{3.49612}\right) \qquad (4.4)$$

where T and C are in degrees centigrade and wt% sodium sulfate respectively. This result is also plotted

in Fig. 4-1. Finally, for selected temperatures between 350 and 375 °C at pressures of 191, 231 and 305

bar Shvedov and Tremaine [79] recently obtained solubility data in the Na_2SO_4-H_2O system as well. The

following expression accurately represented all of the Shvedov and Tremaine data:

$$ln(x_A) = -10.47 - \frac{27550}{T} + \frac{4805}{T}ln(\rho^*),$$ (4.5)

where x_A is the mole fraction of sodium sulfate, T is temperature in degrees Kelvin and ρ^* is the density of

pure water in kg/m^3 at the temperature and pressure of interest. The solubility of sodium sulfate in water

at 250 bar predicted by Shvedov and Tremaine's expression is also shown in Fig. 4-1.

Overall the sodium sulfate solubility data from the six existing studies are reasonably consistent. The

Tremaine expression appears to be too low by about 10 °C at concentrations larger than 15 wt%. Also,

it appears that the Armellini solubility datum at 3 wt% sodium sulfate might be high by a few degrees.

Aside from these two discrepancies and ignoring the Shvedov and Tremaine expression for sodium sulfate

concentrations above 6 wt%, the discrepancies between the 6 studies do not exceed about 5 °C. It is noted,

however, that in the context of the deposition experiments conducted for this dissertation 5 °C is very

significant. However, as per Fig. 2-1, the solubility curve used to select the operating conditions in the

deposition experiments and subsequently analyze the results from them was consistent with the solubility

measurements in this dissertation.

Benrath et al. [10] measured the solubility of potassium sulfate in water for temperatures ranging from

179 to 357 °C. However, apparently no other investigators have measured the solubility of potassium sulfate

in water at the elevated temperatures of interest to this dissertation. Benrath et al. acquired their solubility

data by heating a constant volume mixture of salt and water enclosed inside a high-melting point glass tube

and visually observed at what temperature all of the potassium sulfate dissolved. However, pressure could

not be measured. The Benrath results at temperatures between 310 and 357 °C are plotted along with

the potassium sulfate solubility data obtained for this dissertation at 250 bar in Fig. 4-2. The solubility

temperature measured at 2, 4, 6 and 8 wt% potassium sulfate concentrations exceeded what the linear fit to

the Benrath et al. data predicts by about 20-25 °C. However, it is very possible that 250 bar substantially
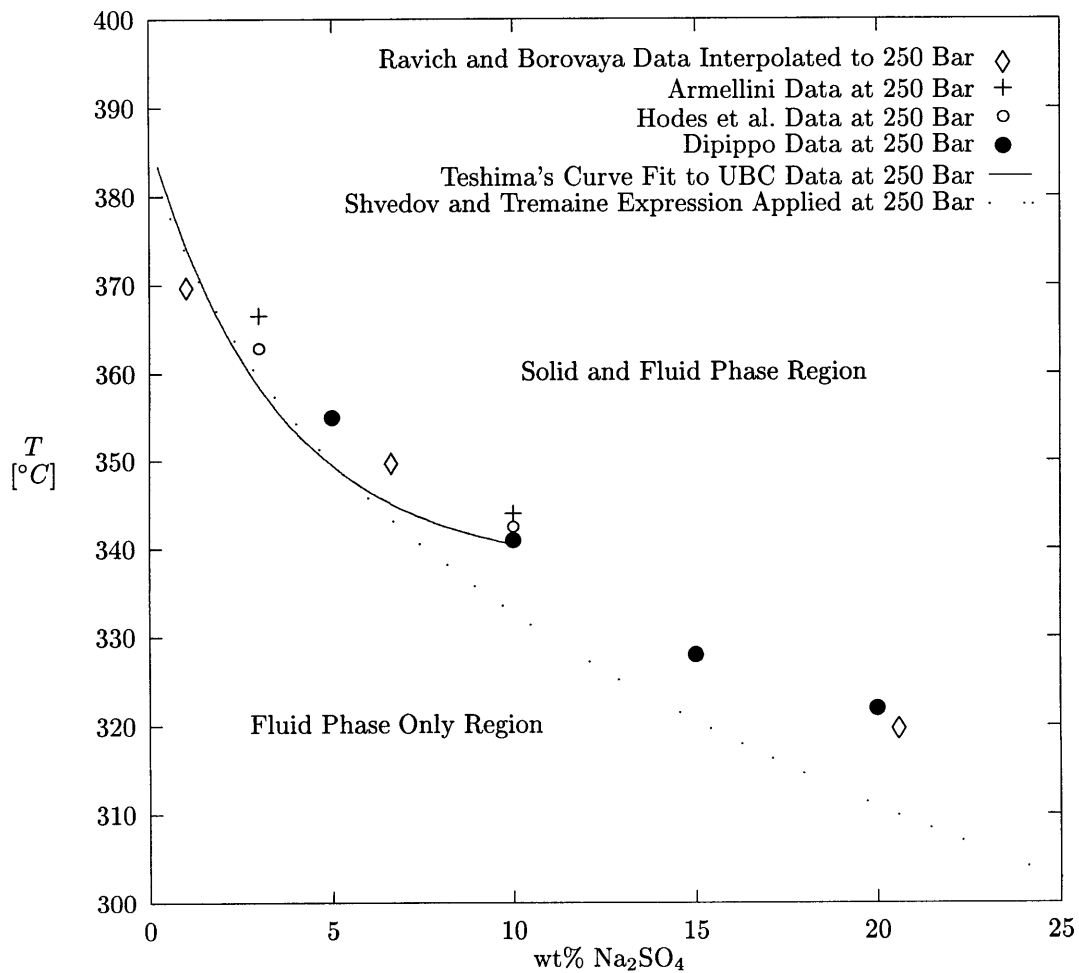
Figure 4-1: Plot of sodium sulfate in water solubility data at 250 bar based on data from the Ravich and Borovaya study [76], Armellini dissertation [4], this dissertation and DiPippo dissertation [24]. The curve fit to the Teshima solubility data [85] and empirical expression proposed by Shvedov and Tremaine [79] are also provided.
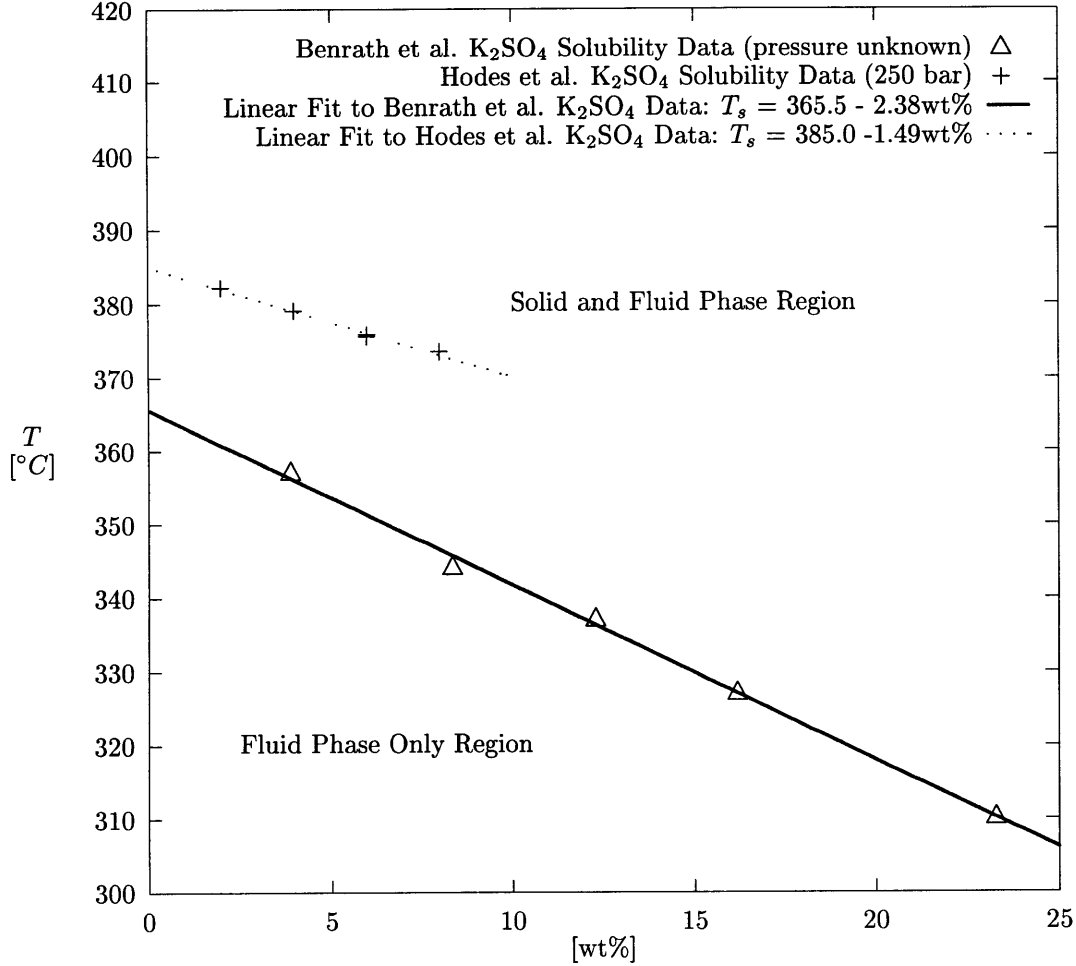
Figure 4-2: Plot of potassium sulfate in water solubility data from this dissertation and the Benrath et al. [10] study.

exceeds the pressures in the sample tubes used by Benrath et al. Since the density of water increases with pressure and the static dielectric constant of water increases with density one expects solutions at higher pressures to have higher solubility temperatures for the same potassium sulfate concentration.

4.4 Solution of Deposition Rate Formulation

The deposition rate formulation as given by Eqs. 3.193 through 3.196 is solved by numerically marching forward in time using a FORTRAN 77 program. After K_A and K_B have been determined, the numerical

solution procedure begins. At time equal to zero the diameter of the salt layer-solution interface is set equal to the diameter of the hot finger D_{io}. Next, Eqs. 3.193 and 3.194 are solved simultaneously for $\frac{dm}{dt}$ and T_i by the Newton-Raphson method using a subroutine written by Press et al. [74]. The Newton-Raphson method is applicable for the solution of systems of N nonlinear equations of the form:

$$F_i(x_1, x_2, ..., x_N) = 0 \qquad i = 1, 2, ..., N. \tag{4.6}$$

Denoting the entire vector of variables by $\mathbf{x}$ and the entire vector of functions by $\mathbf{F}$ it follows from a Taylor series expansion that:

$$F_i(\mathbf{x} + \delta\mathbf{x}) = F_i(\mathbf{x}) + \sum_{j=1}^{N} \frac{\partial F_i}{\partial x_j} \delta x_j + O(\delta\mathbf{x}^2) \tag{4.7}$$

The matrix of partial derivatives appearing in Eq. 4.7 is the Jacobian matrix $\mathbf{J}$, i.e.,

$$J_{i,j} \equiv \frac{\partial F_i}{\partial x_j} \tag{4.8}$$

Thus in matrix notation Eq. 4.7 becomes:

$$\mathbf{F}(\mathbf{x} + \delta\mathbf{x}) = \mathbf{F}(\mathbf{x}) + \mathbf{J} \cdot \delta\mathbf{x} + O(\delta\mathbf{x}^2) \tag{4.9}$$

Neglecting terms of second order and higher in Eq. 4.9 and setting $\mathbf{F}(\mathbf{x} + \delta\mathbf{x})$ equal to zero results in a set of linear equations for corrections $\delta\mathbf{x}$ that simultaneously move each function closer to zero provided the initial guess of the vector $\mathbf{x}$ is one which will cause the method to converge. Thus the corrections $\delta\mathbf{x}$ are obtained by solving Eq. 4.10.

$$\mathbf{J} \cdot \delta\mathbf{x} = -\mathbf{F} \tag{4.10}$$

The corrections are added to the solution vector $\mathbf{x}$ as per Eq. 4.11 and iterations are performed until the required level of accuracy is achieved.

$$\mathbf{x}_{new} = \mathbf{x}_{old} + \delta\mathbf{x} \qquad (4.11)$$

Convergence is assumed if either the summed absolute variable increments are less than the tolerance "tolx" or the summed absolute function values are less than the tolerance "tolf". Mathematically stated, the convergence criteria for the case at hand are:

$$\left| \frac{dm}{dt}(i) - \frac{dm}{dt}(i-1) \right| + |T_i(i) - T_i(i-1)| < \text{tolx} \qquad (4.12)$$

$$\left| f\left(\frac{dm}{dt}, T_i \right) \right| + \left| g\left(\frac{dm}{dt}, T_i \right) \right| < \text{tolf} \qquad (4.13)$$

where the functions $f\left(\frac{dm}{dt}, T_i \right)$ and $g\left(\frac{dm}{dt}, T_i \right)$ are Eqs. 3.193 and 3.194 respectively expressed in a form suitable to the Newton-Raphson method. For the purpose of computing the deposition rate both tolx and tolf are set equal to 0.0001. After dm/dt at time (t) has been computed the mass of salt on the hot finger at time (t + Δt) is computed from Eq. 4.14

$$m(t + \Delta t) = m(t) + \frac{dm}{dt}\Delta t \qquad (4.14)$$

For the sodium sulfate-water system at 250 bar, Eq. 3.191 is used to express C_i in terms of T_i. Expressed

266

in a form suitable to solution by the Newton-Raphson Method, Eqs. 3.193 and 3.194 become:

$$f\left(\frac{dm}{dt}, T_i\right) = \eta P + \frac{dm}{dt} H_{diss} - K_A D_i^{\frac{3}{4}}\left(1 + \frac{D_i}{4L}\right)$$

$$\left[\beta(T_i - T_B) + 0.01\rho\beta^*\left(A_1 - \sqrt{B_1 + C_1 T_i} - C_{in} + \frac{100\frac{dm}{dt}}{\dot{m}_{soln}}\right)\right]^{\frac{1}{4}}(T_i - T_B) = 0 \tag{4.15}$$

$$g\left(\frac{dm}{dt}, T_i\right) = \frac{dm}{dt} - K_B D_i^{\frac{3}{4}}\left(1 + \frac{D_i}{4L}\right)$$

$$\left[\beta(T_i - T_B) + 0.01\rho\beta^*\left(A_1 - \sqrt{B_1 + C_1 T_i} - C_{in} + \frac{100\frac{dm}{dt}}{\dot{m}_{soln}}\right)\right]^{\frac{1}{4}}$$

$$\left(C_{in} - \frac{100\frac{dm}{dt}}{\dot{m}_{soln}} - A_1 + \sqrt{B_1 + C_1 T_i}\right) = 0 \tag{4.16}$$

The Jacobian matrix for these two equations is given by Eqs. 4.17 through 4.20.

$$J_{11} = H_{diss} - \frac{0.25\rho\beta^*}{\dot{m}_{soln}} K_A D_i^{\frac{3}{4}} \left(1 + \frac{D_i}{4L}\right)$$ (4.17)

$$\left[\beta(T_i - T_B) + 0.01\rho\beta^* \left(A_1 - \sqrt{B_1 + C_1 T_i} - C_{in} + \frac{100\frac{dm}{dt}}{\dot{m}_{soln}}\right)\right]^{-\frac{3}{4}} (T_i - T_B)$$

$$J_{12} = -K_A D_i^{\frac{3}{4}} \left(1 + \frac{D_i}{4L}\right) \left\{ \left[\beta(T_i - T_B) + 0.01\rho\beta^* \left(A_1 - \sqrt{B_1 + C_1 T_i} - C_{in} + \frac{100\frac{dm}{dt}}{\dot{m}_{soln}}\right)\right]^{\frac{1}{4}} \right.$$ (4.18)

$$+ \frac{T_i - T_B}{4} \left[\beta(T_i - T_B) + 0.01\rho\beta^* \left(A_1 - \sqrt{B_1 + C_1 T_i} - C_{in} + \frac{100\frac{dm}{dt}}{\dot{m}_{soln}}\right)\right]^{-\frac{3}{4}}$$

$$\left. \left[\beta - \frac{0.01\rho C_1 \beta^*}{2\sqrt{B_1 + C_1 T_i}}\right] \right\}$$

$$J_{21} = 1 - K_B D_i^{\frac{3}{4}} \left(1 + \frac{D_i}{4L}\right) \left\{ \frac{-100}{\dot{m}_{soln}} \right.$$ (4.19)

$$\left[\beta(T_i - T_B) + 0.01\rho\beta^* \left(A_1 - \sqrt{B_1 + C_1 T_i} - C_{in} + \frac{100\frac{dm}{dt}}{\dot{m}_{soln}}\right)\right]^{\frac{1}{4}}$$

$$+ \frac{0.25\rho\beta^*}{\dot{m}_{soln}} \left[\beta(T_i - T_B) + 0.01\rho\beta^* \left(A_1 - \sqrt{B_1 + C_1 T_i} - C_{in} + \frac{100\frac{dm}{dt}}{\dot{m}_{soln}}\right)\right]^{-\frac{3}{4}}$$

$$\left. \left(C_{in} - \frac{100\frac{dm}{dt}}{\dot{m}_{soln}} - A_1 + \sqrt{B_1 + C_1 T_i}\right) \right\}$$

$$J_{22} = -K_B D_i^{\frac{3}{4}} \left(1 + \frac{D_i}{4L}\right) \left\{ \left[\beta(T_i - T_B) + 0.01\rho\beta^* \left(A_1 - \sqrt{B_1 + C_1 T_i} - C_{in} + \frac{100\frac{dm}{dt}}{\dot{m}_{soln}}\right)\right]^{\frac{1}{4}} \right.$$ (4.20)

$$\left(\frac{C_1}{2\sqrt{B_1 + C_1 T_i}}\right) + \frac{1}{4}\left(\beta - \frac{0.01\rho C_1 \beta^*}{2\sqrt{B_1 + C_1 T_i}}\right)$$

$$\left[\beta(T_i - T_B) + 0.01\rho\beta^* \left(A_1 - \sqrt{B_1 + C_1 T_i} - C_{in} + \frac{100\frac{dm}{dt}}{\dot{m}_{soln}}\right)\right]^{-\frac{3}{4}}$$

$$\left. \left(C_{in} - \frac{100\frac{dm}{dt}}{\dot{m}_{soln}} - A_1 + \sqrt{B_1 + C_1 T_i}\right) \right\}$$

Setting

$$P_A = D_i^{\frac{3}{4}} \left(1 + \frac{D_i}{4L}\right)$$ (4.21)

$$P_B = \left[\beta(T_i - T_B) + 0.01\rho\beta^* \left(A_1 - \sqrt{B_1 + C_1 T_i} - C_{in} + \frac{100\frac{dm}{dt}}{\dot{m}_{soln}}\right)\right],$$ (4.22)

Eqs. 4.16 and 4.17 and the corresponding Jacobian matrix can be expressed more succinctly as:

$$f\left(\frac{dm}{dt}, T_i\right) = \eta P + \frac{dm}{dt}H_{diss} - K_A P_A P_B^{\frac{1}{4}}(T_i - T_B) = 0 \tag{4.23}$$

$$g\left(\frac{dm}{dt}, T_i\right) = \frac{dm}{dt} - K_B P_A P_B^{\frac{1}{4}}\left(C_{in} - \frac{100\frac{dm}{dt}}{\dot{m}_{soln}} - A_1 + \sqrt{B_1 + C_1 T_i}\right) = 0 \tag{4.24}$$

$$J_{11} = H_{diss} - \frac{0.25\rho\beta^*}{\dot{m}_{soln}}K_A P_A P_B^{-\frac{3}{4}}(T_i - T_B) \tag{4.25}$$

$$J_{12} = -K_A P_A\left\{P_B^{\frac{1}{4}} + \frac{T_i - T_B}{4}P_B^{-\frac{3}{4}}\left[\beta - \frac{0.01\rho C_1\beta^*}{2\sqrt{B_1 + C_1 T_i}}\right]\right\} \tag{4.26}$$

$$J_{21} = 1 - K_B P_A\left\{\frac{-100}{\dot{m}_{soln}}P_B^{\frac{1}{4}} + \frac{0.25\rho\beta^*}{\dot{m}_{soln}}P_B^{-\frac{3}{4}}\left(C_{in} - \frac{100\frac{dm}{dt}}{\dot{m}_{soln}} - A_1 + \sqrt{B_1 + C_1 T_i}\right)\right\} \tag{4.27}$$

$$J_{22} = -K_B P_A\left\{P_B^{\frac{1}{4}}\left(\frac{C_1}{2\sqrt{B_1 + C_1 T_i}}\right)\right.$$
$$\left. + \frac{1}{4}\left(\beta - \frac{0.01\rho C_1\beta^*}{2\sqrt{B_1 + C_1 T_i}}\right)P_B^{-\frac{3}{4}}\left(C_{in} - \frac{100\frac{dm}{dt}}{\dot{m}_{soln}} - A_1 + \sqrt{B_1 + C_1 T_i}\right)\right\} \tag{4.28}$$

For the potassium sulfate-water system at 250 bar, the solubility relationship given by Eq. 3.192 is used to express C_i in terms of T_i. Expressed in a form suitable to solution by the Newton-Raphson Method, Eqs. 3.193 and 3.194 become:

$$f\left(\frac{dm}{dt}, T_i\right) = \eta P + \frac{dm}{dt}H_{diss} - K_A D_i^{\frac{3}{4}}\left(1 + \frac{D_i}{4L}\right) \tag{4.29}$$
$$\left[\beta(T_i - T_B) + 0.01\rho\beta^*\left(A_2 - B_2 T_i - C_{in} + \frac{100\frac{dm}{dt}}{\dot{m}_{soln}}\right)\right]^{\frac{1}{4}}(T_i - T_B) = 0$$

$$g\left(\frac{dm}{dt}, T_i\right) = \frac{dm}{dt} - K_B D_i^{\frac{3}{4}}\left(1 + \frac{D_i}{4L}\right) \tag{4.30}$$
$$\left[\beta(T_i - T_B) + 0.01\rho\beta^*\left(A_2 - B_2 T_i - C_{in} + \frac{100\frac{dm}{dt}}{\dot{m}_{soln}}\right)\right]^{\frac{1}{4}}$$
$$\left(C_{in} - \frac{100\frac{dm}{dt}}{\dot{m}_{soln}} - A_2 + B_2 T_i\right) = 0$$

269

The Jacobian matrix for the foregoing equations is:

$$J_{11} = H_{diss} - \frac{0.25\rho\beta^*}{\dot{m}_{soln}} K_A D_i^{\frac{3}{4}} \left(1 + \frac{D_i}{4L}\right) \tag{4.31}$$

$$\left[\beta(T_i - T_B) + 0.01\rho\beta^* \left(A_2 - B_2 T_i - C_{in} + \frac{100\frac{dm}{dt}}{\dot{m}_{soln}}\right)\right]^{\frac{-3}{4}} (T_i - T_B)$$

$$J_{12} = -K_A D_i^{\frac{3}{4}} \left(1 + \frac{D_i}{4L}\right) \left\{ \left[\beta(T_i - T_B) + 0.01\rho\beta^* \left(A_2 - B_2 T_i - C_{in} + \frac{100\frac{dm}{dt}}{\dot{m}_{soln}}\right)\right]^{\frac{1}{4}} + \right. \tag{4.32}$$

$$\left. \frac{T_i - T_B}{4} \left[\beta(T_i - T_B) + 0.01\rho\beta^* \left(A_2 - B_2 T_i - C_{in} + \frac{100\frac{dm}{dt}}{\dot{m}_{soln}}\right)\right]^{\frac{-3}{4}} [\beta - 0.01\rho\beta^* B_2] \right\}$$

$$J_{21} = 1 - K_B D_i^{\frac{3}{4}} \left(1 + \frac{D_i}{4L}\right) \tag{4.33}$$

$$\left\{ \frac{-100}{\dot{m}_{soln}} \left[\beta(T_i - T_B) + 0.01\rho\beta^* \left(A_2 - B_2 T_i - C_{in} + \frac{100\frac{dm}{dt}}{\dot{m}_{soln}}\right)\right]^{\frac{1}{4}} + \right.$$

$$\left. \frac{0.25\rho\beta^*}{\dot{m}_{soln}} \left[\beta(T_i - T_B) + 0.01\rho\beta^* \left(A_2 - B_2 T_i - C_{in} + \frac{100\frac{dm}{dt}}{\dot{m}_{soln}}\right)\right]^{\frac{-3}{4}} \left(C_{in} - \frac{100\frac{dm}{dt}}{\dot{m}_{soln}} - A_2 + B_2 T_i\right) \right\}$$

$$J_{22} = -K_B D_i^{\frac{3}{4}} \left(1 + \frac{D_i}{4L}\right) \tag{4.34}$$

$$\left\{ \left[\beta(T_i - T_B) + 0.01\rho\beta^* \left(A_2 - B_2 T_i - C_{in} + \frac{100\frac{dm}{dt}}{\dot{m}_{soln}}\right)\right]^{\frac{1}{4}} B_2 + \right.$$

$$\frac{1}{4} \left(C_{in} - \frac{100\frac{dm}{dt}}{\dot{m}_{soln}} - A_2 + B_2 T_i\right) \left[\beta(T_i - T_B) + 0.01\rho\beta^* \left(A_2 - B_2 T_i - C_{in} + \frac{100\frac{dm}{dt}}{\dot{m}_{soln}}\right)\right]^{\frac{-3}{4}}$$

$$\left. (\beta - 0.01\rho\beta^* B_2) \right\} \tag{4.35}$$

Equations 4.30 and 4.31 as well as the corresponding Jacobian matrix may be expressed more succinctly in terms of the quantities P_A and P_C which are defined by Eqs 4.22 and 4.36 respectively.

$$P_C = \left[\beta(T_i - T_B) + 0.01\rho\beta^* \left(A_2 - B_2 T_i - C_{in} + \frac{100\frac{dm}{dt}}{\dot{m}_{soln}}\right)\right] \tag{4.36}$$

The result is:

$$f\left(\frac{dm}{dt}, T_i\right) = \eta P + \frac{dm}{dt} H_{diss} - K_A P_A P_C^{\frac{1}{4}} (T_i - T_B) = 0$$

$$g\left(\frac{dm}{dt}, T_i\right) = \frac{dm}{dt} - K_B P_A P_C^{\frac{1}{4}} \left(C_{in} - \frac{100\frac{dm}{dt}}{\dot{m}_{soln}} - A_2 + B_2 T_i\right) = 0 \tag{4.37}$$

270

$$J_{11} = H_{diss} - \frac{0.25\rho\beta^*}{\dot{m}_{soln}} K_A P_A P_C^{\frac{-3}{4}} (T_i - T_B) \tag{4.38}$$

$$J_{12} = -K_A P_A \left\{ P_C^{\frac{1}{4}} + \frac{T_i - T_B}{4} P_C^{\frac{-3}{4}} [\beta - 0.01\rho\beta^* B_2] \right\} \tag{4.39}$$

$$J_{21} = 1 - K_B P_A \left\{ \frac{-100}{\dot{m}_{soln}} P_C^{\frac{1}{4}} + \frac{0.25\rho\beta^*}{\dot{m}_{soln}} P_C^{\frac{-3}{4}} \left(C_{in} - \frac{100\frac{dm}{dt}}{\dot{m}_{soln}} - A_2 + B_2 T_i \right) \right\} \tag{4.40}$$

$$J_{22} = -K_B P_A \left\{ P_C^{\frac{1}{4}} B_2 + \frac{1}{4} \left(C_{in} - \frac{100\frac{dm}{dt}}{\dot{m}_{soln}} - A_2 + B_2 T_i \right) P_C^{\frac{-3}{4}} \right. \tag{4.41}$$

$$\left. (\beta - 0.01\rho\beta^* B_2) \right\}$$

After determining $\frac{dm}{dt}$ and T_i at time equal to zero, D_i, C_i, C_B, Ra and $\tilde{N}$ are calculated. C_i is determined from the appropriate solubility relationship and D_i, C_B, Ra and $\tilde{N}$ are calculated using Eqs. 3.188, 3.181, 3.167, and 3.161 respectively. Then m, D_i, T_i, C_i, C_B, Ra and $\tilde{N}$ are output to a file. Next, m(t + Δt) is determined from Eq. 4.14 and the process repeated until $\frac{dm}{dt}$ approaches zero, i.e., steady state conditions are reached. The value of $\frac{dm}{dt}$ decreases with time; consequently, the value of the time step, Δt, is increased with time to improve the efficiency of the numerical solution procedure.

4.4.1 Thermodynamic and Transport Properties

Aqueous Sodium Sulfate Solutions

Thermodynamic and transport properties of an aqueous sodium sulfate solution at conditions relevant to the sodium sulfate deposition experiments are given in this section. Table 4.3 gives temperatures and concentrations relevant to the sodium sulfate deposition experiments and determination of the solution properties required in the deposition rate formulation. The quantities $T_{bulk,ic}$ and $T_{bulk,fc}$ are the bulk solution temperatures measured by the thermocouple in the test cell which characterize the beginning and end respectively of a set of runs with the same concentration of sodium sulfate in the inlet stream. The solubility temperature corresponding to the sodium sulfate concentration in the inlet stream is determined using the second order curve fit to the solubility data in Fig. 2-2 and denoted by T_s. The quantities $\Delta T_{i,c}$ and $\Delta T_{f,c}$ are the difference between the solubility temperature corresponding to the sodium sulfate

C_{in} wt%	Runs	$T_{bulk,ic}$ °C	$T_{bulk,fc}$ °C	T_s °C	ΔT_i °C	ΔT_f °C	T_f °C	C_f wt%
2	15	363.3	365.8	367.1	3.8	1.3	370.8	1.5
4	6,8,9,17-19	355.0	357.5	360.0	5.0	2.5	362.5	3.5
6	14,V,W	347.7	350.0	353.3	5.6	3.3	355.0	5.5
8	13,U	340.8	343.5	347.2	6.4	3.7	348.5	7.5

Table 4.3: Various concentrations and temperatures relevant to the sodium sulfate deposition experiments.

concentration in the inlet stream and $T_{bulk,ic}$ and $T_{bulk,fc}$ respectively. Maintaining $\Delta T_{i,c}$ constant while varying the concentration of salt in the inlet stream is the optimal way to isolate the effect of increased salt concentration in the bulk solution on the deposition rate. If ΔT_i is constant, curvature of the solubility curve is modest and solution properties vary modestly as the solute concentration in and temperature of the inlet stream are changed, the deposition rate predicted by the deposition rate formulation remains essentially constant. Thus when the concentration of salt in the inlet stream was changed during the deposition experiments the intention was to hold ΔT_i constant. Unfortunately, only the Ravich and Borovaya [76] data and the Armellini [4] data for the solubility of sodium sulfate in water at 250 bar were available during the planning of the sodium sulfate deposition experiments. Consequently, ΔT_i varies from 3.8 to 6.4 °C based upon Eq. 3.190. The sensitivity analysis presented in Section 4.4.2 shows that the deposition rate is a strong function of ΔT_i.

The thermodynamic and transport properties of the aqueous sodium sulfate solution vary with temperature and concentration across the boundary layer; therefore, they are evaluated at a film temperature and, when possible, film concentration. Since the pressure drop in the test cell is below 1 atmosphere, all solution properties are evaluated at 250 bar. The film temperature is assumed to be 5 °C above the bulk solution temperature characterizing the end of each set of runs with the same concentration of sodium sulfate in the inlet stream. The film concentration is assumed to be 0.5 wt% below the concentration of sodium sulfate in the inlet stream. The use of a film temperature and film concentration is appropriate because the variations in the thermodynamic and transport properties across the boundary layer are relatively small. For example, at the beginning of the set of experiments in which the sodium sulfate concentration in the inlet stream was 4 wt% and the initial bulk solution temperature was about 355 °C, the deposition rate formulation predicts

initial values for C_i, C_B and T_i are approximately 1.75 wt%, 3.3 wt% and 365 $^\circ C$ respectively. At the bulk condition, i.e., 3.3 wt% sodium sulfate, 355 $^\circ C$ and 250 bar, the solution density predicted by the program produced by the Gallagher study is 666.7 kg/m^3 and at the interface condition, i.e., 1.75 wt% sodium sulfate, 365 $^\circ C$ and 250 bar, the same program predicts a solution density of 604.1 kg/m^3. Thus $\frac{\rho_B - \rho_i}{\rho_B}$ is only about 9.0% at the beginning of the runs and diminishes with times. (This number is also small enough for the Boussinesq approximation to be valid.) Similarly, at the foregoing bulk and interface conditions the NIST steam tables predict that for pure water the bulk solution and salt layer-solution interface thermal conductivity are 0.443 and 0.469 $\frac{W}{mk}$ respectively. The film temperatures and concentrations used to determine solution properties are representative of conditions in the boundary layer during the deposition experiments. The film temperature and concentration appropriate for evaluation of solution properties changes as salt builds on the hot finger but this effect is unimportant and, thus, neglected.

The solution properties ρ_{H_2O}, C_P, k, and μ in Tables 4.4 and 4.5 are determined directly from the NIST steam tables [30] at the appropriate film temperature and 250 bar. The densities of the aqueous sodium sulfate solution given in Table 4.4 at the corresponding film temperature and film concentration are determined using the program produced by the Gallagher study discussed in Section 3.7.3. The volumetric thermal and species expansion coefficients are determined using densities determined from the program produced by the Gallagher study following the procedure described in Section 3.7.3 The heat of dissolution, H_{diss}, is determined by extrapolating the Nikolskii data presented in Section 3.7.9 to the film temperature of interest. The Nikolskii data is for an infinitely dilute aqueous sodium sulfate solution and pressure is not provided in the tabulation of the Nikolskii data in Properties of Aqueous Solutions of Electrolytes [94]. The uncertainty in the heat of dissolution values given in Table 4.4 is further compounded because the Nikolskii data are extrapolated to film temperatures near the critical point of pure water. In Table 4.5 the kinematic viscosity, ν, is set equal to $\frac{\mu_{H_2O}}{\rho_{soln}}$ and the self diffusion coefficient of pure water, $\mathfrak{D}_{AA}$, is calculated using the expression provided by Lamb et al. (Eq. 3.130) based on T_f and ρ_{H_2O}. $\mathfrak{D}_{AB}$ is the estimated value of the binary molecular diffusion coefficient based on the Butenhoff et al. data discussed in Section 3.7.5. The Prandtl number is based on pure water properties and the Schmidt number is based on the kinematic viscosity of pure water and $\mathfrak{D}_{AB}$, i.e., Sc = $\frac{\nu}{\mathfrak{D}_{AB}}$.

C_{in} wt%	Runs	T_f °C	C_f wt%	ρ_{soln} $\frac{kg}{m^3}$	ρ_{H_2O} $\frac{kg}{m^3}$	C_P $\frac{J}{kg°C}$	β_{soln} $\frac{1}{°C}$	β^*_{soln} $\frac{1}{\frac{kg}{m^3}}$	H_{diss} $\frac{J}{kg}$
2	15	370.8	1.5	570	535	1.10e4	0.01	-0.007	-2.40e6
4	6,8,9,17-19	362.5	3.5	646	579	8.53e3	0.005	-0.004	-2.24e6
6	14,V,W	355.0	5.5	698	609	7.46e3	0.0036	-0.0028	-2.11e6
8	13,U	348.5	7.5	739	631	6.88e3	0.003	-0.0022	-1.99e6

Table 4.4: Thermodynamic properties used in the sodium sulfate deposition rate predictions.

C_{in} wt%	Runs	T_f °C	C_f °C	k wt%	μ $\frac{W}{m°C}$	ν $\frac{kg}{ms}$	$\mathfrak{D}_{AA}$ $\frac{m^2}{s}$	$\mathfrak{D}_{AB}$ $\frac{m^2}{s}$	Pr	Sc
2	15	370.8	1.5	0.43	6.16e-5	1.08e-7	5.82e-8	2.5e-8	1.58	4.32
4	6,8,9,17-19	362.5	3.5	0.45	6.68e-5	1.03e-7	5.32e-8	2.5e-8	1.27	4.12
6	14,V,W	355.0	5.5	0.47	7.05e-5	1.01e-7	5.02e-8	2.5e-8	1.12	4.04
8	13,U	348.5	7.5	0.48	7.35e-5	9.95e-8	4.80e-8	2.5e-8	1.05	3.98

Table 4.5: Transport properties used in the sodium sulfate deposition rate predictions.

Potassium Sulfate

The equivalent of Tables 4.3 through 4.5 for the potassium sulfate deposition experiments are given in Tables 4.6 through 4.8. The density of an aqueous potassium sulfate solution is unavailable at conditions of interest. Hence, the density and thermal expansion coefficient given in Table 4.7 are based on the NIST steam tables [30] and a species expansion coefficient is not included in the tabulation of thermodynamic properties. The sources and methods used to determine the remainder of the thermodynamic properties are identical to those used for the sodium sulfate-water system in the previous section. (The heat of dissolution data for an infinitely dilute potassium sulfate-water solution given in Properties of Aqueous Solutions of Electrolytes [94] are referenced to studies by Tsvetkov and Rabinovich [89] and Zarembo and Puchkov [93].) The same uncertainties associated with estimation of the heat of dissolution for the sodium sulfate-water solution are present.

C_{in} wt%	Runs	$T_{bulk,ic}$ °C	$T_{bulk,fc}$ °C	T_s °C	ΔT_i °C	ΔT_f °C	T_f °C	C_f wt%
2	T	374.7	376.7	382.0	7.3	5.3	380.7	1.5
4	Q,Z	372.0	373.6	379.0	7.0	5.4	377.6	3.5
6	S	369.0	371.1	376.1	7.1	5.0	375.1	5.5
8	R,Y	366.2	368.5	373.1	6.9	4.6	372.5	7.5

Table 4.6: Various concentrations and temperatures relevant to the potassium sulfate deposition experiments.

C_{in} wt%	Runs	T_f °C	ρ_{H_2O} $\frac{kg}{m^3}$	C_P $\frac{J}{kg°C}$	β_{H_2O} $\frac{1}{°C}$	H_{diss} $\frac{J}{kg}$
2	T	380.7	439	26.53e3	0.035	-1.93e6
4	Q,Z	377.6	481	17.07e3	0.023	-1.87e6
6	S	375.1	504	13.81e3	0.018	-1.83e6
8	R,Y	372.5	524	11.84e3	0.014	-1.78e6

Table 4.7: Thermodynamic properties used in the potassium sulfate deposition rate predictions.

C_{in} wt%	Runs	T_f °C	k °C	μ $\frac{W}{m°C}$	ν $\frac{kg}{ms}$	$\mathcal{D}_{AA}$ $\frac{m^2}{s}$	$\mathcal{D}_{AB}$ $\frac{m^2}{s}$	Pr	Sc
2	T	380.7	0.39	5.11e-5	1.16e-7	7.18e-8	0.25e-7	3.48	4.64
4	Q,Z	377.6	0.40	5.55e-5	1.15e-7	6.53e-8	0.25e-7	2.37	4.60
6	S	375.1	0.41	5.81e-5	1.15e-7	6.21e-8	0.25e-7	1.96	4.60
8	R,Y	372.5	0.42	6.03e-5	1.15e-7	5.96e-8	0.25e-7	1.70	4.60

Table 4.8: Transport properties used in the potassium sulfate deposition rate predictions.

4.4.2 Results

Introduction

The deposition rate predicted by the deposition rate formulation is compared to the experimental deposition rate data in this section. For conditions corresponding to selected deposition experiments values for D_i, T_i, C_i, C_B, Ra, $\tilde{N}$ and $\frac{\Delta\rho_{B-i}}{\rho_B}$ are also presented. The numerical solution of the deposition rate formulation predicts that up to 10000 minutes (one week) are required before steady state conditions are reached, i.e., the deposition rate equals zero in the experiments. (The time required to reach steady state conditions is a strong function of some of the parameters varied in the sensitivity analysis and in some cases is far below one week.) The time scale of the experiments (10 minutes) is extremely small relative to the time required for steady state conditions to be reached. Therefore, the deposition rate and other pertinent variables are examined separately for time scales characteristic of the duration of the experiments and for time scales large enough to capture steady state behavior.

The thermodynamic and transport properties required in the deposition rate formulation are inherently uncertain. Measurements of the porosity within the salt layer and the bulk solution temperature have uncertainties associated with them as well. Moreover, the temperature of the bulk solution increases during each run and the porosity of the salt layer may decrease dramatically before steady state conditions are reached as discussed in Section 4.5. Thus, the results of the numerical solution of the deposition rate formulation are presented in the context of a sensitivity analysis. The sensitivity analysis is performed on the solution properties H_{diss}, $\mathfrak{D}_{AB}$ and β^* as well as the porosity of the salt layer formed on the hot finger, ϕ, and the bulk temperature of solution in the cell, T_B. The rest of the solution properties, i.e., ρ, C_P, β, k, and μ as well as the density of the solid salt, ρ_s, are assumed to be accurately known. The initial and asymptotic behavior of m, D_i, T_i, C_i, C_B, Ra, $\tilde{N}$ and $\frac{\Delta\rho_{B-i}}{\rho_B}$ when the concentration of sodium sulfate in the inlet steam is 4 wt% are presented first. Then the results of the sets of deposition experiments for which the concentration of sodium sulfate and potassium sulfate in the inlet stream were varied are compared against the predictions of the deposition rate formulation.

276

Sodium Sulfate

The theoretically predicted deposition rate as a function of time for the set of runs in which the concentration of sodium sulfate in the solution entering the cell is 4 wt% is shown in Figs. 4-3 through 4-6. (Figures 4-3 and 4-5 are plots of the deposition rate versus run time up to a run time of 15 minutes. Since the duration of the experiments ranged from about 6 to 12 minutes, these figures are useful for comparing the theoretical deposition rate predictions against the experimental data. Figs. 4-4 and 4-6 are the same plots extended to run times required for the establishment of steady state conditions.) The sensitivity analysis is performed relative to a baseline case in which best estimates of variables required in the deposition rate formulation are used. For the baseline case, the binary molecular diffusion coefficient of Na_2SO_4 in SCW is assumed to equal $0.25*10^{-7}$ m^2/s. The rationale for this value of the binary molecular diffusion coefficient is discussed in Section 3.7.5. The baseline bulk solution temperature is set equal to that characterizing the end of the set of runs in which the concentration of sodium sulfate in the inlet stream was 4 wt%, i.e., 357.5 $°C$. The baseline heat of dissolution is set equal to zero because of the uncertainties associated with its estimation. The baseline species expansion coefficient is set equal to -0.004 m^3/kg based on densities determined from the program produced by the Gallagher and Sengers study. Finally, the baseline porosity is assumed to be 2/3 based on the experimentally determined porosity values given in Table 2.12.

Plots of the mass of salt on the hot finger versus time for the baseline case and for variations in the heat of dissolution and binary molecular diffusion coefficient relative to the baseline case are provided in Figs. 4-3 and 4-4. Conditions correspond to the experiments in which the concentration of sodium sulfate in the inlet stream was 4 wt%. The experimental deposition rate data are shown in Fig. 4-3. The baseline prediction for the mass of salt deposited on the hot finger agrees with the experimental data to within 20% at all times. An exothermic precipitation process (positive heat of dissolution) increases the heat rate at the salt layer-solution interface by a factor of $H_{diss}\frac{dm}{dt}$. Thus, if precipitation is exothermic the temperature of the salt layer-solution interface at a given salt layer-solution interface diameter increases relative to the baseline case because it must accommodate a larger heat flux. The increase in temperature at the salt layer-solution interface is accompanied by a decrease in salt concentration. This, in turn, increases the mass transfer driving force and the mass transfer rate at the salt layer-solution interface. Therefore, relative to

277

the baseline case, when the heat of dissolution equals zero, exothermic precipitation increases the mass of salt on the hot finger as a function of time until steady state conditions are reached. Conversely, for an endothermic precipitation process the mass of salt on the hot finger as a function of time decreases relative to the baseline case until steady state conditions are reached because the heat rate at the salt layer-solution interface is decreased by a factor of $H_{diss} \frac{dm}{dt}$. The importance of the heat of dissolution diminishes with increasing time because the magnitude of $H_{diss} \frac{dm}{dt}$ decreases with time. Moreover the mass of salt on the hot finger at steady state conditions is independent of the heat of dissolution. Finally, the time required to reach steady state conditions is a weak function of the heat of dissolution.

Extrapolation of the Nikolskii heat of dissolution data to the film temperature characterizing the set of runs in which the concentration of sodium sulfate in the inlet stream was 4 wt% results in a value of -2.40*10^6 J/kg. (The precipitation process is endothermic.) The mass of salt on the hot finger as a function of time predicted by the deposition rate formulation when the heat of dissolution equals +2.40*10^6 and -2.40*10^6 J/kg is shown in Figs. 4-3 and 4-4. Increasing the heat of dissolution from 0 to 2.40*10^6 J/kg increases the mass of salt on the hot finger by close to 40% relative to the baseline case for time scales on the order of the duration of the experiments. Decreasing the heat of dissolution from 0 to -2.40*10^6 J/kg decreases the mass of salt on the hot finger by about 25% for time scales on the order of the duration of the experiments. The importance of the heat of dissolution diminishes with time and does not affect steady state behavior.

The remaining curve in Figs. 4-3 and 4-4 shows the effect of doubling the binary molecular diffusion coefficient on the deposition rate. Although the Sherwood number and, thus, the mass transfer coefficient are directly proportional to the binary molecular diffusion coefficient, the deposition rate is not. This is largely because as the mass transfer coefficient and deposition rate increase, the depletion of salt in the bulk solution becomes more pronounced which causes a reduction in the mass transfer driving force. Doubling the binary diffusion coefficient increases the mass of salt on the hot finger by up to about 40% for time scales on the order of the duration of the experiments. The deposition rate formulation does not account for the extremely small effect that the value of the binary molecular diffusion has on the mass of salt deposited on the hot finger at steady state conditions. The rationale for this feature of the deposition rate formulation was provided in Section 3.11.3. It is noted that steady state conditions are achieved about 10% faster when

$\mathfrak{D}_{AB}$ is doubled.

The sensitivity of the mass of salt on the hot finger as a function of time to the species expansion coefficient is shown in Figs. 4-5 and 4-6. Contrary to what one might expect, changing the species expansion from -0.004 m^3/kg to zero increases the mass of salt on the hot finger as a function of time until steady state conditions are reached. This is an example of weakened transport resulting in an increased deposition rate as discussed in Section 3.2. The salt layer-solution interface concentration predicted by the deposition rate formulation at the beginning of the run is about 1.75 wt% and decreases with time. Thus the salt layer-solution interface temperature is below the temperature corresponding to zero salt solubility and, equivalently, the mass transfer coefficient is above the critical value of the mass transfer coefficient at all times. Thus it follows from the simple model presented in Section 3.2 that weakened transport will increase the deposition rate. In the case at hand, changing the species expansion coefficient from -0.004 m^3/kg to zero reduces the heat and mass transfer coefficients corresponding to a given temperature difference between the salt layer-solution interface and bulk solution. This happens because both the Nusselt and Sherwood numbers scale as Gr$^{\frac{1}{4}}$ and Gr is reduced when the species expansion coefficient is changed to zero and the other variables which the Grashof number depends on are held constant. Thus, a larger temperature difference across the boundary layer is required to remove the heat at the salt layer-solution interface when the species expansion coefficient is changed to zero. This, in turn, increases the mass transfer driving force. The net effect of the reduced mass transfer coefficient and increased mass transfer driving force results in an increased deposition rate. Thus the mass of salt on the hot finger as a function of time increases relative to the baseline case until steady state conditions are established when the species expansion coefficient is changed from -0.004 m^3/kg to zero as shown in Fig. 4-6. The mass of salt on the hot finger is reduced by less than 10% for time scales on the order of the duration of the experiments when the species expansion coefficient is changed from -0.004 m^3/kg to zero. Nonetheless this reduction is evidence that the qualitative relationship between transport coefficients and deposition rate deduced from the simple model in Section 3.2 holds for the more complex deposition rate formulation as well. The value of the species expansion coefficient does not significantly affect steady state behavior or the time required to achieve it.

The sensitivity of the mass of salt on the hot finger as a function of time to the porosity in the salt layer

and the bulk solution temperature is shown in Figs. 4-5 and 4-6. Small changes in these quantities strongly impact the mass of salt on the hot finger as a function of time. Moreover, the mass of salt on the hot finger at steady state conditions and the time required to reach steady state conditions are strongly affected by these quantities. The bulk solution temperature at the beginning of the set of runs in which the sodium sulfate concentration in the inlet stream was 4 wt% was 355 $°C$ and increased to about 357.5 $°C$ by the end of each run. The temperature difference between the salt layer-solution interface and the bulk solution is about 10 $°C$ during the deposition experiments and a weak function of the bulk solution temperature. Thus, lowering the bulk solution temperature from 357.5 $°C$ to 355.0 $°C$ substantially decreases the amount by which the salt layer-solution interface temperature exceeds the solubility temperature corresponding to the concentration of salt in the bulk solution. Hence, lowering the bulk solution temperature from 357.5 $°C$ to 355.0 $°C$ causes a substantial reduction in the mass transfer driving force and mass of salt deposited on the hot finger as a function of time. For time scales on the order of the duration experiments the mass of salt on the hot finger predicted by the deposition rate formulation is reduced by a factor of about 1/3 when the bulk solution temperature is lowered from 357.5 $°C$ to 355.0 $°C$. Decreasing the bulk solution temperature from 357.5 $°C$ to 355.0 $°C$ also reduces the mass of salt on the hot finger at steady state conditions from about 38 grams to about 6 grams, a more than sixfold effect. This is consistent with Eq. 3.198. Finally, the time required to reach steady state conditions drops by an order of magnitude when the bulk solution temperature is decreased from 357.5 $°C$ to 355.0 $°C$.

The deposition rate decreases as the salt layer-solution interface diameter increases. Since less salt is required to obtain the same salt layer-solution diameter when the porosity of the salt layer is increased, the mass of salt on the hot finger as a function of time decreases with increasing porosity. The diameter of the salt layer-solution interface at steady state conditions is not a function of porosity; therefore, increasing the porosity of the salt layer reduces the mass of salt on the hot finger at steady state conditions. Increasing the porosity in the salt layer from 2/3 to 0.85 decreases the mass of salt on the hot finger at steady sate conditions by a factor of about 55% and the time required to reach steady state conditions by a factor of about 2/3. However, for time scales on the order of the duration of the experiments, increasing the porosity from 2/3 to 0.85 causes the mass of salt on the hot finger to decrease by only slightly more than 10%.

Values of the variables D_i, T_i, C_i, C_B, Ra_{D_i}, $\tilde{N}$ and $\frac{\Delta \rho_{B-i}}{\rho_B}$ predicted by the deposition rate formulation as a function of time for the deposition experiments in which the concentration of sodium sulfate in the inlet stream was 4 wt% are given in Figs. 4-7 through 4-20. Each of these quantities is plotted on a time scale corresponding to the duration of the experiments and a time scale which captures steady state behavior. A detailed sensitivity analysis of these variables to $\mathfrak{D}_{AB}$, H_{diss}, T_B, β^* and ϕ was performed. The effects of changing the heat of dissolution and binary molecular diffusion coefficient on the behavior of these variables are shown in Figs. 4-7 through 4-20. Moreover, from these figures and the results of the sensitivity analysis on the mass of salt on the hot finger to T_B, β^* and ϕ, the effect of changing T_B, β^* and ϕ on D_i, T_i, C_i, C_B, Ra_{D_i}, $\tilde{N}$ and $\frac{\Delta \rho_{B-i}}{\rho_B}$ are easily inferred. Physical explanations for the behavior of D_i, T_i, C_i, C_B, Ra_{D_i}, $\tilde{N}$ and $\frac{\Delta \rho_{B-i}}{\rho_B}$ at baseline conditions and upon changing $\mathfrak{D}_{AB}$, H_{diss}, T_B, β^* and ϕ are very similar to those which explain the mass of salt deposited on the hot finger as a function of time and, thus, the discussion of Figs. 4-7 through 4-20 is brief. For example, the diameter of the salt layer-solution interface and the mass of salt on the hot finger are related directly by Eq. 3.188; therefore, rationale for the behavior of D_i as a function of time has been provided by the explanations for the behavior of m as a function of time.

The salt layer-solution interface condition approaches the bulk condition as time is increases. This process is shown in Fig. 3-30 and the results from the solution of the deposition rate formulation are consistent with Fig. 3-30. (The material capacitance of the cell is not included in the deposition rate formulation, thus the concentration of salt in the bulk solution is lowest when time approaches zero.) At steady state conditions the concentration of salt at the salt layer-solution interface and in the bulk solution equals the concentration of salt in the inlet stream as shown in Fig. 4-12 and 4-14. The steady state value of the Rayleigh number is almost $1.3*10^9$ as shown in Fig. 4-16. The transition Rayleigh number for a natural convection on a horizontal cylinder is about 10^9 [41]; therefore, the natural convection boundary layer may become turbulent before steady state conditions are established. Moreover, if the deposition rate formulation is underpredicting the Rayleigh number for time scales associated with the experiments by close to two orders of magnitude a transition to turbulence may have occurred in the experiments. Turbulence on the downstream side of the natural convective boundary layer may play a role in the formation of the bumps and pronounced dendrites in the salt layer there as discussed in Section 3.5.12. The value of $\tilde{N}$ monotonically decreases from about

0.8 at time equal to zero to zero at steady state conditions. This behavior is consistent with the discussion about $\tilde{N}$ in Section 3.10. Figs. 4-19 and 4-20 show that the quantity $\frac{\Delta\rho_B - \iota}{\rho_B}$ does not exceed 0.1 at any point in the solution of the deposition rate formulation and, thus, justify the use of the Boussinesq approximation.

The mass of salt deposited on the hot finger as a function time predicted by the deposition rate formulation at conditions corresponding to the runs in which the sodium sulfate concentration in the inlet stream was 2, 4, 6 and 8 wt% is plotted in Fig 4-21. The results of all the sodium sulfate deposition experiments are also shown. The deposition rate formulation predicts the mass of salt on the hot finger as a function of time does not change for run times on the order of the duration of the experiments as the concentration of salt in the inlet stream was varied from 2 to 8 wt% at the conditions investigated. This is shown in Fig. 4-21 by the four closely-packed curves corresponding to baseline conditions when the salt concentration in the inlet stream is 2, 4, 6 and 8 wt%. The amount by which the bulk solution temperature at time equal to zero is below the solubility temperature corresponding to the salt concentration in the inlet stream monotonically increased from 3.8 to 6.4 $^\circ C$ as the salt concentration in the inlet stream was increased from 2 to 8 wt% as documented in Table 4.3. However, as is evident from the temperature-composition diagram for sodium sulfate-water system shown in Fig. 2-1, the slope of the solubility line decreases with increasing salt concentration. Thus the change in salt solubility corresponding to a given temperature difference increases with increasing sodium sulfate concentration. This partially compensates for the reduction in bulk solution temperature relative to the solubility temperature corresponding to the concentration of salt in the inlet stream as inlet concentration is increased. In summary, as the sodium sulfate concentration in the inlet stream was increased, the difference between the salt layer-solution interface temperature and solubility temperature corresponding to the bulk salt concentration decreased, the slope of the relevant portion of the solubility curve decreased and the thermodynamic and transport properties changed. The net effect of these three phenomena is that the deposition rate formulation predicts the deposition rate is independent of the inlet condition for time scales on the order of the duration of the experiments.

The sensitivity analysis conducted for the set of runs in which the salt concentration in the inlet stream was 4 wt% shows that the mass of salt deposited on the hot finger decreases most relative to the baseline case when the bulk solution temperature is lowered from the baseline bulk solution temperature to the

bulk solution temperature at the beginning of the run. Conversely, the largest increases in the mass of salt deposited on the hot finger as a function time relative to the baseline case happens when the binary molecular diffusion coefficient is doubled. Hence only the bulk solution temperature and binary molecular diffusion coefficient are examined in the sensitivity analysis for the sodium sulfate weight percent sweep. (The phrase "weight percent sweep" is used to describe series of experiments using the same salt with different salt concentrations and temperatures in the inlet stream.) The results of the sensitivity analysis are shown in Table 4.9 along with the experimental deposition rate data for the runs which were approximately nine minutes long. All of the experimental data were normalized to 9 minutes, e.g., for a run 9.3 minutes long the mass of salt deposited during the run was multiplied by 9/9.3 before being included in Table 4.9. The results of the sensitivity analysis show that for each inlet conditions the deposition rate changes by approximately the same amount when the bulk solution temperature is changed from that corresponding to the end of the run to that corresponding to the beginning of the run and when the binary molecular diffusion coefficient is doubled. Thus only one set of curves is included in Fig. 4-21 to represent the entire sensitivity analysis performed on all four inlet conditions. This set of curves is labelled "Envelope Boundary from Sensitivity Analysis" in Fig. 4-21. For times on the order of the duration of the experiments, the lowering of the bulk solution temperature decreases the mass of salt on the hot finger by about a factor of 1/3 and the doubling of the binary molecular diffusion coefficient increases the mass of salt on the hot finger by about 60%. The experimental data collected at salt concentrations of 2 and 4 wt% in the inlet stream almost fall within the bounds of the sensitivity envelope. The experimental data at 6 wt% is up to about 25 % higher than the envelope boundary and those at 8 wt% are up to about twice the upper bound of the envelope. A logical explanation for the discrepancy between the predictions of the deposition rate formulation and the experimental data is that mass transfer within the porous salt layer becomes more important as the concentration of salt in the inlet stream increases. Mass transfer within the porous salt layer is discussed in Section 4.5.

283

Potassium Sulfate

The experimental results along with the predictions of the deposition rate formulation for the potassium sulfate weight percent sweep are shown in Fig. 4-22. The solubility data for the potassium sulfate-water system presented in Chapter 2 was collected before the potassium sulfates deposition experiments were run. This allowed the temperature difference between the solubility temperature corresponding to the salt concentration in the inlet stream and the bulk solution temperature to be maintained essentially constant at 7 $^\circ C$, as per Table 4.6, at the beginning of each run. Moreover, the solubility relationship between temperature and concentration at 250 bar is linear for the potassium sulfate-water system as shown in Fig. 2-2. Thus the rational for the deposition rate formulation predicting the deposition rate is independent of the inlet condition for the sodium sulfate weight percent sweep does not apply to the potassium sulfate weight percent sweep. The deposition rate formulation predicts the mass of salt on the hot finger as a function of time is a substantial function of the inlet condition for the potassium sulfate weight percent sweep because of variations in the thermodynamic and transport properties. For example the specific heat of pure water drops from 26.53 to 11.84 kJ/kg between the film temperatures characterizing the experiments for which the concentration of potassium sulfate in the inlet stream was 2 wt% and 8 wt%. It is noted that the deposition rate formulation predicts that the salt layer-solution interface concentration is identically zero for the first 2-3 minutes of the experiments with a concentration of potassium sulfate of 2 wt% in the inlet stream at baseline conditions. This does not occur for the other three inlet conditions.

The sensitivity of the theoretical prediction of the mass of salt on the hot finger as a function of time to changes in the bulk solution temperature and binary molecular diffusion coefficient is given in Table 4.10. As with the sodium sulfate case, when the concentration of salt in the inlet stream was 2 and 4 wt%, deposition rate data fall almost within the bounds of the sensitivity analysis. When the concentration of potassium sulfate is 6 and 8 wt% in the inlet stream mass transfer within the porous salt layer is again a logical explanation for the discrepancy between the theory and experiments.

C_{in} wt%	Designation	T_B °C	$\mathcal{D}_{AB}$ $\frac{m^2}{sec}$	m grams
2	Baseline	365.8	0.25E-7	0.59
	Case II	363.3	0.25E-7	0.41
	Case III	365.8	0.50E-7	0.86
	Exp. Data	NA	NA	0.36
4	Baseline	357.5	0.25E-7	0.59
	Case II	355.0	0.25E-7	0.40
	Case III	357.5	0.50E-7	0.86
	Exp. Data	NA	NA	0.57, 0.60
6	Baseline	350.0	0.25E-7	0.58
	Case II	347.7	0.25E-7	0.40
	Case III	350.0	0.50E-7	0.84
	Exp. Data	NA	NA	1.38, 1.06, 1.10
8	Baseline	343.5	0.25E-7	0.59
	Case II	340.8	0.25E-7	0.38
	Case III	343.5	0.50E-7	0.88
	Exp. Data	NA	NA	1.8,1.55

Table 4.9: Results of the sensitivity analysis conducted for conditions corresponding to the sodium sulfate weight percent sweep. The experimental deposition rate data for the runs which were approximately nine minutes long are also shown. The experimental data were normalized to 9 minutes.

C_{in} wt%	Designation	T_B °C	$\mathcal{D}_{AB}$ $\frac{m^2}{sec}$	m grams
2	Baseline	376.7	0.25E-7	0.52
	Case II	374.7	0.25E-7	0.23
	Case III	376.7	0.50E-7	0.71
	Exp. Data	NA	NA	0.27
4	Baseline	373.6	0.25E-7	0.59
	Case II	372.0	0.25E-7	0.34
	Case III	373.6	0.50E-7	0.80
	Exp. Data	NA	NA	0.99, 0.85
6	Baseline	371.1	0.25E-7	0.71
	Case II	369.0	0.25E-7	0.38
	Case III	371.1	0.50E-7	0.97
	Exp. Data	NA	NA	1.37
8	Baseline	368.5	0.25E-7	0.81
	Case II	366.2	0.25E-7	0.44
	Case III	368.5	0.50E-7	1.12
	Exp. Data	NA	NA	1.96, 1.73

Table 4.10: Results of the sensitivity analysis conducted for conditions corresponding to the potassium sulfate weight percent sweep. The experimental data deposition rate data normalized to 9 minutes are also given.
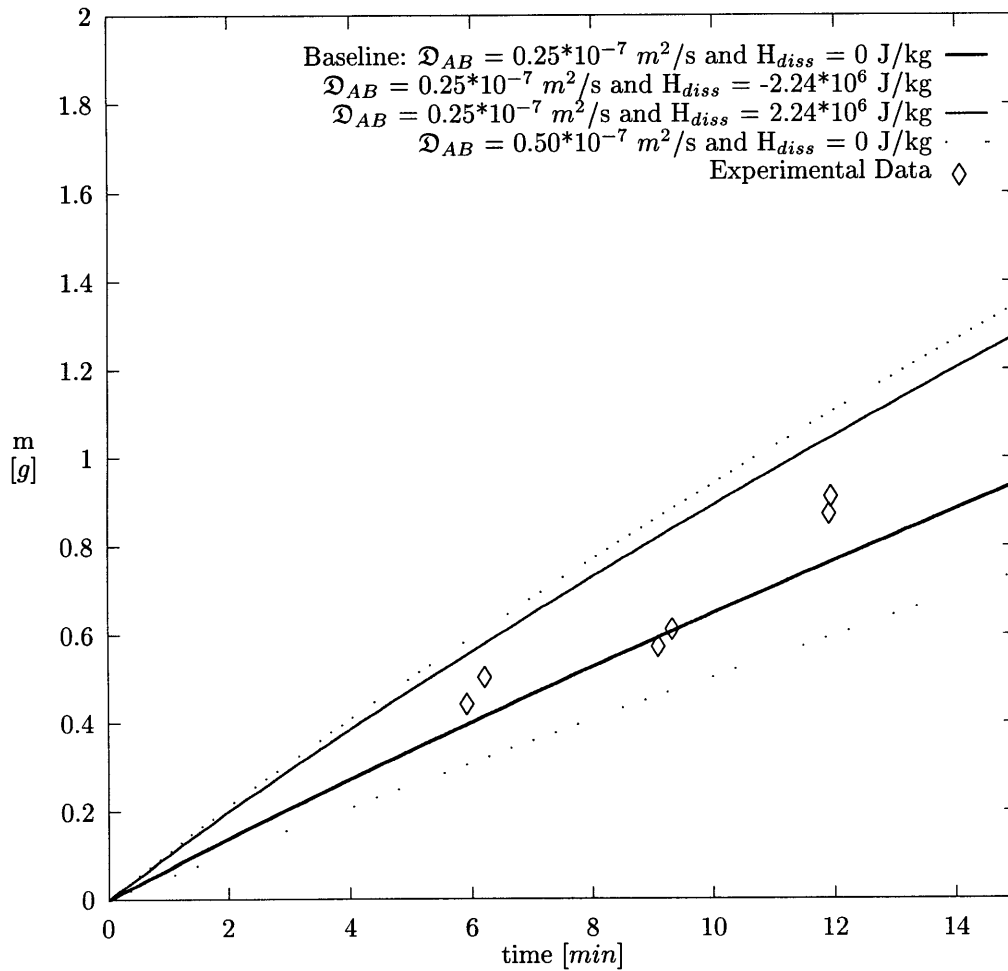
Figure 4-3: Mass of salt deposited on the hot finger versus time from the experimental data in Table 2.12 and predicted by the deposition rate formulation at the conditions indicated and a pressure of 250 bar. The concentration of sodium sulfate in the inlet stream was 4 wt%.

Figure 4-4: Mass of salt deposited on the hot finger versus time predicted by the deposition rate formulation at the conditions indicated and a pressure of 250 bar. The concentration of sodium sulfate in the inlet stream was 4 wt%.
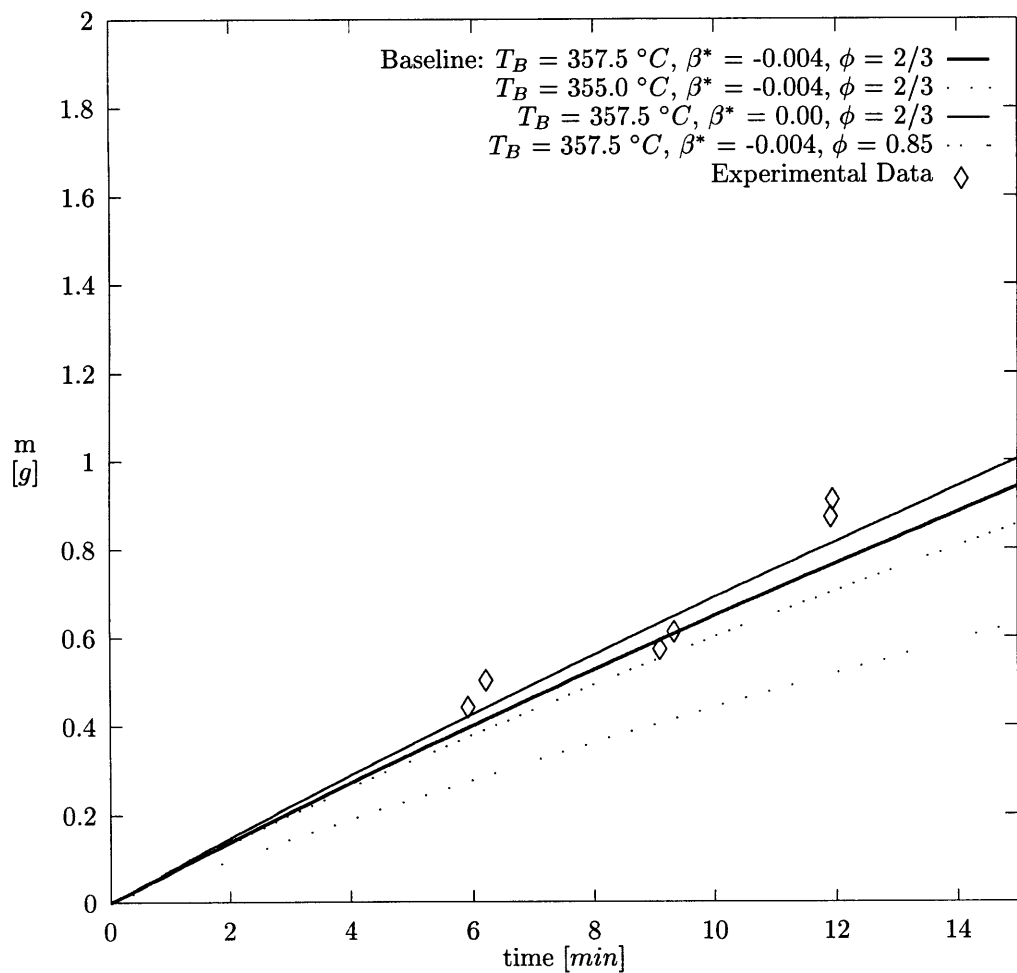
Figure 4-5: Mass of salt deposited on the hot finger versus time from the experimental data in Table 2.12 and from the deposition rate formulation at the conditions indicated and a pressure of 250 bar. The concentration of sodium sulfate in the inlet stream was 4 wt%.
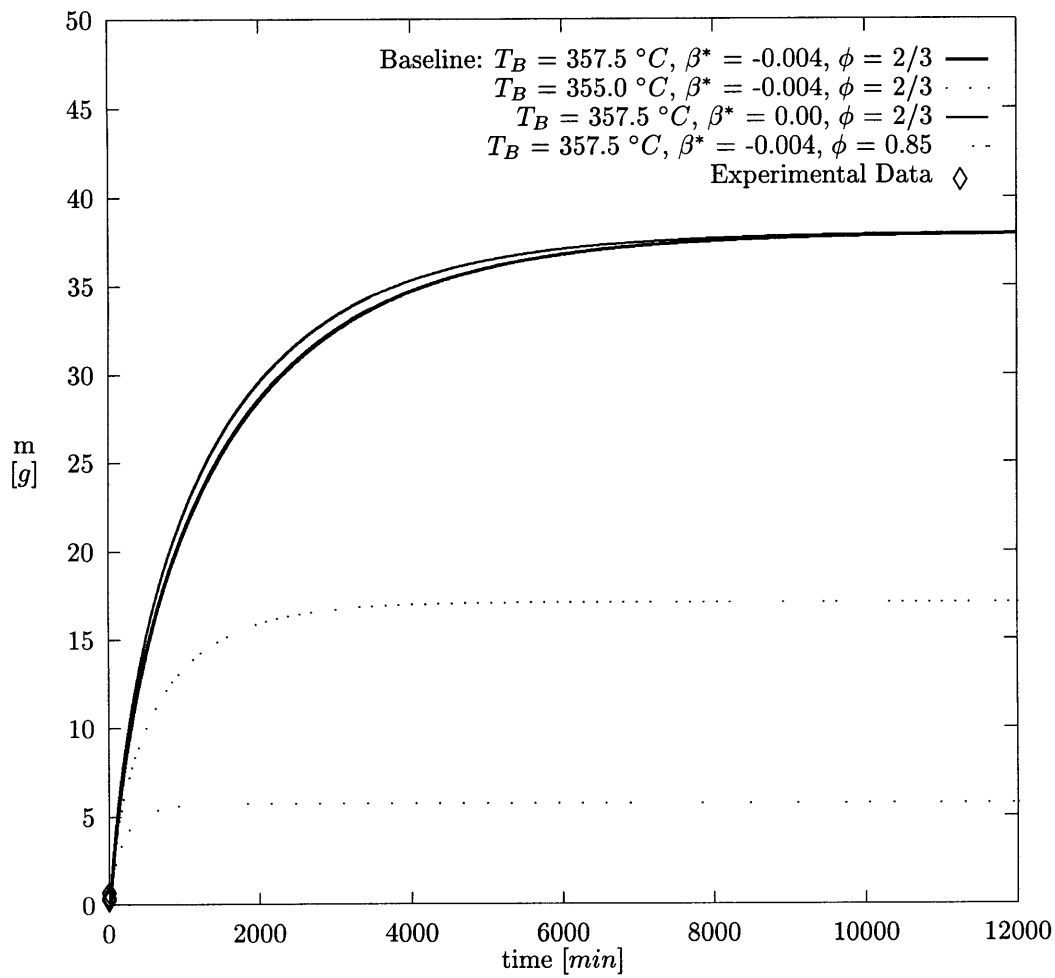
Figure 4-6: Mass of salt deposited on the hot finger versus time from the experimental data in Table 2.12 and from the deposition rate formulation at the conditions indicated and a pressure of 250 bar. The concentration of sodium sulfate in the inlet stream was 4 wt%.
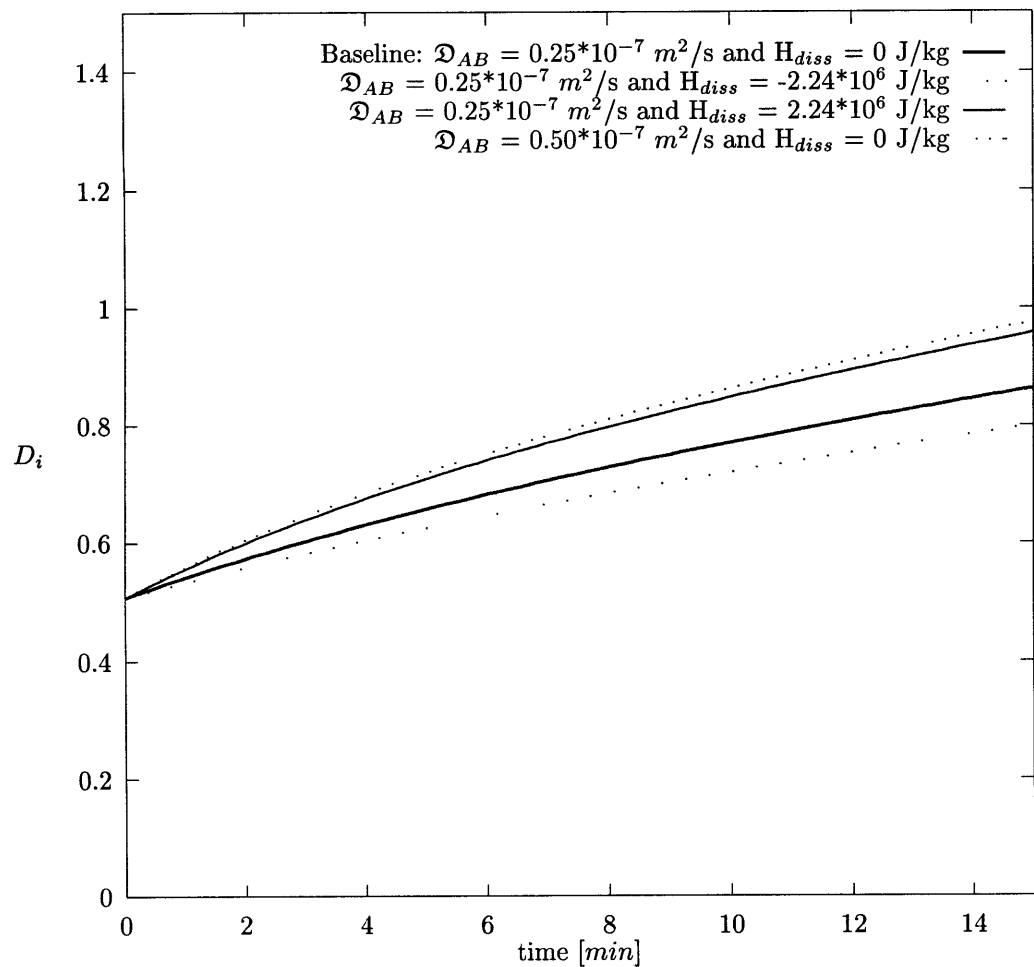
Figure 4-7: Salt layer-solution interface diameter versus time determined from the deposition rate formulation at the conditions indicated and a pressure of 250 bar. The concentration of sodium sulfate in the inlet stream was 4 wt%.
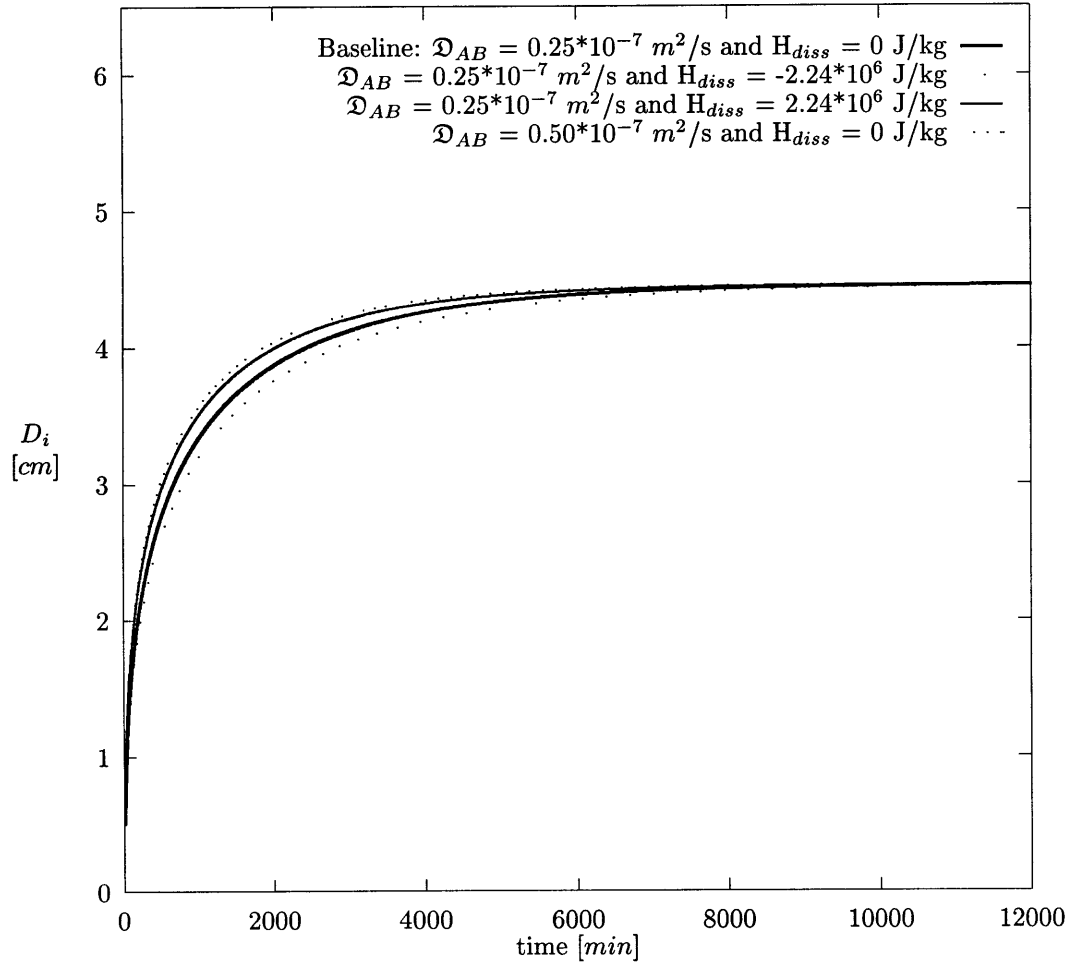
Figure 4-8: Salt layer-solution interface diameter versus time determined from the deposition rate formulation at the conditions indicated and a pressure of 250 bar. The concentration of sodium sulfate in the inlet stream was 4 wt%.
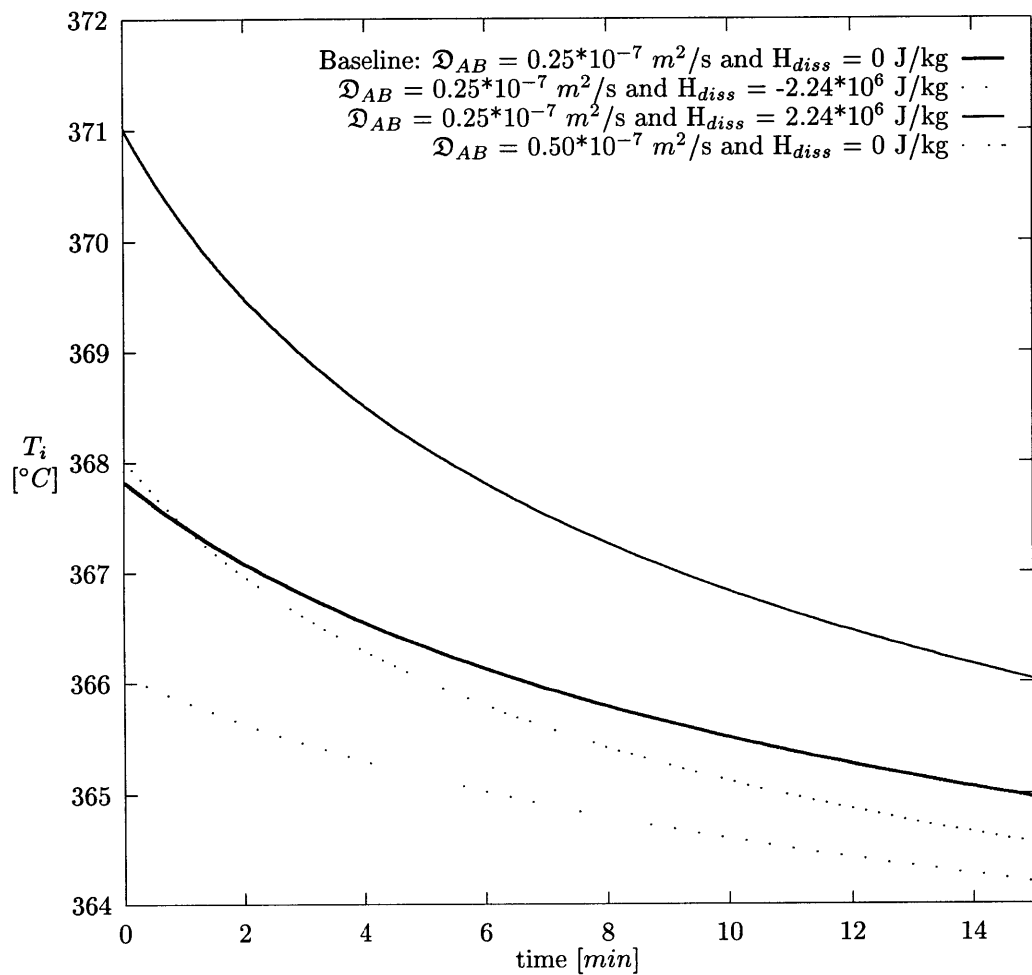
Figure 4-9: Salt layer-solution interface temperature versus time determined from the deposition rate formulation at the conditions indicated and a pressure of 250 bar. The concentration of sodium sulfate in the inlet stream was 4 wt%.
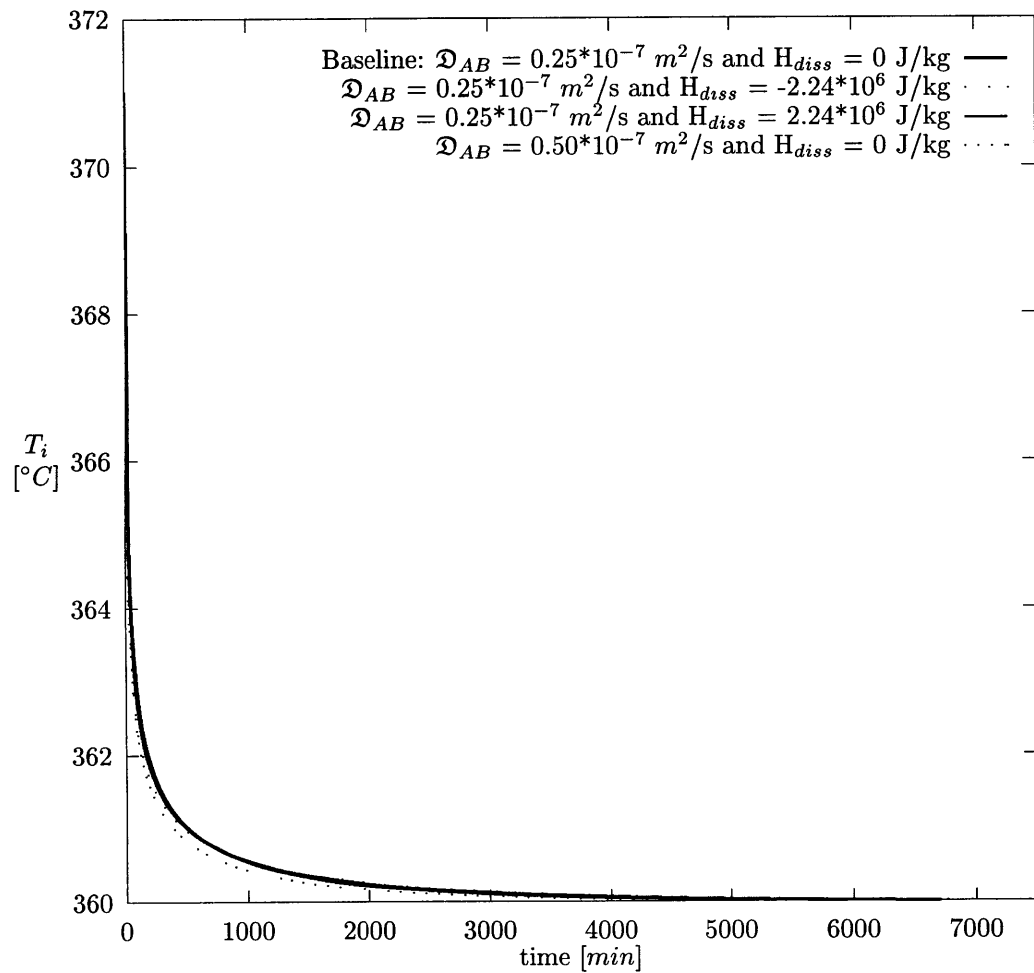
Figure 4-10: Salt layer-solution interface temperature versus time determined from the deposition rate formulation at the conditions indicated and a pressure of 250 bar. The concentration of sodium sulfate in the inlet stream was 4 wt%.
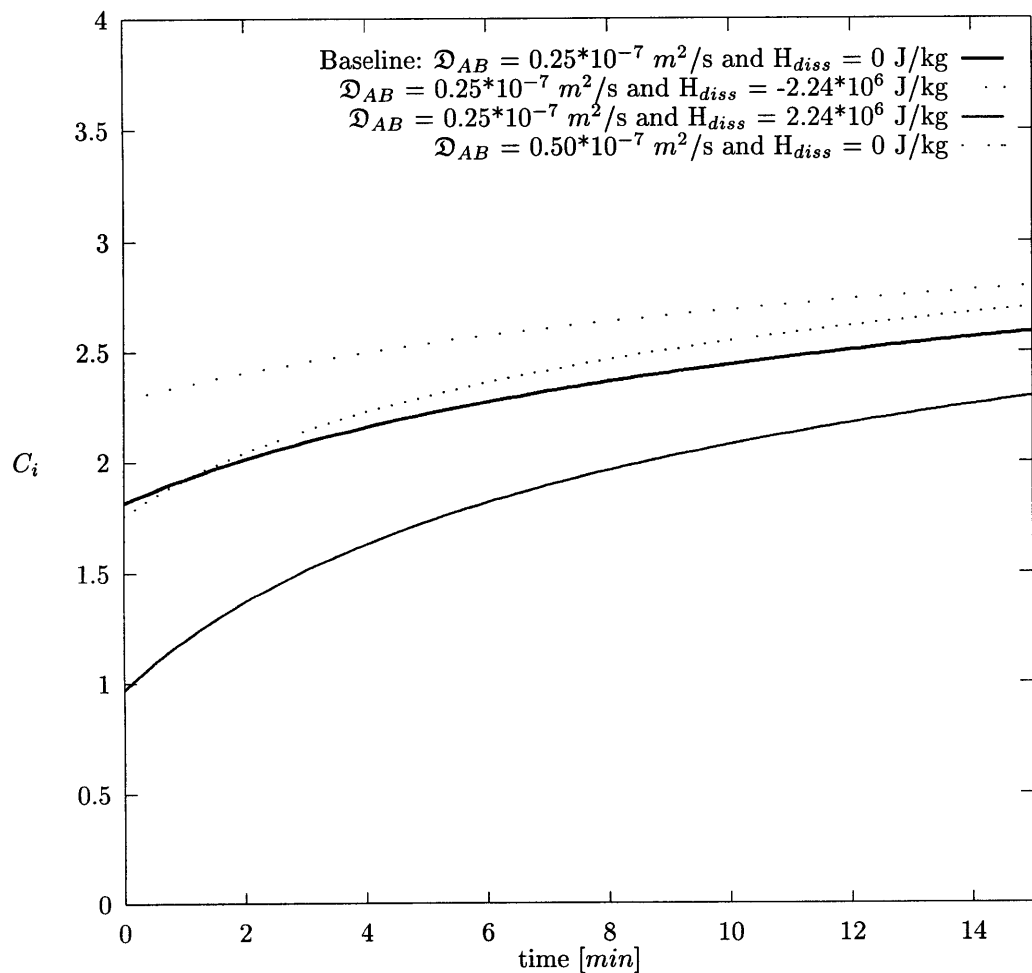
Figure 4-11: Salt layer-solution interface concentration versus time determined from the deposition rate formulation at the conditions indicated and a pressure of 250 bar. The concentration of sodium sulfate in the inlet stream was 4 wt%.
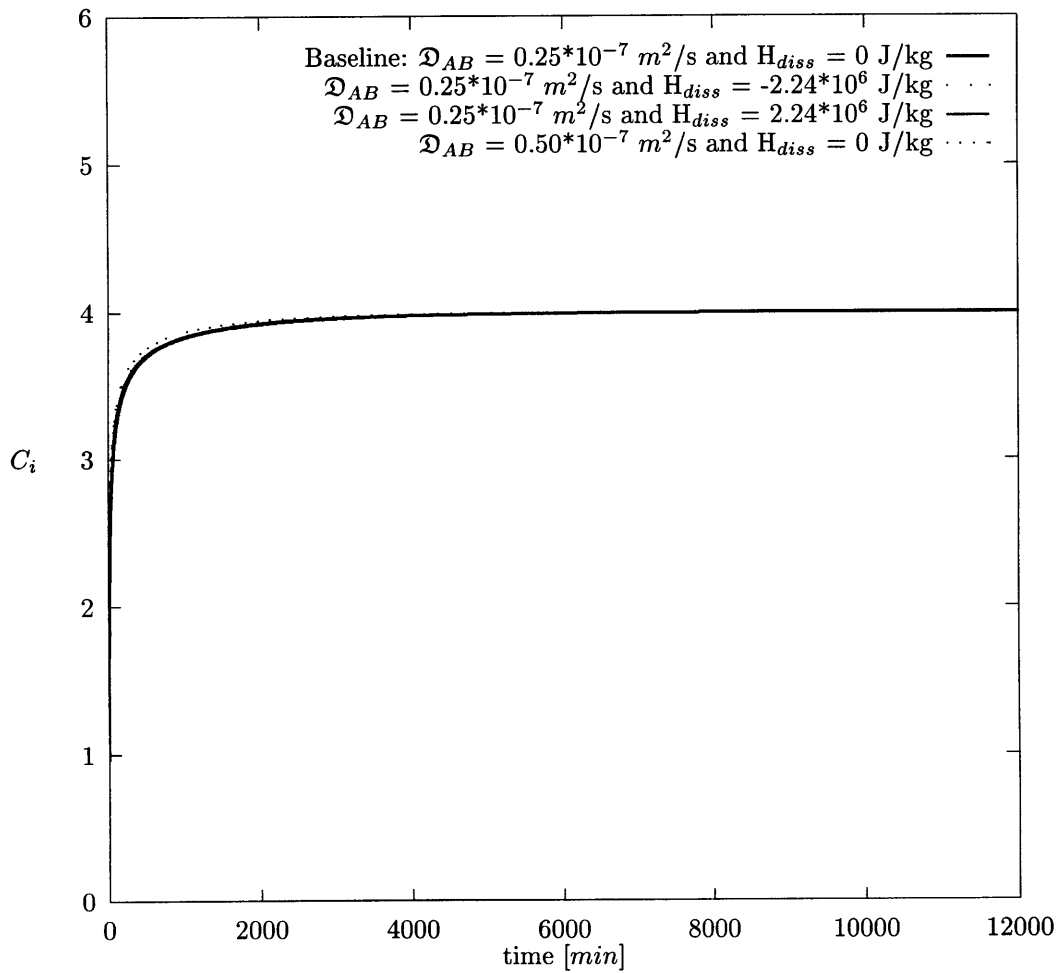
Figure 4-12: Salt layer-solution interface concentration versus time determined from the deposition rate formulation at the conditions indicated and a pressure of 250 bar. The concentration of sodium sulfate in the inlet stream was 4 wt%.
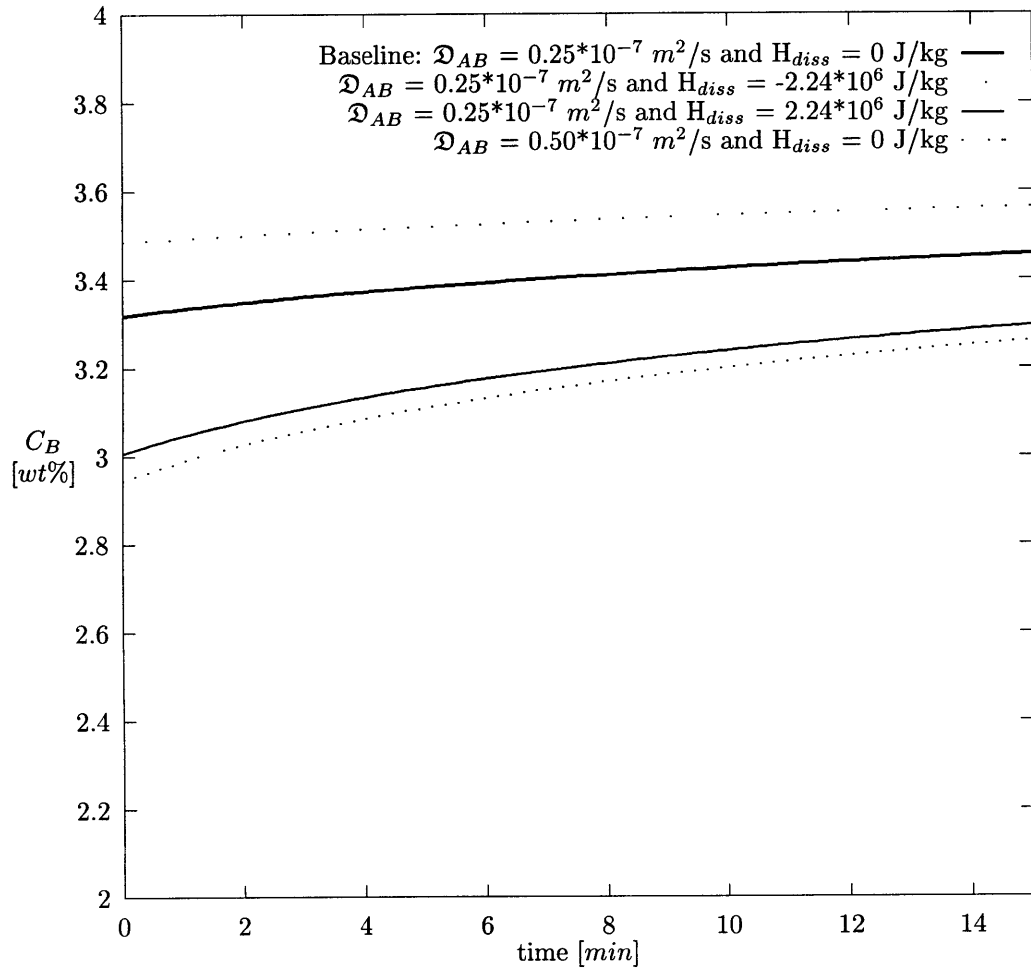
Figure 4-13: Bulk solution concentration versus time determined from the deposition rate formulation at the conditions indicated and a pressure of 250 bar. The concentration of sodium sulfate in the inlet stream was 4 wt%.
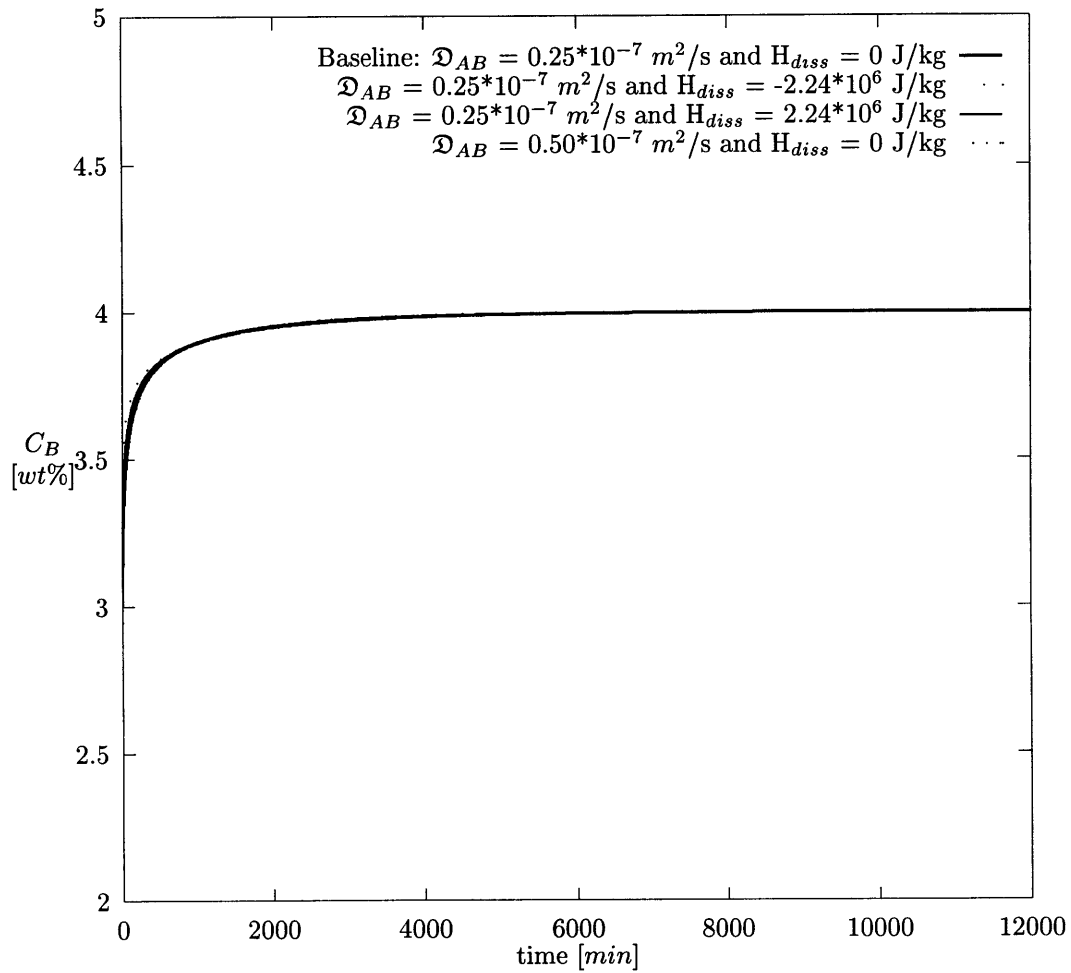
Figure 4-14: Bulk solution concentration versus time determined from the deposition rate formulation at the conditions indicated and a pressure of 250 bar. The concentration of sodium sulfate in the inlet stream was 4 wt%.
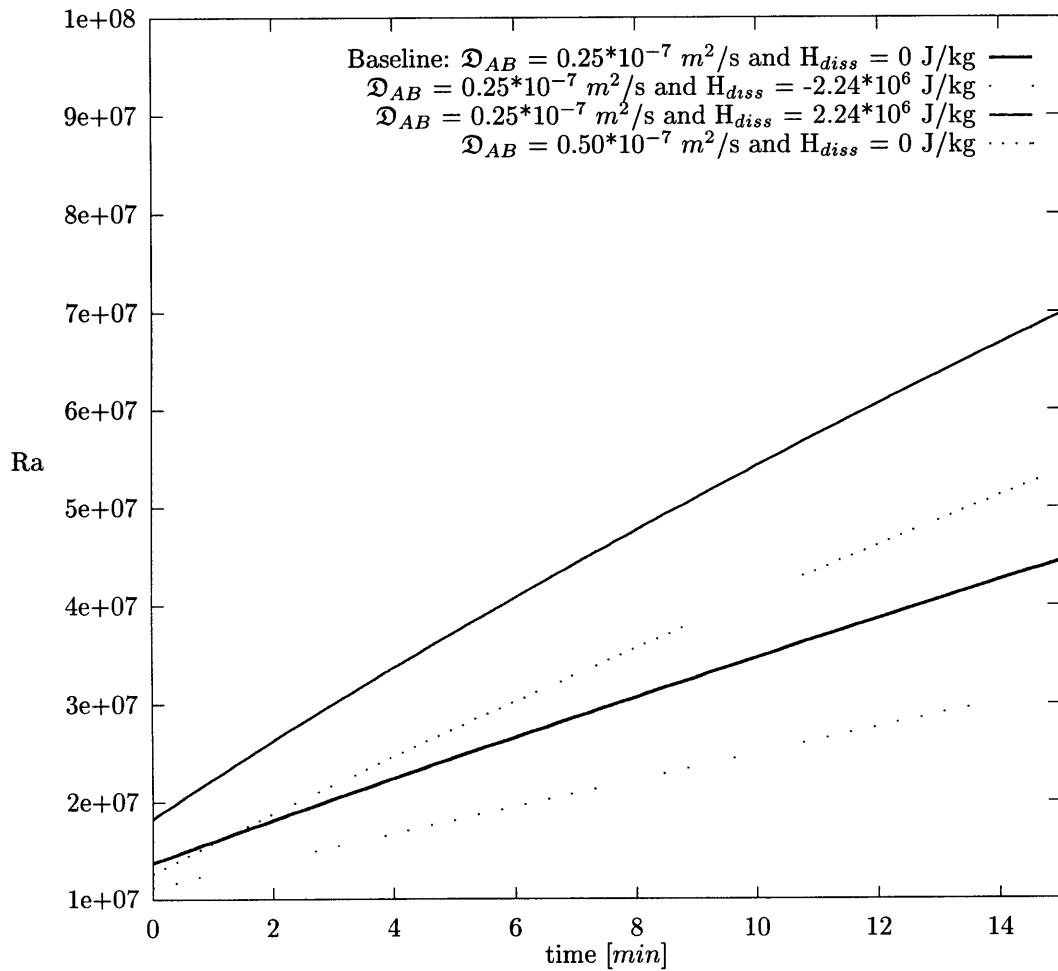
Figure 4-15: Rayleigh number based on the salt layer-solution interface diameter versus time determined from the deposition rate formulation at the conditions indicated and a pressure of 250 bar. The concentration of sodium sulfate in the inlet stream was 4 wt%.
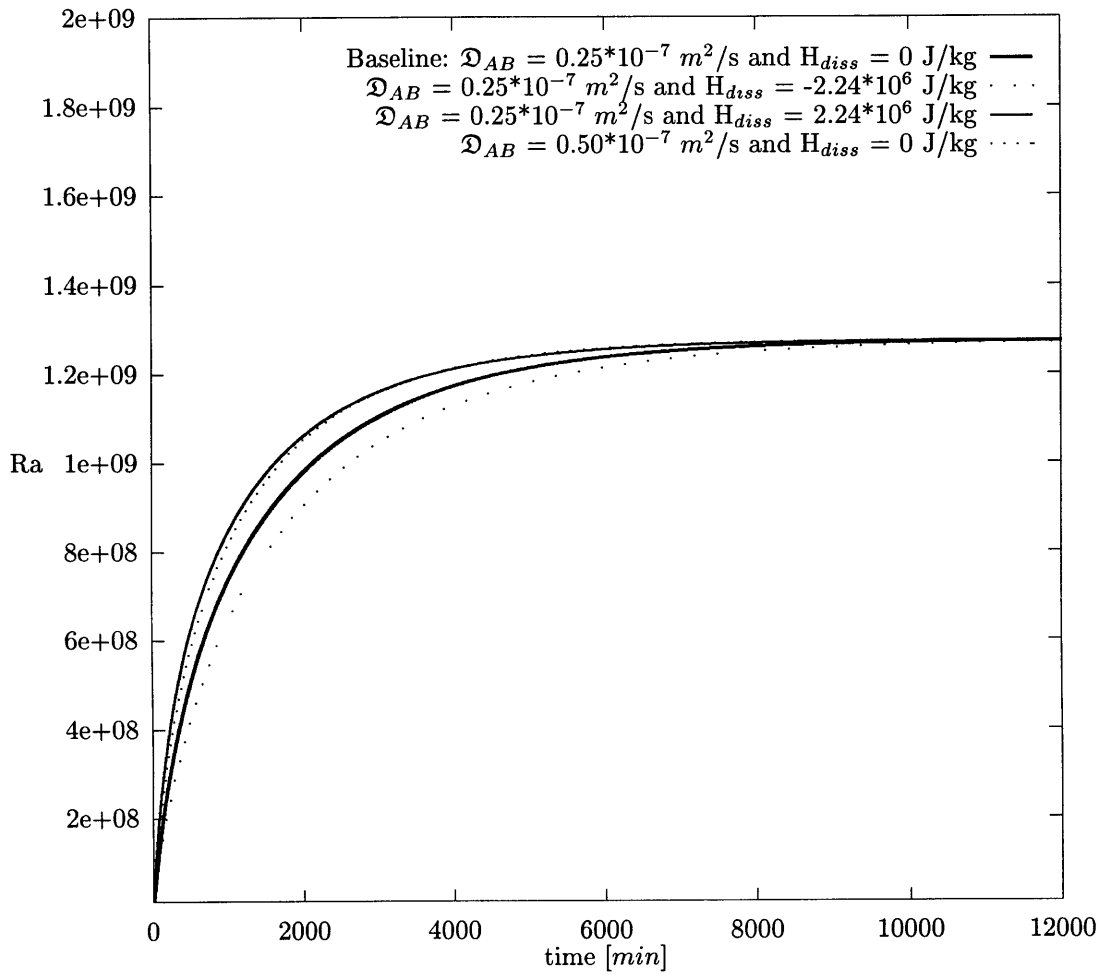
Figure 4-16: Rayleigh number based on the salt layer-solution interface diameter versus time determined from the deposition rate formulation at the conditions indicated and a pressure of 250 bar. The concentration of sodium sulfate in the inlet stream was 4 wt%.
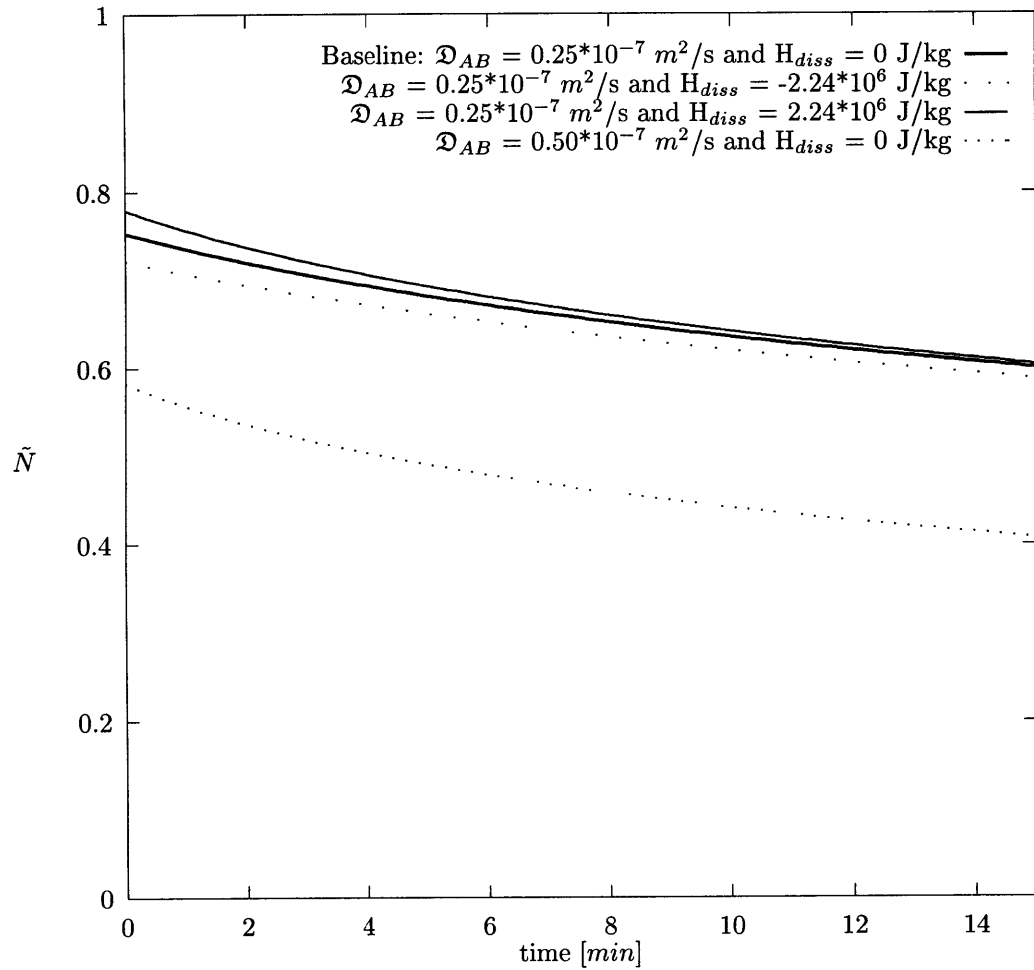
Figure 4-17: $\tilde{N}$ versus time determined from the deposition rate formulation at the conditions indicated and a pressure of 250 bar. The concentration of sodium sulfate in the inlet stream was 4 wt%.
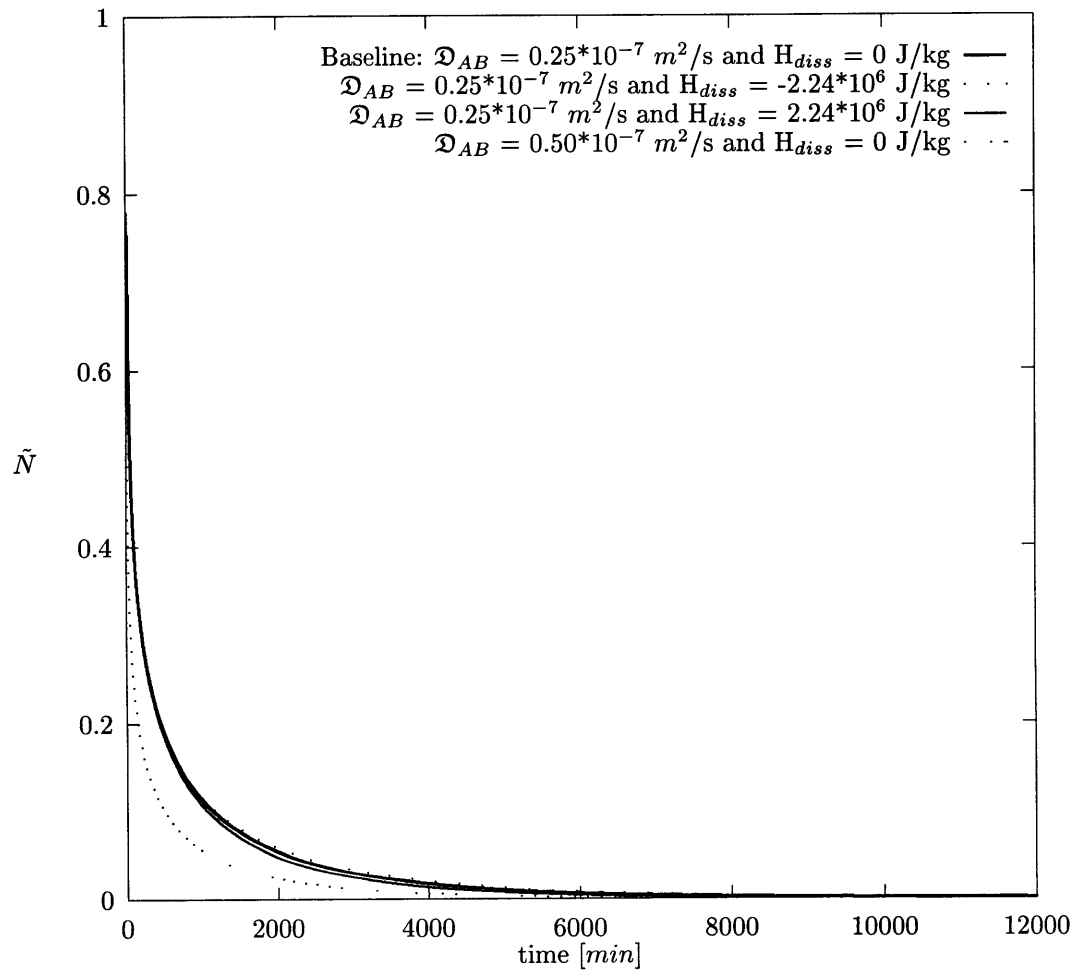
Figure 4-18: $\tilde{N}$ versus time determined from the deposition rate formulation at the conditions indicated and a pressure of 250 bar. The concentration of sodium sulfate in the inlet stream was 4 wt%.
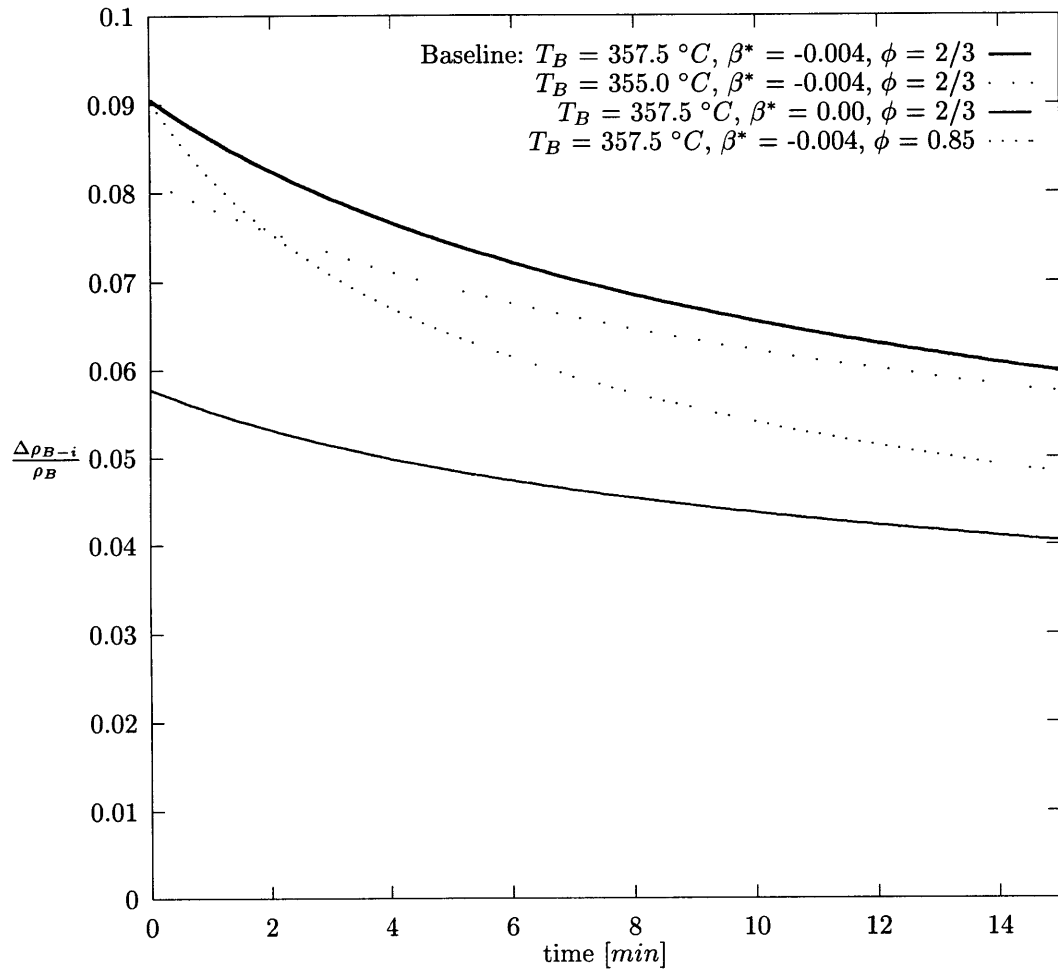
Figure 4-19: $\frac{\Delta \rho_{B-i}}{\rho_B}$ versus time determined from the deposition rate formulation at the conditions indicated and a pressure of 250 bar. The concentration of sodium sulfate in the inlet stream was 4 wt%.
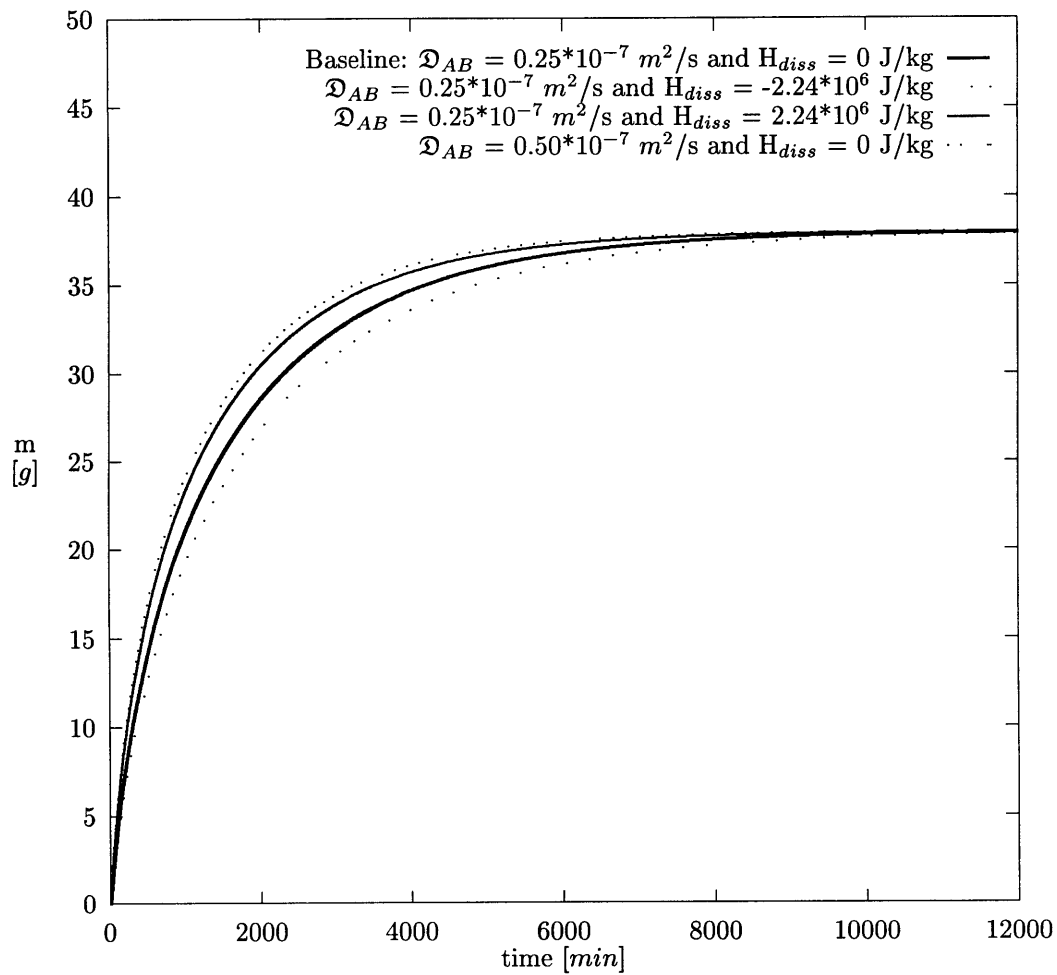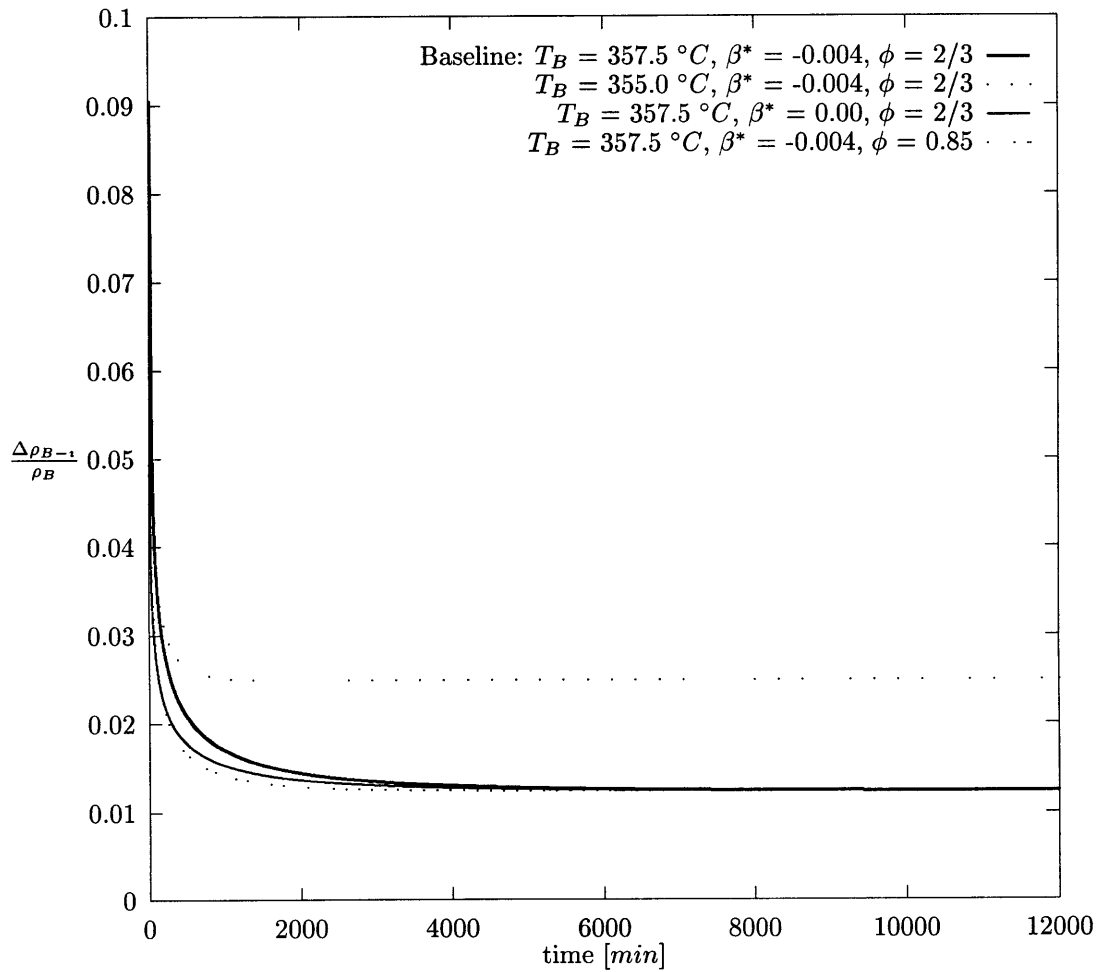
Figure 4-20: $\frac{\Delta\rho_{B-\imath}}{\rho_B}$ versus time determined from the deposition rate formulation at the conditions indicated and a pressure of 250 bar. The concentration of sodium sulfate in the inlet stream was 4 wt%.
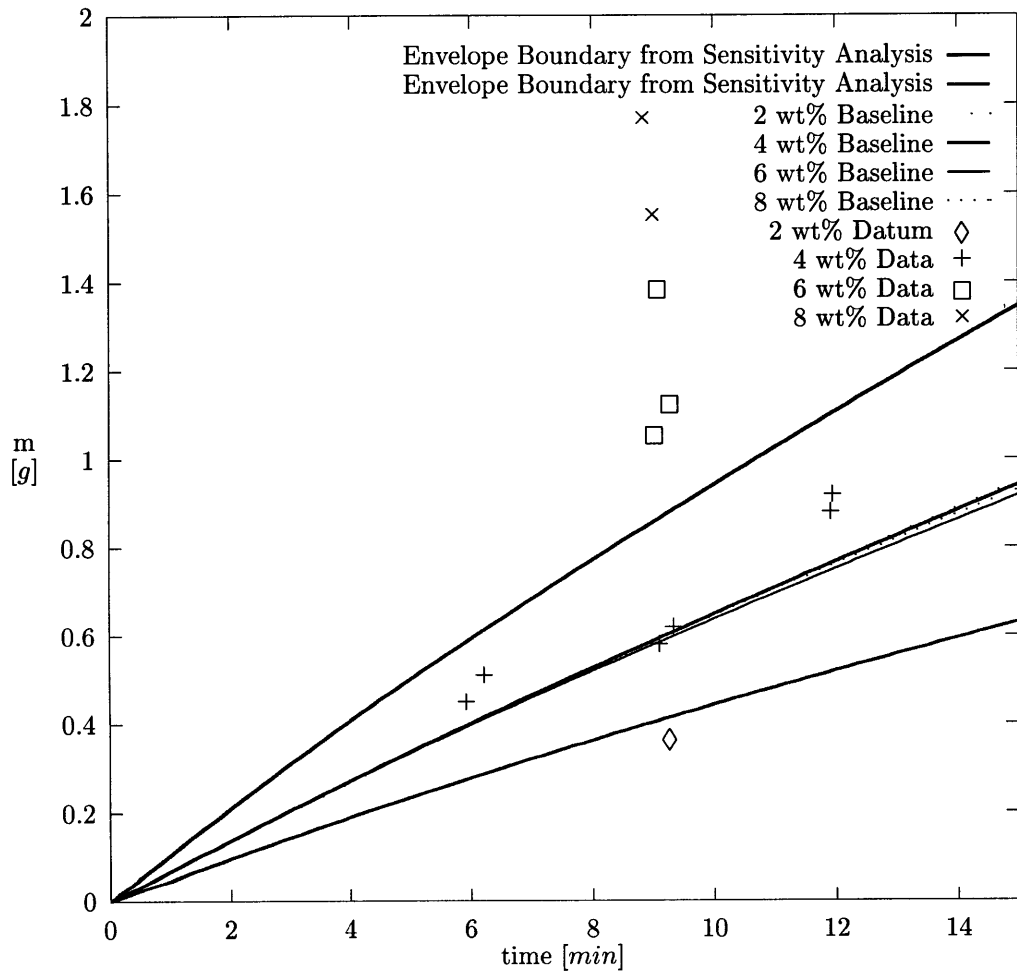
Figure 4-21: Experimental data and theoretical predictions for all of the sodium sulfate deposition experiments. (The same "envelope boundary" bounds the theoretical predictions corresponding to all experimental operating conditions.)
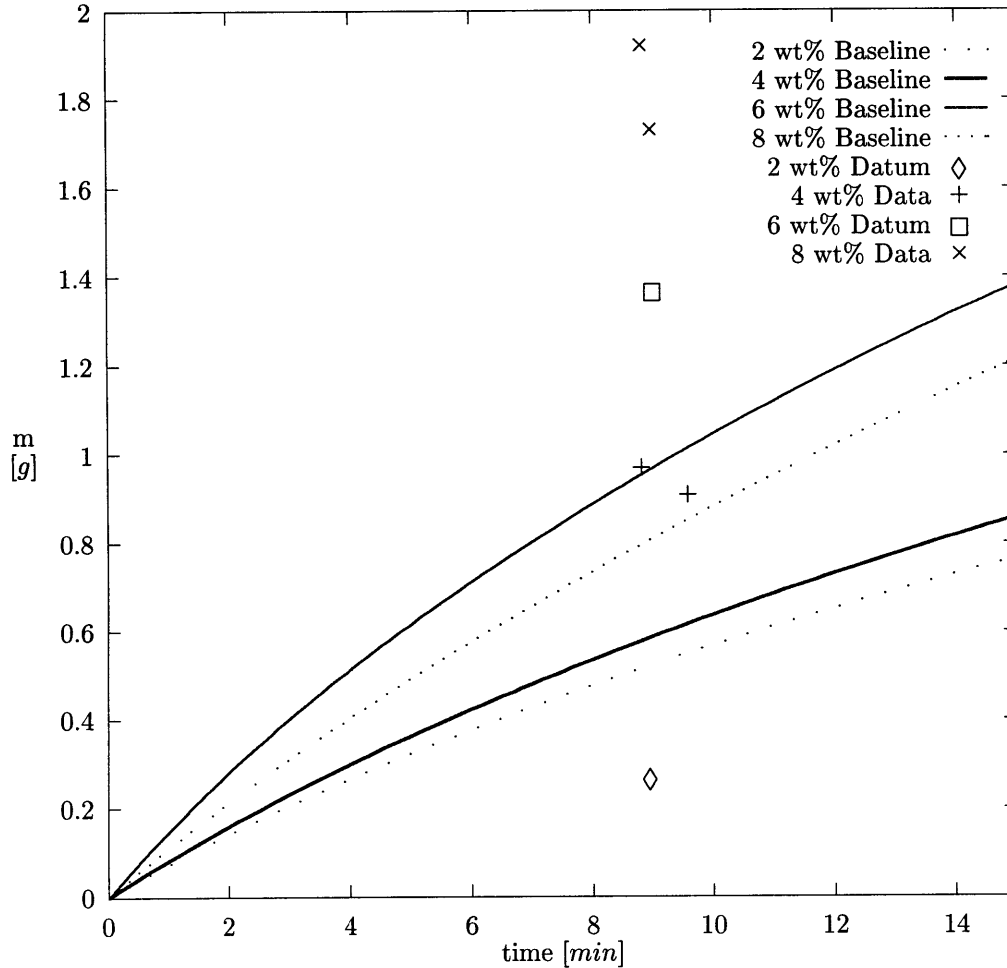
Figure 4-22: Experimental data and "baseline" theoretical predictions for all the potassium sulfate deposition experiments.

4.5 Transport Inside the Porous Salt Layer

This section explains why deposition inside the porous salt layer formed on the hot finger is likely important for some of the operating conditions in the deposition experiments. Throughout this section, it is assumed that the aqueous salt solutions can not tolerate any metastability, i.e., all salt beyond the solubility concentration at a given temperature is assumed to precipitate. The interfacial boundaries separating regions surrounding the hot finger which contain various combinations of solid salt, pure water and aqueous salt solution are delineated in Fig. 4-23. (The circular geometry of the boundaries is an idealization and the radii of them shown in Fig. 4-23 do not correspond to any of the experimental operating conditions as the figure

305

is used only for a general discussion.) In this figure, the innermost circle corresponds to the surface of the hot finger. Progressing radially outward from the surface of the hot finger, the temperature corresponding to zero salt solubility at 250 bar, salt layer-solution interface temperature and bulk solution temperature delineate the other three boundaries. Adjacent to the surface of the hot finger may exist a region containing solid salt and (essentially) pure water. The temperature-composition diagram for the Na_2SO_4-H_2O system at 250 bar together with the surface temperature profile of the hot finger measured during a deposition experiment elucidate why, for some operating conditions, the water in this region is essentially pure. The experimental sodium sulfate solubility data presented by Teshima [85] shows that at a pressure of 250 bar sodium sulfate becomes essentially insoluble in water at the pseudocritical temperature of pure water (385 $°C$). (At 250 bar and 385 $°C$, the solubility of sodium sulfate in water is about 0.1 wt% [85].) However, the surface temperature of the hot finger can exceed 385 $°C$ during the sodium sulfate deposition experiments. For example, Fig. 2-16 shows that during a 4 wt% sodium sulfate deposition experiment the surface temperature of the hot finger reaches about 390 $°C$. When the hot finger surface temperature exceeds 385 $°C$, a mixture of solid sodium sulfate and (essentially) pure water must exist in the region adjacent to the surface of the hot finger assuming no metastability is present. (Similar arguments may be made for the potassium sulfate-water system.) At some radial distance beyond the surface of the hot finger, temperature equals that corresponding to zero salt solubility (the pseudocritical temperature in the case of the Na_2SO_4-water system at 250 bar) and beyond this radius lies a region containing a mixture of solid salt and aqueous salt solution. This region ends at the salt layer-solution interface, beyond which solid salt is no longer present. The concentration of salt in the solution at the salt layer-solution interface increases to that in the bulk solution across the boundary layer formed around the salt layer-solution interface. This boundary layer is idealized as a thin annulus in Fig. 4-23. (Of course, the true boundary layer thickness is a increasing function of x and a plume forms towards the top of the salt layer-solution interface.) Outside the boundary layer region, i.e., in the bulk solution, the concentration of salt in solution is assumed to be uniform as per Section 3.11.2.

The importance of deposition within the porous salt layer may be elucidated by examining the mass transfer driving forces present within the four regions surrounding the hot finger delineated in Fig. 4-23. The bulk solution temperature (T_B), solubility temperature corresponding to the concentration of salt in

306
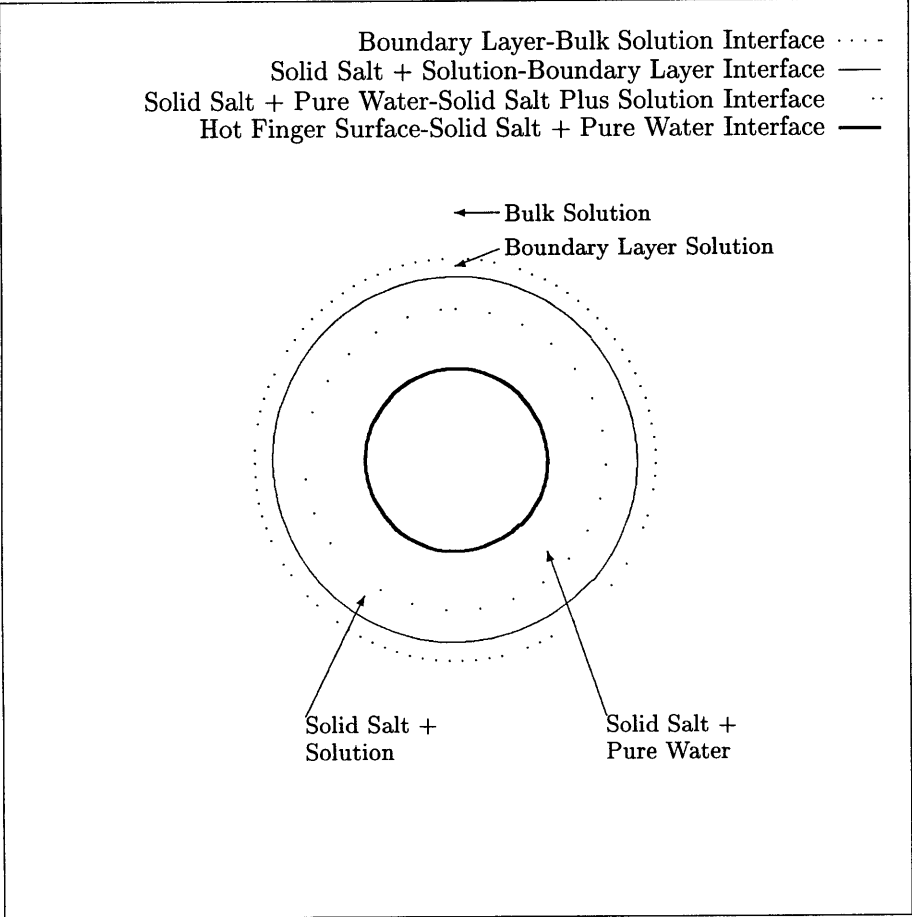
Figure 4-23: Idealized boundaries between regions containing various combinations of solid salt, pure water and aqueous salt solution surrounding the hot finger.

the bulk solution (T_s), salt layer-solution interface temperature (T_i), temperature corresponding to zero solubility (T_o) and hot finger surface temperature (T_{HF}) are shown on a temperature-composition diagram in Fig. 4-24 for an arbitrary set of operating conditions. In the bulk solution the driving force for mass transfer is, obviously, zero. The driving force for mass transfer across the boundary layer, i.e., salt deposition at the salt layer-solution interface, equals the salt concentration in the bulk solution minus the salt concentration at the salt layer-solution interface as shown in Fig. 4-24. (Salt does not nucleate homogeneously in the boundary layer at conditions of interest; therefore, there is not "deposition" on particles inside the boundary layer.) The driving force for mass transfer within the region containing solid salt and aqueous salt solution is a bit more complex. At the outer boundary of this region the concentration of salt in solution corresponds to that at the salt layer-solution interface, C_i. At the inner boundary of this region, the concentration of salt in solution equals (essentially) zero, i.e., the solution is essentially pure water. Thus, a logical choice for a mass transfer driving force representative of this region is simply C_i as shown in Fig. 4-24. (The driving force for mass transfer in the porous salt layer is denoted by ΔC_{i-PSL}.) However, the surface area available for deposition inside the porous salt layer is very important and by no means obvious. The driving forces for mass transfer across the boundary layer and within the porous salt layer pertain to two very different types of transport problems. The driving force for mass transfer across the boundary layer is used to compute the rate of deposition by natural convective mass transfer over the surface area of the salt layer-solution interface (approximately $\pi D_i L$). Conversely, the driving force for mass transfer inside the porous layer applies to a volume. Moreover, mass diffusion is probably the dominant mechanism for deposition inside the porous salt layer. As per Section 6.2, if the morphology of the porous salt layers were carefully examined, it might be possible to determine unequivocally whether or not natural convective mass transfer was important within the porous salt layers. In the region bounded by the hot finger surface and temperature corresponding to zero salt solubility, lies (essentially) pure water and solid salt; therefore, the driving force for mass transfer/deposition is (essentially) zero.

The analyses performed earlier in this Chapter suggest that during all the deposition experiments, the concentration of salt in the bulk solution approaches that in the inlet stream and the concentration of salt at the salt layer-solution interface is about 2 wt% less than that in the bulk solution. Thus, for example, in the

deposition experiments for which the concentration of salt in the inlet stream is 4 wt%, the concentration

of salt in the bulk solution and at the salt layer-solution interface are, roughly, 4 and 2 wt% respectively.

Measurements of the hot finger surface temperature profile during selected deposition experiments show it

reaches or exceeds the temperature corresponding to zero salt solubility. Thus, the concentration of salt at

the hot finger surface is subsequently assumed to equal zero in this section. It follows that in the deposition

experiments for which the concentration of salt in the inlet stream is 4 wt%, for example, the driving forces

for mass transfer to the salt layer-solution interface (ΔC_{B-i}) and within the porous layer (ΔC_{i-PSL}) are

both approximately 2 wt%. The approximate values of the salt concentration in the bulk solution, at the

salt layer-solution interface and at the surface of the hot finger as a function of the salt concentration in

the inlet stream are provided in Table 4.11. The corresponding driving forces for deposition at the salt

layer-solution interface and within the porous salt layer are provided as well. As per Table 4.11, the driving

force for deposition of salt at the salt-layer solution interface is, to a first approximation, independent of

the concentration of salt in the inlet stream at the conditions investigated in the deposition experiments,

i.e., it is always approximately 2 wt% . Conversely, the driving force for deposition within the porous salt

layer is equal to the salt concentration in the inlet stream minus 2 wt% to a first approximation. Moreover,

the driving force for mass transfer inside the porous layer is close to zero in the experiments for which the

concentration of salt in the inlet stream equals 2 wt%. Deposition rates at the salt layer-solution interface

were computed earlier in this chapter. However, as previously noted, deposition inside the porous salt layer

was neglected. The foregoing discussion suggests that deposition within the porous salt layer increases with

the concentration of salt in the inlet stream, but the deposition rate at the salt layer-solution interface is

essentially constant. Hence, it is not surprising that the deposition computations earlier in this Chapter

agreed better with the experimental data when the concentration of salt in the inlet stream was 2 and 4

wt% than when the concentration of salt in the inlet stream was 6 and 8 wt%.

Fig. 4-25 also illustrates a set of circumstances when changing the inlet concentration/bulk concentration

of salt can more dramatically affect the driving force for mass transfer inside the porous layer than at the salt

layer-solution interface. (The magnitudes of the mass transfer driving forces shown in this figure are used

for illustrative purposes and do not correspond to any experimental conditions.) For conditions "1" and "2"
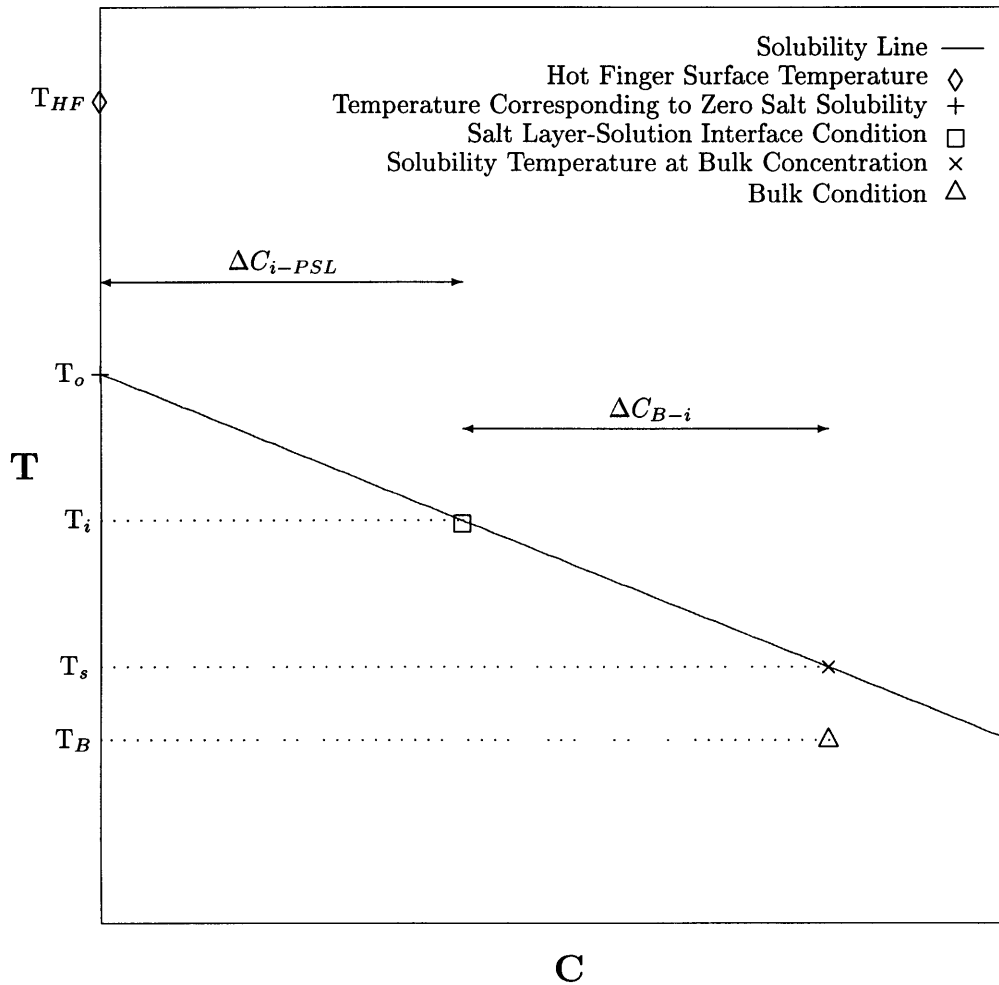
Figure 4-24: Driving forces for deposition at the salt layer-solution interface and within the porous salt layer shown on a temperature composition diagram for an arbitrary set of operating conditions.

C_{inlet} wt%	C_B wt%	C_i wt%	C_{HF} wt%	ΔC_{B-i} wt%	ΔC_{i-PSL} wt%
2	2	0	0	2	0
4	4	2	0	2	2
6	6	4	2	2	4
8	8	6	4	2	6

Table 4.11: Approximate concentrations of salt in the bulk solution, at the salt layer-solution interface and on the surface of the hot finger and corresponding mass transfer driving forces as a function of the salt concentration in the inlet stream for the conditions investigated in the deposition experiments.

in Fig. 4-25, the temperature differences between the salt layer-solution interface and bulk and between the hot finger surface and salt layer-solution interface are constant. Moreover, in both cases the solubility of salt at the hot finger surface temperature equals zero. Under these conditions, the driving force for mass transfer at the salt layer-solution interface is the same in cases "1" and "2"; however, the mass transfer driving force inside the porous salt layer in case "2" is double that in case "1."
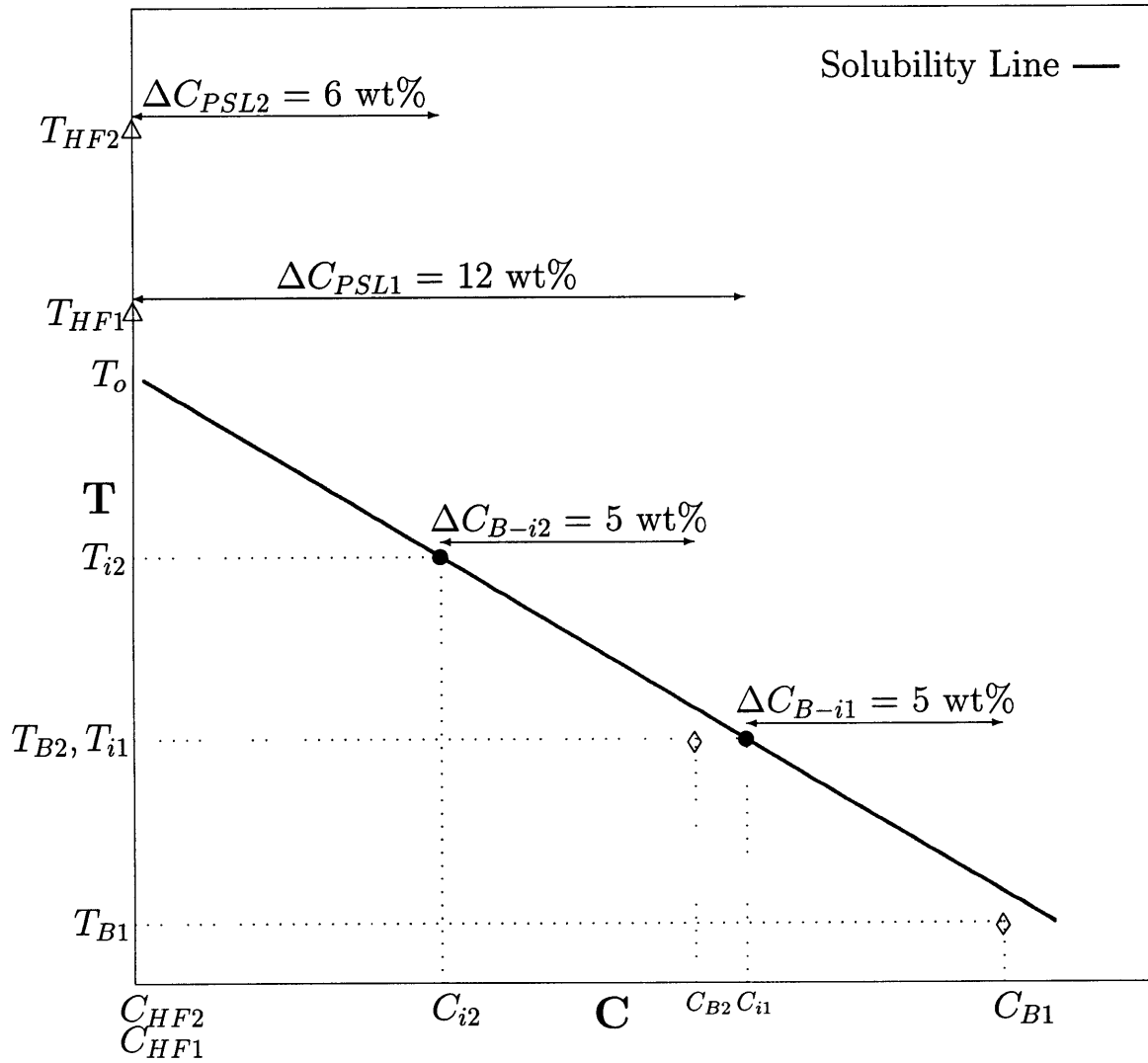
Figure 4-25: Illustration of a set of circumstances when changing the inlet concentration has a more dramatic effect on the mass transfer driving force within the porous salt layer than the mass transfer driving force at the salt layer-solution interface.

Chapter 5

Nucleation

5.1 Introduction

Armellini [4] performed flow experiments to simulate the rapid precipitation of salts at conditions typical of the SCWO process. Observed values of the particle diameters for sodium sulfate and sodium chloride typically ranged from 1 to 20 microns and 5 to 100 microns respectively. Hence, based on the Armellini study, 0.1 microns serves as a conservative lower bound for the diameter of (Brownian) salt particles potentially present in SCWO systems. The Brownian diffusion coefficient of a 0.1 micron-diameter, spherical particle in pure supercritical water at 250 bar and 450 $°C$, for example, is $2.10*10^{-10}$ m^2/sec according to the Stokes-Einstein equation. Molecular diffusion coefficients for dissolved salts in supercritical water are orders of magnitude larger than Brownian diffusion coefficients for salt particles of diameter 0.1 μm or larger in supercritical water. For example, Butenhoff et al. [15] measured the binary molecular diffusion coefficient of sodium nitrate in supercritical water in the single phase region of the sodium nitrate-water system using the laser-induced grating technique. The diffusivity ranged, for example, from $1.06*10^{-8}$ to $2.02*10^{-8}$ m^2/sec as pressure was increased from 409.5 to 600.1 bar at 450 $°C$ in a 0.25 m aqueous sodium nitrate solution. Thus, at a temperature and pressure of about 450 $°C$ and 500 bar, the Brownian diffusion coefficient of a 0.1 micron-diameter particle in pure supercritical water is approximately 2 orders of magnitude lower than the binary molecular diffusion coefficient in a 0.25 m aqueous sodium nitrate solution. Moreover, Armellini's

measurements suggest that the diameter of Brownian particles present at typical SCWO process conditions will often exceed 0.1 microns. Since Brownian diffusion coefficients are inversely proportional to particle diameter, typical molecular diffusion coefficients in SCW may well exceed their Brownian counterparts by more than the foregoing example suggests. Deposition of larger particles by an inertial mechanism is not thought to be relevant at the conditions of interest to this dissertation.

The laminar natural convection mass transfer coefficient for transport of salt from the bulk solution to the salt layer-solution interface scales as the diffusion coefficient to the 3/4 power. Thus, if molecular clusters of salt nucleate homogeneously in the boundary layer and grow to Brownian-sized particles which diffuse to the salt layer-solution interface, the deposition rate will be substantially slower than if salt molecules diffuse to the interface and then nucleate heterogeneously. Obviously, under some conditions diffusion of both Brownian particles and salt molecules to the salt layer-solution interface needs to be considered. Under such conditions the calculation of the deposition rate at the salt layer-solution interface is very complex.

Since the nucleation mechanism and deposition rate at the salt layer-solution interface are strongly coupled, nucleation must be addressed in any meaningful deposition rate model. Nucleation will not occur in the natural convective boundary layer formed around the salt layer-solution interface if the solution there can not become supersaturated. If solution in the natural convective boundary layer becomes supersaturated, salt may or may not nucleate homogeneously there depending upon the amount of metastability which may be sustained. At sufficiently high levels of supersaturation a metastable limit is surpassed and thermodynamics dictates that salt must precipitate from solution. (Unfortunately, metastable limits for phase boundaries of interest to this dissertation are unavailable.) It is noted that if supersaturation is not present in the natural convective boundary layer formed adjacent to the nominal salt layer-solution interface, nucleation is not necessarily confined to this nominal interface. Indeed, comparison of the deposition rate data provided in Chapter 2 against the deposition rate model's predictions in Chapter 4 suggested that a significant amount of nucleation and deposition may occur within the porous salt layer formed around the hot finger. This topic was discussed in Section 4.5.

In this chapter a qualitative relationship between the Lewis number of the aqueous salt solution, phase boundary curve and potential for homogeneous nucleation is developed. Then quantitative criteria which

predict whether or not supersaturation and/or homogeneous nucleation within the boundary layer formed around the salt layer-solution interface must occur are developed and applied to the conditions investigated in the deposition experiments. Next, characteristics of aqueous salt solutions which are conducive to supersaturation and/or homogeneous nucleation within the boundary layer are identified. Then some examples of salts which are prime candidates to nucleate homogeneously in the boundary layer are given. Finally, the results of a nucleation experiment using lithium carbonate are presented.

5.2 Qualitative Relationship Between Lewis Number and Nucleation Mechanism

The Lewis number of the aqueous salt solution of interest, together with the appropriate phase boundary may be used to determine if supersaturation and/or homogeneous nucleation in the solution in the natural convective boundary layer will happen. Fig. 5-1 illustrates the relationship between the Lewis number of the aqueous salt solution, phase boundary and nucleation mechanism. It shows a bulk solution condition, salt layer-solution interface condition and phase boundary. Saturation conditions are assumed to exist at the salt layer-solution interface in Fig. 5-1 and throughout this chapter. For selected Lewis numbers, trajectories of temperature-concentration states connecting the bulk condition to the salt layer-solution interface condition are also shown in 5-1. The phase boundary shown in Fig. 5-1 is linear, but the physics elucidated in this section apply to an arbitrarily shaped phase boundary which separates a one-phase-fluid region from a solid-fluid region. One should not consider Fig. 5-1 in the context of a constant heat flux at the salt layer-solution interface. This is because the temperature difference between the salt layer-solution interface and bulk solution is a function of the thermophysical properties of the fluid, i.e., Lewis number, etc. Instead, one might consider this figure in terms of a boundary condition of the first kind at the salt layer-solution interface.

The ratio of the thermal boundary layer thickness to the concentration boundary layer thickness roughly equals the Lewis number to the 1/3 power as per Eq. 3.127. Consequently, as the Lewis number approaches zero, the thermal boundary layer thickness becomes infinitesimal relative to the concentration boundary

Figure 5-1: Loci of temperature-concentration states connecting the bulk condition to the salt layer-solution interface condition for selected Lewis numbers. Below the solubility line a one-phase-fluid region exists and above it a two-phase, solid-fluid region exists.

layer thickness. Thus as Le → 0, salt concentration decreases from its bulk value to its salt layer-solution interface value at the bulk temperature. Analogously, temperature increases from its bulk value to its value at the salt layer-solution interface at the salt layer-solution interface concentration. As the Lewis number approaches infinity, the concentration boundary layer thickness becomes infinitesimal relative to the thermal boundary layer thickness. The Le → ∞ trajectory in Fig. 5-1 is readily understood by using a rationale analogous to that which explained the Le → 0 trajectory. Maximum potential supersaturation in the boundary layer occurs as Le → ∞ as depicted in Fig. 5-1. It is noted that the amount of potential supersaturation corresponding to Le → ∞ is independent of the slope of the phase boundary provided two conditions are satisfied. Namely, the temperature difference between the salt layer-solution interface and bulk as well as the temperature difference between the solubility temperature corresponding to the bulk concentration and bulk must be constant. This argument applies to nonlinear phase boundaries as well. It is noted, however, that maintaining a constant difference between the solubility temperature corresponding to the bulk concentration of solution and a constant heat flux at the salt layer-solution interface is not sufficient to hold constant the maximum amount of potential supersaturation. This is because the thermophysical properties of aqueous salt solutions are functions of temperature, salt concentration and pressure.

When the Lewis number equals one, the dimensionless boundary layer form of the energy equation is identical to the dimensionless boundary layer form of the species equation as per Eqs. 3.123 and 3.124. Thus, assuming the boundary conditions for the two equations are of the same kind, e.g., all Dirichlet, dimensionless temperature equals dimensionless concentration throughout the boundary layer and a straight line connects the bulk condition to the salt layer-solution interface condition on the temperature-composition diagram in Fig. 5-1. To be sure, the boundary conditions on concentration and temperature at the salt layer-solution interface are not rigorously identical in the deposition experiments. However, they must be close. Moreover, the transport coefficients are modest functions of these boundary conditions; therefore, the straight line connecting the bulk condition to the salt layer-solution interface condition is a useful approximation when the Lewis number of the aqueous salt solution is near unity. It is noted that if the phase boundary is linear, the Lewis number must be larger than one for supersaturation and/or homogeneous nucleation to occur in the boundary layer. The rectangle bounded by the Le → 0 and Le → ∞ trajectories envelopes the physically

plausible (T,C) states which may exist between the bulk and interface conditions.

If nucleation is assumed not to occur in the boundary layer, the salt concentration corresponding to a given temperature increases with the Lewis number of the aqueous salt solution as illustrated in Fig. 5-2. For illustrative purposes, the thermal boundary layer thickness in Fig. 5-2 is assumed to extend approximately 5.4 radial units beyond the salt layer-solution interface at some arbitrary location in the boundary layer. (The purpose of Fig. 5-2 is to qualitatively illustrate the relationship between Lewis number and nucleation mechanism and 5.4 is an arbitrary number. In the context of natural convection induced exclusively by buoyancy forces arising from temperature differences, assuming a constant thermal boundary layer thickness implies the Prandtl number is fixed and variations in the Lewis number are, therefore, entirely due to variations in the Schmidt number.) Dimensionless temperature decreases from 1 to 0, i.e., from "hot" to "cold" over 5.4 radial units. When the Lewis number is equal to one, the concentration boundary layer thickness equals the thermal boundary layer thickness; therefore, dimensionless concentration increases from 0 to 1, i.e., from "low" to "high" in approximately 5.4 radial units. Increasing the Lewis number causes a reduction in the thickness of the 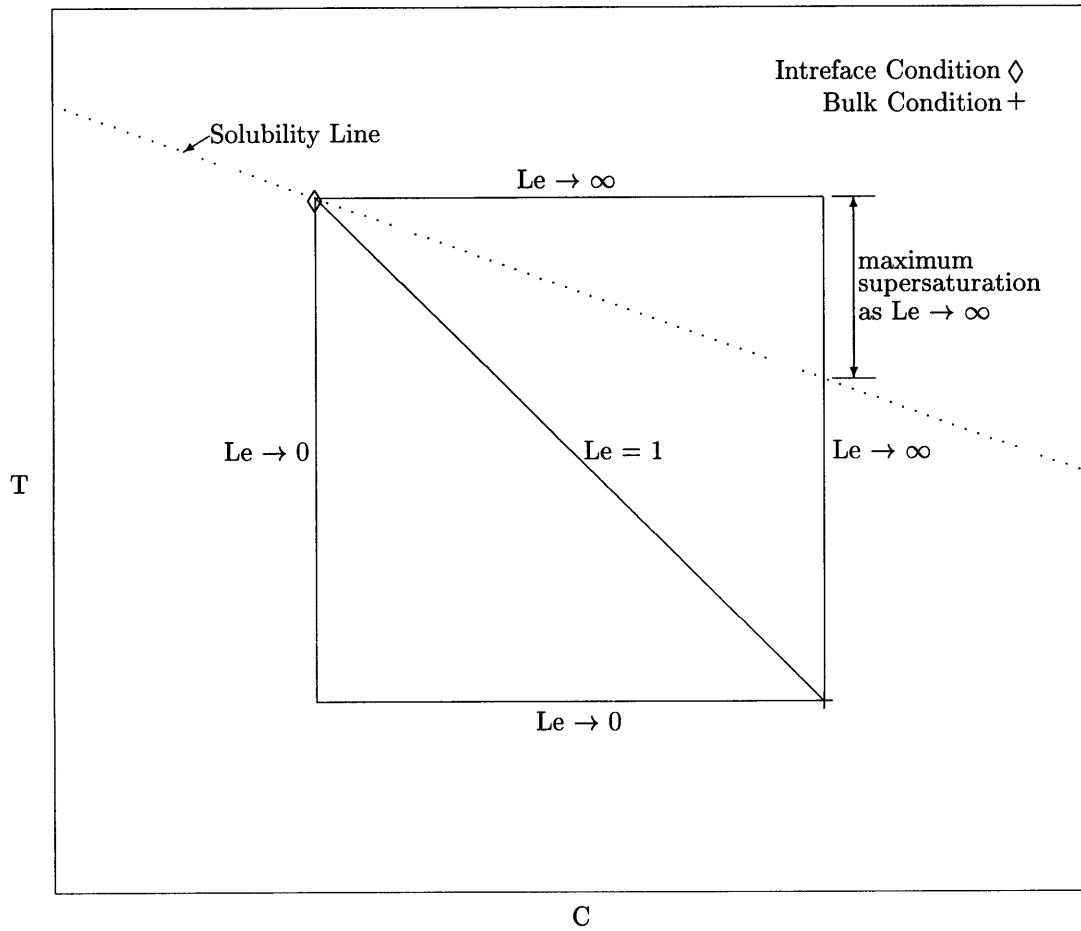concentration boundary layer relative to the thermal boundary layer thickness. Trajectories of temperature-concentration states connecting the bulk condition to the salt layer-solution interface condition are shown for $Le = 1$, $Le > 1$, and $Le \gg 1$. The salient principle illustrated by the three trajectories is that for a given temperature in the boundary layer a higher Lewis number results in a higher salt concentration. For example, at 1 radial unit from the salt layer-solution interface, dimensionless temperature equals about 0.5. The corresponding dimensionless concentrations are approximately 0.5, 0.8, and 1.0 for the $Le = 1$, $Le > 1$, and $Le \gg 1$ trajectories respectively. Moreover, beyond some critical Lewis number, salt concentration exceeds the solubility concentration at the corresponding temperature and supersaturation and/or homogeneous nucleation must occur. The Lewis number beyond which supersaturation and/or homogeneous nucleation must occur is henceforth referred to as the critical Lewis number, Le_c. Also, as can be inferred from Fig. 5-2, as the Le number is increased beyond its critical value, the amount of supersaturation increases and, therefore, homogeneous nucleation becomes more likely. In the limit of Le $\rightarrow \infty$, salt concentration changes from the interface condition to the bulk condition over an infinitesimal distance and all of the flow field surrounding the hot finger is at the bulk concentration. Hence, the level of
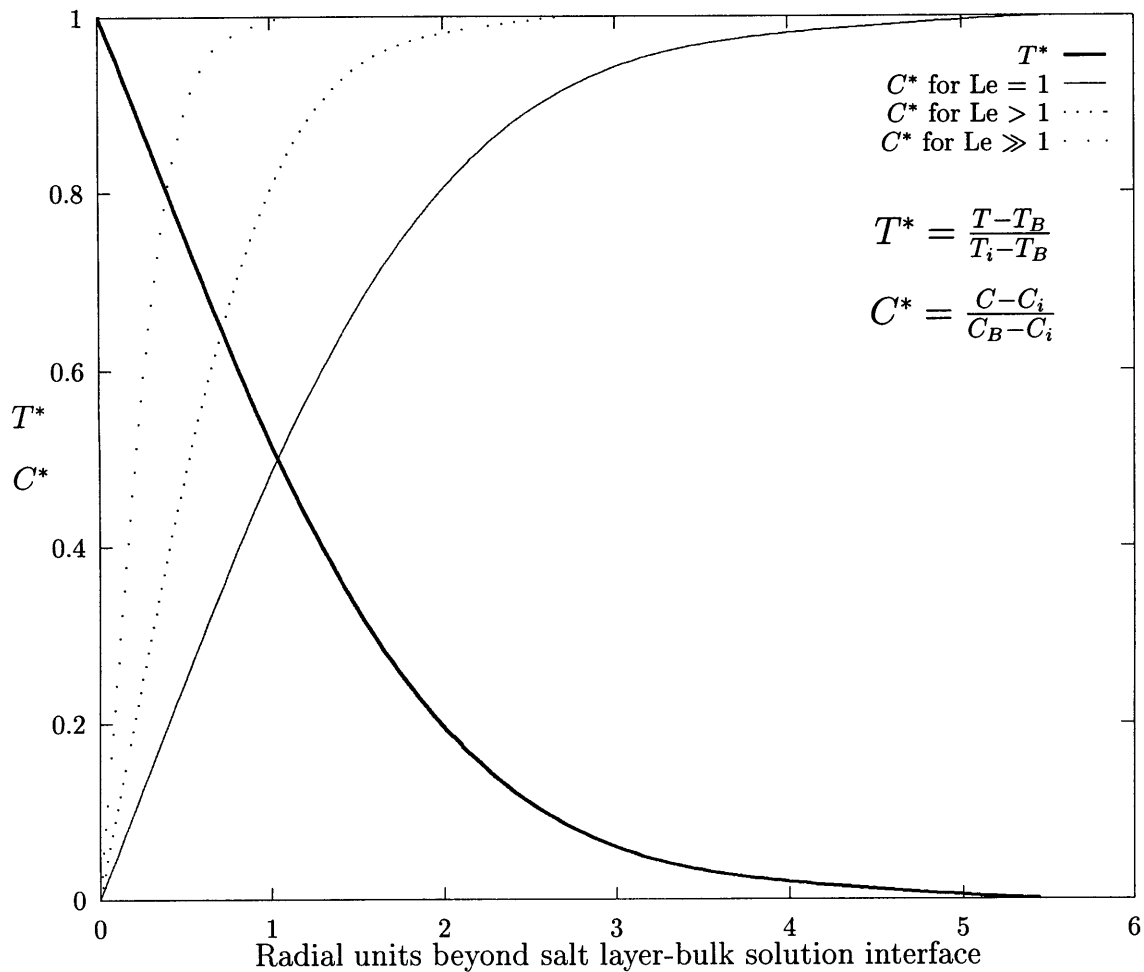
Figure 5-2: Dimensionless temperature and concentration profiles as a function of radial distance from the salt layer-solution interface at different Lewis numbers.

potential supersaturation is at a maximum everywhere.

The critical Lewis number increases as the salt layer-solution interface condition approaches the bulk condition during the deposition process. Fig. 5-3 shows three loci of temperature-concentration states connecting a bulk condition to three different salt layer-solution interface conditions. All three loci correspond to a Lewis number of 100 and Prandtl number of 0.72. (The loci were determined from the analysis presented Section 5.3.3.) At the highest salt layer-solution interface temperature, supersaturation and/or homogeneous nucleation occurs in the boundary layer. As the deposition process continues and the intermediate

salt layer-solution interface temperature is reached, saturation conditions exist as the interface condition is approached. Finally, at the lowest temperature of the salt layer-solution interface, saturation conditions exist only at the interface. As steady state conditions are approached, the salt layer-solution interface concentration approaches the bulk concentration and the critical Lewis number approaches infinity as per Eq. 5.1. Obviously, the Lewis number of any solution is finite. Hence, before deposition stops, salt must be transported to the salt layer-solution interface exclusively by molecular diffusion. Pragmatically, if homogeneous nucleation occurs in the boundary layer at the beginning of an experiment, it will cease substantially before steady state conditions are established.

$$lim_{t \to \infty} Le_c = \infty \qquad (5.1)$$

It is noted in passing that the relationship between the Lewis number of the solution of interest, phase boundary and nucleation mechanism applies to an analogous problem in which a substance is deposited on a cold finger. At ordinary conditions, i.e., near STP, the solubility of most solutes in water increases with increasing temperature as shown on the temperature-composition diagram in Fig. 5-4. Thus, to deposit a solute on a finger immersed in an aqueous solution at "ordinary" conditions, it must be cooled relative to the solution. (Of course this is predicated on the assumption that the substance of interest adheres to the cold finger.) Trajectories of temperature-composition states connecting a bulk condition to a solute layer-solution interface condition corresponding to Lewis numbers of 0, 1 and ∞ are shown in Fig. 5-4. The loci of temperature-composition states as a function of Lewis number are completely analogous to those for the hot finger case. For example, maximum potential supersaturation is achieved as Le $\to \infty$.

5.3 Quantitative Predictions of Nucleation Mechanism

5.3.1 Introduction

The potential for supersaturation and/or homogeneous nucleation in the natural convective boundary layer formed around the salt layer-solution interface is quantitatively evaluated in this section. The salt layer-
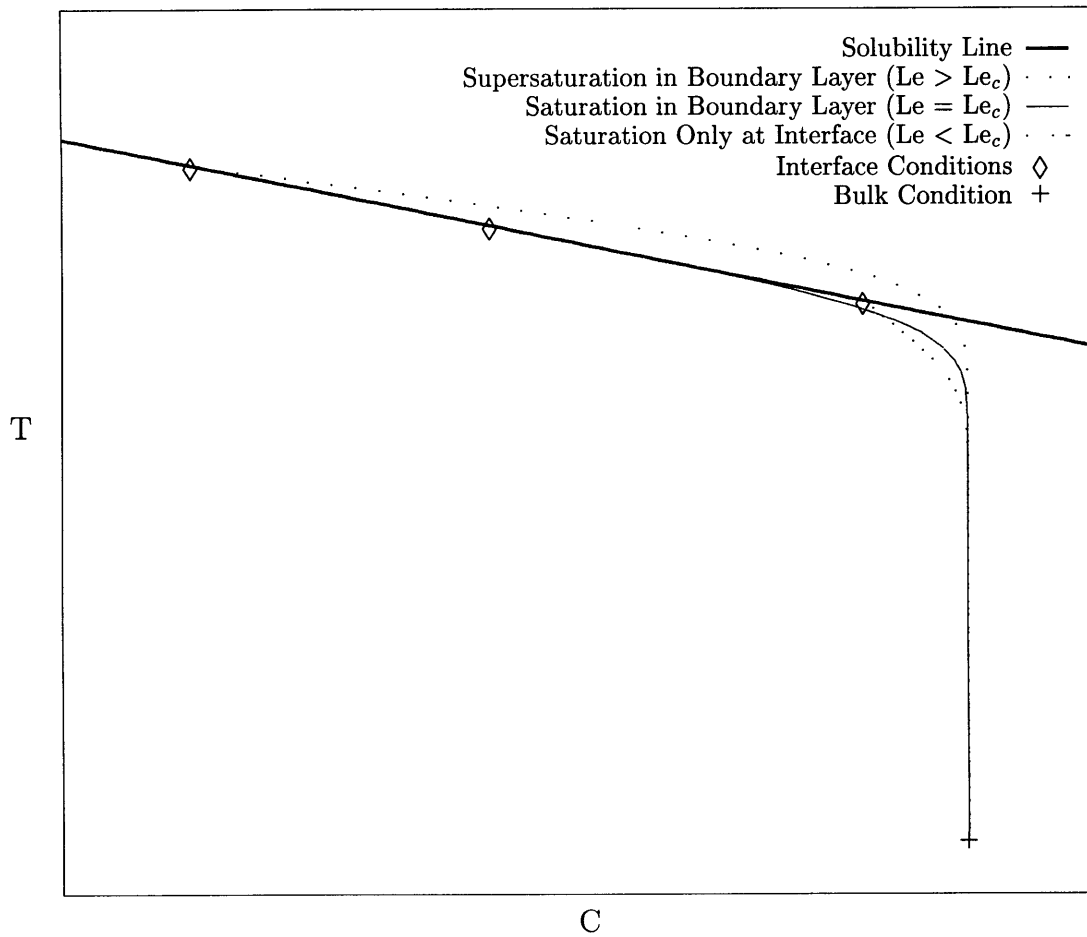
Figure 5-3: Loci of temperature concentration states connecting a bulk condition to three different salt layer-solution interface conditions. All three loci correspond to Le = 100 and Pr = 0.72. Below the solubility line a one-phase-fluid region exists and above it a two-phase, solid-fluid region exists.
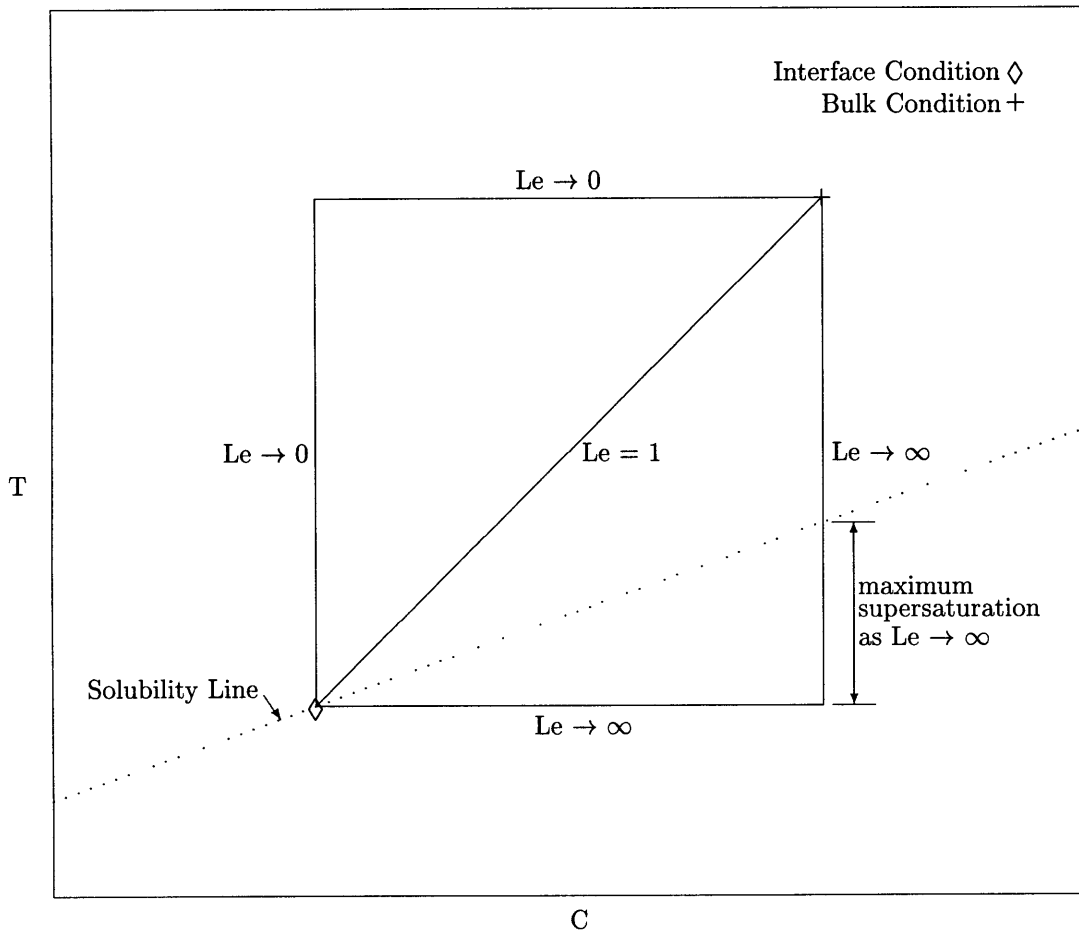
Figure 5-4: Loci of temperature-concentration states connecting a bulk solution condition to a solute layer-solution interface condition as a function of Lewis number during a hypothetical cold finger experiment. Above the solubility line, a one-phase fluid region exists and below it a two-phase, solid-fluid region exists.

solution interface is modeled as a vertical flat plate of height $\frac{\pi D_\perp}{2}$ as in the deposition rate model developed in Chapter 3. This makes the task at hand substantially more analytically/numerically tractable. Loci of temperature-concentration states in the natural convection boundary layer are determined from solutions of the relevant forms of the conservation equations under the assumption that homogeneous nucleation can not occur. If the salt concentration exceeds the solubility concentration anywhere in the boundary layer, the potential for homogeneous nucleation exists. Models are developed first for the case when the Lewis number of the aqueous salt solution equals one and then when it exceeds one.

5.3.2   Le = 1 Case

A method to determine the amount of supersaturation or lack thereof present in the boundary layer when the Lewis number of the aqueous salt solution equals one is developed in this section. Buoyancy is assumed to be driven solely by temperature differences in the development of the method. However, a means to fully account for double-diffusive natural convection is provided at the end of the section. It was shown in Chapter 3 that, when Le = 1 and the relevant boundary conditions are of the same kind, dimensionless temperature equals dimensionless concentration throughout the boundary layer. Throughout this dissertation the boundary conditions at the salt layer-solution interface on both the energy and species "A" conservation laws are assumed to be of the first kind. Rigorously, however, the boundary conditions for the energy and species equations are neither identical nor exactly of the first kind at the salt layer-solution interface. Nonetheless, the transport coefficients are a weak function of the boundary conditions at the salt layer-solution interface provided they are of the first or second kind; hence, for Le = 1, setting dimensionless temperature equal to dimensionless concentration throughout the boundary layer is a reasonable approximation. (It is also assumed that the boundary conditions corresponding to bulk conditions on both of the equations are of the first kind.) Thus, for the case at hand, the species equation does not need to be included in the statement of the conservation laws because the simplest form of the analogy between heat and mass transfer applies. Using the nomenclature illustrated in Fig. 3-4, the laminar boundary layer forms of the mass, momentum and energy conservation equations describing natural convection on a vertical heated plate in a quiescent

medium are given by Eqns. 5.2 through 5.4:

$$\frac{\partial u}{\partial x} + \frac{\partial v}{\partial y} = 0 \tag{5.2}$$

$$u\frac{\partial u}{\partial x} + v\frac{\partial u}{\partial y} = \nu\frac{\partial^2 u}{\partial y^2} + g\beta(T - T_\infty) \tag{5.3}$$

$$u\frac{\partial T}{\partial x} + v\frac{\partial T}{\partial y} = \alpha\frac{\partial^2 T}{\partial y^2} \tag{5.4}$$

The salt layer-solution interface condition is denoted by the subscript "i" and corresponds to y = 0. The bulk solution is denoted by the subscript "B" and corresponds to the edge of the boundary layer. Mathematically stated, the boundary conditions for natural convection from an isothermal vertical plate to a quiescent medium are:

$$u(x,0) = v(x,0) = u(x,\infty) = 0 \tag{5.5}$$

and:

$$T(x,0) = T_0 \tag{5.6}$$

$$T(x,\infty) = T_\infty \tag{5.7}$$

Following Ostrach [68] the transport variables are transformed by introducing the following similarity variable:

$$\eta(x,y) = b(x)y \tag{5.8}$$

A two-dimensional stream function, defined by Eqns. 5.9 through 5.11, satisfies and replaces the continuity

equation.

$$\psi(x,y) = \nu c(x) f(x,y) \tag{5.9}$$

$$u = \psi_y \tag{5.10}$$

$$v = -\psi_x \tag{5.11}$$

It follows from the stream function and definition of the similarity variable η, that u and v are given by:

$$u = \nu c b f' \tag{5.12}$$

$$v = -\nu \left[c f' y b_x + f c_x \right] \tag{5.13}$$

(All derivatives of f(x,y) are with respect to η.) Temperature is non-dimensionalized by:

$$\phi_T(x,y) = \frac{T(x,y) - T_\infty}{T_o - T_\infty} \tag{5.14}$$

Then the momentum and energy equations and their associated boundary conditions become:

$$f''' + \frac{c_x}{b} f f'' - \left(\frac{c_x}{b} + \frac{c b_x}{b^2} \right) f'^2 + \frac{T_0 - T_\infty}{c b^3} \frac{g \beta}{\nu^2} \phi = 0 \tag{5.15}$$

$$\frac{\phi''}{Pr} + \frac{c_x}{b} f \phi' = 0 \tag{5.16}$$

$$f'(0) = f(0) = f'(\infty) = 1 - \phi(0) = \phi(\infty) = 0 \tag{5.17}$$

It can be shown that by defining b(x) and c(x) according to Eqns. 5.18 and 5.19 all the potentially x-dependent coefficients in the momentum and energy equations are constants (see Gebhart et al. [31]); therefore, a similarity solution is possible.

$$b(x) = \frac{1}{x} \left(\frac{Gr_x}{4} \right)^{\frac{1}{4}} \tag{5.18}$$

$$c(x) = 4 \left(\frac{Gr_x}{4} \right)^{\frac{1}{4}} \tag{5.19}$$

Insertion of the foregoing expressions for b(x) and c(x) into Eqs. 5.12 and 5.13 results in the following expressions for η, u and v:

$$\eta = \frac{y}{x} \left[\frac{Gr_x}{4} \right]^{\frac{1}{4}} \tag{5.20}$$

$$u = \frac{2\nu}{x} Gr_x^{\frac{1}{2}} f' \tag{5.21}$$

$$v = \frac{\nu}{x} \left(\frac{Gr_x}{4} \right)^{\frac{1}{4}} (\eta f' - 3f') \tag{5.22}$$

The set of ordinary but nonlinear differential equations which results upon inserting the foregoing expressions for b(x) and c(x) into Eqs. 5.15 and 5.16 is given by Eqns. 5.23 and 5.24 and their associated boundary conditions remain as specified by Eq. 5.17.

$$f''' + 3ff'' - 2f'^2 + \phi = 0 \tag{5.23}$$

$$\phi'' + 3Prf'(\phi) = 0 \tag{5.24}$$

Ostrach [68] numerically solved the foregoing set of differential equations at selected Prandtl numbers. Resulting values for $\phi(\eta)$ and $f'(\eta)$ at a Prandtl number of one, for example, as well as 6th order polynomial curve fits to them are given in Figs. 5-5 and 5-6. As shown in Figs. 5-5 and 5-6, satisfactory curve fits for $\phi(\eta)$ and $f'(\eta)$ are:

$$\phi(\eta) = 1 - .54674\eta - .94867 * 10^{-1}\eta^2 + .14219\eta^3 - .42377 * 10^{-1}\eta^4 + 5.3787 * 10^{-3}\eta^5 - 2.5547 * 10^{-4}\eta^6 \tag{5.25}$$

$$f'(\eta) = .68030\eta - .62626\eta^2 + .23382\eta^3 - 4.3869 * 10^{-1}\eta^4 + 4.1081 * 10^{-3}\eta^5 - 1.5288 * 10^{-4}\eta^6 \tag{5.26}$$

326
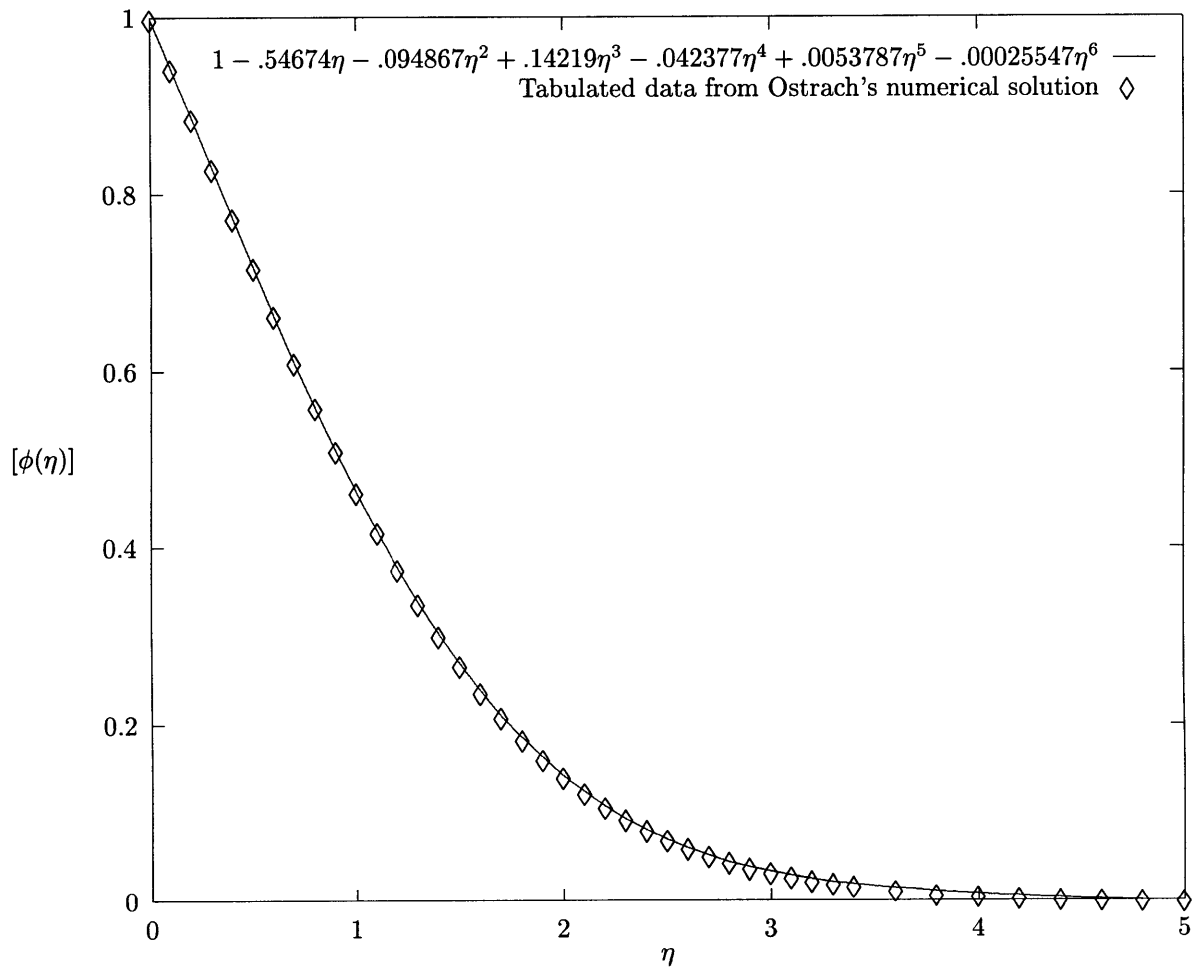
Figure 5-5: Dimensionless temperature distributions as a function of the similarity variable η for thermally-buoyant laminar flow adjacent to a vertical flat plate at $Pr = 1$ from Ostrach [68].
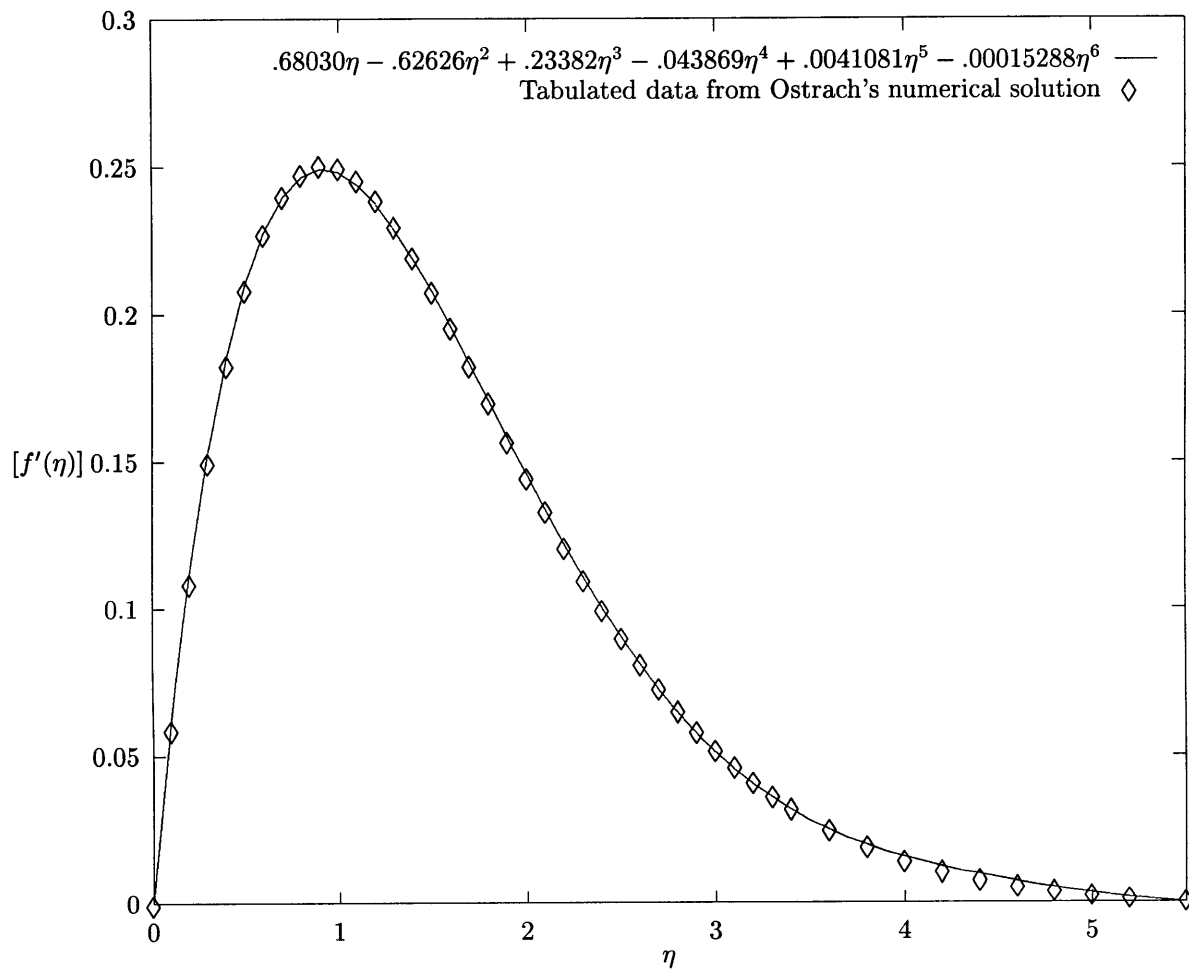
Figure 5-6: $f'(\eta)$ vs. η for thermally-buoyant laminar flow adjacent to a vertical flat plate at Pr = 1 from Ostrach [68].

328

Thus from Eqn. 5.14 the temperature in the boundary layer as a function of the similarity variable η is:

$$T(\eta) = T_\infty + (T_o - T_\infty)[1 - .54674\eta - .94867 * 10^{-1}\eta^2 + .14219\eta^3 - .42377 * 10^{-1}\eta^4 \qquad (5.27)$$
$$+5.3787 * 10^{-3}\eta^5 - 2.5547 * 10^{-4}\eta^6]$$

Since dimensionless concentration equals dimensionless temperature throughout the boundary layer for the case at hand:

$$C(\eta) = C_\infty + (C_o - C_\infty)[1 - .54674\eta - .94867 * 10^{-1}\eta^2 + .14219\eta^3 - .42377 * 10^{-1}\eta^4 \qquad (5.28)$$
$$+5.3787 * 10^{-3}\eta^5 - 2.5547 * 10^{-4}\eta^6]$$

If it is assumed that homogeneous nucleation does not occur, the amount of supersaturation or lack thereof present in the boundary layer may be determined by using the foregoing expressions for $T(\eta)$ and $C(\eta)$ together with the phase boundary of interest. For example, the temperature-composition diagram for the Na_2SO_4-H_2O system at conditions of interest is shown in Fig. 2-1 and the existing solubility data are fit according to:

$$T_s(wt\%) = 374.9 - 3.762 * (wt\%) \quad \text{for} \quad C \leq 6.64 \ wt\% \qquad (5.29)$$

Inserting Eqn. 5.28 into 5.29 it follows that the solubility temperature as a function of the similarity variable η is:

$$T_s(\eta) = 374.9 - 3.762[C_\infty + (C_o - C_\infty)(1 - .54674\eta - .94867 * 10^{-1}\eta^2 + .14219\eta^3 - .42377 * 10^{-1}\eta^4 \ (5.30)$$
$$+5.3787 * 10^{-3}\eta^5 - 2.5547 * 10^{-4}\eta^6)]$$

At the beginning of the set of runs in which the concentration of sodium sulfate in the inlet stream was 4 wt% and the (initial) bulk temperature of solution was 355 °C, for example, the deposition rate model presented in the previous chapter predicts that the temperature and concentration at the salt layer-solution

interface were 365.2 °C and 2.58 wt% respectively. (The given values of T_B, T_i, C_B and C_i correspond to the baseline case of the sensitivity analysis in the previous chapter.) A plot of solubility temperature minus actual temperature versus η corresponding to these conditions is shown in Fig. 5-7. Supersaturation does not occur; hence, homogeneous nucleation in the boundary layer is impossible. As noted in Section 5.2, it is known a priori that supersaturation is impossible when Le = 1 and the phase boundary is linear. However, when the phase boundary of interest has curvature, supersaturation is possible when Le = 1 and the results of this section apply.

Upon redefining the similarity variable η, the results of this section are directly applicable to double-diffusive natural convection. Specifically, Gebhart et al. [31] (see Section 6.3.3 in their book) show that by defining η as

$$\eta = \frac{y}{x} \left[\frac{Gr_x \left(1 + \tilde{N} \right)}{4} \right]^{\frac{1}{4}}, \tag{5.31}$$

Ostrach's results apply to double-diffusive natural convection provided that Le = 1. Then $\tilde{T}$ equals $\tilde{C}$ for all $\tilde{N}$. It is noted that although $\tilde{T}$ and $\tilde{C}$ are independent of $\tilde{N}$, the u- and v-velocity profiles have a significant dependence on $\tilde{N}$.

5.3.3 Le > 1 Case

The preceding analysis predicts that salt can not nucleate homogeneously in the boundary layer at the conditions investigated in the deposition experiments if the Lewis number of the aqueous salt solution is one (or less). However, the measurements by Butenhoff et al. [15] presented in Section 3.5 show the Lewis number of aqueous sodium nitrate solutions ranges from roughly 5 to 10 at supercritical conditions. This suggests that the Lewis number of aqueous sodium sulfate and potassium sulfate solutions at conditions of interest may be substantially larger than one. Moreover, some salts, e.g., lithium carbonate, precipitate from aqueous solutions at liquid-like densities. Lewis numbers are an increasing function of density and particularly high for liquid solutions relative to gas mixtures and supercritical fluids. (See Section 5.4.) Hence the Lewis number for salts such as lithium carbonate may substantially exceed 10, at temperatures

330
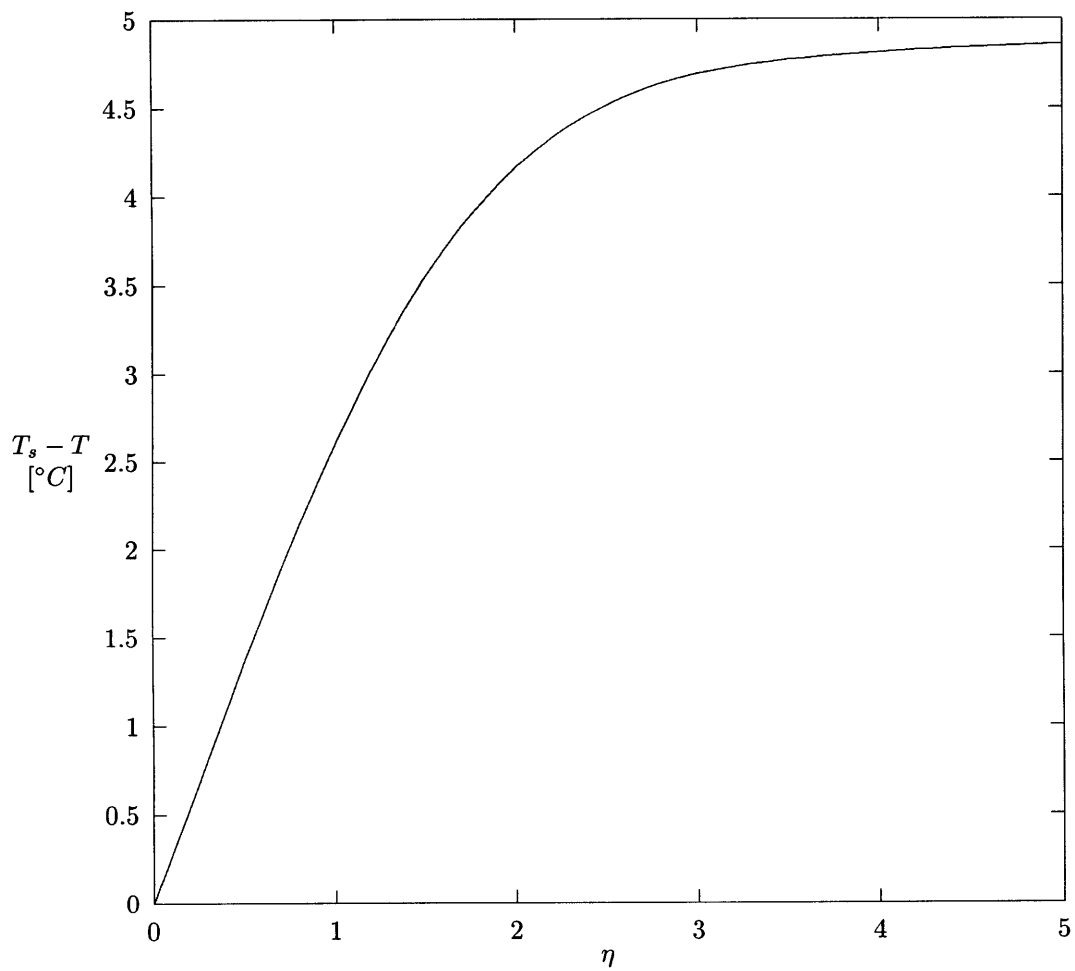
Figure 5-7: Theoretical prediction of solubility temperature minus solution temperature as a function of η at the beginning of the set of experiments in which the concentration of sodium sulfate in the inlet stream was 4 wt%. The Lewis and Prandtl numbers of the aqueous sodium sulfate solution are both set equal to one.

near the (solid+fluid/fluid) phase boundary. Additionally, it was shown in Section 5.2 that the critical Lewis number increases with time and equals infinity at steady state conditions. Hence expressions for the critical Lewis number which apply when it exceeds one are developed in this section. First, a criterion to determine if supersaturation and/or homogeneous nucleation are possible in the boundary layer for $1 \lesssim Le \lesssim 15$ is developed for the case when $Pr \simeq 0.7$ and $\tilde{N} \simeq 0.5$. Then a second criterion applicable for $Le \gtrsim 165$, $Pr \gtrsim 1$ and $\tilde{N} \simeq 0$ is developed. For the latter case, an analytical expression for the loci of temperature-composition states connecting the bulk condition to the salt layer-solution interface condition is also provided. Finally, the criteria valid at low Lewis numbers and high Lewis numbers are united and applied to the conditions investigated in the deposition experiments.

A sufficient criterion for supersaturation and/or homogeneous nucleation to occur in the boundary layer is that dT/dC at the salt layer-solution interface exceeds dT/dC of the phase boundary at the salt layer-solution interface condition, i.e.,

$$\left.\frac{dT}{dC}\right|_i > \left.\frac{dT}{dC}\right|_{sat,i} \tag{5.32}$$

Moreover, for most systems the foregoing criterion is necessary for supersaturation and/or homogeneous nucleation to occur within the boundary layer. However, this condition is not rigorously necessary. For example, a phase boundary and trajectory of (T,C) states connecting a bulk condition to a salt layer-solution interface condition for which supersaturation and/or homogeneous nucleation will occur in the boundary layer, when Eq. 5.32 is not satisfied is shown in Fig. 5-8. The trajectory shown corresponds to $Pr = 0.72$, $Le = 100$ and $\tilde{N} = 0.0$ as per Eq. 5.76.

Upon multiplying Eq. 5.32 by $\frac{k\mathfrak{D}_{AB}}{k\mathfrak{D}_{AB}}$ and applying the definition of the convective heat and mass transfer coefficients, it can be expressed as:

$$\frac{h\mathfrak{D}_{AB}(T_i - T_B)}{h_m k(C_i - C_B)} > \left.\frac{dT}{dC}\right|_{sat,i} \tag{5.33}$$

From the definitions of Nu_x and Sh_x, it follows that the sufficient criterion for supersaturation and/or

332
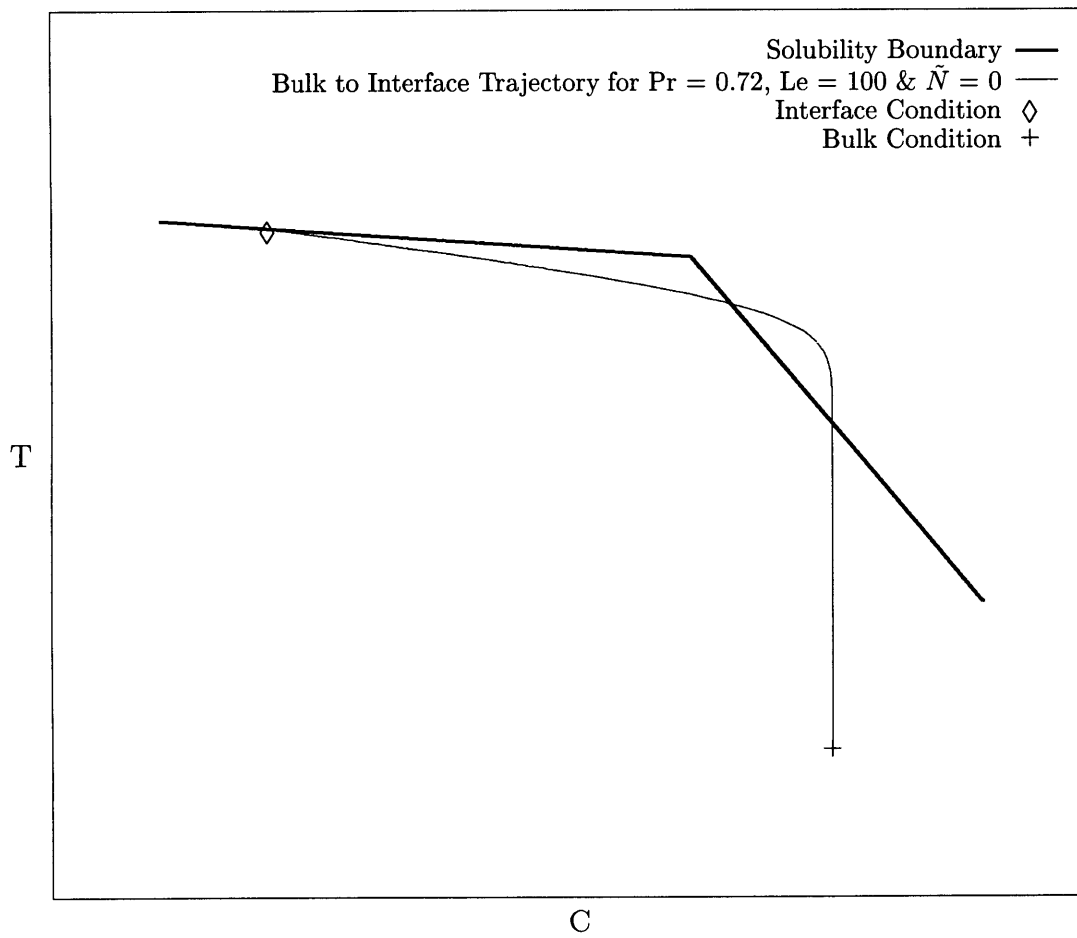
Figure 5-8: Hypothetical set of conditions for which supersaturation and/or homogeneous nucleation occurs in the boundary layer, but $\left.\frac{dT}{dC}\right|_i < \left.\frac{dT}{dC}\right|_{sat,i}$. Above the solubility curve a solid-fluid region exists and below it a single-phase fluid region exists

Pr	$\tilde{N}$	Le	$-\phi'(0)$	$-C'(0)$	$\frac{Nu_x}{Gr_x^{\frac{1}{4}}}$	$\frac{Sh_x}{Gr_x^{\frac{1}{4}}}$	$\frac{Sh_x}{Gr_x^{\frac{1}{4}}Le^{\frac{1}{3}}}$	$\frac{Sh_x}{Ra_x^{\frac{1}{4}}Le^{\frac{1}{3}}}$	$\frac{Nu_x Le^{\frac{1}{3}}}{Sh_x}$
0.7	0.5	1	0.49950	0.49950	0.353	0.353	0.353	0.386	1
0.7	0.5	1.34	0.49292	0.57019	0.349	0.403	0.366	0.400	0.95
0.7	0.5	7.14	0.46880	1.11689	0.331	0.790	0.410	0.448	0.81
0.7	0.5	14.29	0.46330	1.43962	0.328	1.108	0.457	0.500	0.72
7.0	0.5	1	1.05411	1.05411	0.745	0.745	0.745	0.458	1
7.0	0.5	14.29	0.97593	2.75894	0.690	1.951	0.804	0.494	0.86
7.0	0.5	71.43	0.96154	4.79946	0.680	3.394	0.818	0.503	0.83
0.72	0.0	$\gtrsim 165$	0.50467	0.69917	0.357	$0.494Le^{\frac{1}{3}}$	0.494	0.536	0.72

Table 5.1: Transport quantities as a function of Lewis number and Prandtl number for double-diffusive natural convection flows adjacent to an isothermal and constant concentration vertical surface based on the results of the Gebhart and Pera study [32] at $Pr = 0.7$ and $Pr = 7.0$ for $\tilde{N} = 0.5$. In the last row the same transport quantities are provided for $Pr = 0.72$ and $\tilde{N} = 0$, and Le $\gtrsim 165$ based on the analysis contained later in this section. The ratio $\frac{Nu_x Le^{\frac{1}{3}}}{Sh_x}$ is subsequently referred to as A(Le,Pr,$\tilde{N}$).

homogeneous nucleation to occur is:

$$\frac{Nu_x}{Sh_x} < \frac{C_i - C_B}{T_i - T_B}\frac{dT}{dC}\bigg|_{sat,i} \tag{5.34}$$

The direction of the inequality needed to be switched to obtain Eq. 5.34 from Eq. 5.33 because both sides of Eq. 5.33 were multiplied by a negative quantity, namely $(C_i - C_B)/(T_i - T_B)$.

The ratio Nu_x/Sh_x can be determined for double-diffusive natural convection along a vertical flat plate from the values of $-\phi'(0)$ and $-C'(0)$ in Table 3.14 using Eqns. 3.163 and 3.164. Table 5.1 gives $-\phi'(0)$, $-\tilde{C}(0)$, $\frac{Nu_x}{Gr_x^{\frac{1}{4}}}$, $\frac{Sh_x}{Gr_x^{\frac{1}{4}}}$, $\frac{Sh_x}{Gr_x^{\frac{1}{4}}Le^{\frac{1}{3}}}$, $\frac{Sh_x}{Ra_x^{\frac{1}{4}}Le^{\frac{1}{3}}}$ and $\frac{Sh_x}{Nu_x Le^{\frac{1}{3}}}$ as a function of Lewis number at $Pr = 0.7$ and $Pr = 7.0$ for $\tilde{N} = 0.5$ based on the results of the Gebhart and Pera study. The last row of this table provided the same transport quantities for the case when $Pr = 0.72$, Le $\gtrsim 165$ and $\tilde{N} = 0$ based on an analysis presented later in this section. (As per Chapter 4, the Prandtl number and $\tilde{N}$ characterizing the deposition experiments are estimated to be approximately 1 and 0.5 respectively.) Since the ratio of the thermal boundary layer thickness to the concentration boundary layer thickness scales as $Le^{\frac{1}{3}}$ one expects that to a first approximation:

$$Sh_x \simeq Le^{\frac{1}{3}}Nu_x \tag{5.35}$$

Thus, one expects that for constant Prandtl number, the ratio $\frac{Sh_x}{Gr_x^{\frac{1}{4}}Le^{\frac{1}{3}}}$ will be largely constant which is

334

shown to be the case in Table 5.1. Moreover, since both both the Nusselt and Sherwood numbers scale with the Rayleigh number to the 1/4 power, one expects that the ratio $\frac{Sh_x}{Ra_x^{\frac{1}{4}}Le^{\frac{1}{3}}}$ will be relatively constant as both Le and Pr are varied. This is also shown to be the case. The last column shows the ratio $\frac{Nu_x Le^{\frac{1}{3}}}{Sh_x}$. This ratio should be largely constant as per Eq. 5.35. Perhaps it is surprising that increasing the Lewis number from 1 to 14.29 at constant Pr and $\tilde{N}$ causes a 28% reduction in $\frac{Sh_x}{Nu_x Le^{\frac{1}{3}}}$. At a Prandtl number of 7.0 increasing the Lewis number from 1 to 71.43 reduces the ratio by only 17%. Analogously, at constant Prandtl number and $\tilde{N}$ one expects $\frac{Sh_x}{Gr_x^{\frac{1}{4}}}$ to have a more pronounced dependence on Lewis number than $\frac{Nu_x}{Gr_x^{\frac{1}{4}}}$. This is the case.

In general the ratio $\frac{Nu_x}{Sh_x}$ is a function of Le, Pr and $\tilde{N}$ and to determine whether or not supersaturation and/or homogeneous nucleation are possible it is convenient to express it as:

$$\frac{Nu_x}{Sh_x} = \frac{A\left(Le, Pr, \tilde{N}\right)}{Le^{\frac{1}{3}}} \qquad (5.36)$$

$A\left(Le, Pr, \tilde{N}\right)$ is independent of the local Grashof number because both Nu_x and Sh_x scale as $Gr_x^{\frac{1}{4}}$. It is also noted that, in the current notation, the derivative of temperature with respect to concentration at the salt layer-solution interface is:

$$\frac{dT}{dC}\bigg|_i = \frac{A\left(Le, Pr, \tilde{N}\right)}{Le^{\frac{1}{3}}} \frac{T_i - T_B}{C_i - C_B} \qquad (5.37)$$

Inserting Eq. 5.36 into Eq. 5.34, it follows that the critical Lewis number beyond which supersaturation and/or homogeneous nucleation will occur is:

$$Le_c = \left[\frac{A\left(Le, Pr, \tilde{N}\right)(T_i - T_B)}{(C_i - C_B)\frac{dT}{dC}\big|_{sat,i}} \right]^3 \qquad (5.38)$$

At Prandtl = 0.7 and $\tilde{N} = 0.5$, which are characteristic of the deposition experiments, the ratio $\frac{Sh_x}{Nu_x Le^{\frac{1}{3}}}$ ranges from 0.72 to 1. Its mean value based on these two extremes is 0.86 and if it is assumed that the ratio

Nu_x/Sh_x equals $\frac{0.86}{Le^{\frac{1}{3}}}$ for Pr $\simeq$ 1, $\tilde{N} \simeq 0.5$ and $1 \lesssim$ Le $\lesssim 15$, the critical Lewis number becomes:

$$Le_c = \left[\frac{0.86(T_i - T_B)}{(C_i - C_B)\frac{dT}{dC}\Big|_{sat,i}} \right]^3 \quad \text{for } 1 \lesssim \text{Le} \lesssim 15, \text{ Pr} \simeq 0.72 \text{ and } \tilde{N} \simeq 0.5 \quad (5.39)$$

As discussed above, the critical Lewis number increases with time and substantially exceeds 15 before steady state conditions are achieved. Additionally, $\tilde{N}$ is a decreasing function of time and approaches zero as steady state conditions are established. Thus an expression for the critical Lewis number applicable when Le $\gg$ 1 and $\tilde{N} \to 0$ is developed next.

For Sc $\gg$ 1 the concentration boundary layer thickness is much smaller than the velocity boundary layer thickness; therefore, it's plausible to assume that the velocity profile is a straight line in the concentration boundary layer, a la Lèvêque [46]. The "Lèvêque approximation" results in an analytically tractable form of the species equation. However, caution must be exercised when invoking the "Lèvêque approximation." Boundary layer profiles for natural convection on a vertical, heated plate are shown in Fig. 3-4. The values of η corresponding to the maximum u-velocity and to the velocity boundary layer thickness are approximately 1.0 and 5.5 respectively at Prandtl numbers of interest to this study. Since the "Lèvêque approximation" clearly does not apply beyond the value of η corresponding to the maximum u-velocity, it should not be invoked when the ratio of the concentration boundary thickness to the velocity boundary layer thickness exceeds 1/5.5. To be sure, the Lèvêque approximation rigorously applies only so long as the slope of the velocity profile is constant, but some curvature in the velocity profile occurs before u-velocity reaches a maximum. Hence the Lèvêque approximation is not rigorously applicable even up to η equals one at conditions of interest. The ratio of the velocity boundary layer thickness to the concentration boundary layer thickness is approximately equal to $Sc^{\frac{1}{3}}$ (see Sections 3.6.2 and 3.6.4). Therefore, justification of the "Lèvêque approximation" is somewhat suspect for Schmidt numbers below 165. It is noted, however, that although rigorously the Schmidt number must be at least 165 for the "Lèvêque approximation" to be valid, pragmatically it does surprising well at substantially smaller Schmidt numbers. An example of the "Lèvêque approximation" resulting in a surprisingly accurate Sherwood number expression when Sc = 0.72 and Le = 1 is provided later in this section.

A number of other key assumptions are present in the subsequent analysis. The solution density is assumed to be independent of salt concentration, i.e., it is assumed that $\tilde{N} = 0$. However, treating solution density as independent of salt concentration was shown to have a small effect on transport for the conditions investigated in the deposition experiments in Section 4.4.2. Moreover, because as steady state conditions are approached $\tilde{N}$ approaches zero, neglecting buoyancy induced by concentration differences becomes less relevant as time increases. The Boussinesq approximation is assumed to apply and it was shown to be valid at the conditions investigated in the deposition experiments in Section 4.4.2.

For the purposes of the subsequent analysis the u-velocity is defined as:

$$u = \left[\frac{\partial u}{\partial y}\bigg|_{y=0} \right] y \tag{5.40}$$

To accomplish this, the function f(η) is expanded in a Taylor Series and only the first nonzero term is kept:

$$f = \overbrace{f(0)}^{0} + \overbrace{f'(0)\eta}^{0} + \frac{1}{2}f''(0)\eta^2 + \dots \tag{5.41}$$

Thus:

$$\frac{\partial f}{\partial \eta} \cong f''(0)\eta \tag{5.42}$$

Insertion of this expression into Eq. 5.21 gives:

$$u = \frac{4\nu}{x} \left[\frac{Gr_x}{4} \right]^{\frac{1}{2}} f''(0)\eta \quad \text{(for small } \eta\text{)} \tag{5.43}$$

Since y is directly proportional to η for all x the u-velocity profile given by Eq. 5.43 is linear in y for all x and consistent with the "Lévêque approximation". Insertion of Eqs. 5.41 and 5.42 into Eq. 5.22 results in the following expression for v-velocity:

$$v = -\frac{1}{2}\nu \left[\frac{Gr_x}{4} \right]^{\frac{1}{4}} \frac{\eta^2}{x} f''(0) \quad \text{(for small } \eta\text{)} \tag{5.44}$$

The boundary layer form of the species equation is given by:

$$u \frac{\partial \rho_A}{\partial x} + v \frac{\partial \rho_A}{\partial y} = \mathfrak{D}_{AB} \frac{\partial^2 \rho_A}{\partial y^2} \tag{5.45}$$

By using the chain rule, the derivatives in the species equation may be expressed as:

$$\frac{\partial \rho_A}{\partial x} = -\frac{1}{4} \frac{\eta}{x} \frac{\partial \rho_A}{\partial \eta} \tag{5.46}$$

$$\frac{\partial \rho_A}{\partial y} = \frac{1}{x} \left[\frac{Gr_x}{4} \right]^{\frac{1}{4}} \frac{\partial \rho_A}{\partial \eta} \tag{5.47}$$

$$\frac{\partial^2 \rho_A}{\partial y^2} = \frac{1}{x^2} \left[\frac{Gr_x}{4} \right]^{\frac{1}{2}} \frac{\partial^2 \rho_A}{\partial \eta^2} \tag{5.48}$$

Then it follows that the species equation becomes:

$$\frac{d^2 \rho_A}{d\eta^2} + \frac{3}{2} Sc f''(0) \eta^2 \frac{d\rho_A}{d\eta} = 0 \tag{5.49}$$

A dimensionless concentration is defined as:

$$\phi_{\rho_A}(x, y) = \frac{\rho_A(x, y) - \rho_{A,\infty}}{\rho_A - \rho_{A,\infty}} \tag{5.50}$$

and the species equation may then be expressed as:

$$\frac{d^2 \phi_{\rho_A}}{d\eta^2} + \frac{3}{2} Sc f''(0) \eta^2 \frac{d\phi_{\rho_A}}{d\eta} = 0 \tag{5.51}$$

It is assumed that the salt layer-solution interface is at a uniform concentration and the bulk solution is well mixed. Hence, the appropriate boundary conditions for the species equation are given by Eqs. 5.52 and 5.53.

$$\phi_{\rho_A} = 1 \quad \text{at} \quad \eta = 0 \tag{5.52}$$

$$\phi_{\rho_A} = 0 \quad \text{as} \quad \eta \to \infty \tag{5.53}$$

338

With

$$p = \frac{d\phi_{\rho_A}}{d\eta} \tag{5.54}$$

it follows that:

$$\frac{dp}{d\eta} = -\frac{3}{2}Scf''(0)\eta^2 p \tag{5.55}$$

and upon integration:

$$\frac{d\phi_{\rho_A}}{d\eta} = K\,exp\left[-\frac{1}{2}Scf''(0)\eta^3\right] \tag{5.56}$$

where K is the integration constant. After applying the boundary conditions specified in Eqns. 5.52 and 5.53 to Eq. 5.56, it may be expressed as:

$$K \int_0^\infty exp\left[-\frac{1}{2}Scf''(0)\eta^3\right]d\eta = -1 \tag{5.57}$$

The integral in Eq. 5.57 may be evaluated analytically by defining ζ according to Eq. 5.58 and performing the necessary substitutions.

$$\zeta = \frac{1}{2}Scf''(0)\eta^3 \tag{5.58}$$

Since

$$d\eta = \frac{1}{3\zeta}\left[\frac{2}{Scf''(0)}\right]^{\frac{1}{3}}\zeta^{\frac{1}{3}}d\zeta \tag{5.59}$$

it follows that Eqn. 5.57 may be expressed as:

$$\frac{K}{3}\left[\frac{2}{Scf''(0)}\right]^{\frac{1}{3}}\int_0^\infty \frac{e^{-\zeta}}{\zeta^{\frac{2}{3}}}d\zeta = -1 \tag{5.60}$$

339

The gamma function is defined as [1],

$$\Gamma(z) = \int_0^\infty t^{z-1} e^{-t} dt \tag{5.61}$$

therefore, the integration constant, K, is:

$$K = \frac{-3}{\Gamma(\frac{1}{3})} \left[\frac{Sc f''(0)}{2} \right]^{\frac{1}{3}} \tag{5.62}$$

Moreover, as per Eq. 5.56:

$$K = \frac{d\phi_{\rho A}}{d\eta} \bigg|_{y=0} \tag{5.63}$$

and from the definition of the mass transfer coefficient, h_m,:

$$-\mathfrak{D}_{AB} \frac{\partial \phi_{\rho A}}{\partial y} \bigg|_{y=0} = h_m \tag{5.64}$$

Thus:

$$h_m = -\mathfrak{D}_{AB} \frac{\partial \phi_{\rho A}}{\partial \eta} \bigg|_{y=0} \frac{\partial \eta}{\partial y} \tag{5.65}$$

If it is noted that $\Gamma\left[\frac{1}{3}\right] = 2.67894$ [1], then after some simple calculus, it follows that:

$$Sh_x = 0.62849 \left[f''(0) \right]^{\frac{1}{3}} Sc^{\frac{1}{3}} Gr_x^{\frac{1}{4}} \tag{5.66}$$

The effect of Prandtl number on the Sherwood number is embedded in the constant $f''(0)$. Gebhart et al. [31] and LeFevre [49] provide $f''(0)$ for $Pr = 0.72$ and $Pr \to \infty$ respectively as given by:

$$f''(0) = .6760 \quad \text{for} \quad Pr = 0.72 \tag{5.67}$$

$$f''(0) = .8245 Pr^{-\frac{1}{4}} \quad \text{for} \quad Pr \to \infty \tag{5.68}$$

By inserting the foregoing expressions into the Sherwood number expression given by Eq. 5.66, it follows that:

$$Sh_x = 0.5367 Le^{\frac{1}{3}} Ra_x^{\frac{1}{4}} \quad \text{for} \quad Pr = 0.72 \text{ and } Sc \gtrsim 165 \tag{5.69}$$

$$Sh_x = 0.5893 Le^{\frac{1}{3}} Ra_x^{\frac{1}{4}} \quad \text{for } Pr \to \infty \text{ and } Sc \gtrsim 165 \tag{5.70}$$

Sherwood numbers at other Prandtl numbers may be computed using the tabulation of $f''(0)$ values as a function of Prandtl number for Prandtl numbers between 0.01 and 100.0 available in Gebhart et al. [31]. It is noted that when the Lewis number equals one, the heat and mass transfer analogy rigorously applies and $Sh_x = Nu_x$. At Le = 1 and Pr =0.72, for example, $Sh_x = Nu_x = 0.3874 Ra_x^{\frac{1}{4}}$ [31]. Thus the constant in Eq. 5.69 is 39% too high when Le = 1 and Pr = 0.72 as a consequence of the "Lévêque approximation". Considering the conditions necessary for the "Lévêque approximation" to rigorously apply, a 39% error is surprisingly small. As already discussed, the Lévêque approximation becomes more applicable at higher Lewis numbers. Based upon the Sherwood number expression given by Eq. 5.69 and Ostrach's Nusselt number results $A\left(Le, Pr, \tilde{N}\right)$ is equal to 0.72 at Pr = 0.72 and $\tilde{N}$ = 0.0 as per Table 5.1.

Provided the salt layer-solution interface temperature does not exceed the temperature corresponding to zero salt solubility and the phase boundary is linear, the slope of the solubility line may be used to express $(C_B - C_i)$ in terms of $(T_i - T_s)$ as per Eq. 3.3 and the critical Lewis number becomes:

$$Le_c = \left[\frac{A\left(Le, Pr, \tilde{N}\right)(T_i - T_B)}{T_i - T_s(C_B)} \right]^3 \tag{5.71}$$

Hence the critical Lewis number is independent of the slope of the phase boundary when the temperature difference between the salt layer-solution interface and bulk, temperature difference between the solubility temperature corresponding to the bulk concentration and bulk and $A\left(Le, Pr, \tilde{N}\right)$ are constant. A caveat to this assessment is that $\tilde{N}$ and, therefore, $A\left(Le, Pr, \tilde{N}\right)$ are functions of the slope of the solubility line. Hence, the foregoing argument does not rigorously apply to double-diffusive natural convection. Moreover, if the bulk condition and heat flux are held constant, then the ratio $(T_i - T_B)/(T_i - T_s(C_B))$ is a function

of the slope of the phase boundary. Conversely, if, the heat flux is held constant and the bulk condition changed it is possible to hold the ratio $(T_i - T_B)/(T_i - T_s(C_B))$ constant for phase boundaries of different slope.

Table 5.1 summarizes the results for $A\left(Le, Pr, \tilde{N}\right)$ based on the Gebhart and Pera results and the current analysis. As previously noted, Lewis numbers of aqueous sodium sulfate and potassium sulfate solutions are estimated to be of order 10 at the conditions investigated in the deposition experiments. For Le = 10, $\tilde{N} =$ 0.5 and Pr = 0.72, $A\left(Le, Pr, \tilde{N}\right)$ is about 0.75. Moreover, for $Le_c \gtrsim 165$ and $\tilde{N} \simeq 0$, i.e., if the experiments could be run until steady state conditions were reached, $A\left(Le, Pr, \tilde{N}\right)$ is about 0.70. For the purposes of estimating Le_c in the deposition experiments it is assumed that $A\left(Le, Pr, \tilde{N}\right)$ is well behaved between these two cases and $A\left(Le, Pr, \tilde{N}\right)$ is set equal to 0.725.

Critical Lewis numbers at the beginning of the sodium sulfate and potassium sulfate deposition experiments at all of the conditions investigated in the deposition experiments are given in Table 5.2. The critical Lewis numbers after 6 and 12 minutes of run time have elapsed are provided as well. $A\left(Le, Pr, \tilde{N}\right)$ was set equal to 0.725 to determine the Le_c values in the table and conditions correspond to the baseline case of the sensitivity analysis in the previous chapter. At the beginning of the sodium sulfate deposition experiments, the critical Lewis number ranges from 4.79 to 9.68. It is unlikely that the Lewis numbers of the aqueous sodium sulfate solutions at the conditions investigated substantially exceed 4.79, if at all. Moreover, when the Lewis number of the aqueous salt solution exceeds the critical Lewis number, the amount of metastability which may be tolerated in the boundary layer is not known. After 12 minutes of run time have elapsed the critical Lewis numbers range from 17.95 to 30.50. It is highly unlikely that the Lewis numbers of the aqueous sodium sulfate solutions are as high as 17.95. Thus, the critical Lewis numbers in Table 5.2 are consistent with few, if any, particles being observed during the sodium sulfate deposition experiments.

At the beginning of the potassium sulfate deposition experiments the critical Lewis number corresponding to the baseline case of the sensitivity analysis ranges from 28.19 to 112.70. It is extremely unlikely that the Lewis numbers of the aqueous potassium sulfate solutions at conditions of interest exceed 28.19. After 12 minutes of run time have elapsed the theory predicts that the critical Lewis number in the potassium sulfate deposition experiments ranges from 326.80 to 2342.10. Thus the fact that particles were not observed during

SALT	C_{in}	T_{Bo}	T_{io}	C_{Bo}	C_{io}	$Le_c(0^+\ min)$	$Le_c(6\ min)$	$Le_c(12\ min)$
-	wt%	°C	°C	wt%	wt%	-	-	-
Na_2SO_4	2	363.3	373.2	1.51	0.42	4.79	7.21	17.95
Na_2SO_4	4	355.0	365.6	3.51	2.42	7.20	12.09	17.95
Na_2SO_4	6	347.7	358.5	5.52	4.43	9.47	17.75	28.11
Na_2SO_4	8	340.8	352.4	7.54	6.29	9.68	18.65	30.50
K_2SO_4	2	374.7	383.9	1.64	0.76	131.97	627.91	2342.10
K_2SO_4	4	372.0	381.8	3.48	2.19	50.64	221.54	713.66
K_2SO_4	6	369.0	379.1	5.44	4.01	40.70	177.31	556.96
K_2SO_4	8	366.1	376.6	7.36	5.68	28.19	112.70	326.80

Table 5.2: Prediction of critical Lewis numbers at the beginning of the deposition experiments and after 6 and 12 minutes of run time. Relevant temperatures and concentrations at the beginning of the experiments are also provided. All numbers in the table correspond to the baseline case of the sensitivity analyses for each deposition run and $A\left(Le, Pr, \tilde{N}\right)$ is set equal to 0.725 in the critical Lewis number calculations.

the potassium sulfate deposition experiments is consistent with the theory.

The critical Lewis number as a function of run time corresponding to the baseline case of the sensitivity analysis for the sodium sulfate and potassium sulfate runs in which the salt concentration in the inlet stream was 4 wt% is plotted in Fig. 5-9. It was shown in the previous chapter that steady state conditions are not reached until hours and sometimes days have passed. However, as is evident from Fig. 5-9, after only thirty minutes the critical Lewis number has increased by factors of about 6 and 250 at conditions corresponding to the sodium sulfate and potassium sulfate runs respectively. The larger increase in the critical Lewis number for the potassium sulfate conditions over the same time interval happens because the time constant associated with the establishment of steady state conditions is substantially smaller in the potassium sulfate experiments. (Of course, for both salts the critical Lewis number approaches infinity as steady state conditions are approached.) If homogeneous nucleation in the boundary layer were to occur at the beginning of a sodium sulfate experiment, it is evident from Fig. 5-9 that it would cease long before steady state conditions were reached. It should be noted, however, that homogeneous nucleation could dramatically affect the time required to establish steady state conditions. This is because until enough salt accrued on the hot finger for the nucleation mechanism to be predominantly heterogeneous, the Brownian diffusion coefficient associated with particles formed in the boundary layer would substantially slow down the deposition process.
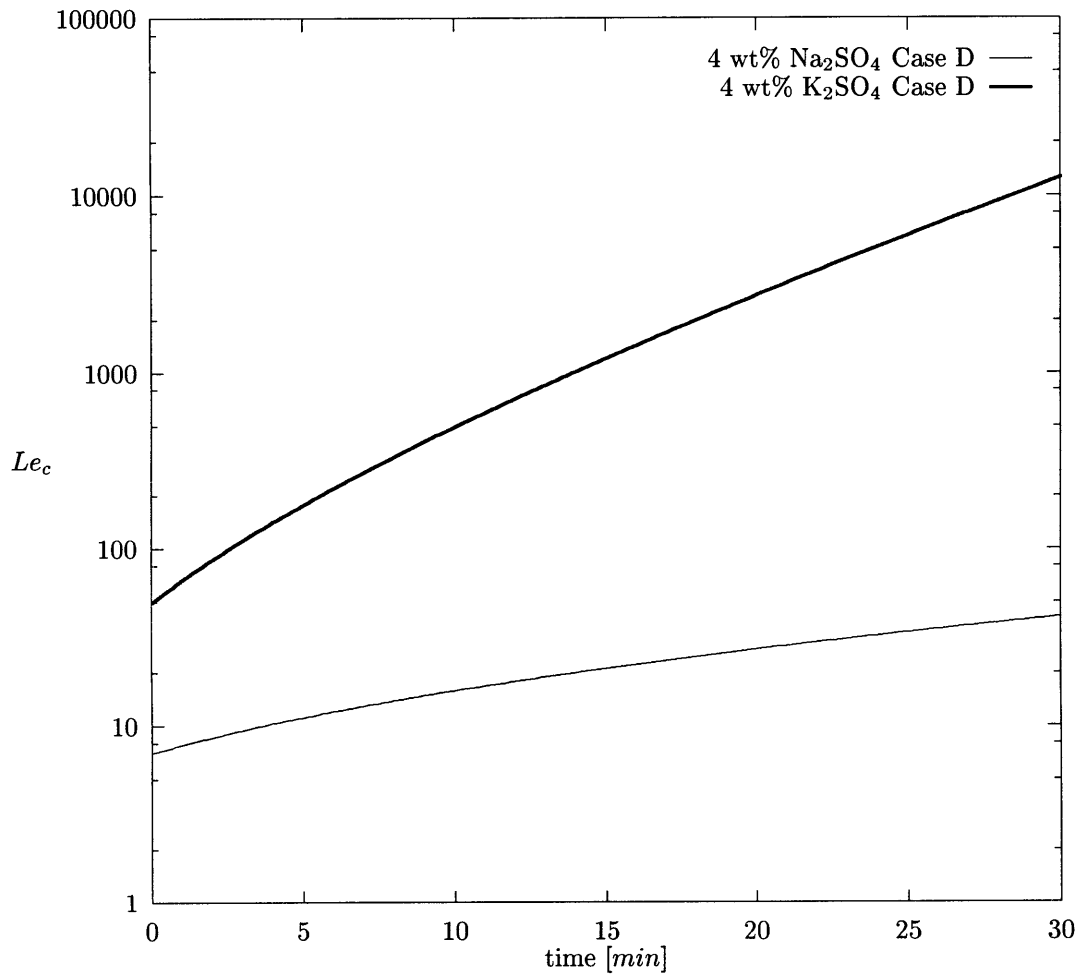
Figure 5-9: Critical Lewis number as a function of time corresponding to the baseline case of the sensitivity analyses conducted for the sodium sulfate and potassium sulfate deposition experiments in which the concentration of salt in the inlet stream was 4 wt%.

5.3.4 Trajectories of temperature-concentration states

The salt concentration in the boundary layer may be computed as a function of η by extension of the analysis in the previous section. After inserting the expression for the integration constant K given by Eq. 5.62 into the integral given in Eq. 5.57, it may be evaluated between zero and η. The same substitution for ζ in terms of η as before yields:

$$\phi_C = 1 - \frac{1}{\Gamma(\frac{1}{3})} \int_0^{\frac{Scf''(0)\eta^3}{2}} \frac{e^{-\zeta}}{\zeta^{\frac{2}{3}}} \tag{5.72}$$

This integral is defined by an incomplete gamma function according to [1]:

$$P(a, x) = \frac{1}{\Gamma(a)} \int_0^x e^{-t} t^{a-1} dt \tag{5.73}$$

Thus, setting:

$$x = \frac{Scf''(0)\eta^3}{2} \tag{5.74}$$

$$a = \frac{1}{3} \tag{5.75}$$

results in:

$$\phi_C = 1 - P\left(\frac{1}{3}, \frac{Scf''(0)\eta^3}{2}\right) \quad \text{for Sc} \gtrsim 165 \text{ and } \tilde{N} \simeq 0 \tag{5.76}$$

A FORTRAN 77 subroutine written by Press et al. [74] was used to evaluate the incomplete gamma function in Eq. 5.72 at discrete values of $\frac{Scf''(0)\eta^3}{2}$. The results for ϕ_C as a function of $\frac{Scf''(0)\eta^3}{2}$ are plotted in Fig. 5-10. Since $f''(0)$ is a known function of Prandtl number a la the Ostrach study [68], ϕ_C as a function of η at Schmidt and Prandtl numbers of interest is easily computed. Moreover, by using Ostrach's results [68] for ϕ_T as a function of η, loci of temperature-concentration states in the boundary layer surrounding the salt layer-solution interface at Sc and Pr numbers of interest may be plotted on a temperature-composition diagram.

Figure 5-10: ϕ_C vs. $\frac{Scf''(0)\eta^3}{2}$.

Trajectories of temperature-composition states which connect the bulk solution condition to the salt layer-solution interface condition as a function of Lewis number at the conditions investigated in the deposition experiments for which the concentration of sodium sulfate in the inlet stream was 4 wt% are plotted in Fig. 5-11. The bulk and interface conditions shown correspond to the beginning of the experiments. The interface condition was determined from the baseline case of the sensitivity analysis in the previous chapter. Complete trajectories may be computed only if Eq. 5.76 applies, i.e., for $Sc \gtrsim 165$ and $\tilde{N} \simeq 0$. Howeve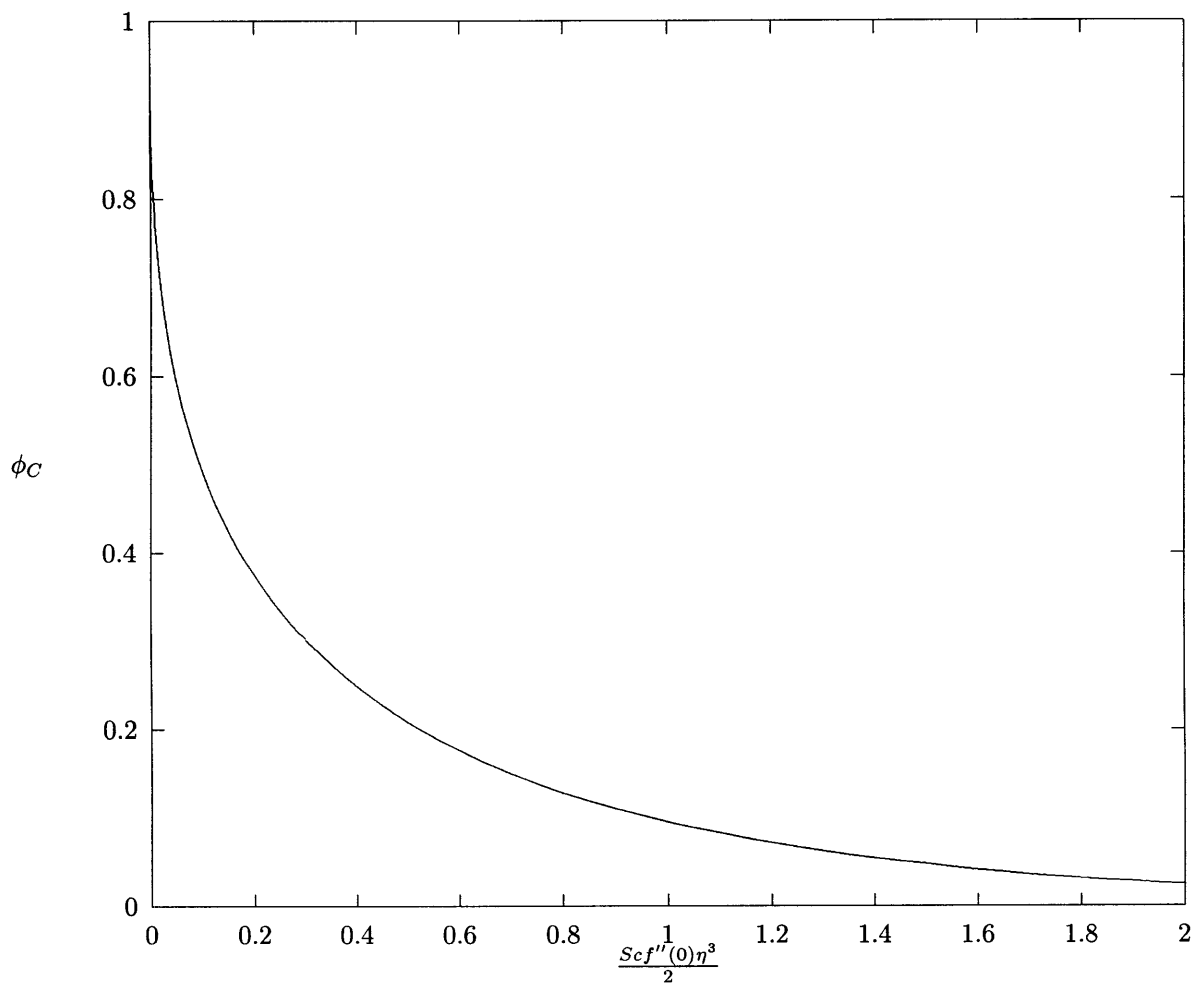r, $\frac{dT}{dC}$ at the salt layer-solution interface may be determined from Eq. 5.37 even when Eq. 5.76 is not valid. Thus partial trajectories of temperature-composition states based on $\frac{dT}{dC}\big|_i$ at the salt layer-solution interface are shown in the figure as well. In the trajectory at $Le = 100$ in Fig. 5-11, the value used for $f''(0)$ in Eq. 5.76 corresponded to a Prandtl number of 0.72. Rigorously, Le should be at least 165 for Eq. 5.76 describe the trajectory of (T,C) states connecting the bulk and interface conditions; nonetheless it is used to approximate the $Le = 100$ trajectory. The four partial trajectories between $Le = 1$ and $Le = 100$ correspond to $Le = 7.20$, 15, 25 and 50 respectively at $Pr = 0.72$ and $\tilde{N} = 0.5$. $A\left(Le, Pr, \tilde{N}\right)$ was set equal to 0.725 to compute the slope of each partial trajectory. The critical Lewis number equals 7.20 as indicated in the figure. It is likely that the Lewis number of the aqueous salt solution is about equal to this critical Lewis number and this is consistent with few and often zero particles being observed in the sodium sulfate deposition experiments. The theory predicts that increasing the Lewis number from 7.20 to 100, well over an order of magnitude, causes less than two degrees centigrade of supersaturation at the conditions investigated.

The equivalent of Fig. 5-11 for the deposition experiments in which the concentration of potassium sulfate in the inlet stream was 4 wt% is shown in Fig. 5-12. The interface condition was again determined from the baseline case of the sensitivity analysis in the previous chapter. For the $Le = 100$ and $Le = 1000$ trajectories, Pr was set equal to 0.72 to determine $f''(0)$ in Eq. 5.76. The three partial trajectories between $Le = 1$ and $Le = 100$ correspond to $Le = 15$, 50.64 and 75 respectively at $Pr = 0.72$ and $\tilde{N} = 0.5$. $A\left(Le, Pr, \tilde{N}\right)$ was set equal to 0.725 to compute them. The critical Lewis number is 50.64. The critical Lewis number of the aqueous potassium sulfate solution is likely to be much less than this values and, thus, the fact that particles were not observed during the potassium sulfate deposition runs is consistent with the nucleation theory. It is noted that even at a Lewis number equal to 1000, less than 2 $°C$ of supersaturation is predicted; hence,

metastability could be a serious issue.

5.4 Candidates for Homogeneous Nucleation

In this section, qualities of aqueous salt solutions conducive to homogeneous nucleation in the boundary layer formed around the salt layer-solution interface are identified. Then, based on these qualities, some example of salts which are prime candidates to homogeneously nucleate are provided. High Lewis number aqueous salt solutions are conducive to supersaturation and/or homogeneous nucleation in the boundary layer formed around the salt layer-solution interface. Thus large molecular diameter/mass salts are prime candidates for homogeneous nucleation. The UO_2F_2-H_2O system, for example, is one worthy of consideration. Uranyl fluoride is a somewhat large molecule with a molecular mass of 308.02 $\frac{gm}{gmol}$. Moreover, it is likely that the Lewis numbers of aqueous uranyl fluoride solutions exceed those of aqueous sodium sulfate and potassium sulfate solutions at conditions of interest. (The molecular masses of sodium sulfate and potassium sulfate are 142.04 and 174.27 $\frac{gm}{gmol}$ respectively and all three salts precipitate from solution at somewhat similar temperatures.) The temperature-composition equilibrium diagram for $UO_2F_2H_2O$ was determined by Marshall et al. [57] and is shown in Fig. 5-13. (Apparently, pressure was not measured during the phase equilibria experiments from which Fig. 5-13 constructed.) Line DE separates a single-phase region from a solid plus fluid phase region, albeit at UO_2F_2 concentrations of about 70-80 wt%. Nonetheless, deposition experiments could be performed in this region and, depending on the Lewis number of the solution, homogeneous nucleation may occur in the boundary layer. If performed, the experiments would be complicated by the presence of the α-solid phase of hydrated uranyl fluoride until a temperature of approximately 150 $^\circ C$ was reached. Thus, preheating the UO_2F_2-H_2O mixture up to a temperature of, 175 $^\circ C$, say, would be necessary before pumping it through a flow system.

Generally Lewis numbers of binary gas mixtures are about two orders of magnitude larger than Lewis numbers of binary liquid solutions. For example, Table 5.3 gives the Lewis number of binary mixtures of air and various species as well as water and various species at approximately 25 $^\circ C$ and atmospheric pressure. (The table was extracted from the study by Gebhart and Pera [32].) Lewis numbers of mixtures of air with

348
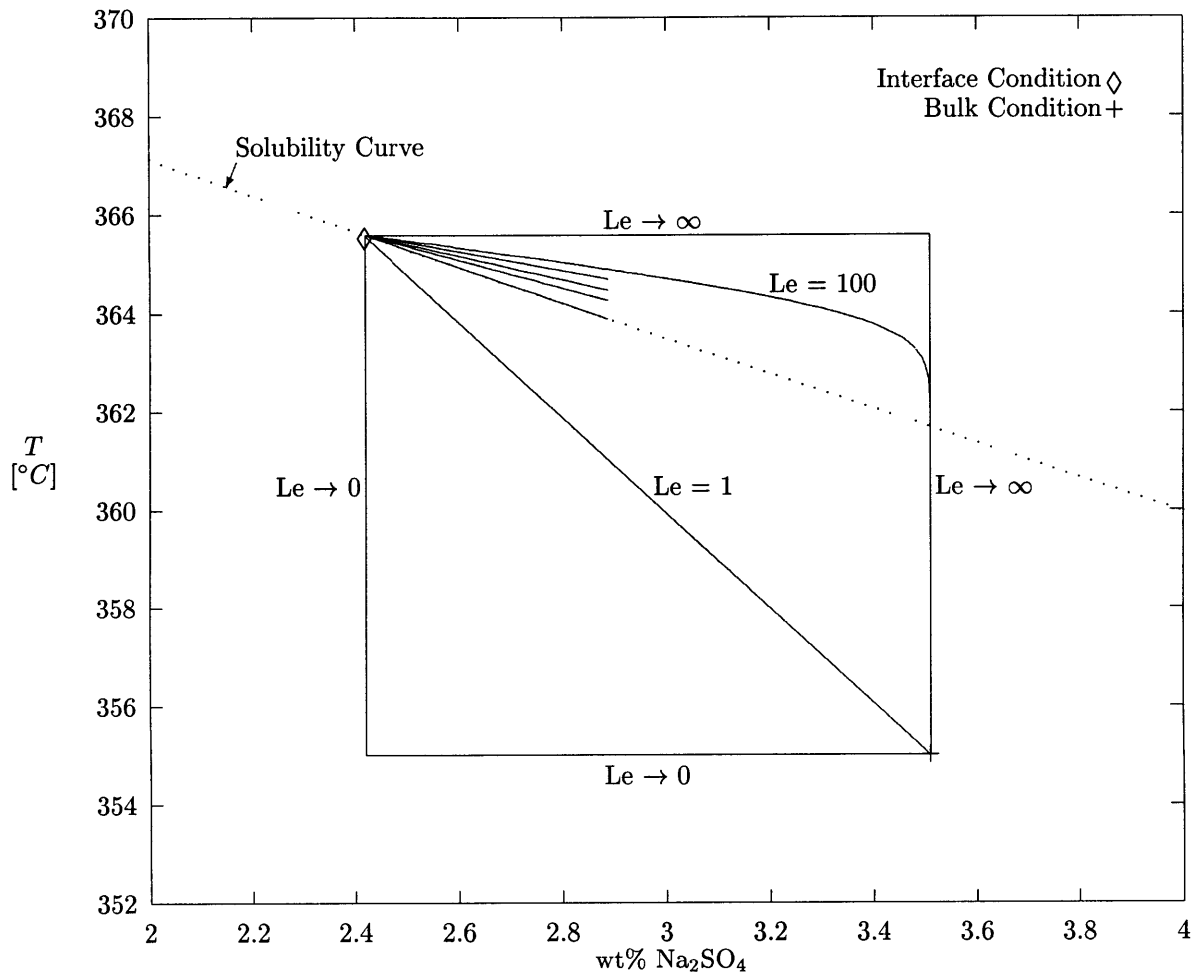
Figure 5-11: Trajectories of temperature-concentration states connecting the bulk and salt layer-solution interface conditions at the beginning of the sodium sulfate deposition experiments in which the salt concentration in the inlet stream was 4 wt%. Unlabelled trajectories correspond to Le = 7.20, 15, 25 and 50 respectively between the Le = 1 and Le = 100 trajectories. See text for $\tilde{N}$ and Prandtl number corresponding to each trajectory.
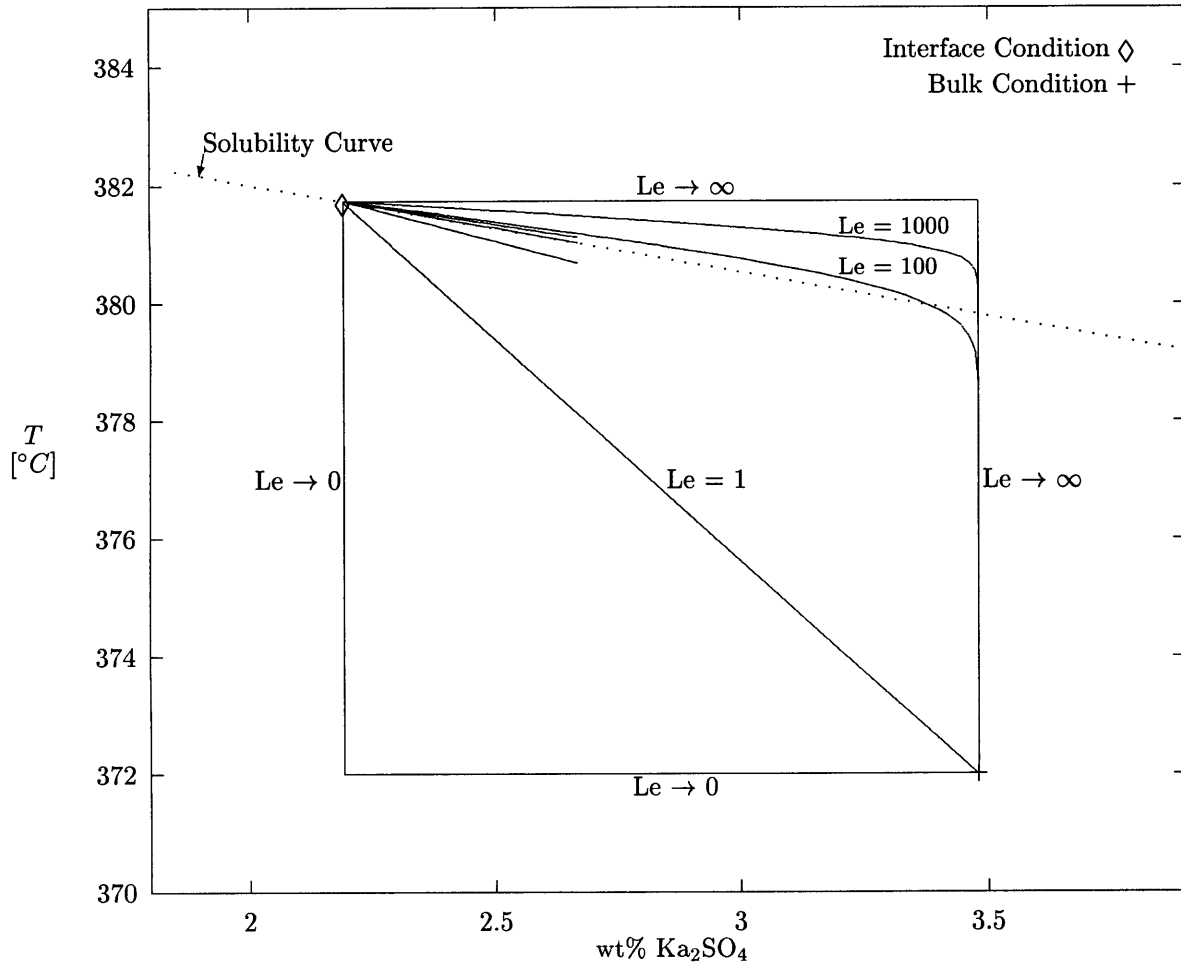
Figure 5-12: Trajectories of temperature-concentration states connecting the bulk and salt layer-solution interface conditions at the beginning of the potassium sulfate deposition experiments in which the salt concentration in the inlet stream was 4 wt%. Unlabelled trajectories correspond to Le = 15, 50.64 and 75 respectively between the Le = 1 and Le = 100 trajectories. See text for $\tilde{N}$ and Prandtl number corresponding to each trajectory.
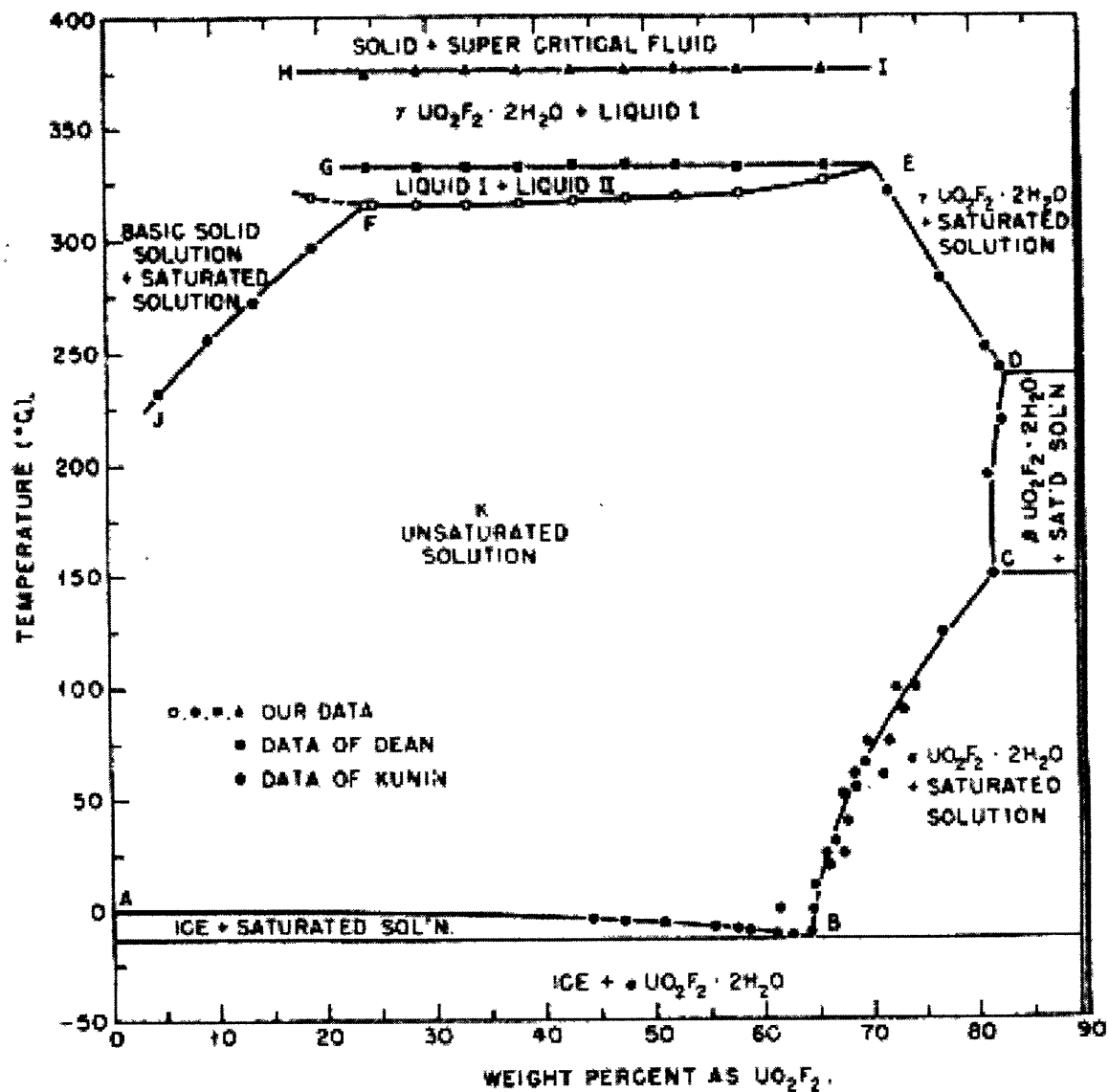
Figure 5-13: UO_2F_2-H_2O temperature composition-diagram. Pressures corresponding to the data shown were not provided. This figure was extracted from a study by Marshall et al. [57].

various species are of order 1, while those of the aqueous solutions are of order 100. As mentioned above, small molecular diameter/mass solutes also result in small Lewis numbers. Not surprisingly, in Table 5.3 the hydrogen-air and hydrogen-water mixtures have the smallest Lewis numbers of the gas mixtures and aqueous solutions respectively.

It is evident from the preceding discussion that Lewis numbers of aqueous salt solutions at liquid-like densities are substantially larger than Lewis numbers of aqueous salt solutions at gas-like densities. Thus salts which precipitate from aqueous solutions at liquid-like densities are prime candidates to homogeneously nucleate in the boundary layer. "Solubilities of Inorganic and Metal Organic Compounds" [54] edited by Linke and "Solubilities of Inorganic and Organic Compounds Volume I, Part I" [83] edited by Stephens and Stephens are especially rich sources of solubility data for salts in aqueous solutions. (Unfortunately, both of these compilations were discontinued about 40 years ago and contemporary equivalents do not exist.) The solubility data contained in these references show that the solubility of many salts in water decreases substantially over temperature ranges below 150 $°C$, i.e., at liquid-like conditions. Some examples include sodium orthophosphate [Na_3PO_4], magnesium sulfate [$MgSO_4$], lanthanum selenate [$La_2(SeO_4)_3$] and lithium carbonate [Li_2CO_3]. The latter two salts are subsequently discussed in some detail.

In addition to the Lewis number of the aqueous salt solution, the phase boundary can also dramatically affect the probability that salt will homogeneously nucleate in the boundary layer formed around the salt layer-solution interface. The shape of the hypothetical phase boundary shown in Fig. 5-14, for example, is extremely conducive to homogeneous nucleation. Interestingly, the shape of this idealized phase boundary is identical to that of the Le $\rightarrow$ 0 trajectory which connects bulk conditions to interface conditions in the deposition experiments. As shown in Fig. 5-14, if homogeneous nucleation does not occur the same amount of (maximum) supersaturation is present at both Le = 1 and Le $\rightarrow$ ∞ provided two criteria are satisfied. Namely, the temperature difference between the salt layer-solution interface and bulk as well as the temperature difference between the solubility temperature corresponding to the bulk concentration and bulk must be constant. A caveat to this discussion is that the Lewis number of the solution will affect the temperature difference between the salt layer-solution interface and bulk if the heat flux at the salt layer-solution interface is maintained constant. Therefore, the preceding discussion should be thought of in the

Species	Le
Air-Ammonia	1.11
Air-Carbon dioxide	1.34
Air-Hydrogen	0.314
Air-Oxygen	1.07
Air-Water	0.86
Air-Benzene	2.51
Air-Ether	2.37
Air-Methanol	1.39
Air-Ethyl alcohol	1.86
Air-Ethylbenzene	2.87
Water-Ammonia	63.57
Water-Carbon dioxide	64.71
Water-Hydrogen	21.71
Water-Oxygen	50.86
Water-Nitrogen	66.86
Water-Chlorine	88.14
Water-Sulfur Dioxide	74.71
Water-Calcium chloride	107.14
Water-Sodium chloride	82.86
Water-Methanol	79.43
Water-Sucrose	242.86

Table 5.3: Lewis numbers of various binary gas mixtures and binary aqueous solutions at approximately 25 $°C$ and atmospheric pressure. Source: Gebhart and Pera [32].

context of a boundary condition of the first kind at the salt layer-solution interface.

The solubility of lanthanum selenate in water was determined in a study by J.A.N. Friend [28] and is shown in Fig. 5-15. (Pressures were not reported.) The phase boundary mimics the idealized phase boundary in Fig. 5-14 to a significant degree. Moreover, lanthanum selenate is a very large molecule with a molecular mass of 706.69 $\frac{gm}{gmol}$. Additionally, at the conditions shown in Fig. 5-15 the solid phase is hydrated with 12 waters and hydration of lanthanum selenate in solution would serve to decrease the binary diffusion coefficient of the solution and increase its Lewis number. Trajectories which connect a bulk condition to a salt layer-solution interface condition corresponding to Le = 1 and Le = 60 are also shown in Fig. 5-14. Eq. 5.76 was used to compute the Le = 60 trajectory. The Prandtl number was set equal to 2 in the computation because the Prandtl number of pure water in the temperature range shown in Fig. 5-15 is about 2. When Prandtl number equals 2 and Le = 60, Sc = 120; therefore; Eq. 5.76 is approximately valid if it is assumed that $\tilde{N} = 0$. Even at a Lewis number of one supersaturation and/or homogeneous nucleation is expected to occur. Given the very large size of the lanthanum selenate molecule, the fact that it may be hydrated in solution and the liquid-like temperature/density at which it precipitates from solution, a Lewis number of 60 or higher is quite likely. At a Lewis number of 60, 20 $°C$ of supersaturation would occur at the proposed conditions in the absence of homogeneous nucleation in the boundary layer. Thus lanthanum selenate appears to be a salt which is a prime candidate to nucleate homogeneously in the boundary layer formed around the salt layer-solution interface.

Seidell and Linke [54] compiled the solubility data for lithium carbonate in water shown in Fig. 5-16 from a number of sources all dating back to the late 19th century. Based on this data, a nucleation experiment was conducted in an effort to validate, at least for one salt, the theory developed in this chapter at conditions where a salt would be expected to become supersaturated and/or nucleate homogeneously in the boundary layer. A 1 wt% salt, aqueous lithium carbonate solution preheated to 53 $°C$ was circulated through the system at 10 ml/min at STP and 250 bar as per the bulk condition in Fig. 5-16. The hot finger instrumented with thermocouples was used in this experiment and 10.61 watts of power were supplied to the cartridge heater inside it. The power supplied to the hot finger caused its measured surface temperature to increase to about 71 $°C$ as per the figure. At 71 $°C$, provided the solubility data shown in Fig. 5-16 is accurate
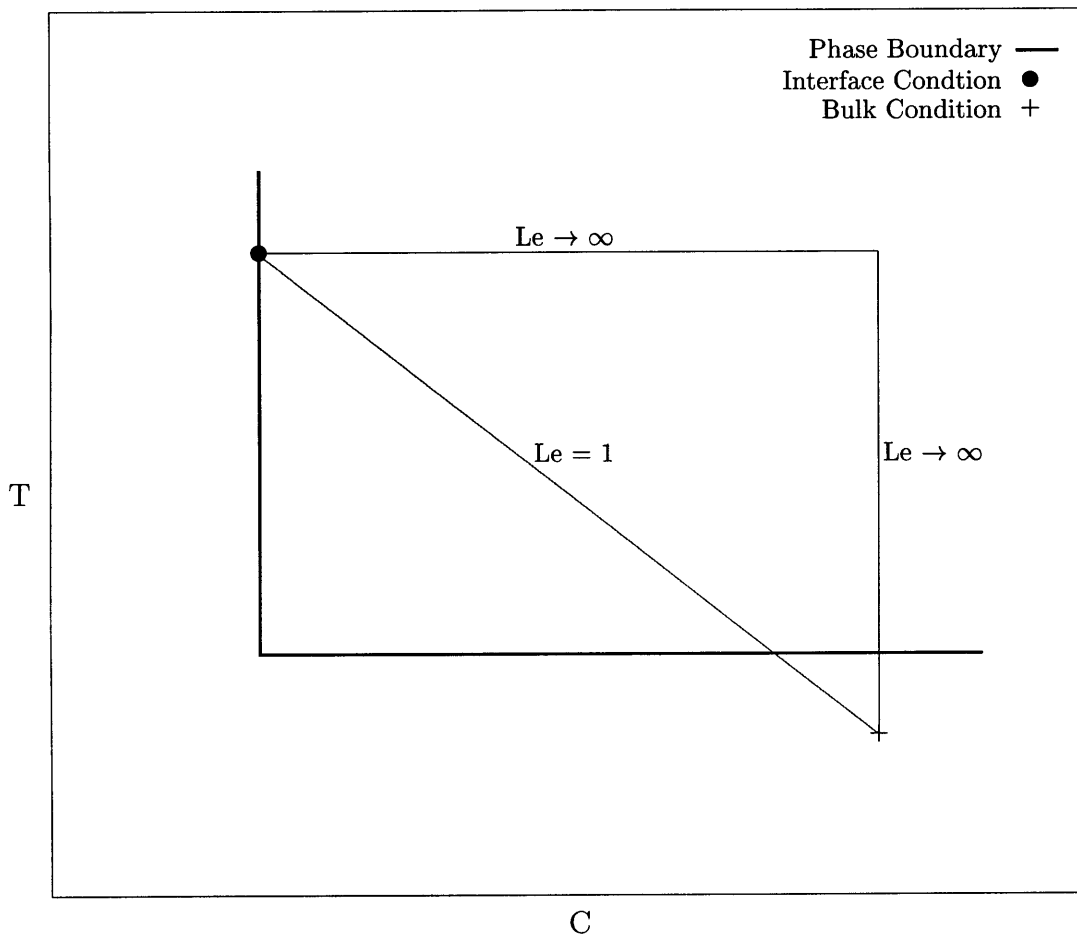
Figure 5-14: Idealized phase boundary conducive to homogeneous nucleation in the boundary layer and trajectories connecting a bulk condition to a salt layer-solution interface condition for Le = 1 and Le → ∞. Below the solubility line a one-phase-fluid region exists and above it a two-phase, solid-fluid region exists.

Figure 5-15: Lanthanum sulfate solubility data [28] and trajectories connecting a bulk condition to a salt layer-solution interface condition at Le = 1, Le = 60 and Le → ∞. Below the solubility data a one-phase-fluid region exists and above it a two-phase, solid-fluid region exists.

and applies at 250 bar, the salt layer-solution interface condition would correspond to the point labelled "Hypothetical Interface Condition". A trajectory corresponding to Le = 60 and Pr = 2 which connects the "Initial Bulk Condition" to the "Hypothetical Interface Condition" is also shown in Fig. 5-16. Since the lithium carbonate precipitates from solution at liquid-like densities, a Lewis number of 60 is a reasonable estimate. Moreover, at Le = 60, about 10 $^\circ C$ of supersaturation is predicted to occur in the absence of homogeneous nucleation. However, absolutely no deposition and/or nucleation was observed at these conditions. (One hour was allowed to elapse at these conditions.)

Metastability within the aqueous lithium carbonate solution may explain why deposition and/or nucleation were not observed at the aforementioned conditions. Thus, in an effort to overcome metastability in case it were present the bulk temperature of the solution in the cell was gradually ramped upward at the rate of approximately 1 degree $^\circ C$ per minute. At a bulk temperature of about 99 $^\circ C$ and hot finger surface temperature of about 116.7 $^\circ C$ deposition began. Moreover, bright bursts of light were observed around the hot finger and especially in the plume at a frequency of about 0-3 hertz throughout the deposition process which was allowed to continue for about one hour. It is possible that the bright bursts of light are attributable to homogeneous nucleation events occurring in the boundary layer. Nothing resembling these bright bursts of light was observed during the sodium sulfate and potassium sulfate deposition experiments.
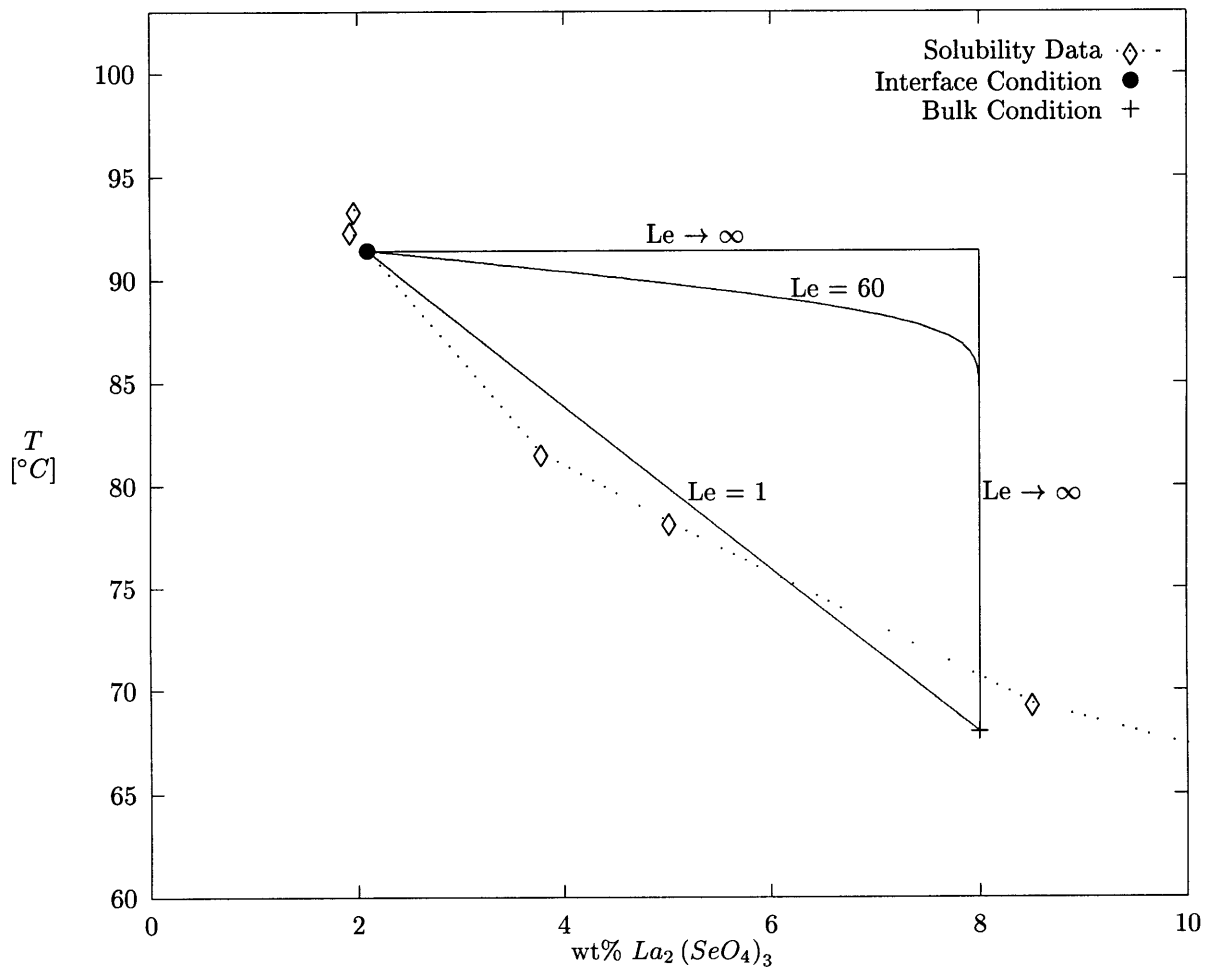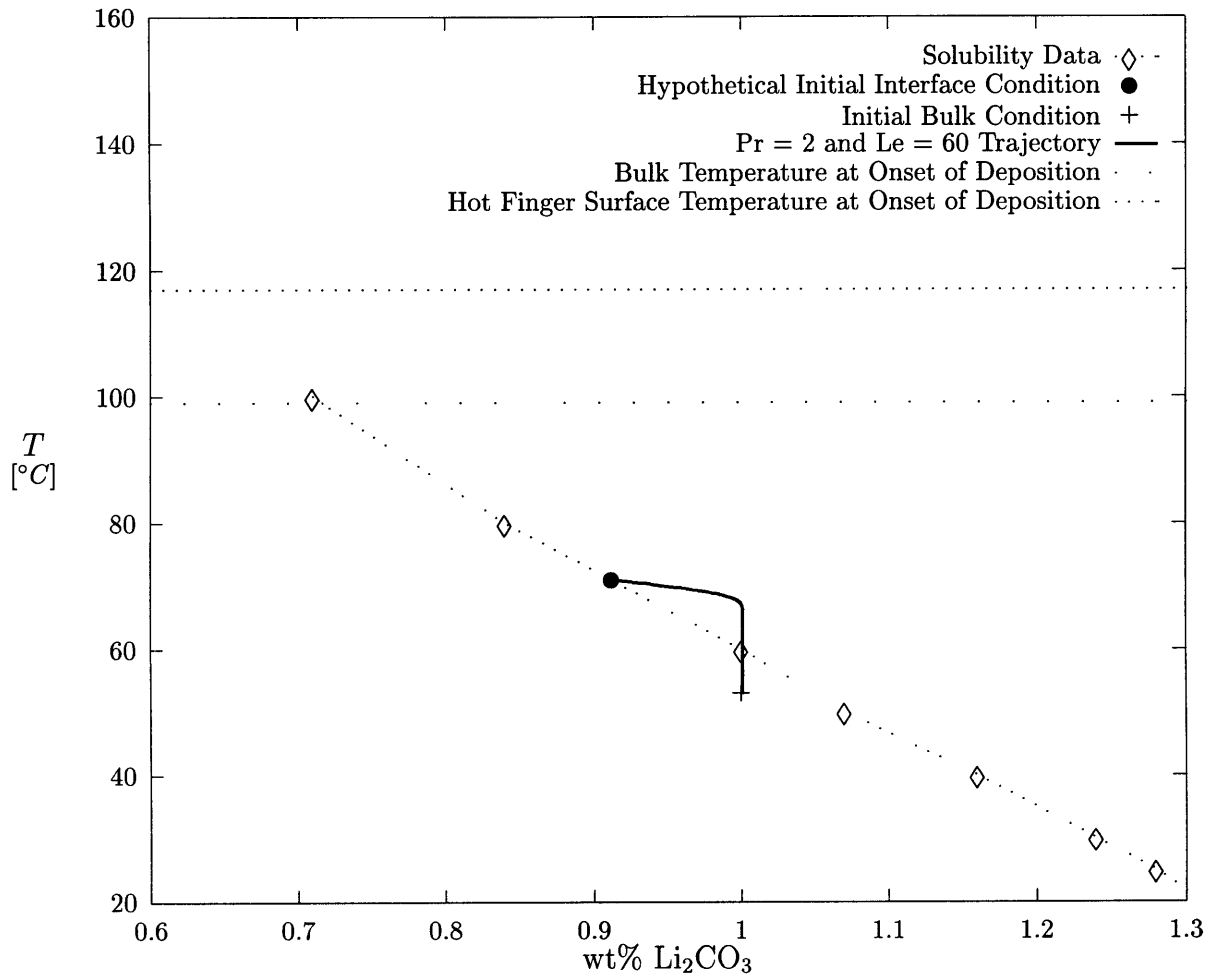
Figure 5-16: Lithium carbonate solubility data [54] and trajectories connecting a bulk condition to a salt layer-solution interface condition at Le = 1, Le = 60 and Le → ∞. Below the solubility data a one-phase-fluid region exists and above it a two-phase, solid-fluid region exists.

Chapter 6

Conclusions and Recommendations

6.1 Conclusions

1. Experiments: An optically accessible apparatus to measure deposition rates from near-supercritical, aqueous, salt solutions to a heated cylinder (hot finger) at conditions relevant to the SCWO process was designed, constructed and run.

2. Deposition Rate Data: Transient deposition rate data from near-supercritical, aqueous, sodium sulfate and potassium sulfate solutions to the hot finger were collected. Salt concentrations in the bulk solution around the hot finger ranged from 2 to 8 wt%. The deposition rate in the experiments was on the order of 1 gram of salt per minute. The porosity of the salt layer was measured to be approximately 70% for all conditions investigated.

3. Solubility Data: Solubility data for the sodium sulfate- and potassium sulfate-water systems at 250 bar were collected for salt concentrations between 2 and 10 wt% using the same apparatus.

4. Transport Mode: Natural convection was the dominant mechanism of heat and mass transport for all the experimental conditions.

5. Relationship between transport coefficients and deposition rate: Reduced heat and mass transfer coefficients can increase, decrease, or not affect the deposition rate at the salt layer-solution interface formed on the hot finger. A simple means to predict how changes in transport coefficients will affect this deposition rate for a given set of operating conditions was developed. At the conditions investigated in the deposition experiments, reduced transport coefficients increase the deposition rate at the salt layer-solution interface.

6. Simplified Deposition Rate Modeling: At the conditions investigated in the deposition experiments, a simple calculation using the analogy between heat and mass transfer and neglecting buoyancy forces induced by concentration gradients suffices to predict the deposition rate to within a factor of about 3, and often does much better.

7. Deposition Rate Modeling: Dissolved and predominantly associated salt molecules are transported to the salt layer-solution interface by natural convective mass transport and subsequently nucleate heterogeneously there. (See Conclusion Number 11.) A model to compute the transient deposition rate at the salt layer-solution interface under these conditions was developed and solved at the operating conditions corresponding to all of the deposition rate experiments. This model accounted for buoyancy forces induced by both temperature and concentration gradients in the boundary layer and for the heat of precipitation when salt nucleated. For the deposition experiments in which salt concentration in the solution entering the test cell was 4 wt% or less, the experimental data fall essentially within the range of the model's predictions in the context of a realistic sensitivity analysis accounting for various uncertainties. When the concentration of salt in the solution entering the test cell was increased to 6 and 8 wt%, the predictions were low by a factor of up to about 2 likely because deposition within the porous salt layer was not accounted for.

8. Mass Transfer Within the Porous Salt Layer: Mass transfer inside the porous salt layer becomes more important as the concentration of salt in the solution entering the test cell increases. This is likely the reason the predictions of the model compare better with the experimental data at lower salt concentrations.

9. Sorét and Dufour Effects: Very limited data for the thermal diffusion ratio in aqueous salt solutions at near-supercritical conditions are available. However the importance (or lack thereof) of the Sorét and Dufour effects on transport can not be properly accounted for without this transport property. Analyses in this dissertation which used available thermal diffusion ratio data showed that the Sorét and Dufour effects are potentially very important to transport at near-supercritical conditions. More thermal diffusion ratio data for aqueous salt solutions at near-supercritical conditions are needed to see if this is the case.

10. Nucleation: In general, to determine whether or not supersaturation and/or homogeneous nucleation will occur at near-supercritical conditions the following algorithm can be applied:

A) Assume homogeneous nucleation is impossible, i.e., nucleation occurs heterogeneously on a surface.

B) Calculate the resulting temperature and salt concentration profiles.

C) Calculate the solubility temperature profile from the temperature-concentration solubility relationship and the salt concentration profile calculated in step B).

D) If the above calculated temperature exceeds the solubility temperature at any location, then supersaturation and/or homogeneous nucleation must occur.

(This algorithm applies to both forced and free convective systems.)

11. Nucleation in the Deposition Experiments: The algorithm given in Conclusion Number 10 was applied to the conditions investigated in the deposition experiments. Supersaturation and/or homogeneous nucleation (in the boundary layer formed around the salt layer-solution interface) was predicted to be very unlikely to occur and visual observations as well as measured deposition rates were consistent with homogeneous nucleation not happening. A simple relationship between the Lewis number of the aqueous salt solution and temperature-composition solubility relationship was developed to determine whether or not supersaturation and/or homogeneous nucleation must occur in natural convective boundary layers along a flat plate or around a horizontal cylinder.

6.2 Recommendations

Of course, the existing apparatus could be used to perform solubility and deposition experiments with many different types of aqueous salt solutions. For example, it would be interesting to study salt depositing on the hot finger from an aqueous sodium-chloride solution because the salt precipitates from a liquid-vapor region in the NaCl-H$_2$O system. Before more experiments are performed, however, it should be checked that the mass fraction of salt in the solution entering the test cell is the same as the mass fraction of the salt in the solution supplied to the system. To accomplish this, a small fraction of the solution entering the test cell could be diverted through a sampling loop and the salt concentration within this stream measured using an ion specific electrode. The mass fraction of sodium sulfate in the effluent during the deposition experiments should also be measured. Moreover, a mass balance on the mass of salt supplied to the system, deposited on the hot finger and egressing from the system should be conducted for each run. This is the only way to insure that the system is completely free from salt at the beginning of each deposition experiment and that salt is not depositing in the system at undesirable locations, e.g., on the wall of the preheater. (As per Chapter 1, the UBC SCWO group and the Sandia National Laboratory SCWO group both conducted these kinds of mass balances during their respective deposition experiments [85, 36].)

An effort should be made to quantitatively estimate the fraction of salt eroded from the hot finger during the blow-down process. Alternatively, one could attempt to refine the blow-down process such that visual observations during the blow-down process suggests erosion is positively insignificant. In the deposition experiments the compressor supplied nitrogen at a pressure of about 0-3 bars higher than the 250 bar pressure at the inlet to the back pressure regulator. Thus up to about a 3 bar pressure drop pumped nitrogen through the system during blow-down. This resulted in the nitrogen-solution interface clearing the salt layer-solution interface at a velocity between roughly 0.1 and 1 inch per second. (The slower the nitrogen-solution interface cleared the salt layer-solution interface, the less problematic erosion appeared to be, but in no experiment did visual observations suggest that more than 20%, at most, of the salt deposited on the hot finger was eroded from it.) The same compressor is used to pressurize the back pressure regulator before each deposition experiment. However, during the deposition experiments, the pressure of the back pressure

regulator increases by up to a couple of bars. The air within the back pressure regulator is inside a constant volume, hermetic chamber, but it is heated by a few degrees centigrade by the "hot" solution egressing from the regulator. This air temperature increase at constant volume increases the pressure of the air according to the ideal gas law and hence increases the pressure of the solution flowing through the back pressure regulator by up to about 3 bar. If the solution entering the back pressure regulator was sufficiently close to room temperature this pressure increase could be eliminated. This could be accomplished by increasing the length of the heat exchanger upstream of the back pressure regulator. Then, after the compressor was used to pressurize the back pressure regulator before each experiment, the compressor output pressure could be increased by a few psig before blow-down instead of a few atmospheres. A smaller pressure drop across the system during blow-down would reduce the volumetric flow rate of nitrogen through the system and reduce the mass of salt eroded from the hot finger as the nitrogen-solution interface cleared the salt layer-solution interface. The pressure drop across the system must, however, remain sufficiently large for the time required for blow-down to be a small fraction of total run time because it is virtually impossible to model the deposition process during blow-down.

The next logical step in improving the theoretical model for predicting the deposition rate is to account for mass transfer inside the porous salt layer formed on the hot finger. Before doing so, the morphology of the salt layer as a function of time should be analyzed experimentally. This could be nicely accomplished at the expense of the top portion of a few hot fingers by the following procedure. Run sodium sulfate deposition experiments for 3, 6, 9, and 12 minutes, say, at identical operating conditions following the experimental procedure given in Chapter 2. After removing each hot finger from the system immerse the protruding portion of it in a polymer to preserve/harden the structure of the porous salt layer. Then, using a fly cutter, say, machine off the top (axial) half of the protruding portion of the hot finger. Next, photograph to the required resolution the morphology of the annulus of salt remaining on each hot finger. Inspection of these photographs to determine the morphology of the porous salt layer may prove very fruitful. First, a length scale for natural convection inside the pores within the salt layer could be determined. Once this length scale is established, it may be used to determine whether heat transfer through the salt layer is purely by conduction or natural convection and conduction are both important. From the same photographs, porosity

363

as a function of radial position, azimuthal position and time could be quantified. Comparing the photographs from the four different experiments, one could easily determine if the salt layer was, in fact, densifying with time and place the importance of mass transfer inside the porous salt layer in far better context. It would also be interesting to determine if porosity reached some limiting values as the aqueous salt solution near the surface of the hot finger gradually changed to (essentially) pure water. Finally, to properly model mass transfer inside the porous salt layer it is critical to quantify the surface area available for deposition there.

Bibliography

[1] M. Abramowitz and I.A. Stegun, editors. *Handbook of Mathematical Functions with Formula, Graphs, and Mathematical Tables.* Dover, 1972.

[2] K.S. Ahluwalia, M.F. Young, B.L. Haroldsen, B.E. Mills, M.C. Stoddard, and C.D. Robinson. Testing and application of a transpiring wall platelet reactor for supercritical water oxidation of harzardous wastes. In *Briefing Book from* 1^{rst} *Int. Workshop on SCWO*, Jacksonville, Florida, February 1995.

[3] A. Anderko and K.S. Pitzer. Equation of state representation of phase-equilibria and volumetric properties of the system nacl-h$_2$o above 573 k. *Geochimica et Cosmochimica Acta*, 57:1657,1680, 1993.

[4] F.J. Armellini. *Phase Equilibria and Precipitation Phenomena of Sodium Chloride and Sodium Sulfate in Sub- and Supercritical Water.* PhD thesis, MIT, 1993.

[5] ASTM. *1992 Annual Book of ASTM Standards*, volume 14.03. ASTM (American Society for Testing and Materials), Philadelphia, 1992.

[6] Z. Balenovic, M.N. Myers, and J.C. Giddings. Binary diffusion in dense gases to 1300 atm by the chromatographic peak-broadening method. *J. Chem. Phys.*, 52:915,922, 1970.

[7] H.E. Barner, C.Y. Huang, T. Johnson, G. Jacobs, M.A¿ Martch, and W.R. Killilea. Supercritical water oxidation: An emerging technology. *Journal of Hazardous Materials*, 31:1,17, 1992.

[8] K.D. Bartle, J.L. Carroll, A.A. Clifford, and L. Smith. Measurement of the diffusion coefficient of benzene in liquid and supercritical water. to be published, 1994.

[9] A. Bejan, editor. *Convection Heat Transfer*. John Wiley and Sons, 1 edition, 1984. see pages 323.

[10] V.A. Benrath, F. Gjedebo, B. Schiffers, and H. Wunderlich. Über die löslichkeit von salzen and salzgemischen in wasser bei temperaturen oberhalb von 100° 1. *Z. Anorg. All. Chemie*, 231:285,297, 1937.

[11] J.A. Bettinger and W.R. Killilea. Development and demonstration of supercritical water oxidation. In *Federal Environmental Restoration Conference*, May 26 1993.

[12] R. Byron Bird, W.E. Stewart, and E.N. Lightfoot. *Transport Phenomena*. John Wiley and Sons, 1960.

[13] L.D. Bond, C.C. Mills, P. Whiting, S.L. Koutz, D.A. Hazlebeek, and K.W. Downey. Method to remove inorganic scale from a supercritical water oxidation reactor, 1996. This reference is a United States Patent (Patent number 5,501,799) and the Assignees are Abitibi-Price, Inc. (Missouga, Canada) and Generat Atomics (San Diego, CA).

[14] G.E. Brodale and W.F. Giauque. The relationship of crystalline forms i, iii, iv, and v of anhydrous sodium sulfate as determined by the third law of thermodynamics. *Journal of Physical Chemistry*, 76(5):737,743, 1972.

[15] T.J. Butenhoff, M.G.E. Goemans, and S.J. Buelow. Mass diffusion coefficients and thermal diffusivity in concentrated hydrothermal nano3 solutions. *J. Phys. Chem.*, 100:5982, 1996.

[16] J.P.C. Chan, C.A. LaJeunesse, and S.F. Rice. Experimental techniques to determine salt formation and deposition in supercritical water oxidation reactors. In *ASME Proceedings of the 29th National Heat Transfer Conference: Fire, Combustion and Hazardous Wastes Processing Session*, volume HTD-296, pages 171,176. ASME, 1994.

[17] Raymond Chang. *Chemistry*. Random House, 2 edition, 1984.

[18] S. Chapman and T.G. Cowling. *The Mathematical Theory of Non-Uniform Gases*. Cambridge University Press, 3 edition, 1970.

[19] S. Chapman and T.G. Cowling. *The Mathematical Theory of Non-Uniform Gases*. Cambridge University Press, 3 edition, 1970. Thorne's generalization is discussed on P.311.

[20] A.P. Colburn. *Trans. AIChE*, 29:174, 1933.

[21] W.M. Deen. *Analysis of Transport Phenomenon*. Oxford University Press, 1997. in press.

[22] P.C. Dell'Orco, H.K. Eaton, R.T. Reynolds, and S.J. Buelow. The solubility of 1-1 electrolytes in supercritical water. Technical Report LA-UR-92-3359, Los Alamos National Laboratory, 1992.

[23] P.C. Dell'Orco, L. Li, and E.F. Gloyna. *Separation Science and Technology*, 28:625, 1993.

[24] M.M. Dipippo. *Phase Behavior of Inorganic Salts in Sub- and Supercritical Water*. PhD thesis, MIT, 1997.

[25] Economics of scwo "looking good". *Supercritical Water Oxidation (SCWO) Newsletter*, 2(2), 1997. Published by Eco Waste Technologies (EWT).

[26] R. Feist and G.M. Schneider. Determination of binary diffusion coefficients of benzene, phenol, naphthalene and caffeine in supercritical co2 between 308 and 333 k in the pressure range 80 to 160 bar with supercritical fluid chromatography (sfc). *Separation Science and Technology*, 17(1):261,270, 1982.

[27] E.U. Franck. Concentrated electrolyte solutions at high temperatures and pressures. *Journal of Solution Chemistry*, 2-3(1):339,356, 1973.

[28] J.A.N. Friend. The selenates of lanthanum and their solubilities in water. *J. Chem. Soc.*, page 1597, 1932.

[29] J.S. Gallagher. A model for the liquid, vapor and supercritical regions of aqueous solutions of na_2so_4 for temperatures from 200 to 500 °c and pressures to 1000 bar. Technical report, National Institute of Standards and Technology, 1996. This technical report was produced for the Process Measurements Division of the Chemical Science and Technology Laboratory at NIST.

[30] J.S. Gallagher and L. Haar. Nbs standard reference database 10 steam tables, 1985. This reference is a computer program produced by the Thermophysics Division of the U.S. National Bureau of Standards.

[31] B. Gebhart, Y. Jaluria, R.L. Mahajan, and B. Sammakia. *Buoyancy-Induced Flow and Transport (Reference Edition)*. Hemisphere, 1988.

[32] B. Gebhart and L. Pera. The nature of vertical natural convection flows resulting from the combined buoyancy effects effects of thermal and mass diffusion. *Int. J. Heat Mass Transfer*, 2025(14):2025, 1971.

[33] E.F. Gloyna and L. Li. Supercritical water oxidation research and development update. *Environmental Progress*, 14(3):182,192, 1995.

[34] M.G.E. Goemans, L. Li, and E.F. Gloyna. Separation of inorganic salts from supercritical water by cross-flow microfiltration. *Separation Science and Technology*, 30(7-9):1491,1509, 1995.

[35] M.G.E. Goemans, F.M. Tiller, L. Li, and E.F. Gloyna. Separation of α-alumina particles from super-critical water by cross-flow microfiltration using a sintered metal filter element. In *Briefing Book from 1^{rst} Int. Workshop on SCWO*, Jacksonville, Florida, February 1995.

[36] B.L. Haroldsen, D.Y. Ariizumi, B.E. Mills, B.G. Brown, and D. Greisen. Transpiring wall supercritical water oxidation reactor salt deposition studies. Technical Report SAND96-8255-UC-702, Sandia National Laboratories, 1996.

[37] B.L. Haroldsen, D.Y. Ariizumi, B.E. Mills, B.G. Brown, and D.C. Rousar. Transpiring wall supercritical water oxidation test reactor design report. Technical Report SAND96-8213-UC-402, Sandia National Laboratories, 1996.

[38] R. Hilpert. *Forsch. Geb. Ingenieurwes*, 4:215, 1933.

[39] J.O. Hirschfelder, C.F. Curtiss, and R.B. Bird. *Molecular Theory of Gases and Liquids*. John Wiley and Sons, Inc., 1954.

[40] M.S. Hodes, K.A. Smith, W.S. Hurst, Jr. W.J. Bowers, and P. Griffith. Measurements and modeling of deposition rates from a near supercritical aqueous sodium sulfate solution to a heated cylinder. In *ASME Proceedings of the 32nd National Heat Transfer Conference*, volume 12, pages 107,119. ASME, 1997.

[41] F.P. Incropera and D.P. DeWitt. *Fundamentals of Heat and Mass Transfer*. John Wiley and Sons, 3 edition, 1990.

[42] T. Isono. Densities, viscosities, and electrolytic conductivities of concentrated aqueous solutions of 31 solutes in the temperature range 15-55°c and empirical equations for the relative viscosity. *Rikagaku Kenkyusho Hokoku*, 61:53, 1985. Data was taken from The Handbook of Electrolyte Solutions: Part B, edited by V.M.M. Lobo and J.L. Quaresma.

[43] W.R. Killilea, G.T. Hong, K.C. Swallow, and T.B. Thomason. 1988. SAE Technical Paper Ser. No. 881038.

[44] J.D. Knudsen and D.L. Katz. *Fluid Dynamics and Heat Transfer*. McGraw-Hill, 1958.

[45] T.H. Kuehn and R.J. Goldstein. Numerical solution to the navier-stokes equations for laminar natural convection about a horizontal isothermal circular cylinder. *Int. J. Heat Mass Transfer*, 23:971,979, 1980.

[46] J. Lévêque. *Annales des mines*, 12(13):201,305 and 381, 1928.

[47] W.J. Lamb, G.A. Hoffman, and J. Jones. Self-diffusion in compressed supercritical water. *Journal of Chemical Physics*, 74(12):6875,6880, 1981.

[48] A. Lee. Effect of shape and orientation on the performance of supercritical water oxidation reactors. In *ASME Proceedings of the 32nd National Heat Transfer Conference*, volume 12, pages 99,106. ASME, 1997.

[49] E.J. LeFevre. In *Proc. 9th Int. Cong. Apppl. Mech.*, volume 4, page 168, 1956.

[50] S. Leistikow. Selection of potential corrosion resistant scwo reactor materials. In *Briefing Book from 1^{rst} Int. Workshop on SCWO*, Jacksonville, Florida, February 1995.

[51] D.R. Lide, editor. *CRC Handbook of Chemistry and Physics*. CRC Press, 74 edition, 1993.

[52] J.H. Lienhard. On the commonality of equations for natural convection from immersed bodies. *Int. J. Heat Mass Transfer*, 16:2121, 1973.

[53] J.H. Lienhard. *A Heat Transfer Textbook*. Prentice Hall, 1987.

[54] W.F. Linke, editor. *Solubilities of Inorganic and Metal-Organic Compounds: A Compilation of Solubility Data from the Periodic Literature*. D. Van Nostrand Company, Inc., 1958. Originally edited by Atherton Seidell.

[55] V.M.M. Lobo and J.L. Quaresma, editors. *Handbook of Electrolyte Solutions*. Elsevier, 1989.

[56] W.L. Marshall and E.U. Franck. Ion product of water substance, 0-1000 °c, 1-10000 bars new international formulation and its background. *J. Phys. Chem. Ref. Data*, 10(2):295,304, 1981.

[57] W.L. Marshall, J.S. Gill, and C.H. Secoy. Phase equilibria of uranium trioxide and aqueous hydrofluoric acid in stochiometric concentrations. *Journal of the American Chemical Society*, page 4279, 1954.

[58] W.H. McAdams. *Heat Transmission*. McGraw-Hill, 3 edition, 1954.

[59] T.G. McGuinness. Developments in transpiring-wall scwo reactor technology. In *Briefing Book from 1^{rst} Int. Workshop on SCWO*, Jacksonville, Florida, February 1995.

[60] J.H. Merkin. Free convection boundary layers on cylinders of elliptic cross section. *ASME Journal of Heat Transfer*, 99:453,457, 1977.

[61] A.F. Mills. *Heat Transfer*. Irwin, 1992.

[62] L. Monchick and E.A. Mason. *J. Chem. Phys.*, 35:1676, 1961.

[63] M.J. Moran and H.N. Shapiro. *Fundamentals of Engineering Thermodynamics*. John Wiley, 1 edition, 1988.

[64] V.T. Morgan. The overall convective heat transfer from smooth circular cylinders. In T.F. Irvine and J.P. Hartnett, editors, *Advances In Heat Transfer*, volume 11, pages 199–264. Academic Press, New York, 1975.

[65] G. Némethy and H.A. Scheraga. *Journal of Chemical Physics*, 36:3383, 1962.

[66] B.P. Nikolskii, editor. *Spravochnik Khimika (Reference Book for Chemists)*, volume 3. Khimiya Press, Moscow, Leningrad, 1965.

[67] C.H. Oh, R.J. Kochan, and J.M. Beller. Numerical analysis and data comparison of a supercritical water oxidation reactor. *AIChE Journal*, 43(6):1627,1636, June 1997.

[68] S. Ostrach. Technical Report 1111, NACA, 1953.

[69] R.T. Pabalan and K.S. Pitzer. Heat capacity and other thermodynamic properties of na$_2$so$_4$(aq) in hydrothermal solutions and the solubilities of sodium sulfate minerals in the system na-cl-so$_4$-oh-h$_2$o to 300 °c. *Geochimica et Cosmochimica Acta*, 52:2393,2404, 1988.

[70] P.G. Papavergos and A.B. Hedley. Particle deposition behaviour from turbulent flows. *Chem. Eng. Res. Des.*, 62:275,295, sep 1984.

[71] S.P. Parker, editor. *McGraw-Hill Dictionary of Physics*. McGraw-Hill, 2 edition, 1997.

[72] B.D. Phenix. *Hydrothermal Oxidation of Simple Organic Compounds*. PhD thesis, MIT, 1998.

[73] R.W. Potter and D.L. Brown. The volumetric properties of aqueous sodium chloride solutions from 0 to 500 °c at pressures up to 2000 bars based on a regression of available data in the literature. Technical Report 1421-C, US Geological Survey Bulletin, 1976.

[74] W.H. Press, S.A. Teukolsky, W.T. Vetterling, and B.P. Flannery. *Numerical Recipes in Fortran 77: The Art of Scientific Computing*. Cambridge University Press, 2 edition, 1992.

[75] A.S. Quist and W.L. Marshall. Electrical conductances of aqueous sodium chloride solutions from 0 to 800°c and at pressures to 4000 bars. *Journal of Physical Chemistry*, 72(2):684,703, 1968.

[76] M.I. Ravich and F.E. Borovaya. Phase equilibria in the sodium sulfate-water system at high temperatures and pressures. *Russian J. Inorg. Chem.*, 9(4):520,532, 1964.

[77] Jr. R.N. McBrayer, J.G. Swan, and J.S Barber. Method and apparatus for reacting oxidizable matter with particles, 1996. This reference is a United States Patent (Patent number 5,620,606) and the Assignee is RPC Waste Management Services Inc. (Austin, TX).

[78] R.W. Shaw, T.B. Brill, A.A. Clifford, C.A. Eckert, and E.U. Franck. Supercritical water a medium for chemistry. *C&EN*, pages 26,39, December 1991.

[79] D.M. Shvedov and P.R. Tremaine. The solubility of aqueous sodium sulphate and the reduction of sulphate by magnetite under near-critical conditions. In *Proceedings of the 5th International Symposium on Hydrothermal Reactions*, Gatlinburg, Tennessee, jul 1993.

[80] K.A. Smith, P. Griffith, J.G. Harris, H.J. Herzog, J.B. Howard, R. Latanison, W.A. Peters, and J.W. Tester. Supercritical water oxidation: Principles and prospects. In *International Water Conference*, Pittsburgh, PA, 1995. Paper #49.

[81] E.M. Sparrow, W.J. Minkowycz, and E.R.G. Eckert. Transpiration-induced buoyancy and thermal diffusion-diffusion thermo in a helium-air free convection boundary layer. *ASME Journal of Heat Transfer*, pages 508,514, 1964.

[82] P.D. Spohn and T.B. Brill. Raman spectroscopy of the species in concentrated aqueous solutions of $zn(no_3)_2$,$ca(no_3)_2$,$cd(no_3)_2$,$lino_3$ and $nano_3$ up to 450 °c and 30 mpa. *J. Phys. Chem.*, 93:6224, 1989.

[83] H. Stephen and T. Stephen, editors. *Solubilities of Inorganic and Organic Compounds: Volume 1-Binary Systems*. Macmillan, 1963.

[84] H.S. Swenson, J.R. Carver, and C.R. Kakarala. Heat transfer to supercritical water in smooth-bore tubes. *Journal of Heat Transfer*, pages 477,484, November 1965.

[85] P. Teshima. Fouling rates from a sodium sulphate-water solution in supercritical water oxidation reactors. Master's thesis, University of British Columbia, 1997.

[86] P. Teshima, S. Rogak, D. Frase, E. Hauptmann, S. Gairns, and J. Lota. Fouling of supercritical water oxidation reactors. In *Air and Waste Management Association's 90th Annual Meeting and Exhibition*, number 97-A230, Toronto, Ontario, Canada, June 1997.

[87] J.W. Tester, H.R. Holgate, F.J. Armellini, P.A. Webley, W.T. Killilea, G.T. Hong, and H.E. Barner. Supercritical water oxidation technology: A review of process development and fundamental research. In *Emerging Technologies for Hazardous Waste Management (1991 ACS Symposium Series)*. ACS, 1992.

[88] Y.S. Touloukian, R.W. Powell, C.Y. Ho, and P.G. Klemens, editors. *Thermophysical Properties of Matter Volume 2: Thermal Conductivity of Nonmetallic Solids*. IFI/Plenum, 1970.

[89] V.G. Tsvetkov and I.B. Rabinovich. *ZhFKh*, 43(5):1213,1217, 1969.

[90] M. Uematsu and E.U. Franck. Static dielectric constant of water and steam. *J. Phys. Chem. Ref. Data*, 9(4):1291,1306, 1980.

[91] P.A. Webley, J.W. Tester, and H. Richard Holgate. Oxidation kinetics of ammonia and ammonia-methanol mixtures in supercritical water in the temperature range 530-700 °c at 246 bar. *Ind. Eng. Chem. Res.*, 30(8):1745,1754, 1991.

[92] E. Wilhelm. On the temperature dependence of the effective hard sphere diameter. *J. Chem. Phys.*, 58:3558, 1973.

[93] V.I. Zarembo and L.V. Puchkov, editors. *Obzory po teplofizicheskim svoistvam veschestv (Reviews on Thermophysical Properties of Substances*. USSR Academy of Sciences, Moscow, 1981.

[94] I.D. Zaytsev and G.G. Aseyev, editors. *Properties of Aqueous Solutions of Electrolytes*. CRC Press, 1992. Book was translated by M.A. Lazarev and V.A. Sorochenko and the heat of solution data was referenced to a different Russian publication [66].